

RECENT ADVANCES in BIOMEDICAL & CHEMICAL ENGINEERING and MATERIALS SCIENCE

**Proceedings of the 2014 International Conference on Chemical
Engineering and Materials Science (CEMS '14)**

**Proceedings of the 2014 International Conference on Biology and
Biomedical Engineering (BBE '14)**

**Venice, Italy
March 15-17, 2014**

RECENT ADVANCES in BIOMEDICAL & CHEMICAL ENGINEERING and MATERIALS SCIENCE

**Proceedings of the 2014 International Conference on Chemical
Engineering and Materials Science (CEMS '14)
Proceedings of the 2014 International Conference on Biology and
Biomedical Engineering (BBE '14)**

**Venice, Italy
March 15-17, 2014**

Copyright © 2014, by the editors

All the copyright of the present book belongs to the editors. All rights reserved. No part of this publication may be reproduced, stored in a retrieval system, or transmitted in any form or by any means, electronic, mechanical, photocopying, recording, or otherwise, without the prior written permission of the editors.

All papers of the present volume were peer reviewed by no less than two independent reviewers. Acceptance was granted when both reviewers' recommendations were positive.

ISBN: 978-1-61804-223-1

RECENT ADVANCES in BIOMEDICAL & CHEMICAL ENGINEERING and MATERIALS SCIENCE

**Proceedings of the 2014 International Conference on Chemical
Engineering and Materials Science (CEMS '14)**

**Proceedings of the 2014 International Conference on Biology and
Biomedical Engineering (BBE '14)**

**Venice, Italy
March 15-17, 2014**

Organizing Committee

General Chairs (EDITORS)

- Prof. Manijeh Razeghi
Walter P. Murphy Professor
Director, Center for Quantum Devices
Department of Electrical Engineering and Computer Science
- Prof. Jun Zhang, Deputy Director
College of Chemistry and Chemical Engineering
Inner Mongolia University, Hohhot 010021, P. R. China
- Prof. Samuel Lofland, Rowan University,
Glassboro, New Jersey, USA
- Prof. Emanuel E. Strehler, Ph.D.
Professor of Biochemistry and Molecular Biology
Mayo Clinic College of Medicine
Rochester, MN 55905, USA
- Prof. George Perry, Ph.D.
Dean and Professor
Semmes Foundation Endowed Chair in Neurobiology
College of Sciences
The University of Texas at San Antonio
- Prof. John Gordon Lindsay,
(Professor of Medical Biochemistry)
University of Glasgow,
Glasgow, UK
- Prof. Photios A. Anninos
Professor Emeritus
Democritus University of Thrace.
Alexandroupolis, Greece

Senior Program Chair

- Prof. Ashutosh Tiwari
Biosensors and Bioelectronics Centre
IFM-Linköpings Universitet
581 83 Linköping, Sweden
- Dr Sukhvinder Badwal, FTSE, FAIE
Chief Research Scientist
CSIRO Energy Technology
Private Bag 33, Clayton South 3169
Victoria, Australia
- Prof. Peter Dieter,
Faculty of Medicine
'Carl Gustav Carus',
Dresden, Germany

Program Chairs

- Prof. Paul H. Holloway
Distinguished Professor Emeritus
- Ellis D. Verink Jr. Professor Emeritus
Dept. of Materials Science and Engineering,
Gale Lemerand Drive
University of Florida Gainesville FL, USA
- Prof. Vesselin Dimitrov
Department of Silicate Technology
University of Chemical Technology and Metallurgy,
8 Kl. Ohridski Blvd., Sofia 1756,
Bulgaria
- Dr. Stefano Bellucci,
Frascati National Laboratory (LNF)
National Institute of Nuclear Physics (INFN)
Via Enrico Fermi, 40 - 00044 Frascati (RM), Italy
- Prof. Andrei Korobeinikov,
Centre de Recerca Matematica,
Barcelona, Spain
- Prof. Florin Gorunescu,
University of Medicine and
Pharmacy of Craiova, Craiova, Romania
- Prof. Ivana Horova, Masaryk
University, Czech Republic

Tutorials Chair

- Prof. Takeshi Fukuda
Saitama University
Sakura-ku, Saitama 338-8570, Japan
- Prof. Charles A. Long
Professor Emeritus
University of Wisconsin
Stevens Point, Wisconsin, USA

Special Session Chair

- Prof. Byron Gates
Canada Research Chair in Surface Chemistry
Department of Chemistry
Simon Fraser University
8888 University Drive
Burnaby, B.C. V5A 1S6
Canada
- Prof. Seong Ihl Woo,
Korea Advanced Institute of Science
and Technology,
Korea
- Prof. Wolfgang Wenzel,
Institute for Nanotechnology,
Germany

Workshops Chair

- Prof. David N. Seidman
Walter P. Murphy Professor
Northwestern University
Evanston, IL 60208-3108, USA
- Prof. Anita H. Corbett,
Emory University School of Medicine,
Atlanta, GA, USA

Local Organizing Chair

- Assistant Prof. Klimis Ntalianis,
Tech. Educ. Inst. of Athens (TEI), Athens, Greece
- Prof. Photios A. Anninos
Professor Emeritus
Democritus University of Thrace.
Alexandroupolis, Greece

Publication Chair

- Prof. Jim P. Zheng
Florida A&M University and
Florida State University
Aero-Propulsion,
Mechatronics and Energy (AME) Center
Center for Advanced Power Systems (CAPS)
Florida State University, USA
- Prof. Tuan Pham,
James Cook University,
Townsville, Australia

Publicity Committee

- Prof. Victor Mosquera Tallon
Universidade de Santiago de Compostela
Santiago de Compostela, Galicia,
Spain
- Prof. Myriam Lazard
Institut Supérieur d'Ingenierie de la Conception
Saint Die, France
- Prof. Gertz I. Likhtenshtein,
Ben-Gurion University of the Negev, Israel

International Liaisons

- Prof. Marie-Paule Pileni
Distinguish Professor University P&M Curie,
UPMC.
Member of Institut Universitaire de France
France
- Prof. Tadaaki Nagao
Group Leader, National
Institute for Materials Science
Tsukuba, Ibaraki, Japan
- Prof. Vincenzo Niola
Departement of Mechanical Engineering for Energetics
University of Naples "Federico II"
Naples, Italy
- Prof. Eduardo Mario Dias
Electrical Energy and Automation
Engineering Department
Escola Politecnica da Universidade de Sao Paulo
Brazil
- Prof. Ka-Lok Ng
Department of Bioinformatics
Asia University
Taichung, Taiwan
- Prof. Olga Martin
Applied Sciences Faculty
Politehnica University of Bucharest
Romania

Steering Committee

- Prof. Aida Bulucea, University of Craiova, Romania
- Prof. Zoran Bojkovic, Univ. of Belgrade, Serbia
- Prof. Metin Demiralp, Istanbul Technical University, Turkey
- Prof. Imre Rudas, Obuda University, Budapest, Hungary

Program Committee

Prof. Gang-Yu Liu, University of California, Davis Campus, CA, USA
Prof. Zhibing Zhang, University of Birmingham, Birmingham, UK
Prof. Jean-Francois Gohy, Université catholique de Louvain, Belgium
Prof. Waler Caseri, ETH, Zurich, Switzerland
Prof. Jacques Desbrieres, Universite De Pau Et Des Pays De L'Adour, France
Prof. Adrian Schumpe, Technical University of Braunschweig, Germany
Prof. Chris Bowen, University of Bath, Bath, UK
Prof. Jerzy Baldyga, Technical Univeristy Warszawska, Poland
Prof. Alirio Rodrigues, University of Porto, Portugal
Prof. Mostafa Barigou, University of Birmingham, Birmingham, UK
Prof. Jaime Wisniak, Ben-Gurion University of the Negev, Beer-Sheva, Israel
Prof. Sohail Murad, University of Illinois at Chicago, USA
Prof. Konstantinos E. Kakosimos, Texas A&M University at Qatar, Doha, Qatar
Prof. Raghunath V. Chaudhari, University of Kansas, USA
Prof. Xijun Hu, The Hong Kong University of Science and Technology, Kowloon, Hong Kong
Prof. Deepak Kunzru, Indian Institute of Technology, Kanpur, India

Prof. Amit Bandyopadhyay, AAAS Fellow , ASM International Fellow , AIMBE Fellow and ACerS Fellow, Washington State University, Pullman, State of Washington, USA

Prof. Yong Ding, Georgia Institute of Technology, Atlanta, GA, USA

Prof. Yulin Deng, Georgia Institute of Technology, Atlanta, GA, USA

Prof. Paul H. Holloway, Distinguished Prof., University of Florida, Gainesville FL, USA

Prof. Saad Khan, North Carolina State University, Raleigh, North Carolina, USA

Prof. Manijeh Razeghi, Northwestern University, Evanston, IL, USA

Prof. Igor Sevostianov, New Mexico State University, Las Cruces, New Mexico, USA

Prof. Mohindar S. Seehra, West Virginia University, Morgantown, West Virginia, USA

Prof. Tao Liu, Florida State University, Tallahassee, Florida, USA

Prof. Daniel Guay, Institut National de la Recherche Scientifique (INRS), Universite du Quebec, Quebec, Canada

Prof. Tian Tang, University of Alberta, Edmonton, Alberta, Canada

Prof. Roland Frankenberger, University of Marburg, Marburg, Germany

Prof. Mohamedally Kurmoo, Universite de Strasbourg, Strasbourg, France

Prof. C. C. Sorrell, University of New South Wales, Sydney, NSW, Australia

Prof. Concepcion Lopez, Universitat de Barcelona, Barcelona, Spain

Prof. Alan Dalton, University of Surrey, Guildford, Surrey, UK

Prof. Kourosh Kalantar-Zadeh, RMIT University, Melbourne, Australia

Prof. Constantinos Tsitsilianis, University of Patras, Patras, Greece

Prof. Tetsu Yonezawa, Hokkaido University, Kita Ward, Sapporo, Hokkaido Prefecture, Japan

Prof. Daolun Chen, Ryerson University, Toronto, Ontario, Canada

Prof. Mohamed M. Chehimi, Universite Paris Diderot, Paris, France

Prof. Vincenzo Fiorentini, Universita degli studi di Cagliari, Cagliari, Italy

Prof. Tamas Ungar, Eotvos Lorand University (ELTE), Budapest, Hungary

Prof. Anthony W. Coleman, Universite Claude Bernard Lyon 1, Lyon, France

Prof. Albert Chin, IEEE Fellow, OSA Fellow, National Chiao Tung University, Hsinchu, Taiwan

Prof. Artur Cavaco-Paulo, Universidade do Minho, Braga, Portugal

Prof. Yoshihiro Tomita, Kobe University, Kobe, Japan

Prof. Jian Wang, Los Alamos National Laboratory, Los Alamos, NM, USA

Prof. Byung K. Kim, Pusan National University, Busan, South Korea

Prof. John T. Sheridan, University College Dublin, Belfield, Dublin, Ireland

Prof. Chi-Wai Chow, National Chiao Tung University, Hsinchu, Taiwan

Prof. Christian M. Julien, Universite Paris-6, Paris, France

Prof. Chun-Hway Hsueh, National Taiwan University, Taipei, Taiwan

Prof. Hyung-Ho Park, Yonsei University, Seodaemun-gu, Seoul, Korea

Prof. Victor M. Castano, Universidad Nacional Autonoma de Mexico, Mexico City, Mexico

Prof. Peter Chang, University of Saskatchewan, Saskatoon, Saskatchewan, Canada

Prof. Dean-Mo Liu, National Chiao Tung University, HsinChu, Taiwan

Prof. Rui Vilar, Instituto Superior Tecnico, Lisboa, Portugal

Prof. Hugh J. Byrne, Dublin Institute of Technology, Dublin, Ireland

Prof. Won-Chun Oh, Hanseo University, Seosan-si, Chungcheongnam-do, South Korea

Prof. Yuanhua Lin, Tsinghua University, Haidian, Beijing, China

Prof. S.C. Tjong, City University of Hong Kong, Sham Shui Po District, New Kowloon, Hong Kong

Prof. Huan-Tsung Chang, National Taiwan University, Taipei City, Taiwan

Prof. Yoshitake Masuda, National Institute of Advanced Industrial Science and Technology (AIST), Tokyo, Japan

Prof. Jing Zhang, Donghua University, Shanghai, China

Prof. Veronica Cortes de Zea Bermudez, Universidade de Tras-os-Montes e Alto Douro, Vila Real, Portugal

Prof. Jun Zhang, Inner Mongolia University, Hohhot, Inner Mongolia, China

Prof. Israel Felner, Hebrew University of Jerusalem, Jerusalem, Israel

Prof. Sukhvinder Badwal, CSIRO Energy Technology, Australia

Prof. Te-Hua Fang, National Kaohsiung University of Applied Sciences (KUAS), Kaohsiung, Taiwan

Prof. Belkheir Hammouti, Mohammed Premier University, Oujda, Morocco

Prof. Mohd Sapuan Salit, Universiti Putra Malaysia, Selangor, Malaysia
Prof. Kwansoo Chung, Seoul National University, Seoul, South Korea
Prof. Zhongfang Chen, University of Puerto Rico, San Juan, Puerto Rico
Prof. Soon-Ku Hong, Chungnam National University, Daejeon, South Korea
Prof. Hannes Jonsson, University of Iceland, Reykjavik, Iceland
Prof. Byron Gates, Simon Fraser University, 8888 University Drive, Burnaby, B.C., Canada
Prof. Culea Eugen, Technical University of Cluj-Napoca, Cluj-Napoca, Romania
Prof. Vesselin Dimitrov, University of Chemical Technology and Metallurgy, Sofia, Bulgaria
Prof. Shadpour Mallakpour, Isfahan University of Technology, Isfahan, Iran
Dr. Stergios Pispas, National Hellenic Research Foundation (NHRF), Athens, Greece
Dr. Anna Lukowiak, Polish Academy of Science, Wroclaw, Poland
Dr. Dimitris Tsiourvas, NCSR "Demokritos", IAMPPNM, Dept. of Physical Chemistry, 15310 Aghia Paraskevi, Attiki, Greece.
Prof. Peter Dieter, Faculty of Medicine 'Carl Gustav Carus', Dresden, Germany
Prof. Andrei Korobeinikov, Centre de Recerca Matematica, Barcelona, Spain
Prof. Florin Gorunescu, University of Medicine and Pharmacy of Craiova, Craiova, Romania
Prof. Wolfgang Wenzel, Institute for Nanotechnology, Germany
Prof. Seiji Shibasaki, Hyogo University of Health Sciences, Japan
Prof. Gary A. Lorigan, Miami University, USA
Prof. Ziad Fajloun, Universite Libanaise, Lebanon
Prof. Nikolai N. Modyanov, University of Toledo, USA
Prof. Dhavendra Kumar, University of South Wales, UK
Prof. Geoffrey Arden, European Vision Institute, UK
Prof. Photios Anninos, Democritus University of Thrace, Alexandroupolis, Greece
Prof. Charles A. Long, Prof. Emeritus, University of Wisconsin, Stevens Point, Wisconsin, USA.
Prof. Tuan Pham, James Cook University, Townsville, Australia
Prof. W. Lakin, University of Vermont, USA
Prof. Lucio Tommaso De Paolis, University of Salento, Italy
Prof. Jean-Michel Jault, Institut de Biologie Structurale, France
Prof. Hassane Oudadesse, University of Rennes 1, France
Prof. Anita H. Corbett, Emory University School of Medicine, Atlanta, GA, USA
Prof. Toshiharu Horie, Teikyo Heisei University, Japan
Prof. Vadim V. Sumbayev, University of Kent, UK
Prof. Andre Surguchov, University of Kansas Medical Center, Kansas City, USA
Prof. Rona R. Ramsay, University of St Andrews, North Haugh, St Andrews, UK
Prof. Daniel Martins-de-Souza, University of Cambridge, UK
Prof. Roberta Chiaraluce, Sapienza Universita di Roma, Roma, Italy
Prof. George Perry, The University of Texas at San Antonio, USA
Prof. Gertz I. Likhtenshtein, Ben-Gurion University of the Negev, Israel
Prof. Vivo Turk, Jozef Stefan Institute, Slovenia
Prof. Makoto Komiyama, University of Tsukuba, Japan
Prof. Shunsuke Meshitsuka, Tottori University, Japan
Prof. Jean-Michel Jault, Institut de Biologie Structurale, Jean-Pierre Ebel, France
Prof. Ziad Fajloun, Ecole Doctorale des Sciences et Technologie, Universite Libanaise Tripoli, Libya

Additional Reviewers

Angel F. Tenorio	Universidad Pablo de Olavide, Spain
Ole Christian Boe	Norwegian Military Academy, Norway
Abelha Antonio	Universidade do Minho, Portugal
Xiang Bai	Huazhong University of Science and Technology, China
Genqi Xu	Tianjin University, China
Moran Wang	Tsinghua University, China
Minhui Yan	Shanghai Maritime University, China
Jon Burley	Michigan State University, MI, USA
Shinji Osada	Gifu University School of Medicine, Japan
Bazil Taha Ahmed	Universidad Autonoma de Madrid, Spain
Konstantin Volkov	Kingston University London, UK
Tetsuya Shimamura	Saitama University, Japan
George Barreto	Pontificia Universidad Javeriana, Colombia
Tetsuya Yoshida	Hokkaido University, Japan
Deolinda Rasteiro	Coimbra Institute of Engineering, Portugal
Matthias Buyle	Artesis Hogeschool Antwerpen, Belgium
Dmitrijs Serdjuks	Riga Technical University, Latvia
Kei Eguchi	Fukuoka Institute of Technology, Japan
Imre Rudas	Obuda University, Budapest, Hungary
Francesco Rotondo	Polytechnic of Bari University, Italy
Valeri Mladenov	Technical University of Sofia, Bulgaria
Andrey Dmitriev	Russian Academy of Sciences, Russia
James Vance	The University of Virginia's College at Wise, VA, USA
Masaji Tanaka	Okayama University of Science, Japan
Sorinel Oprisan	College of Charleston, CA, USA
Hessam Ghasemnejad	Kingston University London, UK
Santoso Wibowo	CQ University, Australia
M. Javed Khan	Tuskegee University, AL, USA
Manoj K. Jha	Morgan State University in Baltimore, USA
Miguel Carriegos	Universidad de Leon, Spain
Philippe Dondon	Institut polytechnique de Bordeaux, France
Kazuhiko Natori	Toho University, Japan
Jose Flores	The University of South Dakota, SD, USA
Takuya Yamano	Kanagawa University, Japan
Frederic Kuznik	National Institute of Applied Sciences, Lyon, France
Lesley Farmer	California State University Long Beach, CA, USA
João Bastos	Instituto Superior de Engenharia do Porto, Portugal
Zhong-Jie Han	Tianjin University, China
Francesco Zirilli	Sapienza Universita di Roma, Italy
Yamagishi Hiromitsu	Ehime University, Japan
Eleazar Jimenez Serrano	Kyushu University, Japan
Alejandro Fuentes-Penna	Universidad Autónoma del Estado de Hidalgo, Mexico
José Carlos Metrôlho	Instituto Politecnico de Castelo Branco, Portugal
Stavros Ponis	National Technical University of Athens, Greece

Table of Contents

Keynote Lecture 1: On the Distinguished Role of the Mittag-Leffler and Wright Functions in Fractional Calculus	17
<i>Francesco Mainardi</i>	
Keynote Lecture 2: Latest Advances in Neuroinformatics and Fuzzy Systems	18
<i>Yingxu Wang</i>	
Keynote Lecture 3: Recent Advances and Future Trends on Atomic Engineering of III-V Semiconductor for Quantum Devices from Deep UV (200nm) up to THz (300 microns)	20
<i>Manijeh Razeghi</i>	
Quasi-Quantum Model of the Nerve Fiber Formation	23
<i>Marcin Molski</i>	
Density of States and Electrical Resistivity in Epitaxial Graphene at Low Temperatures	27
<i>N. Melnikova, N. Bobenko, V. Egorushkin, A. Ponomarev</i>	
Optical Response of a Strongly Driven Asymmetric Quantum Dot Molecule	30
<i>Spyridon G. Kosionis, John Boviatsis, Emmanuel Paspalakis</i>	
Integration of Modified K-Means Clustering and Morphological Operations for Multi-Organ Segmentation in CT Liver-Images	34
<i>Walita Narkbuakaew, Hiroshi Nagahashi, Kota Aoki, Yoshiki Kubota</i>	
A Theoretical Study of an Electronic Structure of the Infinite and Finite-Length Carbon Nanotubes	40
<i>A. V. Tuchin, A. A. Ganin, D. A. Zhukalin, L. A. Bityutskaya, E. N. Bormontov</i>	
Design of a Training System for Intrapedicular Screw Positioning in the Lumbar Region	47
<i>Nataly A. Garcia, Daniel Lorias, Vicente Gonzalez, Fernando Chico</i>	
Dose Profile Variation with Pitch in Head CT Scans Using Gafchromic Films	51
<i>Mourão A. P., Gonçalves Jr. R. G., Alonso T. C.</i>	
Cell Nuclei Classification in HE-stained Biopsy Images	55
<i>C. Atupelage, H. Nagahashi, M. Yamaguchi, F. Kimura, T. Abe, A. Hashiguchi, M. Sakamoto</i>	
Intelligent Classification of Middle Cognitive Impairment and Alzheimer's Disease Using Heterogeneous Information Source Features	61
<i>O. Valenzuela, F. Ortuño, G. Ruiz-García, F. Estrella, I. Rojas</i>	
Testing for Non-Linearity in Spontaneous Pupil Signal of Health Subjects: Preliminary Approach Based on Non-Stationary Surrogate Data Methods	67
<i>W. Nowak, A. Hachol, M. Misiuk-Hojlo</i>	

A New Approach for Selective Optical Fiber Sensors Based on Localized Surface Plasmon Resonance of Gold Nanostars in Molecularly Imprinted Polymer	71
<i>Maria Pesavento, Nunzio Cennamo, Alice Donà, Piersandro Pallavicini, Girolamo D'Agostino, Luigi Zeni</i>	
Structural Determinant for Helicobacter pylori Resistance to Sulfonamides	76
<i>Anna Roujeinikova</i>	
Charge Properties and Fractal Aggregation of Carbon Nanotubes	79
<i>Dmitry A. Zhukalin, Andrey V. Tuchin, Sviatoslav V. Avilov, Larisa A. Bityutskaya, Evgeniy N. Bormontov</i>	
Implementation of Smart Ovulation Detection Device	82
<i>Hazem M. Eissa, Amr M. Ahmed, Ehab A. Elsehely</i>	
Proposal for a Gastrointestinal Simulator System with Anatomical Location and Emulator Mechanism of an Endoscope	87
<i>Efren Moncisvalles, Daniel Lorias, Arturo Minor, Jesus Villalobos</i>	
Electronic Structure of Two Isomers of Fluorine Derivatives of Single-Walled Carbon Nanotubes of C₂F Stoichiometry within the Density Functional Theory	92
<i>Alexander A. Ganin, Larissa A. Bityutskaya, Evgeniy N. Bormontov</i>	
Dynamic Behavior of Polymer at High Strain Rate	97
<i>Khelif M., Bradai C., Masmoudi N.</i>	
Binding Sites of the miR-1273 Family, miR-1285-3p and miR-5684 in Human mRNAs	102
<i>Anatoly T. Ivashchenko, Olga A. Berillo, Anna Y. Pyrkova, Raigul Y. Niyazova</i>	
Composite Ceramics Based on Nanostructured Refractory Oxide Whiskers	108
<i>T. M. Ulyanova, P. A. Vitiaz, N. P. Krutko, L. V. Ovseenko, A. A. Shevchonok, L. V. Titova, A. R. Luchenok</i>	
Metal Mixed Oxides and Zeolites in Oxidation of Ethanol and Isopropanol	113
<i>Jana Gaálová, Květuše Jirátová, Jan Klempa, Olga Šolcová, Irene Maupin, Jérôme Mijoin, Patrick Magnoux, Jacques Barbier Jr.</i>	
A Vibrational Stark Effect In The Fullerene C₆₀	121
<i>Andrey V. Tuchin, Larisa A. Bityutskaya, Eugene N. Bormontov</i>	
A Bench Scale Study on the Enrichment of Saudi Phosphate Rock Used for H₃PO₄ Production	125
<i>Yasir Arafat, T. F. Al-Fariss, Muhammad Awais Naeem</i>	

Assessment of Orthopedic Device Associated with Carbonated Hydroxyapatite on the Metabolic Response in Liver Tissue	130
<i>Samira Jebahi, Hassane Oudadesse, Zoubeir Ellouz, Tarek Rebai, Hafedh El Feki, Hassib Keskes, Abdelfatteh Elfeki</i>	
The Performance of SnO₂/CdS/CdTe Type Solar Cell under Influence of CdS Buffer Layer Thickness and Series Resistance RS	134
<i>H. Tassoult, A. Bouloufa</i>	
Fabrication, Sealing and Hydrophilic Modification of Microchannels by Hot Embossing on PMMA Substrate	138
<i>Alireza Shamsi, Saeed Delaram, Mehrnaz Esfandiari, Hasan Hajghassem</i>	
The Arrangements of the Locations of miR-619, miR-5095, miR-5096 and miR-5585 Binding Sites in the Human mRNAs	144
<i>Anatoly T. Ivashchenko, Olga A. Berillo, Anna Y. Pyrkova, Raigul Y. Niyazova, Shara A. Atambayeva</i>	
Process Hazard Management System (PROHAMS) Based on PSM	150
<i>A. M. Shariff, H. A. Aziz, K. H. Yew</i>	
Predicted Formation and Deposition of Slag from Lignite Combustion on Pulverized Coal Boilers	155
<i>Pakamon Pintana, Nakorn Tippayawong</i>	
Real Time IVUS Segmentation and Plaque Characterization by Combining Morphological Snakes and Contourlet Transform	160
<i>Mohamed Ali Hamdi, Karim Saheb Etabaa, Mohamed Lamine Harabi</i>	
Preliminary Proteomic Analysis and Biological Characterization of the Crude Venom of Montivipera bornmuelleri; A Viper from Lebanon	167
<i>Accary C., Hraoui-Bloquet S., Hamze M., Sadek R., Hleihel W, Desfontis J.-C., Fajloun Z.</i>	
A Computational Model of the Modulation of Basal Ganglia Function by Dopamine Receptors	174
<i>Mohammad Reza Mohagheghi-Nejad, Fariba Bahrami, Mahyar Janahmadi</i>	
GSM Based Artificial Pacemaker Monitoring System	179
<i>Santhosh Ganesh, Lavanya Jagannathan, Sasikala Thirugnanasambandam, Mahesh Veezhinathan</i>	
Effect of Genetic Lines and Season on Body Weights of Chicks	184
<i>Hani N. Hermiz, Kamarn A. Abas, Aram M. Ahmed, Tahir R. Al-Khatib, Shayma M. Amin, Dastan A. Hamad</i>	
On the Optimization of Non-Dense Metabolic Networks in Non-Equilibrium State Utilizing 2D-Lattice Simulation	188
<i>Erfan Khaji</i>	

Antibacterial Study of Copper Oxide Nanoparticles synthesized by Microemulsion Technique	197
<i>Harish Kumar, Renu Rani</i>	
Authors Index	202

Keynote Lecture 1

On the Distinguished Role of the Mittag-Leffler and Wright Functions in Fractional Calculus



Professor Francesco Mainardi

Department of Physics, University of Bologna, and INFN
Via Irnerio 46, I-40126 Bologna, Italy
E-mail: francesco.mainardi@bo.infn.it

Abstract: Fractional calculus, in allowing integrals and derivatives of any positive real order (the term "fractional" is kept only for historical reasons), can be considered a branch of mathematical analysis which deals with integro-differential equations where the integrals are of convolution type and exhibit (weakly singular) kernels of power-law type. As a matter of fact fractional calculus can be considered a laboratory for special functions and integral transforms. Indeed many problems dealt with fractional calculus can be solved by using Laplace and Fourier transforms and lead to analytical solutions expressed in terms of transcendental functions of Mittag-Leffler and Wright type. In this plenary lecture we discuss some interesting problems in order to single out the role of these functions. The problems include anomalous relaxation and diffusion and also intermediate phenomena.

Brief Biography of the Speaker: For a full biography, list of references on author's papers and books see:

Home Page: <http://www.fracalmo.org/mainardi/index.htm>

and <http://scholar.google.com/citations?user=UYxWyEEAAAJ&hl=en&oi=ao>

Keynote Lecture 2

Latest Advances in Neuroinformatics and Fuzzy Systems



Yingxu Wang, PhD, Prof., PEng, FWIF, FICIC, SMIEEE, SMACM

President, International Institute of Cognitive Informatics and Cognitive Computing (ICIC)

Director, Laboratory for Cognitive Informatics and Cognitive Computing

Dept. of Electrical and Computer Engineering

Schulich School of Engineering

University of Calgary

2500 University Drive NW,

Calgary, Alberta, Canada T2N 1N4

E-mail: yingxu@ucalgary.ca

Abstract: Investigations into the neurophysiological foundations of neural networks in neuroinformatics [Wang, 2013] have led to a set of rigorous mathematical models of neurons and neural networks in the brain using contemporary denotational mathematics [Wang, 2008, 2012]. A theory of neuroinformatics is recently developed for explaining the roles of neurons in internal information representation, transmission, and manipulation [Wang & Fariello, 2012]. The formal neural models reveal the differences of structures and functions of the association, sensory and motor neurons. The pulse frequency modulation (PFM) theory of neural networks [Wang & Fariello, 2012] is established for rigorously analyzing the neurosignal systems in complex neural networks. It is noteworthy that the Hopfield model of artificial neural networks [Hopfield, 1982] is merely a prototype closer to the sensory neurons, though the majority of human neurons are association neurons that function significantly different as the sensory neurons. It is found that neural networks can be formally modeled and manipulated by the neural circuit theory [Wang, 2013]. Based on it, the basic structures of neural networks such as the serial, convergence, divergence, parallel, feedback circuits can be rigorously analyzed. Complex neural clusters for memory and internal knowledge representation can be deduced by compositions of the basic structures.

Fuzzy inferences and fuzzy semantics for human and machine reasoning in fuzzy systems [Zadeh, 1965, 2008], cognitive computers [Wang, 2009, 2012], and cognitive robots [Wang, 2010] are a frontier of cognitive informatics and computational intelligence. Fuzzy inference is rigorously modeled in inference algebra [Wang, 2011], which recognizes that humans and fuzzy cognitive systems are not reasoning on the basis of probability of causations rather than formal algebraic rules. Therefore, a set of fundamental fuzzy operators, such as those of fuzzy causality as well as fuzzy deductive, inductive, abductive, and analogy rules, is formally elicited. Fuzzy semantics is quantitatively modeled in semantic algebra [Wang, 2013], which formalizes the qualitative semantics of natural languages in the categories of nouns, verbs, and modifiers (adjectives and adverbs). Fuzzy semantics formalizes nouns by concept algebra [Wang, 2010],

verbs by behavioral process algebra [Wang, 2002, 2007], and modifiers by fuzzy semantic algebra [Wang, 2013]. A wide range of applications of fuzzy inference, fuzzy semantics, neuroinformatics, and denotational mathematics have been implemented in cognitive computing, computational intelligence, fuzzy systems, cognitive robotics, neural networks, neurocomputing, cognitive learning systems, and artificial intelligence.

Brief Biography of the Speaker: Yingxu Wang is professor of cognitive informatics and denotational mathematics, President of International Institute of Cognitive Informatics and Cognitive Computing (ICIC, <http://www.ucalgary.ca/icic/>) at the University of Calgary. He is a Fellow of ICIC, a Fellow of WIF (UK), a P.Eng of Canada, and a Senior Member of IEEE and ACM. He received a PhD in software engineering from the Nottingham Trent University, UK, and a BSc in Electrical Engineering from Shanghai Tiedao University. He was a visiting professor on sabbatical leaves at Oxford University (1995), Stanford University (2008), University of California, Berkeley (2008), and MIT (2012), respectively. He is the founder and steering committee chair of the annual IEEE International Conference on Cognitive Informatics and Cognitive Computing (ICCI*CC) since 2002. He is founding Editor-in-Chief of International Journal of Cognitive Informatics and Natural Intelligence (IJCINI), founding Editor-in-Chief of International Journal of Software Science and Computational Intelligence (IJSSCI), Associate Editor of IEEE Trans. on SMC (Systems), and Editor-in-Chief of Journal of Advanced Mathematics and Applications (JAMA). Dr. Wang is the initiator of a few cutting-edge research fields or subject areas such as denotational mathematics, cognitive informatics, abstract intelligence (AI), cognitive computing, software science, and basic studies in cognitive linguistics. He has published over 160 peer reviewed journal papers, 230+ peer reviewed conference papers, and 25 books in denotational mathematics, cognitive informatics, cognitive computing, software science, and computational intelligence. He is the recipient of dozens international awards on academic leadership, outstanding contributions, best papers, and teaching in the last three decades.

<http://www.ucalgary.ca/icic/>

<http://scholar.google.ca/citations?user=gRVQjskAAAAJ&hl=en>

 Editor-in-Chief, International Journal of Cognitive Informatics and Natural Intelligence
 Editor-in-Chief, International Journal of Software Science and Computational Intelligence
 Associate Editor, IEEE Transactions on System, Man, and Cybernetics - Systems
 Editor-in-Chief, Journal of Advanced Mathematics and Applications
 Chair, The Steering Committee of IEEE ICCI*CC Conference Series

Keynote Lecture 3

Recent Advances and Future Trends on Atomic Engineering of III-V Semiconductor for Quantum Devices from Deep UV (200nm) up to THz (300 microns)



Professor Manijeh Razeghi

Center for Quantum Devices

Department of Electrical Engineering and Computer Science

Northwestern University

Evanston, Illinois 60208

USA

E-mail: razeghi@eecs.northwestern.edu

Abstract: Nature offers us different kinds of atoms, but it takes human intelligence to put them together in an elegant way in order to realize functional structures not found in nature. The so-called III-V semiconductors are made of atoms from columns III (B, Al, Ga, In, Tl) and columns V (N, As, P, Sb, Bi) of the periodic table, and constitute a particularly rich variety of compounds with many useful optical and electronic properties. Guided by highly accurate simulations of the electronic structure, modern semiconductor optoelectronic devices are literally made atom by atom using advanced growth technology such as Molecular Beam Epitaxy (MBE) and Metal Organic Chemical Vapor Deposition (MOCVD). Recent breakthroughs have brought quantum engineering to an unprecedented level, creating light detectors and emitters over an extremely wide spectral range from 0.2 μm to 300 μm . Nitrogen serves as the best column V element for the short wavelength side of the electromagnetic spectrum, where we have demonstrated III-nitride light emitting diodes and photo detectors in the deep ultraviolet to visible wavelengths. In the infrared, III-V compounds using phosphorus, arsenic and antimony from column V, and indium, gallium, aluminum, and thallium from column III elements can create interband and intrasubband lasers and detectors based on quantum-dot (QD) or type-II superlattice (T2SL). These are fast becoming the choice of technology in crucial applications such as environmental monitoring and space exploration. Last but not the least, on the far-infrared end of the electromagnetic spectrum, also known as the terahertz (THz) region, III-V semiconductors offer a unique solution of generating THz waves in a compact device at room temperature. Continued effort is being devoted to all of the above mentioned areas with the intention to develop smart technologies that meet the current challenges in environment, health, security, and energy. This talk will highlight my contributions to the world of III-V semiconductor Nano scale optoelectronics. Devices from deep UV-to THz.

Brief Biography of the Speaker: Manijeh Razeghi received the Doctorat d'État es Sciences Physiques from the Université de Paris, France, in 1980.

After heading the Exploratory Materials Lab at Thomson-CSF (France), she joined Northwestern University, Evanston, IL, as a Walter P. Murphy Professor and Director of the Center for

Quantum Devices in Fall 1991, where she created the undergraduate and graduate program in solid-state engineering. She is one of the leading scientists in the field of semiconductor science and technology, pioneering in the development and implementation of major modern epitaxial techniques such as MOCVD, VPE, gas MBE, and MOMBE for the growth of entire compositional ranges of III-V compound semiconductors. She is on the editorial board of many journals such as *Journal of Nanotechnology*, and *Journal of Nanoscience and Nanotechnology*, an Associate Editor of *Opto-Electronics Review*. She is on the International Advisory Board for the Polish Committee of Science, and is an Adjunct Professor at the College of Optical Sciences of the University of Arizona, Tucson, AZ. She has authored or co-authored more than 1000 papers, more than 30 book chapters, and fifteen books, including the textbooks *Technology of Quantum Devices* (Springer Science+Business Media, Inc., New York, NY U.S.A. 2010) and *Fundamentals of Solid State Engineering*, 3rd Edition (Springer Science+Business Media, Inc., New York, NY U.S.A. 2009). Two of her books, *MOCVD Challenge Vol. 1* (IOP Publishing Ltd., Bristol, U.K., 1989) and *MOCVD Challenge Vol. 2* (IOP Publishing Ltd., Bristol, U.K., 1995), discuss some of her pioneering work in InP-GaInAsP and GaAs-GaInAsP based systems. The *MOCVD Challenge*, 2nd Edition (Taylor & Francis/CRC Press, 2010) represents the combined updated version of Volumes 1 and 2. She holds 50 U.S. patents and has given more than 1000 invited and plenary talks. Her current research interest is in nanoscale optoelectronic quantum devices.

Dr. Razeghi is a Fellow of MRS, IOP, IEEE, APS, SPIE, OSA, Fellow and Life Member of Society of Women Engineers (SWE), Fellow of the International Engineering Consortium (IEC), and a member of the Electrochemical Society, ACS, AAAS, and the French Academy of Sciences and Technology. She received the IBM Europe Science and Technology Prize in 1987, the Achievement Award from the SWE in 1995, the R.F. Bunshah Award in 2004, and many best paper awards.

Quasi-quantum model of the nerve fiber formation

Marcin Molski

Abstract — The second-order Gompertz kinetics is employed in analysis of the axon diameter spectrum of the olfactory nerve of garfish *Lepisosteus osseus* and optic nerve of horse *Thoroughbred*, buffalo *Bos bubalis*, monkey *Macaca fascicularis* and C57BL strain mice. It is proved that the cumulative distribution of axons is a quasi-quantum phenomenon described by the Gompertz function, which is solution of the quantum eigenvalue equation for the Morse oscillator endowed with anharmonicity constant equal to one. The diameter at which the Morse potential attains a minimum precisely reproduces the experimental mean diameter of the nerve fibers. The calculations are performed for nonmyelinated and myelinated axons and then are extended to the myelin sheath, whose mean thickness is also reproducible in the approach proposed.

I. Keywords — Gompertz kinetics, fiber diameter, spectrum cumulative distribution, Morse potential, coherent states, quasi-quantum phenomena.

II. INTRODUCTION

The spatiotemporal first-order Gompertz kinetics is a powerful and descriptive tool for neurosciences researches ranging from cognitive to molecular levels. A cumulative distribution of axon diameter in the nerve, conditioning-testing response of excitable nerve, time-course of synaptic current or conductance of membrane during voltage clamp of squid axons and fractal dimension of the synapse formation are examples supporting this thesis [1]-[4]. The basic equations governing those processes can be specified in the form [1]

$$\frac{dG(q)}{dq} = \pm f(q)G(q) \quad \frac{df(q)}{dq} = -af(q) \quad (1)$$

Here, the sign + characterizes the decelerated exponential growth, whereas the sign – the decelerated exponential decay ($a > 0$). In the above equations $q=r$ for space-dependent processes, e.g. size distribution, or $q=t$ for time-course processes, e.g. synaptic or axon currents. For the Gompertzian systems the function $f(q)$ takes the form ($b > 0$)

$$f(q) = b \exp(-aq) \quad (2)$$

hence, the first of equations (1) provides the Gompertz [1] function of growth (+) or decay (-)

$$G(q) = G_\infty \exp\left[\mp \frac{b}{a} \exp(-aq)\right] \quad (3)$$

$$G_\infty = G(q = \infty) = G_0 \exp\left(\pm \frac{b}{a}\right)$$

In the above formulae a is retardation constant, whereas b the initial growth or regression rate constant; $G_0 = G(q=0)$ stands for the initial characteristics of the system, for instance the initial mass, volume, diameter, voltage, electric current or number of entities under consideration; G_∞ denotes the limiting value of the Gompertz function for $q = \infty$.

Recent investigations in the field revealed that the Gompertzian growth can be described also in terms of the second-order Gompertzian kinetics [6] Differentiating the first of equations (1) for the growth case, with respect to q -coordinate one gets

$$-\frac{d^2G(q)}{dq^2} + \left(\frac{a^2}{4}\right) \{1 - \exp[-a(q - q_e)]\}^2 G(q) = \frac{a^2}{4} G(q) \quad (4)$$

in which

$$q_e = \frac{1}{a} \ln\left(\frac{2b}{a}\right) \quad (5)$$

denotes the point at which the second term appearing in (4) attains a minimum equal to zero (equilibrium point). The point q_e differs from the inflection point q_i defined for the Gompertzian systems as follows

$$\left[\frac{d^2G(q)}{dq^2}\right]_{q=q_i} = 0 \quad q_i = \frac{1}{a} \ln\left(\frac{b}{a}\right) \quad (6)$$

The differential equation (4) has the standard eigenvalue form (see Appendix) in which the second term represents the q -dependent Morse potential [7]

$$V(q) = D_e \{1 - \exp[-a(q - q_e)]\}^2 \quad (7)$$

widely used to describe vibrations in anharmonic oscillators characterized by the dissociation energy D_e , range parameter a and equilibrium distance q_e . The form of Eq. (4) indicates that

the Gompertzian systems behave like a space- or time-dependent oscillators, whose spatial organization or temporal pattern formation is influenced by the Morse potential [6].

Eq. (4) can be specified in the dimensionless form [6]

$$-\frac{1}{2} \frac{d^2 G(\tau)}{d\tau^2} + D \left\{ 1 - \exp[-\sqrt{2}\tau] \right\}^2 G(\tau) = DG(\tau) \quad (8)$$

in which

$$\tau = a(q - q_e) / \sqrt{2}, \quad D = 1/4 \quad (9)$$

$$G(\tau) = G_\infty \exp[-(1/2) \exp(-\sqrt{2}\tau)]$$

The plots of the Gompertz function $G(\tau)$, Morse potential $V(\tau) = D \{ 1 - \exp[-2^{1/2}\tau] \}^2$ equilibrium $\tau_e = 0$ and inflection $\tau_i = -\ln(2)2^{-1/2}$ points are presented in Figure 1.

Recently, Easton [1] demonstrated that cumulative distribution of axon diameter in the olfactory nerve of garfish is described by the sigmoidal (S-shaped) curve, which is very well reproduced by the spatial Gompertz function of growth (3). Since this function is the solution of the second-order differential Eq. (4), the spatial distribution (spectrum) of the axon diameter in the nerve should be strictly connected with the Morse potential characteristics (a , q_e). The main objective of the present work is to determine the Morse function (7) from the axon diameter spectrum in the olfactory and optic nerve of the representative group of species. In particular it is shown that the mean size of the nerve fibres not only in olfactory but also in optic nerve can be precisely determined as it is equal to the equilibrium point q_e of the Morse potential (7). The calculations are extended to include the mean value of the axon myelin sheath thickness, which is also reproducible in the approach proposed. The results obtained reveal that the axon membrane is endowed with mechanical properties well characterized by the Morse model of anharmonic oscillator in the dissociation state.

III. MATERIALS AND METHOD

In the test calculations, we used the space-dependent Gompertz function of growth to describe the cumulative distribution of fibres in the olfactory nerve of garfish *Lepisosteus osseus*, which is an easily accessible source of numerous, long and homogenous nonmyelinated axons [3]. The calculations performed by Easton [1] provided the function

$$G(q) = G_\infty \exp[-k \exp(-aq)] \quad (10)$$

in which $k = b/a = 250$, $a = 25 \mu\text{m}^{-1}$, q denotes the diameter of a fibre, whereas $G_\infty = 1577$ is the total population of fibres in the nerve. Since, the standard errors of the fitted parameters were not specified by Easton [1], we repeated calculations employing the experimental data published by Easton [3]. They provided the values of the Gompertzian parameters $a = 25.1750(3485) \mu\text{m}^{-1}$ and $b = 5698.7(531.0) \mu\text{m}^{-1}$, which

satisfactorily reproduce the value of the dimensionless Easton's parameter $k = 226(21)$. Employing the above specified values of the Gompertzian parameters and Eq. (5) one may calculate the equilibrium point q_e for the Morse potential (7) and the associated standard errors propagating from the errors Δa and Δb of the parameters fitted, according to the formula

$$\Delta q_e(a, b) = \sqrt{\left[\left(\frac{dq_e}{da} \right)^2 \Delta a^2 + \left(\frac{dq_e}{db} \right)^2 \Delta b^2 \right]} \quad (11)$$

The similar calculations have been performed also for the axon distribution in the optic nerve of horse *Thoroughbred* [9], buffalo *Bos bubalis* [10] and monkey *Macaca fascicularis* [11], C57BL strain mice, and then they are extended to the myelin sheath thickness in the optic nerve of buffalo [10]. To this aim the following procedure has been applied:

1. The published data reporting: (i) frequency histograms of myelinated and nonmyelinated axon diameters and (ii) frequency histogram of myelin sheath thickness are converted to the data representing the cumulative distribution of the pertinent quantities in the space.
2. The data from point (1) has been fitted to the Gompertz growth function (3) using nonlinear least square routine.
3. The Gompertzian parameters a and b obtained in the point 2. have been employed to calculate the equilibrium diameter q_e and its standard error according to Eqs. (5) and (9).

The results of calculations are presented in Table 1. The point 1. indicates that one may apply also an alternative procedure: direct fit to the frequency spectrum, reproduced by the first derivative of the Gompertz function (3) [1]

$$F(q) = G_0 b \exp\left\{ \frac{b}{a} [1 - \exp(-aq)] \right\} \exp(-aq) \quad (12)$$

In this case, however, we have to fit not only a and b parameters but also G_0 which has no biological meaning as zero-diameter axons do not exist. In consequence the fitted values of a and b parameters differ significantly on those obtained from the Gompertz function (3), which contains the well-defined parameter G_∞ .

IV. RESULTS AND DISCUSSION

Inspection of the Table 1 reveals that the experimental mean axon diameter obtained for olfactory nerve of garfish and optic nerve of buffalo, horse, monkey and mice are equal within the quoted standard errors with those theoretically estimated in the approach proposed. It is interesting to note that the accuracy of the calculations by taking advantage of Eq. (8), is about one order of magnitude better than the precision of experimental estimations. The only one exception is the mean axon diameter in mice. Hence, the method is not only simple but also

accurate. It requires only experimental fibre diameter spectrum (Bell shaped) in the nerve, which is transformed to the cumulative distribution (S-shaped) reproduced by the Gompertz function (3). Its parameters and the associated standard errors are evaluated for the data under consideration with the nonlinear regression coefficient $R > 0.99$. It indicates the high reliability of the calculations performed by taking advantage of the Sigma Plot 2001 vs 7.0 software. Having determined the Gompertzian parameters one may calculate the equilibrium distance (5) for the Morse potential (7), and its standard error propagating from the errors of the parameters fitted according to Eq. (10).

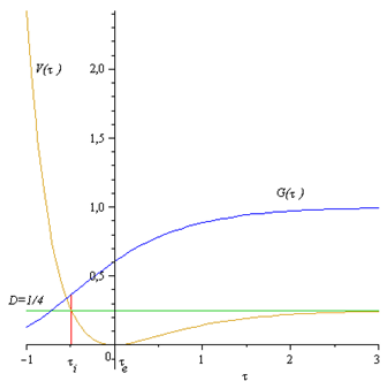


FIGURE I. Plots of the dimensionless Gompertz function $G(\tau) = G_{\infty} \exp[-(1/2)\exp(-21/2\tau)]$ representing cumulative distribution ($G_{\infty}=1$), the Morse potential $V(\tau) = D\{1 - \exp[-21/2\tau]\}^2$, the eigenvalue equal to the dissociation energy $D=1/4$ of the system, inflection and equilibrium points $\tau_e=0$ and $\tau_i = -\ln(2)2-1/2$.

Analysing the optic nerve fibres histogram obtained for monkey by Sanches et al. [11] one may distinguish three peaks at $0.55 \mu\text{m}$, $0.85 \mu\text{m}$ and $1.55 \mu\text{m}$. According to Sanches et al. [11], they correspond to the three groups of cells and associated functions: (i) γ -cells (W-cells) which have the smallest cell body and axon diameter, hence the slowest axonal conduction velocity, (ii) β -cells (X-cells), whose dimension and axon diameter are larger than γ -cells but still near the mean size for ganglion cells, and (iii) α -cells (Y-cells), which are the largest in size and whose axons are fastest in conduction and their responses are more transient. It is interesting to note that the equilibrium point for the Morse potential $q_e = 0.836(25)$ agrees very well (in the range of the standard errors) with the peak observed at the diameter equal to $0.85(5) \mu\text{m}$. On the other hand, the inflection point and its associated standard error calculated from the Eqs. (6) and (11) take the values $q_i = 0.612(22)$, which conform acceptably with the peak observed at $0.55(5) \mu\text{m}$ by Sanches et al. [11]. Those results indicate a possible connection between the function-structure characteristics of the axon and the inflection (6) and equilibrium (5) positions of the Gompertz and Morse functions. We conclude that, the equilibrium point q_e characterizes the diameter at which the β -cells and associated axons are formed. Hence, q_e may be applied to estimate the dimension of β -cells and connected with them axons, at least in the optic nerve of monkey. On the other hand q_i characterizes

the dimension connected with the γ -cells.

V. CONCLUSIONS

To summarize, a few important results have been obtained in this work. First, the space-dependent second-order Gompertz kinetics has been introduced. It permits interpretation of the distribution of entities in the space in terms of anharmonic Morse oscillator. Hence, the Gompertz cumulative distribution of fibres in the nerve can be related to the Morse potential. Secondly, it has been proved that the mean fibre diameter in olfactory and optic nerves can be precisely determined using the analytic expression for the equilibrium point of the Morse potential connected with the parameters of the Gompertz cumulative distribution function. The method permits estimation of the mean diameter of fibres and axons with the precision better than that achieved on the basis of experimental data and the method proposed links parameters q_i and q_e with the functional characteristics of the optic nerve. Thirdly, the nerve fibre formation

TABLE I. The values of the Morse equilibrium point q_e calculated from the Gompertzian parameters a , b and the mean values $\langle d \rangle$ of the diameter of fibres, axons and fiber myelin sheath thickness for the nerve of buffaloes *Bos bubalis*. The results of calculations for the mean fibre diameter of the olfactory nerve of garfish *Lepisosteus osseus* and optic nerve of horse and monkey are also presented. Parameters a , b and q_e are given in $[\mu\text{m}^{-1}]$; their standard errors are presented in parentheses in the unit of the last quoted digits of the parameters fitted and calculated.

G_{∞}	a	b	q_e	$\langle d \rangle$	Animal
Ref.	MYELINATED AXON DIAMETER				
100 [13]	4.6581(2030)	33.0953(4.79)	0.570(46)	0.62(2)	Mice
5774 [9]	0.9426(180)	5.5610(3353)	2.62(10)	2.56(1.45)	Horse
650 [10]	0.6646(129)	11.3916(9260)	5.32(18)	5.6(2.0)	Buffalo
219541 [11]	3.0994(490)	20.666(1.068)	0.836(25)	0.80(9)	Monkey
NONMYELINATED AXON DIAMETER					
1577 [3]	25.1750(3485)	5698.7(531.0)	0.243(5)	0.24(5)	Garfish
6224 [10]	0.9021(104)	6.1893(2343)	2.90(06)	3.3(1.5)	Buffalo
AXON MYELIN SHEATH THICKNESS					
815 [10]	6.0266(5019)	148.33(54.71)	0.64(9)	0.6(2)	Buffalo

APPENDIX

To explain the connection between the second-order Gompertzian kinetics and eigenvalue formalism let's consider the quantal (microscopic) equation for a particle of a rest mass m_0 vibrating in the field of the Morse potential [7]

$$-\frac{1}{2} \frac{\hbar^2}{m_0} \frac{d^2 G(q)}{dq^2} + D_e \{1 - \exp[-aq]\}^2 G(q) = EG(q)$$

This equation for $q=r$ is the Schrödinger equation, whereas for

$q=r$ it represents the so-called Feinberg-Horodecki equation [12]. For $q=r$ its first term is interpreted as the kinetic energy, the second one as the potential Morse energy, whereas E is the total energy of the system. This equation can be specified in the standard eigenvalue form

$$\hat{H}G(q) = [\hat{T} + V(q)]G(q) = EG(q)$$

in which \hat{T} is the kinetic energy operator, \hat{H} stands for the Hamilton's operator, whereas $G(q)$ is its eigenfunction. Employing the dimensionless coordinate $\tau = (m_0\omega_e/\hbar)^{1/2}r$, in which $\omega_e = a(2D_e/m_0)^{1/2}$ is the vibrational frequency, one may transform the starting equation to the form

$$-\frac{1}{2} \frac{d^2G(\tau)}{d\tau^2} + \left(\frac{1}{4x_e}\right) \left\{1 - \exp[-\sqrt{2x_e}\tau]\right\}^2 G(\tau) = \left(\frac{E}{\hbar\omega_e}\right) G(\tau)$$

in which $x_e = \omega_e\hbar/(4D_e)$ is the so-called anharmonicity constant. As has been proved by Morse [7], the eigenvalue E takes only discrete values (is quantized) according to the vibrational quantum number ν

$$E = \hbar\omega_e \left[\left(\nu + \frac{1}{2}\right) - x_e \left(\nu + \frac{1}{2}\right)^2 \right] \quad \nu = 0, 1, 2, \dots$$

It is easy to verify that for the anharmonicity constant $x_e=1$ and $\nu=0$ (ground state) the original eigenvalue equation converts to the macroscopic Eq.(8)

$$-\frac{1}{2} \frac{d^2G(\tau)}{d\tau^2} + \left(\frac{1}{4}\right) \left\{1 - \exp[-\sqrt{2}\tau]\right\}^2 G(\tau) = \left(\frac{1}{4}\right) G(\tau)$$

equivalent to Eq.(4), which represents the second-order Gompertzian kinetics. The above specified equation reveals that for equilibrium position $\tau_e = 0$ the Morse oscillator reaches the minimum value of the potential energy equal to zero and maximum value of the kinetic energy equal to the dissociation energy $D=1/4$ of the system. As this equation does not contain the Planck's constant and is the special case of the quantum equation for $x_e=1$, it belongs to the class of the quasi-quantum equations, hence the formation of the nerve fibre can be viewed as a quasi-quantum phenomenon.

REFERENCES

- [1] Easton D. M. (2005). Gompertzian growth and decay: A powerful descriptive tool for neuroscience. *Phys Behav* 86: pp. 407-414.
- [2] Easton D. M. (1978). Exponentiated exponential model (Gompertz kinetics) of Na⁺ and K⁺ conductance changes in squid giant axon. *Biophys J* 22: 15-28.
- [3] Easton D. M. (1971). Garfish olfactory nerve: Easily accessible source of numerous long, homogenous, nonmyelinated axons. *Science* 172: pp. 952-955.
- [4] Molski M, Konarski J. (2006). Neuronal differentiation and synapse formation in the space-time with temporal fractal dimension. *Synapse* 60: pp. 567-572.
- [5] Gompertz B. (1825). On the nature of the function expressive of the law of human mortality, and on a new mode of determining the value of life contingencies. *Phil Trans Roy Soc London*. 115: pp. 513-585.
- [6] Molski M, Konarski J. (2003). Coherent states of Gompertzian growth. *Phys Rev E* 68: pp. 021916(1-7).
- [7] Morse P. M. (1929). Diatomic molecules according to the wave mechanics. II. Vibrational levels. *Phys Rev* 34: pp. 57-64
- [8] Brandt S. (1997). "Computational Methods in Data Analysis". 3rd ed. New York, Springer Verlag p. 71 (Polish Edition).
- [9] Guo X, Aoyama M, Sugita S. (2001). Quantitative analysis of the optic nerve of the horse (Thoroughbred). *J Vet Med Sci* 63: pp. 971-975.
- [10] Kassab A, Aoyama M, Sugita S. (2002). Quantitative study of the optic nerve in buffaloes (*Bos bubalis*). *Animal Sci J* 73: pp. 59-65.
- [11] Sanchez R M, Dunkelberg G R, Quigley H A. (1986). The number and diameter distribution of axons in the monkey optic nerve. *Invest Ophthalmol Visual Sci* 27: pp. 1342-1350.
- [12] Molski M. (2006). Space-like coherent states of time-dependent Morse oscillator. *Eur. Phys J E* 40: pp. 411-416.
- [13] Dangata Y.Y. Kaufman M.H. (1997). Morphometric analysis of the postnatal mouse optic nerve following prenatal exposure to alcohol. *J Anat.* 191: PP. 49-56.

Density of states and electrical resistivity in epitaxial graphene at low temperatures

N. Melnikova, N. Bobenko, V. Egorushkin and A. Ponomarev

Abstract—The low-temperature electrical resistivity of epitaxial graphene is investigated in the frame of the temperature Green functions method developed for carbon nanosystems. The calculations of contribution to resistivity is carried out taking into account the multiple elastic scattering of electrons by impurities and structural inhomogeneities of short-range order type.

Keywords— graphene, low temperature, electronic transport properties, density of states, short-range order.

I. INTRODUCTION

IT is generally known that the low-temperature behavior of electrical resistivity and electron density of states (DOS) in non-ideal graphene strongly depends on its structure which is characterized by some distribution of impurities and structural defects of different types [1]. That is why doping and degassing may affect the temperature dependence of DOS and resistivity and even change the type of conductivity (semiconductor - metal) in graphene [2]. The aim of our investigation is to study DOS and resistivity in graphene in order to understand the influence of structure disordering on electron transport in graphene.

The low-temperature peculiarities of electrical resistivity and DOS in graphene may be investigated by the temperature Green functions (GF) method [3] which was used in [4-8] to describe the low-temperature electron transport properties and DOS in carbon nanotubes. We have calculated the contributions to DOS, resistivity and thermopower taking into account the multiple elastic scattering of electrons by impurities and structural inhomogeneities of short-range order and obtained the encouraging results which are in a good agreement with experimental data.

N. Melnikova is with the V.D. Kuznetsov Siberian Physical Technical Institute of Tomsk State University, Tomsk 634050, Russia (corresponding author to provide phone: +7-906-949-8566; e-mail: phdmelnikova@gmail.com).

N. Bobenko is with the Institute of Strength Physics and Materials Science Siberian Branch of Russian Academy of Sciences, Tomsk 634021, Russia (e-mail: nlitvin86@mail.ru).

V. Egorushkin is with the Institute of Strength Physics and Materials Science Siberian Branch of Russian Academy of Sciences, Tomsk 634021, Russia (e-mail: vall110@mail.ru).

A. Ponomarev is with the Institute of Strength Physics and Materials Science Siberian Branch of Russian Academy of Sciences, Tomsk 634021, Russia (e-mail: alex@ispms.tsc.ru)

II. DOS AND RESISTIVITY

In order to develop our approach for graphene we have to use in our calculations electronic spectrum for this system and go to 2d-dimension. To describe graphene as a system with impurities and structural inhomogeneities of short-range order type we shall consider a solid with randomly distributed defects such as catalyst impurities, retained atoms, etc. (irrespective of their origin). For simplicity, let us introduce a random field of adsorbed atoms of one sort

$$V(R) = \sum_i c(\vec{R}_i)U(\vec{R}_i - \vec{R}), \quad (1)$$

where $c(R_i)$ are the occupation numbers and U is the site potential of an electron in graphene. In the absence of long-range ordering the representation $c(R_i) = c + \delta c(R_i)$ allows us to introduce a new quantity $\langle \delta c(R_i)\delta c(R_j) \rangle$ which defines either new chemical bonds or new short-range ordering in a system with defects via fluctuations of concentration $\delta c(R_i)$ in site R_i and averaged (macro-) concentration $c = \langle c(R_i) \rangle$. The angle brackets mean averaging over a random field. The Fourier image $\langle \delta c(R_i)\delta c(R_j) \rangle \sim \langle |c_k|^2 \rangle$ determines the structure of short-range order so $\langle |c_k|^2 \rangle = \frac{c(1-c)}{N} \sum_{i=1}^N \alpha_i \cos(k \cdot R_i)$. Here α_i are the short-range order coefficients ($\alpha_0 = 1$), N is the number of atoms inside the structure inhomogeneity of the short-range order type. For all $\alpha_{i \neq 0} = 0$ and $c \rightarrow 0$, $\langle |c_k|^2 \rangle = \frac{c(1-c)}{N}$ determines the input system impurities.

To calculate single-particle properties such as electron relaxation time, let us represent the single-particle Green function in the following form:

$$G = G_0 + \sum_i G_i^{(1)} + \sum_{ij} G_{ij}^{(2)} + \dots, \quad (2)$$

where G_0 is the electron Green function in an ideal graphene and $G_i^{(1)} = c(R_i) \int G_0(\vec{r}, R)U(R - R_i)G_0(R, \vec{r}')dR$

In a p – representation after averaging over disorder we shall obtain the GF in a “dirty” graphene

$$\langle G \rangle = G_0 + G_0^2 \Sigma, \quad (3)$$

where Σ is the self-energy part which includes multiple elastic scattering of electrons on impurities and structural inhomogeneities of the short-range order type given by the following expression:

$$\begin{aligned} \Sigma(p, \varepsilon) = & -i2\pi C U_0^2 \nu_0 \text{sign} \varepsilon \left(1 - \frac{1-C}{N} \sum_{i=0}^N \alpha_i + \right. \\ & \left. + \frac{1-C}{N} \sum_{i=0}^N \alpha_i \frac{R^2 m}{\hbar^2} (\varepsilon + \varepsilon_F + i0 \text{sign} \varepsilon) \right). \end{aligned} \quad (4)$$

Here U_0 is the effective potential and $\nu_0 = \frac{m}{2\pi\hbar^2}$ is the origin DOS at the Fermi level. The first term in (4) corresponds to contribution from scattering only on impurities and two other terms correspond to electron scattering on the structural inhomogeneities of the short-range order type.

To calculate inverse relaxation time in a epitaxial graphene we have to use electronic spectrum in ideal graphene plane near ε_F : $\varepsilon = \hbar k \nu_F$, where $\nu_F \approx 10^6$ m/s [9].

The obtained expression for the relaxation time is the following:

$$\frac{1}{2\tau} = \frac{1}{2\tau_{imp}} \left[1 + \frac{1-c}{N} \sum_{i=0}^N \alpha_i B T \right]. \quad (5)$$

Here $B = \pi \frac{R^2 m}{\hbar^2} k \approx 0.1 \text{ K}^{-1}$, R is the radius of the first coordination sphere and m is electron mass. The inverse relaxation time of electron scattered only by impurities τ_{imp}^{-1} is in order of $2 \cdot 10^{15} \text{ s}^{-1}$.

The contribution to DOS in graphene is defined as follows

$$\Delta \nu = -\frac{1}{\pi} \text{Im Sp} \langle \langle G \rangle - G_0 \rangle, \quad (6)$$

where $G_0 = (\varepsilon - \varepsilon_p + i0)^{-1}$ is the electron GF in a perfect graphene, $\langle G \rangle$ is the averaged GF in a epitaxial graphene. Calculating $\langle G \rangle$ we have to take into account the multiple elastic scattering by impurities and structural defects of short-range order type.

So we have

$$\Delta \nu = \text{Im Sp} \Delta G = \frac{\hbar}{2\tau} \int \frac{p dp}{(\varepsilon - \varepsilon_p)^2 + \left(\frac{\hbar}{2\tau}\right)^2}.$$

The resulting expression for contribution to DOS in epitaxial graphene consists of two terms:

$$\begin{aligned} \Delta \nu = & \frac{1}{\hbar^2 \nu_F^2} \left[\frac{\hbar}{2\tau} \ln \left(1 + \frac{p_0 \nu_F (p_0 \nu_F - 2\varepsilon)}{\varepsilon^2 + \left(\frac{\hbar}{2\tau}\right)^2} \right) + \right. \\ & \left. + 2\varepsilon \text{arctg} \left(\frac{p_0 \nu_F \left(\frac{\hbar}{2\tau}\right)}{\left(\frac{\hbar}{2\tau}\right)^2 + (\varepsilon - p_0 \nu_F) \varepsilon} \right) \right], \end{aligned} \quad (7)$$

where p_0 is the Fermi momentum.

This expression was analyzed near the Fermi level at the fixed temperature in dependence on the sign of sum of parameters of short-range order because the latter may be changed after doping and degassing of graphene. In Figure 1A the calculated DOS in graphene is represented as a sum of two terms corresponding to electron scattering in ideal graphene and scattering on the structural inhomogeneities of the short-range order type. From this figure one may see that the contribution $\Delta \nu(\varepsilon)$ (the dash-dot line) calculated at $T=10$ K for $\sum \alpha_i = -0.6$ is negative, nonlinear and has a minimum at ε_F . In an ideal graphene DOS $\nu_0(\varepsilon)$ (the dotted line) is linear and positive. As a result the sum of these two contributions gives a gap in curve $\nu(\varepsilon)$ (the solid line) near ε_F which is in a good agreement with the data [2] represented in Figure 1B.

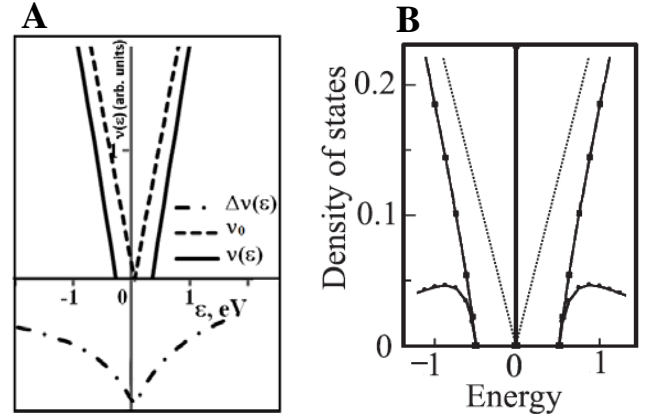


Fig. 1A. The contribution to DOS in graphene calculated at $T=10$ K for $\sum \alpha = -0.6$ (the dash-dot line), DOS in an ideal graphene $\nu_0(\varepsilon)$ (the dotted line) and the full DOS $\nu(\varepsilon) = \nu_0 + \Delta \nu$ (the solid line). Figure 1B. The data of [2] - the dotted line corresponds to DOS in ideal graphene and the solid line - to DOS in hydrogenated graphene.

Figure 2 represents contribution to DOS in graphene $\Delta \nu(\varepsilon)$ calculated at $T=1$ K, 20 K and 50 K. From this figure one may see that $\Delta \nu(\varepsilon)$ at the Fermi level increases when temperature rises if $\sum \alpha > 0$ and decreases if $\sum \alpha < 0$.

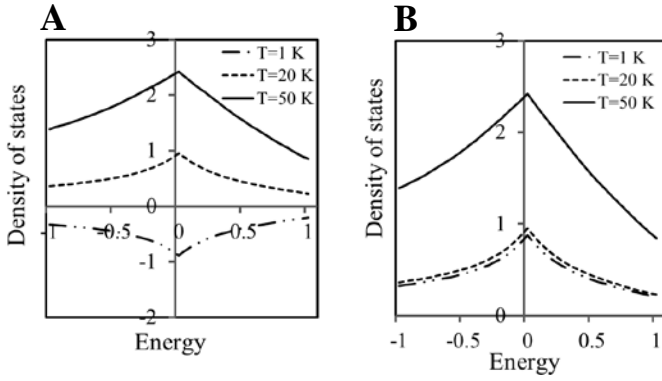


Fig. 2. Contribution to DOS $\Delta\nu(\varepsilon)$ calculated for $\Sigma\alpha = 0.2$ (A) and $\Sigma\alpha = -0.2$ (B) at $T = 1, 20, 50$ K.

Contribution to resistivity in graphene from electron scattering by impurities and structural inhomogeneities may be also calculated similar to [4-6] using electronic spectrum for graphene and 2d-dimension as it was shown above. That is why we shall give here the final expression for electrical resistivity:

$$R(T) = \frac{m}{e^2 n} \left(\frac{1}{\tau_{imp}} + 2\pi U_0^2 v_0 \frac{c(1-c)}{N} \sum_i \alpha_i B T \right), \quad (8)$$

where n is concentration of charge carriers. The calculated resistivity consists of two terms corresponding to electron scattering on impurities (the first one) and structural inhomogeneities of the short-range order type (the second one). From Equation (8) one may see that resistivity in graphene is linear on temperature and sum of parameters of short-range order and nonlinear on impurity concentration. Then R strongly depends on concentration of charge carriers n which is known to differ in the different ranges of graphene and even change the value by several orders.

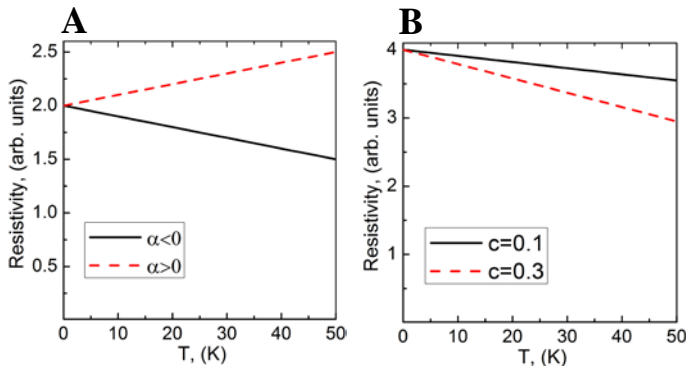


Fig. 3. Contribution to resistivity, calculated for $\alpha = -0.1$ (solid line), $\alpha = 0.1$ (dashed line) (A) and $c = 0.1$ (solid line), $c = 0.3$ (B).

Figures 4 and 5 represent the temperature dependence of the calculated resistivity at fixed impurity concentration (Fig.3, A) and fixed sum of parameters of short-range order (Fig.3, B).

III. CONCLUSIONS

The resulting expressions for the contribution to DOS (7) and electrical resistivity (8) depend on concentration of impurities and the parameters of short-range order (structural heterogeneity). Analyzing these expressions we concluded the following:

1. Gas adsorption in graphene leads to appearance of a gap in the DOS at the Fermi level, which can be explained by the negative contribution to DOS from multiple elastic electron scattering by structural inhomogeneities of short-range order.

2. Change in the defect structure of graphene results in metallization of epitaxial graphene due to the increasing contribution to DOS at the Fermi level from the electron scattering by structural inhomogeneities of short-range order. This result is in a good agreement with data [2].

3. The value of $\Delta\nu(\varepsilon_F)$ increases when temperature rises in graphene without impurities (the case of metallization) and decreases in graphene saturated gas [2, 10].

4. The sorption of gases results in the inverse temperature dependence of resistivity at low temperatures. This is in a good agreement with data [10].

5. The variation of the impurities concentration does not change the type of electrical resistivity in graphene - this is in a good agreement with data [11].

The results of our calculations showed that the low-temperature behavior of electrical resistivity and DOS is determined by the short range ordered structure of non-ideal graphene. At the same time the change in concentration of impurities does not strongly influence on the low-temperature electrical resistivity and DOS.

REFERENCES

- [1] S.Yu. Davydov, *Physics and Technics of Semiconductors*.vol. 46, no. 2, pp. 204-209, 2012.
- [2] S.Dröscher, P. Roulleau, F. Molitor, P. et all, *Appl. Phys. Lett.*, vol. 96, pp. 152104-1-152104-3, 2010.
- [3] A.A. Abrikosov, L.P. Gorkov, I.E. Dzyaloshinskii, *Methods of quantum field theory in statistical physics*. Moscow: Fizmatgiz, 1962.
- [4] V.E. Egorushkin, N.V. Melnikova, A.N. Ponomarev et al., *J. Physics: Conference Series*, vol. 248, pp. 012005, 2010.
- [5] V. Egorushkin, N. Mel'nikova, A. Ponomarev et al. *J. Mat. Sci. Eng.* vol. 1, no. 2, pp. 161-167, 2011.
- [6] V Egorushkin, N Melnikova, N Bobenko and A. Ponomarev. *Phys Sci Appl*, vol. 2, no. 7, pp. 224-232, 2012.
- [7] V.E. Egorushkin, N.V. Melnikova, A.N. Ponomarev and N.G. Bobenko, *Nanosystems*, vol. 4, no. 5, pp. 622-629, 2013.
- [8] V.E. Egorushkin, N.G. Bobenko N.V. Melnikova and A.N. Ponomarev, *Physica E*, vol. 60, pp. 11-16, 2014.
- [9] P. R. Wallace, *Phys. Rev.*, vol. 71, pp. 622-634, 1947.
- [10] Y.-W. Tan, Y. Zhang, H.L. Stormer et all. *Eur. Phys. J. Special Topics*, vol. 148, pp. 15-18, 2007.
- [11] S.V.Morosov et al., *Phys Rev Lett*, vol. 100, pp. 016602, 2008.

Optical Response of a Strongly Driven Asymmetric Quantum Dot Molecule

Spyridon G. Kosionis, John Boviatsis, and Emmanuel Paspalakis

Abstract—We study the interaction of an asymmetric double semiconductor quantum dot molecule with a weak probe field and a strong pump field. We show that the optical properties of the system are controlled by a gate voltage and the pump field. For example, we find that the application of the pump field leads to probe absorption, optical gain and the ac-Stark effect for weak tunneling rates, while for stronger tunneling rates optical gain disappears.

Keywords— Asymmetric quantum dot molecule, probe field, pump field, gate voltage, optical transparency, gain.

I. INTRODUCTION

THE nonlinear optical response of a two-level quantum system interacting with a strong pump field and a weak probe field has been the subject of several studies for many years. The subject started 40 years ago with the seminal work of Mollow [1]. He showed that depending on the frequency and intensity of the pump field the probe field can be either absorbed, enhanced or remain intact [1]. In addition, ac-Stark shift effect is found to occur in this system [1]. Furthermore, significantly enhanced nonlinear mixing processes [2], enhanced self-Kerr nonlinearity with low absorption [3] and even slow light [4] can occur in this system. In the area of semiconductor quantum dots, Xu *et al.* [5] investigated similar phenomena in a singly charged quantum dot under a strong optical driving field by probing the system with a weak optical field and found absorption, the ac-Stark effect, and optical gain. Also, Chang and Chuang [6] demonstrated that slow light can be created in the interaction of a quantum dot with a weak probe and a strong pump field due to population oscillation.

Here, we consider an asymmetric double semiconductor quantum dot molecule [7]-[9] that interacts with a weak probe field and a strong pump field. The nanostructure that is depicted in Fig. 1 consists of two quantum dots with different band structures coupled by tunneling. At nanoscale interdot

This research has been co-financed by the European Union (European Social Fund – ESF) and Greek national funds through the Operational Program "Education and Lifelong Learning" of the National Strategic Reference Framework (NSRF) - Research Funding Program: Archimedes III.

Spyridon G. Kosionis is with the Physics Department, University of Patras, Patras 265 04, Greece (e-mail: kosionis@upatras.gr).

John Boviatsis is with the Technological and Educational Institute of Western Greece, Megalou Alexandrou 1, Patras 263 34, Greece (e-mail: bovat@teipat.gr).

Emmanuel Paspalakis is with the Materials Science Department, University of Patras, Patras 265 04, Greece (corresponding author, phone: 0030-2610-969346; fax: 0030-2610-996358; e-mail: paspalak@upatras.gr).

separation the hole states are localized in the quantum dots and the electron states are rather delocalized. With the application of an electromagnetic field an electron is excited from the valence band to the conduction band of one of the quantum dots. This electron can be transferred by tunneling to the other quantum dot. The tunneling barrier can be controlled by placing a gate electrode between the two quantum dots. In this system, tunneling induced transparency and slow light have been analyzed under its interaction with a weak probe field [7]-[9]. For the theoretical analysis of the optical properties of the system under pump and probe excitation we use a density matrix approach where we assume that the pump field is strong and should be treated to all the orders, while the probe field is weak and should be treated to first order [10], [11]. We show that the optical response of the system can be controlled by the gate voltage and the pump field. For example, we find that the application of the pump field leads to probe absorption, optical gain and the ac-Stark effect for weak tunneling rates, while for stronger tunneling rates optical gain disappears.

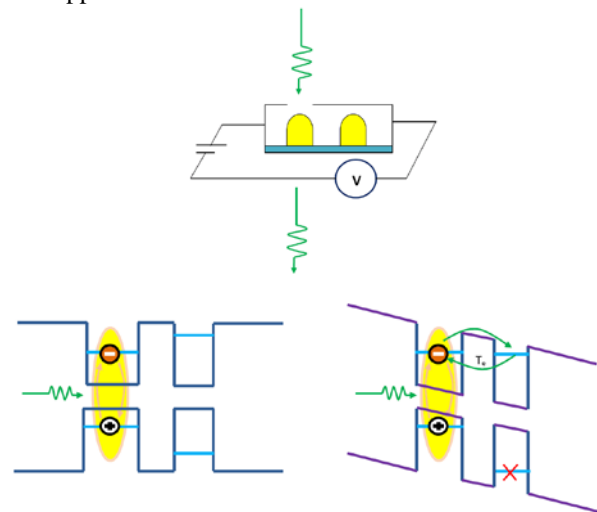


Figure 1. Upper: Schematic of the setup. An electromagnetic field drives strongly the left quantum dot. V is a bias voltage. Lower: Schematic of the band structure. On the left: without a gate voltage, electron tunneling is weak. On the right: With applied gate voltage, conduction band levels get into resonance, increasing their coupling, while valence-band levels become even more off-resonance, resulting in effective decoupling of those levels.

In the next section, we present the theoretical methodology used for the description of the interaction of the semiconductor quantum dot nanostructure with the two applied

electromagnetic fields. We use the described methodology and in section III we present basic results for the optical response of the quantum system. Our results are summarized in section IV.

II. THEORETICAL METHODOLOGY

The interaction of the quantum dot structure with the applied electromagnetic fields can be described by three quantum states [12], [13], as it is schematically shown in Fig. 2: the ground state $|0\rangle$, where the system has no excitations, the (direct) exciton state $|1\rangle$, where a pair of an electron and a hole are bound in the first quantum dot, and finally the indirect exciton state $|2\rangle$, where the hole is in the first quantum dot and the electron is in the second quantum dot.

The Hamiltonian that describes the interaction of the three-level system with the two applied fields, in the dipole and the rotating wave approximations, is given by

$$\begin{aligned}
 H = & E_0 |0\rangle\langle 0| + E_1 |1\rangle\langle 1| + E_2 |2\rangle\langle 2| \\
 & + \frac{\hbar\Omega_a}{2} \left(e^{-i\omega_a t} |1\rangle\langle 0| + e^{i\omega_a t} |0\rangle\langle 1| \right) \\
 & + \frac{\hbar\Omega_b}{2} \left(e^{-i\omega_b t} |1\rangle\langle 0| + e^{i\omega_b t} |0\rangle\langle 1| \right) \\
 & + \hbar T_e (|1\rangle\langle 2| + |2\rangle\langle 1|).
 \end{aligned} \quad (1)$$

Here, E_n is the energy of state $|n\rangle$, $\Omega_a = -\mu E_a / \hbar$ is Rabi frequency of the pump field and $\Omega_b = -\mu E_b / \hbar$ is the Rabi frequency of the probe field, where μ is the associated dipole transition matrix element for the transition $|0\rangle \leftrightarrow |1\rangle$. Also, E_a , ω_a are, respectively, the electric field amplitude and the angular frequency of the pump field, and E_b , ω_b are, respectively, the electric field amplitude and the angular frequency of the probe field. Finally, T_e denotes the electron tunneling coupling coefficient.

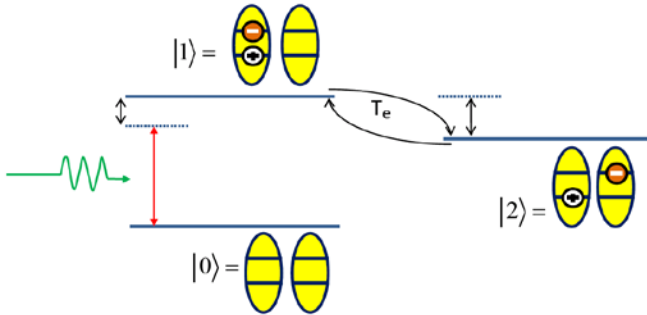


Figure 2. Schematic level configuration of the double quantum dot system. T_e is the electron tunneling coupling coefficient between the two quantum dots.

Using (1) we write the following differential equations for the density matrix elements:

$$\begin{aligned}
 \dot{\rho}_{01}(t) = & i(\Delta + i\gamma_{01})\rho_{01}(t) - i\frac{(\Omega_a + \Omega_b e^{i\delta t})}{2} \times \\
 & [\rho_{11}(t) - \rho_{00}(t)] + iT_e \rho_{02}(t),
 \end{aligned} \quad (2)$$

$$\begin{aligned}
 \dot{\rho}_{12}(t) = & -i(\omega_{12} - i\gamma_{12})\rho_{12}(t) - i\frac{(\Omega_a + \Omega_b e^{-i\delta t})}{2} \times \\
 & \rho_{02}(t) - iT_e [1 - \rho_{00}(t) - 2\rho_{11}(t)],
 \end{aligned} \quad (3)$$

$$\begin{aligned}
 \dot{\rho}_{02}(t) = & i(\Delta - \omega_{12} + i\gamma_{02})\rho_{02}(t) \\
 & - i\frac{(\Omega_a + \Omega_b e^{i\delta t})}{2} \rho_{12}(t) + iT_e \rho_{01}(t),
 \end{aligned} \quad (4)$$

$$\begin{aligned}
 \dot{\rho}_{00}(t) = & i\frac{(\Omega_a + \Omega_b e^{-i\delta t})}{2} \rho_{01}(t) \\
 & - i\frac{(\Omega_a + \Omega_b e^{i\delta t})}{2} \rho_{10}(t) \\
 & + \Gamma_{10}\rho_{11}(t) + \Gamma_{20}[1 - \rho_{00}(t) - \rho_{11}(t)],
 \end{aligned} \quad (5)$$

$$\begin{aligned}
 \dot{\rho}_{11}(t) = & -i\frac{(\Omega_a + \Omega_b e^{-i\delta t})}{2} \rho_{01}(t) \\
 & + i\frac{(\Omega_a + \Omega_b e^{i\delta t})}{2} \rho_{10}(t) \\
 & - (\Gamma_{12} + \Gamma_{10})\rho_{11}(t) - iT_e [\rho_{21}(t) - \rho_{12}(t)].
 \end{aligned} \quad (6)$$

Here, $\rho_{00} + \rho_{11} + \rho_{22} = 1$, $\rho_{nm} = \rho_{nm}^*$, $\Delta = (E_1 - E_0)/\hbar - \omega_a$ is the detuning of the pump field from resonance, $\delta = \omega_b - \omega_a$ is the detuning between the two applied electromagnetic fields, and $\omega_{12} = (E_1 - E_2)/\hbar$. We also define as Γ_{nm} the population decay rate from state $|n\rangle$ to state $|m\rangle$ and by γ_{nm} the decay of coherence of the density matrix element ρ_{nm} , with $n \neq m$.

Now, we assume that the pump field is strong and all the orders of its interaction with the quantum dot system will be taken into consideration, while the probe field is weak and we just maintain the terms up to first order while studying its interaction with the system [2], [10], [11]. This approach is applicable when the Rabi frequency of the pump field is much larger than the Rabi frequency of the probe field, i.e. $\Omega_a \gg \Omega_b$. We proceed to the expansion of the density matrix elements, according to the first order approximation to the probe field

$$\rho_{nm} = \rho_{nm}^{(0)} + \rho_{nm}^{(+)} e^{i\delta t} + \rho_{nm}^{(-)} e^{-i\delta t}, \quad (7)$$

with $|\rho_{nm}^{(0)}| \gg |\rho_{nm}^{(+)}|, |\rho_{nm}^{(-)}|$ and obtain the differential equations for the various density matrix elements.

In this study we are interested in the analysis of the absorption and dispersion properties of the probe field in first order, under the presence of a strong pump field. These effects are determined, respectively, by the imaginary and real parts

of the density matrix element $\rho_{01}^{(+)}$, as the linear susceptibility for the probe field, under the presence of the pump field is given by

$$\chi^{(1)}(\delta) = -\frac{\Gamma}{V} \frac{\mu^2}{\varepsilon_0 \hbar \Omega_b} \left[\rho_{01}^{(+)} \right]^*, \quad (8)$$

where Γ is the optical confinement factor [7], V is the volume of the quantum dot, and ε_0 is the dielectric constant of vacuum. The susceptibility is calculated from the solution of the derived density matrix equations in steady state.

III. RESULTS

In this section we will present results for the pump-probe optical response of the system for different values of the pump field Rabi frequency and especially the tunneling coupling coefficient. In the calculations we present here we consider the case that $\omega_{12} = 0$ (exact resonance between states $|1\rangle$ and $|2\rangle$). We also choose typical parameters for InAs/GaAs quantum dots for the decay and dephasing parameters [9], [14] $\hbar\Gamma_{10} = 0.025$ meV, $\hbar\Gamma_{20} = 0.000025$ meV, $\Gamma_{12} = 0$, $\hbar\gamma_{01} = 0.22$ meV, $\hbar\gamma_{12} = 0.1$ meV and $\hbar\gamma_{02} = 0.001$ meV.

We first present the absorption and dispersion of the probe field in the absence of the pump field in Fig. 3. This has been studied in Refs. [7], [9]. We obtain a strong optical transparency window at the center and the absorption peaks are separated by $2T_e$. The chosen case of weak tunneling leads to optical transparency mainly due to quantum interference and not due to Autler-Townes splitting [9].

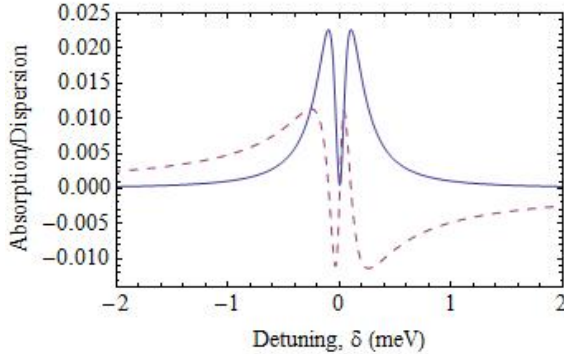


Figure 3. The absorption (solid curve) and the dispersion (dashed curve) spectrum, in arbitrary units, for $\Omega_a = 0$ and $\hbar T_e = 0.1$ meV.

We then present the absorption and dispersion of the probe field in the presence of the pump field but in the absence of tunneling between the two quantum dots in Fig. 4, i.e. only for single quantum dot. This has been studied in [5], [6]. The pump field is taken on-resonance with the $|0\rangle \leftrightarrow |1\rangle$ transition, i.e. $\Delta = 0$. In this case, we obtain zero absorption at $\delta = 0, \pm\Omega_a$, and for values of δ between $-\Omega_a$ and Ω_a optical gain occurs.

Results for the case of simultaneous tunneling between the quantum dots and the application of the pump field are shown in Figs. 5 and 6. We present results for on-resonance excitation of the quantum dot and for various values of the electron tunneling coupling coefficient ranging from very low values to the same value as the Rabi frequency of the pump field. As can be seen from Fig. 5 for very weak tunneling a significant structure is created in the region of δ between $-\Omega_a$ and Ω_a . This structure shows both gain and absorption, with specific zeroes in absorption as well. In addition, a pronounced absorption peak is created at $\delta = 0$.

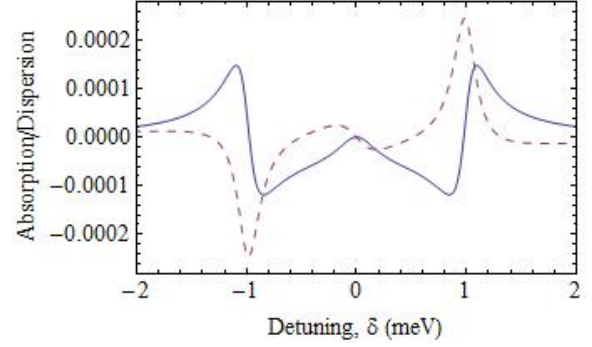


Figure 4. The absorption (solid curve) and the dispersion (dashed curve) spectrum, in arbitrary units, for $\hbar\Omega_a = 1$ meV, $\Delta = 0$ and $T_e = 0$.

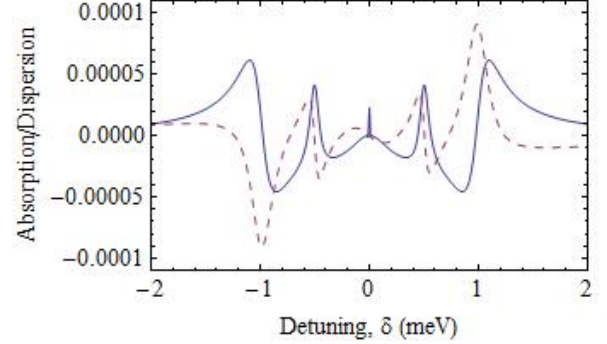


Figure 5. The absorption (solid curve) and the dispersion (dashed curve) spectrum, in arbitrary units, for $\hbar\Omega_a = 1$ meV, $\Delta = 0$ and $\hbar T_e = 0.03$ meV.

For larger values of the tunneling coupling coefficient the structure between the two strong absorption peaks essentially disappears and strong suppression of absorption occurs in this region. This is shown in Fig. 6. The suppression of absorption also becomes more pronounced and in addition the gain essentially disappears, as the tunneling becomes stronger. Moreover, two weak dispersion-like peaks appear at the tails of the strong absorption peaks. Furthermore, the strong absorption peaks move further apart from each other, as the tunneling coupling coefficient increases. The positions of the two strong absorption peaks can be understood using a dressed state analysis [11].

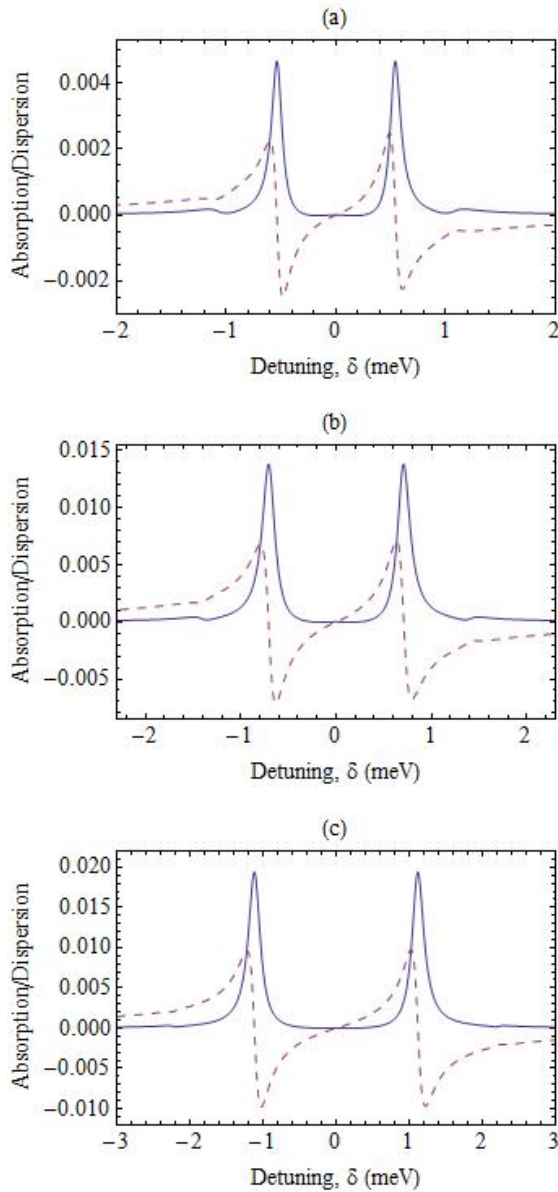


Figure 6. The absorption (solid curve) and the dispersion (dashed curve) spectrum, in arbitrary units, for $\hbar\Omega_a = 1$ meV, $\Delta = 0$ and (a) $\hbar T_e = 0.2$ meV, (b) $\hbar T_e = 0.5$ meV and (c) $\hbar T_e = 1$ meV.

IV. SUMMARY

We considered an asymmetric double semiconductor quantum dot molecule that interacts with a weak probe field and a strong pump field. The nanostructure consists of two quantum dots with different band structures coupled by tunneling. We have shown that the optical response of the system can be controlled by the gate voltage and the pump field. For example, we have found that the application of the pump field leads to probe absorption, optical gain and the ac-Stark effect for weak tunneling rates, while for stronger tunneling rates optical gain disappears. We will continue this study with the analysis of the dependence of the absorption and dispersion spectrum on Δ and Ω_a . We will also analyze the self-Kerr nonlinearity in the driven quantum dot system, as

there is potential for high self-Kerr nonlinearity with low or zero absorption in this system [3].

ACKNOWLEDGMENT

We thank Prof. A. F. Terzis for useful discussions and help.

REFERENCES

- [1] B. R. Mollow, "Absorption and emission line-shape functions for driven atoms," *Phys. Rev. A*, vol. 5, pp. 2217-2222, 1972.
- [2] R.W. Boyd, M.G. Raymer, P. Narum, and D.J. Harter, "Four-wave parametric interactions in a strongly driven two-level system," *Phys. Rev. A*, vol. 24, pp. 411-423, 1981.
- [3] R.S. Bennink, R.W. Boyd, C.R. Stroud, Jr., and V. Wong, "Enhanced self-action effects by electromagnetically induced transparency in the two-level atom," *Phys. Rev. A*, vol. 63, p. 033804, 2001.
- [4] G.S. Agarwal and T.N. Dey, "Non-electromagnetically induced transparency mechanisms for slow light," *Laser Photon. Rev.*, vol. 3, pp. 287-300, 2009.
- [5] X.-D. Xu *et al.*, "Single charged quantum dot in a strong optical field: Absorption, gain, and the ac-Stark effect," *Phys. Rev. Lett.*, vol. 101, p. 227401, 2008.
- [6] S.-W. Chang and S. L. Chuang, "Slow light based on population oscillation in quantum dots with inhomogeneous broadening," *Phys. Rev. B*, vol. 72, p. 235330, 2005.
- [7] C.-H. Yuan and K.-D. Zhu, "Voltage-controlled slow light in asymmetry double quantum dots," *Appl. Phys. Lett.*, vol. 89, p. 052115, 2006.
- [8] M. Ioannou, J. Boviatsis, and E. Paspalakis, "Transient properties of voltage-controlled transparency in an asymmetric double quantum dot," *Physica E*, vol. 40, pp. 2010-2012, 2008.
- [9] H.S. Borges, L. Sanz, J.-M. Villas-Boas, O. O. Diniz Neto, and A. M. Alcalde, "Tunneling induced transparency and slow light in quantum dot molecules," *Phys. Rev. B*, vol. 85, p. 115425, 2012.
- [10] S. G. Kosionis, A. F. Terzis, and E. Paspalakis, "Pump-probe optical response and four-wave mixing in intersubband transitions of a semiconductor quantum well," *Appl. Phys. B*, vol. 104, pp. 33-43, 2011.
- [11] S. G. Kosionis, A. F. Terzis, and E. Paspalakis, "Transient four-wave mixing in intersubband transitions of semiconductor quantum wells," *J. Lumin.*, vol. 140, pp. 130-134, 2013.
- [12] J.-M. Villas-Boas, A. O. Govorov, and S. E. Ulloa, "Coherent control of tunneling in a quantum dot molecule," *Phys. Rev. B*, vol. 69, p. 125342, 2004.
- [13] E. Voutsinas, A. F. Terzis, and E. Paspalakis, "Control of indirect exciton population in an asymmetric quantum dot molecule," *Phys. Lett. A*, vol. 378, pp. 219-225, 2014.
- [14] H.-F. Yao, N. Cui, Y.-P. Niu, and S.-Q. Gong, "Voltage controlled coherent population transfer in an asymmetric semiconductor quantum dot molecule," *Photon. Nanostr.: Fund. Appl.*, vol. 9, pp. 174-178, 2011.

Integration of Modified K-Means Clustering and Morphological Operations for Multi-Organ Segmentation in CT Liver-Images

Walita NARKBUAKAEW¹, Hiroshi NAGAHASHI², Kota AOKI², and Yoshiki KUBOTA³

¹ Interdisciplinary Graduate School of Science and Engineering, Tokyo Institute of Technology, Kanagawa, Japan

² Imaging Science and Engineering Laboratory, Tokyo Institute of Technology, Kanagawa, Japan

³ Gunma University Heavy-Ion Medical Center, Gunma, Japan

Abstract—This paper presents a combination of two ideas to segment multi-organs in CT images. First, we modified the K-means clustering through a hierarchical concept. It was aimed to get a correlation between clustered indexes and different types of tissues. Second, we proposed a simple method to segment multiple organs. The proposed method was based on tissue types, some morphological operations, and basic information of anatomical structures. We applied the proposed method to the CT liver-images acquired by a 4D-CT imaging system. From our experiment, the proposed clustering method described clustered indexes in accordance with five types of regions including background and four different types of tissues. Further, it could reduce the ratio of losing regions, which were randomly occurred when using the original K-means and fuzzy C-means. Further, the multi-organ segmentation method gave attractive outlines on liver, kidneys, and spleens. Moreover, liver-regions were compared with manual-drawing regions performed by a radiologist. From ten sets of 3D-CT images, the proposed method demonstrated the average similarity measures about 87.4 percent.

Keywords—multi-organ segmentation, modified K-means clustering, and morphological operations

I. INTRODUCTION

Medical image segmentation is a fundamental process of computer-aided diagnosis (CAD), which requires analysis of anatomical structures and tissue types. Since specific organ segmentation occasionally gives inadequate information for diagnosis, multi-organ segmentation is an alternate procedure to add further information. It probably illustrates correlation between a target organ and its neighbors. However, it is a challenging task due to a variety of anatomical structures, which largely vary in shapes and sizes. Furthermore, this challenge becomes more complicated when the conditions of image acquisition and a respiratory status cause the deterioration of image quality as demonstrated in 4D-CT measurements [1].

Due to a requirement for multiple-region segmentation, a clustering method is one of the appropriate solutions. Clustering is an unsupervised method that simultaneously divides data points into several groups. Further, it supports multiple-dimensions feature vectors. Therefore, each pixel will be clustered into an appropriate region through an objective function that is designed to measure distance and similarity. For example, Mignotte M. [2] used K-means clustering to segment natural images by fusion of clustered results in different color

spaces. Lee, T.H *et al.* [3] studied CT brain segmentation by using K-means clustering to segment normal and abnormal regions. Then, they constructed the decision tree based on six features for classifying the abnormal regions. Further, they used an expectation-maximization (EM) algorithm to extract cerebrospinal fluid (CSF) and brain matter. Juang, L.H *et al.* [4] proposed a tumor tracking method by applying K-means clustering to converted color-spaces of the MRI brain images. Yusoff I.A *et al.* [5] obtained a dynamic number of clusters to modify K-mean clustering for natural image segmentation. Chu *et al.* [6] used clustering method to divide an atlas database for seeking the good matching between a target image and a template image. Then, they generated a dynamic weight function for performing multi-organ segmentation from maximum a posterior probability (MAP) estimation. Further, they refined the results by using a graph-cut method.

This paper aims to introduce an optional method for multi-organ segmentation in CT liver-images. The proposed method consists of two processes. First, we proposed a modified K-mean clustering through a hierarchical segmentation process. This modification helps to determine the number of clusters and define initial centers of clusters. Further, it is expected to give cluster indexes that correlate to the types of tissues. Second, we present a simple method of multi-organ segmentation. It is based on tissue types, morphological operations, and information of anatomical shapes and locations. This method is expected to segment kidneys, spleen and liver organs.

The rest of paper begins with briefly explaining the K-means algorithm. Section 3 describes the modified K-means clustering method in details. Then, Section 4 explains the proposed method of multi-organ segmentation. Next, experiment and results are shown in Section 5. Finally, we summarize this study in the last section.

II. K-MEANS CLUSTERING ALGORITHM

In order to group a set of data points $\{x_1, \dots, x_N\}$ into K clusters, the K-mean clustering [7] is normally introduced. Since, it supports multidimensional vectors and its computa-

tion is high efficient. It minimizes the distortion measure of

$$J = \sum_{n=1}^N \sum_{k=1}^K b_{nk} \|x_n - c_k\|^2, \quad (1)$$

$$b_{nk} = \begin{cases} 1 & \text{if } k = \arg \min_a \|x_n - c_a\|^2, a = 1, \dots, K, \\ 0 & \text{otherwise,} \end{cases}$$

$$c_k = \frac{1}{N_k} \sum_{x \in C_k} x,$$

where $\|\cdot\|$ is a distance measure. The variables c_k and N_k denote the center and the number of data points in the cluster C_k . This algorithm can be summarized as follows.

step 1: Initialize K cluster centers by random sampling from the data set.

step 2: Measure distances among all data points and all cluster centers.

step 3: Assign cluster index to each data point in accordance with the shortest distance.

step 4: Calculate new cluster centers from all data points in the same cluster.

step 5: Repeat step 2 to 4 until the cluster assignment does not change.

III. MODIFIED K-MEANS CLUSTERING

A. Constrained K-means (C-KM) clustering

Typically, the original K-means (KM) clustering requires three inputs including feature vectors, the number of clusters, and initial centers of clusters. We introduce some ideas to cope with these three requirements.

First, we determine two dimensional feature vectors from a given image. We use gray intensity in each pixel to present the first feature of the image (I_G). On the other hand, we apply a 5x5 median filter to the image, and the result is called a median-gray image (I_M). Then, the median-gray value in each pixel is represented the second feature. Subsequently, we plot feature vectors in a two dimensional space (see Fig.1). The gray intensity values are represented in a horizontal axis, and a vertical axis illustrates the median gray values. Therefore, feature vectors \mathcal{F} can be defined as

$$\mathcal{F} = \left[\left\{ v_G(i) \right\}_{i=1}^N, \left\{ v_M(i) \right\}_{i=1}^N \right], \quad (2)$$

$$v_G(i) = I_G(x, y), \quad v_M(i) = I_M(x, y),$$

$$i = (y \times \text{width of image}) + x,$$

where variables v_G and v_M are a gray intensity and a median gray in a pixel at coordinates x and y in a gray-intensity image I_G and a median-gray image I_M , respectively. Further, N is a total number of features.

Second, we aim to construct a clustering procedure under a hierarchical model, which requires only two clusters in each level to represent background and foreground regions. Further, we define a background region as a stable region, and all feature members of the background region are removed before clustering in the next level.

Third, we symmetrically divide feature vectors \mathcal{F} in each dimension of feature vectors into two parts. Then, we compute

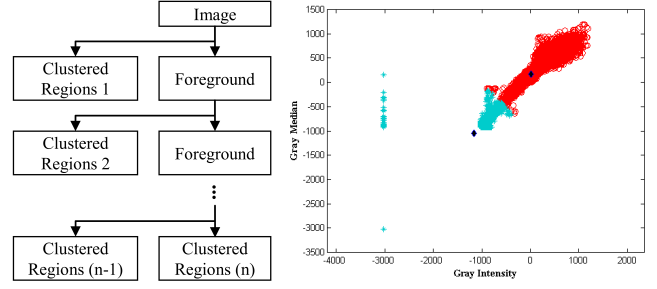


Figure 1. A diagram of clustered-region construction (left) and an example of clustering computed by the constrained K-means (C-KM) clustering in one level (right). In this result, all features are divided into two groups as shown in blue and red points. Meanwhile, two centers of clusters are plotted by two black diamond points.

median of features in each part to represent the initial center of cluster.

$$c_1 = (m_x^1, m_y^1) \quad \text{and} \quad c_2 = (m_x^2, m_y^2),$$

$$m_x^k = \text{Median} \left(\left\{ v_G(i) \right\}_{i=1+\frac{N \times (k-1)}{2}}^{\frac{N \times k}{2}} \right), \quad (3)$$

$$m_y^k = \text{Median} \left(\left\{ v_M(i) \right\}_{i=1+\frac{N \times (k-1)}{2}}^{\frac{N \times k}{2}} \right), \quad k = 1, 2,$$

where c_1 and c_2 are centers of two clusters. Further, the KM clustering under the proposed inputs is called the constrained K-means (C-KM) clustering.

B. Apply C-KM clustering to a hierarchical concept

In this section, we proposed a procedure to get a correlation between clustered indexes and tissue types in CT images. Indeed, this procedure is based on a hierarchical concept, and it performs the following steps to cluster regions in each axial CT image.

Step 1: We obtain a body region (R_{body}). It starts from using C-KM to divide all features into two groups $\{C_1, C_2\}$, and then we construct binary region for each group, $\{r_1, r_2\}$. We remap gray intensity into each clustered region by multiplying gray intensities and a binary region together,

$$f(r_k, I) = r_k(x) \cdot I(x), \quad k = 1, 2, \quad (4)$$

where I is an image and x is a coordinate inside each clustered region. Next, we compute a summation of gray intensities inside each binary region, and obtain the region given the maximum result to identify the direct body-region as

$$r_{\text{body}} = \arg \max_{r_1, r_2} \left\{ \sum f(r_1, I), \sum f(r_2, I) \right\}, \quad (5)$$

where $\sum(\cdot)$ is the summation of function over all element x in the considered region. Afterward, the direct body-region is refined by using morphological operations to remove some undesirable fragment regions as

$$R_{\text{body}} = [[HF(r_{\text{body}}) \ominus s] \oplus s] \cap r_{\text{body}}, \quad (6)$$

where $HF(\cdot)$ denotes a holes-filling filter, and s is the disk-structure element. The operations \oplus and \ominus are morphological

Algorithm 1 Modified K-Means under a hierarchical concept for foreground regions

Repeat:

1. Compute feature vectors in the foreground region r_f
2. Construct regions from results of C-KM: $\{r_1, r_2\}$
3. Refine the clustered regions by morphological operations:

$$r_k \leftarrow [[r_k \oplus s] \ominus s], k = 1, 2$$

4. Determine mean intensities μ_k and index T in each region:

$$\mu_k = \frac{1}{N_k} \sum_{x \in r_k} (r_k(x) \cdot I(x)), N_k = \sum_{x \in r_k} x,$$

$$T = \left(\arg \min_t |P(t) - \mu_k| \right) + 1,$$

5. Check conditions and Assign clustered region r_s

if $\left(\frac{\max\{N_1, N_2\}}{\min\{N_1, N_2\}} > threshold \right)$ **then**

$r_f = \arg \max_{r_1, r_2} \{N_1, N_2\}$ and

$r_s = r_a T_a$ where $r_a = r_f^c$.

else

if $(T_1 - T_2 > 1)$ **then** $r_f \leftarrow r_1$ and $r_s = r_2 T_2$

elseif $(T_2 - T_1 > 1)$ **then** $r_f \leftarrow r_2$ and $r_s = r_1 T_1$

else $r_s = r_1 T_1 + r_2 T_2$ and a stop-iteration flag is true

end if

end if

6. Combine clustered regions without intersection regions:

$$R_{\text{final}} \leftarrow R_{\text{final}} + R_{\text{pre}} \text{ where } R_{\text{pre}} = r_s \cap R_{\text{final}}^c.$$

Until the stop-iteration flag is true

dilation and erosion. Thus, a background region is a complement set of the body region $(R_{\text{bkg}} = R_{\text{body}}^c)$. Subsequently, we define the body region as a foreground region ($r_f \leftarrow R_{\text{body}}$), which is used to obtain regions of target organs.

Step 2: We define possible mean-intensities of clusters $P = \{0, 40, 80, 250\}$ to obtain remaining regions. These values are designed and adjusted by considering average intensity of standard CT numbers in each organ. Next, we set the background region as the final clustered regions ($R_{\text{final}} \leftarrow R_{\text{bkg}}$), and apply Algorithm 1 to determine the remaining regions.

According to the proposed method, we get the final clustered regions, which are explained by simple indexes as $\{R_{\text{bkg}}, R_{\text{fat}}, R_{\text{soft1}}, R_{\text{soft2}}, R_{\text{hard}}\} = \{1, 2, 3, 4, 5\}$. These indexes relate to the regions and tissue types. For example, if we want to reconstruct regions of ribs that is a hard-tissue type, we just select clustered regions indexed by five.

IV. MULTI-ORGAN SEGMENTATION APPLICATION

This section aims to demonstrate an advantage of the proposed clustering method, which can describe a correlation among tissue types, clustered region, and clustered indexes. Since, the proposed clustering method explains the clustered regions without random indexes although we change axial CT images. Thus, it helps to segment multiple organs in 3D or 4D-CT liver-images by referring to the index of a desirable tissue-type. In this study, we consider three organs including liver, kidneys, and spleen. However, the clustered results cannot

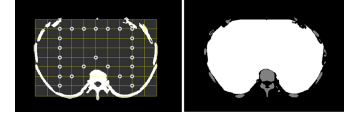


Figure 2. Example of initial seed points (left) and a constructed region inside the ribcage (right)

completely separate regions of different organs due to the problems of overlapped intensity ranges, high level of image noises, and some image artifacts. Therefore, we proposed a simple procedure based on some morphological operations to correct the segment regions in each organ.

First, we construct regions inside the ribcage to limit a boundary of multi-organ segmentation since regions outside ribs mostly contain fat and muscle regions. We construct the region inside ribs in each axial image by performing the following steps.

Step 1: We do not construct the region inside ribs, $R_{\text{in_ribs}} = \emptyset$, when axial planes are located above or at the top section of lung because no soft tissue appears in these positions. We simply check this condition by measuring a proportion of width to height of the body region R_{body} . If this proportion is less than a predefined threshold, we will start the next step.

Step 2: We combine hard-tissue regions extracted from a specific set of images, which contain the target axial image and its twelve-neighbor axial images in the upper and lower positions, $\mathcal{I} = \{I_t | -6 \leq t \leq 6\}$. This combination helps to enhance a boundary of the ribcage in the target axial-image.

$$R_{\text{com_test}} = \bigcup HF(R_{\text{hard}}(\mathcal{I})), \quad (7)$$

where $R_{\text{hard}}(\mathcal{I})$ denotes the region in the hard-tissue type extracted from the specific set of images \mathcal{I} .

Step 3: We construct the region inside the combined test-region ($R_{\text{com_test}}$). However, ribs and vertebral regions, which are defined as hard-tissue regions, in each axial image do not always present a clear boundary. Thus, we have to obtain an optional boundary. This study checks a quality of the combined test-region from a summation of pixels in an upper half of the combined test-region. This summation should be more than a predefined threshold. Otherwise, we replace the combine test-region as $R_{\text{com_test}} = R_{\text{soft1}} \cup R_{\text{soft2}} \cup R_{\text{hard}}$. Then, we create a 10x8-grids rectangular region that is fit to the combined test-region. (See Fig.2) Next, we initialize 24 seed points, and we move these points to a boundary of the combined test-region. Consequently, we will get the region inside ribs $R_{\text{in_ribs}}$ after moving these initial points. Lastly, we refine the result by using morphological operations as

$$R_{\text{in_ribs}} = HF(R_{\text{in_ribs}} \cap R_{\text{com_test}}^c) \ominus s. \quad (8)$$

Afterward, we introduce several steps and some templates (See Fig.3) to segment specific organs. These templates contain one type of kidneys, one type of spleen, and three types of livers, $T_m = \{T_{\text{kidneys}}, T_{\text{spleen}}, T_{\text{liver_t}}, T_{\text{liver_m}}, T_{\text{liver_b}}\}$. In fact, it is necessary to use three templates for a liver organ in order to deal with large variation in liver shapes among different axial image slices. We manually divide the liver organ into three zones from top to bottom, and each zone is related to



Figure 3. Examples of template regions of interests used for identifying the specific organ: one template for kidney, one template for spleen, and three templates for liver in left-to-right order. Three templates of liver regions relate to three zones of liver from top-to-bottom.

these three templates. Further, the final clustered region R_{final} approximates each specific organ through a combination of some clustered regions. According to our data set, the kidney requires three clusters including two soft clusters and a hard cluster as $C_m = R_{\text{soft1}} \cup R_{\text{soft2}} \cup R_{\text{hard}}$. Meanwhile, spleen and liver require two soft clusters as $C_m = R_{\text{soft1}} \cup R_{\text{soft2}}$. Subsequently, we perform the following steps.

Step 1: Select an appropriate template (T_m), which relates to the specific organ.

Step 2: Select a representative clustered-region (C_m) of the specific organ.

Step 3: Identify a range of axial image indexes, which covers the specific organ and relates to the template.

Step 4: Construct the region of interest (ROI) over the target organ as $R_{\text{ROI}} = C_m \cap R_{\text{in_ribs}} \cap T_m$

Step 5: Create test region from the ROI by using morphological erosion and the holes-filling filter, $R_{\text{test}} = HF(R_{\text{ROI}} \ominus s)$. Further, we construct a complement region of the test region as $R_{\text{comp}} = R_{\text{test}}^c \cap T_m$

Step 6: Extract the pre-target and alternate regions by using Algorithms 2 and 3, respectively. In both algorithms, we enhance border regions of the target organ by using an entropy filter. In fact, we begin with remapping gray intensities into the test region as $R_{\text{test}}(x) \cdot I(x)$ where $x \in R_{\text{test}}$, and then we apply the entropy filter to this remapped region. These border regions are denoted by R_{entropy} .

Step 7: Infer the final target regions under the following conditions. First, if we consider the first image of the specific range of images, the pre-target region will represent the final result. Second, we use a combination of pre-target and alternate regions to create the kidneys regions. Further, the alternate region can illustrate the spleen regions in the remaining axial image slices in the specific range of images. Lastly, we use pre-target regions to present liver regions in the top and middle zones whereas the liver regions in the bottom zone are constructed by the alternate regions. In addition, we use segmented regions of kidneys to subtract regions in the liver segmentation to prevent regions of kidneys appear in the results of liver segmentation.

Step 8: Refine the results by applying a 13x13-pixels Gaussian smooth filter with the standard deviation $\sigma = 2.5$ to the volume of the final target regions in coronal and sagittal planes. Then, we apply morphological-dilation with preserving holes regions to the liver regions in axial planes.

V. EXPERIMENT AND RESULTS

A. Data set

We applied the proposed method to 3D-CT images of ten respiratory phases (10 sets of 3D-CT data) of a 4D-

Algorithm 2 Extract the pre-target regions

$$R_{\text{entropy}} = \text{EntropyFilter}(R_{\text{test}}(x) \cdot I(x)), x \in R_{\text{test}}$$

$$R_{\text{check}} = R_{\text{comp}} \cup R_{\text{entropy}}$$

$$N_{\text{check}} = \sum_{x \in R_{\text{check}}} x$$

Repeat: $R_{\text{check}} \leftarrow R_{\text{check}} \ominus s$

Until: $N_{\text{check}} < \text{threshold}$

$$R_{\text{pre_target}} = HF(R_{\text{check}}) \cap R_{\text{check}}^c$$

Algorithm 3 Extract the alternate regions

Retrieve the target region from the last image: $R_{\text{prior_target}}$

$$R_{\text{check}} = R_{\text{prior_target}} \text{ and } N_{\text{check}} = \sum_{x \in R_{\text{check}}} x$$

Repeat: $R_{\text{check}} \leftarrow [R_{\text{prior_target}} \oplus s] \cap R_{\text{test}}$

Until: $N_{\text{check}} > \text{threshold}$

$$R_{\text{temp}} = R_{\text{test}} \cap R_{\text{check}} \cap R_{\text{entropy}}^c$$

$$R_{\text{temp}} \leftarrow R_{\text{temp}}^c \cap T_m \text{ and } R_{\text{check}} = R_{\text{temp}}$$

Repeat: $R_{\text{check}} \leftarrow R_{\text{temp}} \ominus s$

Until: $N_{\text{check}} < \text{threshold}$

$$R_{\text{alternate}} = HF(R_{\text{check}}) \cap R_{\text{check}}^c$$

CT liver-data set, which is collected from a patient by using a GE Discovery ST and a Varian RPM system in a cine mode. It is provided by the MIDAS community, <http://midas.kitware.com/community/view/47>. This data set contains 150 axial image slices of 16-bit gray scales. Each axial image sizes 512x512 pixels with resolution 0.98 square millimeters, and slice thickness is 2.5 millimeters.

B. Qualitative Examination

First (See Fig.4), we compared the proposed clustering-method to the original K-means (KM) [5] and Fuzzy C-means (FCM) [8] by observing three sample axial CT-images. We set the number of clusters to be five for all clustering, and we used gray intensity and median-gray to produce feature vectors (see Section III-A). Further, we selected the best result in five times of testing to demonstrate the result of KM and FCM since their results depend on the initial centers of clusters. In contrast, the proposed method used cluster indexes to represent types of tissues. Thus, it is not necessary to repeat the experiment to collect good representative results. Considering the first column, the arrows on the right corner show the difference gray levels between some image noises and real background intensity values. Conversely, it should be represented as one region of background, and the proposed method can achieve this requirement. Meanwhile, both KM and FCM generated these different regions. Further, the arrow at the center image indicates the lost regions of bones in FCM's result. Next, we observed a large region of soft tissue including high level of image noises as shown in the second column. In this image, KM, FCM and the proposed method were unable to distinguish regions between liver and spleen. One reason is that some intensity ranges of both organs are overlapped and slightly different from each other. In addition, although the image

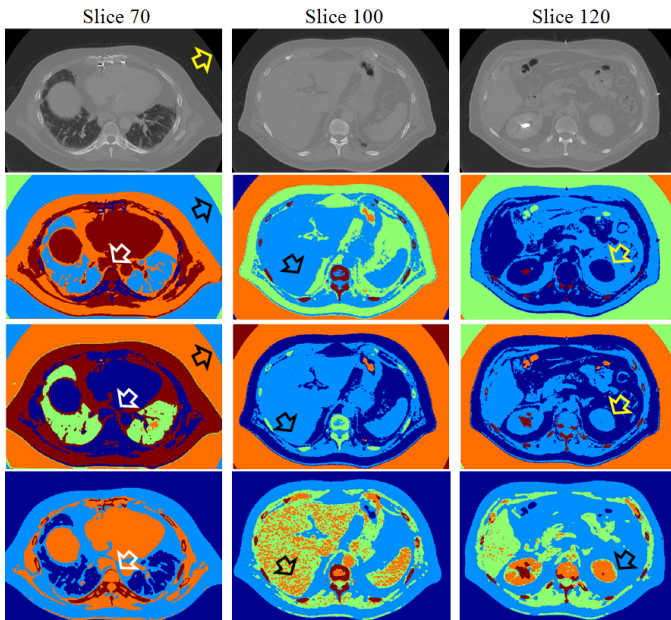


Figure 4. Three examples of comparison in clustered regions performing on three axial images at slice 70, 100, and 120 (the first row) when the number of clusters is five. Further, feature vectors are gray intensities and median of the target image. The clustered results of K-means, Fuzzy C-means, and the proposed method are demonstrated from the second to the fourth rows, respectively.

noise caused the proposed method to define soft tissue as fragmentary regions, we can merge the regions in R_{soft1} and R_{soft2} together to improve the soft tissue region. Focusing on the last column, some artifacts caused large changes in intensities of kidneys in the original image. The KM and FCM cannot separate the kidney regions from the others. Meanwhile, the proposed method can show some different regions.

Next, we consider a combination of the proposed clustering and the region-correction methods. We extract ribcage, kidney, liver, spleen, and body regions excluding air volumes. These organs were well delineated in different colors and displayed in axial, coronal and sagittal planes (see Fig. 5). The proposed method was able to display the boundary of a hole region inside the liver, but they were not exact shapes. Further, it was possible to deal with some image artifacts inside kidneys by giving good global shapes. In contrast, the proposed method sometimes failed to extract vertebral-body regions because intensities inside these regions are equivalent to another and the boundary of these regions are thin. In addition, we could observe the global shapes of the target organs by reconstructing a surface model on each segmented organ. We simply reconstructed the surface models by using the marching cubes algorithm [9], and example results were illustrated in Fig. 6.

C. Accuracy of Liver segmentation

In this section, we selected a liver-segmentation application to study an accuracy of the proposed method since its shape includes high complexity and large variation in size. Three similarity measures and its average were used to evaluate the accuracy. The segmented liver-regions (V_S) were compared

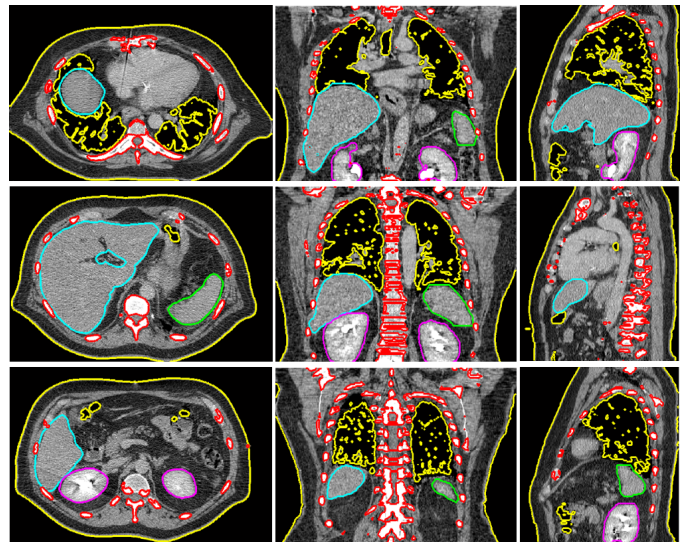


Figure 5. Nine examples of multi-organ segmentation displayed in axial planes at slices 70, 100, and 120 in the first column, coronal planes at slices 180, 210, and 240 in the second column, and sagittal planes at slices 161, 250, and 322 in the last column. Five region-types are delineated in different colors. They contain the body region excluding air volumes (yellow), ribcage (red), kidneys (magenta), liver (cyan), and spleen (green).

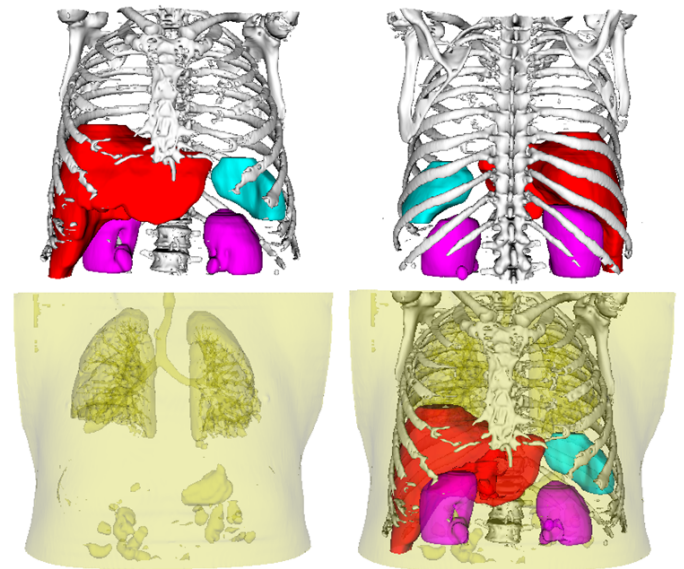


Figure 6. Four examples of surface reconstruction. On the top left, it shows the ribcage, liver, kidneys, and spleen in a front view whereas their back views are illustrated on the top right. The bottom left figure presents the body surface excluding air volumes. Lastly, on the bottom right, it shows a combination of liver, kidneys, spleen, and body excluding air volume.

with manual segmentation (V_M), which was performed by a radiologist. These measures contained the volume overlapped region coefficient (VOC), the relative absolute volume similarity (RAVS), and the dice similarity coefficient (DSC) [10]. From comparison over 10 sets of 3D-CT images, the liver volumes extracted by the proposed method were similar to the manual delineation 87.4 percent on average, and some details

of measure values are shown on Table. I.

$$\begin{aligned}
 VOC &= \frac{V_S \cap V_M}{V_S \cup V_M} \times 100\% \\
 RAVS &= \left(1 - \frac{|V_S - V_M|}{V_M}\right) \times 100\% \\
 DSC &= \frac{2|V_S \cap V_M|}{|V_S| + |V_M|} \times 100\%
 \end{aligned} \quad (9)$$

Table I
COMPARISON OF SIMILARITY MEASURES OF LIVER SEGMENTATION
ON 10 SETS OF 3D-CT DATA (unit:%)

Measure values	VOC	RAVS	DSC	Average
Minimum	84.3	83.4	91.5	86.4
Mean	85.5	84.5	92.2	87.4
Maximum	86.5	85.5	92.7	88.2
SD	0.68	0.74	0.40	0.60

VI. CONCLUSION

This study introduced an idea to integrate the modified K-means clustering to a hierarchical process of segmentation for improving the clustered results. We applied the proposed clustering method to the CT liver-images acquired by a 4D-CT imaging system. From our results, the proposed clustering gave better results than the original K-mean (KM) and Fuzzy C-means (FCM) by presenting the clustered indexes in accordance with types of tissues. Meanwhile, KM and FCM randomly described the clustered regions. In addition, this randomization sometimes caused several regions of different tissue-types to be merged. However, the proposed clustering cannot distinguish the regions of different organs, which locate inside the ribcage, and their intensities are overlapped or slightly different. Thus, we proposed a region-correction method to achieve this purpose. The idea of this method relied on a combination of tissue types, morphological operations, and basic information of anatomical structures. We created simple-template regions of interests from locations and shapes of specific organs to segment the target regions. The results showed attractive outlines and shapes of multiple segmented-organs. Moreover, we selected the liver regions to examine the accuracy of the proposed method by measuring similarity between segmented regions and manual drawing. The proposed method was applied to 10 sets of 3D-CT images, and the result showed the percentage of similarity at 87.4 percent on average.

In contrast, the proposed method occasionally fails to segment the region including high convex and concave areas. Further, it requires parameters adjustments on sample images of the target 3D volumetric images. Consequently, these problems will be addressed in our future work.

REFERENCES

- [1] S. B. Jiang, "Radiotherapy of mobile tumors," *Seminars in radiation oncology*, vol. 16, no. 4, pp. 239–248, 2006.
- [2] M. Mignotte, "Segmentation by fusion of histogram-based k-means clusters in different color spaces," *IEEE Transactions on image processing*, vol. 17, no. 5, pp. 780–787, 2008.
- [3] T. H. Lee, M. F. A. Fauzi, and R. Komiya, "Segmentation of ct brain images using k-means and em clustering," in *Computer Graphics, Imaging and Visualisation, 2008. CGIV'08. Fifth International Conference on*, pp. 339–344, IEEE, 2008.
- [4] L.-H. Juang and M.-N. Wu, "Mri brain lesion image detection based on color-converted k-means clustering segmentation," *Measurement*, vol. 43, pp. 941–949, 2010.
- [5] I. A. Yusoff, N. A. Mat Isa, and K. Hasikin, "Automated two-dimensional k-means clustering algorithm for unsupervised image segmentation," *Computers & Electrical Engineering*, 2012.
- [6] C. Chu, M. Oda, T. Kitasaka, K. Misawa, M. Fujiwara, Y. Hayashi, R. Walz, D. Rueckert, and K. Mori, "Multi-organ segmentation from 3d abdominal CT images using patient specific weighted-probabilistic atlas," in *Medical Imaging 2013: Image Processing*, pp. 86693Y–1–86693Y–7, Proc. of SPIE, 2013.
- [7] C. M. Bishop and N. M. Nasrabadi, *Pattern recognition and machine learning*, vol. 1. springer New York, 2006.
- [8] K.-S. Chuang, H.-L. Tzeng, S. Chen, J. Wu, and T.-J. Chen, "Fuzzy c-means clustering with spatial information for image segmentation," *computerized medical imaging and graphics*, vol. 30, no. 1, pp. 9–15, 2006.
- [9] W. E. Lorensen and H. E. Cline, "Marching cubes: A high resolution 3d surface construction algorithm," in *ACM Siggraph Computer Graphics*, vol. 21, pp. 163–169, ACM, 1987.
- [10] L. R. Dice, "Measures of the amount of ecologic association between species," *Ecology*, vol. 26, no. 3, pp. 297–302, 1945.

A Theoretical Study of an Electronic Structure of the Infinite and Finite-length Carbon Nanotubes

A. V. Tuchin, A.A. Ganin, D. A. Zhukalin, L. A. Bityutskaya and E. N. Bormontov

Abstract— The paper describes results of a theoretical study of the electronic structure of infinite- and finite-length single-walled carbon nanotubes in the region of ultra-small diameters (<2nm). Clear oscillation of the gap energy and the work function on the diameter of the zigzag and on the length of the armchair nanotubes are presented. An applied electric field leads to the energy gap decreasing in finite-length nanotubes due to Stark shifting of the frontier orbital energies.

Keywords— single-walled carbon nanotube, electronic structure, size effect, energy gap, work function.

I. INTRODUCTION

THE broad application of carbon nanotubes in nanoelectronics [1], [2], [3], [4], [5] is impeded by difficulties to control their properties which strongly depend on their structure. General classification of single-walled carbon nanotubes (SWCNT) is based on their chirality indices n , m [6], [7]. In the nineties of the 20th century the first calculations of the band structure of SWCNTs and graphene were carried out within the tight binding model (TBM) [7], [8], [9], [10], [11]. It was found that the nanotube has a metallic conductivity if the difference ($n - m$) is a multiple of three, otherwise its conductivity is semiconducting (“3k” rule) [12]. It was also obtained that the band gap in semiconducting SWCNTs is inversely proportional to their diameter. Team led by Blasé has found that this dependence is true in the region of radiuses from infinity to 2.4 angstroms [13].

Odom et al. [14] (for diameters ranged 0.7 – 1.1 nm) and Wildoer et al. [15] (for diameters ranged 1.0 – 2.0 nm) have experimentally determined E_g of nanotubes using density of states (DOS) spectra (obtained by measuring of the tunneling current from SWCNT to scanning tunneling microscope (STM) probe). Significant difference between the experimental and theoretical values has been found for SWCNT in the

region of ultra-small diameters. Ouyang et al. [16] have experimentally found the following values of E_g for SWCNTs (0, 9), (0, 12) and (0, 15): 0.080 eV, 0.042 eV and 0.029 eV correspondingly, which contradicts to the 3k rule.

A band structure of the SWCNTs also depends on their length. The first ab-initio investigations of impact of length on the electronic band structure of SWCNTs were carried out in 1999 [17]. It was shown that the electronic density of states in finite-length tubes is close to that of infinite nanotubes only from lengths of about several nanometers. Rocherfort et al. [18] have studied an electronic band structure of open-ended armchair SWCNT (6, 6). Calculations within the Hartree-Fock, DFT, semiempirical MNDO-PM3 and extended Huckel model have shown that an additional confinement of electrons along the tube axis leads to a non-zero band gap. The energy gap shows clear oscillations with the length of the tube.

Wang et al. [19] have investigated open-ended armchair and zigzag SWCNTs properties using semiempirical PM3 method. According to the results, the band gap versus length dependency of armchair nanotubes has oscillating character while the same dependency for zigzag tubes shows no oscillations. On the other hand, the gap for zigzag SWCNTs oscillates with a change in their diameter, but there are no oscillations observed in armchair tubes. Cioslowski et al. [20] have calculated ionization energies, electron affinities and a band gap of finite-length capped armchair (5, 5) and zigzag (9, 0) SWCNTs using B3LYP method and 6-311G* basis set. They concluded that SWCNTs properties depend on the length of tubes and, in case of SWCNT (9, 0) and on the mutual orientation of the caps.

Thus, in the region of ultra-small diameters (less than 2 nm) and lengths (less than 10 nm), the principle of the monotonous change of a band gap is not valid, the dependence acquires signs of nonlinearity and consequently the 3k rule is not always correct. The investigation of the impact of length on the band structure of SWCNTs is motivated by the tendency to decrease the active element sizes in nanoelectronics devices and the latest achievements in the technologies of short nanotubes production [18]. High curvature and small sizes of finite-length SWCNTs lead to the high local electric field even if a low voltage is applied [21]. An Electric field can significantly change the electronic structure of the nanotubes [3], [22].

The aim of the investigation is to reveal the impact of a diameter and length change on the band gap, work function and electron density distribution of single-walled carbon nanotubes of ultra-small diameter and the field induced

This work was supported by RFBR, research project No. 14-02-31315 mol_a and by the project FP7-IRSES-295260 “ECONANOSORB” under Marie Curie Actions of the 7th Framework Program of European Union.

A. V. Tuchin is with the Voronezh State University, 394006, Voronezh, Russia (tel.: +7(473)2208481; e-mail: a.tuchin@bk.ru).

A. A. Ganin is with the Voronezh State University, 394006, Voronezh, Russia (tel.: +7(473)2208481; e-mail: me144@phys.vsu.ru).

D. A. Zhukalin is with the Voronezh State University, , 394006, Voronezh, Russia (tel.: +7(473)2208481; e-mail: d.zhukalin@mail.ru).

L. A. Bityutskaya is with the Voronezh State University, 394006, Voronezh, Russia (tel.: +7(473)2208481; e-mail: me144@phys.vsu.ru).

E. N. Bormontov is with the Voronezh State University, 394006, Voronezh, Russia (tel.: +7(473)2208481; e-mail: me144@phys.vsu.ru).

electronic structure modulation of the capped finite-length SWCNTs.

II. METHODOLOGY

Firstly, we observe infinite-length SWCNTs (zigzag in chiralities range from (0, 3) to (0, 25) and armchair in chiralities range from (2, 2) to (15, 15) – 23 zigzag and 14 armchair nanotubes total). Secondly, we investigate properties of finite-length capped tubes (24 armchair (5, 5) and 11 zigzag (0, 9) total) and finite-length open-end nanotubes passivated by hydrogen atoms (chiralities ranging from (3, 3) to (15, 15) and lengths ranging from 2 to 20 segments - 247 tubes total). Then, an analysis of the highest occupied and the lowest unoccupied molecular orbitals (HOMO and LUMO) of the selected tubes is presented. Finally, the effect of an electric field on the electronic structure of the capped finite-length SWCNTs (5,5) is observed.

For infinite tubes we used periodic boundary conditions (PBC) and the density functional theory within the local spin-density approximation (LSDA) and 6-31G basis. The calculation was performed for 200 points in the Brillouin zone. In order to take the curvature effects into account properly, we used a cylindrical unit cell of a nanotube. Work function was calculated as difference between vacuum level and Fermi level.

A stoichiometric formula of capped SWCNT (5, 5) is C_{60+10j} , where j denotes the number of segments which form the body of the tube while the caps essentially are halves of the fullerene molecule (fig.1a). These halves are obtained by dissection of

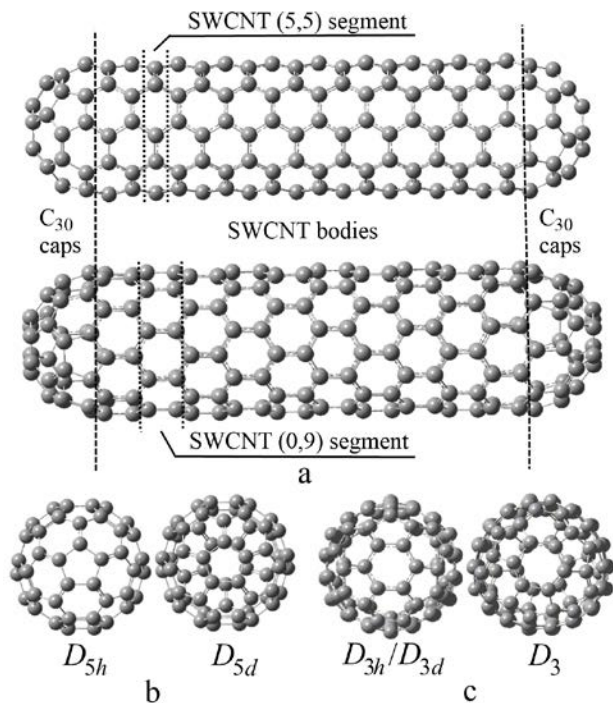


Fig. 1. Structural images of capped SWCNTs (5, 5) and (0, 9) (a). The mutual orientation of two C_{60} hemisphere of the capped SWCNTs (5, 5) D_{5h} and D_{5d} symmetries (b) and SWCNTs (0, 9) D_{3h}/D_{3d} and D_3 symmetries (c).

the fullerene molecule perpendicularly to the C_{5v} axis. Each increase of j by 1 leads to a rotation of the caps relatively to each other through $\pi/5$ angle. Thus, one of the caps is a mirror image of another every 2 segments and j defines the symmetry of SWCNT (5, 5): D_{5h} (when $j = 2p + 1$) or D_{5d} (when $j = 2p$), where p is integer (fig. 1b).

A stoichiometric formula of capped SWCNT (0, 9) is C_{60+18j} . Caps are obtained by dissection of the fullerene molecule perpendicularly to the C_{3v} axis. Regardless of j there may be two orientations of the caps, corresponding to: 1 - D_{3h} (when $j = 2p + 1$) and D_{3d} (when $j = 2p$) and 2 - D_3 symmetry (fig.1c).

According to the Coopmans theorem, the ionization potential E_I and electron affinity E_A equals to the HOMO and LUMO energy with opposite sign. Our calculated values for fullerene C_{60} are $E_I=6.69$ eV and $E_A=4.86$ eV differ from the average experimental values $E_I = 7.56 \pm 0.06$ eV [23], [24], [25], [26] and $E_A = 2.68 \pm 0.02$ eV [27], [28]. Using the assumption of Cioslowski et al. [20], the difference between average experimental data and calculated values for fullerene C_{60} and finite-length SWCNTs (5,5) and (0,9) are equal. We used following corrections: $\Delta E_I=0.87$ eV и $\Delta E_A=-2.18$ eV in our research.

All the calculations were performed in the Supercomputing center of the Voronezh State University using the Gaussian software [29].

III. RESULTS

A. An Influence of the diameter on electronic structure of the infinite-length single-walled carbon nanotubes

In zigzag SWCNTs one of the chirality indices equals zero and in armchair nanotubes both indices are equal. In these cases it is sufficient to use only one index to denote the nanotube chirality. In the further discussion we are going to use the chirality indices instead of the diameter in all plots which show only zigzag or only armchair tubes. The diameter of SWCNTs tubes equals $d = a\sqrt{n^2 + m^2 + nm} / \pi$ [12].

The energy gap of infinite-length zigzag SWCNTs strongly depends on the chirality indice (fig.2a). Tubes with chiral indexes $n \geq 9$ can be divided into three groups with n multiply to $3k$, $3k+1$, $3k+2$ ($k=3, 4, 5, \dots$) with a low, mediate and high energy gap respectively. SWCNTs with $n=3k$ are semiconductors with the small band gap of 20-140 meV, which contradicts to the “3k” rule. The energy gap of the zigzag SWCNTs in the range of ultra-small diameters is a function of $1/d^2$ (fig.2a) rather than of $1/d$, as was predicted by TBM calculation [12]. Tubes with $n < 9$ also violate the “3k” rule, because of the high curvature effects and degenerated levels. The band gap of armchair SWCNTs do not depend on the diameter (fig.2b). All tubes have small E_g in the range =0-30 meV.

The work function of infinite-length armchair and zigzag SWCNTs as function of diameter in the range from 0.3 to 2 nm are presented in the fig.3.

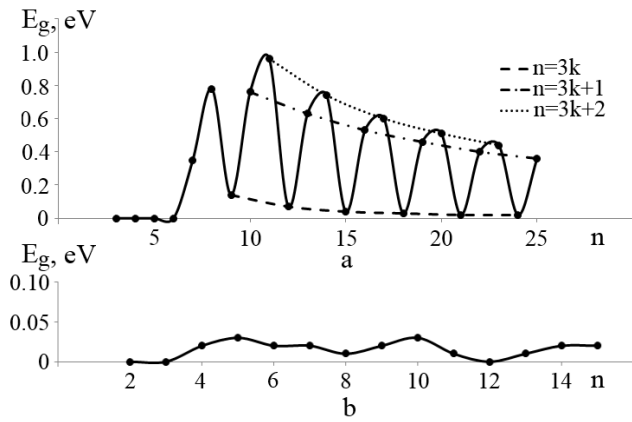


Fig. 2. The band gap dependence on chirality indexes (diameter) of infinite-length zigzag (a) and armchair (b) SWCNTs.

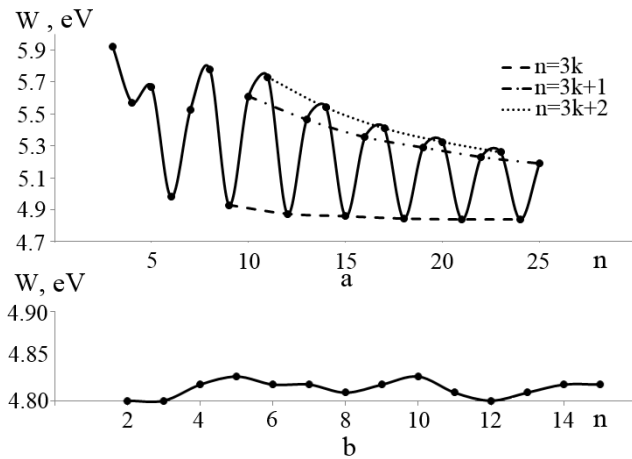


Fig. 3. The work function dependence on chirality indexes (diameter) of infinite-length zigzag (a) and armchair (b) SWCNTs.

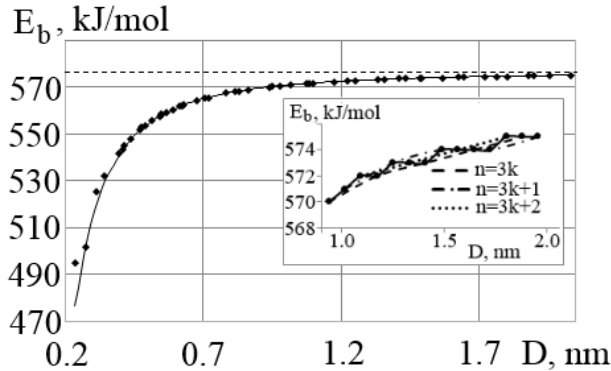


Fig. 4. Binding energy dependence on diameter for armchair and zigzag SWCNTs. Solid line represents fitting formula $E_b = E_b^{\text{Graphene}} - 5.5/D^2$. Dashed line represents calculated bond energy in graphene 576 kJ/mol. The inset shows the binding energy of (3k), (3k+1) and (3k+2) groups of zigzag tubes in the range from 1 to 2 nm.

The work function of all armchair and 3k-group zigzag SWCNTs have little to none dependence on diameter and chirality with two exceptions for tubes (0, 3) and (0, 6) where W equals 5.92 and 4.98 eV correspondingly. For all other tubes this value appears to be close to the one in graphene, (our calculated value is 4.8 eV). The work function of zigzag tubes of 3k+1 and 3k+2 groups oscillates with the chirality indices.

A binding energy of carbon nanotubes dependence on their diameter appears to have a monotonic increasing -character. Following fitting formula can be used $E_b = E_b^{\text{Graphene}} - C / D^2$ (fig. 4), in which D is a diameter of the tube, C is a coefficient (which we take to be equal 5.5) and E_b^{Graphene} is a binding energy of graphene. We consider this formula to be a consequence of the fact that the repulsion of π electrons becomes smaller and inversely proportional to the cross-sectional area of the nanotube and thus increases stability of the structure. Zigzag nanotubes of the (3k+1) group with the diameter less than 1.5 nm are slightly more stable, than (3k) and (3k+2) groups. In the range $D=1.5-2$ nm binding energy of the SWCNTs of the (3k+2) group is slightly more than for zigzag tubes with a smaller energy gap.

B. Capped finite-length SWCNTs (5, 5)

The capped finite-length armchair SWCNT have a non-zero value of its energy gap LUMO-HOMO with an oscillating dependency on the length (fig.5). According to the 3k rule, the infinite-length SWCNT (5,5) has a zero energy gap. Finite-length tubes can be divided into three groups depending on the number of section j : 1) $j = 3p$, 2) $j = 3p+1$ and 3) $j = 3p+2$ (where p is an integer). The groups mentioned correspond to the average, maximal and minimal $E_{\text{LUMO-HOMO}}$.

The energy gap LUMO-HOMO of the SWCNTs of the first and second groups monotonically decreases with the number of segments. $E_{\text{LUMO-HOMO}}$ of SWCNT of the $(3p + 2)$ group has no dependency on lengths larger than 8 segments. The following system of inequalities is correct for tubes (fig.5):

$$E_{\text{LUMO-HOMO}}(3p+2) < E_{\text{LUMO-HOMO}}(3p) < E_{\text{LUMO-HOMO}}(3p+1) \quad (j \leq 12)$$

$$E_{\text{LUMO-HOMO}}(3p) < E_{\text{LUMO-HOMO}}(3p+2) < E_{\text{LUMO-HOMO}}(3p+1) \quad (12 < j \leq 23)$$

$$E_{\text{LUMO-HOMO}}(3p) < E_{\text{LUMO-HOMO}}(3p+1) < E_{\text{LUMO-HOMO}}(3p+2) \quad (j > 23)$$

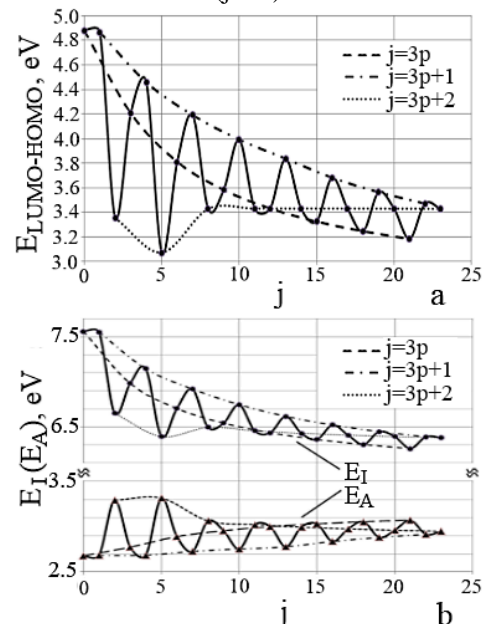


Figure 5. Electronic structure of capped armchair SWCNTs (5, 5) depending on its length: a) energy gap LUMO-HOMO, b – ionization potential (E_I) and electron affinity (E_A).

A decrease of the LUMO-HOMO gap in the nanotubes of (3p) and (3p+1) groups is conditioned by a stabilization of LUMO and destabilization of HOMO. Destabilization of both orbitals of SWCNTs, which are members of (3m+2) group, is observed at $j \geq 8$. Equality of the slopes of the curves, which is almost a straight line, leads to the constant gap LUMO-HOMO (fig.5a)

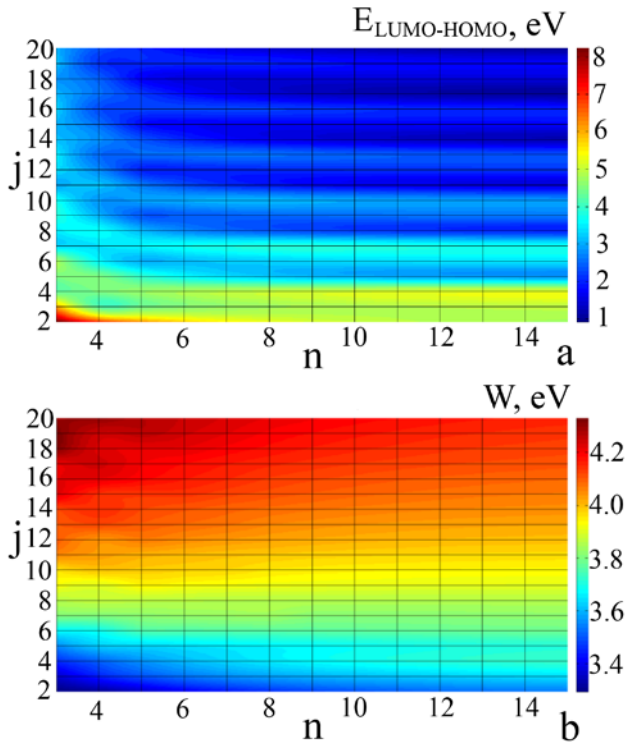


Fig. 6. Energy gap LUMO-HOMO (a) and work function (b) dependencies on length and diameter for open-end armchair finite-length nanotubes.

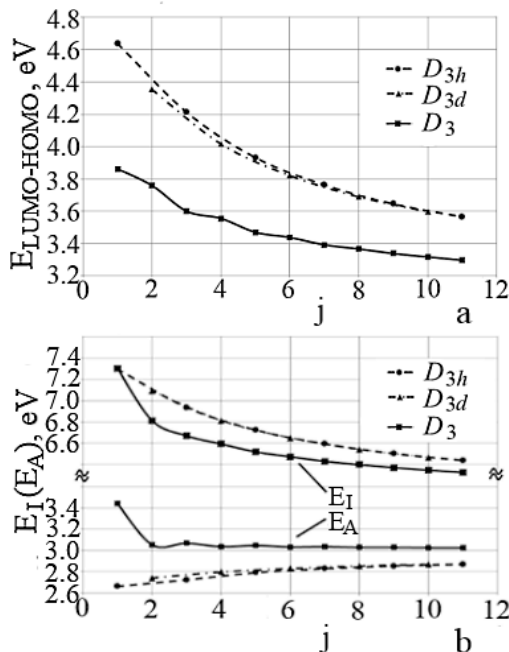


Fig. 7. Electronic structure of capped armchair SWCNT (0, 9) depending on its length: a) energy gap LUMO-HOMO; b) ionization potential (E_I) and electron affinity (E_A).

The calculation results shows that the electronic structure of the finite-length SWCNTs (5, 5) is determined mainly by the number of segments j but not by a mutual orientation of the caps. Using the investigation results of the influence of length on the electronic structure of the open-end armchair SWCNT family of different diameters, which were performed by Wang et. al [19], it can be stated that the oscillating dependence of fundamental parameters on length is typical for all open-ended and closed armchair nanotubes in the range of ultra-small diameters ($d < 2$ nm). With this aim, we calculated the energy gap LUMO-HOMO in the open-end finite-length armchair single-walled carbon nanotubes (chiralities ranging from (3, 3) to (15, 15) and lengths ranging from 2 to 20 segments) passivated by hydrogen. According to the obtained results, the open-end armchair nanotubes have non-zero $E_{\text{LUMO-HOMO}}$ with clear oscillation as a function of tube length (fig.6a). A magnitude of the energy gap decreases slightly with the diameter change.

The work function dependency on length and diameter is shown in fig. 6b. According to the obtained results, the work function grows with the length increase. The values lie in range from 3.3 to 4.3 eV.

C. Capped finite-length SWCNTs (0, 9)

Figure 7 shows a dependency of the energy gap $E_{\text{LUMO-HOMO}}$, ionization potential and electron affinity on the length of capped zigzag SWCNT (0, 9). The character of the change of the fundamental parameters is monotonic. The energy E_{LUMO} (E_{HOMO}) of nanotubes D_{3h} and D_{3d} symmetry are greater (less) than the same parameter of SWCNT of the D_3 symmetry (fig.7a). That is why $E_{\text{LUMO-HOMO}}$ of the last mentioned one is less. The electron affinity of the nanotubes of the D_{3h} and D_{3d} symmetry increases with increase of the j , but it decreases in case of the D_3 symmetry (fig.7b).

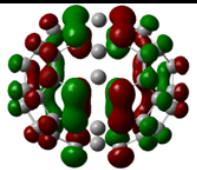
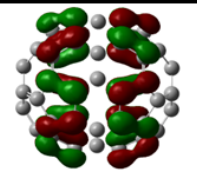
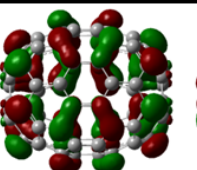
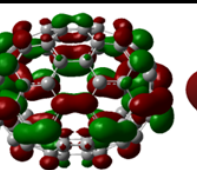
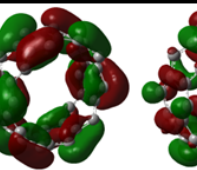
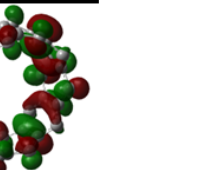
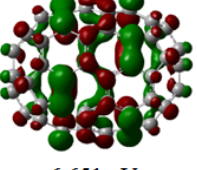
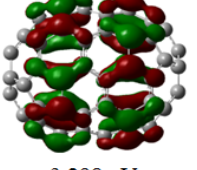
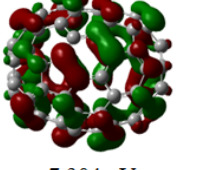
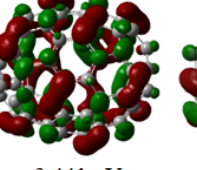
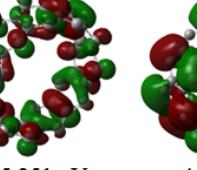
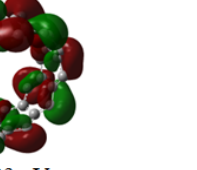
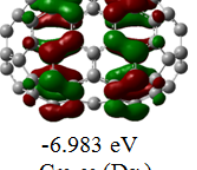
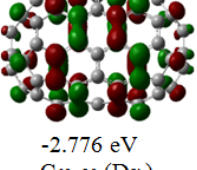
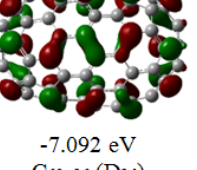
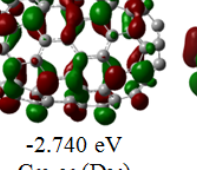
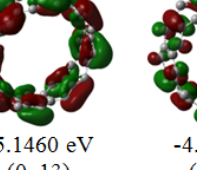
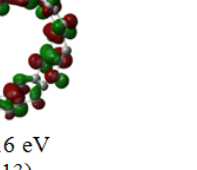
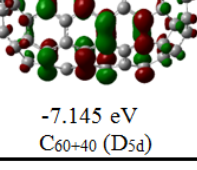
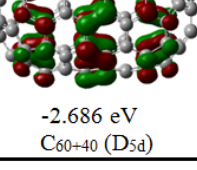
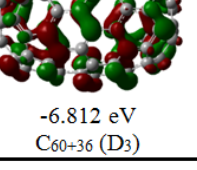
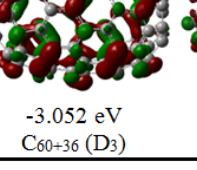
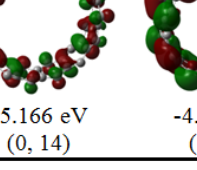
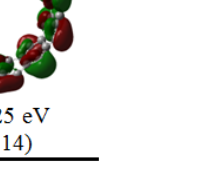
The investigation demonstrates that nanotubes of the D_{3h} and D_{3d} symmetry are more stable than SWCNTs of the D_3 symmetry with the exception of nanotube C_{60+18} . The obtained result is confirmed by the calculation of the standard enthalpy of the SWCNT (0, 9) formation which is reported in [20].

IV. DISCUSSION

A distribution of the electron density gives a pictorial presentation of the transformation of the σ , π and σ^* , π^* hybridized levels in the nanotubes of a ultra-small diameter. Table 1 gives a detailed description of the frontier orbitals electron density distribution of the finite-length SWCNTs (5, 5) and (0, 9) with $j \geq 1$ and infinite-length zigzag SWCNTs of (3k+1) and (3k+2) groups.

Firstly, let us consider the SWCNT (5, 5) with $j = 1$ and $j = 2$. Two segments in the equatorial region of C_{60+20} cause the highest occupied molecular orbital to be less stable than that of C_{60+10} . LUMO binds the two segments and the caps of C_{60+20} . Thus, the HOMO energy increases, and the LUMO energy decreases. This leads to decrease of the band gap. HOMO C_{60+30} is bonding for the first and the third segments. Binding nature of the C_{60+20} LUMO changes to the loosening one for C_{60+30} . Thus, the HOMO energy decreases while the LUMO

Table 1. Visualization of the electronic density distribution of low unoccupied (LUMO) and high occupied (HOMO) molecular orbitals of finite-length SWCNT (5, 5), (0,9) and low unoccupied (LUCO) and high occupied (HOCO) crystal orbital of infinite SWCNTs (0, 10), (0, 11), (0, 13), (0, 14) and (0, 16).

HOMO (5,5)	LUMO (5,5)	HOMO (0,9)	LUMO (0,9)	HOCO	LUCO
 -7.552 eV C ₆₀₊₁₀ (D _{5h})	 -2.685 eV C ₆₀₊₁₀ (D _{5h})	 -7.296 eV C ₆₀₊₁₈ (D _{3h})	 -2.660 eV C ₆₀₊₁₈ (D _{3h})	 -5.226 eV (0, 10)	 -4.471 eV (0, 10)
 -6.651 eV C ₆₀₊₂₀ (D _{5d})	 -3.298 eV C ₆₀₊₂₀ (D _{5d})	 -7.304 eV C ₆₀₊₁₈ (D ₃)	 -3.441 eV C ₆₀₊₁₈ (D ₃)	 -5.251 eV (0, 11)	 -4.293 eV (0, 11)
 -6.983 eV C ₆₀₊₃₀ (D _{5h})	 -2.776 eV C ₆₀₊₃₀ (D _{5h})	 -7.092 eV C ₆₀₊₃₆ (D _{3d})	 -2.740 eV C ₆₀₊₃₆ (D _{3d})	 -5.1460 eV (0, 13)	 -4.516 eV (0, 13)
 -7.145 eV C ₆₀₊₄₀ (D _{5d})	 -2.686 eV C ₆₀₊₄₀ (D _{5d})	 -6.812 eV C ₆₀₊₃₆ (D ₃)	 -3.052 eV C ₆₀₊₃₆ (D ₃)	 -5.166 eV (0, 14)	 -4.425 eV (0, 14)

energy increases and this leads to a larger band gap value. C₆₀₊₁₀, C₆₀₊₂₀ and C₆₀₊₃₀ are the first species of the (3p+1), (3p+2) and 3p groups and they have the maximal, minimal and average values of the band gap correspondingly (tab. 1). A distribution of the electronic density of the second species from (3p+1) group C₆₀₊₄₀ is similar to the distribution of C₆₀₊₁₀, with the main difference being an additional electronic density in the equatorial region. This addition slightly destabilizes HOMO and stabilizes LUMO, and, thus, the band gap is smaller than that of the C₆₀₊₁₀.

The electron density distribution of LUMO and HOMO capped finite-length SWCNTs (0, 9) depends mainly on symmetry. Increase of the number of segments makes HOMO destabilized along the nanotube axis, which causes a monotonic decrease of the gap LUMO-HOMO. There are two kinds of electronic density distribution in the infinite-length semiconducting zigzag SWCNTs. The first one is observed for HOCO/LUCO of (0, 3k+1)/(0, 3k+2) tubes. Local regions are destabilized by adjacent similar regions along both the axial and the radial directions of the tube. The second kind of the electronic density distribution is specific for LUCO/HOCO of SWCNTs (0, 3k+1)/(0, 3k+2). The orbitals mentioned are partially antibonding in the radial direction and are partially

bonding along the axis. The sequential change of the two kinds of the orbitals leads to a band gap oscillations in zigzag semiconducting SWCNTs with the diameter change.

The electron density distribution of the frontier orbitals depends on the diameter, length and symmetry of nanotubes. An external electric field can be used for electronic structure modulation. An application of the electric field leads to a charge redistribution and polarization of nanotubes. A strong electric field ($\epsilon > 0.1 \text{ V/\AA}$) deforms frontier orbitals and shifts their energy due to Stark effect [30], [31].

We calculated the electronic structure of capped SWCNTs (5,5) in the electric field of the strength 0-1 V/Å. The electric field was directed parallel to the nanotube axis.

Figure 7 clearly shows that the energy gap LUMO-HOMO decreases in the electric field as a quadratic function. The calculation reveals that the energy gap LUMO-HOMO $\Delta E_{\text{LUMO-HOMO}} = E_{\text{LUMO-HOMO}}(E=0) - E_{\text{LUMO-HOMO}}(E=1 \text{ V/\AA})$ decrease, which is caused by the electric field, depends on the length and type of a nanotube. For SWCNTs that are members of 3p+1, 3p и 3p+2 groups, $\Delta E_{\text{LUMO-HOMO}}$ possesses the maximum, average and minimal values, that corresponds with the previously introduced classification based on the calculations of the dependency of the gap LUMO-HOMO on a

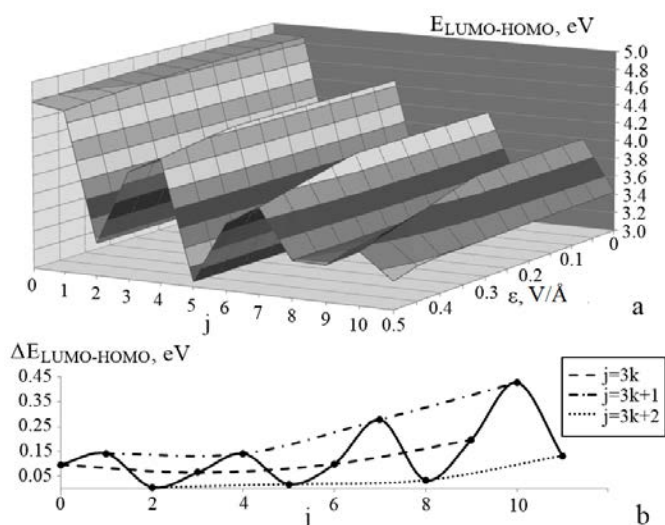


Fig. 8. Energy gap of the capped finite-length SWCNTs (5,5) under an applied electric field in the range from 0 to 0.5 V/Å (a) and energy gap tuning on the number of section j under an applied electric field $\varepsilon=0.5$ V/Å.

nanotube length. For each of the SWCNTs groups, the field decrease of the gap LUMO-HOMO is in square proportion to a nanotube length $\Delta E_{\text{LUMO-HOMO}} \sim l^2$.

V. CONCLUSION

We have investigated the electronic structure, band gap and work function of infinite- and finite length single-walled carbon nanotubes with diameters in range from 0.2 to 2.0 nm using the density functional theory. The dependence of the energy gap of SWCNTs in the range of ultra-small diameters is a function of $1/d^2$ rather than of $1/d$. The energy gap of infinite zigzag and capped finite-length SWCNT (5,5) shows clear oscillation on the diameter and length respectively. Mutual orientation of caps in the armchair nanotubes (5, 5) does not strongly affect their electronic structure, while in the case of the zigzag nanotubes (0, 9) difference in caps orientation may lead to difference in a band gap up to 1 eV. An applied electric field leads to the decreasing of the energy gap LUMO-HOMO of capped SWCNTs (5,5).

ACKNOWLEDGMENT

Special thanks to Galina Tuchina for the help and support.

REFERENCES

- [1] Q. Cao, S.-j. Han, G. S. Tulevski, Y. Zhu, D. D. Lu and W. Haensch "Arrays of single-walled carbon nanotubes with full surface coverage for high-performance electronics" *Nature Nanotech.*, vol. 8, pp. 180-186, 2013.
- [2] G. Szèchenyi and A. Pályi "Current hot spot in the spin-valley blockade in carbon nanotubes" *Phys. Rev. B*, vol. 88, pp. 235414 (8), 2013.
- [3] J. Klinovaja, M. J. Schmidt, Bernd Braunecker and D. Loss "Carbon nanotubes in electric and magnetic fields" *Phys. Rev. B*, vol. 84, pp. 085452 (22), 2011.
- [4] J. Tan, L. Jiang, L. He, H. Dong and W. Hu "Photovoltaic effect of individual polymer nanotube" *Appl. Phys. Lett.*, vol. 100, pp. 173902, 2012.
- [5] M. Ganzhorn, S. Klyatskaya, M. Ruben and W. Wernsdorfer "Strong spin-phonon coupling between a single-molecule magnet and a carbon nanotube nanoelectromechanical system" *Nature Nanotech.*, vol. 8, pp. 165-169, 2013.
- [6] N. A. Poklonski, S. V. Ratkevich, S. A. Vyrko, E. F. Kislyakov, O. N. Bubel, A. M. Popov, Y. E. Lozovik, N. N. Hieu, N. A. Viet "Structural phase transition and band gap of uniaxially deformed (6,0) carbon nanotube" *Chem. Phys. Lett.*, vol. 545, pp. 71-77, 2012.
- [7] C. T. White, D. H. Robertson and J.W. Mintmire "Helical and rotational symmetries of nanoscale graphitic tubules" *Phys. Rev. B*, vol. 47, pp. 5485-5488, 1993.
- [8] N. Hamada, S. Sawada and A. Oshiyama "New one-dimensional conductors: Graphitic microtubules" *Phys. Rev. Lett.*, vol. 68, pp. 1579-1581, 1992. 68 1579-81.
- [9] R. Saito, M. Fujita, G. Dresselhaus and M. Dresselhaus "Electronic structure of graphene tubules based on C_{60} " *Phys. Rev. B*, vol. 46, pp. 1804-1811, 1992.
- [10] R. Saito, M. Fujita, G. Dresselhaus and M. Dresselhaus "Electronic structure of chiral graphene tubules" *Appl. Phys. Lett.* vol. 60, pp. 2204-2206, 1992.
- [11] H. Yorikawa and S. Muramatsu "Electronic properties of semiconducting graphitic microtubules" *Phys. Rev. B*, vol. 50, pp. 12203-12206, 1994.
- [12] M. S. Dresselhaus, G. Dresselhaus and R. Saito "Physics of carbon nanotubes" *Carbon*, vol. 33, N. 7, pp. 883-891, 1995.
- [13] X. Blase, L. X. Benedict, E. L. Shirley and S. G. Louie "Hybridization effects and metallicity in small radius carbon nanotubes" *Phys. Rev. Lett.*, vol. 72, pp. 1878-1881, 1994.
- [14] T. W. Odom, J.-L. Huang, P. Kim and C. M. Lieber "Atomic structure and electronic properties of single-walled carbon nanotubes" *Nature*, vol. 391, pp. 62-64, 1998.
- [15] J. W. G. Wilder, L. C. Venema, A. G. Rinzler, R. E. Smalley and C. Dekker "Electronic structure of atomically resolved carbon nanotubes" *Nature*, vol. 391, pp. 59-62, 1998.
- [16] M. Ouyang, J.-L. Huang and C. M. Lieber "Fundamental electronic properties and applications of single-walled carbon nanotubes" *Acc. Chem. Res.*, vol. 35, pp. 1018-1025, 2002.
- [17] R. A. Jishi, J. Bragin and L. Lou "Electronic structure of short and long carbon nanotubes from first principles" *Phys. Rev. B*, vol. 59, pp. 9862-9865, 1999.
- [18] A. Rocherfort, D. R. Salahub and P. Avouris "Effects of finitlength on the electronic structure of carbon nanotubes" *J. Phys. Chem. B*, vol. 103, pp. 641-646, 1999.
- [19] B.-C. Wang, H.-W. Wang, I.-C. Lin, Y.-S. Lin, Y.-M. Chou and H.-L. Chiu "A semiempirical study of carbon nanotubes with finite tubular length and various tubular diameters" *J. Chin. Chem. Soc.*, vol. 50, pp. 939-945, 2003.
- [20] J. Cioslowski, N. Rao and D. Moncrieff "Electronic structure and energetics of [5,5] and [9,0] single-walled carbon nanotubes" *J. Am. Chem. Soc.*, vol. 124, pp. 8485-8489, 2002.
- [21] C.-P. Huang, W.-S. Su, C.-C. Su and M.-S. Ho.

“Characteristics of Si(111) surface with embedded C_{84} molecules” *RSC Adv.*, vol. 3, pp. 9234-9239, 2013.

[22] C. Kim and B. Kim B. “Electronic structures of capped carbon nanotubes under electric fields” *Phys. Rev. B*, vol. 65, pp. 165418(6), 2002.

[23] I. V. Hertel, H. Steger, J. de Vries, B. Weisser, C. Menzel, B. Kamke “Giant plasmon excitation in free C_{60} and C_{70} molecules studied by photoionization” *Phys. Rev. Lett.*, vol. 68, pp. 784-787, 1992.

[24] R. K. Yoo, B. Ruscic, J. Berkowitz “Vacuum ultraviolet photoionization mass spectrometric study of C_{60} ” *J. Chem. Phys.*, vol. 96, pp. 911-918, 1992.

[25] J. de Vries, H. Steger, B. Kamke, C. Menzel, B. Weisser, W. Kamke, I. V. Hertel “Single-photon ionization of C_{60}^- and C_{70}^- fullerene with synchrotron radiation: determination of the ionization potential of C_{60} ” *J. Chem. Phys. Lett.*, vol. 188, pp. 159-162, 1992.

[26] H. Steger, J. Holzapfel, A. Hielscher, W. Kamke, I. V. Hertel “Single-photon ionization of higher fullerenes C_{76} , C_{78} and C_{84} . Determination of ionization potentials” *J. Chem. Phys. Lett.*, vol. 234, pp. 455-459, 1995.

[27] C. Brink, L. H. Andersen, P. Hvelplund, D. Mathur, J. D. Voldstad “Laser photodetachment of C_{60}^- and C_{70}^- ions cooled in a storage ring” *J. Chem. Phys. Lett.*, vol. 233, pp. 52-56, 1995.

[28] X.-B. Wang, C.-F. Ding and L.-S. Wang “High resolution photoelectron spectroscopy of C_{60} ” *J. Chem. Phys.*, vol. 110, N. 17, pp. 8217-8220, 1999.

[29] <http://www.gaussian.com>

[30] Wehrli S., Koch E. and M. Sigrist. “Field doping of C_{60} crystals: Polarization and Stark splitting” *Phys. Rev B*, vol. 68, pp. 115412. **68**, 115412(14), 2003.

[31] A. Tuchin, L. Bityutskaya, E. Bormontov “The Quadratic Stark Effect in The Fullerene C_{60} ” *19th International Vacuum Congress*, Paris, pp. 1168, 2013.

Design of a training system for intrapedicular screw positioning in the lumbar region

Nataly A. Garcia, Daniel Lorias, Vicente Gonzalez, and Fernando Chico

Abstract— The main objective of this article is to develop a minimum invasion surgery simulator for the implantation of intrapedicular screws by using both, a model of the lumbar area, and a program that simulates the fluoroscope imagery. In addition to the teaching technique, this device will also allow to measure the surgeon's movement's metrics, and thus to evaluate her learning progress.

Keywords— intrapedicular needle; lumbar instrumentation; surgery minimally invasive; simulator

I. INTRODUCTION

LUMBAR region illnesses are very common among those in labor age, with a prevalence of 53% [1] among this group of people. As a result different procedures have been developed for their treatments that vary according to the severity and pathology of the problem. For some maladies such as scoliosis, trauma, and nerve compression [2], spine instrumentation is used as a form of treatment [3]. There are many kinds of spine instrumentation that vary according to the affected area and the provider's preferences [4]. One of these kinds of spine instrumentation is the implantation of interpedicular screws that represents an advantage due to a better fixation on Pull out tests [5]. The collocation of these screws generally comes from the back, around the lumbar vertebrae (low back). The exact technique to implant these screws depends on the surgeons' preferences and abilities.

A recent technique for interpedicular nail implantation is by a minimum invasion surgery. This technique is recommended because of the benefits it represents, a small incision during surgery, and shorter recovery time among others [6]. In order to perform this surgery the physician should use a fluoroscope to observe the exact path of the entrant needle on the lumbar vertebra and later to implant the screw. The use of a fluoroscope means radiation exposure to the patient and to the provider, and a high exposure will result in health consequences [7].

This work was supported by the Research and Advanced Studies Center of IPN (CINVESTAV).

N. A. Garcia is with the Bioelectronic Section of Electrical Engineering Department, Research and Advanced Studies Center of IPN, Mexico DF, CO 06360 MEX (phone: +521-5528844297; e-mail: garciam@cinvestav.mx).

D. Lorias, is with the Bioelectronic Section of Electrical Engineering Department, Research and Advanced Studies Center of IPN, Mexico DF, CO 06360 MEX (e-mail: dlorias@cinvestav.mx).

V. Gonzales is with Neurosurgery Department, Federico Gómez Pediatric Hospital of Mexico, Mexico DF, CO 06720 MEX, (e-mail: drvicentegonzalez@me.com).

Minimum invasion surgery training is needed in order to minimize radiation exposure and to improve physician's performance [8]. Current training techniques in the matter require the use of animals and death subjects, which is a problem because of its cost and its shortage; moreover the physician in training has to use a fluoroscope, which represents exposure to radiation. As a result many simulators have been developed since the 70's. Some examples of these simulators are the Greengrocer Model, which only presents the way an insertion is made [9], the Lumbar Spine Surgery MIS-Model, by CREAPLAST [10], which allow the practitioner to have anatomic references, the Bristol Epidural Simulator, a computer-based simulator that emulates the tissue resistance to a needle [9], and those that integrate anatomical landmarks with the use of a software developed by Vortex [11].

Despite the early use of these lumbar area simulators, there is no record of the metric of the movements realized during the collocation of intrapedicular screws procedures, and of the exact movements required for a successful procedure [12].

II. METHOD

The device proposed in this project is planning on incorporate: a model with anatomic marks to allow the surgeon to locate the anatomic structures as he normally would do during surgery, surgical instrumental similar to the one use in surgery that will permit to measure the metrics, and computer software that in addition to process information obtained through sensors, will also function as an interphase with the surgeon allowing for visual feedback simulating the fluoroscope imagery.

The system will focus on the needle insertion process to collocate interpedicular screws on the lumbar area; at the moment this process used a model of an adult spine. In order to measure the metric of the movements, a two-camera system is used to register the needle's movements and to develop a 3D projection

A. Instrument used

To make the preliminary trials we used a metal platform in a box shape with the following dimensions: 35 cm width, 30 cm of length, and 18 cm of height. On the top of the platform, we established an insertion zone that consists on a quarter of circle with a radio of 18 cm; this allows for a natural surgical movement. Inside of the platform there are located two cameras on the X and Y planes with a similar visual field.

These cameras are connected to a computer and will digitalize the image of the nail in order to register its movement (Fig. 1). The system uses a lighting structure made of a strip of high luminosity LED's to maintain the light stable, and to make the system environmentally-light independent.

We also use a needle with color marks to follow the path of the needle (Fig. 2).

B. Image Digitalization

In order to perform the imagery digitalization, two Microsoft LifeCam HD-500 cameras were connected to the computer through USB ports. The image is got using MatLab and the image acquisition toolbox. The images was obtained in RGB format. Once that the images were captured we obtained the profile of the markers to establish the threshold needed to perform a color based filter.

C. Image Filtration Figures

Once that the saturation color profile of the image was obtained, we found that the markers have a RGB value, for the marker blue we got $R < 80$, $G < 140$ and $B > 140$, for marker red we got $R > 150$, $G < 100$ and $B < 100$. Later we made two copies of the image, in the first copy we delete all the pixels with a saturation color outside the range of the red marker, and in the second copy we delete all the pixels with a saturation color outside the range of the blue marker. To accomplish that, the image is filtered by the next equation (1).

$$y = \begin{cases} 255 & u > x \\ 0 & u < x \end{cases} \quad (1)$$

Where 'y' is the new pixel value, 'x' is the original pixel value and 'u' is the threshold established by the color profile of the image

D. Metrics Calculation

Angle calculation: To measure this metric we used the image with only blue components. In order to reduce the noise in the image we use a dilation and erosion process. Once that the possible noise is removed we transform it to a binary image. Only then we use the Hough transformation [13] which constructs a parametric space containing all the parameter

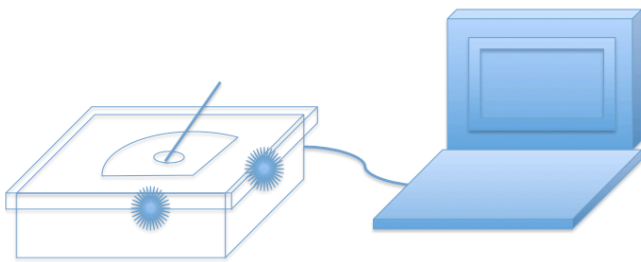


Fig.1: Preliminary model that provides a platform for the cameras and an insertion zone, also allows the connection with a computer for analyze the movements of the needle

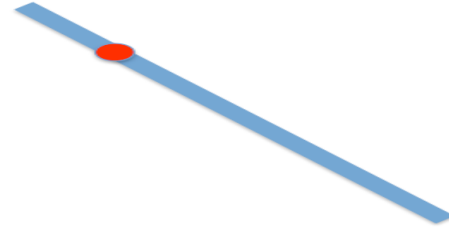


Fig2: instrument used to make the simulation of the needle; it uses colors that software will recognize as marks (red and blue)

combinations characterizing Equation (2)

Once that the parametric field was obtained, a system based on votes allows us to obtain the parameters with the highest number of votes, transforming them into values that better describe the desired equation to find the needle path.

$$\rho = x * \cos(\theta) + y * \sin(\theta) \quad (2)$$

This is the equation is used to find the parametric field, where ρ is the value of a parameter that takes the values of $0, \Delta\rho, 2\Delta\rho \dots S$, where S is the size of the image, 'x' and 'y' are the variables of the equation line and θ that takes the values of $0, \Delta\theta, 2\Delta\theta \dots 360^\circ$

We use the dot product definition to get the angle. Since the dot product needs two vectors, first we estimate the one corresponding to the base of the needle insertion and we fix this line it in the program.

$$\alpha = \cos^{-1} \frac{a \cdot b}{|a||b|} \quad (3)$$

Where α is the angle of interest, 'a' is the estimated from Equation 2 and 'b' is the previously fixed needle insertion vector [14].

Distance calculation: in this case we look for the red marker in the needle. We used the image with only the red components; again we process the image with a dilation and erosion operation in order to reduce noise. Once that the possible noise is gone we transform it into a binary image. Hence we compute the centroid of the red marker to obtain a single point. Later we used the Euclidian equation (4) to calculate the distance (in pixels) between the insertion point and the mark [15].

Notice that the point of insertion remains unchanged, thus we calculate and fixed the centroid coordinates in the program. Finally we match the estimated distance in pixels to centimeters using Excel's linear regression.

$$d = \sqrt{(x_2 - x_1)^2 + (y_2 - y_1)^2} \quad (4)$$

Where 'd' corresponds to the distance between the insertion

point and the mark on the needle, x_2 and y_2 are the coordinates for the insertion point and x_1 and y_1 are the coordinates for the mark.

Associated Metrics to other Variables Calculations: once we could measure the angle and the distance, it is possible to quantify others metrics such as velocity and acceleration (5)(6).

$$v = dx \quad (5)$$

$$a = dv \quad (6)$$

Where 'v' belongs to velocity and can be obtained as the first derivative of the distance with respect to time and 'a' corresponds to acceleration that corresponds to the first derivative of velocity with respect to time.

These results will allow us to evaluate not only the movement being made, but also its characteristics, providing us with valuable information to evaluate a surgeon's skills.

E. Matching the two cameras to get XY Plane

The needle is capable of tri-dimensional movement in the space corresponding to the insertion area of the previously described platform. As a result the recording-camera system was placed in a way that the planes XZ and YZ can be recorded to permit a 3D reconstruction of the movement.

It is important to mention that the surgeon has a visual feedback in only two dimensions, lateral and posterior views are generally used. Lateral view is obtained from the XY plane; however, in order to obtain the posterior view the XZ plane is needed, we can calculate this plane with the previously mentioned 3D reconstruction.

Since both cameras have the same visual field, we assume the Z coordinates to be the same for both images to construct the XY plane using only the X and Y coordinates. Notice that the insertion point is assumed to remain fixed, as a result its coordinates are calculated first. Once the centroid of the red marker is obtained, we calculate the needle vector. Finally extracorporeal distance and area are computed using the algorithms previously described.

F. Display of the visual feedback

The visual feedback is made with an image of a lumbar model. First the image was characterized using circular tags, we found that 24.8 pixels is equivalent to 5 mm. Once the

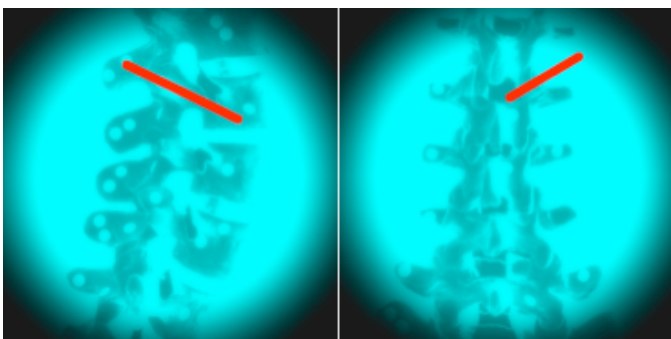


Fig.3: Image shown in the graphic interface if the lateral and posteroanterior view with the projection of the needle getting into the pedicle

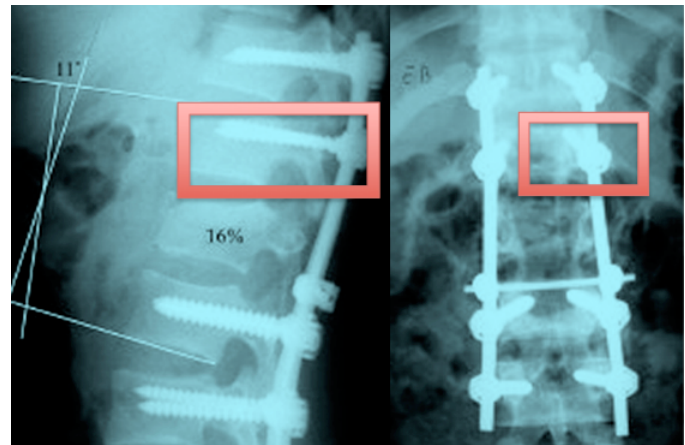


Fig.4: Example of a column with intrapedicular screw placed in a successful way.

image was obtained the color was changed as to give the appearance of fluoroscopy imagery. When this image is displayed, the line representing the needle is also drawn (Fig. 3). This is made using the extracorporeal parameters.

To calculate the intra-corporeal distance, we subtract the extracorporeal distance from the total distance. To compute the angle we simply consider the complementary angle.

With this information we can trace the segment of the line representing the needle, as a result we obtain a good approximation of what is shown on the fluoroscope during a real procedure. The training technique will require the user to try and to put the needle in the place that corresponds to the intrapedicular screw. (Fig. 4)

III. RESULTS

To the moment, the platform and the instrument with colors allow us to measure a minimum intra corporeal distance of 5 cm and angles ranging from 35° to 90° in both sides of the insertion point. The image is refresh every 0.7 seconds, from the moment that the image is obtained to the moment that the metrics and the needle projection are displayed. Data and images are displayed using a graphic interphase on MatLab.

To evaluate the mechanism's precision to measure distances, we estimated a variation coefficient (7) for distances ranging from 5cm to 12cm of intra corporeal length. The variation coefficients are shown in Table 1.

$$CV = (A/B) * 100 \quad (7)$$

Where 'CV' is the variation coefficient, 'A' is the standard deviation and 'B' is the average of the acquired data.

IV. DISCUSSION AND CONCLUSIONS

We design a preliminary system that allows for the simulation of a needle insertion on a model of the lumbar vertebrae to position intrapedicular screws. The platform and

TABLE I
VARIATION COEFFICIENTS (CV)

Distance (cm)	Variation Coefficient
1	0.49
2	0.48
3	0.14
4	0.53
5	0.28
6	0.24
7	0.34

^a It is shown that the CV does not depend on distance

the software used, allowed us to register and record the metrics and to provide visual feedback simulating the visual imagery proper to a fluoroscope.

The refresh time of the system is 0.7 seconds, however this is a consequence of the resolution of the camera, which is 1200x800 pixels. This system could also use cameras with a lower resolution, as a result, the data of the images that need to be processed would decrease, thus reducing the required processing time. This will result in smaller refreshing times and a more video-like fluid movements.

The system currently uses color markers for instrument recognition. Because of the format in which the image is obtained, we have variations on the pixel information resulting from extreme environmental light changes, even when the LED's lighting of system tries to keep the light constant.

Future work should consider the use of pressure sensors on the instruments being used to measure the resistance of the tissue to the needle and the strength needed for insertion into the pedicle.

The platform used for this work does not have any anatomic references, however it is intended to improve this platform to integrate such references as well as textures and materials simulating tissue.

The results and the metrics obtained have a variation coefficient that decreases along with the intra corporeal distances, resulting from the system evaluating and measuring extracorporeal information from the camera. These results can vary depending on the camera resolution and the environmental light.

The preliminary characteristics of the system are listed in Table 2.

ACKNOWLEDGMENT

We thank to CONACYT, CINVSTAV and Federico Gomez Pediatric Hospital for give us the chance of develop this project.

REFERENCES

- [1] Clinica MEDS. (2011, Septiembre 13). *Dolor Lumbar (Espalda)*. Retrieved Octubre 30, 2013, from <http://www.meds.cl/lesiones-y-enfermedades/articulo/dolor-lumbar-espalda>
- [2] P. C. A. J. Vroomen, M. C. (1999, Marzo 17). *Diagnostic value of history and physical examination in patients suspected of sciatica due to*

TABLE II
TECHNICS ESPECIFICACIONES

Characteristics	Value
Image refresh	0.7 s
Size of the obtained image	800x1280 pixels
Size of the image shown	720x720 pixels
Views	Lateral and anterior
Angle range	35° a 90°
Maximum Extracorporeal Distance	7 cm
Minimum Extracorporeal Distance	1 cm
Maximum Intracorporeal Distance	11 cm
Minimum Intracorporeal Distance	5 cm
CV Average in distance	0.36

- disc herniation: a systematic review*. Retrieved Noviembre 5, 2013, from <http://link.springer.com/article/10.1007/s004150050480#page-1>
- [3] Gil, J. A. (2012, Diciembre 10). *Patología Lumbar*. Retrieved Octubre 28, 2013, from Comentarios Medicos.com: <http://comentariosmedicos.com/documentos/PatologiaLumbar.pdf>
 - [4] Daniel H. Kim, A. R. (2005). *Spinal Instrumentation: Surgical Techniques*. Stuttgart: Thieme
 - [5] Jean-Raymond, M. (1995). *Patent No. 6132464*. United States.
 - [6] C. Moncerrat, e. a. (2004). Estado del Arte en Simulación Quirúrgica. *Informática y Salud*, (47).
 - [7] FDA. (2009, Junio 08). *Radiation-Emitting Products*. Retrieved octubre 2013, 18, from Medical X-ray imaging: <http://www.fda.gov/radiation-emittingproducts/radiationemittingproductsandprocedures/medicalimaging/medicalx-rays/ucml15329.htm>
 - [8] D. Lorias, e. a. (2010, Noviembre). Computer System for the Evaluation of Laparoscopic Skills. *DOI 10.1109*.
 - [9] Neil Vaughana, V. N. (2012, Mayo 24). A review of epidural simulators: Where are we today? . *Medical Engineering & Physics* , 2258-2274.
 - [10] CREAPLAST. (2010). *LUMBAR SPINE SURGERY SIMULATOR*. Retrieved Noviembre 10, 2013, from <http://www.creaplast.eu/lumbar-spine-surgery-simulator--prd2-fp.php>
 - [11] CM LABS. (n.d.). *Vortex VxMaster*. Retrieved Noviembre 20, 2013, from <http://www.cm-labs.com/market/construction/products/vortex-vxmaster>
 - [12] Fuster, S., A., V., Barrios, G., Urdaneta, I., Ojeda, O., Macchia, M., et al. (2010). *Fiabilidad del navegador en la colocación de tornillos pediculares toracolumbares*. Retrieved Noviembre 8, 2013, from Elsevier: http://apps.elsevier.es/watermark/ctl_servlet? f=10&pident articulo=90138755&pident_usuario=0&pcontactid=&pident_revista=340&ty=38&accion=L&origen=neurocirugia&web=http://www.revistaneurocirugia.com&lan=es&fichero=340v21n04a90138755pdf001.pdf
 - [13] Xiaohui Chen, X. L. (2010). A sub peak tracker based Hough transform for accurate and robust linear edge extraction. *International Conferende on Electrical and Control Engineering* (pp. 288-291). ICECE'10.
 - [14] Serway, R. A., & Jewett, J. W. (2013). *Physics for Scientists and Engineers*. USA: Brooks Cole Pub Co.
 - [15] Patricia, J., Ana, L., Carmen, R., & Manuel, G. (2007). *Geometría Analítica*. México: Umbral.

Dose profile variation with pitch in head CT scans using gafchromic films

Mourão A. P., Gonçalves Jr R. G. and Alonso T. C.

Abstract - Exposures arising from computed tomography examinations cause higher doses than those caused by other modalities for diagnostic radiology using attenuation of X-ray beams. Technological advances have increased the clinical applications of X-ray computed tomography (CT). Dose reduction strategies are difficult to implement because of a lack of guidance on the examination of CT scanning. However, the technique offers the possibility of adjustment of the CT scanner operating parameters of according to the patient's physical profile and diagnostic application for which the scan is intended. Among various parameters that are common to the TC protocols (kV, mA, tube time, etc) the pitch is responsible for significant variation of patient's dose. In this work was used a PMMA head phantom to observe the dose variation for different pitch values (0.8, 1.0 and 1.5) keeping the other protocol parameters constant. Radiochromic films were used for the registry of dose variation on the peripheral and in central region of PMMA phantom to each one of the scans. The films were used to record the dose profiles and they were calibrated for a pencil ionization chamber, in particular experiment for this purpose. The records of the films were converted to digital images and these were worked to obtain the various degrees of darkening caused by energy deposition. After the treatment of irradiated films were obtained the longitudinal profiles of dose. The results showed the dose dependence of the pitch values.

Keywords – Computed tomography, Dosimetry, X-ray radiation, CT Protocol.

I. INTRODUCTION

The technology of the computed tomography (CT) scanner has a great development since the early 1970s. This evolution to the helicoidal acquisition data, multi-detector row (MDCT) has revolutionized the role of imaging in medical diagnosis. State of the art CT scanners are able to provide diagnostic, artifact free, whole body scans from head to toe in less than 5 s. These CT scans provide in vivo images that have similar information content to visual inspection at gross anatomic

dissection. The scans can be quickly obtained with minimal patient preparation in essentially all body types and clinical situations. There are minimal restrictions imposed by implanted medical devices or medical monitoring equipment. Finally CT is well accepted by patients and referring clinicians since examinations require minimal patient co-operation, have minimal discomfort and are usually highly accurate. These conditions promotes a significant increase in the number of computed tomography (CT) examinations. [1]

Standards for dosimetry in radiology were launched during the Conference of Malaga, in 2001, aimed at the radiation protection of patients undergoing diagnostic examinations or therapy, both in radiotherapy, radiodiagnostic and nuclear medicine. Use of ionizing radiation in medicine has grown due to the benefits associated with it and its technological development, such as the application of new radiopharmaceuticals, the digital radiographic images and the new generations of scanners [2].

Currently, computed tomography (CT) scanners used in radiodiagnostic services are from third generation. There are several factors that differentiate them, such as the axial (conventional), helical and helical multislice scans, the variety of manufacturers, different X-ray tube powers, tube current and tube time values. Each service, regardless of the type of scanner used, adopts its own protocol, and this is the principal reason differences exist between the image acquisition protocols [3].

Many countries have introduced in their legislation the obligation to report the doses imparted to patients undergoing radiodiagnostic examinations. Brazilian legislation established diagnostic reference levels (DRLs) only in terms of the multi-slice average dose (MSAD) of 50 mGy for the head, 35 mGy for the lumbar spine and 25 mGy for the abdomen/chest in a typical adult patient [4].

As part of an optimization program, DRLs should be used for quality control of CT scanners to review and adjust procedures and techniques when doses exceed the specified values, Brazil (1998). DRL values were adopted from international recommendations, IAEA (1996), and they may not represent the actual conditions of Brazilian examinations [5].

In the Minas Gerais state, quality control CT tests have been mandatory since July 1, 2009, but a better understanding of the methodology to perform such tests is still needed. In this work,

A. P. Mourão is with the Minas Gerais Federal Technological Center, Brazil (corresponding author to provide e-mail: aprata@des.cefetmg.br).

R. L. Gonçalves Jr., was with Minas Gerais Federal University, Nuclear Engineering Dpto. (e-mail: juniorgonc@gmail.com:).

T. C. Alonso is with the University of Colorado, Boulder (e-mail: alonso@cdtn.br).

experimental measurements in a PMMA head CT dosimetry phantom with radiochromic films were performed to obtain dose profiles generated by a CT scanner. Irradiations were performed using an image protocols for an adult head.

II. MATERIALS AN METHODS

The experiment to observe the dose profile variation was conducted in a Toshiba Aquilion CT scanner and using the clinical protocol defined for head scans. Scan parameters are shown in Table 1. A head phantom was utilized to position a pencil ionizing chamber and radiochromic film strips.

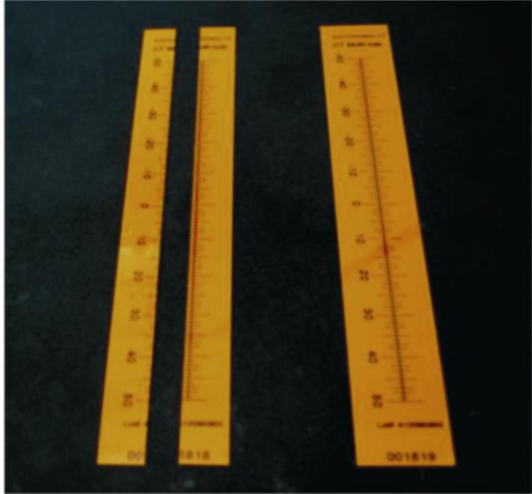


Fig. 1. Radiochromic film strips.

Measurements were performed using GAFCHROMIC XR-CT radiochromic film strips (Fig. 1) [7, 8].

TABLE 1
CT Scan Parameters

Voltage (kV)	Time mAs	Time (s)	Thickness beam (mm)
135	150	1.5	10



Fig. 2. Pencil ionization chamber.

The head phantom is a PMMA cylinder with a diameter of 160 mm and length of 150 mm. The PMMA cylinder contains five parallel probe holes, one in the center and four around the perimeter, 90° apart and 10 mm from the edge. These holes are used for a pencil ionization chamber placement. The Figure 2 shows a image of the pencil ionization chamber. The inside diameter of the holes is 12.67 mm. This head phantom includes five acrylic sticks for plugging all the holes in the phantom, and it is specifically applicable to CT systems [8, 9].

Figure 3 shows as design of the PMMA head phantom with

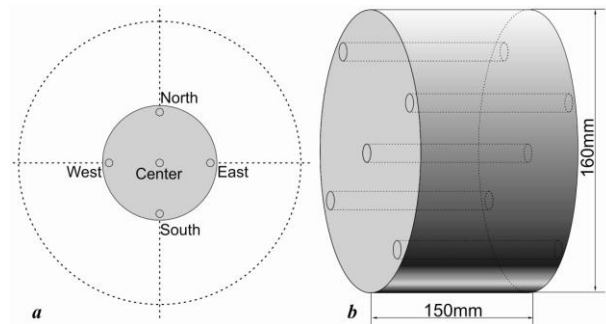


Fig. 3. PMMA head phantom.

its peripheral holes denoted as North, South, East and West. The Fig. 4 shows a diagram phantom sticks developed to accommodate the film strips. After charge the strips the sticks are charged in the head phantom holes.

This work investigated the deposited in a PMMA cylindrical

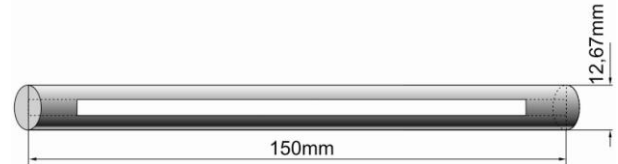


Fig. 4. Radiochromic film in the PMMA stick.

head phantom that had been subjected to three scans. Three CT scanning protocols were used with two different pitch values: 8.8, 1.0 and 1.5. The phantom volume was irradiated and radiochromic films were employed to record dose profiles. Measurements were performed with a calibrated pencil ionization chamber, which was positioned in the center and in four peripheral bores of the head PMMA phantom, to calibrate the radiochromicfilms. The central slice was then irradiated. This procedure allowed finding of the conversion factors to obtain dose values recorded in the films.

Metrological reliability of the radiochromic films was demonstrated through homogeneity and repeatability tests and by calibrating it in a reference radiation for CT (RQT9) that were reproduced in the Calibration Laboratory of the Development Center of Nuclear Technology (CDTN/CNEN). For the calibration, the film strips were positioned in the phantom holes to reproduce the position of the ionization chamber [9]. Optical alignment aids were used to place the phantom in the CT scanner isocenter. A scout was made to check position of the phantom and to demarcate the region where the irradiation was to be performed. A single axial

rotation of the scanner was selected, and the central slice of the phantom was irradiated several times using the protocols for an adult head (Table 1).

To record dose profiles, new radiochromic film strips were inside the PMMA phantom, and the phantom was scanned (15cm length) using protocol defined in the Table 1, changing the pitch. The film strips were used to record the dose of 10 cm in the central region of the phantom. The exposed films were digitized using a HP Photosmart C4480 reflective-type scanner. The scanning parameters used were RGB mode (48-bit) and 300 ppi. The red channel was selected for calibration and measurement because these radiochromic films have a main absorption peak in the red region of the visible spectrum (636 nm)[6].

III. RESULTS

All the measurements were converted to dose in PMMA with the air to PMMA attenuation coefficient ratio equal to 1.0682 [10]. The radiochromic films had homogeneity of 6.9% and a repeatability of 4.3%. Their calibration factors were obtained using dose recorded by the ionization chamber (mGy) and radiochromic films (grayscale). Table 2 presents radiochromic film calibration factors obtained.

TABLE 2
CT Scan Parameters

Mesures	North	South	East	West	Center
Grayscale	99.89	87.05	88.92	94.07	98.61
Dose (mGy)	65.71	50.73	55.01	61.25	52.65
Conversion factor (mGy.grayscale ⁻¹)	0.658	0.583	0.619	0.651	0.534

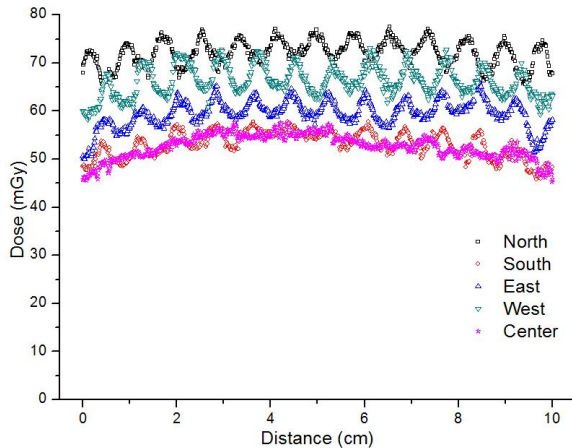


Fig. 5 Dose variation profile for pitch equal to 0.8.

The calibration factors used were 0.534 mGy.grayscale⁻¹ for the central region and 0.628 mGy.grayscale⁻¹ for the peripheral region. Dose profiles along the longitudinal axis in the five phantom holes for pitch equal to 0.8 are shown in Fig. 5.

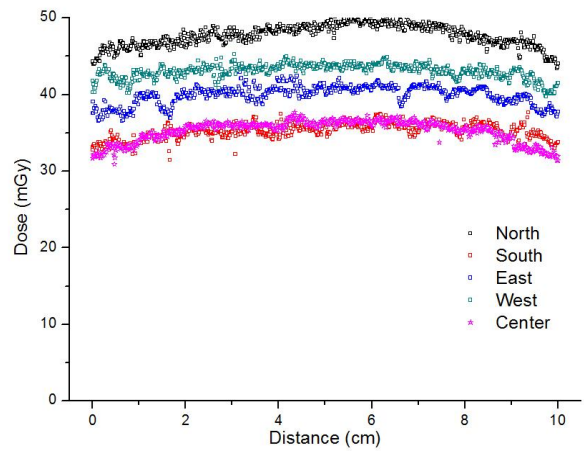


Fig. 6. Dose variation profile for pitch equal to 1.0.

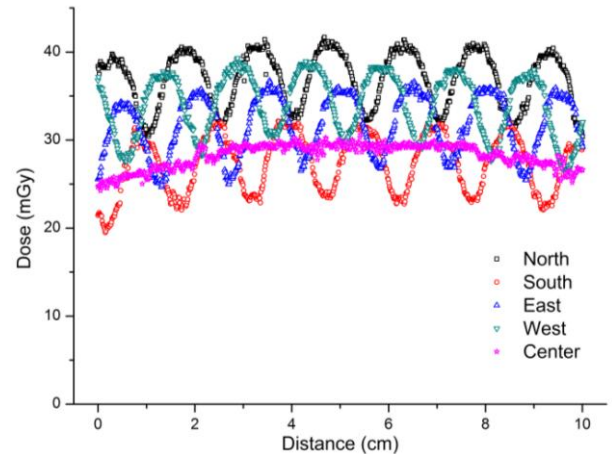


Fig. 7. Dose variation profile for pitch equal to 1.5.

Dose profiles along the longitudinal axis in the five phantom holes for pitch equal to 1.0 are shown in Fig. 6 and the Fig. 7 show the Dose profiles for pitch equal to 1.5. The average dose values (MSAD) obtained with the three scans, are shown in the Table 3.

TABLE 3
Absorbed Dose (mGy)

Pitch		North	South	East	West	Center
0.8	Average	72.03	53.05	59.54	66.22	52.57
	SD	2.64	2.74	2.81	3.14	2.52
1.0	Average	47.66	35.23	39.92	43.01	35.24
	SD	1.39	1.04	1.23	0.94	1.43
1.5	Average	36.97	27.38	31.84	33.99	28.23
	SD	3.10	3.32	3.33	3.49	1.37

IV. DISCUSSION

By analyzing the PMMA cylinders, dose profiles in the five phantom regions were recorded, and the maximum values were found at the midpoint of the axis due to the significant contribution of scattered radiation generated in the scans.

The peripheral region of the phantom showed higher dose values than those of the central region for scans with both

voltage values: approximately 31% higher for scanning with 120 kV and 25% higher with 100 kV. This result occurs due to the beam filtration at the central region which receives the X-ray beam with a higher attenuation than the peripheral.

The peripheral region of the phantom showed higher dose values than those of the central region for scans with both voltage values: approximately 31% higher for scanning with 120 kV and 25% higher with 100 kV. This result occurs due to the beam filtration at the central region which receives the X-ray beam with a higher attenuation than the peripheral.

Doses recorded at the highest voltage are significantly higher: approximately 50% higher in the peripheral region and 40% higher in the central region. A longitudinal variation could be observed, and the maximum dose was recorded at the peripheral region at the midpoint of the longitudinal axis. The MSAD values are in accordance with the DRL of 25 mGy established by Brazilian legislation for both protocols. The use of a pitch value of approximately 1 did not generate oscillations in the peripheral recorded dose profile [11].

V. CONCLUSIONS

Results obtained with the two protocols allowed for observation of the dose variation in the PMMA head phantom and the dose variation with the voltage. Pencil ionization chambers have some advantages for dose measurements such as easy handling, the possibility of reuse, an acceptable uncertainty (~4.3%) and its adoption in international procedures. Its disadvantage is the high cost. Radiochromic films showed some advantages such as a continuous output, easy handling and acceptable uncertainty (~5.2%). They seemed to be suitable for quality control measurements of CT scanners, although they are expensive and not reusable. Considering that radiochromic films have not been used for dosimetry in radiology in Brazil, this work contributes to the dissemination of proper procedure to hospitals and radiologists for MASD calculations from CT dose profiles measured with radiochromic films.

REFERENCES

- [1] Y. Thakur, P. D. McLaughlin and J. R. Mayo, "Strategies for Radiation Dose Optimization," *Curr Radiol Rep*, vol. 1, 2013, pp. 1–10.
- [2] IAEA - International Atomic Energy Agency, *Dosimetry in diagnostic radiology: an international code of practice*. TRS Serie 457, Vienna. 2007.
- [3] A. P. Mourão, *Computed tomography: Technologies & aplicações*. Difusão. São Paulo. 2007. ISBN: 978-85-88489-97-4 [in Portuguese].
- [4] Brazil, 1998. *Radiological Protection Directives for Medical and Dental Radiodiagnostic*. Portaria 453, Brasília, DF, [in Portuguese].
- [5] IAEA - International Atomic Energy Agency, *International basic safety standards for protection against ionizing radiation and for safety of radiation sources*. Safety Series, 115, Vienna. 1996.
- [6] ISP - International specialty products, 2010. *Gafchromic XR catalogue*. 8p.
- [7] AAPM - American Association of Physicists in Medicine, 1998. *Radiochromic film dosimetry: AAPM Report 63*. Med. Phys. 25, pp. 2093-2115.
- [8] O. Rampado, E. Garelli and Ropolo, R., "Computed tomography dose measurements with radiochromic films and a flatbed scanner," *Med. Phys.*, vol. 37, 2010, pp. 189-196.

- [9] A. P. Mourão, T. C. Alonso and T. A. DaSilva, T.A. "Study of the CT peripheral dose variation in a head phantom," *Int. Nucl. Atl. Conf. - INAC 2009*. Rio de Janeiro. 2009. ISBN: 978-85-99141-03-8.
- [10] NIST - National Institute of Standards and Technology, at <http://www.nist.gov/pml/data/xraycoef/index.cfm>. - Access 15 Oct. 2011
- [11] B. B. Oliveira, A. P. Mourão and T. A. DaSilva, "Kerma profile measurements in CT chest scans: a comparison of methodologies," *World Acad. Sci. Eng. Technol.*, vol. 80, 2011, pp 88-91.

Cell Nuclei Classification in HE-stained Biopsy Images

C. Atupelage*, H. Nagahashi*, M. Yamaguchi†, F. Kimura†, T. Abe*†, A. Hashiguchi*† M. Sakamoto*†

*Imaging Science and Engineering Laboratory,

†Global Scientific Information and Computing Center,

Tokyo Institute of Technology, Japan.

*†Department of Pathology, School of Medicine, Keio University, Japan.

Abstract—Pathological diagnoses are based on visual characteristics of tissues. According to the symptoms of patients, pathologists manually localize particular type of cells and analyze their structural changes and diagnose disease and its stage. Generally, cells are identified based on the characteristics of nuclei. Subsequently, pathologists investigate the structures of neighboring tissue components for further verification. In fact, a nucleus contains substantial discriminative characteristics compared with other tissue components.

This paper proposes a methodology to classify cell nuclei by observing their textural and morphological characteristics. In particular, we segment every nucleus by using a supervised segmentation method and extract nuclear characteristics for classifying five classes of cell nuclei such as liver, fibrocytes, lymphocytes, endothelial, and histiocytes. Texture of the nuclei is observed by multifractal computation based textural feature extraction method. Morphological features are computed using the properties of nuclear contours. The results indicated that the proposed method is significant for classifying cell nuclei, in which we obtained over 85% classification accuracy for five classes of nuclei.

Index Terms—Nuclei classification, Cell nuclear features, Multifractal computation, Feature descriptor, HE-stained specimens

I. INTRODUCTION

Cell classification plays an important role in pathological examination. Observations of the structural changes of the cells helps a pathologist to understand the disease and its grade. In addition, specific structural changes of particular cells indicate specific disease. For example, neoplastic liver cells are utilized for grading of hepatocellular carcinoma (HCC); lymphocyte are used to investigate the viral hepatitis; structures of collagen fiber and fibrocytes describes the degree of functional damages in the liver; histiocytes and endothelial cells are important to locate sinusoids (sinusoids are used to investigate the cancer cell structures and differentiation).

Generally, HE-stained specimens show the nuclei in purplish blue and other tissue component such as cytoplasm in pinkish red. Pathologists mainly observe the nuclei and surrounding tissue components such as cytoplasm and sinusoid to distinguish different cells. Pathological observations of five different types of cells are summarized¹ in Table I [1]. Manual

examination of cells or cellular components in a large image is inefficient. In addition the result may be depend on the experience of the pathologist. Therefore, it is necessary to utilize computational methods to improve the efficiency and consistency of cell classification. From computational medical image analysis point of view, nuclei can be segmented by using supervised or non-supervised methods. However, it is hard to segment the cells, because of the chaotic texture of cytoplasm and inconsistent appearance of cell membranes. In literature, very less number of studies have been reported for cellular or nuclei classification in microscopic images [2], [3].

It is reasonable to assume that a nucleus contains enough discriminative information for computational classification. In this research, we utilized textural and morphological features to describe the nuclear characteristics. Inspired from our previous work [4], we segmented all nucleus in the images using supervised segmentation method. Subsequently, we computed the nuclear feature and utilized them for discriminating nuclei into five classes. We utilized five classes of cell nuclei such as liver cells (*Liv.*), fibrocytes (*Fib.*), lymphocytes (*Lym.*), histiocytes (*His.*), and endothelial cells (*End.*). Fig.1 visualizes five classes of nuclei captured in several specimens. Fig.1 describes that liver cells are slightly large and round; lymphocytes are small and round; fibrocytes are long and thin; endothelial cells and histiocytes nuclei have slightly similar structural patterns and some of them have close appearance with fibrocytes; histiocytes present variable structural patterns. Furthermore, each nuclei has distinct textural patterns.

II. MATERIALS

A. Multifractal analysis on digital image

Fractal dimension (FD) is a non-integer exponent used to describe the complexity of fractal structures. Multifractal analysis is a generalization of fractal analysis that can be used to characterize natural images as a spectrum of FDs, i.e., multifractal spectrum [5]. Multifractal computation for digital images is illustrated below.

We can find the local irregularity at a given point (x, y) in an image using a function μ called “multifractal measure”, which is a non-integer exponent and described by the Hölder

¹In fact, it is very difficult to tabulate all the structural characteristics of the cells. Because these structures may changes upon diseases, patient, three dimensional location of the cell in the specimen, etc.

TABLE I: Pathological observations of cell characteristics.

Cell type	Characteristics			
	Shape	Size	Cytoplasm	Nuclei texture
<i>Liv.</i> (including HCC)	Round to oval	Relatively large	Relatively large, Round to square shape, Granular	Granular to reticular, Fine to coarse
<i>Fib.</i>	Long and thin	Often vary	Thin, long, granular	Granular and pyknotic
<i>Lym.</i>	Round	Small	Very Scanty	Thick Granular
<i>His.</i>	Bean shape to elliptic	Small to large	Fuzzy appearance	Lacy and foamy
<i>End.</i>	Oval	Relatively small	Long, relatively wide, granular	Granular and pyknotic

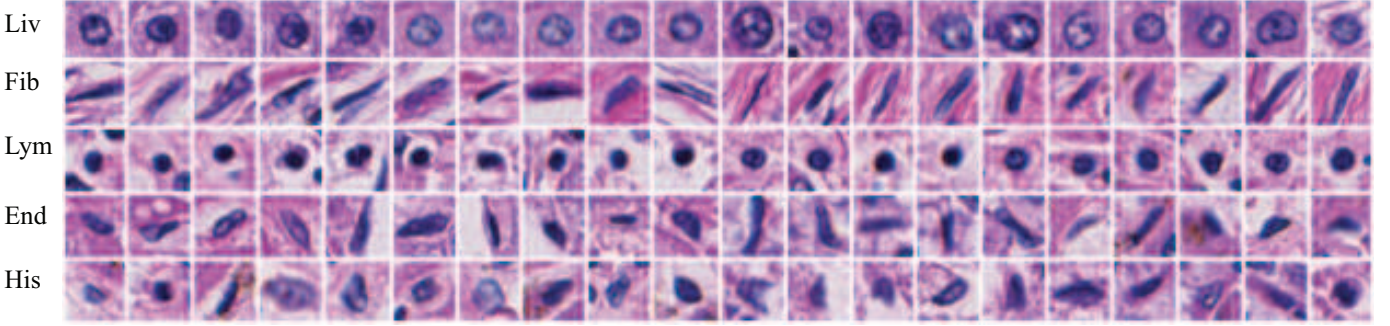


Fig. 1: Five classes of nuclei dataset.

Exponent $h_\mu(x, y)$,

$$h_\mu(x, y) = \lim_{\varepsilon \rightarrow 1} \frac{\log(\mu(W_\varepsilon(x, y)))}{\log(\varepsilon)}, \quad (1)$$

where, $W_\varepsilon(x, y)$ denotes a square window of side length ε centered at (x, y) . We plot $\log(\mu(W_\varepsilon(x, y)))$ against $\log(\varepsilon)$ for different sizes of neighbors and estimate $h_\mu(x, y)$ by computing the gradient of the linear regression line. This $h_\mu(x, y)$ is called α exponent. Accordingly, we compute α exponents for each pixel in the image and derive a matrix called α feature matrix.

Subsequently, we quantize the entire range of α (from minimum to maximum) into R discrete sub-ranges and derive a binary image for each sub-range. Let α_r be all α values quantized into r^{th} sub-range and I_{α_r} gives a binary value matrix as,

$$I_{\alpha_r}(x, y) = \begin{cases} 1, & \alpha_{rMin} \leq \alpha(x, y) < \alpha_{rMax} \\ 0, & \text{otherwise} \end{cases} \quad (2)$$

where, α_{rMin} and α_{rMax} denote lower and upper limits of r^{th} sub-range and $\alpha(x, y)$ is the value at point (x, y) in α matrix. Then, we compute the FD for each I_{α_r} using a method called box-counting algorithm. This method covers the entire image with grids of side length ε' , and counts the number of non-empty boxes $N_{\varepsilon'}(I)$. When ε' tends to 1, the limiting value of $N_{\varepsilon'}(I)$ follows the power law $N_{\varepsilon'}(I) \sim \varepsilon'^{-d_B}$, where d_B is a constant, i.e., the FD of I .

$$d_B(I) = \lim_{\varepsilon' \rightarrow 1} \frac{\log(N_{\varepsilon'}(I))}{\log(\varepsilon'^{-1})} \quad (3)$$

We compute the FD of I by plotting $\log(N_{\varepsilon'}(I))$ against $\log(\varepsilon'^{-1})$, and estimate the gradient of the linear regression line, i.e., the FD of I . The FDs obtained for each sub-range

α_r form a spectrum called $f(\alpha)$, i.e., multifractal spectrum. In addition, for each element in the α matrix has a corresponding FD in the $f(\alpha)$ and it yields a matrix called $f(\alpha)$ feature matrix.

The above description shows that α features observe the pixel's local behavior with respect to the neighborhood and $f(\alpha)$ features contain the pixel's spatial characteristics.

B. BOF-based classification model

The BOF classification model involves computing a codebook, in which the most representative patterns are codified as codewords, and characterizing given images by a frequency analysis of the codewords. When the texture is presented in a high-dimensional feature space, the codebook is a collection of distinct feature vectors. These codewords can be used to represent the characteristics of the pixels of a particular image domain. The frequency analysis of the codewords in an image derives a histogram, in which each bin represents a codeword and its value indicates the frequency. When different sizes of images or image regions are used, the areas of the histograms are different. Therefore, these histograms are required to be normalized.

III. METHODOLOGY

A. Feature descriptor

The α and $f(\alpha)$ features are associated with the multifractal measure μ that was used in (1). In particular, different textural characteristics can be obtained for different multifractal measures. We utilize four multifractal measures to extract α and $f(\alpha)$ feature matrices.

The proposed feature descriptor utilizes four multifractal measures: Maximum: μ_{Max} , Minimum: μ_{Min} , Summation: μ_{Sum} , and Ndiff: μ_{Ndiff} as defined in (4a), (4b), (4c),

and (4d), respectively [5], [6]. These four measures observe the disparity of the intensities from four different viewpoints.

$$\mu_{Max}(m, n) = \max_{(k,l) \in \Omega} g(k, l) \quad (4a)$$

$$\mu_{Min}(m, n) = \min_{(k,l) \in \Omega^*} g(k, l) \quad (4b)$$

$$\mu_{Sum}(m, n) = \sum_{(k,l) \in \Omega} g(k, l) \quad (4c)$$

$$\mu_{Ndiff}(m, n) = \frac{\left(\max_{(k,l) \in \Omega} g(k, l) - \min_{(k,l) \in \Omega^*} g(k, l) \right)}{\varepsilon}, \quad (4d)$$

where, $\mu_{(\cdot)}(m, n)$ represents the measurement at point (m, n) . Ω is the square window with side length ε centered at point (m, n) . Ω^* represents all of the non-zero pixels of Ω . $g(k, l)$ is the intensity at point (k, l) .

In this study, we compute α and $f(\alpha)$ feature matrices for Red, Green, and Blue (RGB) color channels using the above mentioned four multifractal measures, which yield a 24 dimensional multifractal feature space. Subsequently, we combine the RGB color intensities with the multifractal features and obtain 27-dimension of feature space. More precisely, each pixel of an image can be characterized by a 27-dimension feature vector in the combined feature space.

B. Nuclear segmentation

Nuclei were segmented by using our previously proposed method [4]. In particular, using a annotated dataset (nuclei and their background regions were annotated by experts), we computed multifractal features of each annotated pixels and trained a classifier for two classes: nucleus and background. The nuclei segmentation process is graphically illustrated in Fig.2. For a given image, we computed multifractal features for every pixels and classified them using the classifier. Subsequently, we obtained each pixel's posterior probability for nucleus class and normalized these probabilities into range a [0, 255] to obtain a gray-scale image, in which high intensities represent the regions of nucleus (Fig.2(b)). This image is enhanced by using morphological closing operator with three pixels radius of disk shape structural element. Consequently, noises are removed and boundaries of the nuclei are refined (Fig.2(c)). Then, we obtained the contours of the nuclei by using the level-set contour estimation method (Fig.2(d)). Finally, we excluded smaller region to avoid unusual predictions (Fig.2(e)).

C. Nuclear feature extraction and classification

As shown in Fig.1 different classes of nuclei have various textural and morphological characteristics. As a consequence, we utilized both textural and morphological features to describe nuclear characteristics.

The multifractal feature descriptor was used to obtain textural features of the nucleus. Multifractal feature descriptor computes pixel's local and spatial characteristics. Incorporating BOF model, we obtained the textural characteristics of a nuclear (segmented region) as a histogram. Since sizes of the

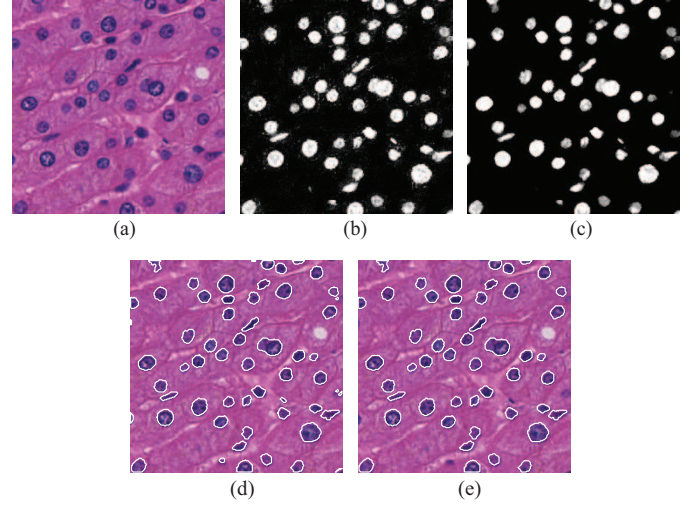


Fig. 2: Nuclei segmentation process. (a) A given image. (b) Posterior probability prediction of nuclear class. (c) Output of morphological closing. (d) Nuclear contours. (e) Final refined results.

nuclei are differed, we normalized each histogram obtained for each nuclear by dividing frequencies of each bin using the integral computed for all frequencies in the histogram. This histogram is used as the feature vector that presents all the textural characteristics of the nuclei.

To obtain morphological characteristics, we computed eight feature including area, perimeter, circularity, radius of long axis, radius of short axis, complexity, linear factor, and circular ratio. Computations of circularity, complexity linear factor, and circular ratio are given in Eq.5, 6, 7, and 8, respectively.

$$Circularity = \frac{perimeter^2}{4\pi \times area} \quad (5)$$

$$Complexity = \frac{perimeter^2}{area} \quad (6)$$

$$Linear\ factor = \frac{\pi \times radius\ of\ long\ axis^2}{4} \quad (7)$$

$$Circular\ ratio = \frac{radius\ of\ long\ axis}{radius\ of\ short\ axis} \quad (8)$$

Combining both textural and morphological features derives high-dimensional feature vector to describe the characteristics of a nuclear.

IV. EXPERIMENTS AND RESULTS

A. Data acquisition

In this experiment, we utilized a HE-stained liver biopsy specimens of 30 HCC patients and each specimen was scanned into a WSI (whole slide image) by a scanner called Nano-Zoomer (Hamamatsu Photonics K.K.) with an objective lens of 20x magnifications. The approximate size of the WSI is 33600×21000 pixels. Among these 30 WSIs, we obtained 40 ROIs 2174×2174, which were categorized into four grades (non-neoplastic and three tumor grades; G1, G2, and G3) [7],

TABLE II: Two-Class classification results

	CCR(%)	Precision/Recall	F-measure
<i>Liv.</i> vs. <i>Fib.</i>	97.42±2.06	0.98/0.97	0.97
<i>Liv.</i> vs. <i>Lym.</i>	96.86±2.48	0.97/0.96	0.96
<i>Liv.</i> vs. <i>End.</i>	97.49±3.36	0.96/0.98	0.97
<i>Liv.</i> vs. <i>His.</i>	95.05±5.27	0.95/0.92	0.93
<i>Fib.</i> vs. <i>Lym.</i>	97.73±2.25	0.96/0.98	0.97
<i>Fib.</i> vs. <i>End.</i>	84.35±8.09	0.89/0.90	0.89
<i>Fib.</i> vs. <i>His.</i>	90.81±5.69	0.95/0.95	0.95
<i>Lym.</i> vs. <i>End.</i>	95.50±4.01	0.98/0.98	0.98
<i>Lym.</i> vs. <i>His.</i>	88.44±6.21	0.92/0.96	0.94
<i>End.</i> vs. <i>His.</i>	79.44±9.01	0.82/0.90	0.86

[8]. We segmented the nuclei in each ROI, as described in Sec.III-B. Several experienced pathologists annotated a set of clearly segmented² nuclei into five classes. The annotated dataset contains 365, 365, 345, 365, and 190 nuclei for *Liv.*, *Fib.*, *Lym.*, *End.*, and *His.* categories, respectively.

B. Implementation

We computed α -features according to (1) by setting ε as 1, 3, 5, ..., 13 and quantized the α range (minimum to maximum) into 70 discrete sub-ranges to obtain 70 binary images. $f(\alpha)$ was computed according to (3) by setting ε' as 1, 2, 4, ..., 16.

The nuclei segmentation process utilized MATLAB random forest implementation [9] for classifying pixels into nuclei and background classes. The nuclear contour estimation method utilised MATLAB level-set implementation [10].

Nuclei classification process utilized BOF model to observe nucleus textural characteristics. The codebook in BOF model was computed as follows. We randomly selected 5000 feature vectors from the annotated regions, clustered them into 10 clusters using k -mean algorithm, and their centroids were selected as the codebook. As the classifier, SVM (support vector machine) MATLAB implementation: LIBSVM [11] was utilized. We set the parameters of LIBSVM as SVM type: C-SVM and kernel: radial basis function and estimated the optimal values for penalty parameters c and γ using entire dataset.

To evaluate the significance of the proposed method, we performed two experiments. In each experiment, the results were computed using 10-fold cross validation method. Analysis of the results was performed by computing several statistics such as CCR (correct classification rate), precision, recall, and F -measure. For a multi-class classification problem, the CCR is defined as [12],

$$CCR = \sum_{i=1}^M P(c_i) \frac{n_i}{N_i} \quad (9)$$

where M is total number of classes, n_i is the number of samples that are correctly classified to the i^{th} class, N_i is the total number of samples in the i^{th} class, and $P(c_i)$ refers to the prior probability that the observed data falls in class c_i .

²Biopsy images show that some nuclei are placed very close or bind together. Our segmentation algorithm falsely identified these nuclei into a single region (nuclei). Therefore, pathologist excluded these falsely segmented nuclei during the annotations

TABLE III: Multiclass classification results

	CCR(%)	Precision/Recall	F-measure
Five classes	88.95±6.06	0.87/0.86	0.87

TABLE IV: Multiclass classification detail results

Nuclei class	# of nuclei	Predictions					Rate(%)
		<i>Liv.</i>	<i>Fib.</i>	<i>Lym.</i>	<i>End.</i>	<i>His.</i>	
<i>Liv.</i>	365	347	0	6	0	12	95.07
<i>Fib.</i>	365	0	328	2	29	6	89.86
<i>Lym.</i>	345	1	4	318	8	14	92.17
<i>End.</i>	365	0	31	9	304	21	83.29
<i>His.</i>	190	5	13	8	11	153	80.53

C. Evaluation

As visually illustrated in Fig. 1, classifying fibrocytes, endothelial nuclei and histiocytes is challenging. To evaluate the discrimination capacity of the proposed method, we performed two-class classification among each nuclei group, in which every combination of each classes was classified and measured evaluation statistics. Table II shows the results of two-class classification.

Microscopic images of specimens contains a different categories of nuclei in different numbers. Therefore, we performed a multiclass classification on the annotated dataset. Summary and detail results of multiclass classifications are tabulated in Table III and IV, respectively. Table IV presents the classification performance in confusion matrix form. The second column shows the total number of nuclei used in each class, and the spanned column "Predictions" shows the predictions of each nucleus group. For example, the second row indicates that 365 nuclei were labeled as fibrocytes; there were 328 correctly classified, two nuclei were classified as lymphocyte, 29 nuclei were classified as endothelial, six nuclei were classified as histiocyte and classification rate for fibrocytes is 89.86%.

For a visual evaluation of the proposed method, it is necessary to classify every nucleus in the WSI to visualize the result more interactively. Therefore, we designed a visualization module using the proposed method. Generally, images of HE-

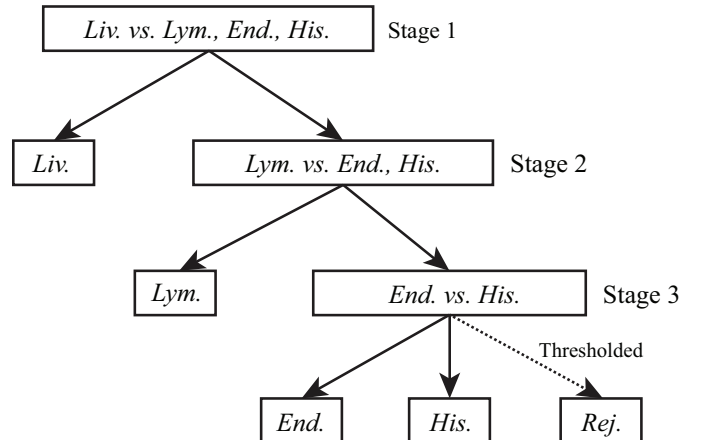


Fig. 3: Hierarchical classifier

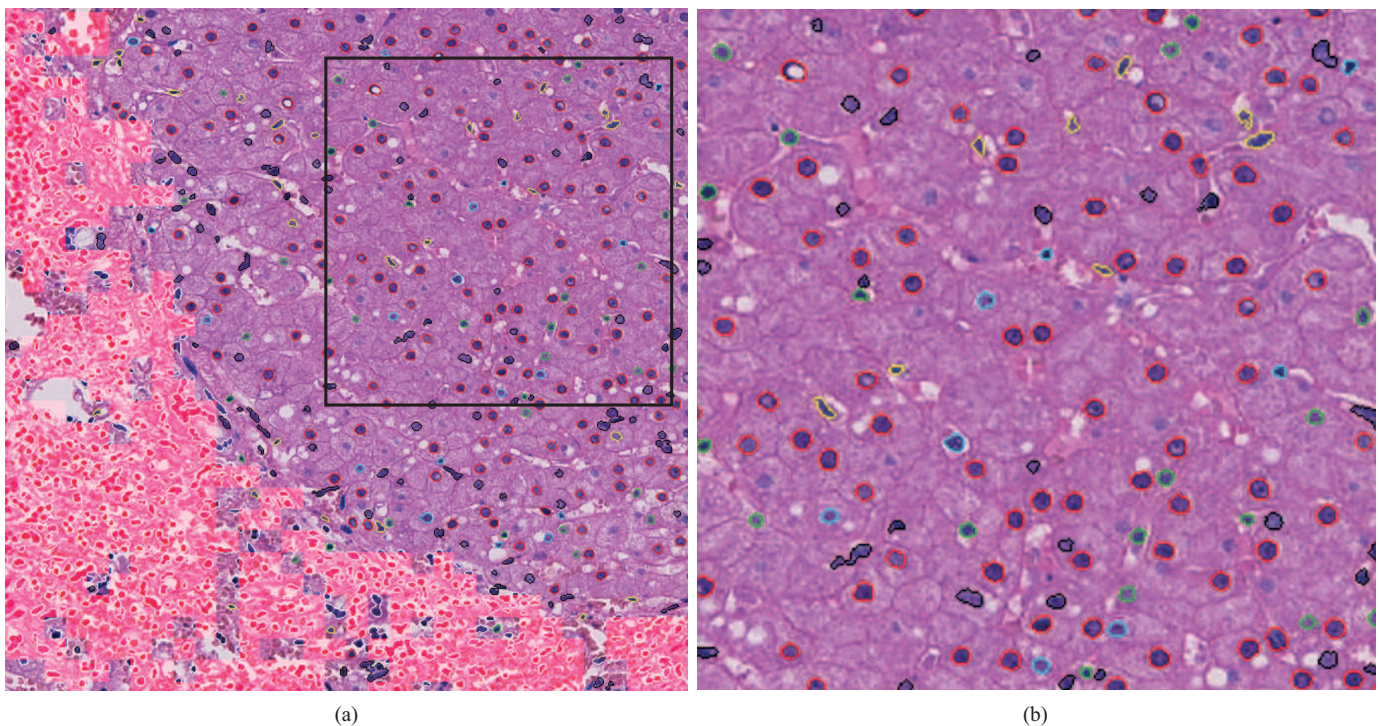


Fig. 4: An example of the visualization module for HE-stained biopsy specimen. (a) Computational labels in 1024×1024 pixels image. (b) Selected regions (black square) of (a) in higher resolution. Labels of computational annotations: *Liv.*: red, *Fib.*: blue, *Cyt.*: green, *End.*: yellow, *His.*: cyan, *Rej.*: black, Nuclei overlapped with fibrosis region: white, Fibrosis region: shaded in red

stained specimen shows complex tissue structures and appearance of some tissue components may differ with respect to their three dimensional location. In addition, some cells locate very closer or bind together and computational segmentation methods may unable to segment these regions properly. As a results, classifying these regions becomes a crucial task. Therefore, it is necessary to predetermine these regions or categorized them into separate group. Nuclei in fibrosis regions often place very close or bind. On the other hand, detection of fibrosis region is important than classifying the fibroblast. In this visualization module, we utilized our previously proposed a supervised regional segmentation method to localize fibrosis regions [4]. As a consequence, all the nuclei overlapped with fibrosis regions were excluding from the classification. To classify the rest of the nuclei, we empirically utilized hierarchical classification method as shown in Fig. 3. At the first stage, we classified liver cell nuclei using the morphological features. From the rest of the nuclei lymphocytes were classified using both texture and morphological features in the second stage. The rest of the nuclei were classified as two-class classification and prediction of each nuclei was threshold based on prediction's posterior probability. We empirically decided the threshold value as 0.6, in which the prediction below the threshold was categorizes as rejected (*Rej.*). As a consequence, visualization module excludes most of the falsely segmented regions (bound nuclei). To construct the visualization module, we computed three classifiers using the annotated dataset. Fig. 4 shows outcome of the visualization module for a HE-stained liver biopsy image.

D. Discussion

Liver cell nuclei can be easily differentiated from other nuclei and it is indicated in Table II that liver cell nuclei class vs. every other have obtain over 95% CCR. Fibrocytes and endothelial nuclei have slightly similar appearance and it is indicated that CCR value of *Fib.* vs. *End.* becomes 84.35%. Histiocytes has heterogeneous structural characteristics and particularly its appearances are similar to endothelial nuclei. As a consequence, *End.* vs. *His.* has obtained the lowest CCR 79.44%.

Table III shows that CCR of multiclass classification obtained 88.95%. Consequences for this low CCR is further described in Table IV. As it indicated, *End.* and *His.* have obtain 83.29% and 80.53%, respectively. All other nuclei classes have obtained over 89% classification rate.

Generally, pathologists identify the cells by from the characteristics of nuclei and its surrounding cellular components such as cytoplasm. In some cases such as endothelial, they further investigate the neighbor of the cell membrane. Nuclear texture contains computationally observable adequate discriminative characteristics. In addition, combination of inner and its neighborhood texture may improve the discrimination capacity. Multifractal feature descriptor observes pixel's characteristics with respect to its neighborhood pixels. According to our parameter setting, pixel's feature vector observes its behavior with respect to six pixels of neighborhood. As a consequence, the feature vector computed for the segmented region (nuclear) comprise inner and six pixels width of neighboring textural

information. Therefore, multifractal feature descriptor is significant for cell nuclei classification process.

V. CONCLUSION

In pathological investigations, cell classification is very important for diagnosing various diseases. Generally, cell classification is performed based on the structural characteristics of the nuclei. In addition, pathologists observe the characteristics of surrounding tissue components to confirm the classification of particular cells such as endothelial and histiocytes. Computational systems cannot observe the characteristics of entire cell because of the inconsistent appearance of the cellular membrane in HE stained specimen. However, cell nuclear comprises most discriminative characteristics.

In this paper, we presented a methodology to characterize cell nuclei based on its textural and morphological features. The textural characteristics were obtained from multifractal feature descriptor. We computed eight morphological features from the contours of the nuclei regions. The proposed nuclei classification method was evaluated by using five categories of annotated nuclei. As the experimental results indicated, histiocyte and endothelial nuclei have obtained slightly lower accuracy and others obtain around 90% accuracy.

In an automated diagnostic environment, cell nuclei classification depend on the sensitivity of the segmentation. In practice, we often find a circumstances that some nuclei are placed very close or bound together. Several methods have been proposed in literature for re-segmenting bound nuclei regions. Our nuclei segmentation method has not utilized any re-segmentation techniques. This paper focused on the discrimination characteristics contains in the nuclei. In future, it is necessary to optimize segmentation process and utilize the nuclei classification technique to derive high-throughput system.

ACKNOWLEDGMENT

This research is supported by the New Energy and Industrial Technology Development Organization (NEDO) in Japan

under the research and development project of Pathological Image Recognition.

REFERENCES

- [1] M. Takahashi, *Color Atlas of Cancer Cytology*, third edition ed. Igaku-Shoin Tokyo, New York, 2000.
- [2] M. Gnen, A. Ula, P. Schffler, U. Castellani, and V. Murino, "Combining data sources nonlinearly for cell nucleus classification of renal cell carcinoma," *Similarity-Based Pattern Recognition*, pp. 250–260, 2011.
- [3] J. Kong, L. Cooper, F. Wang, C. Chisolm, C. Moreno, T. Kurc, P. Widener, D. Brat, and J. Saltz, "A comprehensive framework for classification of nuclei in digital microscopy imaging: An application to diffuse gliomas," in *Biomedical Imaging: From Nano to Macro, 2011 IEEE International Symposium on*, 2011, pp. 2128–2131.
- [4] C. Atupelage, H. Nagahashi, M. Yamaguchi, F. Kimura, T. Abe, A. Hashiguchi, and M. Sakamoto, "MULTIFRACTAL COMPUTATION FOR NUCLEAR CLASSIFICATION AND HEPATOCELLULAR CARCINOMA GRADING," in *Proceedings of the IASTED International Conference on Biomedical Engineering (BioMed 2013)*, Innsbruck, Austria, Feb. 2013, pp. 415–420.
- [5] T. Stoji, I. Reljin, and B. Reljin, "Adaptation of multifractal analysis to segmentation of microcalcifications in digital mammograms," *Physica A: Statistical Mechanics and its Applications*, vol. 367, pp. 494–508, 2006.
- [6] A. Grski, "Pseudofractals and the box counting algorithm," *Journal of Physics A: Mathematical and General*, vol. 34, pp. 7933–7940, 2001.
- [7] C. Atupelage, H. Nagahashi, M. Yamaguchi, T. Abe, A. Hashiguchi, and M. Sakamoto, "Computational grading of hepatocellular carcinoma using multifractal feature description," *Computerized Medical Imaging and Graphics*, vol. 37, no. 1, pp. 61 – 71, 2013. [Online]. Available: <http://www.sciencedirect.com/science/article/pii/S0895611112001565>
- [8] H. Edmondson and P. Steiner, "Primary carcinoma of the liver. a study of 100 cases among 48,900 necropsies," *Cancer*, vol. 7, no. 3, pp. 462–503, 1954.
- [9] A. Jaientilal, "Randomforest-matlab," 2010.
- [10] L. A. Vese and T. F. Chan, "A multiphase level set framework for image segmentation using the mumford and shah model," *Int. J. Comput. Vision*, vol. 50, no. 3, pp. 271–293, Dec. 2002.
- [11] C.-C. Chang and C.-J. Lin, "LIBSVM: a library for support vector machines," *ACM Transactions on Intelligent Systems and Technology*, vol. 2, no. 3, p. 27, 2011, software available at <http://www.csie.ntu.edu.tw/~cjlin/libsvm>.
- [12] W. Lee, Y. Chen, and K. Hsieh, "Ultrasonic liver tissues classification by fractal feature vector based on m-band wavelet transform," *Medical Imaging, IEEE Transactions on*, vol. 22, no. 3, pp. 382–392, 2003.

Intelligent Classification of Middle Cognitive Impairment and Alzheimer's Disease Using Heterogeneous information source features

O.Valenzuela, F. Ortuño, G. Ruiz-García, F. Estrella, I.Rojas

Abstract— There are three main objectives in this paper: the first one is to develop a classification method to tag MR images as either normal or with the Alzheimer's disease (AD); the second, which is more ambitious, is the identification and classification in normal subjects, MCI (Middle Cognitive Impairment) patients and AD patients; and finally (and most interesting), the third goal is the possibility to classify in Middle Cognitive Impairment Converters (MCI-C, i. e. , people that suffer a MCI and in the future will suffer from Alzheimer's disease within 18 months), and Middle Cognitive Impairment Non Converters (MCI-NC, i. e., people that suffer a MCI and in the future will not suffer from Alzheimer's disease). It is noteworthy that with this last study we could offer a tool to assist the early diagnosis of dementia.

Keywords—MRI, SVM, Alzheimer's disease .

I. INTRODUCTION

There are several possible causes for dementia, but Alzheimer Disease (AD) is leading cause of dementia in the world. There are an estimated 35.6 million people in the world with dementia and more than 18 million of them have Alzheimer disease, which represents more than 50% of the total people with dementia. Besides, the number of people with dementia is expected to increase to 65.7 million in 2030 and 115.4 million in 2050.

Today, the diagnosis of Alzheimer disease is made by using clinical criteria; however these criteria are not capable of diagnosing the disease in its pre-clinical stage, not allowing for an early diagnosis.

At this point, it is necessary to identify the condition prior to dementia which is Mild Cognitive Impairment (MCI). Subjects with MCI are in an intermediate clinical situation between normality and dementia, which is characterized by the presence of subjective cognitive impairment, but do not make a significant alteration in activities of daily living. As there are studies which show that between 10% and 15% of patients with MCI have developed dementia within a year, it is really important to be able to identify this pathology.

This work has been partially supported by the projects: Spanish Ministry of Science and Innovation SAF2010-20558; Genil Start-Up Projects For Young Researchers PYR-2012-8 and Excellence projects Junta de Andalucía P09-TIC-5476,P07-TIC-02906.

Second Third, Fourth and Fifth Authors are with the Dpt. Computer Architecture and Computer Technology. University of Granada, Spain.

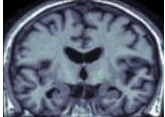
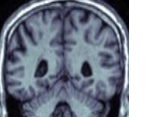
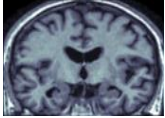
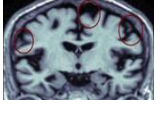
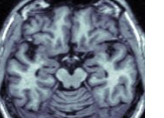
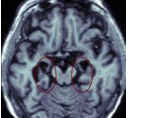
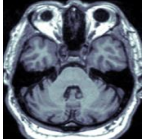
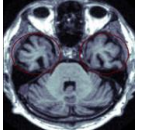
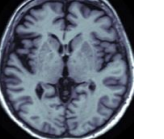
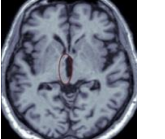
First Authors is with Dpt. Applied Mathematics. University of Granada Spain.

It is important to note that neuroimaging, using mainly magnetic resonance, is a powerful tool that adds a positive predictive value to the diagnosis and includes measurements using structural MRI to evaluate medial temporal lobe atrophy and positron emission tomography using fluorodeoxyglucose (FDG) or amyloid markers [1]. Many studies have focused on quantifying focal atrophy in the temporal lobe [2], [3] and there even exist visual scales to quantify the degree of atrophy, which are quick and easy to use. Recently, validations of computerized methods to measure the degree of temporal atrophy have been published. In comparison, these methods have a similar discriminatory power [4] with the advantage that they would facilitate measurements and would provide more objective results by standardizing the methods of analysis [5].

There are new development in automatic classification systems based on computer intelligent paradigms, mainly such as support vector machine (SVM), that present new diagnosis tools based on T1-weighted MRI [7][8][9][10][11][12]. These approaches can be divided into three different categories, taking into account the type of features extracted from the MRI (voxel-based, vertex-based or ROI-based) [1]. For the voxel-based, the features are the probability of the different tissue classes in a given voxel [13] [14]. In the second category, vertex-based, the features are defined at the vertex-level on the cortical surface [12] [15]. Finally, the methods based on ROI include mainly the analysis of the hippocampus (study of the volume, shape and specific characteristic of the hippocampus) [16] [17].

Even though these approaches achieve high accuracy (over 85%), they were calculated on different studied populations (in fact, the variability between evaluations statistically increases mainly in case where the number of subject is small; typically, there are several approaches in which less than a hundred subjects are used) making it difficult to compare the obtained results. It is important to note that most of articles published to date using intelligent classification systems in

Table 1. Alzheimer's disease on MRI

Healthy Patient	Patient with AD	Comment	Healthy Patient	Patient with AD	Comment
		In clinical practice, the width of the horn of the lateral ventricle is the most reproducible measure to assess the atrophy.			Dilatation of the ventricular system as a result of general atrophy.
		Cortical volume loss. General atrophy of the cortex.			Atrophy in the hippocampal region.
		Atrophy of the temporal lobes.			It is possible to observe the dilatation of the third ventricle.

Alzheimer's disease diagnosis have three major drawbacks:

- They use a low number of data for both training and test (in some cases less than a hundred).
- Classification is performed between patients with dementia and healthy patient, but does not make difference between patients with Mild Cognitive Impairment (MCI), Middle Cognitive Impairment Converters (MCI-C) and Middle Cognitive Impairment Non Converters (MCI-NC), since it is a complex task.
- They use only one type of feature (voxel-based, vertex-based or ROI-based), but not all together.

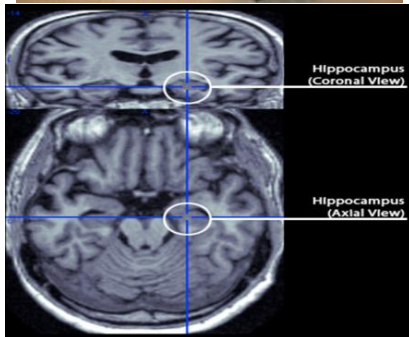


Fig.1. The hippocampus is a major component of the brain. It belongs to the limbic system and plays important roles in the consolidation of information from short-term memory to long-term memory and spatial navigation. In AD, the hippocampus is one of the first regions of the brain to suffer damage; memory problems and disorientation appear among the first symptoms.

In this paper, a new methodology for classification of MR images is proposed using a large data base (more than one thousand patient), for the classification of MCI patients, especially in the case of MCI-C and MCI-NC, using simultaneously all kind of features. An important goal in this

paper is the identification and classification between normal subjects, MCI (Middle Cognitive Impairment) patients and AD patients. Finally, a very interesting objective is the possibility to classify Middle Cognitive Impairment Converters (MCI-C, this is, people that suffer a MCI and in the future will have Alzheimer's disease, within 18 months), and Middle Cognitive Impairment Non Converters (MCI-NC, this is, people that suffer a MCI and in the future will not have Alzheimer's disease). Besides, throughout the entire paper different techniques and methods are tested to compare them and determine which of them offers better results are.

II. ALZHEIMER'S DISEASE ON MAGNETIC RESONANCE IMAGING

Imaging findings in patients with MCI are typically inconspicuous, and often considered as normal. The main problem is that there exist no standardized criteria to determine if the impairment observed in a MR image is caused by normal aging or if it can be admitted as pathological. In patients older than 65 years, it is considered normal to detect mild signs of atrophy and little impairments of the white matter, but the evaluation of the damage degree (which will determine if it is considered pathological) remains subjective [18]. The table below shows the principal slices were AD symptoms could be detected [19]. The main feature of the disease is the general atrophy of the cerebral cortex. As the disease progresses, an accelerated loss of focal volume is shown in the medial temporal lobes, in particular in the hippocampus, entorhinal cortex and amygdala.

The structural imaging of the brain with cranial MRI has become a fundamental part of the evaluation of patients suspected of having cognitive impairment or dementia; therefore, it has been included in the new research criteria for AD [2]. So, patients with significant episodic memory impairment and temporal lobe atrophy evaluated with MRI may be diagnosed as probable AD. This is a significant step for the detection of the disease in early stages, with the medical, psychological and social advantages that benefit the patient and the caregiver. Nevertheless, despite many articles have set the relevance of cerebrospinal fluid biomarkers for early and prodromal diagnose of AD, few studies have

determined the characteristic changes in MRI of prodromal AD group according to the new proposed criteria, which establish the pattern of atrophy in those patients with a pattern of amnesia typical of AD and positive biomarkers [7]. Finally, it is important to note that, even if it is possible to detect alterations in normal images, the external symptom of the patient can occur several years later, mainly in the MCI-NC [1] (see Fig. 2). Therefore, improvement of the imaging process, characterization criteria and standardization of results, as well as the development of new techniques with new tracers, is a promising start for the pre-clinical diagnosis of AD.

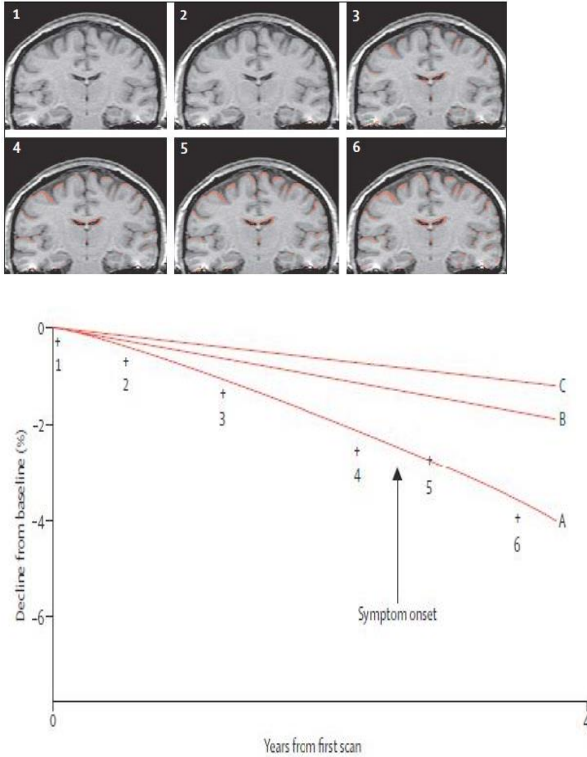


Fig. 2. Progressive atrophy in presymptomatic AD

III. DATA BASE

Data used in the preparation of this article were obtained from the Alzheimer's Disease Neuroimaging Initiative (ADNI) database (adni.loni.ucla.edu). The ADNI was launched in 2003 by the National Institute on Aging (NIA), the National Institute of Biomedical Imaging and Bioengineering (NIBIB), the Food and Drug Administration (FDA), private pharmaceutical companies and non-profit organizations, as a \$60 million, 5-year public-private partnership. The primary goal of ADNI has been to test whether magnetic resonance imaging (MRI), positron emission tomography (PET), other biological markers, and clinical and neuropsychological assessments can be combined to measure the progression of mild cognitive impairment (MCI) and early Alzheimer's disease (AD) [1].

In this paper, images from 1.5-T and 3-T were simultaneously used. It is important to note that a pre-

processing (normalization) of all the images obtained has been carried out, and all the images were visualized one by one, taking into account both the normal image, the gray matter and white matter. Abnormal or defective images were considered corrupted and therefore discarded. The following tables show the total number of images and patients used for this study:

	Normal		MCI-C		MCI-NC		AD		Total	
	Initial	Final								
Patient	229	229	134	134	266	251	188	177	815	739
MRI	913	811	620	539	987	819	554	467	3071	2636

Table 2. Data base from 1.5-T MRI

	Normal		MCI-C		MCI-NC		AD		Total	
	Initial	Final								
Patient	61	56	38	35	50	47	41	37	190	175
MRI	248	187	183	130	210	160	135	98	776	575

Table 3. Data base from 3-T MRI

IV. FEATURE EXTRACTION

In this paper, we need to extract from an image the feature vector that characterizes it. Thus, our features are the approximate wavelet coefficients, using them to generate a classification rule to assist with diagnosis. As described in the following sections, the number of features is not as important as robustness to get the best classification accuracy (being *robustness* in an image application understood as the consistency of the results that certain feature provides across the entire application). Wavelets are mathematical functions that decompose data into different frequency components and then study each component with a resolution matched to its scale.

While the Fourier Transform only provides representation of an image based on its frequency content (losing time information of the signal), the Wavelet Transform provides both time and frequency information. Therefore, the Wavelet Transform is a better tool for feature extraction from images. The Discrete Wavelet Transform (DWT) is a linear transformation that operates on a data vector whose length is an integer power of two, transforming it into numerically different frequency components, and then studies each component with resolution matched to its scale.

Assume $x(t)$ is a square-integrable function; then the continuous wavelet transform of $x(t)$ relative to a given wavelet $\psi(t)$ is defined as:

$$W_{\psi}(a,b) = \int_{-\infty}^{+\infty} x(t)\psi_{a,b}(t)dt \quad (1)$$

Where:

$$\psi_{a,b}(t) = \frac{1}{\sqrt{a}}\psi\left(\frac{t-a}{b}\right) \quad (2)$$

To get the DWT, previous equation can be discretized by restraining a and b to a discrete lattice ($a = 2^m b$; $a > 0$; $a, b \in \mathfrak{R}$). Then, the DWT can be expressed as follows:

$$ca_{j,k}(n) = DS \left[\sum_n x(n) g_j^*(n - 2^j k) \right] \quad (3)$$

$$cd_{j,k}(n) = DS \left[\sum_n x(n) h_j^*(n - 2^j k) \right] \quad (4)$$

Here $ca_{j,k}$ and $cd_{j,k}$ refer to the coefficients of the approximation components and detail components, respectively. $g(n)$ and $h(n)$ denote the low-pass filter and high-pass filter, respectively. j and k represent the wavelet scale and translation factors, respectively; and DS operator means the “down sampling” or decimation operation. The above decomposition process can be iterated decomposing successively the approximations in turn, so that the signal is broken down into various levels of resolution.

In case of images, the DWT is applied to each dimension separately, decomposing an image into four sub-bands, which are low-low (LL), low-high (LH), high-high (HH) and high-low (HL); where the LL sub-band can be regarded as the approximation component and it is used for the next level of the 2D-DWT, whereas the other sub-bands would be regarded as the detailed component of the image. A 2D-DWT scheme is shown in fig. 4.

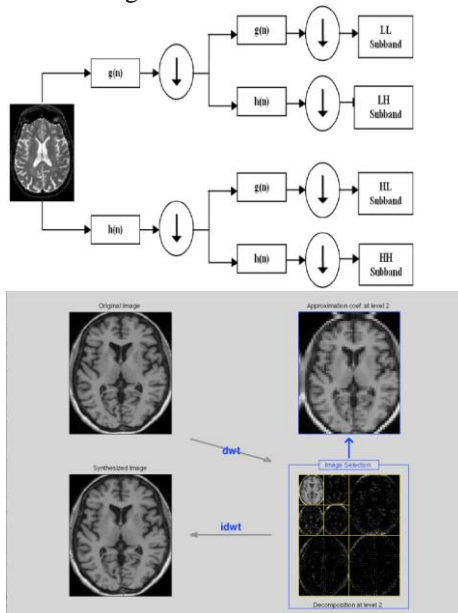


Fig. 4. A) 2D DWT decomposition scheme; B) Level 2 decomposition of an image using DWT

At each decomposition level, the half band filters produce signals spanning only half of the frequency bands. As the level decomposition is increased, a more compact and less resolution image is obtained.

V. FEATURE SELECTION

Often the extraction of image features provides a large number of them, but as we explained before, that do not guarantee the best classification accuracy because part of the data may be

redundant. Therefore, we have used the Principal Component Analysis (PCA) in our experiments as a feature reduction technique, and we have also studied the effects of including two other techniques that set a ranking of features in order of importance, based on different criteria: minimum Redundancy-Maximum Relevance (mRMR) and Normalized Mutual Information Feature Selection (NMIFS).

VI. SIMULATIONS RESULTS

For the classification of the MR images we used Support Vector Machines technique. In particular, the LIBSVM, which is an integrated software for SVM classification with a MATLAB extension. The best improvement that LIBSVM provides is the multi-class classification, while most of SVM tools can only classify between two different classes. Now, we define the procedure to follow. First of all, we use the 2D-DWT to perform the feature extraction; then, we develop a feature selection algorithm based on PCA, and finally we use an SVM classifier. A block scheme of the procedure is shown in Fig.5 .

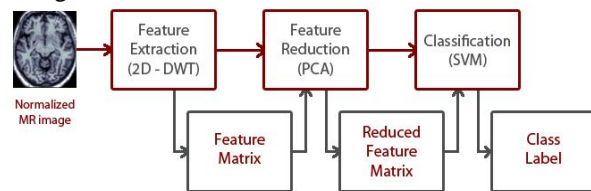


Fig. 5. Structure of Experiment schematically

Once the procedure was defined, we had to know what slice or slices where the best to extract the wavelets from. According to this, we proposed two different starting points: in the first scenario, we had no medical expert help, whereas in the second Doctor Ignacio García Basterra (Neurologist) expert criteria was used to select which slices where the most suitable to make AD diagnosis. Thus, in the first case, we applied the complete procedure shown in Fig. to every slice of every image to set up a ranking of accuracy. Then we used the top 20 slices in the experiment.

Also, in this experiment we would like to compare the behavior of SVM with other classifiers. For a medical human expert (especially for a doctor expert in MRI) it is not easy to understand the knowledge within the model of a SVM. However, there are other types of classifiers which, even though their precision is lower, their interpretability is more clear (for example, decision trees) and therefore, this classifiers are very important to extract knowledge within the weights associated and understand (from the point of view of a human expert) the rules used to perform the classification.

In this paper, decision trees (DT), linear discriminant analysis (LDA), quadratic discriminant analysis (QDA), naive bayes (NB), support vector machines (SVM) and Radial basic function neural networks (RN) were used.

We will also compare the behavior of these classifiers in four different scenarios: a) using information from the wavelet transform (denoted as D42); b) using information from morphological features (there are a total 100 features, denoted as MRF100); using the 50 most relevant morphological features (MRF50) or the 10 most relevant morphological features (MRF10).

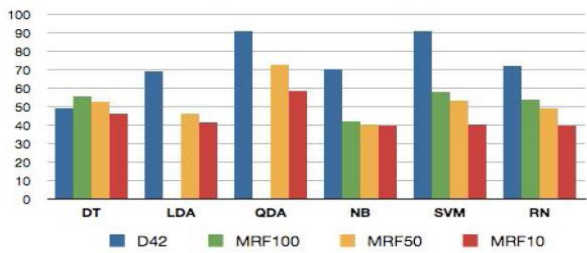


Fig. 6. Comparison of different classifier for classification of the four groups (Normal, AD, MCI-N and MIC-NC).

A second analysis was carried out, but in this case with the purpose of classifying two different groups: MCI-N and MCI-NC. The classifier with best performance was the SVM, with the results presented in the following table:

	Maximum	Minimum	Mean	STD
Wavelet	99,25	95,11	97,41	1,17
Morphol. 100	96,27	91,79	94,55	1,52
Morphol. 50	98,13	89,93	94,14	2,50
Morphol. 10	93,28	85,82	90,19	2,31

Table 4. Results of the SVM classifier for the problem MCI-N, and MCI-NC

The comparison with the rest of the classifiers is presented in Fig. 7, for different configuration of the features used.

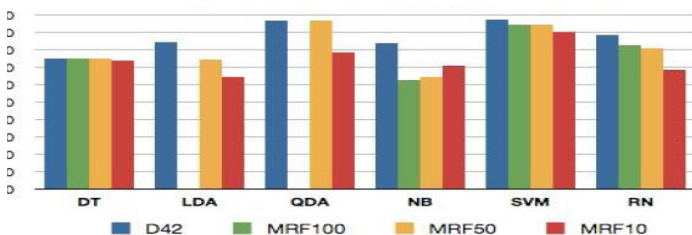


Fig. 7. Comparison of different classifier for classification of MCI-N and MIC-NC.

Finally, it is important to note that better accuracy can be obtained if a combination of features is introduced in the classifier. In this case, we carried out a combination of morphological features and features from wavelets, and also some easy features, as is the gender of the patient. In this scenario, we compare the performance of the SVM for different experiment that are showed in table 5.

	Maximum	Minimum	Mean	STD
Wavelet Female patients	95.59	89.22	92.45	1.76
Wavelet, Male patients	92.88	85.53	90.09	2.22
Wavelet+Morpho (Female)	94.61	88.24	92.55	1.87
Wavelet+Morpho (Male)	90.79	85.53	88.68	1.56

Table 5. Results of the SVM classifier for the problem of four groups using different combinations of features.

VII. CONCLUSION

In this papers an advanced classifier capable of combining different sources of information (features) is proposed and compared in different scenarios. First of all, a classification method is focused in tagging normal subjects, MCI-NC, MCI-N patients and AD patients; a very remarkably capacity of this classifier is the possibility to classify MCI-N and MCI-NC patients. Also, we presented the results of comparing the accuracy of the system for female and male patients. It is noteworthy that with this last study we could offer a tool to assist the early diagnosis of dementia.

ACKNOWLEDGMENT

Thank to David Jaramillo, Antonio Fernandez, Fadel Hamed and Gema Roman for their work

REFERENCES

- [1] Remi Cuingnet et.al. "Automatic classification of patients with Alzheimer's disease from structural MRI: A comparison of ten methods using the ADNI database", *NeuroImage* 56 (2011) 766–781.
- [2] Scheltens, P., Frisoni, G. B., Galluzzi, S., Nobili, F. M., Fox, N. C., Robert, P. H., et al. (2003). Neuroimaging tools to rate regional atrophy, subcortical cerebrovascular disease, and regional cerebral blood flow and metabolism: consensus paper of the EADC. *Neurol Neurosurg Psychiatry*, 71, 1371-81.
- [3] Koedan, E., Lehmann, M., Van der Flier, W. M., Scheltens, P., Pijnenburg, Y., Fox, N., et al. (2011). Visual assessment of posterior atrophy development of a MRI rating scale. *Eur Radiol*, 21, 2618-2615.
- [4] Westman, E., Cavallin, L., Muehlboeck, J. S., Zhang, Y., Mecocci, P., Vellas, B., et al. (2011). Sensitivity and Specificity of Medial Temporal Lobe Visual Ratings and

- Multivariate Regional MRI Classification in Alzheimer's Disease. *PLoS One*, 6 (7).
- [5] Jack, C. R., Barkhof, F., Barnstein, M. A., Cantillon, M., Cole, P. E., DeCarli, C., et al. (2011). Steps to standardization and validation of hippocampal volumetry as a biomarker in clinical trials and diagnostic criterion for Alzheimer's disease. *Alzheimer's & Dementia*, 7, 474-485.
- [6] Koedan, E., Lehmann, M., Van der Flier, W. M., Scheltens, P., Pijnenburg, Y., Fox, N., et al. (2011). Visual assessment of posterior atrophy development of a MRI rating scale. *Eur Radiol*, 21, 2618-2615.
- [7] A. Vandenberghe, Rik; Nelissen, Natalie; Salmon, Eric; et al., "Binary classification of F-18-flutemetamol PET using machine learning: Comparison with visual reads and structural MRI" *NEUROIMAGE* Volume: 64 Pages: 517-525. Published: JAN 1 2013.
- [8] Li, Lin; Wang, James Z.; Lozar, Carl; et al. Automated detection of mild cognitive impairment through mri data analysis, *International Journal On Artificial Intelligence Tools* Volume: 21 Issue: 5. Published: OCT 2012.
- [9] Daliri, Mohammad Reza, "Automated Diagnosis of Alzheimer Disease using the Scale-Invariant Feature Transforms in Magnetic Resonance Images" *Journal Of Medical Systems* Volume: 36 Issue: 2 Pages: 995-1000. Published: APR 2012
- [10] Misra, C., Fan, Y., Davatzikos, C., 2009. Baseline and longitudinal patterns of brain atrophy in MCI patients, and their use in prediction of short-term conversion to AD: results from ADNI. *Neuroimage* 44 (4), 1415–1422.
- [11] Gerardin, E., Chételat, G., Chupin, M., Cuingnet, R., Desgranges, B., Kim, H.-S., Niethammer, M., Dubois, B., Lehericy, S., Garnero, L., Francis, E., Colliot, O., 2009. Multidimensional classification of hippocampal shape features discriminates Alzheimer's disease and mild cognitive impairment from normal aging. *Neuroimage* 47 (4), 1476–1486.
- [12] Querbes, O., Aubry, F., Pariente, J., Lotterie, J.A., Démonet, J.F., Duret, V., Puel, M., Berry, I., Fort, J.C., Celsis, P., Alzheimer's Disease Neuroimaging Initiative, 2009. Early diagnosis of Alzheimer's disease using cortical thickness: impact of cognitive reserve. *Brain* 32 (8), 2036–2047.
- [13] Magnin, B., Mesrob, L., Kinkingnéhun, S., Péligrini-Issac, M., Colliot, O., Sarazin, M., Dubois, B., Lehericy, S., Benali, H., 2009. Support vector machine-based classification of Alzheimer's disease from whole-brain anatomical MRI. *Neuroradiology* 51 (2), 73–83.
- [14] Vemuri, P., Gunter, J.L., Senjem, M.L., Whitwell, J.L., Kantarci, K., Knopman, D.S., Boeve, B.F., Petersen, R.C., Jack Jr., C.R., 2008. Alzheimer's disease diagnosis in individual subjects using structural MR images: validation studies. *Neuroimage* 39 (3), 1186–1197.
- [15] Desikan, R.S., Ségonne, F., Fischl, B., Quinn, B.T., Dickerson, B.C., Blacker, D., Buckner, R.L., Dale, A.M., Maguire, R.P., Hyman, B.T., Albert, M.S., Killiany, R.J., 2006. An automated labeling system for subdividing the human cerebral cortex on MRI scans into gyral based regions of interest. *Neuroimage* 31 (3), 968–980
- [16] Colliot, O., Chételat, G., Chupin, M., Desgranges, B., Magnin, B., Benali, H., Dubois, B., Garnero, L., Eustache, F., Lehericy, S., 2008. Discrimination between Alzheimer disease, mild cognitive impairment, and normal aging by using automated segmentation of the hippocampus. *Radiology* 248 (1), 194–201.
- [17] Chupin, M., Gerardin, E., Cuingnet, R., Boutet, C., Lemieux, L., Lehericy, S., Benali, H., Garnero, L., Colliot, O., Alzheimer's Disease Neuroimaging Initiative, 2009b. Fully automatic hippocampus segmentation and classification in Alzheimer's disease and mild cognitive impairment applied on data from ADNI. *Hippocampus* 19 (6), 579–587.
- [18] Pérez, D. A., Ramos, A., & Álvarez-Linera, J. (2010). *Neuroimagen. Diagnóstico, técnicas, secuencias 2*. Almirall.
- [19] Jaramillo, David; Rojas, Ignacio; Valenzuela, Olga; et al. Advanced systems in medical decision-making using intelligent computing. Application to magnetic resonance imaging, *IEEE International Joint Conference on Neural Networks (IJCNN)* Published: 2012.

Testing for non-linearity in spontaneous pupil signal of health subjects: preliminary approach based on non-stationary surrogate data methods

W.Nowak, A.Hachoł, M. Misiuk-Hojło

Abstract—The papers presents investigation on deterministic and stochastic nature of short-term fluctuations in spontaneous pupil size fluctuations signal.. The Small-Shuffle Surrogate (SSS) Test was performed on the set of SPF signals recorded for healthy subjects by dynamic pupillometry. The results of the test obtained for all SPF signals show that there is short-term dynamics in irregular fluctuations of pupil size.

Keywords— Spontaneous pupil size fluctuations, Small-Shuffle Surrogate (SSS) Test, short-term dynamics in irregular fluctuations.

I. INTRODUCTION

THE spontaneous pupil size fluctuation (SPF) appears even in constant light and accommodation conditions. This complex behavior reflects a dynamical equilibrium modulated by the central nervous system (CNS) and the two branches of the autonomous nervous system (ANS), the sympathetic, which innervate the iris dilator muscle and the parasympathetic, which innervate the iris sphincter muscle [1,2].

The possibility to noninvasive and easy monitoring of nervous systems activity by using SPF signal provokes its intensive research using many analysis approaches/techniques including Fourier Transform [3], Short-Time Fourier Transform [4], Wavelet Transform [5] and Wavelet Entropy [6]. Performed analysis has shown that SPF is nonstationary and its main spectra is below 1 Hz, including respiratory and heart beat components. It has been show that SPF reflect sleepiness, cognitive and affective processes [7,8].

The important question that was not considered so far, is what are the characteristics of the underlying system that

generate SPF Signal? (i.e. it is deterministic or stochastic? Linear or nonlinear?).

If the system is deterministic, its future performance can be clearly determine based on its past behaviour. If it is random, then it can be done only with a certain probability. The answer for this question can be obtain only by careful examination of the nature of the signal/system.

The methods used so far, the spectral analysis allows to resolve the determinism in the form of cycles of different lengths, hence they are used to study the periodicity.

New possibilities for this area creates statistical method based on surrogate data [9, 10]. The surrogate data generated with the original data preserve certain properties of the data and destroy others, and is also consistent with a specified null hypothesis. Generically stated, the procedure can be characterized by four steps:

- (1) A discriminating statistic is applied to the original data,
- (2) Artificial surrogate data that are consistent with some null hypothesis are constructed using the original data,
- (3) The discriminating statistic is applied to the surrogates,
- (4) The discriminating statistic value for the original data is compared with the ensemble of values estimated for the surrogates.

One of the newest statistical tests using surrogate data is the Small-Shuffle Surrogate (SSS) test. The test identifies the short-term dynamics (determinism) in the time series of irregular fluctuations, including those containing long cycles or trends. Hence, its versatility, with respect to the data is its main advantage.

Small-Shuffle Surrogate data proposed by Nakamura in [11, 12] allows for nonstationary data analysis, as contrary to linear surrogate methods which analyze stationary data.

SSS can investigate whether there is some kind of dynamics in irregular fluctuations, even if they are modulated by long term trends. The null hypothesis addressed by this algorithm is that irregular fluctuations are independently distributed random variables (i.e. there is no short term dynamics or determinism).

In this paper, we apply the Small-Shuffle surrogate method (SSS) to SPF signal. The results and analysis of these results will be presented and discussed.

This work was supported This research was supported by a research grant NN518 405338 from the Polish Ministry of Science and Higher Education.

W. Nowak is with Institute of Biomedical Engineering and Instrumentation, Wrocław University of Technology, Poland (corresponding author to provide phone: 713202518; e-mail: wioletta.nowak@pwr.wroc.pl).

A.Hachoł is with Institute of Biomedical Engineering and Instrumentation, Wrocław University of Technology, Poland (e-mail: andrzej.hachol@pwr.wroc.pl).

M.Misiuk-Hojło is with Ophthalmology Department, Wrocław Medical University, Poland (e-mail: misiuk55@wp.pl).

II. MATERIAL AND METHODS

A. Database

SPF was recorded using laboratory version of the pupillometry equipment at a sampling rate of 60 Hz [13]. There are 5 records of healthy subjects, 2 men and 3 women, aged 20-38. All participants were in good health, without any eye disease and they were non-smokers.

Before initiating a measurement series, all subjects participated in a training session concerning the pupillometric measuring procedure. At the beginning the measurement started with adapting the subject to darkness (5 min) and calibrating the system to individual characteristics of the subject. A subject was asked to keep her/his eyes open, look at the fixation point, and avoid blinking and head movements during the recording procedure. Subjects were also asked to avoid drinking coffee and alcohol for 24 hours before the measuring session. Measuring sessions were conducted between 9:00 am and 10:00 am hour. Each measurement lasted for 60 seconds, and the signal length used for the analysis contained 3600 samples. For each subject 4 SPF signals were recorded.

B. Small-Shuffle Surrogate Test and Discriminant Statistic

Small-Shuffle Surrogate (SSS) data are generated as follows: Let the original data be $x(t)$, let $i(t)$ be the index of $x(t)$ (that is, $i(t)=t$, and so $x(i(t))=x(t)$), let $g(t)$ be Gaussian random numbers and $s(t)$ will be the surrogate data. The procedure can be characterized by three steps:

- (1) Obtain $i'(t)=i(t)+Ag(t)$, where A is an amplitude,
- (2) Sort $i'(t)$ by the rank-order and let the index of $i'(t)$ be $\bar{i}(t)$
- (3) Obtain the surrogate data $s(t)=x(\bar{i}(t))$.

In the SS surrogate data the local structures or correlations in irregular fluctuations (short term variability) are destroyed but the global behaviors (trends) are preserved. The SS surrogate data have the same probability distribution as the original data.

The SSS method changes the flow of information in data. Hence, the average mutual information (AMI) has been chosen as the discriminating statistic for surrogate test. AMI, a general nonlinear version of auto-correlation on a time series, can answer the question: on average, how much does one learn about the future from the past?

After calculation of these statistics, the inspection whether a null hypothesis shall be rejected or not is needed. T-test is employed to check whether estimated statistics of the original data fall within or outside the statistic distribution of the surrogate data.

If estimated statistic of the original data fall within the distribution of the surrogate data, the surrogate null hypothesis may not be rejected (in other words, there is no dynamics in irregular fluctuations). Contrary, the null hypothesis may be rejected (the irregular fluctuations have some kind of dynamics) if estimated statistic of the original data fall outside the distribution of the surrogate data.

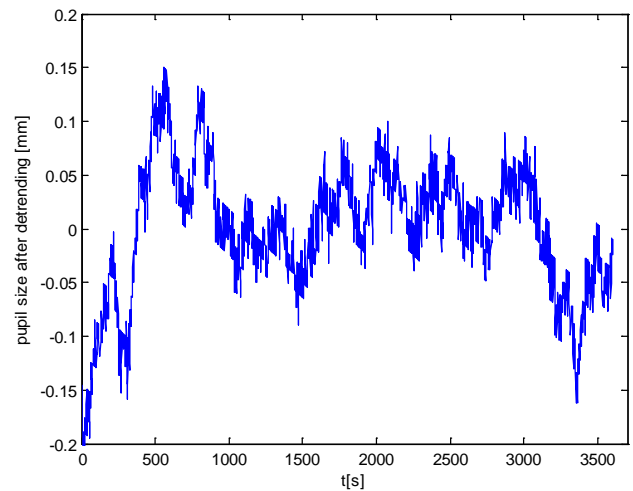
C. Application of the SSS to SPF data

For each of 5 signals of 5 subjects, 50 surrogates time series were generated from the original one. To compare the original and the surrogate series, discriminating statistics (AMI) are calculated for both signals. The significance level is 0.05. This information lead us to reject or not the null hypothesis.

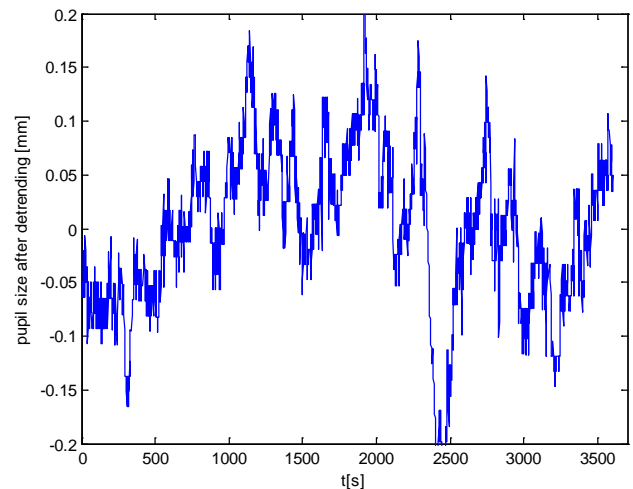
III. RESULTS AND DISCUSSION

Fig. 1a. and Fig. 1b. show two examples of the SPF data. Preliminary observation of time variation of the SPF signals presented in Figure 1 reveals that there are only a few high amplitudes and more medium amplitudes as compared with many small amplitudes ones.

In addition, it is difficult to perceive any regularity in the amplitude changes. Generally, based on this observation it is impossible to determine whether the test system generates random or deterministic values.



a)



b)

Fig. 1. SPF examples signals

Fig. 2 shows the enlarged segments of SPF data and one of the SS surrogate data. Comparison of the course of original data and the course of the surrogate data, shows the large similarity of shapes and only slight (hardly noticeable) differences. This confirms the correctness of the applied SSS data generation algorithm (the SS surrogate method generates data in which long term behaviors are preserved and local structures are destroyed).

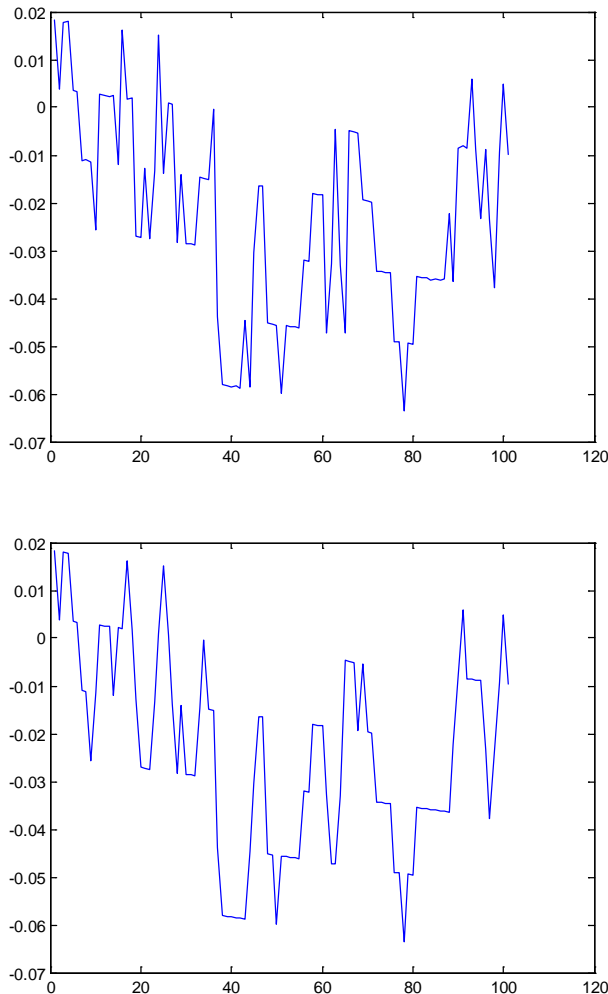


Fig. 2. The enlargement segments of SPF signal (higher panel) and surrogate data (lower panel)

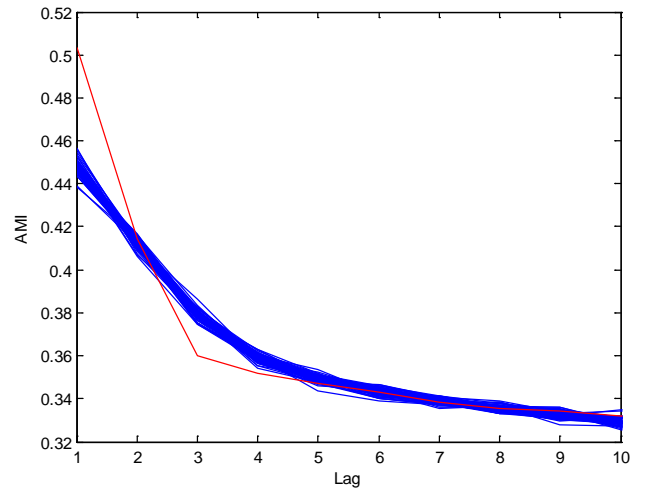
Fig. 3 shows the result of applying the SS surrogate method. The figure shows the AMI estimated for the original data and the AMI distributions of the SS surrogate data.

We noticed that some differences (the original data fall outside the distributions of SS surrogate data) clearly appear when the time lag is relatively small, because the information in the systems is not retained for longer periods of time.

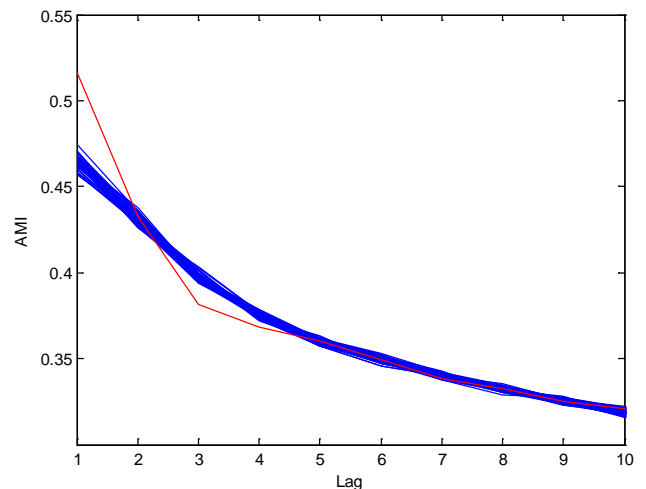
Hence, we conclude that irregular fluctuations in the SPF have some kind of short term (inter second) dynamics.

It is also interesting to note that the course of AMI function for the original data is similar to the course of this function for the surrogate data. This is a confirmation that in the SSS data local structures were destroyed but the global structures were retained.

Tab. 1 shows AMI statistic calculated for all tested subjects.



a)



b)

Fig. 3. The results of SSS test for SPF data presented in Fig. 1. Vertical axis of the plot shows the estimated AMI statistic. Horizontal axis shows the lag. The 'thin' line is the original data and 'thick' lines are the SS data. We use 3600 data points, $A=1.0$ and 50 surrogate data.

Table 1. AMI Statistics for all subjects

SPF signal		AMI (Lag=1)	AMI (Lag=1)
		Original data	Surrogate data
Subject 1	1	0.50	0.45±0.01
	2	0.53	0.45±0.01
	3	0.58	0.52±0.01
	4	0.51	0.44±0.01
Subject 2	1	0.74	0.70±0.01
	2	0.80	0.76±0.01
	3	0.77	0.72±0.01
	4	0.47	0.41±0.01
Subject 3	1	0.34	0.28±0.01
	2	0.53	0.46±0.01
	3	0.44	0.38±0.01
	4	0.40	0.33±0.01
Subject 4	1	0.60	0.57±0.01
	2	0.58	0.56±0.01
	3	0.75	0.70±0.01
	4	0.46	0.39±0.01
Subject 5	1	0.82	0.79±0.01
	2	0.84	0.80±0.01
	3	0.79	0.75±0.01
	4	0.83	0.78±0.01

IV. CONCLUSIONS

In this study we applied a Small-Shuffle Surrogate (SSS) Test for dynamic testing in spontaneous pupil fluctuation (SPF) signal of health subjects. SSS test is capable of testing against the null hypothesis of irregular fluctuations are independently distributed random variables (in other words, there is no dynamics in irregular fluctuations).

Signals which were analyzed represent complex papillary behavior regulated by the sympathetic and parasympathetic innervations of the iris muscles controlled via neural feedback mechanism. As has been shown in Figures and Table, the SSS test detect that irregular fluctuations in the SPF have some kind of short term (inter second) dynamics. These results suggest possible future treatment and understanding SPF signal.

REFERENCES

- [1] I. E. Loewenfeld The Pupil: Anatomy, Physiology, and Clinical Applications (Iowa City, IO: University of Iowa Press) 1993.
- [2] G. Calcagnini, F. Censi, S. Lino, S. Cerutti, " Spontaneous fluctuations of human pupil reflect central autonomic rhythms", *Methods of Information in Medicine*, vol. 39, pp.142-145, 2000.
- [3] B. Wilhelm, H. Giedke, H. Lüdtke, E. Bittner, A. Hoffman, H. Wilhelm, "Daytime variations in central nervous system activation measured by a pupillographic sleepiness test", *J. Sleep Res.*, vol. 10, pp. 1-7, 2001.
- [4] W. Nowak, A. Hachol, H. Kasprzak, "Time-frequency analysis of spontaneous fluctuation of the pupil size of the human eye", *Optica Applicata*, vol. 38, pp. 469-480, 2008.
- [5] G. Leal, C. Neves, P. Viera, "A novel method of measuring autonomic nervous system pupil dynamics using wavelet transform", in *XIII*

- Mediterranean Conference on Medical and Biological Engineering and Computing*, pp. 827-830, 2013
- [6] W. Nowak, E. Szul-Pietrzak, A. Hachol, "Wavelet Energy and Wavelet Entropy as a New Analysis Approach in Spontaneous Fluctuations of Pupil Size Study – Preliminary Research", in *XIII Mediterranean Conference on Medical and Biological Engineering and Computing* pp. 807-810, 2013.
 - [7] H. Wilhelm, H. Lüdtke, B. Wilhelm, "Pupillographic sleepiness testing in hypersomniacs and normals", *Graefe's Arch Clin Exp Ophthalmol.* vol. 236, pp. 725-729, 1998.
 - [8] F.D Bremner., S.E. Smith, "Pupil abnormalities in selected autonomic neuropathies", *Journal of Neuro-Ophthalmology*, vol.26, pp. 209-219, 2006.
 - [9] J. Fell, J.Roöschke, C. Schäffner, "Surrogate data analysis of sleep electroencephalograms reveals evidence for nonlinearity", *Biol. Cybern.*, vol. 75, pp. 85-92, 1996.
 - [10] R.A. Stępień, "Testing for non-linearity in EEG signal of healthy subjects", *Acta Neurobiol. Exp.*, vol. 62, pp. 277-281, 2002.
 - [11] T. Nakamura, M. Small," Small-shuffle surrogate data : Testing for dynamics in fluctuating data with trends", *Physical Review E*, vol. 72, 056216, 2005.
 - [12] T. Nakamura, M. Small, "Applying the method of small-shuffle surrogate data: testing for dynamics in fluctuating data with trends", *International Journal of Bifurcation and Chaos*, vol.16, pp. 3581-3603, 2006.
 - [13] A. Hachol, W. Szczepanowska-Nowak, H. Kasprzak, I. Zawojcka, A. Dudzinski, R. Kinasz, D. Wyględowska-Promienska, „ *Measurement of pupil reactivity using fast pupillometry*". *Physiol Meas* vol. 28, pp. 61-72, 2007.

A new approach for selective optical fiber sensors based on localized surface plasmon resonance of gold nanostars in molecularly imprinted polymer

Maria Pesavento, Nunzio Cennamo, Alice Donà, Piersandro Pallavicini, Girolamo D'Agostino and Luigi Zeni

Abstract— An optical chemical sensor based on localized surface plasmon resonance (LSPR) in a plastic optical fiber (POF) for the selective detection and analysis of trinitrotoluene (TNT) in aqueous solution has been developed. LSPR is excited in five-branched gold nanostars (GNS), suspended in a molecularly imprinted polymer (MIP) specific for TNT, which assures the selectivity. This sensing layer has been deposited directly on the exposed POF core. The sensor shows better performance than a similar one previously proposed, in which the SPR was excited in a thin gold layer at the surface of the POF. In the GNS sensor the sensitivity was $8.5 \cdot 10^4$ nm/M, three times higher than in the gold layer sensor.

Keywords— chemical optical sensors, gold nanostars, localized surface plasmon resonance, molecularly imprinted polymer, trinitrotoluene.

I. INTRODUCTION

Localized surface plasmon resonance (LSPR) is a very sensitive technique for determining small refractive index changes at the interface between a metal and a dielectric medium.

Thus it is a common tool for surface and nano-surface interaction analysis and bio-sensing, widely used as a detection method for sensors that operate in different areas of bio and chemical sensing as reported in several recent review papers [1,2]. The signal, i.e. the change of the refractive index at the

interface, which is measured by SPR techniques, must be due to the adsorption/combination of the considered substance (i.e. the analyte) at the sensor surface.

In the present investigation, LSPR is applied as the transduction optical method to obtain a device with characteristics suitable for on line and remote sensing. As a proof of principle, 2,3,6-trinitrotoluene (TNT), an aromatic nitroderivative explosive with low molecular mass, has been considered.

LSPR biosensors are commonly regarded as suitable for the analysis of medium or large molecular weight analytes, however several approaches have been proposed for the detection of low molecular mass substances too, mainly based on reactions which give by-products inducing measurable refractive index changes at the surface of the optical device. Molecularly imprinted polymers (MIPs) have been proved to present such a characteristics, so that they can be considered as suitable receptors to be used in combination with SPR as transduction method [3]. MIPs are synthetical porous solids obtained by the molecular imprinting methods [4,5], containing specific sites interacting with the molecule of interest according to a “key and lock” model. They present a number of favorable aspects for sensing in comparison to bioreceptors such as, for example, antibodies [6], including a better stability out of the native environment, a better reproducibility and a lower cost. Another relevant feature of MIPs, in comparison with other receptors, is the selectivity. In the case of the MIP for TNT here considered, it has been found to be very good, even against molecules of similar chemical structure [3].

Sensors based on SPR in a plastic optical fiber present several advantages [3]. Indeed, the use of a plastic optical fiber reduces the cost and the dimension of the device, with the possibility of easy integration of SPR sensing platform with optoelectronic devices, such as LEDs and photodetectors, and electronic devices for data processing, as well. Moreover, the multiple reflections of light occurring in the optical fiber allow to excite the sample to a large extent, so the detection

M. Pesavento is with the Department of Chemistry, Pavia University, 27100 Pavia -Italy (corresponding author: xx39 0382 987580; fax: xx39 0382 528544; e-mail: maria.pesavento@unipv.it).

N. Cennamo is with the Department of Industrial and Information Engineering, Second University of Naples, 81031 Aversa - Italy, (e-mail: nunzio.cennamo@unina2.it).

A. Donà is with inLAB, Department of Chemistry, University of Pavia, 27100 Pavia - Italy (e-mail: alice.dona@gmail.com).

P. Pallavicini is with inLAB, Department of Chemistry, University of Pavia, 27100 Pavia - Italy (e-mail: piersandro.pallavicini@unipv.it).

G. D'Agostino is with the Department of Chemistry, Pavia University, 27100 Pavia -Italy (e-mail: girolamo.dagostino@unipv.it).

L. Zeni is with the Department of Industrial and Information Engineering, Second University of Naples, 81031 Aversa - Italy, (e-mail: luigi.zeni@unina2.it).

sensitivity to the analytes could be improved.

Additional benefits are expected from the use of five-branched gold nanostars (GNS) [7] instead of a gold thin film [8]. For example the multiple resonances of GNS [7] may add flexibility to the sensor's design, making it possible to vary the geometry, the material and the indagated wavelength. Besides, the very thin dimensions of GNS would allow a larger interface between the metal and the dielectric, and a direct connection with the interaction sites of TNT in the MIP, in a tridimensional way. All these effects should improve the sensitivity of the detection. In addition the plastic optical fiber sensor based on LSPR effect in gold nanostars may have the benefits of being compact, low cost and high sensitivity devices, well suited for remote/online detection.

II. DEFINITION OF LSPR PARAMETERS

The sensitivity (S) of a sensor based on gold nanoparticles can be defined by calculating the shift in resonance wavelength per unit change in refractive index (LSPR sensors with spectral interrogation). It is usually reported in nanometers of peak shift per Refractive Index Unit (nm/RIU):

$$S = \frac{\delta\lambda_{res}}{\delta n} \left[\frac{nm}{RIU} \right] \quad (1)$$

The simplest sensing application of LSPR-active particles or nanostructures [8,9] is to detect changes in the bulk refractive index of their environment through shifts in the LSPR peak wavelength. LSPR peaks are typically detected by spectral extinction measurements on a dense film or spectral scattering measurements on single nanoparticles.

For this bio-chemical optical sensor the sensitivity is more conveniently defined as:

$$S = \frac{\delta\lambda_{res}}{\delta c} \left[\frac{nm}{M} \right] \quad (2)$$

In other words, the sensitivity can be defined by calculating the shift in resonance wavelength per unit change in analyte concentration (nm/M).

III. OPTICAL SENSING PLATFORM

The fabricated optical sensor system was realized removing the cladding of a plastic optical fiber along half circumference (D-type plastic optical fiber). The sample consisted in a plastic optical fiber without jacket embedded in a resin block, with the purpose of easing the polishing process. This was carried out with a 5 μm polishing. After 20 complete strokes following a "8-shaped" pattern in order to completely expose the core, a 1 μm polishing paper was used for another 20 complete strokes with a "8-shaped" pattern. The realized region was about 10 mm in length. The sensing layer (MIP with suspended GNS) is deposited on the exposed POF core.

The plastic optical fiber has a PMMA core of 980 μm and a fluorinated polymer cladding of 20 μm . The refractive indexes

of the materials, in the visible range of interest, are about 1.49 for PMMA, 1.41 for fluorinated polymer.

IV. SENSING LAYER: MATERIALS AND METHODS

A. Preparation of Five-Branched Gold Nanostars

The preparation of gold nanostars was made according to an established seed growth method [7]. Briefly, a seed solution was prepared as following. In a 20 mL vial, HAuCl_4 (5 mL, 5×10^{-4} M in water) is added to an aqueous solution of TritonX-100 (5 mL, 0.2 M). The mixture is gently hand-shaken and a pale yellow color is obtained. Then, a previously ice-cooled solution of NaBH_4 (0.6 mL, 0.01 M in water) is added. The mixture is gently hand-shaken and a reddish color appears. Growth solution (10 mL) is prepared as following. In a 20 mL vial, AgNO_3 (180 μL , 0.004 M in water) and HAuCl_4 (5 mL, 0.001 M in water) are added in this order to an aqueous solution of TritonX-100 (5 mL, 0.2 M). Then, an aqueous solution of ascorbic acid (170 μL , 0.0788 M) is added. The solution, after gentle mixing, becomes colorless. Soon after, the seed solution (12 μL) was added. The solution is gently hand-shaken and a pink color appears and quickly changes to blue and becomes more intense. After 1 h at room temperature PEG₂₀₀₀-SH is added in a concentration of 5×10^{-5} M. The mixture is stirred for 1h at room temperature, then the nanoparticles undergo four cycles of ultracentrifugation (13,000 rpm, 11 min)/elimination of the supernatant/redissolution of the pellet in 10 mL of bi-distilled water. These steps are required to eliminate excess PEG₂₀₀₀-SH and TritonX-100. The pellet is dried under vacuum to obtain 0.6 mg of gold in the nanostars. Figure 1 shows TEM image of GNS.

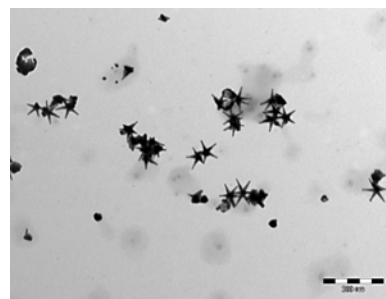


Fig. 1 TEM image of the same sample (acquired on a Jeol JEM-1200 EX II 140 instrument).

B. Prepolymeric mixture for MIP

Divinylbenzene [1321-74-0] (DVB), 2,2'-azobisisobutyronitrile [78-67-1] (AIBN), 2,2-dichloro-N-[1,3-dihydroxy-1-4(4-nitrophenyl)propan-2-yl]acetamide [56-75-7] (CAP, chloramphenicol) were obtained from Sigma-Aldrich and used without any further purification. Methacrylic acid (MAA) [79-41-4] (Sigma-Aldrich cod. M0782) and divinylbenzene (DVB) [1321-74-0] (Sigma-Aldrich cod. 414565) were purified with molecular sieves (Sigma-Aldrich

cod 208604) prior to use in order to remove stabilizers. 2,4,6-trinitrotoluene (TNT) and 2,4,6-trinitrobenzoic acid (TNBA) were synthesized as previously reported [3] (98% purity tested by HPLC). All other chemicals were of analytical reagent grade. The solvent was deionized water.

Stock solutions were prepared by weighing the solids and dissolving in ultrapure water (Milli-Q).

The prepolymeric mixture for MIP was prepared according to a classical procedure [3]. It is composed of trinitrotoluene (TNT) as template (20 mg), methacrylic acid as functional monomer (30 μ l), DVB as cross-linker (665 μ l) and AIBN as the radicalic initiator (15 mg). The reagents were at molar ratio 1 (TNT): 4 (MAA): 40 (DVB). The mixture was uniformly dispersed by sonication (visually omogeneous solution) and de-aerated with nitrogen for 10 min.

C. Sensor preparation by MIP with Gold Nanostars

The pellet of gold nanostars was dissolved in 0.9 mL of prepolymeric mixture by sonication. The final concentration of the nanostars, expressed as mg of gold per mL of prepolymeric mixture, is 0.67 mgAu/mL. The polymeric film was prepared by dropping 100 μ l of prepolymeric mixture on the gold layer, and polymerizing at 70°C for about 16 h. The template molecule was extracted by washing with ethanol 10 times, leaving the imprinted sites free for successive template rebinding. A schematic view of the sensor is reported in Fig 2.

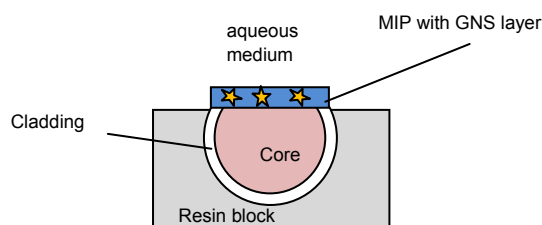


Fig. 2 Section view of sensing region

V. EXPERIMENTAL SETUP

The experimental setup was arranged to measure the transmitted light spectrum and included a halogen lamp, illuminating the optical sensor systems (POF of 1,000 μ m in

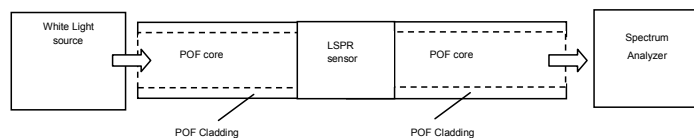


Fig. 3 Top view of sensor system and experimental setup.

diameter), and a spectrum analyzer. The employed halogen lamp (Model no. HL-2000-LL, manufactured by Ocean Optics) exhibits a wavelength emission range from 360 nm to 1,700 nm, while the spectrum analyzer detection range was from 200 nm to 850 nm. An Ocean Optics “USB2000+UV-VIS” spectrometer has been employed.

The spectrometer was finally connected to a computer. The LSPR curves along with data values were displayed online on the computer screen and saved with the help of advanced software provided by Ocean Optics. Fig. 3 shows the experimental setup and top view of the chemical sensor in POF based on LSPR in MIP.

VI. RESULTS AND DISCUSSION

The measurements were performed by dropping 100 μ l of deionized water, or aqueous solution of the target molecule (TNT), over the resin block holding the modified optical fiber, letting the drop to expand over the whole resin block. The transmission spectra were recorded after 5 min incubation. The experimentally obtained SPR transmission spectra were normalized to the reference spectrum, which is the spectrum obtained with air as the surrounding medium when an MIP

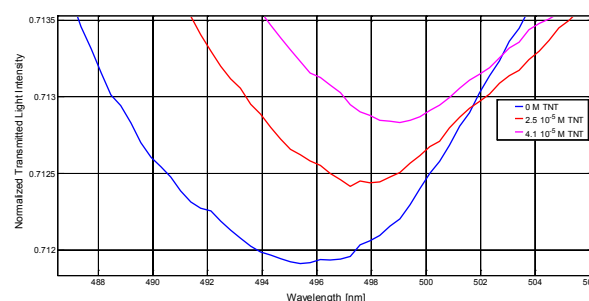


Fig. 4 LSPR transmission spectra, normalized to the reference spectrum, for different concentrations of TNT.

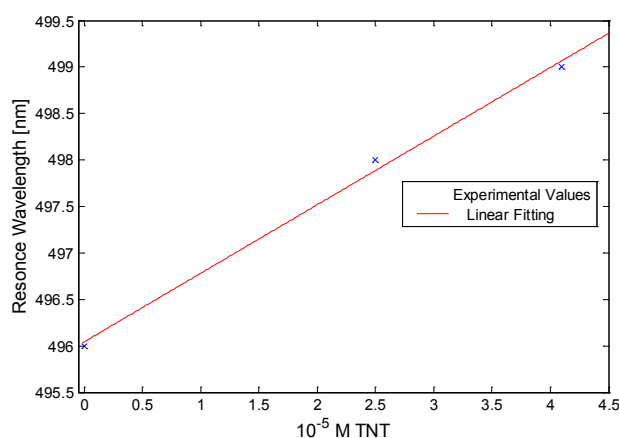


Fig. 5 Plasmon resonance wavelength as a function of TNT concentration.

layer without GNS is placed on the POF core (reference spectrum). Between successive determinations the sensor was washed by repeatedly rinsing with water.

Figure 4 presents the LSPR transmission spectra, normalized to the reference spectrum, for different concentrations of TNT. The spectra reported in Fig 4 show that the localized surface plasmon resonance takes place also when the GNS are suspended in the hydrated polymer phase (blue curve), as when they are in direct contact with the POF [8]. This indicates that the light emerging from the fiber penetrates sufficiently in the polymer to interact with the GNS.

It is also seen that, when increasing concentrations of TNT enter the molecularly imprinted polymer, the LSPR phenomenon varies and the resonance wavelength is shifted to the higher wavelengths. In optical sensors based on LSPR, when the refractive index at the GNS-dielectric interface increases, according to LSPR phenomenon theory, the resonance wavelength is shifted to higher values (red shift). The resonance wavelengths corresponding to the dips in Figure 4 were evaluated by Matlab software.

Figure 5 shows the resonance wavelengths as a function of different concentrations of TNT. In the same figure, the linear fitting to the experimental data is presented too.

The parameters of the regression line are here reported, and compared with the same function previously obtained for the same MIP for TNT, but with a gold layer interposed between the bare POF and the MIP layer [3] ($n=3$ in both cases):

$$\begin{aligned} \text{GNS in MIP} &\rightarrow \lambda_{\text{ex}} = 8.5(3) \cdot 10^4 c_{\text{TNT}} + 495.4(1) & R^2 = 0.998 \\ \text{gold layer} &\rightarrow \lambda_{\text{ex}} = 2.7(8) \cdot 10^4 c_{\text{TNT}} + 758.5(7) & R^2 = 0.925 \end{aligned}$$

These functions (regression line) are illustrated in Figure 6.

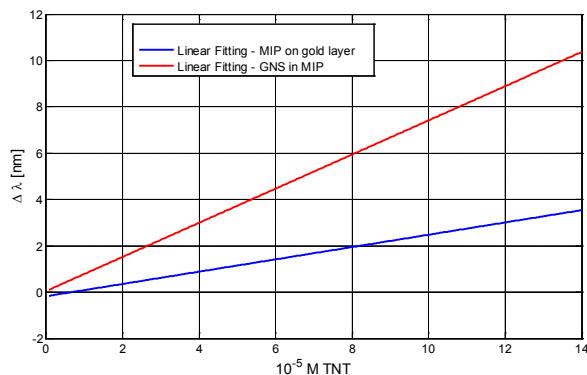


Fig. 6 Blue Line shows the Linear Fitting to the experimental values for the POF sensor with MIP layer on gold film. Red Line shows the Linear Fitting to the experimental values for the POF sensor with GNS in MIP.

The sensitivity is noticeably improved in the sensor based on the gold nanostars suspended in the polymer with respect to the previously proposed sensor based on a thin gold layer [3]. As a consequence the lower detection limit (LOD) was much better too, being $2.4 \cdot 10^{-6}$ M instead of $5.1 \cdot 10^{-5}$ M (detection limit evaluated from twice the standard deviation of the blank).

This indicates that the configuration based on GNS

suspended in the polymer is much more sensitive to the refraction index variation than the thin layer gold, probably because of the three dimensional structure of the nanostars. This allows the metal surface to be directly in contact with more combination sites in the polymer than the bidimensional gold layer.

It must be recalled that an interesting characteristics of MIPs is their very high selectivity. The MIP specific for TNT here prepared and used is equal to that previously applied for a POF sensor [3], which has been proved to be selective even against molecules of very similar structure.

VII. CONCLUSION

In conclusion, the experimental results indicate that the configuration with the five-branched gold nanostars in MIP is actually suitable for TNT detection. The sensitivity of this new POF sensor based on GNS in MIP is about three times the value of the POF sensor with an MIP layer on the gold film.

It has been found that it is possible to dissolve the five branched gold nanostars prepared and purified as described in the prepolymeric mixture for MIP formation at a sufficiently high concentration to obtain a significant LSPR signal. This can be at least in part ascribed to the particular shape of the considered nano-objects

This sensor is easy to prepare, low cost and it opens the door to a new approach in the chemical optical sensor topic.

ACKNOWLEDGMENT

The work was partially supported by POR Campania FSE 2007/2013 and by FAR 2009 of the University of Pavia.

REFERENCES

- [1] K.M. Mayer, J.H. Hafner, "Localized surface plasmon resonance sensors", *Chem. Rev.*, vol. 111 (6), pp. 3828–3857, June 2011.
- [2] E. Petryayeva, U. J. Krull, "Localized surface plasmon resonance: Nanostructures, bioassays and biosensing—A review", *Anal. Chim. Acta*, vol. 706, pp. 8–24, 2011.
- [3] N. Cennamo, G. D'Agostino, R. Galatus, L. Bibbò, M. Pesavento, L. Zeni, "Sensors based on surface plasmon resonance in a plastic optical fiber for the detection of trinitrotoluene", *Sensors and Actuators B*, vol. 188, pp. 221–226, 2013.
- [4] B. Sellergren, "Noncovalent molecular imprinting: antibody-like molecular recognition in polymeric network materials", *Trends in Analytical Chemistry*, vol. 16, pp. 310–320, 1997.
- [5] A.G. Mayes, K. Mosbach, "Molecularly imprinted polymers: useful materials for analytical chemistry?", *Trends in Analytical Chemistry*, vol. 16, pp. 321–332, 1997.
- [6] K. Haupt, K. Mosbach, "Molecularly imprinted polymers and their use in biomimetic sensors.", *Chem Rev*, vol. 100, pp. 2495–2504, 2000.
- [7] P. Pallavicini, A. Donà, A. Casu, G. Chirico, M. Collini, G. Dacarro, A. Falqui, C. Milanese, L. Sironic, A. Taglietti, "Triton X-100 for three-plasmon gold nanostars with two photothermally active NIR (near IR) and SWIR (short-wavelength IR) channels", *Chem. Commun.*, vol. 49, pp. 6265–6267, 2013.
- [8] N. Cennamo, G. D'Agostino, A. Donà, G. Dacarro, P. Pallavicini, M. Pesavento, L. Zeni, "Localized Surface Plasmon Resonance with Five-Branched Gold Nanostars in a Plastic Optical Fiber for Bio-Chemical Sensor Implementation" *Sensors*, vol. 13(11), pp. 14676–14686, 2013.

- [9] M.A. Garcia, "Surface plasmons in metallic nanoparticles: Fundamentals and applications", J. Phys. D Appl. Phys., vol. 44 (28), June 2011.

Maria Pesavento is full professor of analytical chemistry at the Chemistry Department of University of Pavia. Her research interests are in the field of environmental analytical chemistry, in particular in the development of specific adsorbing materials and sensors.

Nunzio Cennamo is a post-doc at the Department of Industrial and Information Engineering at Second University of Naples, Italy. His main interest deals with the design of advanced optical sensors.

Alice Donà is Ph.D. student at the University of Pavia. Her research interest is synthesis of metal nanoparticles and their surface modification for biomedical and sensing applications.

Piersandro Pallavicini is associate professor in the Chemistry Department of the University of Pavia. His research interests are in the synthesis of inorganic nano-objects, modification of inorganic surfaces, biomedical applications of nanomaterials, sensing in micellar nanocontainers.

Girolamo D'Agostino is a post-doc at the Department of Chemistry at University of Pavia, Italy. His main interest deals with specific synthetic receptors and sensors.

Luigi Zeni is full professor of electronics at the Second University of Naples and president of the Research Consortium on Advanced Remote Sensing Systems – CO.R.I.S.T.A., Naples, Italy. His research interests include the design and fabrication of optical fiber sensors and optoelectronic devices.

Structural determinant for *Helicobacter pylori* resistance to sulfonamides

Anna Roujeinikova

Abstract— Bacterial dihydropterolate synthase (DHPS) is a key enzyme in the folic acid biosynthesis. In many pathogens, DHPS is the molecular target of sulfa drugs (sulfonamides). Sulfonamides act as competitive inhibitors by occupying the binding pocket for the substrate p-aminobenzoic acid. Despite the high degree of cross-species sequence conservation in the p-aminobenzoic-acid-binding site, some bacteria are not sensitive to these drugs. This work addresses the molecular mechanism of resistance of *Helicobacter pylori* DHPS to sulfonamides. Homology modelling, structural and sequence analysis identify a single amino acid substitution in the substrate-binding pocket as the major determinant for its resistance. Structure-guided rational modification of sulfonamides to fit the specific architecture of the *H. pylori* enzyme's active site may be a strategy to develop novel antimicrobial agents with specific activity against *H. pylori*.

Keywords—Dihydropterolate synthase, *Helicobacter pylori*, homology model, sulfonamides.

I. INTRODUCTION

SULFONAMIDES (SO₂-NH-), commonly termed sulfa drugs or sulpha drugs, are broad-spectrum bacteriostatic antibiotics that block folic acid synthesis by inhibiting the enzyme dihydropterolate synthase (DHPS) [1]. This enzyme catalyzes the condensation of 6-hydroxymethyl-7,8-dihydropterin-pyrophosphate (DHPP) with p-aminobenzoic acid (pABA) to produce the intermediate in the folic acid synthesis, 7,8-dihydropterolate. Sulfonamides act as competitive inhibitors: they have a greater affinity than pABA for DHPS. DHPS inhibition leads to depletion of folic acid in bacterial cells, and since most bacteria lack a transport system to take up preformed folic acid from their environment, this results in a growth inhibition and cell death. DHPS is not present in mammalian cells. Sulfonamides used clinically include sulfamethoxazole (SMX), sulfadiazine, sulfadoxine and sulfametopyrazine. These drugs kill a wide spectrum of bacteria encompassing most Gram-positive and many Gram-negative bacteria.

Helicobacter pylori is a Gram-negative bacterium present in the stomachs of roughly half of the world's population [2]. It is associated with severe gastroduodenal diseases including gastric and duodenal ulcers, mucosa-associated lymphoid

tissue lymphoma and gastric adenocarcinoma [3], [4]. Eradication of *H. pylori* reduces the recurrence of gastric cancer in patients who received early surgical treatment of gastric cancer and the recurrence of both gastric and duodenal ulcers in patients with peptic ulcer disease [5], [6]. Current treatments of *H. pylori* infections involve the use of a combination of a proton pump inhibitor with two broad-spectrum antibiotics (mainly clarithromycin and either amoxicillin or metronidazole) [7]. However, the efficacy of the treatment has now dropped below 80% [8], mainly due to antibiotic resistance and lack of patient compliance. An increasing prevalence of resistance to the antibiotic components of such regimens requires development of novel drugs against *H. pylori*.

H. pylori is naturally resistant to sulfonamides, despite the fact that it does possess DHPS (fused with a separate, dihydropterolate reductase (DHPR) domain) [9]. This work addresses the molecular mechanism of resistance of *H. pylori* DHPS to sulfonamides with the view to facilitate rational modification of these drugs in order to attain novel specific activity against *H. pylori*. Detailed structural analysis of DHPS-sulfonamide interactions in other bacterial species has been previously hampered by the lack of observable electron density for the flexible conserved loops in the enzyme's active site [10]. The recent report of the crystal structure of *Yersinia pestis* DHPS in complex with sulfonamide drug complex was a breakthrough in the field [10], as it revealed, for the first time, the structure of the loops and the stabilizing interactions that they make with the inhibitor. The significant level of sequence identity (approximately 36%) between the DHPS enzymes from *H. pylori* and *Y. pestis* allowed us to build an accurate homology model for the *H. pylori* protein, based on the known 3D coordinates of its *Y. pestis* counterpart [10], and pinpoint the single amino acid substitution that likely confers resistance.

II. MATERIALS AND METHODS

The homology model of the DHPS domain of the DHPS/DHPR from *H. pylori* was constructed using MODELLER (9v13) [11], [12] based on the coordinates of the 2.1-Å resolution crystallographic model of the complex of *Y. pestis* DHPS with DHPP and SMX (RCSB PDB 3tfz) [10]. The spatial restraints, including distance restraints and torsion angle restraints, were derived from the sequence alignment (Fig. 1) and used in the automated 3D-model building. The model was further optimized with the internal optimizer of

A. Roujeinikova is with the Department of Microbiology and Department of Biochemistry and Molecular Biology, Building 76, Monash University, Clayton Campus, Victoria 3800, Australia (phone: +61 399029194; fax +61 399029222; e-mail: Anna.Roujeinikova@monash.edu).

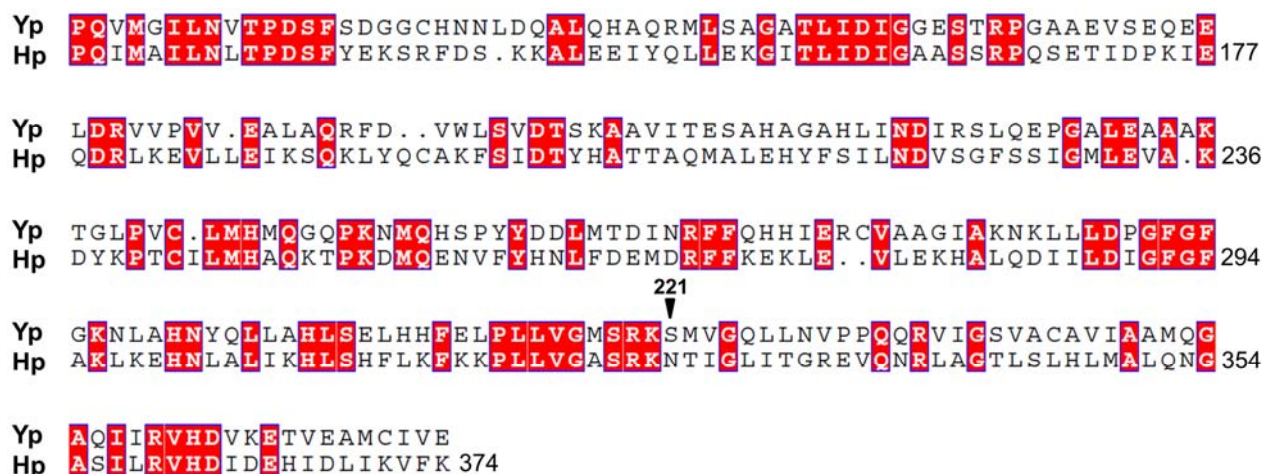


Fig. 1 Alignment of the sequences of *Y. pestis* DHPS (RCSB PDB 3tfz) and the DHPS domain of *H. pylori* DHPS/DHPR (NCBI YP_006226380). Sequence numbering is shown for the *H. pylori* protein. Identical residues are highlighted. The position of Ser221 in *Y. pestis* DHPS is indicated with an arrow.

MODELLER. Model quality was assessed using the Prosa2003 [13], [14], ProQ [15] and Verify3D [16] quality scores.

Sequence alignment was performed with ClustalW2 [17] using the default parameters. Structural superimpositions were carried out using the Swiss PDB viewer [18]. Figures were prepared using ESPript [19] and PYMOL [20].

III. RESULTS AND DISCUSSION

Analysis of the crystal structure of the *Y. pestis* DHPS complex with DHPP and SMX (RCSB PDB 3tfz) [10]

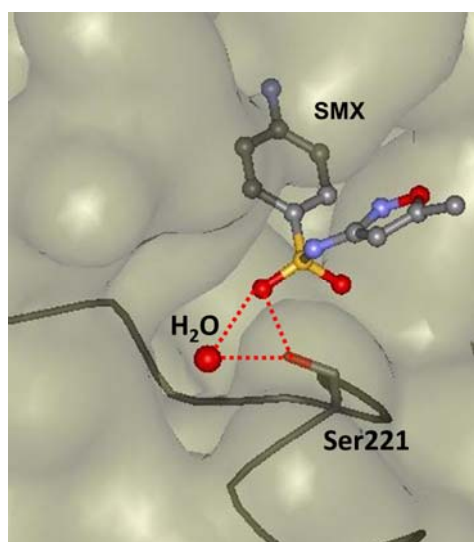


Fig. 2 The SMX molecule occupying the pABA-binding pocket in the crystal structure of the *Y. pestis* DHPS complex with DHPP and SMX (RCSB PDB 3tfz) [10] is stabilized by hydrogen bond interactions between the side chain of Ser221, a water molecule and the oxygen atom of the SMX sulfonyl group.

revealed that SMX fits well into the specific binding pocket for pABA, formed by the two conserved flexible loops one of which harbors Ser221 (Fig. 2). This residue plays an important role in stabilizing the polar moiety of the bound SMX molecule in the pocket that has an overall hydrophobic nature. Its side chain forms hydrogen bonds with the electronegative oxygen atom of the SMX sulfonyl group and with the water molecule which forms an additional hydrogen bond with the same oxygen atom of SMX.

In order to gain an understanding of why sulfonides inhibit *Y. pestis* DHPS but not its homologue from *H. pylori*, a 3D homology model of the complex of *H. pylori* DHPS with SMX was created using the coordinates of the crystal structure of the *Y. pestis* DHPS complex with DHPP and SMX. The ligands were excluded from the initial calculations for the protein moiety. To model the SMX binding in the pABA-binding pocket of *H. pylori* DHPS, the 3D atomic model of the latter was superimposed with the crystal structure of the *Y. pestis* DHPS/DHPP/SMX complex. The conformations of the side chains in the *H. pylori* protein model around the SMX molecule were manually adjusted to remove clashes with the SMX atoms using the manipulation tools implemented in Coot [21]. This model was further optimized by structure idealization through iterative manual model re-building and simulated annealing calculations using an approach similar to the published procedure [22]. The detailed comparative analysis of the generated model and the crystal structure of the *Y. pestis* DHPS/DHPP/SMX complex showed that the residues forming the SMX binding pocket tunnel are highly conserved between the two proteins with exception of one amino acid: Ser221 in *Y. pestis* DHPS is substituted by Asn in its *H. pylori* homologue (Figs 1 and 3). Modelling of the side chain of Asn336 with the same torsion angle χ_1 as in the structure of the *Y. pestis* DHPS indicated in a steric clash with the SMX molecule. Modelling with $\chi_1=180^\circ$ removed clash but generated an unfavorable contact between the aliphatic carbon atom C β and the negatively charged oxygen atoms of the SMX sulfonyl group (Fig. 3). Further structural analysis shows that Asn at the position occupied by Ser221 in *Y. pestis* DHPS would make the pocket, that binds the polar sulfonyl

moiety of SMX, strongly hydrophobic (Fig. 3). Thus, the Ser→Asn substitution is likely to result in poor affinity of *H. pylori* DHPS to sulfonamides. The hypothesis that the presence of Asn at position 326 of *H. pylori* DHPS is the major determinant for its resistance to sulfonamides can be tested using site-directed mutagenesis. Subsequent structure-guided rational modification of sulfonamides to fit the specific architecture of the *H. pylori* enzyme's active site may be a strategy to develop novel antimicrobial agents with specific activity against *H. pylori*.

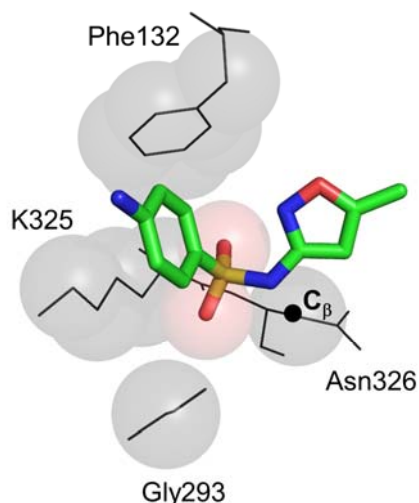


Fig. 3 The binding pocket for SMX in the model of *H. pylori* DHPS. Aliphatic carbon atoms of the protein side chains (shown as grey spheres) form a strongly hydrophobic pocket that does not complement the electronegative sulfonyl group of the inhibitor, likely resulting in the low affinity.

REFERENCES

- [1] L. Huang, K. Crothers, C. Atzori, T. Benfield, R. Miller, M. Rabodonirina *et al.*, "Dihydropteroate synthase gene mutations in pneumocystis and sulfa resistance," *Emerg. Infect. Dis.*, vol. 10, no. 10, pp. 1721–1728, Oct. 2004.
- [2] A. Covacci, J. L. Telford, G. Del Giudice, J. Parsonnet, and R. Rappuoli, "*Helicobacter pylori* virulence and genetic geography," *Science*, vol. 284, no. 5418, pp. 1328–1333, May, 1999.
- [3] B. J. Marshall, and J. R. Warren, "Unidentified curved bacilli in the stomach of patients with gastritis and peptic ulceration," *Lancet*, vol. 1, no. 8390, pp. 1311–1315, Jun., 1984.
- [4] R. M. Peek, Jr., and M. J. Blaser, "*Helicobacter pylori* and gastrointestinal tract adenocarcinomas," *Nat. Rev. Cancer*, vol. 2, no. 1, pp. 28–37, Jan. 2002.
- [5] A. C. Ford, B. C. Delaney, D. Forman, and P. Moayyedi, "Eradication therapy for peptic ulcer disease in *Helicobacter pylori* positive patients," *Cochrane Database Syst Rev*, no. 2, pp. CD003840, 2006.
- [6] N. Uemura, T. Mukai, S. Okamoto, S. Yamaguchi, H. Mashiba, K. Taniyama *et al.*, "Effect of *Helicobacter pylori* eradication on subsequent development of cancer after endoscopic resection of early gastric cancer," *Cancer Epidemiol. Biomarkers Prev.*, vol. 6, no. 8, pp. 639–642, Aug. 1997.
- [7] G. Treiber, S. Ammon, E. Schneider, and U. Klotz, "Amoxicillin/metronidazole/omeprazole/clarithromycin: a new, short quadruple therapy for *Helicobacter pylori* eradication," *Helicobacter*, vol. 3, no. 1, pp. 54–8, Mar. 1998.

- [8] S. D. Georgopoulos, V. Papastergiou, and S. Karatapanis, "Current options for the treatment of *Helicobacter pylori*," *Expert Opin. Pharmacother.*, vol. 14, no.2, pp. 211–223, Feb. 2013.
- [9] I. Levin, M. Mevarech, and B. A. Palfey, "Characterization of a novel bifunctional dihydropteroate synthase/dihydropteroate reductase enzyme from *Helicobacter pylori*," *J. Bacteriol.*, vol. 189, no. 11, pp. 4062–4069, Jun. 2007.
- [10] M. K. Yum, Y. Wu, Z. Li, Y. Zhao, M. B. Waddell, A. M. Ferreira *et al.*, "Catalysis and sulfa drug resistance in dihydropteroate synthase," *Science*, vol. 335, no. 6072, pp. 1110–1114, Mar. 2012.
- [11] A. Sali, and T. L. Blundell, "Comparative protein modelling by satisfaction of spatial restraints," *J. Mol. Biol.*, vol. 234, no. 3, pp. 779–815, Dec. 1993.
- [12] A. Fiser, R. K. Do, and A. Sali, "Modeling of loops in protein structures," *Protein Sci.*, vol. 9, no. 9, pp. 1753–1773, Sep. 2000.
- [13] M. J. Sippl, "Recognition of errors in three-dimensional structures of proteins," *Proteins*, vol. 17, no. 4, pp. 355–362, Dec. 1993.
- [14] M. Wiederstein, and M. J. Sippl, "ProSA-web: interactive web service for the recognition of errors in three-dimensional structures of proteins," *Nucleic Acids Res.*, vol. 35, no. Web Server issue, pp. W407–W410, Jul. 2007.
- [15] B. Wallner, and A. Elofsson, "Can correct protein models be identified?," *Protein Sci.*, vol. 12, no. 5, pp. 1073–1086, May 2003.
- [16] J. U. Bowie, R. Luthy, and D. Eisenberg, "A method to identify protein sequences that fold into a known three-dimensional structure," *Science*, vol. 253, no. 5016, pp. 164–170, Jul. 1991.
- [17] M. A. Larkin, G. Blackshields, N. P. Brown, R. Chenna, P. A. McGettigan, H. McWilliam *et al.*, "Clustal W and Clustal X version 2.0," *Bioinformatics*, vol. 23, no. 21, pp. 2947–2948, Jun. 2007.
- [18] N. Guex, and M. C. Peitsch, "SWISS-MODEL and the Swiss-PdbViewer: an environment for comparative protein modeling," *Electrophoresis*, vol. 18, no. 15, pp. 2714–2723, Dec. 1997.
- [19] P. Gouet, X. Robert, and E. Courcelle, "ESPrInt/ENDscript: extracting and rendering sequence and 3D information from atomic structures of proteins," *Nucl. Acids Res.*, vol. 31, no. 13, pp. 3320–3323, Mar. 2003.
- [20] W. L. DeLano, "The PyMOL Molecular Graphics System: Version 0.90 (DeLano Scientific, Palo Alto, CA)," 2003.
- [21] P. Emsley, B. Lohkamp, W. G. Scott, and K. Cowtand, "Features and development of Coot," *Acta Cryst. D*, vol. 66, no. Pt4, pp. 486–501, Apr. 2010.
- [22] A. Roujeinikova, "Crystal structure of the cell wall anchor domain of MotB, a stator component of the bacterial flagellar motor: implications for peptidoglycan recognition," *Proc. Natl. Acad. Sci. U S A*, vol. 105, no. 30, pp. 10348–53, Jul. 2008.

Anna Roujeinikova received her training in Natural Sciences (BSc, MSc) at the Moscow Institute of Physics and Technology and obtained her PhD in Structural Biology at the Krebs Institute for Biomolecular Research (The University of Sheffield (UK), 2002). Prior to joining Monash University (Australia) as an Associate Professor, Dr. Roujeinikova developed her research programme in the laboratories of the Institute of Bioorganic Chemistry (Moscow, Russia), The Institute for Cancer Studies (Sheffield, UK), Leicester University (UK) and Manchester University (UK). In 2006, she was awarded a Wellcome Trust Research Career Development Fellowship which supported her work on dissecting the molecular architecture and mode of action of bacterial molecular machines using structural biology techniques and enabled her to establish her first laboratory at the University of Manchester (UK). In 2009, she took an academic position as an ASSOCIATE PROFESSOR at Monash University and relocated from the UK to Australia to establish a new structural biology group. Since 2010, she holds an ARC Research Fellowship. She works in the Faculty of Medicine, Nursing and Health Sciences. Her group's research focus is the structural biology of virulence factors of the carcinogenic bacterium *Helicobacter pylori*. Her research page can be found at www.med.monash.edu.au/microbiology/research/roujeinikova/index.html.

Charge properties and fractal aggregation of carbon nanotubes

Dmitry A. Zhukalin, Andrey V. Tuchin, Sviatoslav V. Avilov, Larisa A. Bityutskaya, Evgeniy N. Bormontov

Abstract— A Theoretical and experimental investigation of the influence of internal electric fields on the fractal aggregation of short and long carbon nanotubes was made. Results show that the electric field occurred in the interface of C_{60} – SWNT, and the nanotube length determined the presence of either a point charge (for short nanotubes) or a distributed charge (for long nanotubes).

Keywords—carbon nanotubes, interface, aggregation, electric charge, electric field.

I. INTRODUCTION

THE aggregation process is one of the most important in nanotechnology. During aggregation a big number of interparticle interactions which are significant for composite and hybrid material synthesis take place. Generally, Van-der-Vaals interactions, hydrogen and covalent bonds are characteristic for carbon nanotubes (CNT) [1,2]. Electrostatic interactions are of great interest at synthesis of self-organised structures based on CNT [3]. In a number of papers [4-6] the nanotubes' sensitivity to an external electrical field was discovered and studied. In the 500 Hz - 50 MHz frequency range at 10 V an orientation of CNT occurs in accordance with the field in different liquids. The current work is dedicated to theoretical and experimental studies on the influence of CNT's electrical activity [7] on their fractal aggregation[8].

This work was supported by the project FP7-IRSES-295260 "ECONANOSORB" under Marie Curie Actions of the 7th Framework Program of European Union

Dmitry A. Zhukalin – PhD candidate, Department of Physics of Semiconductors and Microelectronics of Voronezh State University
E-mail: d.zhukalin@mail.ru

Andrey V. Tuchin - PhD candidate, Department of Physics of Semiconductors and Microelectronics of Voronezh State University
E-mail: a.tuchin@bk.ru

Sviatoslav V. Avilov – PhD candidate, Department of Solid State Physics and Nanostructures of Voronezh State University
E-mail: slava_avilov@hotmail.com

Larisa A. Bityutskaya - PhD, Department of Physics of Semiconductors and Microelectronics of Voronezh State University
E-mail: me144@phys.vsu.ru

Evgeniy N. Bormontov – grand PhD, professor, Department of Physics of Semiconductors and Microelectronics of Voronezh State University
E-mail: me144@phys.vsu.ru

II. MODELING

Often armchair single-walled carbon nanotubes seem as a defect free cylindrical conductors with low resistance and without local charges. This approach is applicable for defect free, non functionalized infinite nanotubes. A capped SWCNTs have two general defects – tube caps. A calculation of the electronic structure of the capped SWCNTs were carried out by a semiempirical AM1 method in the Gaussian software

Let us consider the capped SWCNTs (5,5). Nanotube caps are two hemispheres of a fullerene C_{60} dissected perpendicular to a C_{5v} axis. The interface boundary between a SWCNTs body and the cap includes two rings, where each of them consist of ten carbon atoms. The first ring is formed by hexagon sides of the nanotube body. The second ring is formed by pentagon sides of the cap (fig 1).

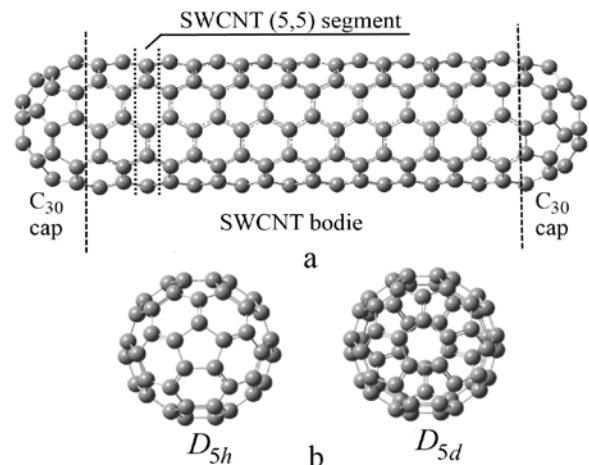


Fig. 1. Structural images of capped SWCNTs (5, 5) and (0, 9) (a). The mutual orientation of two C_{60} hemisphere of the capped SWCNTs (5, 5) D_{5h} and D_{5d} symmetries (b) and SWCNTs (0, 9) D_{3h}/D_{3d} and D_3 symmetries (c).

The charge distribution at the SWCNTs (5,5) interface cap/body is local. Atoms of the cap ring pull back the electron density from atoms of the nanotube body ring. The dependence of a module of the maximum effective charge is the non monotonic and rapidly converges to the constant value $Q_{max}=0.017$ (fig.2).

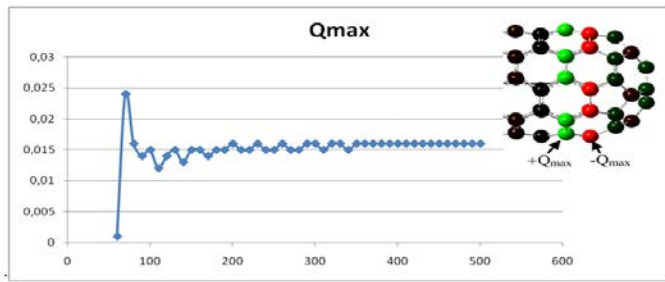


Fig.2 Dependence of the module of the maximal effective charge at the SWCNTs (5,5) interface cap/body on the length of the nanotube (n – number of atoms).

Caps of the SWCNTs (0,9) are hemispheres of the fullerene C60 dissected perpendicular to a C3v axis. The boundary between the cap and the nanotube body is formed by both hexagon and pentagon sides that lead to a less localized charge distribution than in the case of the SWCNTs (5,5). The module of the maximum effective charge increases with the length of the nanotube (fig.3).

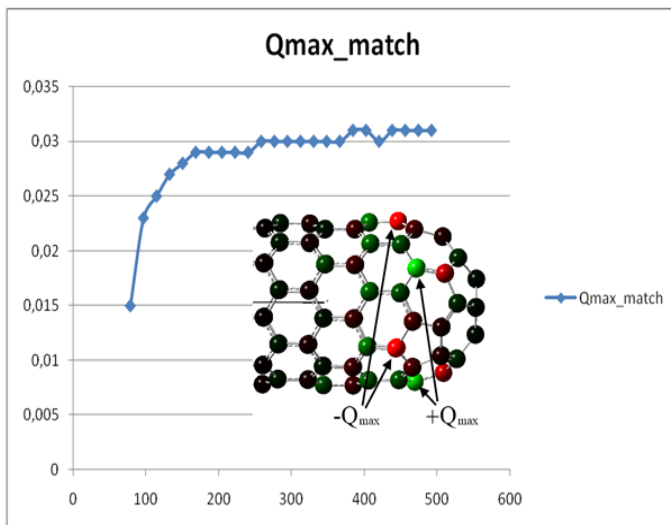


Fig. 3 Dependence of the module of the maximal effective charge at the SWCNTs (0,9) interface cap/body on the length of the nanotube (n – number of atoms).

Thus we have concluded, that the dependence of module of the maximum effective charge rapidly saturates with the length independently to the type and symmetry of nanotubes. The region of the charge that opens up strong electric fields ($\sim 108\text{-}109$ V/m) can be considered as localized. Hence, the induced electric field affects the fractal aggregation of nanotubes.

III. EXPERIMENT

The CNT's fractal aggregation was studied in the point and distributed charge approximations. We used purified CNTs obtained by the CVD technique.

The CNTs were separated by length by sedimentation. A dispersion of CNTs in distilled water was dispersed in an ultrasonic bath (Bandelin SONOREX RK512H) at 45 °C for 10 minutes. Then the obtained dispersion was sedimenting for

5 days at 20 °C. The samples were probed from 3 levels (fig. 4): h ; $h/2$; $h/4$. The solution was separated into fractions with the subsequent extraction of isotropic and anisotropic fractal aggregates of carbon nanotubes (A, B, C). Optic microscopy (NU-2E) and electron microscopy (JEOL JSM-6380) techniques were applied in order to study the topology of these fractal aggregates. An object-plate was used as substrate for optical microscopy studies. A flat conductive substrate was used for electronic microscopy.

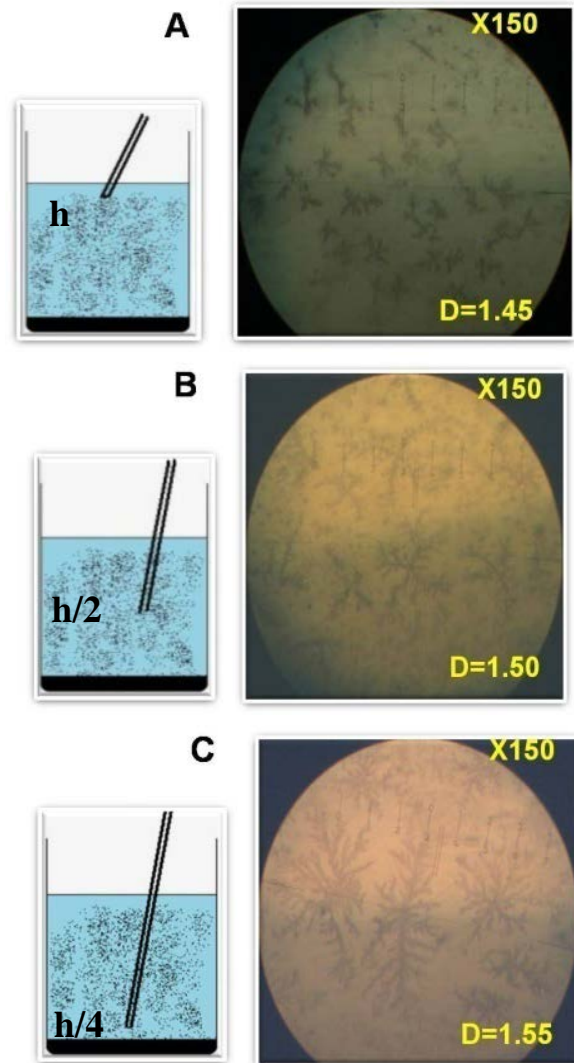


Fig. 4. Sedimentation of the CNT conglomerate in distilled water. A: sampling level h ; B: $h/2$; C: $h/4$.

Depending on the sampling level a hierarchy of clusters was observed, differing in morphology and size. Large anisotropic clusters were found at the $h/4$ level, isotropic and anisotropic clusters at the $h/2$ level and isotropic clusters at the h level.

The fractal dimension D and Anisotropy coefficient A were estimated from the microphotographs. The anisotropy coefficient was calculated as a ratio between the greatest cluster diameter to the greatest orthogonal axicon. The fractal dimension was calculated using the grid method.

It was found that with the increase of the CNT concentration in the dispersion, defined by the level h , the

fractal dimension is decreasing with the increase of the anisotropic aggregate percentage and the anisotropy coefficient (table 1).

Table 1. Fractal dimension versus sample probing level and anisotropy coefficient.

level (h)	Fractal Dimension D	Anisotropy coefficient A
H	1.55	1, 1.4
h/2	1.5	1, 1.4
h/4	1.45	1, 2.1

The scale invariance of the studied fractal clusters was observed using SEM of light CNT dispersions from the pre-surface level (Fig. 5a). With further magnification (Fig. 5b) the morphology of the primary fractal CNT cluster is observed.

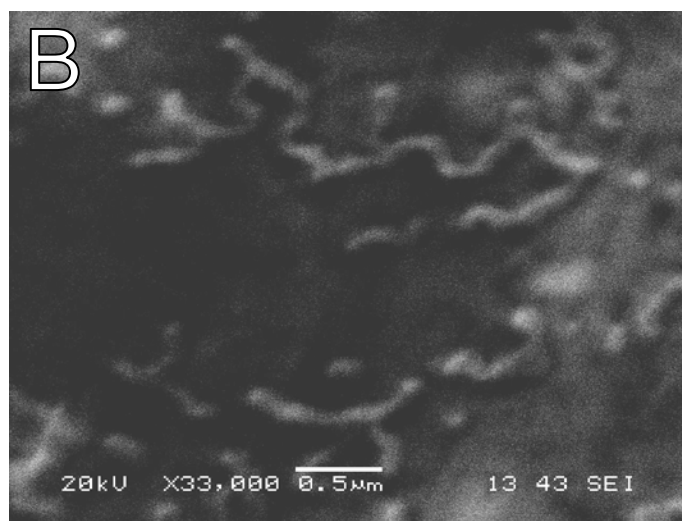
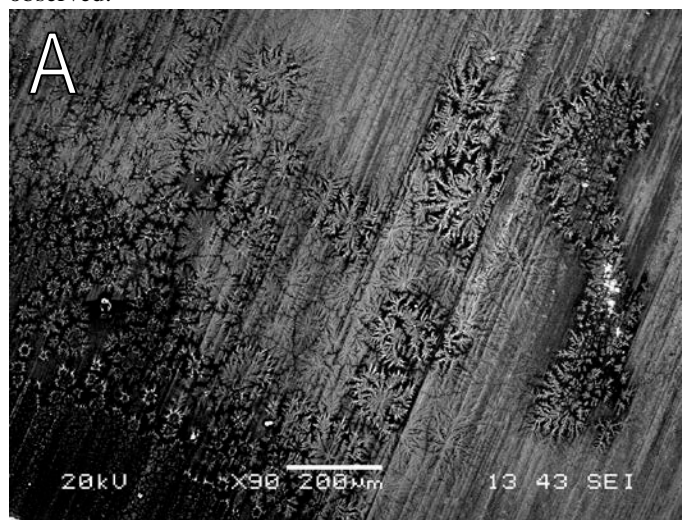


Fig. 5. SEM image (JEOL JSM-6380) of the CNT fractal clusters. A: fractal clusters (50-200 μm) X90. B: fractal clusters (0.5-2 μm) X33000

By characteristic lengths it was determined that the fractal clusters consist of solitary CNTs and their conglomerates.

IV. CONCLUSION

In isolated length-restricted closed SWNT the reorganization of charge occurs at the interface C60 - SWNT. The localization of the induced charge at the interface is determined by the location of the cap's pentagons in relation to the tube's hexagons at a very short distance in two layers. These charges create powerful electric fields ($\sim 10^8 - 10^9$ V/m). The dependence of the maximum effective charge module from the CNT's length quickly reaches saturation, irrespective of tube's symmetry. Therefore, similar mass quantities of short and long SWNT will cause a different charge reorganization in the surrounding medium. We can view short nanotubes as structures with a point charge, and long nanotubes as structures with a distributed charge and electrical fields at each end. Based on this difference in charge distribution, we propose a new interpretation of experimental results for CNT self-organization from water dispersion. With the increase of the CNT's length their ability to aggregate reduces.

ACKNOWLEDGMENT

Dmitry Zhukalin thanks the Center of scientific equipment of the Voronezh State University for the help with electron microscopy.

REFERENCES

- [1] Y. Lan, Y. Wang and Z.F. Ren Physics and applications of aligned carbon nanotubes, *Adv. In Phys.*, Vol. 60, N4, 2011, Pp.553-678;
- [2] O.E. Glukhova, A.S. Kolesnikova, G.V. Torgashov, Z.I. Buyanova Elastic and electrostatic properties of bamboo shaped nanotubes, *Solid State Physics Journal*, 2010, Vol.52, N6 Pp.1240-1244
- [3] D.Walker, B. Kowalczyk, M. Olvera de la Cruz, B. Grzybowski Electrostatics at the nanoscale *Nanoscale Journal*, 2011, Vol.3, Pp. 1316-1344
- [4] X.Q. Chen, T. Saito, H. Yamada, and K. Matsushige, *Appl. Phys. Lett.* 78 (2001), pp. 3714-3716.
- [5] K. Yamamoto, S. Akita, and Y. Nakayama, *Jpn. J. Appl. Phys.* 35 (1996), pp. L917-L918.
- [6] K. Bubke, H. Gnewuch, M. Hempstead, J. Hammer, and M.L.H. Green, *Appl. Phys. Lett.* 71 (1997), pp. 1906-1908.
- [7] N.P. Abanshin, B.I. Garfinkel, A. Yakunin Manage localization of the electrostatic field in field emission structures, *Technical Physics Letters*, 2011, Vol.37, Issue 7, p.94-102.
- [8] Smirnov B.F. *Physics of Fractal Clusters*, Moscow, Nauka, 1991. -134.

Implementation of Smart Ovulation Detection Device

Hazem M. Eissa, Amr M. Ahmed, Ehab A. Elsehely

Department of Electrical Communication and Electronics Systems Engineering

October University for Modern Sciences and Arts

6th of October City, Egypt

hazemone@hotmail.com , amt_bob@hotmail.com , elsehely@yahoo.com

Abstract— An infertility is a major problem facing females causes by many kind of disease that has no side effect, many females facing this problem in Egypt and around the world; so the problem concern the married people, especially the females; thus, the aim of this device is to **detect the day which have the highest ovulation and the percentage of it during the menstrual cycle, without using any chemical analysis or chemical reactions inside the device**, with making the device small, portable, easy to use, private, low cost and smart to serve non-specialized people and to simplify the physics and electronics technology for the people; a lot of money and wasting working time will be saved; This device will work using high accurate temperature sensor and by gathering three parameters: temperature factor, time factor, and decision making, the last parameter is the aim to make the device smart. The final product will produce a new additional idea as a solution of this kind of problem which we called smart ovulation detection device.

Keywords— Ovulation, BBT, Decision Making, Gaussian Distribution, Delta, Temperature Variance.

I. INTRODUCTION

Having a baby is a dream for every married people, but some problems prevent that to happen, according to the Central Agency for Public Mobilization and Statistics, more than 8 million married people have an infertility problem in Egypt, and more than 50 million married people have an infertility problem around the world [1], problems like:

- 1) Late pregnancy.
- 2) Usage of harmful chemical pills, ex: “Contraceptive Pills”.
- 3) Female Temporary Infertility, which is causes by many reasons, ex: “Family interruption”
- 4) Variation of menstrual cycle.

All these problems cause a very low chance for a female to be able to be pregnant.

There are some chemical solutions used for these problems, but any of these solutions have some defects mentioned in steps:

Normal thermometer which can measure from several places of human body which give different measures (multi-measures).

Some kinds of normal thermometer which is using mercury not accurate and very toxic.

Some kinds of normal thermometer which is using thermocouple takes long time (1min-3min) to measure body temperature.

Although Chemical products are inexpensive, it's useless (usage for one time), and not accurate.

Some kinds of Chemical products have strict conditions (no smoke, no eat after 2 hrs.).

This device will work only depend on three parameters:

- 1) Body Temperature
- 2) Variance in Time
- 3) Decision Making

The last parameter is the aim to make the device smart using:

- 1) Processing Mode:
 - Probabilities and distribution analysis.
 - Difference between temperatures (Delta).
- 2) Training Mode:
 - M out of N Decision Criteria.

II. REVIEW OF LITERATURE

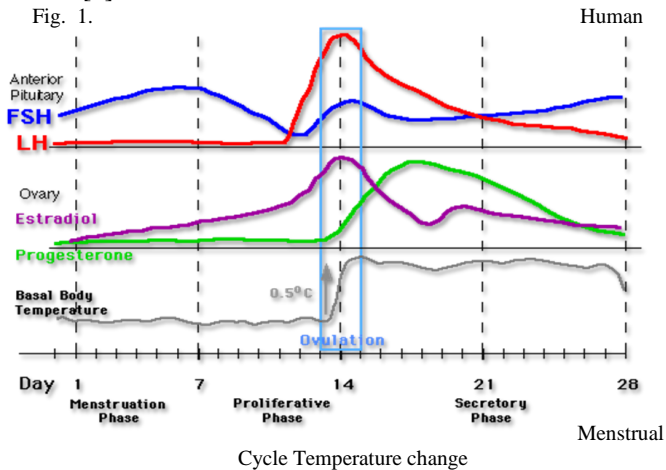
A. Medical Research

➤ Ovulation stage during the Minstrual Cycle

The ovulation happens almost in the middle of the period (between 10 to 18 days from the beginning); the ovule still alive for 24-48 hours then it is lessens even if it is fertilizing [2]. Then the suitable term for fertilization is one day before the period and one day after it end. But if period is irregular the ovule differs from a month to another. The summery; if the period is regular and its term is 28 days the ovulation happens in the middle of the period. Which are mean 14 days before the period and another 14 days after it; for example, if the term of the period is 35 days this term still fixed for 14 days and the ovulation is done within 21days from the last period. But the woman that suffers from irregular periods knows neither the time of the period nor the time of the ovulation precisely.

➤ Sudden change in Temperature (Temperature Variance)

There is another cheap way by measuring the woman's daily temperature, where the woman can limit the time ovule secretion during the days of ovule expectation between the end of the second week and the beginning of third week (from the beginning of the period). The temperature rises slightly on the normal temperature between (0.3°C-0.6°C) during the ovulation day for the flowing of ovulation hormone 12-24 hours [3].



Woman fertile day is the beginning of ovulation (usually 12-16 days before the fertile period starts) and the 5 days before it. But for women averagely between 10-18 days .we notice that few women are in average limit [4]. This way differs from a month to another but it is about the mid periods days for some reasons:

- The condition changes of the woman
 - Health.
 - Sociology.
 - Social Condition (effort, suffer, travelling, etc.).

All these factors play an important part in making woman's brain hormones active, and affect her period. So this way decides the following:

The family quietness.

Without raising temperature as a result of disease or others.

It is known that the temperature is 37C, and any slight change high-low (0.3C-0.6C) tells the happening of ovulation in that day or the term.

B. Chemical and Physical Products

Nowadays, ovulation prediction test is the common products used for detecting ovulation; most of them depend on chemical changes for showing their results and need some samples from the body to show whether if the ovulation has occurred or not, each product have their principles and their disadvantages, the most common products are:

➤ Urinary ovulation predictor kit

Principle of work: ovulation is mediated primarily by a surge of LH, which causes the mature follicle to rupture and

release the ovum. Urinary ovulation test kits work by detecting LH in urine.

Usage: The kits consist of paper strips which change color if they come in contact with urine that contains LH. After being dipped in a container containing urine, the color of the strips is matched with a control strip and ovulation is considered positive if color change is seen [5].

Disadvantages:

Useless, the kit usage is for one time only, and then the users have to use another one.

In some conditions, for example, PCO (Polycystic Ovarian Syndrome) or menopause, a wrong positive result may be seen.

The test can be affected by the concentration of urine. In a dilute sample, LH may be difficult to detect by a few drops.

➤ Salivary ovulation test kit

Principle of work: estrogen levels are raised in the follicular phase as the mature follicle secretes this hormone. High estrogen levels can cause increased secretion of sodium chloride in the saliva. When the dried saliva from a woman with high estrogen level is examined on a slide, a specific crystal pattern called firming is seen [6].

Disadvantages:

Not as reliable as urinary ovulation test kits.

Salt present in the food may contaminate the saliva and give false positive test.

The test is not specific for ovulation and abnormal increases in estrogen levels (cysts, oral contraceptives etc.) may also give a wrong positive result.

➤ Normal Thermometer

One of the physical ways to detect the ovulation time using the body temperature, but it has many defects or disadvantages:

Some thermometers depend on mercury for measuring the temperature which is very toxic to human.

Some thermometers are not accurate (± 0.3) include a chart with it to point the temperature on it; the final result will be a human decision which is not accurate.

III. DEVICE STRUCTURE (HARDWARE AND SOFTWARE)

A. Hardware

The main components of the device, there features, and there effects on the main target of the idea. The device will be introduced the newest technique, low cost and highest accuracy.

The main components of the device are: Infra-Red Thermometer (consist of small components inside it, and the functionality of it is to detect the tympanic membrane inside the ear canal using Infrared Radiation that produced from the body) microcontroller – non-volatile memory ex: (flash memory) and output port for showing data to a display device such as screen ex: (USB Port), and another audio output.

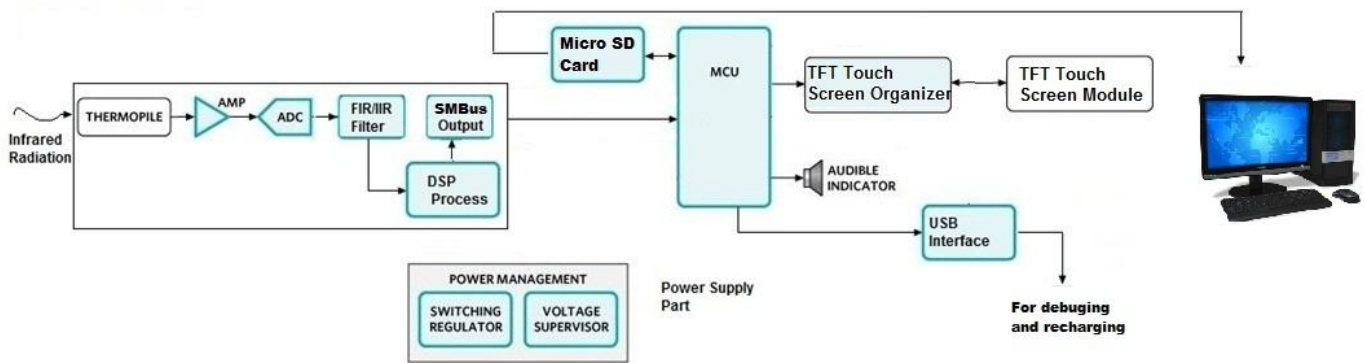


Fig. 2. Main Block Diagram

In this device, the Infra-Red Thermometer will capture the temperature by the multi thermocouple inside the sensor to measure the BBT of the human, and use the standard management bus (SMBus) technique to send the temperature data to the microcontroller unit measure and with a simple equation, we can measure the exact temperature needed to start to detect the ovulation day [7].

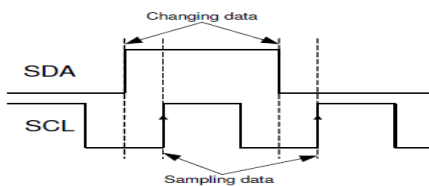


Fig. 3. SMBus format

The infra-red thermometer supports a 2 wires serial protocol, build with pins SDA and SCL, the data on SDA must be changed when SCL is low (min 300ns after the falling edge of SCL). The data is fetched by both MD and SDs on the rising edge of the SCL. The recommended timing for changing data is in the middle of the period when the SCL is low.

The temperature reading can be calculated from the formula:

$$T_o [^{\circ}\text{C}] = \text{RAM}(0x27) \times 0.02 - 273.15 \quad (1)$$

Where:

T_o is the output temperature in Celsius.

RAM (0x27) is the address which is save the temperature in bits.

The SMBus interface is a 2-wire protocol, allowing communication between the Master Device (MD) and one or more Slave Devices (SD). In the system only one master can be present at any given time. The infra-red thermometer can only be used as a slave device; generally, the MD initiates the start of data transfer by selecting a SD through the Slave Address (SA).

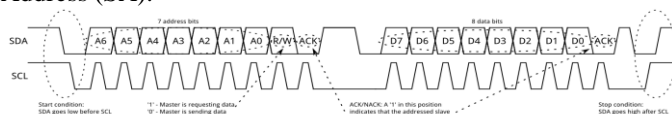


Fig. 4. Procedure of SMBus

After every 8 bits received by the SD an ACK/NACK is followed. When a MD initiates communication, it first sends the SA. Only the SD with recognized SA gives ACK, the rest will remain silent. If the SD does not ACK the MD should stop the communication and repeat the message. A NACK could be received after the PEC. This means that there is an error in the received message and the MD should try sending the message again. The PEC calculation includes all bits except the START, REPEATED START, STOP, ACK, and NACK bits. The PEC is a CRC-8 with polynomial X^8+X^2+X+1 . The Most Significant Bit of every byte is transmitted first.

B. Embedded Software

In this part of the device, we will discuss the whole software of the device, process steps and the effect of the 3 factors inside the software process.

The flow chart of the device contains many processes, starting from selector that separates the normal temperature measurement process from the ovulation process. In the normal temperature measurement, the thermopile will read the temperature through the eardrum in just a second and save it in a specific address and show the result on the LCD touch screen.

In the ovulation process, also the thermopile will read the temperature through the eardrum in just a second then calculate the average of all the readings have taken it before average of all readings = (Total readings / number of readings), but before save the result, there will be a conditional instruction that will check if the reading has taken at minor day (day 10) or not.

If the reading has taken it after day 10, then the result will move through a second sub. Program that save the result in a specific address.

But if the reading has taken it after day 10, the result will move through a third sub. Program that decide whether there is an ovulation or not

Ovulation Average = (Readings from day to day 10 / number of days reading).

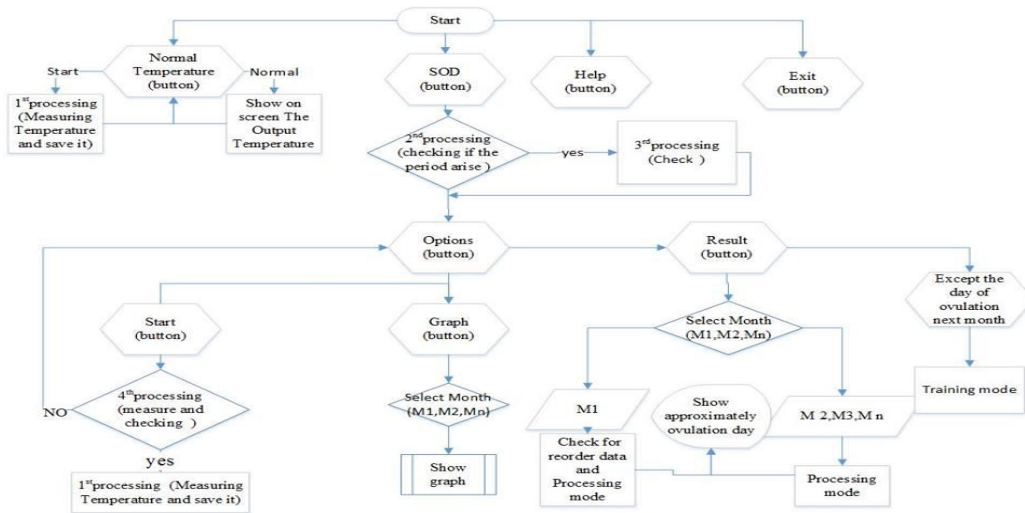


Fig. 5. Simple Flow Chart of the Device

C. Decision Making (Processing and Training)

It is a part of artificial intelligence, is about the construction and study of systems.

Decision Making depends on two records:

- 1) Representation of data instances and functions evaluated on these instances are part of all machine learning systems
- 2) Generalization is the property that the system will perform well on unseen data instances.

Decision Making is divided into two modes:

- Processing Mode
- Training Mode

a) Processing Mode

Processing Mode the mode were the device applied one or more of decision algorithm, in this project, the device will apply two decision algorithms.

- 1) Delta
- 2) Gaussian Probability Distribution Function (PDF).

b) Delta

Delta $\Delta = (\text{new reading} - \text{Ovulation average})$
 There isn't an ovulation (in case of $\Delta < 0.3^\circ\text{C}$)
 Fever (in case of $\Delta > 0.6^\circ\text{C}$)
 There is an ovulation (in case of $0.3^\circ\text{C} = \Delta \leq 0.6^\circ\text{C}$).

c) Gaussian (Normal) Distribution

It is a continuous probability distribution, defined by the formula.

$$f(x) = \frac{1}{\sigma\sqrt{2\pi}} e^{-\frac{(x-\mu)^2}{2\sigma^2}} \quad (2)$$

Where

μ = mean of distribution (also at the same place as mode and median)

σ = standard deviation
 σ^2 = variance of distribution
 χ is a continuous variable ($-\infty < \chi < \infty$)

Normal distributions are extremely important in this device because it will give an additional prove at checking on ovulation by given us the maximum value at the sudden change in the temperature.

d) Training Mode

Training Mode is the mode were the device is learning from the statistical data of the human (user), there are many Techniques used for make the device learn from the human ,it is a decision on reading data but after train the device by stored reading data .

The device will start its training mode using statistical data that already stored inside the device for the first month only. The training mode that will be used is M out of N decision criteria, and the comparison between the months (compare with statistical data for the first month, and then by comparing the average of the previous months results stored on the device, according to the final result of its month.

e) M out of N Decision

It is one of the Technical decisions used to show the accurate result of any decision porpoise needed. It is compared the days after ovulation with the mean for each month
 M out of N decision criteria types are: (4 out of 6) and (7 out of 10) [8].

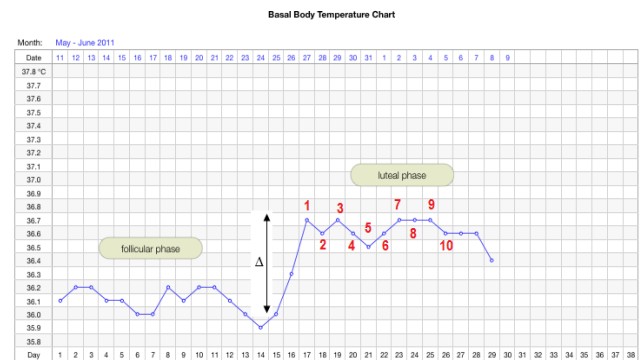


Fig. 6. Processing of M out of N decision

IV. RESULTS AND SIMULATIONS

To ensure that all these algorithms can be applied and detect the ovulation day, we have collect some BBT charts and the detection of the ovulation day (human decision) after a permission from a website called Fertility Friend [9], and made a simulation using MATLAB to test the algorithms and detect the ovulation day depend on these algorithms, we have got these results.

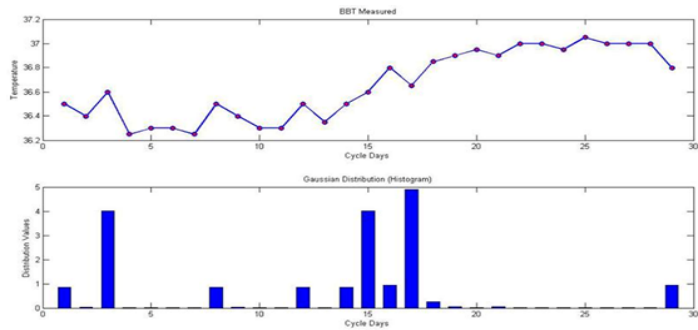


Fig. 7. 1st Case

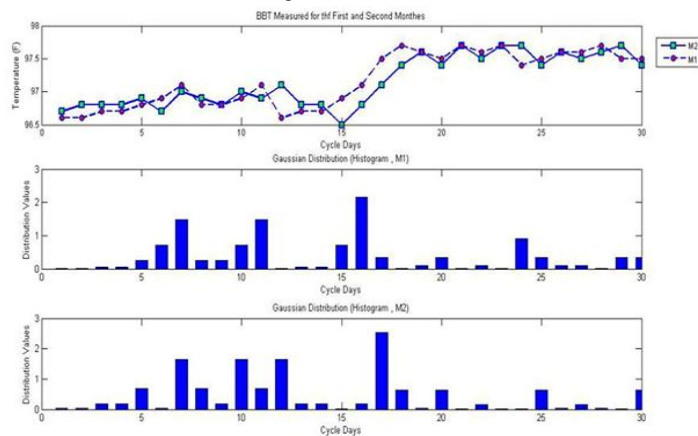


Fig. 8. 2nd Case

Table. 1. Data of the simulation

Figure	Case	Month	Delta (Δ)	Day of Ovulation
7	1	1	Very small	17
8	2	1	0.3	16
		2	0.3	17

REFERENCES

- [1] Key Statistics from the National Survey of Family Growth. (2013, May 30)., "Database of Infertility Problems" [Online]. Available: <http://www.cdc.gov/nchs/fastats/fertile.htm>
- [2] E. Braunwald, K.J. Isselbacher, R.G. Petersdorf, et al, eds. "Harrison's Principles of Internal Medicine". 18th ed., New York: McGraw-Hill, 2012: Chapter 347.
- [3] Dorling Kindersley™ Limited., "Temperature and Mucus Changes during the Menstrual Cycle", Copyright 2009.
- [4] Z.A. Weinberg., IBM, J. Thomas , (2007, March 12)., "Ovulation Detection by Monitoring Temperature During Sleep", Sponsored by IEEE Engineering in Medicine and Biology Society.
- [5] reproductive medicine and surgery center., (n.d.) "FERTILITY TEST URINARY OVULATION PREDICTION KITS", "[Online], Available: <http://www.rmcsva.com/ovulation-prediction.html#>
- [6] The Fertility Blogs., (2010, Jun 23), "Saliva Ferning", [Online], Available: <http://thefertilityblogs.com/product-reviews/saliva-ferning/149/>
- [7] C. Melexis., (2013, April 24), "IR Sensor Thermometer MLX90615 Data Sheet", [Online]. Available: <http://www.melexis.com/Asset/IR-sensor-thermometer-MLX90615-Datasheet-DownloadLink-5477.aspx>
- [8] R. John Zaleski., (2011)., "Medical Device Data and Modeling for Clinical Destion Making", ARTECH HOUSE,.
- [9] Fertilityfriend., (2013, March 11) "Website for collecting data of Ovulation Charts". [Online]. Available: <http://www.fertilityfriend.com>

Proposal for a gastrointestinal simulator system with anatomical location and emulator mechanism of an endoscope.

Efren Moncisvalles, Daniel Lorias, Arturo Minor, and Jesus Villalobos

Abstract — The aim of this paper is to develop a proposal for a simulator system for gastroscopy. A non-virtual system which consists of an anatomical model is proposed, this will affect students in veterinary medicine needed to develop or improve skills in the proper handling of the gastroscope tasks. This is built with vinilica fabric a mechanism that emulates a flexible endoscope and software which allows determining the anatomical location in which the endoscope is located.

Keywords—development, endoscopy, gastroscopy simulator, skills.

I. INTRODUCTION

THE word endoscopy comes etymologically from the Greek words endo meaning inside and skopein that means looking or look [2].

Therefore, we can define endoscopy as a technique based on the exploration of natural cavities through an endoscope, with minimal disruption to the patient. The endoscopic examination can be divided into two groups: by natural orifice endoscopy (esophagoscopy, gastroscopy, duodenoscopy, colonoscopy, rhinoscopy, laryngoscopy, etc.) and artificial opening endoscopy (arthroscopy, laparoscopy, etc.) [1], [3].

Veterinary endoscopy is very important today because there is a greater awareness in the pet care (in this case the canine kind) and come to live with people within the household, for reasons such as oversights or accidents in this, the animals come to swallow a foreign object. Due to this incident frequency veterinary student preparation should have

This work is supported financially and with resources to our research by Research and Advanced Studies Center of IPN (CINVESTAV).

E. Moncisvalles is with Bioelectronic Section of Electrical Engineering Department from Research and Advanced Studies Center of IPN (CINVESTAV), CO 07360 Mexico D.F., Mexico (phone: (+521)55-39726702; e-mail: emoncisvalles@cinvestav.mx).

D. Lorias is with Bioelectronic Section of Electrical Engineering Department from Research and Advanced Studies Center of IPN (CINVESTAV), CO 07360 Mexico D.F., Mexico (e-mail: dlorias@cinvestav.mx).

A. Minor is with Bioelectronic Section of Electrical Engineering Department from Research and Advanced Studies Center of IPN (CINVESTAV), CO 07360 Mexico D.F., Mexico (e-mail: aminor@cinvestav.mx).

J. Villalobos is with Veterinary Hospital Del Valle, CO 03100 Mexico D.F., Mexico (phone: 5639-8392; e-mail: vetlobo@gmail.com).

good handling of the endoscope [10], [8].

Today there are few systems and trainers gastroscopies centers such as the GI MENTOR (2014 simbionix) [11] and The RHIC Simulation Center [12], which are mostly focused on humans. These training systems come to be costly for some institutions or clinics and training centers do not become easily accessible for some populations. These systems are also virtually, which based on research with veterinarians indicate they prefer a system that is physical and anatomical closer to reality.

Another method is to use animals and sometimes due to the lack of experience with the endoscope can eventually cause minor injuries.

The purpose of this system is focused at the moment in veterinary endoscopy, which is a procedure where an endoscope flexible type to look inside the upper gastrointestinal tract, which consists of the esophagus, stomach and duodenum is used (beginning of the small intestine) [2]. Because of this, a proposal of a gastrointestinal simulator system is done, which allows determining the anatomical location where the endoscope is located, all based on research with veterinarians. The purpose of this system is quite accessible due to the type of materials and software used, which are commercial kind. This is developed with the goal of meeting the needs of veterinary students.

II. METHODOLOGY

The purpose of this system consists of the physical model of a canine breed average size stomach; these dimensions have been established from a series of investigations with veterinarians. The construction of the anatomical model was not only the outside, but also on the inside we have implemented a finished so that resembles a real stomach.

This also includes: the construction of a module whose function is to contain the physical model of the stomach, the development of software to determine the anatomical location and the design and development of a mechanism that emulates a flexible endoscope.

One advantage is that the equipment and materials used so far is quite accessible, which comprises: vinilica fabric, vinyl, one connected to a laptop HD USB Endoscope Camera (HUEC) camera [4].

A. Software development for prototype.

The software has been developed up to now to determine the anatomical location where the endoscope is. With respect to the image capture has been up to now using HUEC, this will be only until the mechanism that emulates an endoscopic camera is completed.

General Operation: Using the HUEC is introduced through the trocar which is attached permanently to the model of the stomach. Once inside the model, is explored throughout the anatomy of the stomach to find 5 points previously adhered to the inside of the model, the objective is to find the points and then displayed on the screen of the laptop, the actual anatomic location. The 5 points correspond to certain anatomical areas which are: cardia, fundus, body, antrum and pylorus. The software that is used to capture all of the above is MATLAB, which allows developing an algorithm that recognizes different colored labels which indicate the anatomical position of the stomach, which is currently, located the endoscope.

The software process consists of four steps:

Image capture. Once detected the tag, the image is captured through HUEC and using the software image is processed in RGB. A color is then specified by its trichromatic coefficients defined as (1):

$$\begin{aligned} x &= \frac{X}{X+Y+Z}; \\ y &= \frac{Y}{X+Y+Z}; \\ z &= \frac{Z}{X+Y+Z} \end{aligned} \quad (1)$$

The amounts of green, red and blue needed to form any particular color are called the tristimulus value and are denoted, X, Y and Z, respectively [9].

Image filtering. Once captured and processed in RGB image, allows establishing a threshold which serves to separate the color of the label with respect to all other colors in the image. The algorithm has the filtering stage is based on the equation (2) [9].

$$x = \begin{cases} 0, & u < x \\ 255, & u > x \end{cases} \quad (2)$$

Image Detection. This step is accomplished with a pre-image capture on the labels, which allows be processed in RGB and then obtain a characteristic value for each label [9]. This serves as a basis for any value of any color that not correspond to the label be filtered. The color of the labels corresponds to a specific part of anatomical model, as shown in the following table.

TABLE I.
CORRESPONDENCE LABELS WITH ANATOMICAL PARTS

Color label	Anatomical part
Blue	Cardia
Green	Fundus
Yellow	Body
Purple	Antrum
White	Pylorus

The color selection was based the labels to respond better in the process image detection.

Display screen. After detection of the label is displayed in the screen area in which is located the HUEC. The display screen is accomplished by the moment in the Comand Window of MATLAB because it is completing an interface that will allow better user interaction.

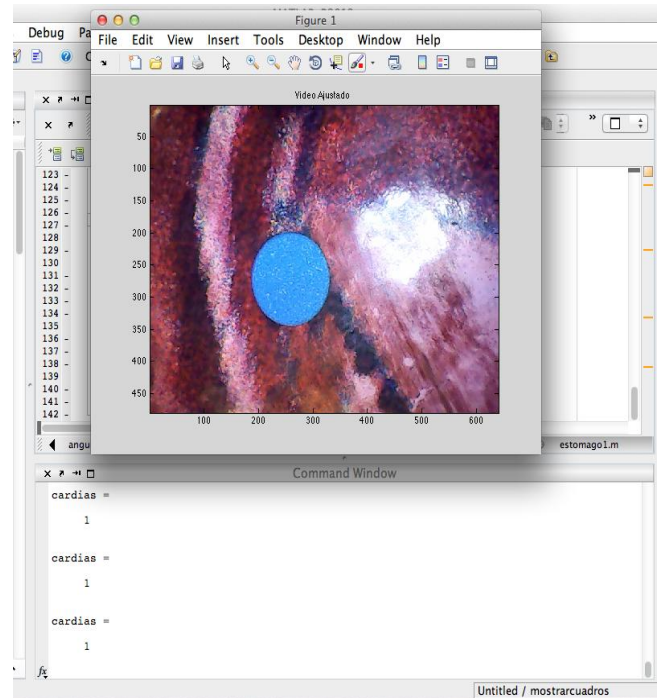
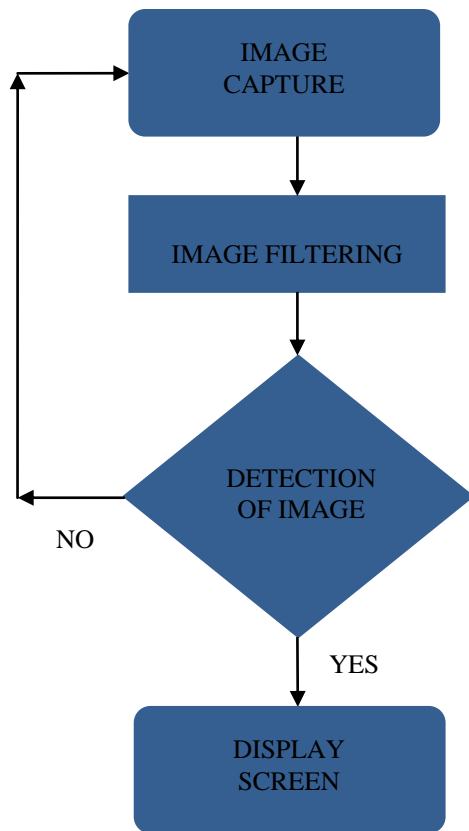


Fig. 1. Screen display

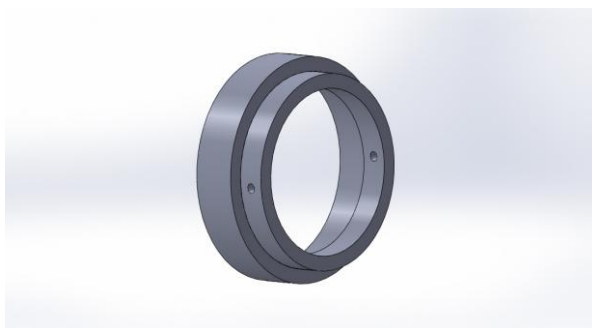
Below is a flow diagram of the process that performs the software is shown.



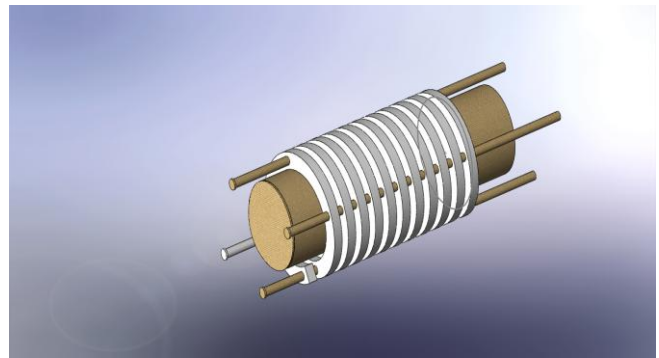
To insufflate an air compressor 250 P.S.I. MIKEL'S connected to the trocar is used. This is to achieve insufflate the stomach model, which is necessary because it would fail to enter the HUEC and no results would be obtained.

B. Development mechanism that emulates an endoscope.

At this stage because of the time has not been able to finish developing, but what is being done is a system that emulates the mechanical properties of a flexible endoscope [6], [7]. Which consists of a HUEC using in the first 10 cm a series of rings, which are subject some tension cables and these at the same time attached to pulleys, where these are handled with some knobs. The operation is based on the principle of tension which in this case consists of two knobs pulling on tension cables and these at the same time move to manipulate the rings allowing the first 10 cm of HUEC in the desired direction [4].



(a)



(b)

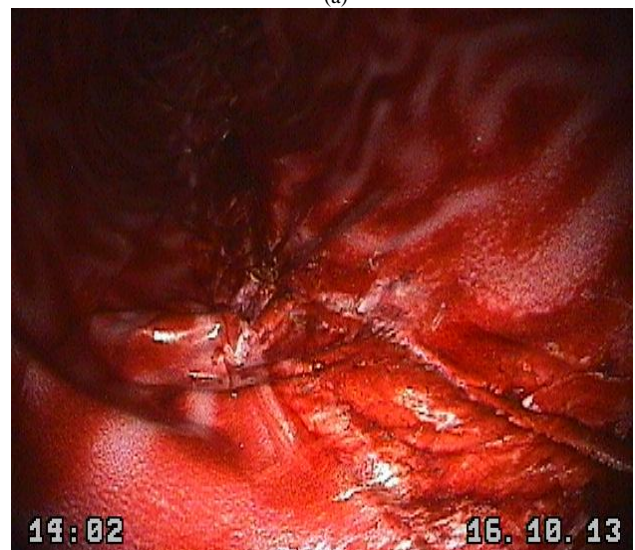
Fig. 2. Design and development of the mechanism that emulates an endoscope. a) Rings to manipulate movement. b) Series rings secured with tensioners.

III. RESULTS

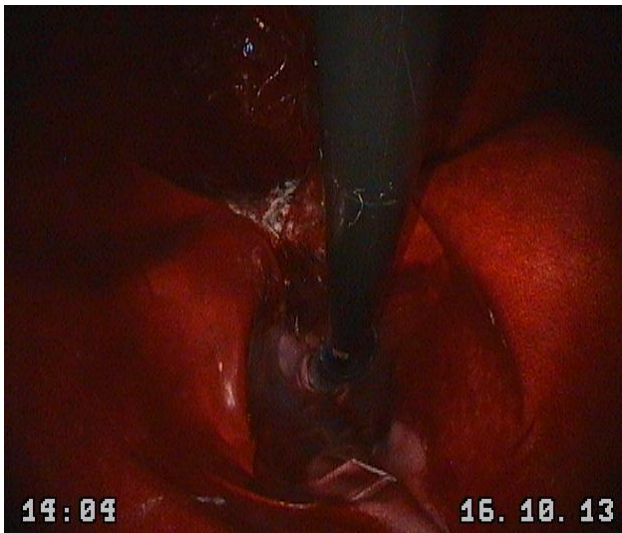
The flexible endoscope was helpful to perform a series of diagnostic tests to the anatomical model, which was widely accepted by veterinarians after a scan through the entire model.



(a)



(b)



(c)

Fig. 3. View of the internal model with a flexible endoscope type. a), b), c).

Moreover in the software design is very successful in the internal anatomical location model, which has already been widely accepted by veterinarians, can be seen in the next image as the HUEC, is positioned on the label and on the screen of the laptop shows the exact location in which it is positioned.

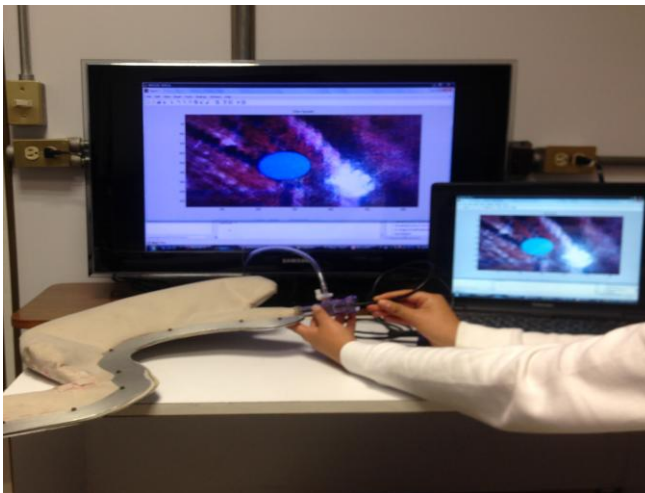


Fig. 4. Interaction and tests HUEC with tags (on cardia).

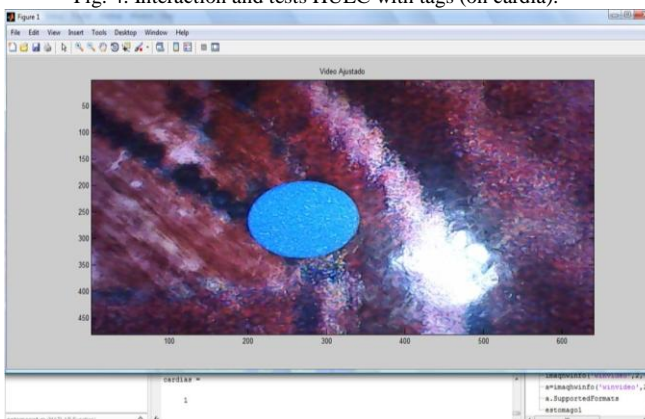


Fig. 5. Screenshot when HUEC is positioned on the cardia.

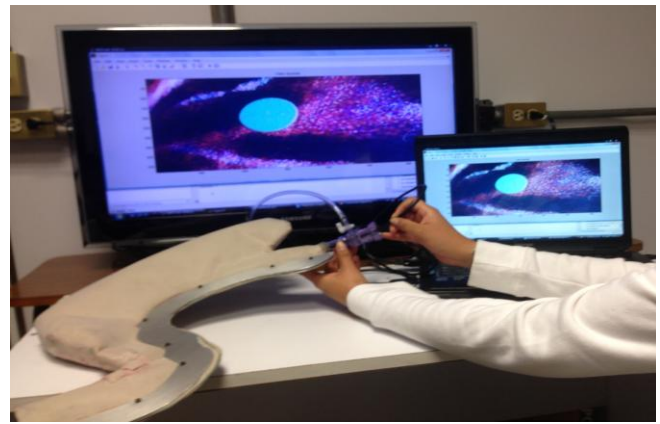


Fig. 6. Interaction and tests HUEC with tags (on fundus).

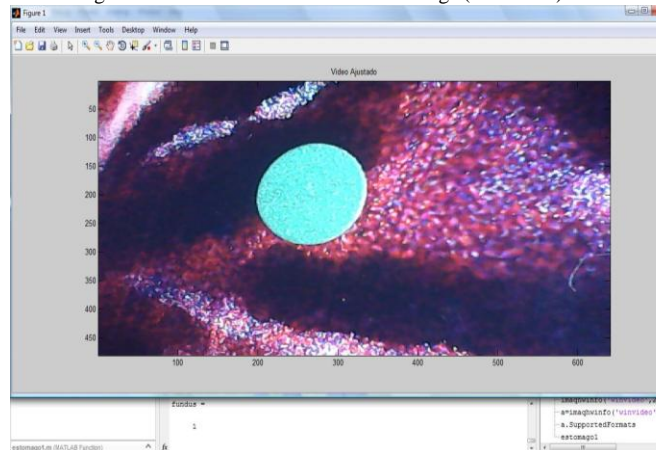


Fig. 7. Screenshot when HUEC is positioned on the fundus.

IV. CONCLUSIONS

Because there are few simulators gastroscopies systems focused on the veterinary area, the decision to work on a system to meet basic needs but very helpful to students and veterinarians as it is practical and appropriate management of a gastroscope was taken.

Due to the great potential that has been seen in this system, is contemplating the parallel work in the medical field because there is a great anatomical similarity with respect to stomach. Because the purpose of this is to provide a system that meets the needs required for a veterinary or a gastroenterologist, and thus benefit both areas.

For this system continues to evolve have considered a series of improvements by the moment the short term, which are described below:

The development of a module that contains the entire system, which is already under construction at this time. This module will contain: the anatomical model of the stomach, the air compressor as well as its power supply. The module is being developed for the model of the stomach, this positioning of the manner in which a dog is time for a gastroscopy.

The completion of the development of a mechanism that emulates a flexible endoscopic camera, this being designed as a HUEC [6]. Because are focusing a part veterinary student, it was decided to develop this mechanism, since a gastroscope is somewhat delicate and the aim here is to begin to develop skills in handling the same [7].

Further develop the algorithm, as this system not only stays in the anatomical location of the stomach. Since it is intended to include a number of tasks which allow veterinary students to develop skills.

ACKNOWLEDGMENT

The authors would like to thank the Research and Advanced Studies Center of IPN (CINVESTAV) and the National Council for Science and Technology (CONACYT, Mexico).

REFERENCES

- [1] Fernando Rodríguez Franco. Hospital Clínico Veterinario (Gastroenterología y Endoscopia). Dpto. Patología Animal II. Facultad de Veterinaria de Madrid.
- [2] http://www.cmp.org.pe/documentos/librosLibres/tsmi/Cap22_Endoscopia_gastrointestinal.pdf
- [3] Vázquez-Iglesias JL. Endoscopia digestiva: Una fascinación diagnóstica y terapéutica, en un viaje alucinante camino del siglo XXI. Asociación Española Endoscopia Digestiva 1995; 3: 13-9.
- [4] Maratka Z. Databases for gastrointestinal endoscopy [letter]. *Gastrointest Endosc* 1992; 38(3):395-396.
- [5] Maish M. Esophagus. In: Townsend CM, Beauchamp RD, Evers BM, Mattox KL, eds. *Sabiston Textbook of Surgery*. 18th ed. Philadelphia, Pa: Saunders Elsevier; 2008:chap 41.
- [6] Pasricha PJ. Gastrointestinal endoscopy. In: Goldman L, Ausiello D, eds. *Cecil Medicine*. 23rd ed. Philadelphia, Pa: Saunders Elsevier; 2008:chap 136.
- [7] Plumeri PA. Informed consent and the gastrointestinal endoscopist. *Gastrointest Endosc* 1985; 31: 218–222.
- [8] Fleischer DE, Al-Kawas F, Benjamín S y cols. Prospective evaluation of complications in an endoscopy unit. *Gastrointest Endosc* 1992; 38:411–414.
- [9] Gonzalez RC, Woods RE. *Digital image processing*. ed. Prentice Hall 2nd ed. Upper Saddle River, New Jersey 2002: chap 6.
- [10] REDVET - Revista electrónica de Veterinaria - ISSN 1695-7504 . (2012) Volumen 13 N° 6 from <http://www.veterinaria.org/revistas/redvet/n060612/061204.pdf>
- [11] Symbionix. (2014). GI MENTOR con sede en Cleveland Ohio, con un centro de investigación y desarrollo en Israel. from <http://symbionix.com/simulators/gi-bronch-gi-mentor/>
- [12] RHIC SIMULATION CENTER from <http://www.rhicsimcenter.org/>

Electronic structure of two isomers of fluorine derivatives of single-walled carbon nanotubes of C_2F stoichiometry within the density functional theory

Alexander A. Ganin, Larissa A. Bityutskaya, and Eugeny N. Bormontov

Abstract—The paper presents the results of calculation of electronic structure and the related fundamental parameters (band gap, Fermi energy and ionization energy) of two isomers of fluorinated armchair (with chirality indices from (3, 3) to (15, 15)) and zigzag (with chirality indices from (0, 3) to (0, 17)) single-walled carbon nanotubes of C_2F stoichiometry within the density functional theory. Transitions from semiconducting to metallic conductivity and vice versa were found depending on the isomer type and chirality indices. It is shown that the Fermi energy decreases during the fluorination. The dependencies of the parameters investigated on the diameter of the nanotubes are given. Based on these dependencies the band gap value of the two isomers of fluorinated graphene is estimated.

Keywords—carbon nanotubes, fluorination, electronic structure, band gap.

I. INTRODUCTION

CARBON nanotubes (CNT) are considered to be one of the most promising materials for development of the electronics in the nanoregion. In order to effectively utilize a material in micro- and nanoelectronics one needs to be able to control the materials electronic structure and the related parameters (in particular, the band gap). The techniques of modification of the electronic structure of single-walled CNTs (SWCNTs) may be divided into two groups: 1) without alteration of the physical structure of the SWCNTs (i.e. by applying an external electric field); 2) with modification of the SWCNTs structure (i.e. by creating defects in the tube's atomic configuration). Among the techniques of the second group the chemical functionalization of walls and ends of CNTs takes a special place and may be considered an analogue to the doping of semiconductors. The functionalized CNTs represent a new class of nanomaterials with applications in both the composite materials and the nanoelectronic devices [1].

A rigorous research of the interactions between the CNT walls and different chemical elements (hydrogen [2], oxygen [3], nitrogen [4] and others) and compounds have been carried out during the last several years. Currently we may admit that

fluorine appears to be one of the most interesting elements for chemical functionalization of CNTs. Firstly, the chemistry of the fluorocarbon bond is well studied. Secondly, an experimental evidence of the possibility of fluorination of CNTs has been obtained and the saturation stoichiometry C_2F has been found. [5, 6]

At this stage of the development of the technology the controlled production of F-CNTs with C_2F stoichiometry and predetermined structure is not feasible. Due to this reason the experimental investigation of their electronic structure is rather difficult. For the theoretical description of pure SWCNTs both the analytical [7] and numerical [8] approaches may be used. Since the geometrical structure of fluorinated SWCNTs is not known, their theoretical description appears to be more feasible with the use of computational methods.

The work by Kudin et al. [9] has proposed four possible isomers of fluorinated SWCNTs with C_2F stoichiometry (A – D on Fig. 1). Using the density functional theory approach in two approximations the authors have calculated the band gap and the Fermi level for tubes (10, 10) and (18, 0). It was confirmed that the bond energy and electronic structure parameters vary between different isomers.

In Ref. [10] Ranjan and Seifert investigated the transport properties of fluorinated SWCNTs (10, 10) (isomer A) and (10, 0) (isomer C) within the density functional theory. They have found that both fluorinated SWCNTs have metallic conductivity. The electronic structure and the band gap for F-SWCNT (10, 0) of isomers B – D were studied by Seifert et al. [11] According to their results the band gap equals 4 eV for isomer B, 0 eV for isomer C and 1 eV for isomer D.

Thus, the fluorine functionalization leads to alteration of the electronic structure of single-walled carbon nanotubes and may switch the metallic nanotube to the semiconducting state and vice versa. So far the electronic structure of the F-SWCNTs is not sufficiently studied. Due to the fact that the results of the ab initio calculations of the electronic structure are available only for several nanotubes (mostly, the primitive ones), the investigation of the properties of a wide range of SWCNTs appears to be interesting both fundamentally and practically.

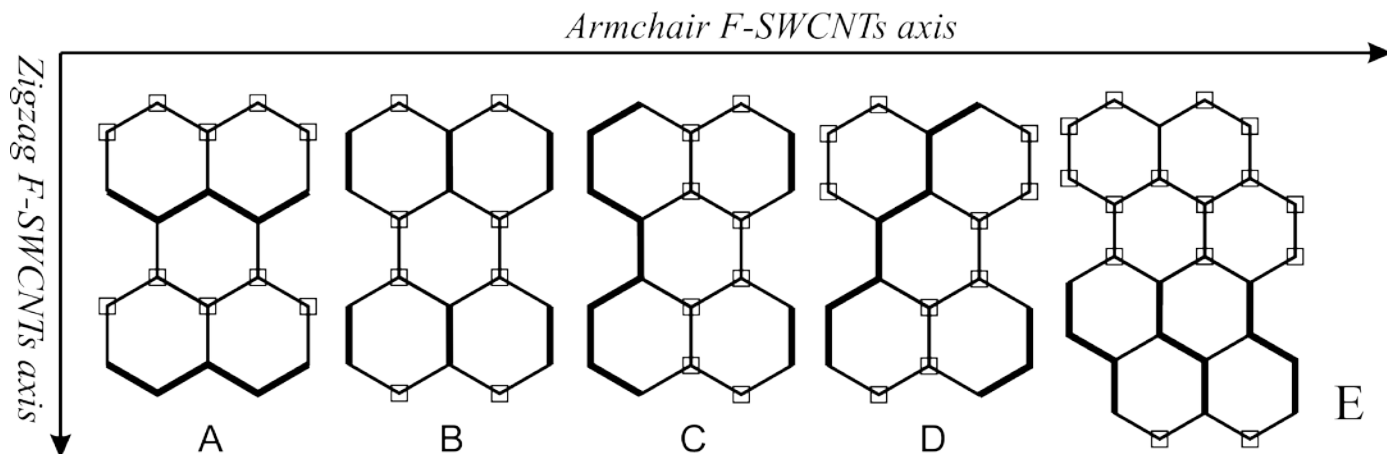


Fig. 1. Isomers of the achiral F-SWCNTs with C_2F stoichiometry. Squares denote fluorinated carbon atoms.

I. METHODOLOGY

From the five isomers depicted on Fig. 1 not all are available in the armchair and zigzag nanotubes with arbitrary chirality indices. In particular from the symmetry consideration standpoint the chirality index is required to be even for isomers D, E of the armchair and for isomers C, D of the zigzag tubes. In order to calculate the properties of the isomers C, D of the armchair and the isomers D, E of the zigzag nanotubes the unit cell must be replicated along the CNT axis. However the isomers A and B do not impose any restrictions on the set of the tubes studied and for this reason we consider only these isomers in the present paper.

The calculation was carried out within the density functional theory in local spin-density approximation and 6–31G basis set which uses 6 primitive gaussian functions to represent each of the core atomic orbitals and each of the valence orbitals is composed of two basis functions (which in turn consist of three and one primitive gaussian functions). For the calculation we used the resources of the Computing center of the Voronezh State University and the Gaussian software package [12].

We used periodic boundary conditions (the nanotubes were approximated to be infinite) for 200 points in the Brillouin zone.

In the works we studied the electronic structure and the related parameters (the energy band gap, the Fermi energy and the ionization energy) for zigzag nanotubes of chiralities from (0, 3) to (0, 17) and armchair nanotubes of chiralities from (3, 3) to (15, 15). The band gap was calculated as the difference between the energies of the lowest unoccupied crystal orbital (LUCO) and the highest occupied crystal orbital (HOCO). In the further text we shall use the term “crystal orbital” instead of “molecular orbital”, because the calculation was carried out for the infinite CNTs and the wave functions were approximated by the Block waves. The Fermi energy was estimated as the HOCO energy for the metallic nanotubes and as the energy corresponding to the middle of the band gap for the semiconducting nanotubes. Also we have estimated the ionization energy of the F-SWCNTs as the HOCO energy

(according to the DFT version of the Koopmans theorem [13]).

In order to account for the curvature effects occurring in the nanotubes of the small diameters we have used a cylindrical model of the unit cell in the calculation.

The method was tested in the calculation of the band structure of pristine carbon nanotubes and the comparison of the data obtained with the theoretical (both analytical [14] and numerical [15, 16]) and experimental [17, 18] data was carried out with satisfactory results [19].

For generation of the input files with the atomic structures of the F-SWCNTs we used the TubeGen 3.4 software [20]. The software was modified in accordance with the license in order to implement the feature of generation of the fluorinated armchair and zigzag SWCNTs of the C_2F stoichiometry (isomers described in [9] and isomer E (Fig. 1)).

The fluorocarbon bond length was taken to be 1.35 Å [21, 22]. The fluorine atoms connected the nanotube walls from the outer side. In the calculation the geometric structure was optimized to the minimum of the total energy.

II. RESULTS AND DISCUSSION

Optimization of the geometric structure of unit cells of isomers A and B of achiral F-SWCNTs to the minimum of the total energy it was found that the fluorination leads to qualitative changes in the atomic configuration of the nanotubes which can be explained as a consequence of two factors: 1) mutual repulsion of partially negatively charged fluorine atoms; 2) orientation of the chemical bonds in functionalized carbon atoms to the vertices of a tetrahedron. Changes in geometric structure and symmetry of the SWCNTs unit cells are followed by radical changes in the electronic structure of the tubes. And depending on the chirality of the CNT and the isomer we may observe transitions from metallic conductivity to the semiconducting and vice versa. Moreover during fluorination we found that the Fermi energy of the CNTs lowers by 2 – 3 eV. The tables 1, 2 summarize the data on the changes of the parameters of the SWCNTs electronic structure caused by fluorination.

Table 1. Changes of the electronic structure parameters in zigzag SWCNTs as a result of fluorination. Letters M, S denote metallic and semiconducting conductivities respectively: the first letter applies to the pristine SWCNT and the second one to the F-SWCNT. Only the second chirality index m is shown since the first one is taken to be zero.

m	Isomer A			Isomer B		
		ΔE_g (eV)	$ \Delta E_F $ (eV)		ΔE_g (eV)	$ \Delta E_F $ (eV)
3	M-S	1.792	1.22	M-S	0.179	2.13
4	M-S	0.837	1.50	M-M	0.000	2.24
5	M-S	1.536	1.84	M-S	0.400	2.53
6	M-M	0.000	1.89	M-S	0.511	3.17
7	S-S	1.456	2.03	S-S	0.558	3.13
8	S-M	-0.785	2.11	S-S	0.206	3.32
9	M-S	1.476	2.48	M-S	1.051	3.63
10	S-M	-0.755	2.54	S-S	0.480	3.61
11	S-S	0.346	2.69	S-S	0.394	3.76
12	M-M	0.000	2.71	M-S	1.376	3.75
13	S-S	0.455	2.78	S-S	0.826	3.78
14	S-M	-0.742	2.90	S-S	0.726	3.84
15	M-S	0.881	2.93	M-S	1.489	3.87
16	S-M	-0.534	2.96	S-S	1.016	3.87
17	S-S	0.196	3.04	S-S	0.975	3.92

Table 2. Changes of the electronic structure parameters in armchair SWCNTs as a result of fluorination. Letters M, S denote metallic and semiconducting conductivities respectively: the first letter applies to the pristine SWCNT and the second one to the F-SWCNT. Only the second chirality index m is shown since the first one is the same.

m	Isomer A			Isomer B		
		ΔE_g (eV)	$ \Delta E_F $ (eV)		ΔE_g (eV)	$ \Delta E_F $ (eV)
3	M-M	0.000	2.72	M-S	2.746	2.57
4	M-M	0.000	3.47	M-S	1.915	3.21
5	M-M	0.000	3.50	M-S	1.828	3.42
6	M-M	0.000	3.64	M-S	1.578	3.65
7	M-M	0.000	3.65	M-S	1.589	3.72
8	M-M	0.000	3.71	M-S	1.489	3.83
9	M-M	0.000	3.72	M-S	1.505	3.86
10	M-M	0.000	3.75	M-S	1.469	3.92
11	M-M	0.000	3.75	M-S	1.493	3.94
12	M-M	0.000	3.76	M-S	1.456	3.98
13	M-M	0.000	3.75	M-S	1.470	3.99
14	M-M	0.000	3.77	M-S	1.449	4.01
15	M-M	0.000	3.77	M-S	1.463	4.02

As it is obvious from the table 1, we can establish a conductivity classification rule for the isomer A of zigzag F-SWCNTs: if the chirality index is even then the conductivity is metallic; if the chirality index is odd then the conductivity is semiconducting. The only exception to this rule is F-SWCNT (A) (0, 4). This rule can be qualitatively understood by

considering the electronic structure of the zigzag F-SWCNTs (isomer A) (Fig. 2). One may notice that the energetic level corresponding to the HOCO of the F-SWCNTs (A) is fourfold degenerate (including the spin related degeneracy). And for F-SWCNTs (A) with even chirality indices this orbital is occupied only halfway, whereas for the SWCNTs with odd chirality indices it is fully occupied. The exception of the (0, 4) tube is explained by the decrease of the degeneracy of the HOCO to the twofold (what leads to the full occupation of the energetic level under consideration and opening of a non-zero band gap).

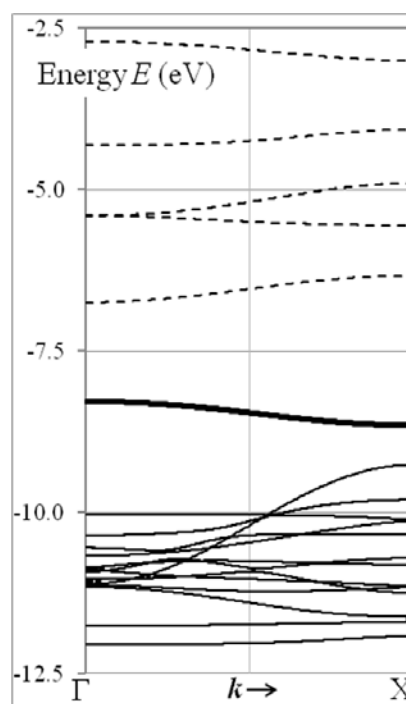


Fig. 2. Electronic structure of the zigzag F-SWCNTs (0, 5) (isomer A). The standard designations of the points in the Brillouin zone are used.

Moreover as it is noticeable from the table 1 all zigzag F-SWCNTs fluorinated in B pattern are semiconducting.

As it is shown in the table 2 armchair F-SWCNTs (isomer A) retain their metallic conductivity, whereas for the armchair SWCNTs fluorinated in B pattern we observe the transition to the semiconducting state. It is also obvious from the table that the band gap is decreasing with the diameter and chirality of the nanotubes in question.

Now let us consider the dependencies of the fundamental parameters of the electronic structure of the F-SWCNTs from their diameter and chirality. On the Fig. 3 the dependency of the band gap on the diameter of the zigzag semiconducting fluorinated SWCNTs (isomer A) is provided. It is noticeable that with the increase of the diameter E_g decreases. This fact lies in accordance with the fact that all armchair F-SWCNTs of this isomer are metallic and testifies that isomer A of fluorinated graphene is likely to be metallic. The Fig. 4 gives the dependency of the band gap on the diameter of the isomer

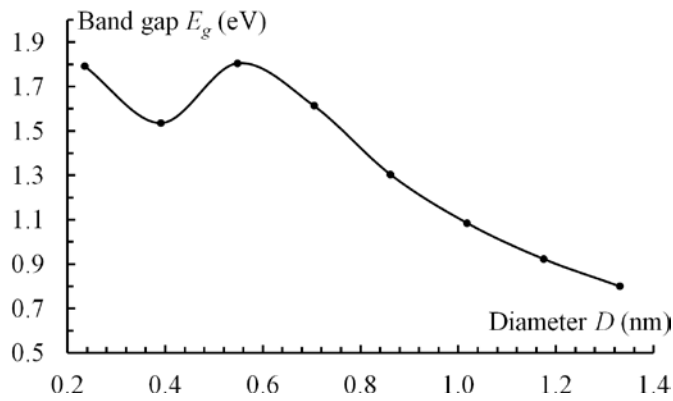


Fig. 3. Dependency of the band gap E_g on the diameter D of the zigzag semiconducting F-SWCNTs (isomer A).

B of the achiral F-SWCNTs. From the plot one may see that on the contrary to all previously considered types of nanotubes (including pristine ones) the band gap of zigzag F-SWCNTs (isomer B) grows with the diameter. The stabilization of this growth occurs at the value of 1.5 eV. In the case of the armchair F-SWCNTs the band gap decreases with diameter. The stabilization of this decrease occurs on the value of 1.5 eV as well. By analyzing the dependencies on the fig. 4 we may expect the band gap of the graphene fluorinated in the B pattern to have a magnitude of 1.5 eV. This result is confirmed by the data on the band gap of the zigzag and armchair F-SWCNTs and testifies in favor of validity of the calculation.

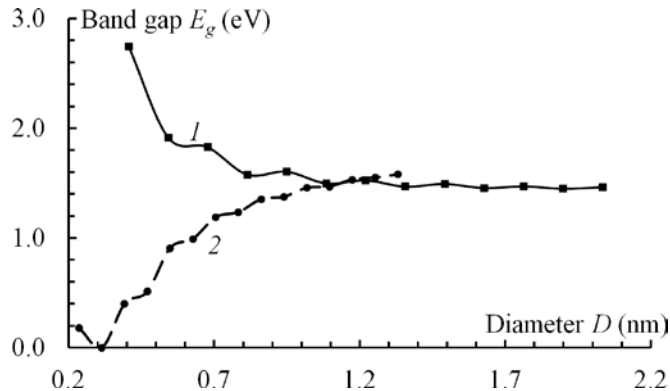


Fig. 3. Dependencies of the band gap E_g on the diameter D of the isomer B of armchair (1) and zigzag (2) F-SWCNTs.

The results obtained for the Fermi level energy and the ionization energy shown on the Fig. 5, 6 are also of certain interest.

As it is well known from the theoretic [23] and experimental [24] studies the Fermi level in the carbon nanotubes lies at the value of $-5.2 - -4.8$ eV. As it is noticeable from the Fig in the fluorinated SWCNTs it is significantly lower. The general tendency of the ionization energy and the modulus of the Fermi energy is to increase with the diameter in the region of small diameters and change insignificantly in the region of larger diameters (Fig. 5, 6). On the contrary, the modulus of the Fermi energy and the ionization energy of pristine tubes do

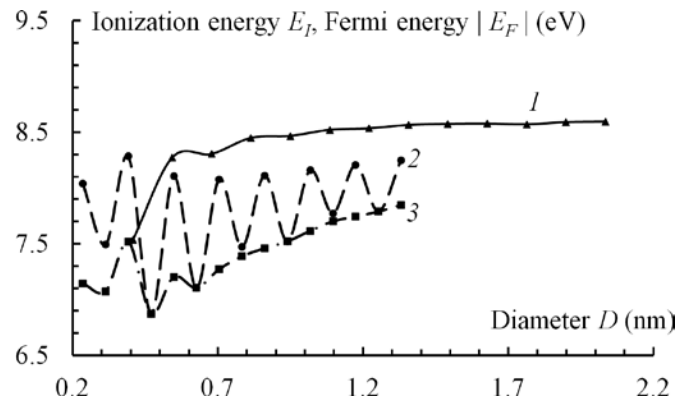


Fig. 5. Dependencies of the modulus of Fermi energy $|E_F|$ and the ionization energy E_I on the diameter D of the isomer A of achiral F-SWCNTs: 1 – $|E_F|$ and E_I of the armchair F-SWCNTs; 2 – E_I of the zigzag F-SWCNTs; 3 – $|E_F|$ of the zigzag F-SWCNTs.

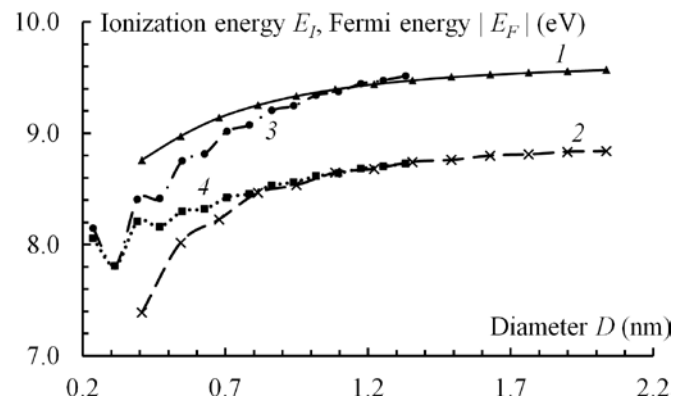


Fig. 6. Dependencies of the modulus of Fermi energy $|E_F|$ and the ionization energy E_I on the diameter D of the isomer A of achiral F-SWCNTs: 1 – E_I of the armchair F-SWCNTs; 2 – $|E_F|$ of the armchair F-SWCNTs; 3 – E_I of the zigzag F-SWCNTs; 4 – $|E_F|$ of the zigzag F-SWCNTs.

decrease with the diameter in the region of $D < 1.0$ nm and do not change with the diameter for larger diameters. From the experiments involving fluorination of SWCNTs it is known that, generally, fluorine atoms do not distribute evenly all along the SWCNT but rather tend to form fluorinated zones. This phenomenon opens opportunities for creation of different structures of lowered dimensionality based on the partially fluorinated SWCNTs (for instance, quantum dots).

III. CONCLUSION

A conclusion section is not required. Although a conclusion may review the main points of the paper, do not replicate the abstract as the conclusion. A conclusion might elaborate on the importance of the work or suggest applications and extensions.

REFERENCES

- [1] V. N. Khabashesku, "Covalent functionalization of carbon nanotubes: synthesis, properties and applications of fluorinated derivatives," *Russian Chemical Reviews*, vol. 80 (8), pp. 705–725, 2011.

- [2] D. A. Bogdanova and S. V. Bulyarskii, "Simulation of chemical adsorption of hydrogen by carbon nanotubes," *Physics of the Solid State*, vol. 55 (3), pp. 567–572, 2013.
- [3] M. K. Ashraf, N. A. Bruque, R. R. Pandey, P. G. Collins and R. K. Lake, "Effect of localized oxygen functionalization on the conductance of metallic carbon nanotubes," *Phys. Rev. B*, vol. 79 (11), pp. 115428 (11 pages), Mar. 2009.
- [4] B. Ruelle et al., "Functionalization of MWCNTs with atomic nitrogen," *Micron*, vol. 40 (1), pp. 85–88, Jan. 2009.
- [5] K. H. An et al., "X-ray photoemission spectroscopy study of fluorinated single-walled carbon nanotubes," *Appl. Phys. Lett.*, vol. 80 (22), pp. 4235–4238, Jun. 2002.
- [6] E. T. Mickelson, C. B. Huffman, A. G. Rinzler, R. E. Smalley and R. H. Hauge, J. L. Margrave, "Fluorination of single-wall carbon nanotubes," *Chem. Phys. Lett.*, vol. 296, pp. 188–194, Oct. 1998.
- [7] P. N. Dyachkov, *Carbon nanotubes: structure, properties, applications*, Moscow: Binom, 2006, ch. 2., pp. 157–162.
- [8] S. Osuna, M. Torrent-Sucarrat, M. Sola, P. Geerlings, C. P. Ewels and G. Van Lier, "Reaction mechanisms for graphene and carbon nanotube fluorination," *J. Phys. Chem.*, vol. 114, pp. 3340–3345, Feb. 2010.
- [9] K. N. Kudin, H. F. Bettinger and G. E. Scuseria, "Fluorinated single-wall carbon nanotubes," *Phys. Rev. B*, vol. 63, pp. 045413 (8 pages), Jan. 2001.
- [10] N. Ranjan and G. Seifert, "Transport properties of functionalized carbon nanotubes: density-functional Green's function calculations," *Phys. Rev. B*, vol. 73, pp. 153408 (3 pages), Apr. 2006.
- [11] G. Seifert, T. Kohler and T. Frauenheim, "Molecular wires, solenoids, and capacitors by sidewall functionalization of carbon nanotubes," *Appl. Phys. Lett.*, vol. 77 (9), pp. 1313–1316, Aug. 2000.
- [12] M. J. Frisch et al. *Gaussian 03. Revision C.2*, Pittsburgh: Gaussian Inc., 2003.
- [13] S. Hamel, P. Duffy, M. E. Casida and D. R. Salahub, "Kohn–Sham orbitals and orbital energies: fictitious constructs but good approximations all the same," *Journal of Electron Spectroscopy and Related Phenomena*, vol. 123, pp. 345–363, May, 2002.
- [14] R. Saito, G. Dresselhaus and M. S. Dresselhaus, *Physical properties of carbon nanotubes*, London: Imperial College Press, 1998, ch. 4.
- [15] V. Zólyomi and J. Kürti, "First-principles calculations for the electronic band structures of small diameter single-wall carbon nanotubes," *Phys. Rev. B*, vol. 70, pp. 085403 (8 pages), Aug. 2004.
- [16] I. Cabria, J. W. Mintmire and C. T. White, "Metallic and semiconducting narrow carbon nanotubes," *Phys. Rev. B*, vol. 67, pp. 121406(R) (4 pages), Mar. 2003.
- [17] J. W. G. Wilder, L. C. Venema, A. G. Rinzler, R. E. Smalley and C. Dekker, "Electronic structure of atomically resolved carbon nanotubes," *Nature*, vol. 391, pp. 59–62, Jan. 1998.
- [18] T. W. Odom, J.-L. Huang, P. Kim and C. M. Lieber, "Atomic structure and electronic properties of single-walled carbon nanotubes," *Nature*, vol. 391, pp. 62–64, Jan. 1998.
- [19] E. N. Bormontov, A. A. Ganin and L. A. Bityutskaya, "Oscillations of the band gap of single-walled carbon nanotubes in the range of very small diameters," *Semiconductors*, vol. 46 (13), pp. 1573–1575, Dec. 2012.
- [20] J. T. Frey and D. J. Doren, *TubeGen 3.2*, Newark, DE: University of Delaware, 2003 [Online]. Available: <http://turin.nss.udel.edu/research/tubegenonline.html>.
- [21] F. H. Allen, O. Kennard, D. G. Watson, L. Brammer, A. G. Orpen, R. Taylor, "Tables of bond lengths determined by X-ray and neutron diffraction. Part 1. Bond lengths in organic compounds," *J. Chem. Soc., Perkin Trans. 2*, vol. 12, pp. S1–S19, 1987.
- [22] D. O'Hagan, "Understanding organofluorine chemistry. An introduction to the C–F bond," *Chem. Soc. Rev.*, vol. 37, pp. 308–319, 2008.
- [23] W. S. Su, T. C. Leung, B. Li and C. T. Chan, "Work function of small radius carbon nanotubes and their bundles," *Appl. Phys. Lett.*, vol. 90 (16), pp. 163103 (3 pages), Apr. 2007.
- [24] M. Shiraishi and M. Ata, "Work function of carbon nanotubes," *Carbon*, vol. 39 (12), pp. 1913–1917, Oct. 2001.

Dynamic Behavior of Polymer at High Strain Rate

KHLIF .M, BRADAI .C., MASMOUDI. N

National School of Engineers of Sfax Tunisia (ENIS)
LASEM (Analysis Laboratory of the Electro-Mechanical Systems)
BP.1173. W. 3038 Sfax, Tunisia

Abstract— The increasing use of charged or not charged polymeric materials in the field of transport requires knowledge of their behavior in fast loading for the optimization of the structures. Such current studies are common in the case of metallic materials. But compared to metals, the particular behavior of polymers marked by a weak density, low Young modulus and visco-plastic behavior; makes the conventional experimental devices inoperative. Thus there doesn't exist nowadays a unanimously recognized test allowing a fine investigation of the fast behavior of these materials. The objective of this work is the development of a fast tensile test reaching 100 to 500 s⁻¹ strain rate inspired from Charpy device and the study of the polypropylene mechanical behavior under transitory dynamic loading. The major problem to be solved consists of the test duration which causes measurement difficulties by means of elastic wave like the case of Hopkinson bars technique..

Keywords— Dynamic tension, Polypropylene, High strain rate, Hopkinson bar ,Sensing block

I. INTRODUCTION

POLYMERIC materials have been used widely in engineering applications due to their low production cost and light weight. Polymeric materials are subjected to dynamic loading and high-strain-rate deformation in a variety of important applications such as aircraft and automotive components, as well as during high-speed processes such as extrusion and blow molding. However, the dynamic mechanical responses of polymeric materials under transitory loading are not completely understood. In particular, it is unclear whether the dynamic compressive behavior would be a reasonable reference for the corresponding tensile behavior since the differences between dynamic tensile and compressive responses have rarely been addressed. The study of materials properties under quasi-static to

dynamic loading depends on the strain rates range. The strain rate for dynamic domain begins at approximately 10 s⁻¹ [1].

Polymeric responses under impact have been studied since Kolsky's [2] pioneering work. For example, [3] used a split Hopkinson pressure bar (SHPB) to determine the dynamic compressive stress-strain behavior of Lucite and Micarta. [4] measured the dynamic compressive behavior of plastics using the same method. [5] used high-speed photography to determine the rapid deformation behavior of a range of polymers in compression. [6] noticed that specimen thickness was an important parameter when using the SHPB to test polymers. A few studies of polymeric material dynamic tensile behavior are found in the literature. In this study, the dynamic response of a heterophasic copolymer polypropylene PPC 7712 under a dynamic uniaxial tensile loading condition has been determined experimentally. In these experiments, a conventional Hopkinson bar was modified and a sensing block is used in order to measure the weak signals transmitted from the specimens of low strength and low mechanical impedance. A pendulum was applied to control the incident pulses in a tensile experiment in order to achieve dynamic stress equilibrium and homogeneous deformation in the specimen. A conventional tensile machine was used to conduct the quasi-static behavior of PP materials. In the following sections, the experiments are described and the results are presented with the appropriate discussions.

II. EXPERIMENTAL SET-UP

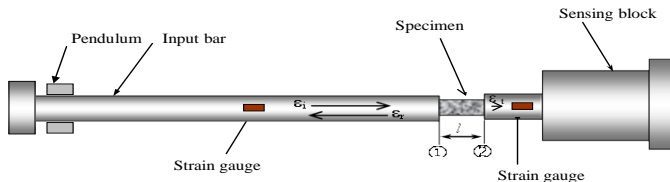
Experimental machine used in this study include a Hopkinson tension bar modified to conduct dynamic tension experiments on polymer specimens and a sensing block to perform dynamic tensile tests [7]. A conventional tensile machine is used for quasi-static experiments.

A. 2.1. Description of the dynamic loading machine

The dynamic loading machine presented in figure 1 is composed of three parts [7]. The first part represents the shock generating system used to excite the input bar. It includes a rotating pendulum that impacts the end part of the input bar. The intensity of the pendulum shock can be changed using a range of

variable masses. The speed of the excitation impact is a function of the pendulum altitude position. To commands the shock generating system and allows only one impact, a pneumatic device is implemented.

The shock receiving system represents the second part; it is illustrated in figure 1. It is composed of an input bar which receives the shock excitation generated by the pendulum and transmits the corresponding strain wave to the specimen located between the input bar and the sensing block. The geometrical sizes of the incident bar and the sensing block as well as the corresponding materials are presented in the following sections. The input bar is instrumented in order to measure the force. The choice of a long bar enables us to solve the waves superposition problem (incident and reflected waves) and to measure the loading force for a dynamic test. Moreover, the transmitting incident wave from the bar is transmitted to the specimen. This wave is finally received by the sensing block which is composed of a sensing receiver and a base block. A strain gage located at the sensing receiver measures the corresponding transmitted stress wave. Due to the important relative large mass of the base block, the stress wave moving from the sensing receiver is dissipated after some reflections between the base block upper surfaces.



The technique described above has many advantages compared with the Hopkinson bar system: The important mass of the base block allows a negligible reflection waves disturbance and the short length of the sensing receiver allows a long measuring time.

The mechanical characteristics (Young' modulus, Poisson's ratio, and density) of the investigated polymer, the bar and the sensing block are presented in Table 1.

Table 1: Mechanical characteristic of polymer PPC7712, the bar and the sensing block

	Materiel	ρ . kg/m ³	E . GPa	ν	Re MPa
specimen	polypropylene	1400	1.4	0.4	9
bar and sensing block	aluminum	2830	71	0.34	41

The last part of the dynamic loading machine represents the data acquisition system which analyses the signals (incident ϵ_i , transmitted ϵ_t and reflected ϵ_r waves) measured by two pairs strain gauges type Kyowa KFG-5-120-C1-11. The strain gauges grill length is 5 mm. The first pair is located in the middle of the input bar, the second pair is mounted on the sensing block. A data acquisition card "NI-PCI-6250" is used to collect signals issued from the gauges which were preably amplified. The visualization and analysis of results are done using Lab-view software.

B. 2.2. Wave propagation analysis

Assuming a homogeneous deformation in the specimen and identical incident and transmitted waves, the analysis based on one-dimensional wave theory [8] showed the nominal strain $\epsilon_s(t)$, in the specimen to be:

$$\epsilon_s(t) = \frac{C_0}{l} \int_0^t (\epsilon_i - \epsilon_r) dt, \quad (1)$$

where,

l is the initial length of the specimen,

$\epsilon_i(t)$ and $\epsilon_r(t)$ are the incident and reflected strain waves in the incident bar,

C_0 is the wave celerity of the bar material.

On the other hand, the forces at the ends of the specimen are obtained by the following equations:

$$F_1 = EA(\epsilon_i + \epsilon_r) \quad (2-a)$$

$$F_2 = EA\epsilon_t \quad (2-b)$$

Where,

A is the cross-sectional area of the bar,

$\epsilon_t(t)$ is the transmitted strain waves in the sensing block of Young's modulus E .

Assuming equal forces at both ends of the specimen ($F_1 = F_2$) and using equations (2-a) and (2-b) yields to:

$$\epsilon_t = \epsilon_i + \epsilon_r \quad (3)$$

Integration of equation (1) with respect to time gives the time-resolved axial strain of the specimen. The nominal axial stress σ_s , in the specimen is determined using the following equation [8]

$$\sigma_s(t) = E \frac{A}{A_s} \epsilon_t(t) \quad (4)$$

Where A_s is the cross-sectional area of the specimen.

The sensing block system has been an effective tool for investigating the dynamic flow behavior of ductile metals [9]. However, when the specimen has a low impedance, low strength material, the limitations of the split Hopkinson bars should be recognized and remedied. First, the low mechanical impedance of the specimen allows the incident bar-specimen interface to move almost freely under stress-wave loading because most of the incident pulse is reflected back into the incident bar. Only a small portion of the loading pulse is transmitted through the specimen into transmission bar, so the transmitted strain signal $\epsilon_t(t)$ has very small amplitude. To solve this problems and to increase the magnitude of a weak transmitted signal we used a sensing block system in aluminum alloy (Figure 1-a). This method is alike to the sensing projection for impact experiments [10]. It is apparent from equation (3) that to increase the transmitted strain $\epsilon_t(t)$ under the same specimen, it is necessary to reduce either the Young's modulus of the bar material, E , or the cross-sectional area ratio, A/A_s , or both. Both the lower Young's modulus of the aluminum alloy and a smaller cross-sectional area of the sensing block contribute to increase in magnitude of the transmitted signal $\epsilon_t(t)$.

At the interface, the fixing of the specimen at the end of the incident bar and the sensing block is performed by three screws. To conserving same cross-sectional area a groove is made at the end of the bar and the sensing block

As pointed out by [11], in order to facilitate dynamic stress equilibrium and constant strain rate in a low-impedance specimen, a pulse shaper must be used. The sensing block undergoes the loading signal from the specimen; the latter will be in dynamic equilibrium. This technique was also used by [9] to determine the dynamic impact strength of mild steels.

To ensure homogeneous deformation of the specimen before fracture occurs, a pulse-shaping technique was applied. Pulse shaping is an experimental technique to ensure stress equilibrium and constant strain rate in the specimen in dynamic tensile testing [12]. The rise time of the loading pulse was designed to be longer than the stress-equilibrating time in the tensile specimen. The bar wave speed of the polypropylene is about 2 km/s. The gage length of the dynamic tensile specimens is 10 mm. This wave takes 25 μ s to reach dynamic stress equilibrium in the gage section. Control of the pulse shape was achieved by launching a pendulum at the end of incident bar. The pendulum material was chosen according to the intensity loading proposed. The gradually increasing disk area upon impact by the striker allows more and more momentum to transfer from the striker to the incident bar, which significantly increases the rise time of the incident pulse. Proper choice of the pulse-shaper material and dimensions controls the profile of the incident pulse. The amplitude and duration of an incident pulse are controlled by varying the pendulum velocity and weight. In dynamic tensile experiments with pulse shaping, the specimen fractured at two places in a short (10 mm) gage section, as shown in (Figure2) which is an indication that dynamic stress equilibrium had been reached before failure occurred.

C. Materials and specimens

A heterophasic multi-phase copolymer polypropylene (named PPC7712) supplied by Total-Petrochemicals was analyzed in this study. Quasi-static loading tests (simple tensile, cyclic, relaxation and torsion tests) had previously been carried out on this grade of polymer [13]. PPC7712 combines good fluidity and mechanical properties. It is characterized by excellent impact resistance and makes for faster cycling because it lends itself to early remolding. Its melt flow index is 13 g/10min. The rate of crystallinity had previously been measured by Differential Scanning Calorimetry (DSC) using the enthalpy of fusion of 209 J g^{-1} in 100% crystalline polypropylene.

The specimens were molded by injection machine with controlled parameters. Figure 2 illustrates the injection mold and the dimensions for the specimens used in dynamic tension tests (The standard NF ISO 8256) [15]. The quasi-static tension specimen is determined by the standard ISO 6200, the gage section length is 55 mm.

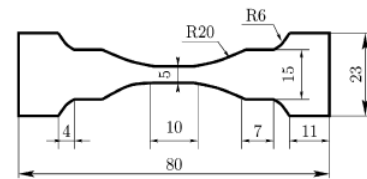
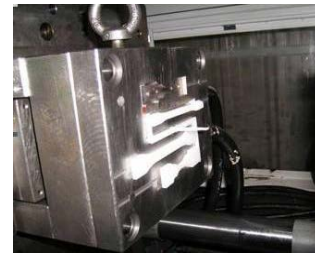


Figure 2: Dynamic tensile specimen (thickness 5mm)

III. EXPERIMENTAL RESULTS

The experiments were conducted in the mechanical department at the University of Sfax. For the dynamic tensile machine (Figure 1) , the length of the incident bar is 3000 mm, The sensing block system, manufactured of aluminum alloy, is composed of a specific sensing receiver with 15mm diameter and 30mm length and a base block with 100mm diameter and 200mm length. This important difference between the two diameters provokes the wave trapping phenomenon.

In this study, uni-axial tension experiments on the PPC7712 were performed using the Static Tensile Machine (MTS) and the dynamic tensile machine described in Figure 1., is used for four strain rates 10^2 s^{-1} , 2.10^2 s^{-1} , 3.10^2 , 4.10^2 s^{-1} and 5.10^2 s^{-1} . The time-resolved engineering stress and engineering strain profiles were recorded during the quasi-static experiments on the MTS. For the quasi-static experiments, the MTS machine parameters are controlled in order to get a constant strain-rate in the specimen. Figure 3 presents the evolution of the stress related to the strain of the polypropylene PPC7712 for 0.8 s^{-1} strain rate. It is clear from this experiment that the PPC 7712 has elastoplastic behavior. For small strain (0 - 0.7%) the material has a linear behavior,

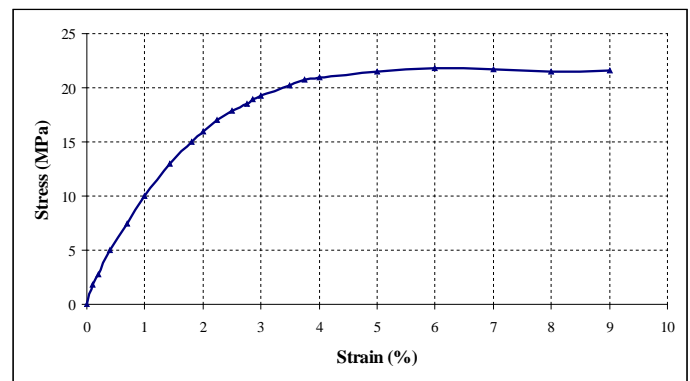


Figure 3: Quasi-static tensile test: stress–strain curve of PPC7712 for 0.8 s^{-1} strain rate

During dynamic tension experiments, the incident, reflected and transmitted strain signals were recorded. Using these signals and

Eqs (1) and (3), the strain and dynamic tensile stress in the specimen are calculated.

Pulse shaping was used to achieve constant strain rates in dynamic experiments, which took a significant amount of experimental effort to find a suitable pulse shaper for a particular set of test conditions. (Figure. 5) shows a typical oscilloscope record of the dynamic tensile experiment on PPC7712 using the dynamic tensile machine. As indicated by the transmitted pulse in figure 4, the use of a pendulum resulted in a transmitted signal. The transmitted signal directly gives engineering stress history through Eq. (3), where the cross-sectional area and Young's modulus of the bar. The incident and reflected signals give the dynamic strain history in the specimen through Eq. (4).

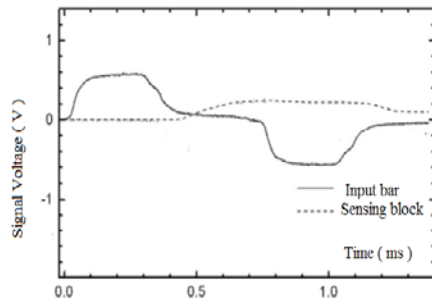


Figure 4: The incident and the transmitted waves recorded by the strain gauges located on the bar and the sensing block under a dynamic tensile test on PPC7712.

Figure 5 presents respectively the typical dynamic strain and the strain history for the specimen. The fact that the strain increases almost linearly with increasing time during the majority of the experiment indicates that a dynamic constant strain rate has been achieved. The slope is taken as the strain rate of the experiment.

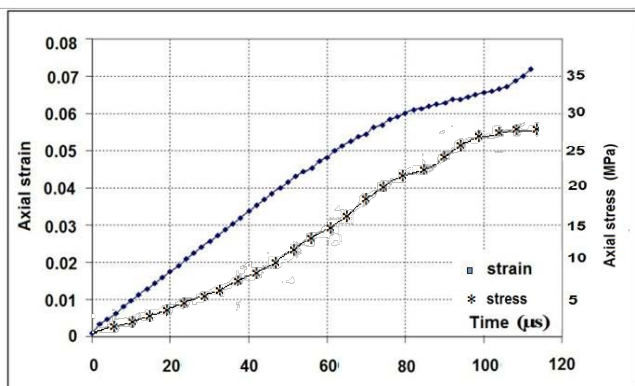


Figure 5: The axial strain and stress on the specimen versus time under a dynamic tensile test on PPC7712.

Figure 6 summarizes the tensile stress–strain curves of PPC7712 over a strain-rate range of 100 s^{-1} , 200 s^{-1} , 300 s^{-1} , 400 s^{-1} and 500 s^{-1} . It should be noted that the stress-strain curves obtained from dynamic tensile machine experiments do not give reliable elastic modulus due to the transient stress state within the specimen during the early stages of the experiment. An

inspection of figure 7 indicates that peak strength was reached during a dynamic test at a smaller strain compared with the quasi-static case. Also, the results in Figure 6 do not show clear strain-rate dependence of the material's peak tensile strength, which is approximately 25 MPa. The specimens fractured in a brittle manner during dynamic tensile loading. In contrast, during quasi-static tests, the specimens failed in a ductile manner with a necking process. The brittle–ductile transition is considered to be the strain-rate effect.

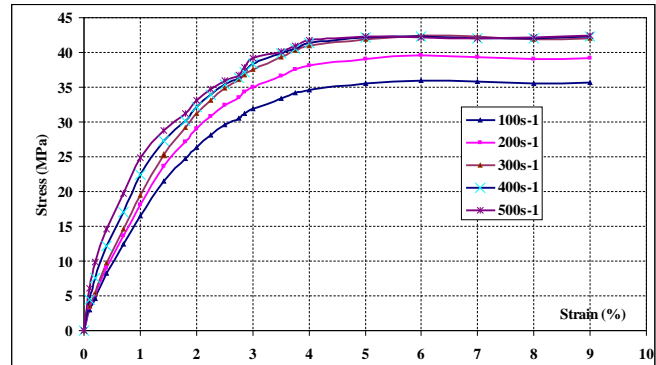


Figure 6: Dynamic tensile test: stress–strain curves of PPC7712 for various strain rates.

Qualitatively, if the polymer is still thermo-rheologically simple at such high strain rates encountered in the dynamic tensile machine range, and time superposition still applies, a higher strain rate would correspond to a shorter loading time. Another possible cause for the brittle–ductile transition is the short gage length of the specimen. The end constraint, in the form of the hydrostatic component of the stress tensor, to the gage section becomes more important as the length of the gage section decreases. The fact that more than one fracture surface exists, as shown in specimen, indicates that dynamic stress equilibrium has been reached before fracture events took place. However, the fracture occurred near the fillets despite a series of changes in the fillet radius in a series of trial experiments. This fact indicates that stress concentration near the fillets played an important role in the dynamic fracture of the short specimen, which may have shadowed the strain-rate effects on the tensile failure strength. As will be shown in the following discussion, the tensile experimental results exhibit much more apparent strain-rate effects on the peak strength of the same material.

Figure 7 presents two specimens after rupture for quasi-static and dynamic tests. From This figure, we can get an idea for the PPC7712 behavior. It is shown that the final length of the specimen is more important for the quasi-static test Figure 7 (a). That means the material has a ductile behavior in the quasi-static test however it has a brittle behavior in the dynamic test.



Figure 7: The specimens after rupture (a) quasi-static test, (b) dynamic test

IV. CONCLUSION

The quasi-static and dynamic stress-strain behavior of a PPC7712 polypropylene has been determined under uniaxial tension loading conditions. To determine the dynamic tensile behavior of low-strength, low-impedance of a PPC7712 polypropylene, a dynamic tensile machine has been developed to capture the low transmitted signal. A pulse-shaping technique was used to ensure a homogeneous deformation at a constant strain rate during experiment, either in tension or in compression.

For quasi-static case, the mechanical behavior of this material is investigated at 0.8 s^{-1} strain rate. It is found the PPC7712 polypropylene has elasto-plastic behavior and the Young's modulus can be determined. The specimen is failed in a ductile manner. It is noted that the dynamic stress-strain behavior under tension differ from the dynamic compressive response for the quasi-static loading conditions. With similar quasi-static strength in both tension and compression states of the testing material, the dynamic compressive strength is higher than the quasi-static counterpart.

For the dynamic case, a strain-rate range of 100 s^{-1} , 200 s^{-1} , 300 s^{-1} , 400 s^{-1} and 500 s^{-1} are considered in the experimental tests. The Young's modulus was found to increase with the strain rate. The experimental results show that, for the PPC7712 materials investigated, the dynamic stress-strain behavior under tension significantly differ from the dynamic compressive response. Specimens are failed in a brittle manner under dynamic tension. Therefore, dynamic compressive results are not indicative for dynamic tensile failures. It is a challenge to design a valid dynamic tensile experiment for a polymeric material. Hence, the low wave speeds in the material significantly restrict the specimen length.

REFERENCES

[1] Hamoda A.M.S., Hashmi M.S.J. (1998). Testing of composite material at high rates of strain: advances and challenges, *Journal of Material Processing and Technology* 77: 327-336.

[2] Kolsky, H. (1949) An Investigation of the Mechanical Properties of Materials at Very High Rates of Loading. *Proc. Roy. Soc. London*, B62: 676-700.

[3] Q.M. Li, Y.B. Lu, H. Meng. (2009)., Further investigation on the dynamic compressive strength enhancement of concrete-like materials based on split Hopkinson pressure bar tests. *International Journal of Impact Engineering*. 36: 1336-1345.

[4] Chou, S. C., Robertson, K. D., Rainey, J. H. (1973) The Effect of Strain Rate and Heat Developed During Deformation on the Stress-Strain Curve of Plastics. *Experimental Mechanics*. 13: 422-432.

[5] Walley. S.M, Field. J.E, Pope. P.H, Safford. N.A, (1989) A study of the rapid deformation behavior of a range of polymers, *Philosophical Transactions of the Royal Society of London* 328: 1-33.

[6] Bo Song and Weinong Chen. (2005). Split Hopkinson pressure bar techniques for characterizing soft Materials. *Latin American Journal of Solids and Structures* 2: 113-152

[7] Khlif .M, Masmoudi. N, Bradai.C, Grolleau. V, Rio G. (2008). Development of a new testing method for polymer materials at high strain rate' *Journal of Theoretical and Applied Mechanics*. 38: 67-82

[8] Khlif, M., Masmoudi, N., Bradai, Ch Polypropylene tensile test under quasi-static and dynamic loading *Materials Science and Technology Conference and Exhibition 2012, MS and T 2012 1* , pp. 567-574

[9] Tanimura S, (2001) 'Evaluation of Accuracy in Measurement of Dynamic Load by Using Load Sensing Block Method', *Proceedings of 4th International Symposium on Impact Engineering ISIE4, Kumamoto, Japan*. 77-82.

[10] Grolleau. V, Guines. D, Umiastowski. S, Ragneau. E, Rio. G, (2005) 'Optimisation de dispositifs d'essais dynamiques sur machine d'impact et presse hydraulique', *MECAMAT, Aussois*,

[11] Chen. W, Lu. F, Zhou. B, (2000) 'A quartz-crystal-embedded split Hopkinson pressure bar for soft materials', *Experimental Mechanics*. 40: 1-6.

[12] Frew. D.J, Forrestal. M.J, Chen. W, (2001). A split Hopkinson bar technique to determine compressive stress-strain data for rock materials', *Experimental Mechanics* 41: 40-46.

[13] Zrida. M, Laurent .H, Rio. G, Pimbert. S, Grolleau. V, Masmoudi. N, Bradai. C, (2009) Experimental and numerical study of polypropylene behavior using an hyper-visco-hysteresis constitutive law. *Computational Materials Science*. 45: 516-527

[14] Krawczak. P (1997), *Essais mécanique des plastiques, Techniques de l'Ingénieur, AM*, 3. 510.

Binding sites of the miR-1273 family, miR-1285-3p and miR-5684 in human mRNAs

Anatoly T. Ivashchenko, Olga A. Berillo, Anna Y. Pyrkova and Raigul Y. Niyazova

Abstract—The search of 2578 miRNA binding sites in 13000 mRNAs of human genes using the MirTarget program has been completed. For the binding sites of the miR-1273 family, miR-1285-3p and miR-5684, the hybridization free energies of the bonds are equal to or greater than 90% of the maximum value free energy. Approximately 90-nucleotide regions of mRNAs containing binding sites for the miR-1273 family, miR-1285-3p and miR-5684 were revealed. These regions are located in the 5'UTRs, CDSs and 3'UTRs of the mRNAs and contain between two and six arranged miRNA binding sites. The miR-1273g-3p, miR-1273a, miR-1273c, miR-1285-3p and miR-5684 binding sites are grouped together and located ahead of another group consisting of miR-1273f, miR-1273d, miR-1273e, miR-1273g-5p and miR-1273h-5p binding sites. The role of these miRNAs in the regulation of gene expression and its participation in different biological processes will be discussed.

Keywords—apoptosis, cancer, cell cycle, miRNA, mRNA.

I. INTRODUCTION

THERE are many unresolved problems in studying the biological role of microRNAs (miRNAs), despite numerous publications in this field [1]. Non-protein-coding miRNAs regulate the expression of protein-coding genes at the post-transcription level [2]. miRNAs participate directly or indirectly in nearly all stages of metazoan development [3]. There are different programs of miRNA prediction of target genes, but many of them generate a large number of false-positive results [4]. This complicates the understanding of

connections among miRNAs and target genes participating in different metabolic processes. For a long time, it has been proposed that binding sites can be located only in 3'UTRs [5]; however, several studies have recently reported binding sites in 5'UTRs and CDSs of mRNAs [6, 7]. The largest type of target genes includes genes participating in the development of cancer and other diseases. miRNAs regulate the expression of different genes and participate in many pathological processes [8-10], including carcinogenesis [11-17]. Changes in the concentration of miRNAs were observed in the development of breast cancer [11], lung cancer [12], gastrointestinal cancer [13, 14] and other cancer types [15-17]. Fold changes in miRNA expression have been revealed in the majority of the studies [11-20], although their target genes have been insufficiently investigated. Thus, it is necessary to establish the properties of miR-1273a, miR-1273c, miR-1273d, miR-1273e, miR-1273f, miR-1273g-3p, miR-1273g-5p, miR-1273h-3p, miR-1273h-5p, miR-1285-3p and miR-5684 binding sites in mRNAs of genes participating in the development of cancer.

II. MATERIAL AND METHODS

The human gene mRNAs were obtained from GenBank (<http://www.ncbi.nlm.nih.gov>) using Lextractor002 script (<http://sites.google.com/site/malaheenee/software>), which was written in our laboratory. The miRNA sequences and information regarding their origin was obtained from the miRBase database (<http://mirbase.org>). The search for target genes of miRNAs was achieved using the MirTarget program, which was written in our laboratory. This program defines the following features of binding: a) the origin of the initiation of miRNA binding to mRNAs; b) the localization of miRNA binding sites in the 5'-untranslated regions (5'UTRs), the coding domain sequences (CDSs) and the 3'UTRs of the mRNAs; c) the free energy of hybridization (ΔG , kJ/mole); and d) the schemes of nucleotide interactions between the miRNAs and mRNAs. The $\Delta G/\Delta G_m$ ratio (%) was determined for each site (ΔG_m equals the free energy of a miRNA binding with its perfect complementary nucleotide sequence). The miRNA binding sites located on the mRNAs had $\Delta G/\Delta G_m$

This study was supported by a grant obtained from the Ministry of Education and Science, Kazakhstan Republic.

A.T. Ivashchenko with the National Nanotechnology Laboratory, al-Farabi Kazakh National University, Almaty, Kazakhstan, 050038 (phone/fax: +7 (727) 3773202; e-mail: a_ivashchenko@mail.ru).

O.A. Berillo with the National Nanotechnology Laboratory, al-Farabi Kazakh National University, Almaty, Kazakhstan, 050038 (e-mail: devolia18@mail.ru).

A.Y. Pyrkova with the National Nanotechnology Laboratory, al-Farabi Kazakh National University, Almaty, Kazakhstan, 050038 (e-mail: Anna.Pyrkova@kaznu.kz).

R.Y. Niyazova with the National Nanotechnology Laboratory, al-Farabi Kazakh National University, Almaty, Kazakhstan, 050038 (e-mail: raiguln@mail.ru).

ratios of 90% or more. We also noted the positions of the binding sites on the mRNA, beginning from the first nucleotide of the mRNA's 5'UTR. The MirTarget program calculated the interactions between the nucleotides of the miRNAs and those of the mRNA target gene. This program identified hydrogen bonds between adenine (A) and uracil (U), guanine (G) and cytosine (C), G and U, and A and C [21]. The distance between A-C was same as that as between G-C, A-U, and G-U [22] nucleotides. The number of hydrogen bonds between G-C, A-U, G-U and A-C and the value of their free energy of binding is equal to 3, 2, 1 and 1, respectively.

III. RESULTS

A. Characteristics of the arranged binding sites in 3'UTRs

In this study, 2578 miRNA binding sites in 13000 mRNAs of human genes were identified. The binding sites with equal to or greater than 90% of the maximum free energy were selected and were analyzed. It was revealed that binding sites of the miR-1273 family, miR-1285-3p and miR-5684 are localized side by side in many mRNAs. Therefore we started study them in detail. miR-1273e, miR-1273g-3p and miR-1273f have several hundreds of target genes and are unique miRNAs (umiRNAs) in comparison with others. The mRNAs of genes that have binding sites with two or more studied miRNAs were analyzed. The data regarding the quantity of genes and binding sites of the selected miRNAs are presented in Table 1.

Table 1 Number target genes and binding sites of miR-1273 family, miR-1285-3p and miR-5684 in mRNA of human genes.

miRNA	Number genes	Number sites	Number sites in 5'UTR	Number sites in CDS	Number sites in 3'UTR
miR-1273a	145	151	6	2	143
miR-1273c	80	81	7	2	72
miR-1273d	102	104	5	6	93
miR-1273e	399	431	18	9	404
miR-1273f	654	742	30	26	686
miR-1273g-3p	809	945	42	28	875
miR-1273g-5p	32	32	2	5	25
miR-1273h-5p	98	99	6	8	85
miR-1285-3p	127	130	8	2	120
miR-5684	189	200	9	7	184

The miRNAs form two groups with arranged binding sites in 90-nucleotide regions of mRNAs (Fig. 1, A). The arranged binding sites are binding sites of different miRNAs, which have overlapping nucleotide sequences or are located within the same distance in different mRNAs of genes. The region of the nucleotide sequence in the 3'UTRs of the *SLC36A2* gene

containing arranged binding sites was selected for comparison with other mRNAs of target genes. The miR-1273g-3p group includes miR-1273a, miR-1273c, miR-1285-3p, and miR-5684 (Fig. 1, A).

The distance between the end of the miR-1273g-3p binding site and the beginning of the miR-1273f binding site is equal to 12 nucleotides (Fig. 1, A). The miR-1273f group includes miR-1273d, miR-1273e, miR-1273g-5p, miR-1273h-5p. There are no arranged miR-1273h-3p binding sites in 90-nucleotide regions of mRNAs with a $\Delta G/\Delta G_m$ ratio equal or greater than 90%. In this study, 2687 arranged binding sites are located in the 90-nucleotide parts of 865 3'UTRs. Six out of ten examined miRNAs are the maximum number of arranged binding sites in two miRNA groups. The aligned nucleotide sequences of the 3'UTR regions with five or six arranged miRNA binding sites are represented in the schematic shown in Fig. 1, A. The nucleotide sequences of the revealed sites of the target genes are highly homologous, which confirms their general origin in the studied genes. The 3'UTRs of 26 genes exhibited arranged miRNA binding sites with a $\Delta G/\Delta G_m$ ratio greater than 96%. Each mRNA of the *CHMP1B*, *MCTS1*, *OPRK1*, *OR7D2*, *SLC36A2*, *TAT* and *ZNF527* genes has one binding site with a $\Delta G/\Delta G_m$ ratio greater than 98%. The high $\Delta G/\Delta G_m$ ratio for binding sites of the miRNAs with the RNAs showed that the expression of these genes may be strongly suppressed in conditions of same concentration of mRNAs and miRNAs.

B. Characteristics of the arranged binding sites in 5'UTRs

In this study, 133 arranged binding sites are revealed in the 90-nucleotide parts of 53 5'UTRs (Fig. 1, B). The miRNA binding sites corresponded to one of two groups and are localized in the corresponding arranged nucleotide sequences as well as in 3'UTRs. The *LGMM* mRNA has miR-1273e, miR-1273f, miR-1273g-3p, miR-1285-3p and miR-5684 binding sites. The *KCNJ11*, *RGS12*, *TMC1* and *ZNF527* mRNAs have four arranged miRNA sites. In addition, 17 mRNAs have three binding sites, and 30 mRNAs have two sites. Moreover, the 5'UTRs of 12 genes have miRNA binding sites with a ratio $\Delta G/\Delta G_m$ greater than 96%. The mRNA of the *CD59*, *FAIM* and *TMC1* genes have one binding site with a $\Delta G/\Delta G_m$ ratio greater than 98%. Thus, the expression of these genes will be strongly suppressed in conditions of comparable concentrations of mRNAs and miRNAs. The homology degree of nucleotide sequences in 5'UTR regions of the genes is high, which confirms the important role of these binding sites in the biological function of these genes (Fig. 1, B). The binding sites of the studied miRNAs are distributed in the 5'UTR as well as in 3'UTR; thus, it is possible that these sites have one general precursor.

```

UUCUUUCUCAGAACGAAACAGCGGG miR-1273a          A          AGGUGAAGGACCCAAGUUCGUU miR-1273e
CUGUCCAGAGCAAACAGCGG miR-1273c                UGACGUCGGAACUGGAGGGUC miR-1273h-5p
UCCAGAGUGAAACACGGGUCU miR-1285-3p             UGACGUCGGAGUUGGAGUACCCAAG miR-1273d
          GACAACGAGUCCGAUCUCA miR-5684          UGAAUGACGUCGGAGUUGGUGG miR-1273g-5p
miR-1273g-3p 3'GAGUCCGACCUCACGUCACCA 5'      3'GUGACGUUGGAGGUAGAGG 5' miR-1273f
5'          ||| 3'
GAGAUGAAGUCUCGUCUCUGUUGCCAGGCUGGAGUGCAAUGGCACAAUCUCGGCUCACUGCAACUCCUCCUGGUAUCAAGCGA SLC36A2 2795
...C.G.....C.....A.....G...U..C...C.....G.....C.....C..G.. ARSA 3193
...C.G.....A.....C.....G.....U.....G.....C.....G.....C... C1orf210 1120
...CAG.....UG...G.G...U.....C.....U.....C.....U..... CHMP1B 2474
...CAGG.....G...GUG...U.....U...G.....U..... FUTI 2666
A...CAG.A...G...UG...U.....UC..... KCNE4 2222
...A.CAGG...U.....G...U.G...U.....U.....C..... MCTS1 1597
A...G...U.....G...A...UG...A.....AU MOB1B 4467
...C.GG.....C.....A.G...UG.C...A.....G...U..... MR11 2593
...CAG.....A.....A.....G...G.G.U.U.....G..... NMUR1 1902
...C.G.....GG.A...G...U..... OPRK1 3440
A...CAG...A.....G...G.G...AU.....CA..... OR7D2 2539
...CAG.....U.....CAG...U.....GU.....U..AG PHKG2 2445
A...CAGG...U.....CC...G...UGUG...AU...G...G...C...A... PPIL2 2051
UU...AAC...G...CA...G...UG...A.G...G...C...A... SERBP1 5369
...G...U.....G...UU...U.....U.....A... SIGLEC8 1911
...G...A.....G...GUG...U.....G...C..... SMC5 5358
U.A.CAGG...A.....A.....UG...A.A...G...A...A... STAT2 3581
...CAG...A.....G...G.C...G...CA...A...A... STK4 4624
...G...U...C...U...G...G.G...TAT 2222
...CAG...U...U...CA...UG...UGUU.C.A...G... USP33 3461
C...CAG.....G...UGU...U.....G...UG.....A... ZNF527 2131

UUCUUUCUCAGAACGAAACAGCGGG miR-1273a          B          AGGUGAAGGACCCAAGUUCGUU miR-1273e
CUGUCCAGAGCAAACAGCGG miR-1273c                UGACGUCGGAACUGGAGGGUC miR-1273h-5p
UCCAGAGUGAAACACGGGUCU miR-1285-3p             UGACGUCGGAGUUGGAGUACCCAAG miR-1273d
          GACAACGAGUCCGAUCUCA miR-5684          UGAAUGACGUCGGAGUUGGUGG miR-1273g-5p
miR-1273g-3p 3'GAGUCCGACCUCACGUCACCA 5'      3'GUGACGUUGGAGGUAGAGG 5' miR-1273f
5'          ||| 3'
AGAUGAAGUCUCGUCUCUGUUGCCAGGCUGGAGUGCAAUGGCACAAUCUCGGCUCACUGCAACUCCUCCUGGUAUCAAGCGAU SLC36A2
U...CAGG...AU...C.....U.G.A.G.G.....U.....CA.....A... CCD36 53
GCCGCC...U.....A.....G...G...U.....G.....G..... CD59 112
...CAG.A...C.....CA...G...UG.....C.....C..... FAIM 258
CUUGAG...A.CG.....A...G...G.G.....A.....G...C..... GPR63 226
C.GCAG...U...GC.ACA...G...U.....G.U...C...A... HMOX2 164
...C.G.....C.....G...GUG...U.....G...UC... KCNJ11 103
CC.CAGG...UA.....G...U.....UG...C.....A... LGMN 230
...G...U...CAUU...G...UG.G...A...G...U.....CAU... LTB4R 520
...G...U...G...C...U...G...GUG...U...G...U...C...U.A... NLRP3 294
...CAG...U...CA...G...GUG...A...G...C...U... POU5F1 203
...CAG...C.A...A...G...G...UG...CA...U... PRRI6 342
...GGA...UA...G...UG.G...U...G...CA...U... RGS12 297
G...G...A.U...C...CC.G...UGUG...A...U...C... TMEM230 365
CAUG...GU.UCGCUCU...U...UGUG.....G...C..... ZNF761 76

UUCUUUCUCAGAACGAAACAGCGGG miR-1273a          C          AGGUGAAGGACCCAAGUUCGUU miR-1273e
CUGUCCAGAGCAAACAGCGG miR-1273c                UGACGUCGGAACUGGAGGGUC miR-1273h-5p
UCCAGAGUGAAACACGGGUCU miR-1285-3p             UGACGUCGGAGUUGGAGUACCCAAG miR-1273d
          GACAACGAGUCCGAUCUCA miR-5684          UGAAUGACGUCGGAGUUGGUGG miR-1273g-5p
miR-1273g-3p 3'GAGUCCGACCUCACGUCACCA 5'      3'GUGACGUUGGAGGUAGAGG 5' miR-1273f
5'          ||| 3'
GAGAUGAAGUCUCGUCUCUGUUGCCAGGCUGGAGUGCAAUGGCACAAUCUCGGCUCACUGCAACUCCUCCUGGUAUCAAGCGA SLC36A2
...CAGG...A.....C.....A.....GCA.UG.U...A.A...G...G.A...C...G...A... FAHD1 664
AGACG...GU.G.UCU...G.....C...GGG.U.....UG...C.....A... FRRS1 216
...CAGG...C.....U.....C...G...UGUG...A.A...G...U...A.A.AUUG...C... RFC5 214
C.AUG...GU.UCGCUC...AGCG...U...G...G...CA...AA.UU... SCGE 1385
UG...GUCUCAUU.A...CA...G...C...CUU.C...G...CC.A...U... SPAG6 429
...A.CAGGA...A.....G...A.A.AA.U...G...UG.U...C.A.C...U... TRIM54 838
C...G...U...C...A...G...C.G...A...G...CA...A... ZNF573 522

```

Fig. 1 the localizations of the aligned nucleotide sequences of five and six arranged miR-1273 family, miR-1285-3p and miR-5684 binding sites in the 3'UTR (A), 5'UTR (B) and CDS (C).

Note: | symbol shows the presence of hydrogen bond between the miRNA and mRNA nucleotides; * after the name of the gene given the start of the binding site of miR-1273g-3p.

C. Characteristics of the arranged binding sites in CDSs

95 arranged binding sites were revealed in the 90-nucleotide parts located in 42 CDSs. The CDSs of 26 mRNAs have two arranged binding sites. The CDSs of the *ARGFX*, *FAHD1*, *FRRS1*, *GINS3*, *MKNK1*, *PRR16*, *RFC5*, *RNF135*, *SPAG6* and *ZNF573* genes have three binding sites. The CDSs of the *SGCE*, *TRIM54*, *NEK4* and *ADARB1* genes have four arranged binding sites. The CDSs of eight mRNAs have miRNA binding sites with a $\Delta G/\Delta G_m$ ratio greater than 96% (Fig. 1, C). In addition, the mRNAs of the *ADARB1* and *GINS3* genes have miRNA binding sites with a $\Delta G/\Delta G_m$ ratio greater than 98%. Furthermore, the miR-1273h-5p has perfect complementation with the *GINS3* mRNA. The expression of these genes may be strongly suppressed under conditions of comparable concentrations of mRNAs and miRNAs. Regions of the CDS containing miRNA binding sites have homologous nucleotide sequences, and they encode homologous oligopeptides. The mRNA of *ADARB1*, *FAHD1*, *FRRS1*, *SGCE* and *ZNF573* genes have one open reading frame (ORF) and their polypeptides are highly homologous in domains corresponding to the miRNA binding sites. For example, regions containing *SGCE* and *ZNF573* proteins have identical AQAGVQW and SLQPPPP oligopeptides. The translation of *SPAG6*, *TRIM54* and *RFC5* mRNAs was processed according to other ORFs and generates the corresponding polypeptides. The obtained data confirmed that the conservation of miRNA binding sites in the CDSs was a more important feature compared with the conservation of amino acids in the protein encoded by the miRNA binding sites.

D. miRNA target genes associated with the cell cycle and apoptosis at cancer

miR-1285-3p, miR-5684 and miRNAs of miR-1273 family have common target genes participating in regulation of cell cycle and apoptosis (Table 2). Therefore, the expression of these genes is under strong miRNA control. For example, five of six target genes have miR-1285-3p and miR-1273g-3p binding sites. Proteins of *CLSPN*, *MDM2*, *NF2* and *TRIM13* genes participate in regulation of cell cycle and their mRNAs are targets for the majority of studied miRNAs. *SPN*, *CASP*, *STK4* and *DFFB* genes participating in regulation apoptosis are targets for the miRNAs too. The number of target genes involved in apoptosis and cell cycle is approximately equal for each miRNA. *ATM* and *VHL* are participants of cell cycle and apoptosis regulations and their mRNAs have common miRNA binding sites (Table 2). Therefore, these genes more than others can define speed ratio between cell cycle and apoptosis.

IV. DISCUSSION

As a result of our study, miR-1273a, miR-1273c, miR-1273d, miR-1273e, miR-1273f, miR-1273g-3p, miR-1273g-5p, miR-1273h-3p, miR-1273h-5p miR-5684 and miR-1285-3p have from 32 to 945 arranged binding sites. The arranged binding sites of these miRNAs are located in the 5'UTRs, CDSs and 3'UTRs of all examined target genes. The miRNAs in different combinations have 2915 arranged binding sites in the examined mRNAs. Management of the expression of target genes is achieved via important regulatory interactions of miRNA binding sites located in the 90-nucleotide parts of mRNAs. The examined miRNAs have a different origin and it is necessary to establish why their target genes contained regions with arranged miRNA binding sites. Precursors of the studied miRNAs (pre-miRNAs) are encoded in the introns of different protein-coding genes, except the pre-miR-1273h-3p, which is coded in an intergenic sequence. In addition, miR-1273h-3p is the only miRNA from the miR-1273 family that did not have arranged binding sites in the two revealed groups. pre-miR-1273a is coded in an intron of the regulator of G-protein signaling 22 gene (*RGS22*). The pre-miR-1273c is coded in an intron of T cell lymphoma invasion and metastasis 2 gene (*TIAM2*). In addition pre-miR-1273d is coded in an intron of the kinesin family member 1B gene (*KIF1B*). The pre-miR-1273f and pre-miR-1273g are encoded in an intron of sterol carrier protein 2 gene (*SCP2*). The origin of the pre-miR-1273e was not established. Furthermore, pre-miR-1285-3p is coded as a pre-mir-1285-1 in an intron of the ankyrin repeat containing gene (*KRIT1*) and in an intergenic sequence of chromosome 2. The pre-mir-1285-1 codes for miR-1285-5p, which did not have any binding sites that were closely located to the arranged miR-1273g-3p and miR-1273f groups.

The miR-5684 is coded in an intron of the hook homolog 2 *Drosophila* gene (*HOOK2*). Precursors of the miR-1273 families were found in a large number of introns and exons in lncRNAs, protein-coding RNAs and repeating sequences [23]. Thus, miRNAs participating in the post-transcription regulation of gene expression are intronic in most cases. The expression of 949 target genes of miR-1273 family, miR-1285-3p and miR-5684 may be dependent on the expression of host *RGS22*, *TIAM2*, *KIF1B*, *KRIT1*, *SCP2* and *HOOK2* genes that encode intronic miRNAs. It is possible, if the intronic miRNAs coexpress with their host genes. Because proteins of the studied target genes participate in different metabolic processes, the estimated regulation of their expression via the interaction with miRNAs has an important biological value and is not casual.

Table 2 miRNA target genes participating in cell cycle and apoptosis at cancer

miRNA	Cell cycle genes	Apoptosis genes
mir-1273a	<i>ATM</i> , 11054, 90; <i>EIF2AK2</i> , 2445, 90; <i>NF2</i> , 4324, 90; <i>TRIM13</i> , 2364, 92.	<i>ATM</i> , 11054, 90; <i>CASP2</i> , 2804, 92; <i>EIF2AK2</i> , 2445, 90; <i>SPN</i> , 1484, 90.
mir-1273c	<i>LZTS1</i> , 3474, 95; <i>RBBP4</i> , 6770, 91; <i>TP53</i> , 2297, 91.	<i>CASP2</i> , 2806, 93; <i>SPN</i> , 1484, 91; <i>TP53</i> , 2297, 91.
mir-1273d		<i>SPN</i> , 4944, 91.
miR-1273e	<i>ATM</i> , 11119, 93; <i>CLSPN</i> , 5984, 93; <i>FLCN</i> , 3179, 93; <i>MDM2</i> , 2521, 93; <i>NF2</i> , 3646, 95; <i>NF2</i> , 5139, 91.	<i>ATM</i> , 11119, 93; <i>SPN</i> , 5693, 91; <i>STK4</i> , 3865, 93; <i>TNFRSF10B</i> , 3661, 95.
mir-1273f	<i>CLSPN</i> , 5974, 92; <i>E2F2</i> , 4161, 92, <i>FLCN</i> , 3169, 92; <i>HECA</i> , 3460, 92; <i>KRAS</i> , 3209, 100; <i>MCC</i> , 5239, 92; <i>MDM2</i> , 6772, 92; <i>NF2</i> , 3636, 98; <i>NF2</i> , 4379, 96; <i>NF2</i> , 5129, 94; <i>RBBP4</i> , 5439, 92; <i>SASH1</i> , 5544, 92; <i>TRIM13</i> , 2419, 92; <i>VHL</i> , 1857, 92.	<i>CTSB</i> , 2449, 92; <i>DFFB</i> , 2243, 92; <i>SPN</i> , 1536, 92; <i>STK4</i> , 3855, 96; <i>STK4</i> , 4657, 96; <i>TP63</i> , 1695, 96; <i>VHL</i> , 1857, 92.
mir-1273g-3p	<i>ATM</i> , 11076, 96; <i>CLSPN</i> , 4911, 91; <i>E2F2</i> , 4128, 96; <i>FLCN</i> , 3136, 93; <i>HECA</i> , 3427, 95; <i>KRAS</i> , 3176, 93; <i>LZTS1</i> , 3326, 96; <i>MCC</i> , 5205, 91; <i>MDM2</i> , 2117, 96; <i>MDM2</i> , 2486, 91; <i>MDM2</i> , 6739, 96; <i>NF2</i> , 4346, 91; <i>NF2</i> , 5096, 93; <i>PPMID</i> , 3509, 95; <i>RASSF2</i> , 4504, 98; <i>SASH1</i> , 5511, 93; <i>TADA3</i> , 1927, 96; <i>TP53</i> , 2317, 91; <i>TRIM13</i> , 2386, 95; <i>VHL</i> , 3423, 98; <i>VHL</i> , 1824, 96.	<i>AIFM2</i> , 2010, 96; <i>APAF1</i> , 4933, 91; <i>APAF1</i> , 5231, 96; <i>ATM</i> , 11076, 96; <i>CASP10</i> , 2589, 93; <i>CASP2</i> , 2826, 93; <i>CASP8</i> , 1256, 96; <i>CFLAR</i> , 3667, 96; <i>CTSB</i> , 2416, 96; <i>DFFB</i> , 1566, 93; <i>DFFB</i> , 2210, 96; <i>SPN</i> , 5650, 93; <i>STK4</i> , 4624, 96; <i>TNFRSF10B</i> , 2050, 95; <i>TNFRSF10B</i> , 3618, 93; <i>TP53</i> , 3217, 91; <i>VHL</i> , 1824, 96; <i>VHL</i> , 3423, 98.
mir-1273h-3p		<i>IRAK1</i> , 2896, 93.
mir-1273h-5p	<i>TP53</i> , 2351, 91; <i>TRIM13</i> , 2420, 93.	<i>CASP10</i> , 2234, 91; <i>CASP10</i> , 2623, 100; <i>TP53</i> , 2351, 91.
mir-1285-3p	<i>AURKA</i> , 352, 91; <i>EIF2AK2</i> , 2450, 91; <i>MAPK1</i> , 3078, 93; <i>MDM2</i> , 3218, 91; <i>RBBP4</i> , 6773, 93; <i>TP53</i> , 2301, 95; <i>VHL</i> , 3407, 91.	<i>CASP10</i> , 2357, 91; <i>DFFB</i> , 2193, 91; <i>EIF2AK2</i> , 2450, 91; <i>STK4</i> , 4607, 93; <i>TP53</i> , 2301, 95; <i>VHL</i> , 3406, 91.
mir-1285-5p	<i>BRCA2</i> , 10821, 91; <i>CLSPN</i> , 7586, 91; <i>GTSE1</i> , 2757, 91; <i>IL2RA</i> , 2322, 92; <i>IRF1</i> , 2899, 94; <i>TADA3</i> , 2317, 91; <i>VHL</i> , 4140, 92; <i>VHL</i> , 4291, 92.	<i>CFLAR</i> , 5666, 91; <i>CFLAR</i> , 6570, 91; <i>DFFA</i> , 2039, 91; <i>DFFA</i> , 2985, 96; <i>DNASE</i> , 1325, 91; <i>IL2RA</i> , 2322, 91; <i>NAIP</i> , 6164, 91; <i>SPN</i> , 2752, 93; <i>SPN</i> , 5497, 94; <i>SPN</i> , 6578, 91; <i>VHL</i> , 4140, 93; <i>VHL</i> , 4291, 93.
mir-5684	<i>CLSPN</i> , 6633, 90; <i>E2F2</i> , 4122, 92; <i>EIF2AK2</i> , 2461, 92; <i>MDM2</i> , 2480, 90; <i>MDM2</i> , 6733, 90; <i>NF2</i> , 4340, 90; <i>TRIM13</i> , 2380, 90; <i>VHL</i> , 3417, 92.	<i>CASP8</i> , 1850, 90; <i>CFLAR</i> , 3661, 90; <i>DFFB</i> , 2204, 92; <i>EIF2AK2</i> , 2461, 92; <i>FOXO1</i> , 461, 90; <i>STK4</i> , 4618, 92; <i>VHL</i> , 3417, 92.

Note. * given gene name, the start of the binding site of miRNA (nt) and the value $\Delta G/\Delta G_m$ ratio (%).

The proteins of the majority of studied target genes and cell cycle. In addition, they define the development of participate in different cellular processes, including apoptosis many pathologies. Other genes are oncogenes, tumor

suppressors, and transcription factors, among others. The genes were selected according to their participation in the development of diseases, including lung cancer, breast cancer, gastrointestinal cancer and cancers of other tissues. Thus, the change in the regulation of target gene expression via these miRNAs might be the reason underlying many diseases. If the concentration of miR-1273 family, miR-1285-3p and miR-5684 is lower, than their target mRNAs, these miRNAs will poorly suppress cell cycle and apoptosis. There are different speed ratios between apoptosis and cell cycle in the cases when miRNAs super express in comparison with mRNAs of the target genes. It was shown that concentration of miR-1273 in tumour cells was significant increased [24]. Unfortunately, there is not enough experimental studies proved the participation of miR-1273 family, miR-1285-3p and miR-5684 in tumorigenesis. However, all target genes of studied miRNAs participate in development of breast cancer, lung cancer and etc. [24].

ACKNOWLEDGMENT

We thank Atambaeva Sh., Moldagaliyeva A. and Sagaydak S. for their help in preparing the materials for analysis. We would also like to thank Dr. Khaylenko V. for writing the Lextractor002 script.

REFERENCES

- [1] Y. Zeng, E. J. Wagner, B. R. Cullen, "Both natural and designed micro RNAs can inhibit the expression of cognate mRNAs when expressed in human cells", *Mol Cell*, vol. 9, pp. 1327–1333, 2002.
- [2] E. C. Lai, "MicroRNAs are complementary to 3'UTR sequence motifs that mediate negative post-transcriptional regulation", *Nat Genet*, vol. 30, pp. 363–364, 2002.
- [3] E. Doxakis, "Principles of miRNA-Target Regulation in Metazoan Models", *Int J Mol Sci*, vol. 14, pp. 16280–16302, 2013.
- [4] H. Hamzei, J. Allmer J, M. Yousef, "Computational Methods for MicroRNA Target Prediction", *Methods Mol Biol*, vol. 1107, pp. 207–221, 2013.
- [5] P. Zhou, W. Xu, X. Peng, Z. Luo, Q. Xing, et al, "Large-Scale screens of miRNA-mRNA interactions unveiled that the 3'UTR of a gene is targeted by multiple miRNAs", *PLoS One*, vol. 8, e68204, 2013.
- [6] J. Hausser, A.P. Syed, B. Bilen, M. Zavolan, "Analysis of CDS-located miRNA target sites suggests that they can effectively inhibit translation", *Genome Res*, vol. 23, pp. 604–615, 2013.
- [7] R.M. Marín, M. Sulc, J. Vaníček, "Searching the coding region for microRNA targets", *RNA*, vol. 19, pp. 467–474, 2013.
- [8] O.M. Niemoeller, M. Niyazi, S. Corradini, F. Zehentmayr, M. Li, et al, "MicroRNA expression profiles in human cancer cells after ionizing radiation", *Radiat Oncol*, vol. 6, pp. 29, 2013.
- [9] T. Derrick, Ch. Roberts, M. Rajasekhar, S.E. Burr, H. Joof, et al, "Conjunctival MicroRNA expression in inflammatory trachomatous scarring", *PLoS Negl Trop Dis*, vol. 7, e2117, 2013.
- [10] D.R. Thapa, X. Li, B.D. Jamieson, O. Martínez-Maza, "Overexpression of microRNAs from the miR-17-92 paralog clusters in AIDS-related non-Hodgkin's lymphomas", *PLoS One*, vol. 6, e20781, 2011.
- [11] D. Serpico, L. Molino, S. Di Cosimo, "MicroRNAs in breast cancer development and treatment", *Cancer Treat Rev*, S0305-7372(13)00230-2, 2013.
- [12] P. Leidinger, A. Keller, E. Meese, "MicroRNAs - Important Molecules in Lung Cancer Research", *Front Genet*, vol. 2, 104, 2012.
- [13] X. Xu, X. Yang, C. Xing, S. Zhang, J. Cao, "MiRNA: The nemesis of gastric cancer", *Oncol Lett*, vol. 6(3), pp. 631-641, 2013.
- [14] L. Bonfrate, D.F. Altomare, M. Di Lena, E. Travaglio, M.T. Rotelli, et al, "MicroRNA in colorectal cancer: new perspectives for diagnosis, prognosis and treatment", *J Gastrointest Liver Dis*, vol. 22(3), pp. 311-320, 2013.
- [15] H. Hidaka, N. Seki, H. Yoshino, T. Yamasaki, Y. Yamada, et al, "Tumor suppressive microRNA-1285 regulates novel molecular targets: aberrant expression and functional significance in renal cell carcinoma", *Oncotarget*, vol. 3, pp. 44–57, 2012.
- [16] N.P. Hessvik, K. Sandvig, A. Llorente, "Exosomal miRNAs as Biomarkers for Prostate Cancer", *Front Genet*, vol. 4, pp. 36, 2013.
- [17] A.A. Zabolotneva, A.A. Zhavoronkov, P.V. Shegay, N.M. Gaifullin, B.Y. Alekseev, et al, "A systematic experimental evaluation of microRNA markers of human bladder cancer", *Frontiers in genetics*, vol. 4, pp. 247, 2013.
- [18] A. Issabekova, O. Berillo, M. Regnier, A. Ivashchenko, "Interactions of intergenic microRNAs with mRNAs of genes involved in carcinogenesis", *Bioinformatics*, vol. 8, pp. 513-518, 2012.
- [19] S. Tian, S. Huang, S. Wu, W. Guo, J. Li, et al, "MicroRNA-1285 inhibits the expression of p53 by directly targeting its 3'untranslated region", *Biochemical and Biophysical Research Communications*, vol. 396, pp. 435–439, 2010.
- [20] K.S. Tan, A. Armugam, S. Sepramaniam, K.Y. Lim, K.D. Setyowati, et al, "Expression profile of MicroRNAs in young stroke patients", *PLoS One*, vol. 4, e7689, 2009.
- [21] E.T. Kool, "Hydrogen bonding, base stacking, and steric effects in DNA replication", *Annu Rev Biophys Biomol Struct*, vol. 30, pp. 1–22, 2001.
- [22] N.B. Leontis, J. Stombaugh, E. Westhof, "The non-Watson–Crick base pairs and their associated isosteric matrices", *Nucleic Acids Res*, vol. 30, pp. 3497–3531, 2002.
- [23] F. Niazi, S. Valadkhan, "Computational analysis of functional long noncoding RNAs reveals lack of peptide-coding capacity and parallels with 3' UTRs", *RNA*, vol. 18, pp. 825-843, 2012.
- [24] C. Xu, C. Liu, W. Huang, S. Tu, F. Wan, "Effect of Mst1 overexpression on the growth of human hepatocellular carcinoma HepG2 cells and the sensitivity to cisplatin in vitro", *ABBS*, vol. 45(4), pp. 268-279, 2013.
- [25] A. Watahiki, Y. Wang, J. Morris, K. Dennis, H.M. O'Dwyer, et al, "MicroRNAs associated with metastatic prostate cancer", *PLoS One*, vol. 6, e24950, 2011.
- [26] M. Ninomiya, Y. Kondo, R. Funayama, T. Nagashima, T. Kogure, et al, "Distinct microRNAs expression profile in primary biliary cirrhosis and evaluation of miR 505-3p and miR197-3p as novel biomarkers", *PLoS One*, vol. 8, e66086, 2013.

Composite Ceramics Based on Nanostructured Refractory Oxide Whiskers

T.M Ulyanova¹, P.A. Vitiaz², N.P. Krutko¹, L.V. Ovseenko¹,
A.A. Shevchonok³, L.V. Titova¹, A.R. Luchenok³

Abstract— In the present work the influences of thermal-baric effect in the process of nanostructured alumina and zirconia powders consolidation on structure and physical-mechanical properties of the composite ceramics have been investigated. The samples of ceramics have been prepared from nanostructured powders (ZrO_2 -3 mol. % Y_2O_3) and Al_2O_3 in ratio from 100 : 0 to 20 : 80 wt. % in two ways: by static uniaxial pressing and by pulse pressing. Then part blanks were annealed in the temperature region 1560-1670 °C. During pulse process a crystal structure of samples was disordered, and monoclinic ZrO_2 lattice was partially deformed. After a heat treatment of a blank the crystal structure of metal oxides was restored. Ceramics of oxide powders with content 100 - 50 wt.% PSZ synthesized at the 1100 °C possessed a higher level of properties than one of active powders prepared at the 900 °C.

Keywords—partially stabilized zirconia, alumina, nanostructured oxide whiskers, structure, properties.

I. INTRODUCTION

Nanomaterials on the base of refractory compounds have been intensively investigated recently in connection with the development of nanotechnology [1] The creation of the ZrO_2 based materials with important operation characteristics is based on the alloying of zirconia by oxides of alkaline earth or rare earth metals which allows to get high temperature ZrO_2 tetragonal or cubic form at relatively low temperatures [2] The compounds on its base are used to get

This work was supported in part by the U.S. Department of Commerce under Grant BS123456 (sponsor and financial support acknowledgment goes here). Paper titles should be written in uppercase and lowercase letters, not all uppercase. Avoid writing long formulas with subscripts in the title; short formulas that identify the elements are fine (e.g., "Nd-Fe-B"). Do not write "(Invited)" in the title. Full names of authors are preferred in the author field, but are not required. Put a space between authors' initials.

F. A. Author is with the National Institute of Standards and Technology, Boulder, CO 80305 USA (corresponding author to provide phone: 303-555-5555; fax: 303-555-5555; e-mail: author@boulder.nist.gov).

S. B. Author, Jr., was with Rice University, Houston, TX 77005 USA. He is now with the Department of Physics, Colorado State University, Fort Collins, CO 80523 USA (e-mail: author@lamar.colostate.edu).

T. C. Author is with the Electrical Engineering Department, University of Colorado, Boulder, CO 80309 USA, on leave from the National Research Institute for Metals, Tsukuba, Japan (e-mail: author@nrim.go.jp).

both: structural (blades of turbines, cutting tool) materials as well as functional ones (solid body power supply, medical products, targets for emitters) [3]. The proportion between tetragonal and monoclinic phases of zirconia, which can be changed depending not only upon the quantity of incorporated additive but also upon temperature or bar impact on the material [4], has a considerable significance in determining the properties of this ceramics. In connection with the aforesaid, to investigate consolidation processes for nanostructured powders including their moulding, solid phase reactions at the phase boundary and structure conversions in heat processing, which determine physical and mechanical properties for the ceramics, is an important task. It should be noted that the moulding and sintering processes of ceramic composites from nanostructured refractory oxides powders are not adequately explored. The influence of synthesis temperature of nanostructured fibrous refractory oxides (ZrO_2 - Y_2O_3) - Al_2O_3 powders, their structure and properties as well as moulding and sintering processes on physical-chemical and mechanical characteristics of the obtained ceramic materials have been studied in the present paper.

II. EXPERIMENT

The initial oxide whiskers were prepared by biomimetic method when hydrated cellulose fibers have been impregnated with aqueous solution of three chloride salts of yttrium, aluminium and zirconium. The ratio of salt components were calculated in terms of metal oxides: (ZrO_2 with 3 mol.% Y_2O_3 for all samples) as a partially stabilized zirconia (PSZ) : Al_2O_3 = 100: 0, 80 : 20, 60 : 40, 50 : 50, 40 : 60 and 20 : 80 wt.%. The detail procedure of oxide fiber synthesis were written in papers [5, 6]. Oxide fibers of the specified compositions have been obtained at 900 and 1100 °C, they were distinguished by crystal structure and physical-chemical properties. Crystal structure of aluminium oxide fibers at 900 °C corresponded to θ - or σ -phase and after annealing at 1100 °C, unstable aluminium oxide phases were passed over to α -corundum. Crystal structure of PSZ fibers corresponded to tetragonal and monoclinic ZrO_2 phases. Their ratio was varied depending upon composition of powders and synthesis conditions. To mould blanks, fibers have been ground in ball mill, and prepared oxide whiskers have been graded by fractions. Every whisker had long 0.1 - 0.5 mm, diameter - 1 - 5 μ m, and

consisted of many nanoparticles with size 5 – 20 nm. Since high disperse powders of refractory oxides as a rule possess low plasticity and low fluidity, plasticizers are usually used. Granules have been obtained from synthesized powders with added polyvinyl alcohol solution (PVA).

Two ways to mould blanks from nanostructured yttria partially stabilized zirconia (PSZ) and aluminium oxide composition powders have been applied. The blanks from granules have been moulded by two-sided static pressing method with 500 MPa effort. Ceramics samples moulding from nanostructured powders (without PVA) has been performed also by impulse pressing method, which in accordance with paper [7], must improve the strength of blanks and provide the density uniformity of sample volume. Powders have been sprinkled into plastic containers, they have been packed into metal foil and have been subjected to impulse pressing by explosion during which pressure has been developing up to 4.0-4.5 GPa. The fixed detonation wave velocity was about 4000 m/s, and explosion impulse duration constituted $7 \cdot 10^{-6}$ s. Then all moulded blanks have been sintered within the temperature range 1560-1670°C.

Crystal structure of powders and moulded blanks has been investigated with the help of X-ray apparatus Advance 8 and DRON-3, the recording of X-ray grams was carried out in the interval of angles 2θ from 5 up to 110° with velocity 0.5 – 1.0 °/min, monochromatic radiation $\text{CuK}\alpha$ ($\lambda=1,54 \text{ \AA}$) has been used. The measurement of particles size was made by CSR (coherent scattering region) by physical widening of reflexes for phases under investigation: tetragonal [111] and monoclinic $[\bar{1}11]$ for ZrO_2 as well as for α -alumina – [012], [113], the calculation was made by Sherrer formula [8]. The investigation of nanostructure and size of particles for fiber alumina and zirconia has been carried out earlier by atomic-force microscopy, transmission electron microscopy and CSR, the investigation has shown a good similarity of results [9]. Surface microstructure for powders and ceramics has been studied by scanning electron microscopy (LEO Zeiss 1420) in accelerating potential 20 kV. Bulked, picnometric density for powder material, apparent density and porosity of ceramics have been measured by standard methods. The specific surface of powders has been assessed by nitrogen adsorption-desorption curve (BET method) (Brunauer – Emmett – Teller) [10] using surface and porosity analyzer (ASAP 2020, Micromeritics, USA).

III. DISCUSSION OF RESULTS

Synthesized powders have been represented by white highly disperse substances agglomerated into micron size particles, each particle, in its turn, consisted of nanograins with the size from 5 - 6 up to 50 nm depending upon composition and synthesis temperature. The higher Al_2O_3 content and the lower temperature synthesis are, the lesser the size of metal oxides crystallites is, the specific surface of powder and its reactive activity are higher. Some properties of powders are represented in table 1 and microstructure in figure 1.

The peculiarity of phase composition of powders, (as we suppose) was the formation of the triple solid ($\text{ZrO}_2\text{-Y}_2\text{O}_3$) – Al_2O_3 solution, based on crystal lattice of ZrO_2 tetragonal phase. The triple solid solution was formed during synthesis of

inorganic fibers and was existed in the temperature range 600 - 1100 °C. When annealing temperature was risen up to 1100 – 1150 °C the solid solution degraded and powder composition included the following three phases: tetragonal and monoclinic ZrO_2 and α -corundum too. In connection with this phenomenon, aluminium oxide reflexes were absent on X-ray grams of powders with ratio 50 – 100 wt. % PSZ. Low crystal system reflexes γ - or θ - Al_2O_3 were established in PSZ compositions with great excess for aluminium oxide 60 – 80 wt. % [11].

During the moulding of blanks by static and impulse pressing, the particles of powders have passed through loads different by their nature. In case with static pressing, temporary bonding for better fluidity and plasticity of powders has been used since particles have experienced friction relative each other and with the walls of die mould and punch. That is why, the ratio between height and cross section did not exceed from 3 : 1 to 5 : 1 for uniform blank density. Besides, the powders were sprinkled into die mould before pressing and they were subject to vibration for better granular laying. During loading, air and adsorbed moisture were partially removed and temporary binder fixed particles between each other. At the same time, crystal structure of powders did not change.

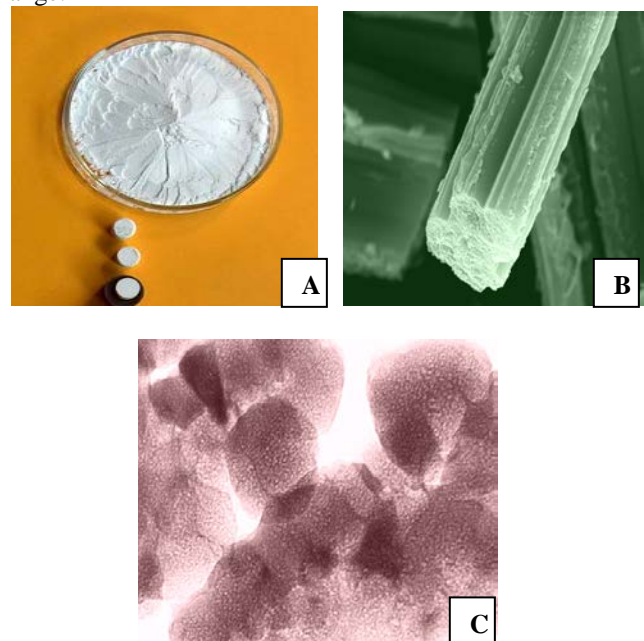


Fig. 1 – Nanostructured 80% PSZ – 20% Al_2O_3 powder: overview – A, microstructure of oxide monofiber - B (SEM x10000), nanostructure of powder particle – C (TEM x100000)

In case with impulse pressing, temporary binder was not used since tangential shock wave was formed in explosion during very short time period and local temperature 600 – 1100 °C is developing by calculation [12]. As a result, disordering for crystal monoclinic zirconia lattice occurred what is marked by inversion of its reflexes on x-ray grams, the widening for contours of all reflexes occurred too. Besides, solid ($\text{ZrO}_2\text{-Y}_2\text{O}_3$) PSZ solution partially degraded, monoclinic phase content increased and substance amorphization was observed. After heat treatment of blanks at 1300 °C, the crystal structure of metal oxides restored and did not change with annealing temperature increase up to 1600 °C (Fig. 2). Tetragonal zirconia phase content was increased up

to 94-96%, porosity was decreased up to 0.1 – 0.5 % what improved strength of ceramic material.

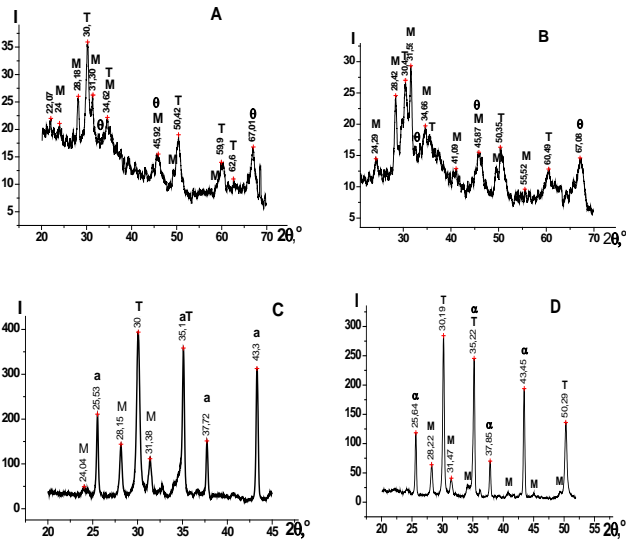


Fig.2 – X-ray grams of 20 % PSZ + 80 % Al_2O_3 powder, synthesized at the 900 °C – **A**, blank after pulse pressing – **B**, ceramics annealed at the 1300 °C – **C**, ceramics annealed at the 1600 °C – **D**;
M – monoclinic phase ZrO_2 , **T** – tetragonal phase ZrO_2 , **θ** – Al_2O_3 , **a** – $\alpha\text{-Al}_2\text{O}_3$

The changes of samples microstructure after their pressing by pulse method and sintering are presented on figure 3.

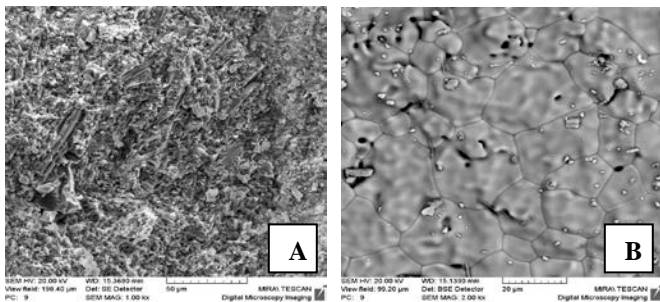


Fig. 3 – Microstructure of 60% PSZ+ 40% Al_2O_3 sample, formed by pulse pressing - (A), and after annealing at the 1600 °C – (B)

The study of physical - mechanical properties of sintered blanks has shown that the use of different moulding methods of blanks from nanostructured powders leads to ambiguous results. Ceramics powders moulded by static pressing from powders with synthesis temperature 900 °C are characterized by higher density and low porosity than from powders obtained at 1100 °C. Probably, this is stipulated by higher plasticity and reaction activity of powders with synthesis temperature 900 °C. The curve course – the dependence of density upon composition is regular since with the increased aluminium oxide content, the true density value decreases from 6.0 g/cm^3 in PSZ up to 4.0 g/cm^3 in α -corundum.

The curves, showing the change in strength depending upon composition, have extreme points in the following ratio of PSZ : Al_2O_3 – 60 : 40 and 50 : 50 wt. %, what is stipulated by their crystal structure. Monoclinic zirconia content did not exceed 5 wt. %. Besides, aluminium oxide was partially

included into triple solid solution in connection with which the growth of crystallites became slower and after heat treatment at 1560-1600 °, the granular tetragonal phase ZrO_2 size constituted 30-35 nm, as for monoclinic one, it constituted 17 – 27 nm, they were consolidated in ceramics blocks. In general, ceramics strength in samples moulded from powders synthesized at 1100 °C is higher for compositions of PSZ : Al_2O_3 - 100 : 0 up to 50 : 50 and becomes lower with the increase in aluminium oxide content in composition powders. In the latter case, the samples from powders synthesized at 900 °C had higher physical-mechanical characteristics (Fig. 4).

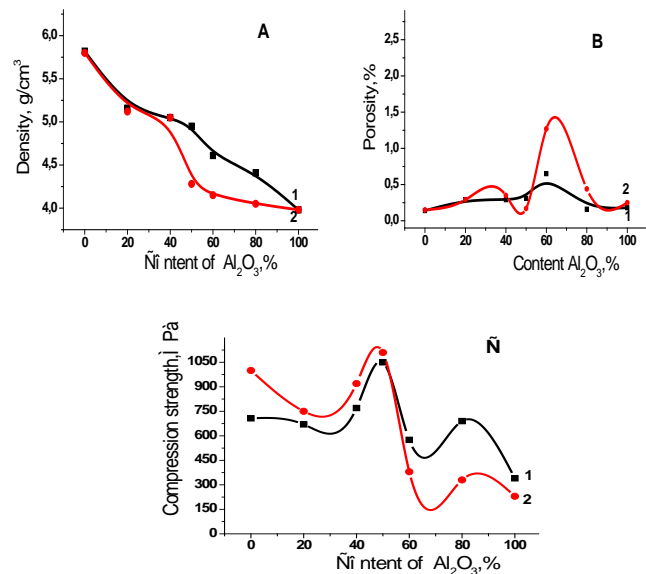


Fig. 4 – Dependences of density – **A**, porosity – **B** and compression strength – **C** of ceramics samples, formed by static pressure from powders synthesized at the 900° C -1, –at the 1100 °C, -2 and annealed at the temperatures: 1580+1670 °C vs. composition

As for ceramic samples from nanostructured aluminium oxide powder, strength in compression was also increasing with their synthesis temperature increase from 750 up to 1500 °C.

In samples, moulded from powders with different synthesis temperature by explosion, the density values were closer, porosity was lower and compression strength was higher in samples the powders of which were synthesized at 1100 °C. The study of heat treatment mode of moulded samples has shown that single annealing at 1670 °C allows to obtain ceramics with higher strength characteristics in comparison with temperature mode: 1560+1670 °C in case powders with synthesis temperature 1100 °C are used in impulse moulding method. Maximal ceramics strength value was observed in samples with ratio: PSZ :- Al_2O_3 – 50 : 50 (Fig. 5) in case with static pressing of blanks and in using explosion method.

After heat treatment of blanks at the 1670 °C the content of tetragonal component ZrO_2 was increased. The size of crystalline particles of a tetragonal phase increased to 45 - 50 nm, and of monoclinic phase – to 55 - 65 nm. Microhardness of ceramic samples PSZ made 13.9 -14.2 GPa and a composite (80% PSZ + 20) – 19.0 – 20.5 GPa -

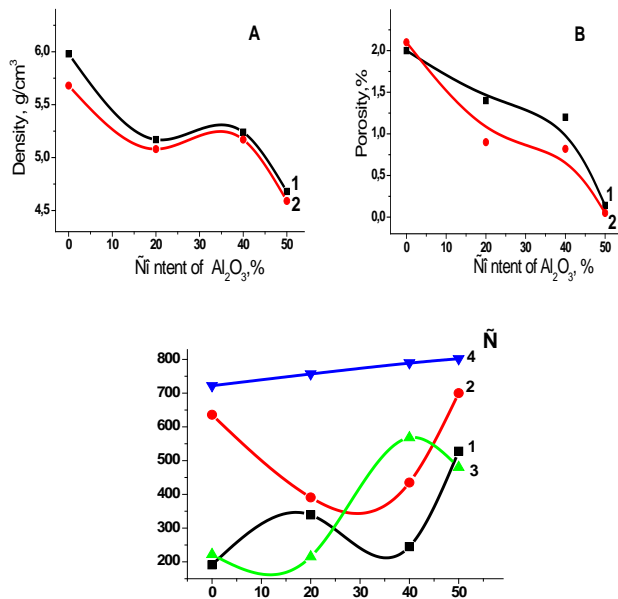


Fig. 5- Dependences of density – A, porosity – B and compression strength –C of ceramics samples, obtained by explosion method and annealed at the temperatures: 1580+1670 °C – 1, 2 and – at the 1670 °C – 3, 4, vs. composition; the samples: 1, 3 were prepared from powders synthesized at the 900°C and 2,4 – were prepared from powders synthesized at the 1100°C

IV. CONCLUSION

Porous as well as high density ceramics with high engineering characteristics can be obtained from nanostructured powders of refractory (ZrO₂-Y₂O₃) – Al₂O₃ oxides in observing definite technology conditions.

Substance amorphization, partial deformation and disordering for crystal oxides lattice occur during the moulding of blanks from nanopowders by explosion method, the crystal lattice is restored in further heat treatment. To get dense ceramics from composition powders having compositions from 100 up to 50 wt. % PSZ, it is advisable to use powders with annealing temperature higher than 1000 °C. Annealing temperature of powders, enriched with aluminium oxide, must not exceed 900 °C. In general, to get small one type parts from nanostructured powders of refractory oxides, one can use one axial static pressing method. To get large blanks, it is expedient to use impulse moulding method with further single annealing at a given temperature.

ACKNOWLEDGMENT

This work was supported by the State Complex Program of Scientific Investigations of the Republic of Belarus “Nanomaterials and Nanotechnologies”, project 2.08.

REFERENCES

- [1] V.F. Petrunin, “Synthesis of nanocrystalline high temperature zirconia phases,” (Periodical style), *J Inorganic materials*, vol. 40, No. 3, pp. 303-311, 2004.
- [2] V.Ya. Shevchenko, S.M. Barinov, *Technical Ceramics* (Book style). Moscow: Science, 1993, 197 p.

- [3] A. Neubrand, R. Schafer “Materials design studies for creep and thermal shock resistant oxide ceramic matrix composites” (Published Conference Proceedings style), in *Proc. of the 5 Int. Conf. HT CMC*, Seattle, 2005, pp. 253-258.
- [4] V.S. Bakunov, E.S. Lukin, “Peculiarities of high-density technical ceramics technology. Chemical methods of initial powders preparation,” (Translation Journals style), *J.Glass and Ceramics*, No 2, pp.3-7, 2008.
- [5] T.M. Ulyanova, N.P. Krut'ko, P.A. Vityaz, and L.V. Titova, “Investigation of Nanostructured Oxides: Synthesis, Structure and Properties”, (Periodical style), *J. Nanosci. Nanotechnol.* vol. 11, No 3, pp. 2107-2112., March, 2011.
- [6] T.M. Ulyanova, N.P. Krutko, Vityaz P.A., “Formation of Nanostructural Oxide Fibers”, (Book style with paper title), *Advanced materials "Fabrication, Control and Properties of Nano-Architected Materials"*, publ. by Y. Champion, ed. Wiley-VCH, Verlag, Germany, 2004, pp. 167-170.
- [7] S.S. Bacsanov, “Peculiarities of solid solution transformations initiated by blast waves”, (Periodical style), *J. Advances in Chemistry*, vol. 75, No 7, pp. 669-686, 2006.
- [8] Ya.S. Umanskiy, *X-ray graphy of metals and semiconductors* (Book style). Moscow: Metallurgy, 1969, 496 p.
- [9] T.M. Ulyanova, L.V. Titova, S.V. Medichenko, Yu.G. Zonov, T.E. Konstantinova, V.A. Glazunova, A. S. Doroshkevich, T. A. Kuznetsova, “Investigation of the structure of nanocrystalline refractory oxides by X-ray diffraction, electron microscopy, and atomic force microscopy”, (Translation Journals style) *J.Crystallography Reports*, vol. 51, Issue 1, December, S144-S149, 2006.
- [10] S. Greg, K. Sing, *Adsorption, specific surface, porosity* (Book style). Translation from English, 2 issue, Moscow: Mir, 1984. 306 p.
- [11] T.M. Ulyanova, P.A. Vityaz, N.P. Krutko, L.V. Titova, S.V. Medichenko, A.A. Shevchenok, “Nano-structured ZrO₂(Y₂O₃) – Al₂O₃ fibrous powders for composite materials”, (Published Conference Proceedings style), in *Proc. of EPMA*, 2010, vol. 1, pp. 423-429.
- [12] O.V. Roman, G.V. Smirnov, I.M. Kozlov, A.E. Suvorov, “Energy flow density cumulation in spreading detonation waves in layer media”, (Book style with paper title and editor), *New materials and technologies: Powder metallurgy, Composition materials, Protective coatings, welding*, Minsk, SSI PMI, 2010, pp. 307-314.

Table 1 – Characteristics of nanostructured (ZrO_2 - Y_2O_3)
- Al_2O_3 powders

Chemical Composition, wt. %	Temperature synthesis, °C	Phase ratio, wt. % $ZrO_2-T : ZrO_2-M$	Particle size, nm $ZrO_2T : ZrO_2M$	Specific surface, m^2/g
100 % PSZ	900	84 : 16	6 : 17	47
	1100	87 : 13	20 : 25	28
80 % PSZ + 20 % Al_2O_3	900	73 : 27	9 : 22	60
	1100	68 : 32	18 : 33	34
60 % PSZ + 40 % Al_2O_3	900	83 : 17	10 : 25	65
	1100	72 : 28	25 : 35	30
50 % PSZ + 50 % Al_2O_3	900	63 : 37	6 : 15	90
	1100	75 : 25	17 : 33	45
40 % PSZ + 60 % Al_2O_3	900	66 : 34	9 : 20	85
	1100	72 : 28	18 : 30	38
20 % PSZ + 80 % $\gamma-Al_2O_3$	900	76 : 24	11:25	140
	1100	72 : 28	20:35	35

Metal mixed oxides and zeolites in oxidation of ethanol and isopropanol

Jana Gaálová, Květuše JirátoVá, Jan Klempa, Olga Šolcová, Irene Maupin, Jérôme Mijoin, Patrick Magnoux, and Jacques Barbier, Jr.

Abstract—The different kinds of catalysts – zeolite, (mixed) oxide – were tested and compared in catalytic oxidation of ethanol and isopropanol respectively. All catalysts proved remarkable activity in catalytic oxidation of selected model compounds. Even the less active catalyst, basic zeolite NaX, converted 50 % of ethanol as well as isopropanol at around 300 °C. The deeper comparison revealed that CeO₂ and zeolite NaX-CeO₂ is more suitable for oxidation of isopropanol while oxidation of ethanol is faster in a presence of the metal mixed oxides, Co₄MnAl and NiMgMn. The additional contribution of the present article is a comparison of certain catalysts' properties linked directly to the catalytic performance in the oxidation processes, such as oxygen storage capacity (OSC), surface properties, acidity/basicity and others.

Keywords—Ethanol, Isopropanol, Metal mixed oxide, Oxidation, and Zeolite.

I. INTRODUCTION

ISOPROPYL alcohol (IPA) is one of the most widely used solvents in the world. It is particularly popular for pharmaceutical applications and is a major ingredient in "gas dryer" fuel additives. Ethanol (EtOH) was selected

This work was supported by Czech-French research program Barrande/Egide of MŠMT/MEN. The financial support of the Ministry of Industry and Trade of the Czech Republic No. FR-TII/059 is gratefully acknowledged.

J. Gaálová is with the Institute of Chemical Process Fundamentals of the CAS, Rozvojová 135, 165 02 Prague 6, Czech Republic (corresponding author to provide phone: 420-220-390-133; fax: 420-220-920-661; e-mail: gaalova@icpf.cas.cz).

K. JirátoVá is with the Institute of Chemical Process Fundamentals of the CAS, Rozvojová 135, 165 02 Prague 6, Czech Republic (e-mail: jiratova@icpf.cas.cz).

J. Klempa is with the Institute of Chemical Process Fundamentals of the CAS, Rozvojová 135, 165 02 Prague 6, Czech Republic (e-mail: klempa@icpf.cas.cz).

O. Šolcová is with the Institute of Chemical Process Fundamentals of the CAS, Rozvojová 135, 165 02 Prague 6, Czech Republic (e-mail: solcova@icpf.cas.cz).

I. Maupin is with the Institut de Chimie des Milieux et Matériaux de Poitiers (IC2MP), UMR CNRS 7285, 4 Rue Michel Brunet, 86022 Poitiers, France (e-mail: irene.maupin@univ-poitiers.fr).

J. Mijoin is with the Institut de Chimie des Milieux et Matériaux de Poitiers (IC2MP), UMR CNRS 7285, 4 Rue Michel Brunet, 86022 Poitiers, France (e-mail: jerome.mijoin@univ-poitiers.fr).

P. Magnoux is with the Institut de Chimie des Milieux et Matériaux de Poitiers (IC2MP), UMR CNRS 7285, 4 Rue Michel Brunet, 86022 Poitiers, France (e-mail: patrick.magnoux@univ-poitiers.fr).

J. Barbier, Jr., is with the Institut de Chimie des Milieux et Matériaux de Poitiers (IC2MP), UMR CNRS 7285, 4 Rue Michel Brunet, 86022 Poitiers, France (e-mail: jacques.barbier.jr@univ-poitiers.fr).

intentionally to focus on the emerging environmental problems of nowadays such as E-85 combustion (linked to the rising biofuel production), which actually augments the output of two different carcinogens such as formaldehyde and acetaldehyde. **IPA and EtOH** are volatile organic compounds (VOCs): organic compounds having an initial boiling point less than or equal to 250 °C measured at a standard atmospheric pressure of 101.3 kPa. VOCs are harmful to human health and recognized as major responsible for the increase in global air pollution. They can also react with NO_x and oxygen to form ozone: $\text{VOC} + \text{NO}_x + \text{O}_2 + h\nu \rightarrow \text{O}_3 + \text{other products}$. Ozone causes human health problems, affects DNA and enzyme functions, is toxic for vegetation, impairs quality of some materials, etc. Fortunately, the clean technologies and the regulations covering VOCs are permanently improving. **Catalytic oxidation** at low temperatures provides the safe and efficient way for removing dangerous VOCs. Catalysts with noble metals are currently preferred for this process, as they are highly active and stable [1], [2]. However, cheaper alternatives such as metal oxide catalysts or zeolites approved their suitability as catalysts for VOCs oxidation too [3]-[6].

Metal oxide catalysts (mainly Cu, Mn, Cr, Co, Mn, and Ni oxides) are appreciably active; though, their weak point is a lower stability than in the case of noble metal catalysts [7], [8]. They are often obtained by controlled thermal decomposition of layered double hydroxides (LDHs). Chemical composition of LDHs can be represented by the general formula: $[\text{M}^{\text{II}}_{1-x}\text{M}^{\text{III}}_x(\text{OH})_2]_x + [\text{A}^{n-}_{x/n}\text{yH}_2\text{O}]^x$ where M^{II} and M^{III} are divalent and trivalent metal cations, Aⁿ⁻ is an n-valent anion and x has usually values between 0.20 and 0.33. After heating at moderate temperatures, LDHs give finely dispersed mixed oxides of M^{II} and M^{III} metals with a sufficiently large surface area and relatively good thermal stability [9]. Metal nitrates are usually used in preparation of such heterogeneous catalysts, as nitrates can be easily removed from the catalysts by calcination. However, metal nitrates are rather expensive and so, other cheaper metal salts like sulphates, could be interesting for catalyst preparation.

The zeolites are crystalline microporous materials with a high surface to volume ratio. They are constituted of three-dimensional tetrahedral units (TO₄), bonded by oxygen atoms. The T atoms can be aluminium, silicon, and iron, copper or other. The combination of these units leads to particular arrangements with the formation of intra-crystalline channels

and cavities, with dimensions in a molecular order of magnitude of 3 to 30 Å. The primary structure of the zeolite (faujasite) used in this work is composed of tetrahedral units with aluminium as central atom (AlO_4^{5-}), and silicon (SiO_4^{4-}). Faujasite zeolites are characterized by the presence of one type of large cages (supercages), 13 Å in diameter and ball-shaped, accessible through a 12 ring window with a free aperture of 7.4 Å, which is larger than the size of most of the organic molecules. Basic zeolites and particularly faujasites ones (NaX) showed interesting properties for oxidation of VOCs [10], [11].

The metal oxides (Co_4MnAl and NiMgMn) as well as the zeolite (NaX and its modification by CeO_2 , well known in literature for its oxygen mobility [12]) have been recently examined by our groups as catalysts for deep VOCs oxidation. The catalysts selected for our research do not differ only in their structure, but also in acid-base characteristics and redox properties. It is known that alcohols can react as both acids and bases in solution phase chemistry depending on the acid-base characteristics of the reaction medium [13]. Scientists suggest that the presence of strong base sites such as O^{2-} , O_2^- , or HOO^- , advances the dehydrogenation of alcohol [14]. Thus, acidic (Co_4MnAl , NiMgMn) or basic (NaX, NaX- CeO_2 , CeO_2) catalysts may become attractive way of varying alcohol oxidation selectivity and activity. Another approach, how to clarify divergent selectivity of catalysts is to evaluate their redox properties [15], [16]. Finally, diverse physical chemical nature of the surface of catalyst leads to promising model systems permitting to give details about the relations between acid-base or redox characteristics of solid phase and catalytic activity in total oxidation of more or less polar chemical compounds.

The additional contributions of present article are characterizations such as BET, XRD, TPR, TPD or determination of oxygen storage capacity of all catalysts.

II. EXPERIMENTAL

A. Preparation of the catalysts

The metal mixed oxide **Co4MnAl** was prepared by coprecipitation from hydrotalcite-like precursors with Co, Mn and Al molar ratio of 4:1:1. An aqueous solution of metal nitrates was added with flow rate of 7.5 ml/min into 1000 ml batch reactor containing 200 ml of distilled water. The flow rate of simultaneously added alkaline solution of 0.5 M Na_2CO_3 and 3 M NaOH was controlled to maintain reaction $\text{pH} = 10.0 \pm 0.1$. The coprecipitation was carried out under vigorous stirring at 25 °C. The resulting suspension was stirred 1 h at 25 °C, the product was then filtered off, washed thoroughly with distilled water and dried overnight at 60 °C in air. The dried and powdered product was formed into pellets and calcined at 500 °C for 4 h in air.

The metal mixed oxide **NiMgMn** was prepared by coprecipitation from hydrotalcite-like precursors with Ni, Mg and Mn molar ratio of 1:1:1. The preparation process differs

from the one of **Co4MnAl** only in the fact that metal sulphates were used instead of metal nitrates.

Zeolite **NaX** was supplied by Axens ($\text{Si/Al} = 1.2$).

Ceria (**CeO₂**) was prepared in the Institut de Chimie des Milieux et Matériaux de Poitiers (IC2MP), by calcining a cerium nitrate salt ($\text{Ce}(\text{NO}_3)_3 \cdot 6\text{H}_2\text{O}$, Fluka, purity > 99.0%) under air flow (200 ml/min) with a heating rate of 1 °C/min from room temperature to 110 °C with a hold of one hour. Then the samples were heated overnight up to 550 °C (2 °C/min).

The hybrid catalyst (**NaX-CeO₂**) is a mechanical mixture of ceria and faujasite in equal mass. The mixture was then pelletized under 1.5 ton/cm² pressure and sieved between 0.2 and 0.4 mm. The sieved sample was then calcined under air flow (150 ml/min) at 100°C (1 °C/min) for one hour and at 600°C (1 °C/min) overnight.

B. Characterization of the catalysts

The specific surface areas and pore volumes of the samples were determined by adsorption-desorption isotherms of nitrogen at -196 °C with a Micromeritics ASAP 2010 apparatus after evacuation at 90 °C for one hour followed by a hold for three hours at 350 °C. Microporous volumes were obtained by the t-plot method and the Dubinin-Radushkevich equation was used to calculate the mesoporosity.

XRD patterns of all catalysts were recorded over a Bruker D5005 diffractometer thanks to Diffrac+ software (XRD Wizard and XRD Commander) and interpreted with Eva and Topas softwares. The experimental conditions were as followed: $\lambda = 1.542$ Å, $10^\circ 2\theta$ to $75^\circ 2\theta$, $0.02^\circ 2\theta$ and 4 seconds by step. Sherrer method was used to calculate the particle sizes for all samples [17].

Temperature-programmed reduction (TPR) measurements of the calcined samples (0.025 g) were performed with a H_2/N_2 mixture (10 mol % H_2), flow rate 50 ml/min and linear temperature increase 20 °C/min up to 1000 °C. A change in H_2 concentration was detected with a mass spectrometer Omnistar 300 (Pfeiffer Vakuu). Reduction of the grained CuO (0.16-0.315 mm) was repeatedly performed to calculate absolute values of the hydrogen consumed during reduction.

Temperature-programmed desorption (TPD) of NH_3 and CO_2 was carried out to examine acid and basic properties of the catalysts surface, respectively. The measurements were accomplished with 0.050 g of a sample in the temperature range 20 - 1000 °C, with helium as a carrier gas and CO_2 or NH_3 as adsorbing gases. The heating rate 20 °C/min was applied. During the experiments the following mass contributions m/z were collected: 2- H_2 , 18- H_2O , 16- NH_3 , and 44- CO_2 . The spectrometer was calibrated by dosing an amount (840 µl) of CO_2 or NH_3 into the carrier gas (He) in every experiment. The TPR and TPD experiments were evaluated using OriginPro 7.5 software with an accuracy of $\pm 5\%$.

The oxygen storage capacities, oxygen storage complete capacity (OSCC) and oxygen storage capacity in dynamic conditions (OSC) were calculated following the reduction

reaction of the catalysts: $\text{CO}(\text{g}) + \frac{1}{2} \text{O}_2(\text{s}) \rightarrow \text{CO}_2(\text{g}) + \square (\text{s})$. Prior the experiments, the samples were brought to 400 °C under flowing He (30 ml/min). Then, the catalysts were pre-treated under O_2 , before undergoing CO pulses (0.267 ml) up to the catalysts maximal reduction. This permits to know the total amount of available oxygen in the samples (OSCC). After that, the samples were re-oxidized by O_2 pulses and underwent alternate pulses of CO and O_2 to calculate the O_2 amount immediately available in the samples. Oxygen storage capacities are expressed in $\mu\text{mol}_{\text{CO}_2}/\text{g}$ from the CO_2 formation (after CO pulses) and transformed by calculation in $\mu\text{mol}_\text{O}/\text{g}$ stored in the samples.

C. Catalytic testing

The catalytic oxidation of **ethanol** was carried out *in Czech Republic* in a fixed-bed glass reactor (5 mm i.d.) in the temperature range from 100 to 400 °C (the temperature of the furnace was linearly increased by the rate of 3.5 °C/min). The catalyst (0.75 g of the sieved grains with the particle size of 0.16 – 0.315 mm) was examined at 10 $\text{m}^3/\text{kg}\cdot\text{h}$ gas hourly space velocity (GHSV). The inlet concentration of VOC in the air was 1 g/m^3 . Reaction products were analysed using a gas chromatograph Hewlett-Packard 6890 equipped with a FID detector and a capillary column (HP-5 19091 J-413, 30 m \times 0.32 mm \times 0.25 mm with 5 % phenylmethyl silicone). The accuracy of the conversion and selectivity determination was ± 2 %. Temperature T_{50} (the temperature at which 50 % conversion of the examined VOC was observed) was chosen as a measure of the catalyst activity. Selectivity in ethanol conversion was evaluated as the GC peak area of by-products analysed at 95 % conversion of ethanol. Complete composition of the ethanol oxidation reaction mixtures were calculated on the basis of mass balance.

The destruction of 1360 ppm of **isopropanol**, mixed in synthetic and wet air (80 % nitrogen, 20 % oxygen, 33 % relative humidity, 1.2 mol % water), was carried out *in France* in a fixed bed reactor (i.d. = 5 mm, length = 90 cm) at atmospheric pressure and followed as a function of time (for 5 hours) at constant temperature. The catalysts used (140 mg) were previously sieved (0.2-0.4 mm) and activated overnight in air at 450 °C in the same reactor, inserted into an oven and the temperature was measured by a thermocouple inserted near the catalyst bed. The gas hourly space velocity (GHSV) was kept constant and equal to 18000/h, calculated at room temperature and pressure. The apparatus was coupled with a gas phase chromatograph (Varian 3400) equipped with a packed column and a thermal conductivity detector (TCD) to analyse air and carbon dioxide and with a capillary column (30 m VF-5ms with 0.25 mm of internal diameter and 0.25 μm film thickness) and a flame ionization detector (FID) to analyse hydrocarbons, namely isopropanol and secondary products, basically acetone and propene.

III. RESULTS AND DISCUSSION

A. Characterization of prepared catalyst

The **specific surface areas and pore volumes** of all prepared catalysts are gathered in Table I. BET surface areas of the metal mixed oxides are close to 100 m^2/g . CeO_2 exhibits only a little bit lower S_{BET} value than the mixed oxides – 80 m^2/g , while NaX boasts with the high specific surface area – more than 700 m^2/g . The hybrid of those two compounds, NaX- CeO_2 , keeps its value someplace in the middle (around 400 m^2/g). The volume of micropores follows the same order $\text{CeO}_2 > \text{Co}_4\text{MnAl} \geq \text{NiMgMn} > \text{NaX-CeO}_2 > \text{NaX}$ in the range 0.03-0.3 cm^3/g . V_{Me} shows rather opposite tendency.

Table I

The specific surface areas S_{BET} and pores volumes of all catalysts

Catalyst	S_{BET} ($\text{m}^2\cdot\text{g}^{-1}$)	V_{Mi} ($\text{cm}^3\cdot\text{g}^{-1}$)	V_{Me} ($\text{cm}^3\cdot\text{g}^{-1}$)
Co4MnAl	94	0.04	0.33
NiMgMn	113	0.04	0.36
NaX	762	0.30	0.01
NaX- CeO_2	423	0.17	0.08
CeO_2	80	0.03	0.19

Powder XRD patterns of all samples are traced on Fig. 1. Concerning the metal mixed oxides, after calcination of the LDH precursors at 500 °C, spinel-type mixed oxides were formed (“S” on Fig. 1).

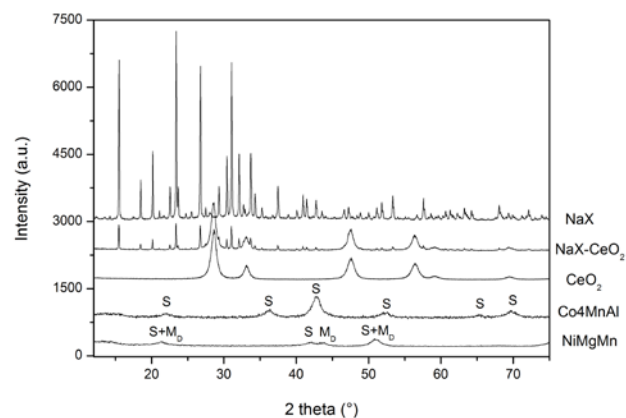


Fig. 1 powder XRD patterns of all prepared catalysts; “S” indicates spinel (Co-Mn-Al or Ni-Mg-Mn) and “Mb” disordered murdochite

Only spinel diffraction lines were found in the powder XRD pattern of Co₄MnAl catalyst. Diffraction lines of non-stoichiometric mixed oxide with murdochite-type structure appear ("M_D" on Fig. 1) with the spinel lines in XRD pattern of NiMgMn. The average particle sizes are 0.8 nm for Co₄MnAl and 0.3 nm for NiMgMn. The crystallographic structures of NaX and CeO₂ do not seem to be affected by the hybrid catalyst preparation or thermal treatment since significant peaks of both compounds are visible in NaX-CeO₂ XRD spectrum. The average particle sizes are equal to 13 nm and 104 nm for respectively ceria and faujasite NaX, with almost no difference for hybrid catalyst.

Temperature program desorption (TPR) patterns of all catalysts are shown in Fig. 2. Temperature-programmed reduction (TPR) measurements of the calcined samples were performed up to 1000 °C, however, catalytic components reducible at temperatures higher than used reaction temperatures cannot likely contribute to the catalytic reaction. For that reason, we zoomed in on a lower temperature region (up to 350 °C) corresponding to our reaction temperature area. Up to selected temperature, CeO₂, NaX-CeO₂ and NaX catalysts showed very similar course of TPR patterns, with practically no reduction behaviour. The first reduction peak appeared at limit temperature 350 °C for NiMgMn as well as Co₄MnAl. For both catalysts, the peak can be ascribed to the reduction of an easily reducible Mn^{IV} phase to Mn^{III} (during the reduction of free MnO_x, the peaks with maxima at 328 and 424 °C were reported [18]). Regarding Co₄MnAl, the same peak can be also ascribed to reduction of Co^{III} to Co^{II} oxides. Observations of Arnoldy and Moulijn [19] explain its slight shift to higher temperatures (indicating worse reducibility of the arising components of Co₄MnAl catalyst comparing to NiMgMn) by influence of Al³⁺ cations.

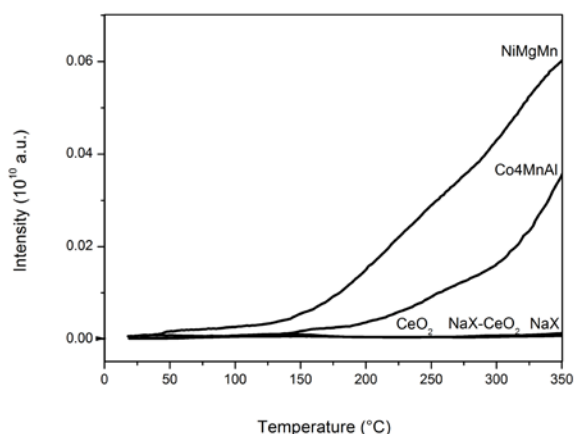


Fig. 2 TPR patterns of all catalysts

Temperature-programmed desorption (TPD) of NH₃ and CO₂ can be applied to determine the density and strength of acidic and basic sites in the samples [20]. **TPD of NH₃** visualized very significant differences in surface acid properties associated to the catalysts. Desorption curves of

NH₃ (TPD) from all catalysts are traced up to 350 °C in the Fig. 3. One main low-temperature desorption peak centred between 110-140 °C with a shoulder at between 180-230 °C, is characteristic for NH₃ desorption curves of all tested samples. The low-temperature peak corresponds to acid centres of moderate strength and the shoulder corresponds to stronger acidic sites. The amount of such centres for the temperature range of 25-350 °C (Table II) decreased in order of corresponding catalysts as following:

NiMgMn (1.34 mmol/g) > Co₄MnAl > CeO₂ ≥ NaX-CeO₂ ≥ NaX (0.22 mmol/g).

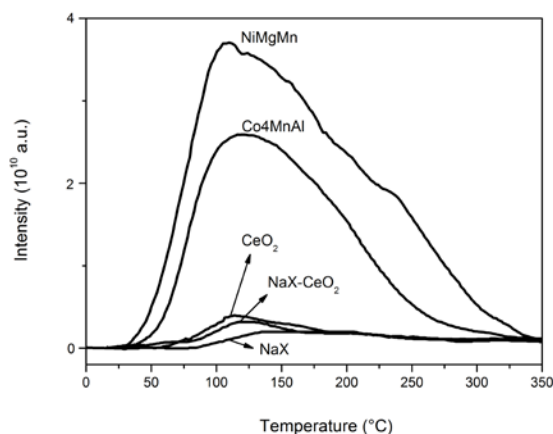


Fig. 3 desorption curves of NH₃ (TPD) from all catalysts

In TPD experiments, carbon dioxide as a probe molecule manifests sufficient acidity to determine all basic sites in a catalyst [21]. **TPD patterns of CO₂** (Fig. 4) from two selected catalysts, Co₄MnAl and NaX-CeO₂, are an example for two peaks identified for all catalysts: very weak (T_{max} around 80 °C) and stronger basic centres (T_{max} around 300 °C).

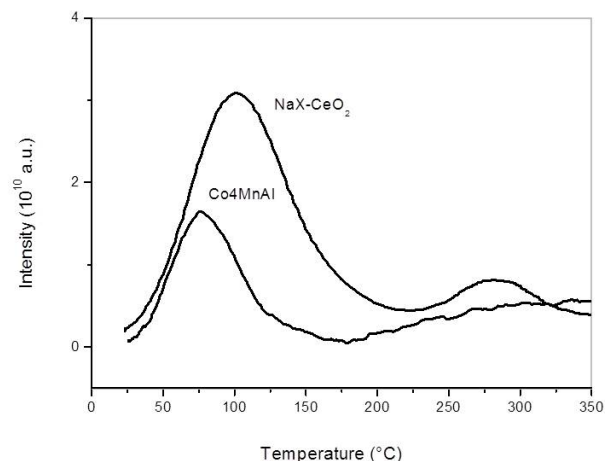


Fig. 4 desorption curves of CO₂ (TPD) from selected catalysts

In Table II, the amount of basic centres for the temperature range of 25-350 °C is given.

Table II

TPD characteristics of all catalysts

Catalyst	TPD NH ₃ (mmol/g) ^a	TPD CO ₂ (mmol/g) ^a
Co4MnAl	0.70	0.16
NiMgMn	1.34	0.09
NaX	0.22	0.20
NaX-CeO ₂	0.23	0.20
CeO ₂	0.25	0.19

^a 25-350 °C.

The overall number of basic sites decreased in opposite order comparing to the amount of acid sites: NaX (0.20 mmol/g) ≥ NaX-CeO₂ ≥ CeO₂ > Co4MnAl > NiMgMn (0.09 mmol/g).

The TPD NH₃ and CO₂ experiments confirmed that Co4MnAl and NiMgMn systems are more acidic than basic while NaX, NaX-CeO₂, CeO₂ are more basic than acidic.

As a rule, two mechanisms can account for **oxygen storage** in oxide materials: (i) either there is diffusion of oxygen species from the bulk to the surface and the reaction with the reducer (CO) takes place at the surface or (ii) the reaction takes place in the bulk, which implies that there is bulk diffusion of the reducer and back-diffusion of the reaction products (CO₂). The second mechanism is quite unlikely for OSC using CO as a reducing agent and such OSC mechanism is mainly controlled by oxygen mobility.

The total amount of available oxygen in the samples (OSCC) and the O₂ amount immediately available in the samples (OSC), expressed in μmol_O/g stored in the samples, are presented in Table III.

Table III

OSC and OSCC of all catalysts

Catalyst	OSCC (μmol _O /g)	OSC (μmol _O /g)
Co ₄ MnAl	2661	1867
NiMgMn	3640	1350
NaX	98	1
NaX-CeO ₂	113	45
CeO ₂	326	80

There are visible differences between OSCC as well as OSC values of measured samples. The metal mixed oxides exhibit extremely high oxygen storage values: OSCC around 3000 μmol_O/g and OSC about 1500 μmol_O/g. The total amount of available oxygen in NiMgMn is the highest comparing to all

other samples, 3640 μmol_O/g. On the other hand, among all catalysts, in Co4MnAl is the highest O₂ amount immediately available, 1867 μmol_O/g. As expected, CeO₂ > NaX-CeO₂ > NaX is decreasing order of OSCC and OSC values respectively. The presence of CeO₂ in NaX structure increased the oxygen storage capacity of a hybrid in comparison to bare NaX, which is able to exchange the oxygen atoms above 600 °C [22]. The increase of oxygen exchange by the introduction of a metal cation can be done via a multiple exchange [23]; a rapid exchange of the oxygen of the ceria surface and a slower exchange of the oxygen atoms from the zeolite lattice is proposed explanation for the hybrid sample [24].

B. Catalytic testing

The samples were tested as catalysts in total **oxidation of ethanol and isopropanol**. The main results of catalytic tests are summarized in Table IV. The temperatures T₅₀ and T₉₀ – at which 50 and 90 % conversion of ethanol and isopropanol was achieved – were chosen as a measure of catalytic activity of the prepared catalysts in oxidation processes.

Table IV

Temperatures of 50 and 90 % conversion of ethanol and isopropanol achieved with all catalysts

Catalyst	Ethanol ^a		Isopropanol ^a	
	T ₅₀	T ₉₀	T ₅₀	T ₉₀
Co4MnAl	132	150	205	240
NiMgMn	129	198	210	234
NaX	309	319	300	325
NaX-CeO ₂	300	316	190	210
CeO ₂	160	178	<120	180

^a GHSV = 18000/h

The catalytic oxidation of **ethanol**, carried out *in Czech Republic*, reveals the best performance for mixed oxides catalysts: NiMgMn and Co4MnAl. The presence of those catalysts assures the values of T₅₀ close to 130 °C (129 °C for NiMgMn and 132 °C for Co₄MnAl). Other very active catalyst was oxide of ceria, which is able to catalyse the half of ethanol oxidation already at 160 °C. The highest values of T₅₀, 300 and 309 °C, are linked to zeolite NaX-CeO₂ and pure NaX respectively. The positive effect of CeO₂ addition to NaX is visible on slightly lower value of T₅₀ for NaX-CeO₂ comparing to pure NaX, anyhow, these catalysts are the less suitable for catalytic oxidation of ethanol from all tested compounds. For better understanding of the differences in catalytic activity, the properties and the characteristics of the catalysts need to be

taken in account. Several connections were found, presented in Fig. 5.

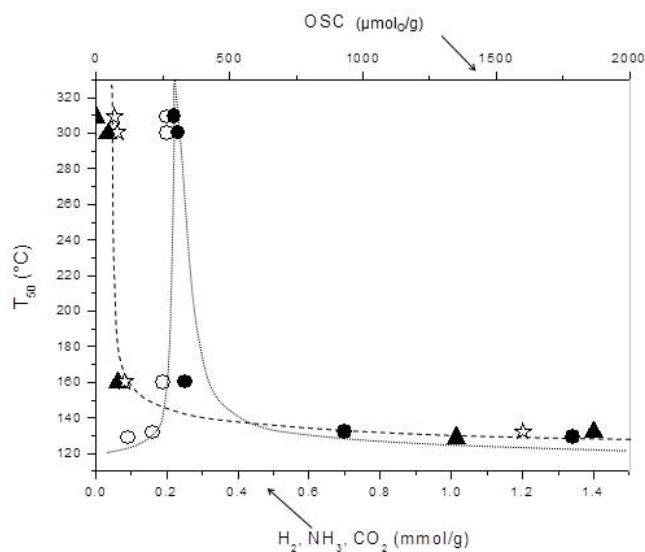


Fig. 5 dependence of catalytic activity in total oxidation of ethanol over tested samples on their OSC (\blacktriangle), the amount of hydrogen consumed during TPR ($*$) and acidic (\bullet) or basic (\circ) properties in the temperature range (25-350 °C)

The dashed exponential curve joins the values of T_{50} in dependence of the ones for OSC (\blacktriangle in Fig. 5) and at the same time the amount of hydrogen consumed during TPR ($*$ in Fig. 5) for all catalysts. The curve describes a growing advantage for catalytic performance in ethanol oxidation with increasing amount of immediately available oxygen in the sample (OSC). Concurrently, it declares that the enhancement of reducibility of the catalyst is reflected in higher activity in ethanol oxidation. Cerium-based heterogeneous catalysts have been widely studied, used, and developed due to their well-known oxygen storage capacity (OSC) and high oxygen mobility, especially in the case of gas-phase reactions [25]. However, a higher oxygen storage and reducibility of metal mixed oxide Co_4MnAl and NiMgMn , comparing to CeO_2 , assured the highest activity in ethanol oxidation. The results of catalytic activity in dependence of TPD measurements in the temperature range (25-350 °C) led to tracing of two dotted curves – one for acidic (\bullet in Fig. 5) and one for basic (\circ in Fig. 5) properties of the compounds. The curves describe the following tendency: more the catalysts are acidic, resp. less basic, higher is the activity in ethanol oxidation. The authors suggest that redox and acid-base parameters are the key factors for ethanol oxidation. Furthermore, the authors interpret the fact that dashed and dotted curves (Fig. 5) has an exponential character by their “mutual influence” on catalytic activity. The further comparisons, analysing also T_{90} for ethanol oxidation, displays the different order of catalytic performance of the samples evaluated by T_{50} and T_{90} . The most active catalyst NiMgMn according to T_{50} values appears at the third place pursuant to T_{90} evaluation. NiMgMn is able to catalyse 90 % of ethanol oxidation at 198 °C, which is later than sample Co_4MnAl ($T_{90} = 150$ °C) or CeO_2 ($T_{90} = 178$ °C). The

possible explanation of a slower catalytic oxidation of NiMgMn than Co_4MnAl and CeO_2 can be the different preparation process. Co_4MnAl and CeO_2 were prepared from nitrates but for synthesis of NiMgMn the sulphate precursors were used. The activity of such catalyst can be inhibited during oxidation process by formation of sulphates on its surface.

Ethanol is a primary alcohol, so the product of its oxidation is first an aldehyde (acetaldehyde) and with further oxidation a carboxylic acid (acetic acid). Oxidation of acetic acid gives the final product of total oxidation of ethanol: CO_2 and H_2O . Depending on the reagents and conditions, different by-products can be detected during ethanol oxidation. Conversion of ethanol as well as selectivity to CO_2 thus may be evaluated. The major path appears to be the direct oxidation of acetaldehyde to CO_2 , while its oxidation via the acetic acid should be a minor path, because no acetic acid is detected in the products [26].

The catalytic oxidation of **isopropanol** was carried out *in France*. The main results of the tests are gathered in Table IV and temperature dependence of isopropanol conversion over the catalysts can be seen on Fig. 6.

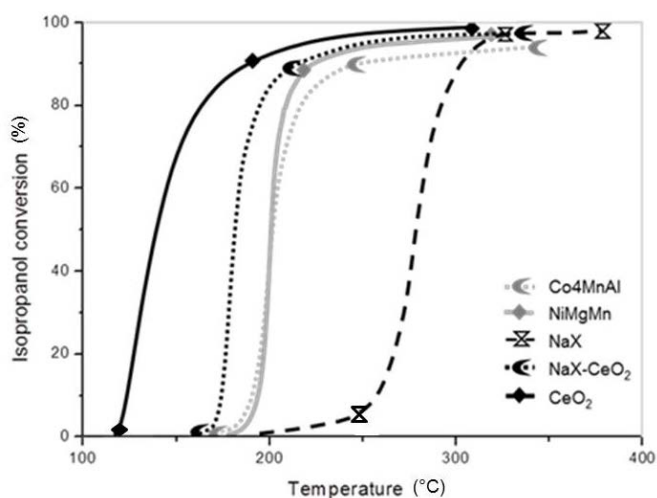


Fig. 6 temperature dependence of isopropanol conversion over all tested catalysts

All catalysts – hybrid zeolite, the metal mixed oxides and cerium oxide – except NaX showed dissimilar activity order in oxidation of isopropanol and ethanol. Different laboratory setup or experimental conditions may move the values if T_{50} or T_{90} to the higher or lower temperature range, but the order of catalytic performance for the tested samples should remain the same. Anyhow, the results between two laboratories will not be compared, but the elementary difference between two tested alcohols simply might be noted. Ethanol is a primary alcohol, which can be oxidised to aldehydes or further to carboxylic acids. Isopropanol is a secondary alcohol and secondary alcohols can be oxidised to ketones but no further. Based on the data from French laboratory for all tested catalysts, isopropanol is quickly and easily transformed into carbon dioxide and for certain samples to one intermediate product –

propene. Other possible intermediate product – acetone, which is corresponding ketone – was not observed. Regarding the fact that reagents useful for the transformation of primary alcohols to aldehydes are normally also suitable for the oxidation of secondary alcohols to ketones, missing acetone in isopropanol oxidation can be coherent with missing aldehyde presence in ethanol oxidation for tested catalysts. Intermediate product propene was observed for more basic catalysts, where isopropanol can be transformed via a basic mechanism into propene before complete oxidation in CO_2 . The advantage of more basic catalysts in isopropanol oxidation might be a stronger adsorption of VOC molecule on the cations and framework oxygen of the zeolite. When isopropanol is adsorbed on a zeolite with alkali cations, it is probable that the OH group of isopropanol will adsorb on the cation (acting as a Lewis acid site), and that hydrogen of molecule will adsorb on the basic framework oxygen. From Table IV and Fig. 6 is noticeable that the most active catalysts among those tested in isopropanol oxidation are CeO_2 and hybrid zeolite NaX- CeO_2 ($T_{50} = 120^\circ\text{C}$ for CeO_2 and $T_{50} = 190^\circ\text{C}$ for the hybrid). TPR and TPD indicated them to be more basic than acidic. On the other hand, the zeolite NaX is the most basic from all the catalysts, however, is the less active in isopropanol oxidation. Here should be repeated that NaX is not able to exchange the oxygen atoms under 600°C and oxygen mobility is minimal in the temperature range of the oxidation process. That might be a handicap for NaX. Also, the mixed oxides NiMgMn and Co4MnAl were evaluated as acidic; still, their great oxygen storage capacity and the good reducibility permit them to perform isopropanol oxidation rather actively.

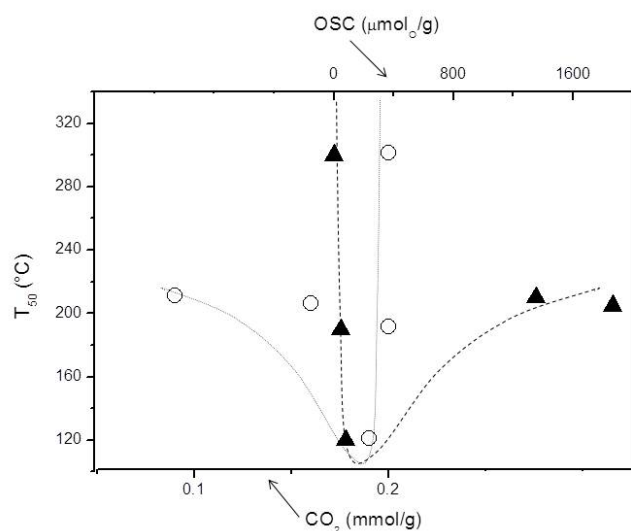


Fig. 7 dependence of catalytic activity in total oxidation of isopropanol over tested samples on their OSC (▲) and basic (○) properties in the temperature range ($25\text{--}350^\circ\text{C}$).

A combination of basicity and oxygen mobility is proposed as advantageous characteristics for isopropanol oxidation. Yet, basicity and OSC values of the catalysts follow the opposite order (Table II and III). Fig. 7 shows the dependence of catalytic activity in total oxidation of isopropanol over tested samples on their OSC (▲) and basic (○) properties in the

temperature range ($25\text{--}350^\circ\text{C}$). OSC values are linked by dashed line and basicity representing points are linked by dotted line. The intersection of the curves illustrates a “compromise” of two key parameters. Closer the values of OSC and basicity for a catalyst are to the intersection, higher activity reveals in isopropanol oxidation.

IV. CONCLUSION

Zeolite NaX, hybrid NaX- CeO_2 , cerium oxide and the mixed oxides – Co4MnAl and NiMgMn – were tested and compared in catalytic oxidation of ethanol and isopropanol respectively. The basic zeolite NaX, converted 50 % of ethanol as well as isopropanol at around 300°C . All other catalysts were more active. The comparison revealed that CeO_2 and zeolite NaX- CeO_2 are the most suitable for oxidation of isopropanol while oxidation of ethanol is the fastest in a presence of the metal mixed oxides, Co4MnAl and NiMgMn. Basicity/acidity appears to be one of the crucial parameter for alcohol oxidation. However, it seems to lead hand by hand with oxygen mobility to a higher performance of the catalysts. The results of ethanol (the primary alcohol) oxidation indicate growing performance with increasing acidity and OSC of the catalysts. Authors suggest, that exponential curve of activity amelioration illustrates a “mutual work” of these two key characteristics. The importance of both parameters was visible also in isopropanol oxidation, though, this secondary alcohol prefers higher basicity. Basicity and OSC values of the catalysts follow the opposite order. Therefore, in this case, the main parameters go “against each other”, ending by the compromise for the best activity: CeO_2 , relatively basic catalyst with rather sufficient OSC.

REFERENCES

- [1] J. J. Spivey, *Ind. Eng. Chem. Res.*, vol. 26, 1987, pp. 2165-2180.
- [2] R. Burch, P. K. Loader, and F. J. Urbano, *Catalysis Today*, vol. 27, 1996, pp. 243-248.
- [3] J. J. Spivey and J.B. Butt, *Catalysis Today*, vol. 11, 1992, pp. 465-500.
- [4] F. Basile, G. Fornasari, M. Gazzano, and A. Vaccari, *Applied Clay Science*, vol. 18, 2001, pp. 51-57.
- [5] L. Pinard, J. Mijoin, P. Ayrault, C. Canaff, and P. Magnoux, *Applied Catalysis B: Environmental*, vol. 51, 2004, pp. 1-8.
- [6] J. Tsou, P. Magnoux, M. Guisnet, J. J. M. Órfão, and J. L. Figueiredo, *Applied Catalysis B: Environmental*, vol. 51, 2004, pp. 129-133.
- [7] K. Bahranowski, R. Dula, M. Gąsior, M. Labanowska, A. Michalik, L.A. Vartikian, and E.M. Serwicka, *Applied Clay Science*, vol. 18, 2001, pp. 93-101.
- [8] S. Vigneron, P. Deprelle, and J. Hermia, *Catalysis Today*, vol. 27, 1996, pp. 229-236.
- [9] A. Vaccari, *Catalysis Today*, vol. 41, 1998, pp. 53-71.
- [10] L. Pinard, J. Mijoin, P. Magnoux, and M. Guisnet, *J. Catal.*, vol. 215, 2003, pp. 234-244.
- [11] L. Pinard, P. Magnoux, P. Ayrault, and M. Guisnet, *J. Catal.*, vol. 221, 2004, pp. 662-665.
- [12] Q. Dai, X. Wang, and G. Lu, *Catalysis Communications*, vol. 8, 2007, pp. 1645-1649.
- [13] R. T. Morrison and R. N. Boyd, *Organic Chemistry*, Allyn and Bacon, 1966.
- [14] R. W. McCabe and P. J. Mitchell, *Industrial & Engineering Chemistry Product Research and Development*, vol. 23, 1984, pp. 196-202.

- [15] J. Mikulova, S. Rossignol, F. Gérard, D. Mesnard, C. Kappenstein, and D. Duprez, *Journal of Solid State Chemistry*, vol. 179, 2006, pp. 2511-2520.
- [16] L. V. Mattos and F. B. Noronha, *Journal of Power Sources*, vol. 145, 2005, pp. 10-15.
- [17] A. L. Patterson, *Physical Review*, vol. 56, 1939, pp. 978-982.
- [18] M. Ferrandon, J. Carnö, S. Järäs, and E. Björnbom, *Applied Catalysis A: General*, vol. 180, 1999, pp. 141-151.
- [19] P. Arnoldy and J. A. Moulijn, *J. Catal.*, vol. 93, 1985, pp. 38-54.
- [20] J. I. Di Cosimo, Apestegui, amp, C.R. a, M.J.L. Ginés, and E. Iglesia, *J. Catal.*, vol. 190, 2000, pp. 261-275.
- [21] S. Abelló, F. Medina, D. Tichit, J. Pérez-Ramírez, X. Rodríguez, J. E. Sueiras, P. Salagre, and Y. Cesteros, *Applied Catalysis A: General*, vol. 281, 2005, pp. 191-198.
- [22] J. Nováková and L. Brabec, *J. Catal.*, vol. 166, 1997, pp. 186-194.
- [23] Y. F. Chang, G. A. Somorjai, and H. Heinemann, *J. Catal.*, vol. 154, 1995, pp. 24-32.
- [24] I. Maupin, J. Mijoin, T. Belin, C. Morais, V. Montouillout, D. Duprez, and N. Bion, *J. Catal.*, vol. 300, 2013, pp. 136-140.
- [25] A. Trovarelli, M. Boaro, E. Rocchini, C. de Leitenburg, G. Dolcetti, *Journal of Alloys and Compounds*, vol. 323-324, 2001, pp. 584-591.
- [26] D. Delimaris and T. Ioannides, *Applied Catalysis B: Environmental*, vol. 84, 2008, pp. 303-312.

A Vibrational Stark Effect In The Fullerene C₆₀

Andrey V. Tuchin, Larisa A. Bityutskaya and Eugene N. Bormontov

Abstract— The method of the density functional theory was used for the investigation of the vibrational spectrum of the fullerene C₆₀ both in the unexcited and excited by the electric field $E=0.5$ V/Å states. It was found, that the active in the Raman spectrum H_g(1), A_g(1), H_g(4), H_g(5), H_g(6) and H_g(7) modes become active in the infrared spectrum of excited state of the molecule. Silent modes G_u(3), G_u(6) and H_u(7) activated in the Raman spectrum. The overlap of the active T_{1u}(1) and silent H_u(2) modes activate one in the infrared spectrum.

Keywords— fullerene, infrared spectrum, Raman spectrum, electric field.

I. INTRODUCTION

FULLERENE C₆₀ is a promising material of organic Electronics [1-3]. Strong acceptor properties of the molecule and its nearly spherical structure let form a bulk heterojunction in polymers for solar converters [2-4]. Structural changes and electron density redistribution between a donor and acceptor occur in the polymer-fullerene C₆₀ system [5]. The result of the changes and redistribution is local electric fields that are potential barriers, which prevent electron-hole-pair from separation. A research of the local electric fields is one of the main ways of the solar converter efficiency increment.

The changes of molecule surroundings are evident in their infrared spectrum [6]. An electric field causes frequency shifts of the vibrational modes (the vibrational Stark effect). The paper [5] determines local electric fields in the mixture of P3HT: PCBM which were determined on the basis of the vibrational Stark effect. It was reported that the electric field strength was ~0.2 V/nm. There are data of frequency shifts in the infrared spectrum for functional groups and small molecules such as acetone, carbon monoxide, glycine, etc [7-8]. Unfortunately, the vibrational Stark effect in fullerene C₆₀ is not studied sufficiently.

It is known that all the 60 atoms of the isolated fullerene C₆₀ are united [9, 10]. The high symmetry of the truncated icosahedron I_h imposes rigid restrictions on a form of the

molecular vibration [11, 12]. All the 174 vibrational modes conform to the irreducible representations of 2(A_g), 1(A_u), 4(T_{1g}), 5(T_{1u}), 4(T_{3g}), 5(T_{3u}), 6(G_g), 6(G_u), 8(H_g) and 7(H_u) [10]. The dimensions of the irreducible representations A, T, G and H equal 1, 3, 4 and 5 correspondingly. Indices g and u denote even and odd modes. The high symmetry imposes rigid restrictions on the active mode numbers in the infrared and Raman spectrums. There are only four active T_{1u} modes in the isolated molecule [10-13].

An external disturbance such as an electric field violates symmetry of the fullerene C₆₀ and can activate silent modes [10]. Investigation of the activated vibrational modes is a powerful tool to study the fullerene C₆₀ properties. Due to the fact that a little perturbation can cause closely spaced modes mixing, an analysis of the fullerene C₆₀ vibrational spectrum in the electric field have to be conducted with taking account all the 174 modes.

The aim of the paper is to present results of a theoretical study of the frequency shifts of the vibrational modes and the modes activation of the isolated fullerene C₆₀ in the electric field.

II. COMPUTATIONAL DETAILS

An electronic structure and infrared spectrum of the fullerene C₆₀ calculations were performed using density functional theory (DFT) computational method [14, 15] with the help of Gaussian software [16] in the Supercomputing center of Voronezh State University. B3LYP (Becke, Lee, Yang, Parr) [17] was chosen as an exchange-correlation potential. We used a 6-31G basis set in the calculations. Firstly, geometry of the fullerene C₆₀ was optimized. Secondly, a vibrational spectrum of the fullerene C₆₀ was calculated. The frequencies were corrected by the factor 0.9613 in accordance with the software guidance [18]. Identification of modes of the symmetry was performed in accordance with the paper [10]. Then, to take an orientation deformation under the influence of ponderomotive force into account, a geometry optimization of the molecule in the electric field $E=0.5$ V/Å was performed without symmetry retention [19]. The electric field was directed parallel to the five-fold axis. Finally, the vibrational spectrum of the perturbed fullerene C₆₀ was calculated and frequency shifts of the vibrational modes were determined in comparison with the ground state of the unexcited fullerene C₆₀.

This work was supported by RFBR, research project No. 14-02-31315 mol_a and by the project FP7-IRSES-295260 "ECONANOSORB" under Marie Curie Actions of the 7th Framework Program of European Union.

A. V. Tuchin is with the Voronezh State University, 394006, Voronezh, Russia (tel.: +7(473)2208481; e-mail: a.tuchin@bk.ru).

L. A. Bityutskaya is with the Voronezh State University, 394006, Voronezh, Russia (tel.: +7(473)2208481; e-mail: me144@phys.vsu.ru).

E. N. Bormontov is with the Voronezh State University, 394006, Voronezh, Russia (tel.: +7(473)2208481; e-mail: me144@phys.vsu.ru).

III. RESULTS AND DISCUSSION

Table 1 shows the calculated vibrational spectrum of the unexcited fullerene C_{60} in comparison with the experimental [10] and theoretical data [11-13]. Paper [10] presents the most

Table.1 Vibrational spectrum of the ground state of the fullerene C_{60} . The level of computational accuracy of our and [11-13] calculations in comparison with the experimental data of [10] are shown within brackets.

Type of symmetry	Activity	ν, cm^{-1} (exp.[10])	ν, cm^{-1} (calc. DFT [11])	ν, cm^{-1} (calc. HF [12])	ν, cm^{-1} (calc. DFT [13])	ν, cm^{-1} (our calc.)
$H_g(1)$	Ram.	272	259 (-4.8%)	268 (-1.5%)	264 (-2.9%)	261 (-4.0%)
$T_{3u}(1)$	-	342	337 (-1.5%)	342 (0.0%)	341 (-0.3%)	339 (-0.9%)
$G_u(1)$	-	353	349 (-1.1%)	355 (0.6%)	354 (0.3%)	351 (-0.6%)
$H_u(1)$	-	403	399 (-1.0%)	413 (2.5%)	403 (0.0%)	401 (-0.5%)
$H_g(2)$	Ram.	433	425 (-1.8%)	432 (-0.2%)	430 (-0.7%)	431 (-0.5%)
$G_g(1)$	-	485	480 (-1.0%)	481 (-0.8%)	485 (0.0%)	480 (-1.0%)
$A_g(1)$	Ram.	496	495 (-0.2%)	470 (0.8%)	496 (0.0%)	477 (-3.8%)
$T_{1u}(1)$	IR	526	527 (0.2%)	522 (-0.8%)	525 (-0.2%)	532 (1.1%)
$H_u(2)$	-	534	530 (-0.7%)	533 (-0.1%)	533 (-0.2%)	533 (-0.2%)
$T_{3g}(1)$	-	553	548 (-0.9%)	578 (4.5%)	552 (-0.2%)	559 (1.1%)
$G_g(2)$	-	567	566 (-0.2%)	587 (3.5%)	567 (0.0%)	570 (0.5%)
$T_{1g}(1)$	-	568	564 (-0.7%)	562 (-1.1%)	560 (-1.4%)	571 (0.5%)
$T_{1u}(2)$	IR	575	586 (1.9%)	557 (-3.1%)	578 (0.5%)	564 (-1.9%)
$H_u(3)$	-	668	662 (-0.9%)	684 (2.4%)	665 (-0.4%)	669 (0.1%)
$H_g(3)$	Ram.	709	711 (0.3%)	692 (-2.4%)	709 (0.0%)	708 (-0.1%)
$G_g(3)$	-	736	762 (3.5%)	715 (-2.9%)	751 (2.0%)	745 (1.2%)
$H_u(4)$	-	743	741 (-0.3%)	721 (-3.0%)	738 (-0.4%)	733 (-1.3%)
$T_{3u}(2)$	-	753	716 (-4.9%)	695 (-7.7%)	706 (-6.2%)	712 (-5.4%)
$T_{3g}(2)$	-	756	767 (1.5%)	637 (-15.7%)	713 (-5.7%)	736 (-2.6%)
$G_u(2)$	-	764	748 (-2.1%)	670 (-12.3%)	741 (-3.0%)	746 (-2.3%)
$H_g(4)$	Ram.	772	783 (1.4%)	752 (-2.6%)	773 (0.1%)	756 (-2.1%)
$G_u(3)$	-	776	782 (0.8%)	780 (0.5%)	756 (-1.3%)	757 (-2.4%)
$T_{3g}(3)$	-	796	794 (-0.3%)	823 (3.4%)	796 (0.0%)	736 (-7.5%)
$T_{1g}(2)$	-	831	823 (-1.0%)	853 (2.6%)	825 (-0.7%)	825 (-0.7%)
$G_u(4)$	-	961	975 (1.5%)	936 (-2.6%)	972 (1.1%)	947 (-1.4%)
$T_{3u}(3)$	-	973	993 (2.1%)	903 (-7.2%)	963(-1.0%)	945 (-2.9%)
A_u	-	984	943 (-4.2%)	1010 (2.6%)	956 (-2.8%)	953 (-3.2%)
$G_g(4)$	-	1079	1118 (3.6%)	994 (-7.9%)	1078 (-0.1%)	1056 (-2.1%)
$H_g(5)$	Ram.	1099	1120 (1.9%)	1075 (-2.2%)	1101 (0.2%)	1085 (-1.3%)
$T_{1u}(3)$	IR	1182	1218 (3.0%)	1130 (-4.4%)	1182 (0.0%)	1161 (-1.8%)
$T_{3u}(4)$	-	1205	1228 (1.9%)	1102 (-8.5%)	1166 (-3.2%)	1154 (-4.2%)
$H_u(5)$	-	1223	1231 (0.7%)	1199 (-2.0%)	1251 (2.3%)	1198 (-2.0%)
$H_g(6)$	Ram.	1252	1281 (2.3%)	1204 (-3.8%)	1251 (-0.1%)	1224 (-2.2%)
$T_{1g}(3)$	-	1289	1296 (0.5%)	1244 (-3.5%)	1260 (-2.2%)	1252 (-2.9%)
$G_u(5)$	-	1309	1334 (1.9%)	1276 (-2.5%)	1307 (-0.2%)	1286 (-1.8%)
$G_g(5)$	-	1310	1322 (0.9%)	1294 (-1.2%)	1315 (0.4%)	1290 (-1.5%)
$H_u(6)$	-	1344	1363 (1.4%)	1313 (-2.3%)	1341 (-0.2%)	1318 (-1.9%)
$T_{3g}(4)$	-	1345	1363 (1.3%)	1319 (-1.9%)	1345 (0.0%)	1317 (-2.1%)
$G_u(6)$	-	1422	1452 (2.1%)	1419 (-0.2%)	1428 (0.4%)	1414 (-0.6%)
$H_g(7)$	Ram.	1425	1450 (1.8%)	1405 (-1.4%)	1426 (0.1%)	1411 (-1.0%)
$T_{1u}(4)$	IR	1429	1462 (2.3%)	1410 (-1.3%)	1433 (0.3%)	1423 (-0.4%)
$A_g(2)$	Ram.	1470	1504 (2.3%)	1457 (-0.9%)	1468 (-0.1%)	1466 (-0.3%)
$G_g(6)$	-	1482	1512 (2.0%)	1514 (2.2%)	1497 (-1.0%)	1487 (0.3%)
$T_{3u}(5)$	-	1525	1535 (0.7%)	1553 (1.8%)	1540 (1.0%)	1520 (-0.3%)
$H_u(7)$	-	1567	1569 (0.1%)	1600 (2.1%)	1566 (-0.1%)	1555 (-0.7%)
$H_g(8)$	Ram.	1575	1578 (0.2%)	1610 (2.2%)	1576 (0.1%)	1565 (-0.6%)

detailed analysis of a vibrational spectrum of the fullerene C_{60} on basis of the results of the infrared spectroscopy, inelastic neutron scattering, fluorescence spectroscopy and high-resolution electron energy-loss spectroscopy. That is why our results were compared with the data of the paper [10].

Our results of the vibrational spectrum calculations are in better agreement than the same calculations shown in papers [11] (the calculations were performed using DFT method) and

[12] (the calculations were performed using Hartree-Fock method) with the exception of $A_g(1)$, $T_{1u}(1)$, $G_u(3)$, $T_{3g}(3)$ and $T_{3g}(4)$ modes. Frequencies defined in [13] are the closest to the experimental results. However, there was an additional correction of the results in order to match the calculated and experimental data.

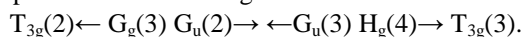
The calculated data shown in Table 1 are in good agreement with the experimental data presented in the research [10].

Moreover, the levels of accuracy of our calculations are higher than accuracy of calculations shown in [11, 12] and slightly less than accuracy of calculations shown in [13].

A geometry optimization of the fullerene C_{60} in the electric field was carried out without symmetry retention. The ponderomotive force causes an orientation deformation of the carbon cage [19, 20]. A reduction of symmetry and electronic system excitation leads to modes splitting and frequency shifts. Table 2 and fig.1 discloses the calculated vibrational spectrum of the fullerene C_{60} in the electric field. Letter \bar{v} denotes an arithmetic mean of the vibrational frequencies with the same symmetry. The frequency shift $\Delta = \bar{v} - v$ is determined in relation to an unexcited state of the molecule. The bandwidth σ is determined as the difference between the minimal and maximal vibrational frequencies of the same symmetry.

There are 3 modes in the frequency range of 200 – 400 cm^{-1} : an active one in the Raman spectrum $H_g(1)$ and two silent modes $T_{3u}(1)$, $G_u(1)$. In the electric field, all the modes shift to 0.1-0.4 cm^{-1} towards the long-wave region. A fivefold degenerated mode $H_g(1)$ becomes slightly active in the infrared spectrum (table 2). There are 2 active modes $T_{1u}(1)$, $T_{1u}(2)$ in the infrared spectrum, 2 active modes $H_g(2)$, $A_g(1)$ in Raman spectrum and 7 silent modes in the frequency range of 400 – 700 cm^{-1} . The red shift of the modes of g-type is 0.5-0.7 cm^{-1} , and A_g -mode becomes active in the infrared spectrum. The active $T_{1u}(1)$ and silent $H_u(2)$ modes are close. In the electric field, the modes overlap each other due to the broad band σ (2.3 cm^{-1} and 4.0 cm^{-1} respectively) and shift to $\Delta = -1.0$ cm^{-1} . As a result of the interaction, $H_u(2)$ becomes active in the infrared spectrum.

There are 9 modes in the frequency range of 700-800 cm^{-1} . The two modes $H_g(3)$ and $H_g(4)$ of the fullerene C_{60} are active in the Raman spectrum. We can observe large widening of the mode bands: $\sigma(H_g(3)) = 4.1$ cm^{-1} , $\sigma(G_u(3)) = 4.2$ cm^{-1} , $\sigma(H_u(4)) = 8.3$ cm^{-1} , $\sigma(T_{3g}(2)) = 7.1$ cm^{-1} . All the modes shift to the long-wave region with the exception of modes $G_u(2)$ and $H_g(4)$. A scheme of the level shift in the range of 735-797 cm^{-1} can be represented as following:



The scheme makes it evident that the blue shift is a result of the interaction of close even and odd modes. The electric field activates one mode $G_u(3)$ in the Raman spectrum. The modes $T_{1g}(2)$, $T_{3u}(3)$, $G_u(4)$ and A_u are silent in both the ground and excited states of the fullerene C_{60} in the range of 800-1000 cm^{-1} .

There are 9 modes in the range of 1000-1300 cm^{-1} . The mode $T_{1u}(3)$ is active in the infrared spectrum, the modes $H_g(5)$ and $H_g(6)$ are active in Raman spectrum. The electric field activates $H_g(5)$ and $H_g(6)$ in the infrared spectrum. All the modes of the range are shifted to 0.5-1.8 cm^{-1} towards the long-wave region. The bandwidth correlate with the degeneracy order of the modes ($\sigma = 0.3$ -1.3 cm^{-1} for T-modes, $\sigma = 0.8$ -1.7 cm^{-1} for G-modes and $\sigma = 1.1$ -2.7 cm^{-1} for H-modes). The widening results in overlapping the following pairs of modes $H_u(4)$ and $T_{3g}(2)$, $G_u(3)$ and $H_g(4)$.

There are following modes in the range of 1300-1600 cm^{-1} : the last active mode $T_{1u}(4)$ in the infrared spectrum, three active modes $H_g(7)$, $A_g(2)$ and $H_g(8)$ in the Raman spectrum. The modes $T_{3g}(4)$ and $H_u(6)$ are very close to each other if they are not excited. Under the influence of the electric field and interactions of even and odd modes, the triply degenerated mode shifts to 5.3 cm^{-1} towards the long-wave region, the band of the fivefold degenerated mode becomes wider $\sigma = 6.8$ cm^{-1} and undergoes the blue shift to 0.5 cm^{-1} . The mode $A_g(2)$ shifts to 0.4 cm^{-1} towards the short-wave region. The modes $H_g(7)$ and $H_g(8)$ become active in the infrared spectrum as well as the mode $H_u(7)$ becomes active in the Raman spectrum.

Table 2 The infrared spectrum of the fullerene C_{60} in the electric field $E = 0.5$ V/Å. \bar{v} – an arithmetical mean of vibrational frequencies of the same symmetry, σ – bandwidth, Δ – a shift of the arithmetical mean vibrational frequency in comparison with the unexcited state of the molecule.

Type of symmetry	v, cm^{-1} (E=0)	\bar{v}, cm^{-1} (E=0.5 V/Å)	Δ, cm^{-1}	σ, cm^{-1}	Activity
$H_g(1)$	260.9	260.6	-0.3	0.9	IR/Ram.
$T_{3u}(1)$	339.1	339.0	-0.1	1.5	-
$G_u(1)$	350.8	350.4	-0.4	1.9	-
$H_u(1)$	401.4	401.0	-0.4	0.5	-
$H_g(2)$	430.8	430.2	-0.6	1.9	Ram.
$A_g(1)$	476.9	476.3	-0.6	0.0	IR/Ram.
$G_g(1)$	479.7	479.0	-0.7	1.6	-
$T_{1u}(1)$	532.1	531.1	-1.0	2.3	IR
$H_u(2)$	532.7	531.7	-1.0	4.0	IR
$T_{3g}(1)$	559.2	558.8	-0.4	0.3	-
$T_{1u}(2)$	563.8	563.1	-0.7	0.6	IR
$G_g(2)$	569.9	569.4	-0.5	2.1	-
$T_{1g}(1)$	571.2	570.7	-0.5	0.5	-
$H_u(3)$	669.3	668.7	-0.6	0.6	-
$H_g(3)$	708.2	705.4	-2.8	4.1	Ram.
$T_{3u}(2)$	712.4	711.9	-0.5	1.6	-
$H_u(4)$	733.1	725.5	-7.6	8.3	-
$T_{3g}(2)$	735.9	735.4	-0.5	7.1	-
$G_g(3)$	745.0	742.3	-2.7	3.6	-
$G_u(2)$	746.3	750.1	3.8	2.3	-
$G_u(3)$	757.0	756.1	-0.9	4.2	Ram.
$H_g(4)$	757.5	757.9	0.4	3.3	IR/Ram.
$T_{3g}(3)$	796.1	795.7	-0.4	0.4	-
$T_{1g}(2)$	824.8	824.2	-0.6	0.4	-
$T_{3u}(3)$	945.4	944.7	-0.7	0.3	-
$G_u(4)$	946.8	945.8	-1.0	0.7	-
A_u	952.9	952.3	-0.6	0	-
$G_g(4)$	1056.0	1055.4	-0.6	1.7	-
$H_g(5)$	1085.2	1084	-1.2	1.1	IR/Ram.
$T_{3u}(4)$	1154.4	1153.9	-0.5	1.3	-
$T_{1u}(3)$	1161.2	1159.9	-1.3	1.2	IR
$H_u(5)$	1197.5	1195.7	-1.8	2.0	-
$H_g(6)$	1224.1	1222.3	-1.8	2.7	IR/Ram.
$T_{1g}(3)$	1252.0	1250.6	-1.4	0.3	-
$G_u(5)$	1286.0	1284.3	-1.7	1.7	-
$G_g(5)$	1290.3	1289.3	-1.0	0.8	-
$T_{3g}(4)$	1317.1	1311.8	-5.3	2.4	-
$H_u(6)$	1317.8	1318.3	0.5	6.8	-

H _g (7)	1410.6	1405.7	-4.9	2.5	IR/Ram.
G _g (6)	1414.1	1412.8	-1.3	2.2	Ram.
T _{1u} (4)	1423.3	1422.4	-0.9	2.2	IR/Ram.
A _g (2)	1466.0	1466.4	0.4	0	Ram.
G _g (6)	1487.3	1485.0	-2.3	0.5	-
T _{3u} (5)	1519.7	1518.0	-1.7	0.6	-
H _u (7)	1555.1	1551.2	-3.9	3.4	Ram.
H _g (8)	1564.9	1564.2	-0.7	2.4	IR/Ram.

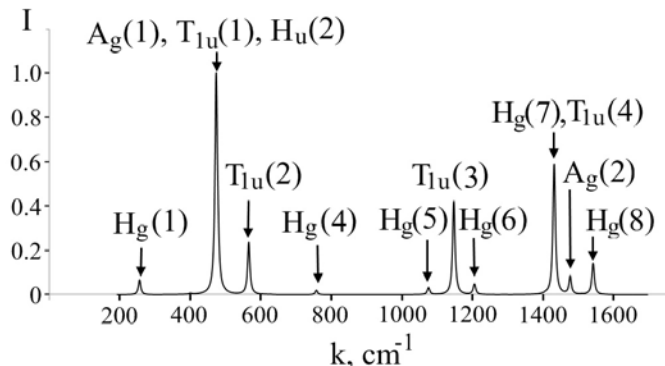


Fig. 1 The normalized IR-spectrum of the fullerene C₆₀ under an applied electric field $E=0.5\text{V}/\text{\AA}$.

Finally, we shall note that the three of five vibrations of the modes H_g(1), H_g(5), H_g(6), H_g(7) and H_g(8) have an by far higher intensity than the two last of the five. Applying the infrared intensity criterion indicates splitting H modes into T and E modes.

IV. CONCLUSION

A vibrational spectrum of the fullerene C₆₀ reflects the influence of the electric field on the molecule. The symmetry violation, excitement of the electronic system of the molecule shifts vibrational modes towards the long-wave region (with the exception of the G_u(2), H_g(4), H_u(6) and A_g(2) modes) and activates “frozen” vibrational modes H_g(1), A_g(1), H_u(2), H_g(4), H_g(5), H_g(6), H_g(7) in the infrared spectrum as well as vibrational modes G_u(3), G_u(6), H_u(7) in the Raman spectrum.

The results of this study are of interest of the research tasks of determining local electric surroundings of the molecule (organic and field-emission electronics, functional and hybrid materials) as well as of the control of its infrared spectrum by electric fields (photonics and quantum- cascade lasers).

ACKNOWLEDGMENT

Special thanks to Galina Tuchina for the help and support.

REFERENCES

[1] Suty S., Williams G., Aziz H. “Role of the donor – acceptor mixing ratio in increasing the efficiency of Schottky junction organic solar cells” *Organic Electr.* Vol. 14, pp. 2392-2400, 2013.

[2] Maeyoshi Y., Saeki A., Suwa S., Omichi M., Marui H., Asano A., Tsukuda S., Sugimoto M., Kishimura A., Kataoka K., and Seki S. “Fullerene nanowires as a versatile platform for organic electronics” *Sc. Rep.* vol. 2, pp. 600 (6), 2012.

[3] Xiaoyu L., Xiaoman C., Boqun D., Xiao B, and Jianfeng F. “Enhanced performance of C₆₀ N-type organic field-effect transistors using a pentacene passivation layer” *J. of Semic.* vol. 34, pp. 084002 (4), 2013.

[4] Banya S., Matsumoto T., Oku T. and Akiyama T. “Fabrication of C₆₀ assembly films via an fullerene-amine addition reaction by using stepwise immersion” *J. of Phys.: Conf. Series* vol. 433, pp. 012007(5), 2013.

[5] Gearba R. I., Mills T., Morris J., Pindak R., Black C. T. and Zhu X. “Quantifying Interfacial Electric Fields and Local Crystallinity in Polymer-Fullerene Bulk-Heterojunction Solar Cells” *Adv. Funct. Mater.*, vol. 21, pp. 2666-2673, 2011.

[6] Ringer A.L. and MacKerell Jr. A. D. “Calculation of the vibrational Stark Effect Using a First Principles QM/MM Approach” *J. Phys. Chem. Lett.*, vol. 2, pp. 553-556, 2011.

[7] Silverman L. N., Pitzer M. E., Ankomah P. O., Boxer S. G. And Fenlon E. E. “Vibrational Stark Effect Probes for Nucleic Acids” *J. Phys. Chem. B* vol. 11, pp. 11611-11613, 2008

[8] Suydam I. T. And Boxer S. G. “Vibrational Stark Effect Calibrate the Sensitivity of Vibrational Probes for Electric Fields in Proteins” *Biochemistry*, vol. 42, pp. 12050-12055, 2003.

[9] Wehrli S., Koch E. and M. Sigrist. “Field doping of C₆₀ crystals: Polarization and Stark splitting” *Phys. Rev B*, vol. 68, pp. 115412. **68**, 115412(14), 2003

[10] Menéndez J. ND Page J. B. “Vibrational Spectroscopy of C₆₀” *Light Scattering in Solids VIII*, ed. By Cardona M. and Güntherodt, Springer, Berlin, 2000, 71p.

[11] Giannozzi P. and Baroni S. “Vibrational and dielectric properties of C₆₀ from density-functional perturbation theory” *J. Chem. Phys.* vol. 100, pp. 8537-8539, 1994.

[12] E. V. Butyrskaya, S. A. Zapryagaev “Computer simulation of the infrared spectra of endohedral metallofullerenes Li₂C₆₀ and Na₂C₆₀” *Sol. St. Phys.*, vol. 3, pp. 649-656, 2009.

[13] Schettino V., Pagliai M., Ciabini L., and Cardini G. “The Vibrational Spectrum of Fullerene C₆₀” *J. Phys. Chem. A* vol. 105, pp. 11192-11196, 2001.

[14] Hohenberg P. and Kohn W. “Inhomogeneous Electron Gas,” *Phys. Rev.* vol. 136, pp. 864-871, 1964.

[15] Kohn W. and Sham L. J. “Self-Consistent Equations Including Exchange and Correlation Effects” *Phys. Rev.* vol. 140, pp. 1133-1138, 1965.

[16] <http://www.gaussian.com>

[17] Becke A. D. “Density-functional thermochemistry. III. The role of exact exchange” *J. Chem. Phys.* vol. 98, pp. 5648-5652, 1993.

[18] Frisch A. “Gaussian 09W Reference” Wallingford, USA, 25p (2009).

[19] A. Tuchin, L. Bityutskaya, E. Bormontov “The Quadratic Stark Effect in The Fullerene C₆₀” *19th International Vacuum Congress*, Paris, pp.1168, 2013.

A bench scale study on the enrichment of Saudi phosphate rock used for H₃PO₄ production

Yasir Arafat, T.F. Al-Fariss and Muhammad Awais Naeem

Abstract—Phosphate rocks are fundamental component in phosphoric acid and ultimately in the phosphatic fertilizers production. The purpose of this study is to provide the cost effective raw material having minimum CaO/P₂O₅ and eventually minimum sulfuric acid consumption for the production of phosphoric acid (H₃PO₄). The phosphate ores situated in the areas of Al-Jalamid and Umm-Wual in Saudi Arabia are of promising nature. In this study, the detailed mineralogical analysis as well as chemical assay is conducted to ascertain the nature and beneficiation technique for two different rocks. The phosphate rock having different grades are compared with commercial grade and segregated. The low grade phosphate rock is beneficiated using calcination in the muffle furnace to meet the market specification for the production of phosphoric acid. The performance of the calcinations was evaluated using different process parameters such as calcination time, calcination temperature and by correlation between CaO/P₂O₅ and sulfuric acid requirement during acidulation. The optimum conditions for calcinations are determined with the aid of XRD, XRF, TGA/DTG, SEM/EDS and calcination experiments to attain efficient, selective and economical enrichment process. The results showed that P₂O₅ content i.e., 25.91% in raw ore may be increased up to 35% in the product. Also, sulfuric acid requirement for acidulation during the phosphoric acid production has been decreased.

Keywords—Calcination, H₂SO₄ consumption, Phosphoric acid, Saudi phosphate ore.

I. INTRODUCTION

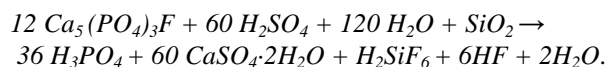
Phosphate rocks are crucial non-renewable resources and vital component in fertilizers and phosphorus-based chemicals. This commodity can neither be substituted nor recycled, that's why the total demand must be met through the mining, beneficiation and chemical processing of naturally occurring phosphate minerals [1], [2], [3]. More or less 95% of the total world's phosphate rock produced is utilized in fertilizer industry [4]. Phosphatic fertilizers constitute higher than 30% of total fertilizer production. In the fertilizer industry, phosphate ore must have (i) P₂O₅ ≥ 30% (ii) CaO/P₂O₅ ratio < 1.6 (iii) MgO < 1% [1]. Therefore the ores which do not fulfil these specification, cannot be used directly

This work was supported by Deanship of Scientific Research and the Research Center at the College of Engineering, King Saud University.

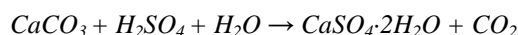
The authors are with the Phosphate and Mineral Processing Chair, Chemical Engineering Department, College of Engineering, King Saud University P.O. Box 800, Riyadh 11421, Saudi Arabia (e-mail: engr.arafat111@yahoo.com, fariss@ksu.edu.sa, ma.naeem@yahoo.com).

and require some beneficiation.

The beneficiation techniques for phosphate ore depend on the type of phosphate minerals present in the ore and the associated gangue minerals [5], [6]. In fact, almost all the phosphoric acid required in the fertilizer industry is produced by wet process. Generally in this process, the raw phosphate ore is changed into phosphoric acid and calcium sulfate dihydrate (gypsum) by adding sulfuric acid [7]. Various chemical reactions occur during the process depending upon the ore complexity, but two main reactions are taken into account here. In the first reaction, fluorapatite ore [Ca₅(PO₄)₃F] is attacked by sulfuric acid according to the following reaction;



While the second reaction is between calcite and sulfuric acid, as follows;



In the presence of free carbonates, phosphate rocks consume an extra acidulent (sulphuric acid) during the manufacture of phosphoric acid. During the course of reaction, carbon dioxide produced is responsible for more foaming and production of smaller size gypsum crystals, that may blind the downstream phosphogypsum filters, and a low quality phosphoric acid may be produced [8], [9]. The phosphate deposits present in the Sirhan-Turayf region of Saudi Arabia are of the most promising nature with favourable mining conditions.

The phosphate ore in the areas of Umm-Wual and Aljalamid is of promising prospects. As the population is increasing, the demand of TSP, NPK and DAP is also increasing rapidly. The demand of phosphoric acid in Saudi Arabia is more than 25000 tons P₂O₅ per year [10]. As Saudi Arabia has a surplus of sulphuric acid, which is second major raw material after phosphate ore for the production of phosphoric acid. The main disadvantage of Saudi phosphate ore as well as other calcareous phosphate ores all over the world is high carbonate content which poses during acidulation such as increase in sulphuric acid consumption, noticeably increase in the phosphoric acid viscosity and foaming problem [11]. Now it's the need of the hour to evaluate the feasible process to reduce the carbonate content of phosphate ore for the economical production of phosphoric acid by utilizing the raw materials

among the available resources.

The objective of this study was to reduce the sulfuric acid consumption by reducing the CaO/P₂O₅ coupled with the removal of carbon dioxide to avoid the problems during downstream operations. Also, to figure out a commercial grade, cost effective raw material (phosphate ore) by applying the efficient, selective and economical enrichment process for the production of phosphoric acid.

II. EXPERIMENTAL

A. Materials

The phosphate samples used in enrichment experiments obtained from phosphate deposits in the two different areas of Umm-Wual and Aljalamid in same Sirhan Turayf region in Saudi Arabia. The samples were subjected to primary and secondary crushing leading to a phosphate ore of 100% -3.36 mm. The grinding of crushed product was carried out to prepare a feed for calcination experiments in a Denver laboratory ball mill submit your manuscript electronically for review as e-mail attachments.

B. Sieving

Dry-sieving was conducted on a vertical vibratory sieve shaker and a series of selected ASTM standard sieves which were arranged in descending order in terms of size. An oscillation of amplitude 2 mm at frequency of about 50 Hz which lasted 25 min.

C. Chemical Analysis

Chemical analysis of phosphate samples was conducted by X-ray Fluorescence (XRF) (Table.1). Phosphorous and associated gangue minerals were determined by X-ray fluorescence, 8 g of the powdered sample and 1.6 g of wax were pressed at 300 N/cm² pressure to produce discs with 4 cm diameter. These discs were subjected to XRF analysis.

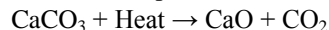
D. X-ray Diffraction

The mineralogical analysis of the phosphate ore was carried out by X-ray diffraction (XRD), using Cu K α ($\lambda = 1.54056 \text{ \AA}$) radiation over the range from 5° to 80° on a X-ray diffractometer (X'Pert PRO, PANalytical, Netherlands) at a scan rate of 0.05°/s. The voltage and anode current were 40 kV and 30 mA, respectively. Phase identification was conducted with the aid of the computer software X'Pert High Score Plus.

E. Thermal Treatment

Thermal Treatment of phosphate ore was carried out by calcinations. Calcination is conducted in a muffle furnace. As per findings of many researchers, coarse particles perform better than fine one in a static bed calciner [12], [13]. So we excluded the fine particles and selected the particles of coarse size (-10+18 mesh). The temperature was raised to 850°C at a rate of 20 °C/min. The 2 g sample taken in porcelain crucibles was calcined for several time intervals in the range of 10-70min at 850 °C in air atmosphere, and then cooled in a

desiccator. The weight of all the samples were recorded before and after calcination to determine loss on ignition and ultimately grade (% P₂O₅) was determined. The decomposition of CaCO₃ takes place at 850°C by the following reaction.



The CaO formed is subsequently removed by washing and a higher-grade phosphate product is achieved [14].

F. Thermo-gravimetric Analysis (TGA) and EDS

The thermo-gravimetric analysis (TGA/DTG) was conducted, to determine the temperature of CaCO₃ decomposition, in air atmosphere using EXSTAR SII TG/DTA 7300 (Thermo-gravimetric/Differential) analyser. For each analysis 20 mg of ore sample, was heated from room temperature to 900°C at a heating rate of 20°C/min and weight changes were measured. The amount of CaCO₃ decomposition was estimated from the weight loss. For samples, calcined at different time span, SEM-EDS technique was employed to identify the chemical composition of the products on SEM-JEOL 840.

III. RESULTS AND DISCUSSIONS

A. Sample characterization

The X-ray diffraction pattern of representative phosphate ore samples Umm-Wual and Al-Jalamid are shown in Fig. 1 and Fig. 2 respectively. The patterns illustrate sharp peaks representing the high crystallinity of Umm-Wual phosphate and Al-Jalamid ores. Also, the XRD pattern indicated that the raw phosphate samples are mainly composed of calcite, fluorapatite and small amount of silica. On the other hand, chemical analysis show that Umm-Wual phosphate ore contains 32.61% P, 50.75% CaCO₃, 2.75% SiO₂ and 1.57 as CaO/P₂O₅, whereas Al-Jalamid phosphate ore contains 25.91% P, 1.31% SiO₂, 53.13% CaCO₃ and 2.046 as CaO/P₂O₅ (Table.1).

Thus both of the chemical assays are in agreement with the XRD analysis. From the analysis (Fig.1 & Fig.2 & Table. 1), it is obvious that Umm-Wual ore contains higher amount of P₂O₅ which is marginally higher than the commercially grade phosphate requirement. In addition, it has lower CaO/P₂O₅ so it requires lower quantity of sulfuric acid i.e., 2.95 tons/ton of P₂O₅ for the production of phosphoric acid. Consequently, it requires no beneficiation and can be used directly for phosphoric acid production.

As far as Al-Jalamid phosphate ore is concerned, it contains lower quantity of P₂O₅ and higher CaO/P₂O₅. Consequently it will consumes higher quantity of sulfuric acid i.e., 3.89 tons/ton of P₂O₅ for the phosphoric acid production if it is used without processing. Eventually, beneficiation is an important step for this ore to raise its P₂O₅ content in order to reduce the high consumption of sulfuric acid and also to overcome the expected foaming problems in the acidulation due to the high organic and carbonate contents. Two main beneficiation techniques can be recommended for the present ore; i.e., flotation and calcination.

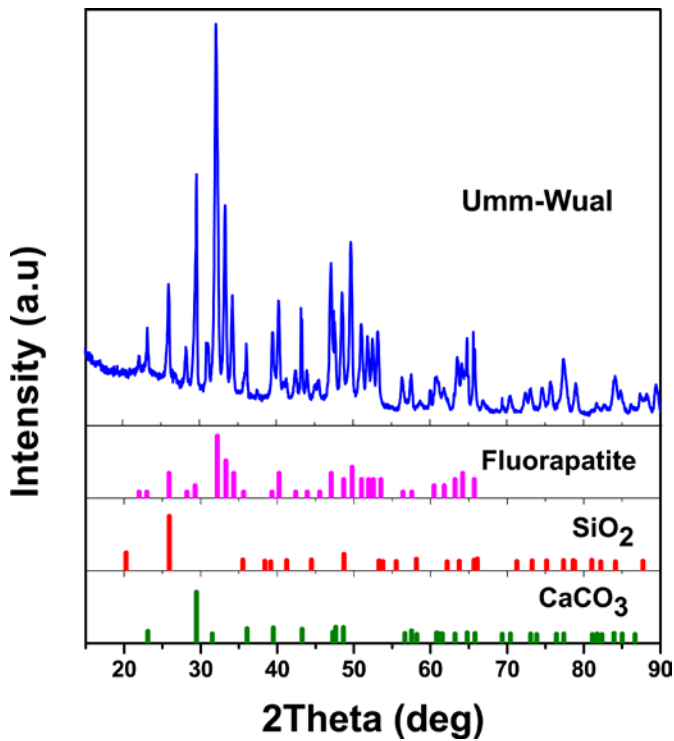


Fig. 1. XRD pattern of Umm-Wual phosphate ore.

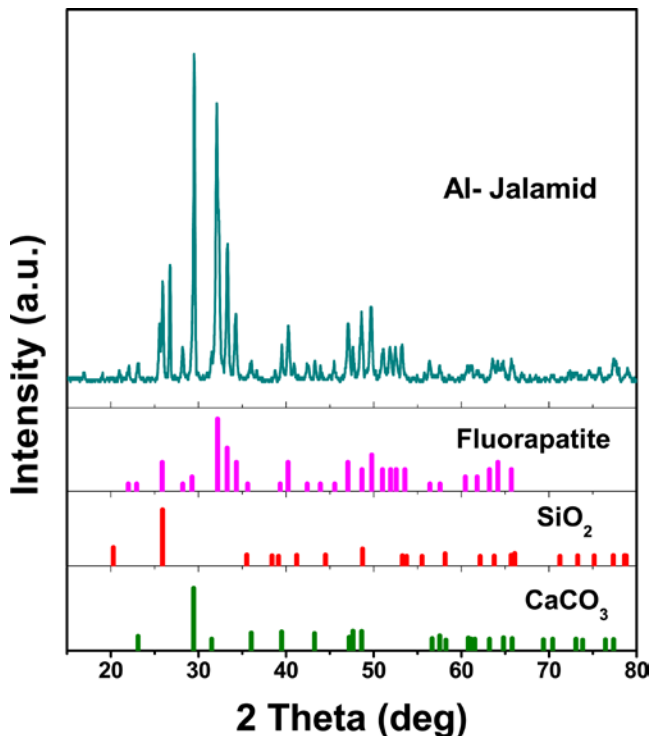


Fig. 2. XRD pattern of Al-Jalamid phosphate ore.

TABLE 1: CHEMICAL ANALYSIS OF SAUDI (AL-JALAMID AND UMM-WUAL) PHOSPHATE ORE.

Constituent	Percentage by Weight
-------------	----------------------

	Saudi Ore		Commercial
	Umm-Wual	Al-Jalamid	Range
P ₂ O ₅	32.61	25.91	29-38
CaO	50.75	53.13	45-54
SiO ₂	2.75	1.31	0.2-8.7
Al ₂ O ₃ +Fe ₂ O ₃	0.44	0.31	0.4-3.4
MgO	0.19	0.5	0.05-0.8
Na ₂ O	0.86	0.21	0.1-0.9
CO ₂	3.8	9.24	0.2-7.5
F	0.84	0.1	2.2-4.35
Cl	2.52	0.03	0-0.5
SO ₃	2.27	2.22	0-3.0
CaO/P ₂ O ₅	1.57	2.046	1.28-1.65

The first operation consumes a large amount of water (about 4.0 kg water kg⁻¹ of ore), which represents a limitation for the process in Saudi Arabia due to scarcity of water. Thus this method seems no more feasible to be used in Saudi Arabia. The second method is a dry process and requires only heat energy which is abundant and not expensive in Saudi Arabia.

B. Effect of temperature

Effect of temperature on phosphate ore size (-10+18 mesh) was determined by using thermo-gravimetric analysis (TGA). Fig. 3 illustrates a nominal weight loss at 100°C due to moisture removal which is termed as drying. While the slightly weight loss at 500- 600°C representing the removal of organic matter which can be considered as roasting [14]. There is a sudden weight loss which starts at 700°C till 850°C and eventually it reaches a plateau.

In the same way, the DTG plot presented in Fig. 3 shows only one very sharp and dominant peak. In fact this peak corresponds to the decomposition, an endothermic reaction, of carbonate species present in the ore. It is also quite worthy to note that no appreciable weight loss has been happened at temperature below 700°C. On the other hand, a noticeable weight loss occurred at temperature range (700–850°C) whereas further increase in calcination temperature (>850°C) has no measurable effect on both weight loss and P₂O₅ content. Consequently the result in Fig. 3 reveals that the most appropriate calcination temperature is 850°C.

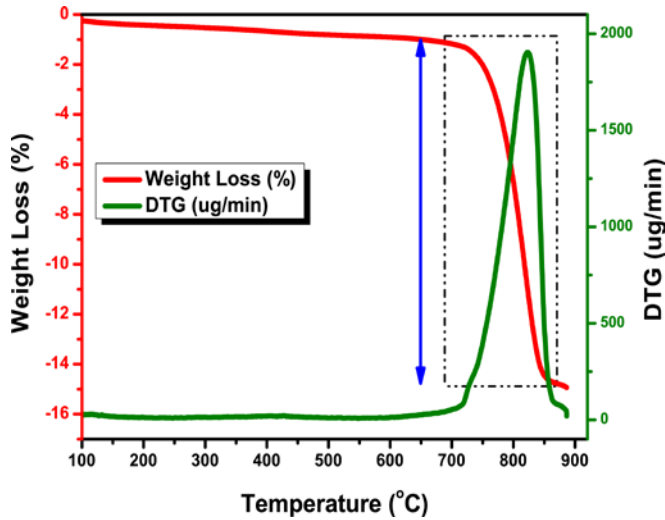


Fig. 3. TGA/DTG data of Al-Jalamid ore.

C. Effect of time

It is clear from the Fig. 4 that there is sudden increase in the grade (P_2O_5 %) of phosphate ore until it reaches its maximum in 50 min and there is no further increment in the grade on increasing the time. Likewise on increasing the time, removal of carbon dioxide takes place abruptly and almost all of the carbon dioxide is removed in 50 min and have no more effect on prolonging the time.

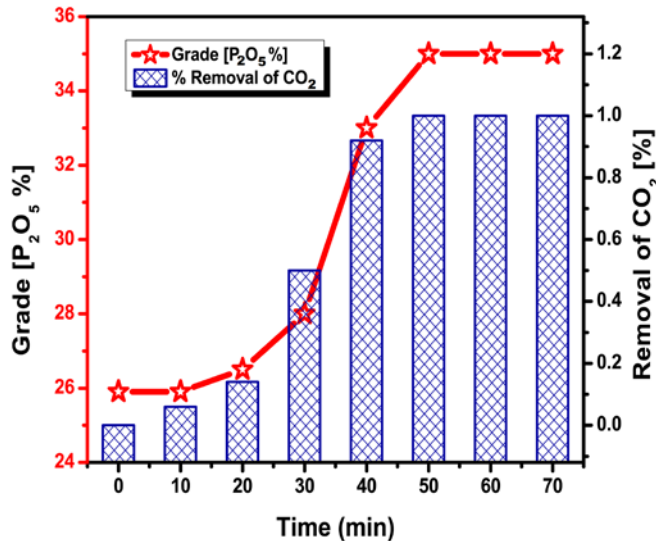


Fig. 4. Effect of time on grade and removal of carbon dioxide for Al-Jalamid phosphate ore.

In addition, SEM-EDX testifies the findings of calcination experiments. Fig. 5a shows the peak of carbon which depicts the presence of calcium carbonate at 30 min. It implies that there is no complete decomposition of $CaCO_3$ achieved at this time and hence the process of calcination is premature now. On the other hand, Fig. 5b shows no sign of carbon and an increase in P_2O_5 content. Since, there is no peak of carbon was observed; hence, it is plausible to say that 100% conversion of

$CaCO_3$ into CaO has been accomplished, for Al-Jalamid phosphate ore of size (-10+18 mesh), after 50 min of heat treatment.

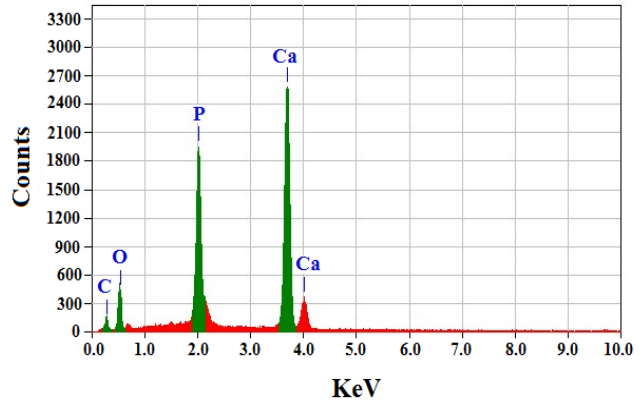


Fig. 5a. EDX of Al-Jalamid ore calcined for 30 min.

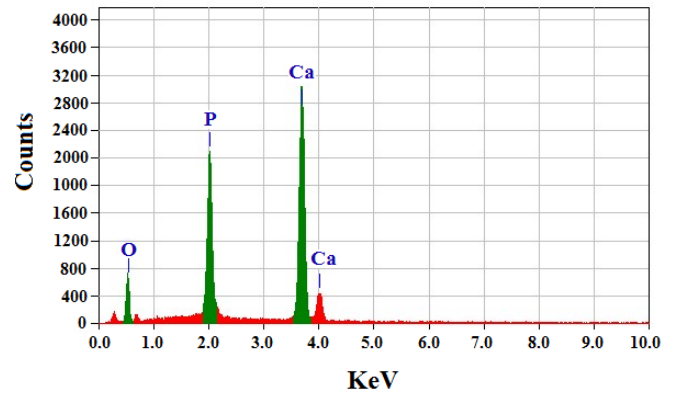


Fig. 5b. EDX of Al-Jalamid ore calcined for 50 min.

D. Reduction in Sulfuric acid consumption

The theoretical amount of H_2SO_4 (100% basis) required per ton P_2O_5 produced can be estimated from the following equation

$$t_{H_2SO_4} = \left(\frac{1.732f_{CaO}}{f_{P_2O_5} - 0.02f_{CaO}} - \frac{1.225f_{SO_3}}{f_{P_2O_5}} + 0.062 \right) * \frac{100}{100 - \%SL}$$

Where $t_{H_2SO_4}$ is tons of 100 w % H_2SO_4 /ton of P_2O_5 produced; $f_{P_2O_5}$, f_{CaO} , f_{SO_3} are weight fractions of P_2O_5 , CaO , SO_3 in the phosphate ore; %S.L. is % water soluble P_2O_5 due to filtration and based on P_2O_5 in the feed ore; %S.L. is usually about 1.5%; %S.L. will be obtained experimentally by the analysis of the dry gypsum cake.

As the grade (P_2O_5 %) of Al-Jalamid phosphate ore has increased so the CaO/P_2O_5 has also been decreased. Consequently the requirement of sulfuric acid (tons sulfuric acid/ton of P_2O_5) for the production of phosphoric acid has decreased from 3.89 (tons sulfuric acid/ton of P_2O_5) to 2.99 (tons sulfuric acid/ton of P_2O_5). Also Fig. 6 shows the comparison of Al-Jalamid ore with different ores. Fig. 6 illustrates a correlation between CaO/P_2O_5 and sulfuric acid requirement that CaO/P_2O_5 and sulfuric acid requirement are directly proportional to each other.

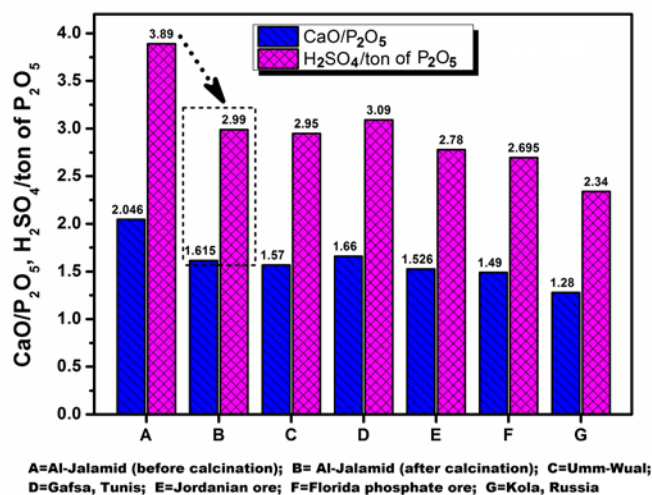


Fig. 6. Relation between CaO/P₂O₅ & tons H₂SO₄/ton of P₂O₅

IV. CONCLUSIONS

In this study, we acquired the lower consumption of sulphuric acid during acidulation in phosphoric acid production by reducing the CaO/P₂O₅. This article leads to the following conclusions:

- XRD and chemical assay reveal that Umm-Wual phosphate ore has higher grade and lower amount of CaCO₃ than Al-Jalamid ore. So its CaO/P₂O₅ is low and it requires lower quantity of sulphuric acid i.e., 2.95. Fortunately, it requires no beneficiation and can be used directly in acidulation process.
- Al-Jalamid phosphate ore has higher CaO/P₂O₅ than market specification for the production of phosphoric acid. Thus it is mandatory to concentrate Al-Jalamid phosphate ore to minimize the sulphuric acid consumption.
- Calcination is considered as the most suitable process to beneficiate the Al-Jalamid ore. Calcination is carried out in static bed Muffle furnace for temperature and different time ranges for the phosphate ore of size -10+18 mesh.
- The optimum calcination duration for which the maximum grade and maximum conversion achieved was found to be 50 min while the optimum temperature was 850°C.
- After calcinations, the grade of the phosphate ore was enhanced by about 35% and eventually CaO/P₂O₅ is reduced.
- The consumption of sulfuric acid has decreased from 3.89 (tons sulfuric acid/ton of P₂O₅) to 2.99 (tons sulfuric acid/ton of P₂O₅) by calcinations of Al-Jalamid phosphate ore and it is comparable with different ores.

ACKNOWLEDGMENT

The authors gratefully acknowledge their appreciation to the Deanship of Scientific Research and the Research Centre at the College of Engineering, King Saud University for supporting this work.

REFERENCES

- [1] H. Sis, and S. Chander, "Reagents used in the flotation of phosphate ores: a critical review," *Min. Eng.*, vol. 16, pp. 577–585, July 2003.

- [2] F. Hernainz, M. Calero and G. Blazquez, "Flotation of low grade phosphate ore," *Adv. Powder Technol.*, vol. 15(4), pp. 421–433, 2004.
- [3] M. Mohammadkhani, M. Noaparast, S. Z. Shafaei, A. Amini, E. Amini and H. Abdollahi, "Double reverse flotation of a very low grade sedimentary phosphate rock, rich in carbonate and silicate," *Int. J. of Min. Process.* vol. 100, pp.157–165, July 2011.
- [4] A.-Z. M. Abouzeid, "Physical and thermal treatment of phosphate ores-An overview," *Int. J. Miner. Process.*, vol. 85, pp. 59-84, Jan. 2008.
- [5] M. Gharabaghi, M. Irannajad and M. Noaparast, "A review of the beneficiation of calcareous phosphate ores using organic acid leaching," *Hydrometallurgy*, vol. 103, pp. 96–107, June 2010.
- [6] A.-Z. M. Abouzeid, A. T. Negm and D. A. Elgillani, "Upgrading of calcareous phosphate ores by flotation: Effect of ore characteristics," *Int. J. Miner. Process.*, vol. 90 pp. 81-89, Feb. 2009.
- [7] S. I. Abu-Eishah and N. M. Abu-Jabal, "Parametric study on the production of phosphoric acid by the dihydrate process," *Chem. Eng. J.*, vol. 81 pp. 231–250, January 2001.
- [8] Melike Sinirkaya, A. Kadir Özer and M. Sahin Gülaboglu, "Investigation of the changes of P₂O₅ content of phosphate rock during simultaneous calcination/sulfation," *Powder Technol.*, vol. 211, pp. 72–76, April 2011.
- [9] T. Heydarpour, B. Rezai and M. Gharabaghi, "A kinetics study of the leaching of a calcareous phosphate rock by lactic acid," *Chem. Eng. Res. Des.*, vol. 89, pp. 2153–2158, October 2011.
- [10] T. F. Al-Fariss, H. O. Ozbelge and H. S. El-shall, "On the phosphate rock beneficiation for the production of phosphoric acid in Saudi Arabia," *J. King Saud Univ. Eng. Sci.*, vol. 4(1), pp. 13-32, 1992.
- [11] X. Zheng and R. W. Smith. "Dolomite depressants in the flotation of apatite and colophane from dolomite," *Min. Eng.*, Vol. 10, No. 5. Pp. 537-545, May 1997.
- [12] R. H. Borgawardt, "Calcination kinetics and surface area of dispersed limestone particles," *AICHE J.*, vol. 31, pp. 103–111, June 1985.
- [13] A. A. El-Midany, F. A. Abd El-Aleem and T. F. Al-Fariss, "Why do relatively coarse calcareous phosphate particles perform better in a static-bed calciner?," *Powder Technol.*, vol. 237, pp. 180–185, March 2013.
- [14] A. K. Özer, "The characteristics of phosphate rock for upgrading in a fluidized bed," *Adv. Powder Technol.*, vol. 14, pp. 33–42, 2003.

Yasir Arafat was born in Pakistan. He obtained his Bachelor degree in



chemical engineering at the Institute of chemical engineering and Technology, University of Punjab, Lahore Pakistan in 2010. During the course of his undergraduate degree, he undertook an internship at Pak-Arab fertilizers, Pakistan's leading fertilizer industry. He served at the National university of Science and technology (NUST), Islamabad Pakistan. He got his M.S degree from the department of chemical engineering, King Saud University (KSU), Riyadh, Saudi Arabia in 2013. Currently, he is serving as a researcher at KSU, KSA. His research interest includes phosphate ore beneficiation through flotation and calcinations, sustainable energy and waste water treatment.

Muhammad Awais Naeem was born in Pakistan in 1988. He has



obtained his bachelor degree in the field of Chemical Engineering from Institute of Chemical Engineering and technology, University of the Punjab, Pakistan in 2010. He got his M.S degree from chemical engineering department, King Saud University (KSU), Riyadh, Saudi Arabia. Currently, he is working as a researcher in Chemical Engineering Department, King Saud University, Kingdom of Saudi Arabia. He has published several research articles in the field of dry reforming of methane. His research interests include syngas production, reforming technology, catalyst development, hydrogen energy, nano-materials, Fisher Tropsch synthesis, greenhouse gases utilization, tri reforming and catalytic decomposition of methane.

Assessment of orthopedic device associated with carbonated hydroxyapatite on the metabolic response in liver tissue

Samira Jebahi, Hassane Oudadesse, Zoubair Ellouz, Tarek Rebai, Hafedh El Feki, Hassib Keskes, Abdelfatteh Elfeki

Abstract-- Bioceramics have been used experimentally and clinically in orthopedic field. Stainless steels device are widely used biomedically especially for fixation of hard. This study aimed to characterize the oxidative stress biomarker and the antioxidant enzyme profiles on the metabolic response in liver tissue. Malondialdehyde (MDA) concentration, superoxide dismutase (SOD), catalase (CAT) and glutathione peroxidase activities (GPx) were measured in tissue liver. Different biochemical parameters such as Aspartate aminotransferase (AST), alanine aminotransferase (ALT) and alkaline phosphatase (ALP) activities were measured in plasma. During the first 4 weeks non significant variation was noted in MDA, SOD and CAT activities. However a significant damage was noted in GPx activities when compared with control. In addition non significant variation for AST and ALT was noted. However a significant variation in PAL activities when compared with that of control was noted. After 8 weeks of implantation, the oxidative stress profile and the biochemical parameters were normalized when compared to that of control. These results suggest the 60-day period was sufficient to re-establish oxidant–antioxidant balance.

Keywords--- Oxidative stress, Liver, Hydroxyapatite, Orthopedic device, Oxidative Stress.

I. INTRODUCTION

Hydroxyapatite (HA) is largely used as bone defect fillers thanks to their biocompatibility, chemical stability, and compositional similarity to the bone mineral phase and thus their ability to form a direct chemical bond with this living tissue [1]. Moreover, this bioactive ceramic is considered as an osteoconductive, non-toxic, non-inflammatory, and nonimmunogenic agent [2]. On the other hand, the use of stainless steels in the field of trauma and orthopedic surgery as well as in orthodontic appliances are widely used biomedically especially for the replacement or support of broken bones with plates or screws, the replacement of joints at the hip or knee, and the fixation of hard tissues in dentistry [3].

Jebahi Samira is with the University of Rennes 1, UMR CNRS 6226, 263 Avenue du General Leclerc, 35042 Rennes Cedex, France (phone: 0021653762227; fax: 0021674 274 437; e-mail: jbahisamira@yahoo.fr).

Hassane Oudadesse, is with the University of Rennes 1, UMR CNRS 6226, 263 Avenue du General Leclerc, 35042 Rennes Cedex, France.

Tarek Rebai, is with the Laboratory of Histologie, Embryologie, Faculty of Medicine, University of Sfax, Sfax, Tunisia.

Hafedh Elfekih is with the Science Materials and Environment laboratory, Sfax Faculty of Science, Sfax, Tunisia.

Zoubair Ellouz Hassib Keskes is with the Orthopaedic and Traumatology laboratory Sfax

Faculty of Medicine Sfax, Tunisia.

Abdelfatteh Elfeki is with the Animal Ecophysiology Laboratory, Sfax Faculty of Science, Department of Life Sciences, Sfax, Tunisia

Despite their highly generalized corrosion resistance, due to the formation of oxide passivation films upon implantation [4] and good mechanical properties, surface corrosion (e.g., crevice corrosion and pitting corrosion) occurs [5], promoting release of small amounts of metal ions into the surrounding biological tissues as well as in extracellular body fluids or in distant organs, such as the liver and kidney [6]. In fact, many reports assessed the performance of the implant through the tissue interaction and the possible migration of metallic ions from the base metal to the nearby tissue [7]. Adverse effects induced by nickel (Ni) have been tackled

and embrace questions of mutagenicity, carcinogenic activity, immunotoxicity and allergic reactions in patients. In our previous study [8], the association between HAP and an orthopedic device (External fixator) (EF) was used to evaluate their effects on oxidative balance in rat bone. Results obtained clearly indicate that the 8-week period was sufficient to re-establish oxidant–antioxidant balance accompanied by bone repair in the tibia rabbit model. In the present study a series of experiments was designed to evaluate the alterations occurring in the liver to explain the toxicity of different ions (Ni, Fe, Cr) when released from metallic implantable biomaterials.

II. MATERIALS AND METHODS

A. Experimental design

Hydroxyapatite (HAP) powder was sterilized by γ -irradiation from a ^{60}Co Source gamma irradiation at a dose of 25 Gy (Theratron external beam teletherapy, Equinox, Ottawa, ON, Canada). The tibia was implanted and stabilized by mini external fixator constitute with Fe + Ni + Cr (>10.5 % + C (<1.2 %)). Anesthesia was induced with 10 mg/kg of ketamine (KetaminoL, Intervet International GmbH, Unterschleibheim, Germany) and 0.1 mg/kg of Xylazine (Rompun, Bayer Healthcare, Puteaux, France). Supplemented local anesthesia was applied after 15–20 min using 4 mg/kg carprofen (Rimadyl, Pfizer, Paris, France). Cutaneous and sub-cutaneous incisions on the inner face of the tibia followed by an opening of the muscular aponeurose were carried out. A gap (1 cm in diameter) in the mid-diaphyseal level of the tibia was created aseptically. HAP and EF were applied for rabbit group (HAP + EF). During a period of 4 and 8 weeks, the subjects were checked daily for clinical lameness or other complications (sacrifice including death). The closure of the wounds was performed in layers (i.e., fascias and the subcutaneous tissue), using resorbable material (Vicryl 3/0;

Ethicon, Germany) in a continuous fashion. The handling of the animals was approved by the Tunisian Ethical Committee for the care and use of laboratory animals.

B. Determination of AST, ALT and ALP activities:

Aspartate aminotransferase (AST) and alanine aminotransferase (ALT) activities were measured colourimetrically in plasma according to the method described by Reitman and Frankel [9]. Total alkaline phosphatase (ALP) were examined using commercial Biomaghreb kits (Tunisia).

C. Hematological and Biochemical assays

White Blood Cell (WBC) count, Red Blood Cell (RBC) count, Hemoglobin Concentration (Hb), Hematocrit (Ht), Platelets, and Mean Corpuscular Volume (MCV) were measured by electronic automate coulter MAXM (Beckman Coulter, Inc., Fullerton, USA), Alkaline phosphatase (ALP) were examined using commercial Biomaghreb kits (Tunisia).

D. Tissue preparation

The bone tissues were carefully removed, cleaned, dried and processed for antioxidant enzyme analysis. The implanted femoral condyles of all groups were minced and homogenized (100 mg/ml) at 4 °C in 0.1 mol/l Tris-HCl buffer pH 7.4 and centrifuged at 3,000G for 10 min.

E. Oxidative Stress Measurements

The lipid peroxidation in the bone tissues of control and all treated animal groups was measured by the quantification of thiobarbituric acid-reactive substances (TBARS) determined by the method of Buege and Aust [10]. The activity of superoxide dismutase (SOD) was assayed by the spectrophotometric method of Marklund and Marklund [11]. The glutathione peroxidase (GPx) activity was measured by the method described by Pagila and Valentine [12]. Catalase (CAT) was assayed calorimetrically at 240 nm and expressed as moles of H₂O₂ consumed per minute per milligram of protein, as described by Aebi [13]. The level of total protein was determined by the method of Lowry et al using bovine serum albumin as the standard at 660 nm [14].

F. Statistical Analysis

The statistical data analysis was made using the Student's t test. All values were expressed as mean ± SE.

III. RESULTS AND DISCUSSION

A large number of metal ions such as nickel (Ni) and chromium (Cr) can be released from stainless steel and cause cytokine release and cytotoxicity in human cells [15]. The present study sought to elucidate whether the chemical composition of the EF (Fe + Ni + Cr (>10.5 % + C (<1.2 %) implantation could induce a set of toxicological activities such as oxidative stress in liver. One study

investigated that nickel oxide (NiO) induced cytotoxicity and apoptosis in cultured human airway epithelial (HEp-2) and human breast cancer (MCF-7) cells. NiO was also found to induce oxidative stress in dose-dependent manner indicated by glutathione depletion, ROS induction, and lipid peroxidation [16,17]. MDA level is the most important factor indicating increased peroxidative level, while glutathione is substance with an important role in cell detoxification and protection from hazardous compounds [18]. Glutathione is synthesized in the erythrocytes and is found in living cells. It has been reported that cellular glutathione has an important function against chemical agents by protecting the cell membrane integrity [19]. The main finding in our study was that during the first 4 weeks, a non significant variation was noted in MDA, SOD and CAT activities. However a significant damage was noted in GPx activities when compared with control (Fig1A, B, C, D).

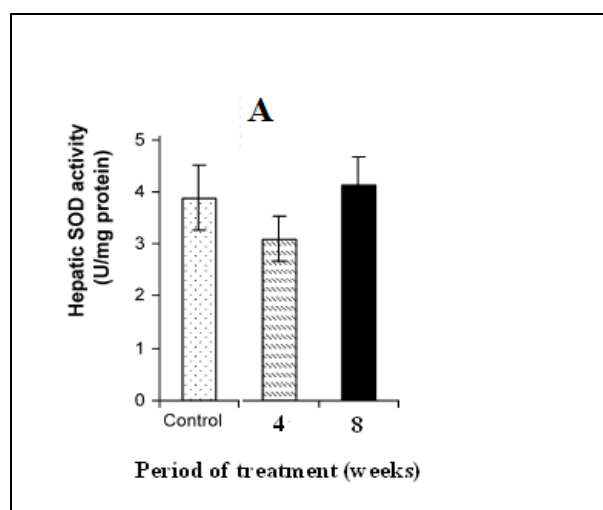


Fig1A. Effects of HAP+EF on superoxide dismutase (SOD). Values are given as mean ± S.E. * significantly less enzymatic activity in the indicated group versus the control group.

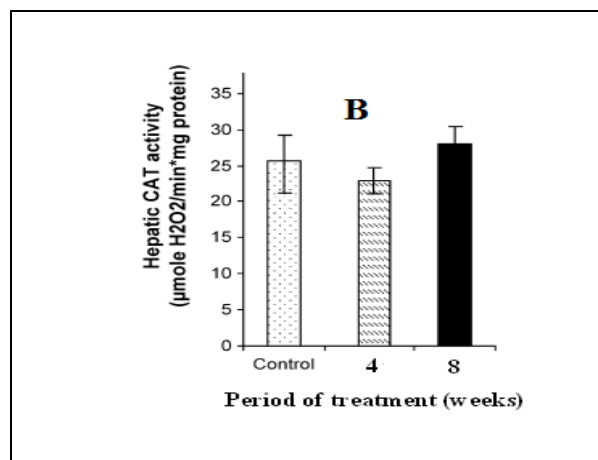


Fig1B. Effects of HAP+EF on catalase (CAT) values are given as mean ± S.E. * significantly less enzymatic activity in the indicated group versus the control group.

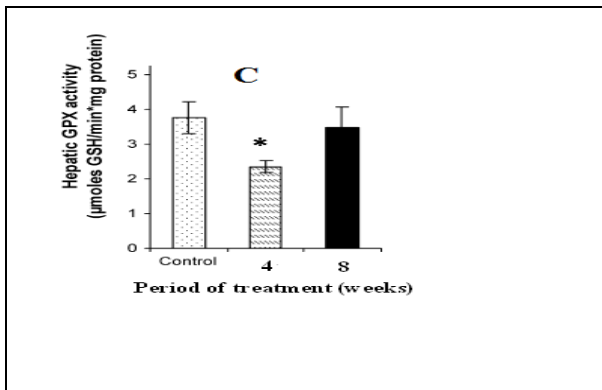


Fig1C. Effects of HAP+EF on glutathione peroxidase (GPx). values are given as mean \pm S.E. * significantly less enzymatic activity in the indicated group versus the control group.

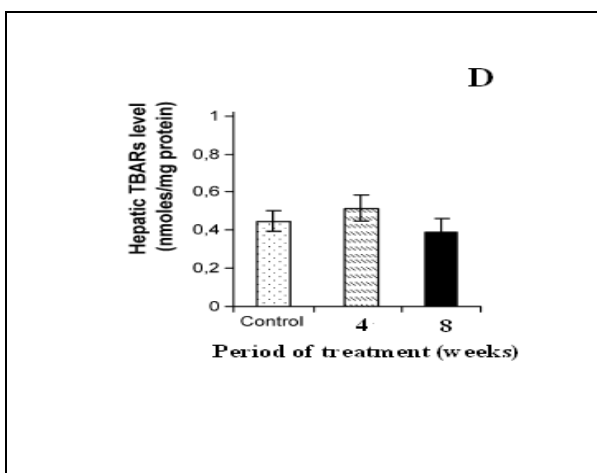


Fig1D. Effects of HAP+EF on MDA (D) concentration in tibia rabbit bone for 4 and 8 weeks. values are given as mean \pm S.E. * significantly less enzymatic activity in the indicated group versus the control group.

In this study, the oxidative stress balance began returned to baseline levels 60 days after surgery. A separate liver enzymes are included on most routine laboratory tests [20]. They are- aspartate aminotransferase (AST) and alanine aminotransferase (ALT). Elevations of these enzymes can indicate the presence of liver disease [21]. In this study, to evaluate the toxicity effect of HAP+EF on the rabbit's liver, the ALT, ALP and AST were measured. ALT and AST were located in cell and ALP was located in cell membrane. Increase of these enzymes are a sign of liver cells damage. ALT and AST indicate status of liver cells [22]. Some metal ions can penetrate lung or dermal (skin) barriers and enter the circulatory and lymphatic systems of humans and animals, reaching most bodily tissues and organs, and potentially disrupting cellular processes and causing disease [23-24]. In the present study, a non significant variation for AST and ALT was noted. However a significant variation in PAL activities when compared with that of control was noted. After 8 weeks of implantation, the the biochemical parameters were normalized when compared to that of control (Fig2, ABC).

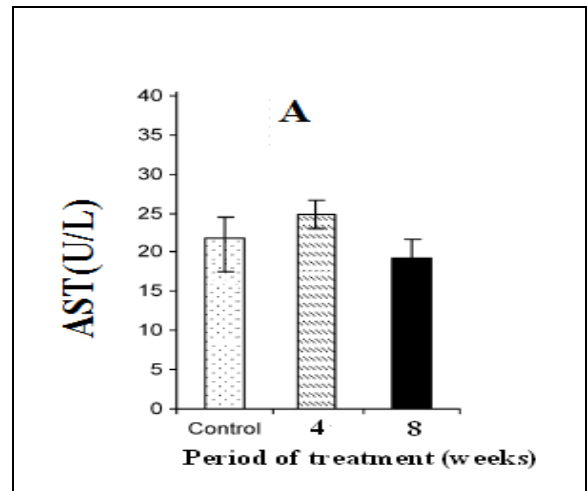


Fig2A. Effects of HAP+EF on AST in tibia rabbit bone for 4 and 8 weeks. Values are given as mean \pm S.E. * significantly less enzymatic activity in the indicated group versus the control group

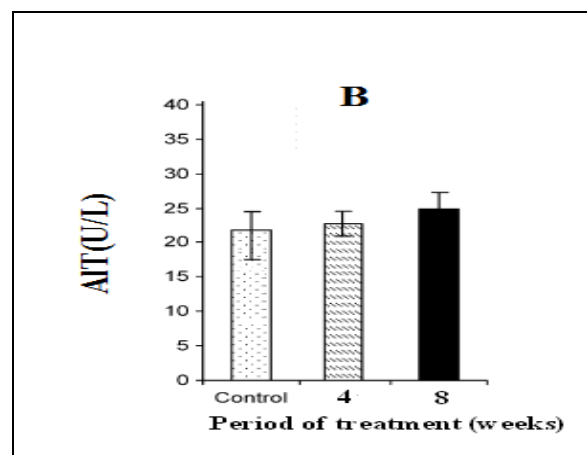


Fig 2B. Effects of HAP+EF on ALT in tibia rabbit bone for 4 and 8 weeks. Values are given as mean \pm S.E. * significantly less enzymatic activity in the indicated group versus the control group

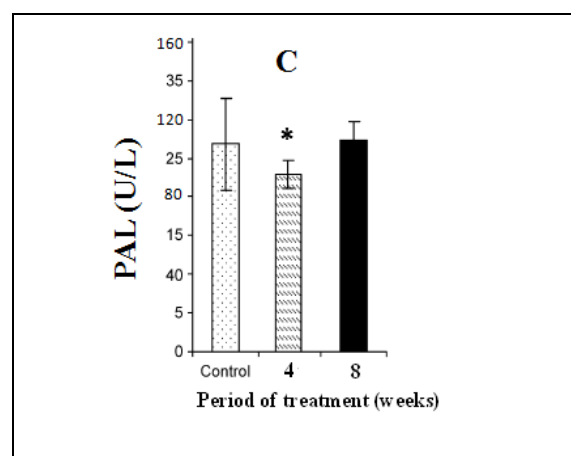


Fig2A. Effects of HAP+EF on PAL in tibia rabbit bone for 4 and 8 weeks. Values are given as mean \pm S.E. * significantly less enzymatic activity in the indicated group versus the control group

The ions, can produce irreversible damage to cells by oxidative stress or/and organelle injury [25]. When the metallic ions accumulated in a tissue, may be absorbed into

the cells or not to be absorbed. If these ions are absorbed, the finally replacement in cell lysosomes or cell cytoplasm will depend on the characteristics of implant materials [26]. If the metallic ions are located in the cytoplasm, the presence of some coarse grain material can cause direct damage or cell death is caused by this interactions. Here we investigated the absence of HAP+EF toxicity effect on ALT, AST and PAL enzymes in male rabbits after after 60 days of implantation.

We conclude that the development of graft material have increased our awareness of device toxicity sources, and hope that this new awareness will lead to significant reduction in human exposure to some potentially toxic materials.

IV.CONCLUSION

According to the present results, the HAP+EF does not lead to liver damage. A significant alteration in liver antioxidant profile and biochemical parameters during the first weeks of implantation was noted. After 8 weeks of treatment, this study demonstrated significantly decrease in MDA concentration level with an increase in the activities of SOD, CAT and GPx. The biochemical parameter such as ALT, AST and ALP were normalized when compared to that of control. In vivo, HAP+ EF had good bioactivity, and oxidative balance stability shown 60 days after surgery. HAP+ EF may be an effective strategy for creating materials for bone repair regeneration therapies.

REFERENCES

- [1] S. Jebahi, M. Saoudi, R. Badraoui, T. Rebai, H. Oudadesse, Z. Ellouz, H. Keskes, A. El Feki, H. El Feki, "Biologic response to carbonated hydroxyapatite associated with orthopedic device: experimental study in a rabbit model", *Korean J Pathol*, vol.46,pp.48-54, Feb. 2012.
- [2] D. Snead, P. Barre, P.K. Bajpai, A. Taylor, D. Reynolds, B. Mehling, A. Longo, D. Nolan, "The use of a zinc based bioceramic as an osteoconductive agent in the rat model". *Biomed Sci Instrum*, vol.31,pp.141-146.1995.
- [3] SA Bencherif, TM Braschler, P Renaud. "Advances in the design of macroporous polymer scaffolds for potential applications in dentistry". *J Periodontal Implant Sci*, Vol.43, pp.251-261.2013.
- [4] M Freedman, LF Stassen, "Commonly used topical oral wound dressing materials in dental and surgical practice--a literature review". *J Ir Dent Assoc*, vol. 59,pp.190-5. 2013.
- [5] N Li, YD Li, YX Li, YH Wu, YF Zheng, Y Han, " Effect of surface mechanical attrition treatment on biodegradable Mg-1Ca alloy". *Mater Sci Eng C Mater Biol Appl*, vol.35,pp.314-21.2014.
- [6] DG Olmedo, DR Tasat, MB Guglielmotti, RL Cabrini, "Biodistribution of titanium dioxide from biologic compartments". *J Mater Sci Mater Med*, vol.19,pp.3049-56, Sep 2008.
- [7] LS Morais, GG Serra, CA Muller, LR Andrade, EF Palermo, CN Elias, M Meyers, "Titanium alloy mini-implants from orthodontic anchorage: immediate loading and metal ion release", *Acta Biomater*, vol. 3,pp:331-9, May 2007
- [8] S Jebahi, R Nsiri, M Boujbiha, E Bourouga, T Rebai, H Keskes, A El Feki, H Oudadesse, H El Feki. "The impact of orthopedic device associated with carbonated hydroxyapatite on the oxidative balance: experimental study of bone healing rabbit model", *Eur J Orthop Surg Traumatol*, vol. 23,pp.759-66.2013
- [9] S .Reitman, S. Frankel, "A colourimetric method for the determination of serum glutamic oxaloacetic and glutamic pyruvic transaminases", *Am J Clin Path*, vol.28,pp. 56-62. 1957
- [10] JA. Buege, SD. Aust, "Microsomal lipid peroxidation". *Methods Enzymol*, vol. 105, pp.302-310.1984.
- [11] S. Marklund, G. Marklund, "Involvement of the superoxide anion radical in the autoxidation of pyrogallol and convenient assay for superoxide dismutase". *Eur J Biochem*, vol. 47,pp. 469-474.1975.
- [12] DE. Pagila, WN. Valentine "Studies on the quantitative and qualitative characterization of erythrocyte glutathione peroxidase". *J Lab Clin Med*, vol. 70,pp.158-169.1967.
- [13] H. Aebi "Catalase in vitro". *Methods Enzymol* vol.105, pp.121-126.1984.
- [14] OH. Lowry, NJ. Rosebrough, AL. Farr, RJ. Randall, "Protein measurement with Folin phenol reagent", *J Biol Chem*, Vol.193,pp.265-275. 1951
- [15] S Alarifi, D Ali, S Alakhtani, ES Al Suhaibani, AA Al-Qahtani. "Reactive oxygen species-mediated DNA damage and apoptosis in human skin epidermal cells after exposure to nickel nanoparticles". *Biol Trace Elem Res*, vol.157,pp.84-93.2014
- [16] M. Ahamed, MJ. Akhtar, MA. Siddiqui, J. Ahmad, J. Musarrat, AA. Al-Khedhairi, MS. AlSalhi, SA. Alrokayan, "Oxidative stress mediated apoptosis induced by nickel ferrite nanoparticles in cultured A549 cells". *Toxicology*, vol.10, pp.101-8. May 2011
- [17] MA. Siddiqui, M. Ahamed, J. Ahmad, M.A. Majeed Khan, J. Musarrat, AA. Al-Khedhairi, SA. Alrokayan. "Nickel oxide nanoparticles induce cytotoxicity, oxidative stress and apoptosis in cultured human cells that is abrogated by the dietary antioxidant curcumin". *Food Chem Toxicol*, vol. 50,pp.641-7. 2012.
- [18] W. Li, J. Chen, P. Xie, J. He, X. Guo, X. Tuo, W. Zhang, L. Wu. "Rapid conversion and reversible conjugation of glutathione detoxification of microcystins in bighead carp (*Aristichthys nobilis*)". *Aquat Toxicol*, vol.8,pp.18-25.2013
- [19] D. Markovic, J. Katic, R. Stojkovic, S. Borovic, N. Zarkovic, A. Fucic, "Lipid peroxidation, detoxification capacity, and genome damage in mice after transplacental exposure to pharmaceutical drugs". *Braz J Med Biol Res.*, vol.10, pp.1014-1020.2013.
- [20] M. Fazilati. "Investigation toxicity properties of zinc oxide nanoparticles on liver enzymes in male rat". *Eur J Exp Biol*, vol. 3,pp. 97-103. 2013
- [21] H. Nyblom, U. Berggren, J. Balldin, R. Olsson. "High AST/ALT ratio may indicate advanced alcoholic liver disease rather than heavy drinking", *Alcohol and Alcoholism*, Vol. 39, pp. 336-339.2004
- [22] P. Das, NB. Chandar, S. Chourey, H. Agarwalla, B. Ganguly, A. Das. "Role of metal ion in specific recognition of pyrophosphate ion under physiological conditions and hydrolysis of the phosphoester linkage by alkaline phosphatase". *Inorg Chem*. Vol.7, pp.11034-41.2013
- [23] S. Silva, G. Pinto, B. Correia, O. Pinto-Carnide, C. Santos, R. ye "oxidative stress under long term Al exposure". *J Plant Physiol.*, vol.1, pp. 879-89.2013.
- [24] L. Lu, M. Zhu. "Protein tyrosine phosphatase inhibition by metals and metal complexes". *Antioxid Redox Signal*. 2014 (Epub ahead of print)
- [25] K. Sakamoto, Y. Suzuki, Y. Kurauchi, A. Mori, T. Nakahara, K. Ishii. "Hydrogen Sulfide Attenuates NMDA-Induced Neuronal Injury via its Anti-oxidative Activity in the Rat Retina". *Exp Eye Res*. 2014. pii: S0014-4835
- [26] HM. Gorr, JM. Zueger, JA .Barnard, "Characteristic size for onset of coffee-ring effect in evaporating lysozyme-water solution droplets", *J Phys Chem B*, vol.11,pp. 12213-20.2012

The performance of $\text{SnO}_2/\text{CdS}/\text{CdTe}$ type solar cell under influence of CdS buffer layer thickness and series resistance R_s

H.TASSOULT and A.BOULOUDA

Abstract— The research in the field of photovoltaic solar energy is expected to improve the conversion efficiency of solar cells while reducing the cost of producing clean energy to ensure a widespread use and make it available to all of us.

The development of photovoltaic energy must go through a search accentuated. Three main axes must be optimized separately by a fundamental choice: the material, the growth technique and structure. In this work we report on the results of the simulation of $\text{SnO}_2/\text{CdS}/\text{CdTe}$ cell type by one-dimensional Scaps-1D simulator [1],[2].

Keywords— Superstrate solar cell, gap, Hall effect..

I. INTRODUCTION

THE operation of the solar cell is generally described by its current-voltage characteristic whose analysis identifies a number of parameters that describe the model non-linear electric solar cells. These parameters are usually the saturation current, the photocurrent, the ideality factor, series resistance and conductance shunts.

Determining the parameters of the solar cell is a very important task in the design phase. Indeed, the model parameters are closely related to internal physical processes acting in the solar cell. Their knowledge is very important to improve the quality of the component during manufacturing and system simulation. Measurements (current-voltage) under illumination and in the dark are usually used to extract these parameters [3],[4], [5].

The aim of this work is to simulate the performance of solar cells under the influence of various CdS buffer layer thickness and series resistance R_s on the parameters of the solar cell using one-dimensional Scaps-1D simulator "Solar Cell Capacitance Simulator in 1 Dimension," for two types of configurations: without SnO_2 : CdS / CdTe / ohmic contact with SnO_2 : $\text{SnO}_2/\text{CdS}/\text{CdTe}/\text{contact}$ resistance and we have presented the results of the simulated current-voltage characteristic and the quantum efficiency of the solar cell based on the variation of these parameters.

II. STRUCTURE OF THE CELL AND MATERIALS PARAMETERS

In this work, we considered a cell type $\text{SnO}_2/\text{CdS}/\text{CdTe}$ whose individual layers constituting it are the following (see Fig.1):

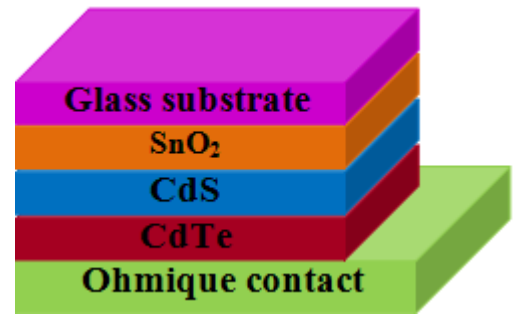


Fig. 1 the structure of the solar cell used

In the simulation, the geometrical parameters of the different layers of the solar cell based on CdTe material were presented in the following table:

The parameters for each layer of the cell have been introduced into Scaps-1D simulator [6].

Table 1: The geometrical parameters of the different layers of the solar cell

parameter	layers		
	SnO_2	CdS	CdTe
W(μm)	0.5	0.025–0.1	4

III. SIMULATION

Simulation calculations discussed in this section use the Scaps-1D simulator application on Windows. It estimates the band diagram, the profile of recombination and a carrier transport one-dimensional and it is based on the Poisson equation and the continuity equations for electrons and holes. The results correspond to the effect of the series resistance and the thickness of the CdS buffer layer on the characteristics and parameters JV: I_{CC} , V_{CO} , and η QE type cells $\text{SnO}_2/\text{CdS}/\text{CdTe}$ determines the performance of the latter.

A. Effect of CdS thickness on the characteristics J-V

Fig.2 represents the characteristic J-V obtained under illumination AM 1.5G in function of the voltage for different values of thickness of the CdS buffer layer.

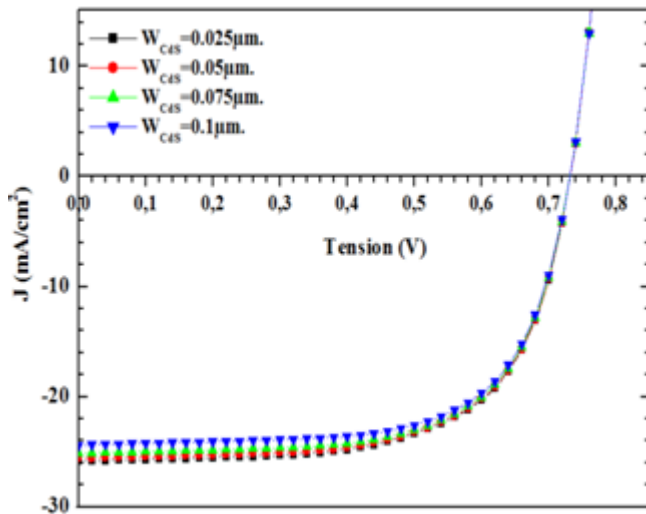


Fig. 2 effect of CdS thickness on the characteristics J-V

We note that the value of the short circuit current I_{CC} is mainly affected and reduced compared to cells using CdS as buffer layer. This is due to recombination at the interface of layers and it can be seen that increasing the thickness of the buffer layer caused a decrease of the latter. As against this, note that the open circuit voltage V_{CO} remains practically constant.

B. Effect of SnO₂ layer on the characteristics J-V

Fig.3 shows the comparison of the current density between the type solar cell SnO₂/CdS/CdTe and the solar cell type CdS / CdTe.

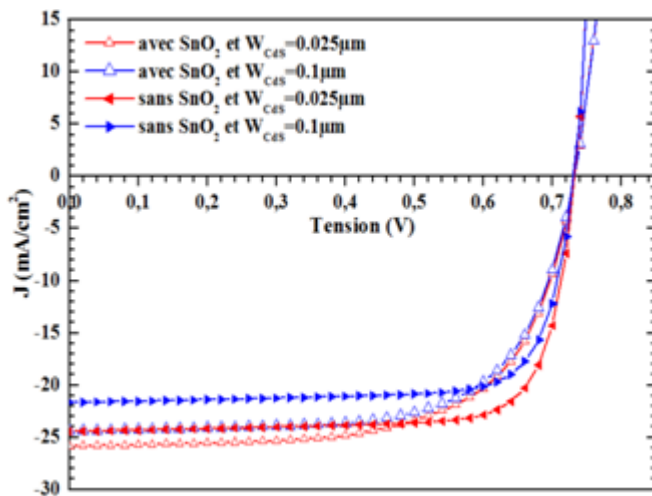


Fig. 3 effect of SnO₂ layer on the characteristics J-V for different thicknesses of the CdS layer

We note that the short-circuit current I_{CC} in a solar cell with SnO₂ layer is higher than that of the solar cell without SnO₂ layer. For cons, efficiency η is less than solar cell without SnO₂ layer and the open circuit voltage V_{CO} remains virtually unchanged after this change.

C. Effect of resistance R_S and thickness W_{CdS} on I_{CC}

Fig.4 shows the effect of thickness on the short-circuit for different values of the series resistance.

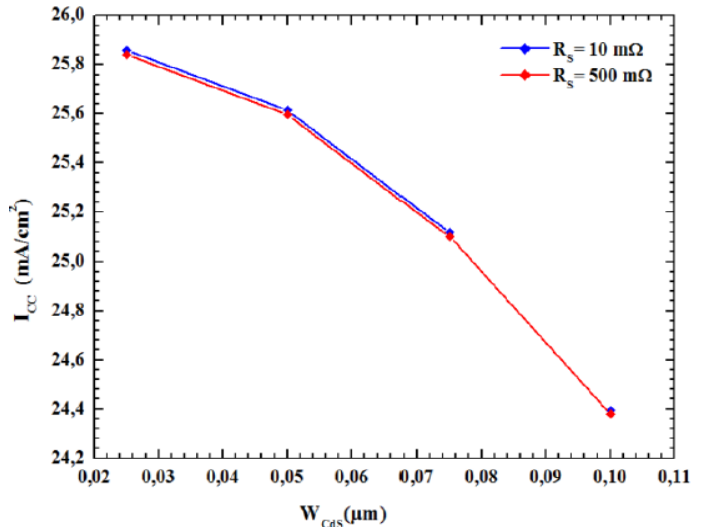


Fig. 4 effect of resistance R_S and thickness W_{CdS} on I_{CC}

We note that the decrease of the short-circuit I_{CC} in accordance with the increase of the thickness of the buffer layer W_{CdS} . For cons, the increase of the series resistance R_S causes only a slight decrease in short-circuits.

D. Effect of resistance R_S and thickness W_{CdS} on V_{CO}

The Fig.5 shows the effect of the thickness of the open circuit voltage for different values of the series resistance.

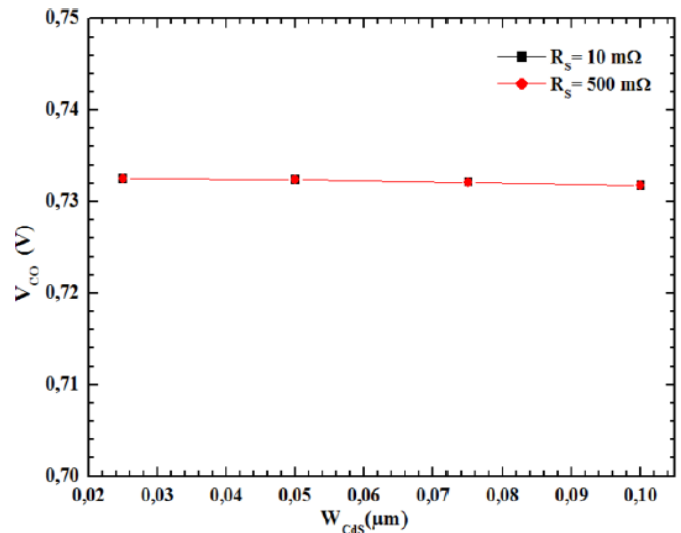


Fig. 5 effect of resistance R_S and thickness W_{CdS} on V_{CO}

We note that when the thickness of the buffer layer increases the open circuit voltage decreases slightly, on the order of a thousandth of millivolt. For cons, the series resistance R_S has no influence on the electrical parameter V_{co} .

E. Effect of resistance R_S and thickness W_{CdS} on the efficiency η

Fig.6 shows the effect of the series resistance and the thickness of the CdS buffer layer on the efficiency η of a solar cell $SnO_2/CdS/CdTe$.

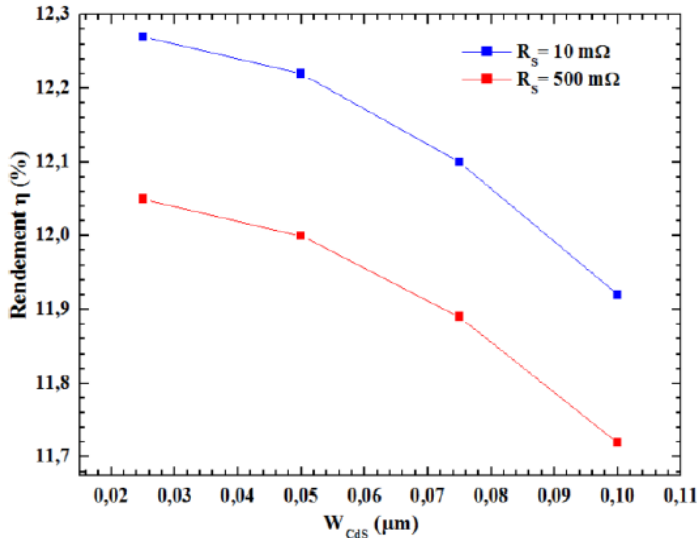


Fig. 6 effect of resistance R_S and thickness W_{CdS} on the efficiency η

We see that when the thickness of the buffer layer increases, the efficiency decreases and even the series resistance. This is due to the decrease in ICC shunt effect caused by a greater thickness of CdS.

F. Effect of SnO_2 on the efficiency η

Fig.7 shows the effect of SnO_2 on the efficiency η for a variation of series resistance R_S and the thickness of the CdS buffer layer.

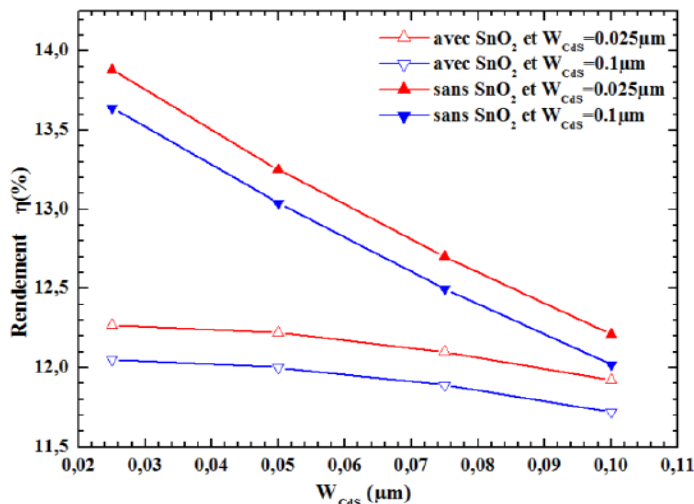


Fig. 7 effect of SnO_2 on the efficiency η

When the thickness of the CdS layer increases, the efficiency decreases more consistently in the absence of the SnO_2 layer and the thickness of CdS affects efficiency the same way.

We note that the performance of the solar cell type CdS / CdTe greater than the efficiency of the solar cell type $SnO_2/CdS/CdTe$.

G. Effect of resistance R_S and thickness W_{CdS} on the QE

Fig.8 represents the variation of quantum efficiency as a function of the wavelength for different values of thickness of the CdS buffer layer.

When the wavelength varies in the range 340-590 microns, increasing of CdS buffer layer thickness reduces the quantum efficiency. In the interval 340-590 microns is the area where the losses are due to the width of the band gap of CdS. These losses are mainly due to the decrease in short-circuit current I_{CC} of the solar cell in the range of the thickness of the CdS layer 500 nm and 250 nm. Therefore, there is a decrease in the quantum efficiency. Thus when the thickness of the CdS buffer layer increases from 250 nm to 500 nm, the quantum efficiency decreases. While in the interval 590-800 microns in wavelength, the influence of CdS buffer layer thickness on the quantum efficiency is very low.

H. Effect of SnO_2 on the quantum efficiency QE

Fig.9 represents the variation of quantum efficiency as a function of the wavelength for different values of thickness of the CdS buffer layer.

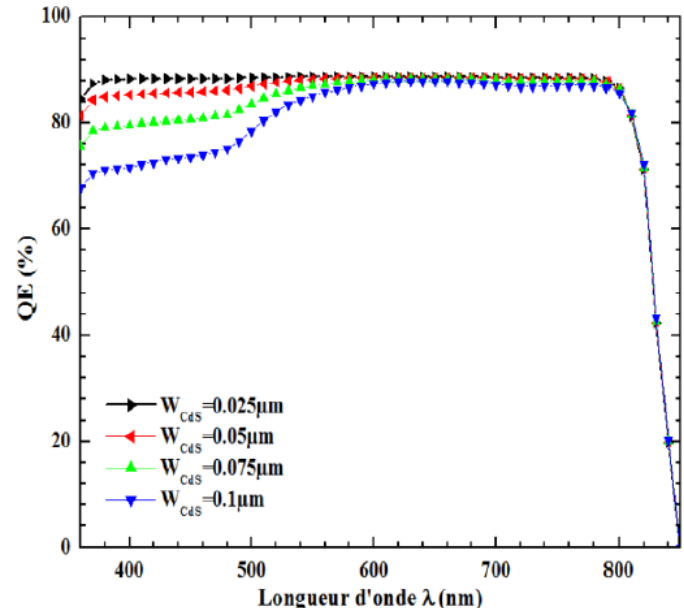


Fig. 8 the quantum efficiency for different thicknesses of CdS layer of cell solaire $SnO_2/CdS/CdTe$.

We note that the first structure $SnO_2/CdS/CdTe$ provides a higher short circuit current J_{CC} compared to the second structure CdS / CdTe. This is due to absorption losses of the conductivity of SnO_2 contact on the second structure, while in

the first structure there are no losses due to SnO_2 , therefore better quantum efficiency QE for the first structure.

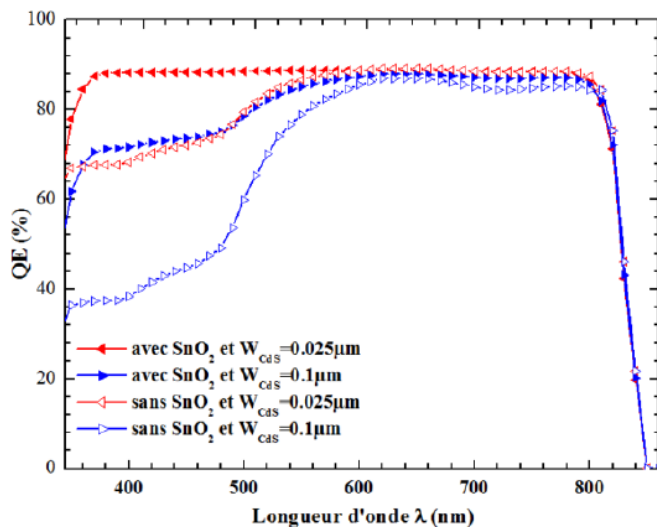


Fig. 9 effect of SnO_2 on the quantum efficiency QE for different thicknesses of the CdS layer

IV. CONCLUSION

A simulation model for a solar cell based on a structure of type $\text{SnO}_2/\text{CdS}/\text{CdTe}$ with a surface inversion layer and using as CdS buffer layer was characterized with a simulation program Scaps component.

It has been shown numerically that the performance of the solar cell $\text{SnO}_2/\text{CdS}/\text{CdTe}$ are much more sensitive to the thickness of the CdS layer compared to the standard cell CdS / CdTe. The results show the influence of the thickness, the series resistance and the SnO_2 layer on the properties of solar cells based on CdTe

The simulation led us to results that clearly show the influence of these parameters on the JV and QE curve for the cell types studied. We note that the performance of the cell depends on the thickness of CdS and the series resistance RS.

- The decrease in the thickness of the CdS buffer layer and series resistance provide the best photovoltaic performance of the solar cell.

- The first $\text{SnO}_2/\text{CdS}/\text{CdTe}$ structure provides a higher short circuit current J_{CC} in relation to the second structure CdS / CdTe
- Better quantum efficiency QE for the first structure
- The presence of the SnO_2 layer plays a very important role in improving performance

REFERENCES

- [1]. A.Bouloufa, K. Djessas, and A. Zegadi, *Thin Solid Films* vol 515 ,2007, pp.6285-6287.
- [2]. S. Khelifi and A. Belghachi, “Le Rôle de la Couche Fenêtre dans les Performances d’une Cellule Solaire GaAs”, BP N° 417, Vol.7, pp. 13-21, Algérie, 2004.
- [3]. A.Bouloufa, “Etude et Caractérisation des Semi-conducteurs Ternaires et Quaternaires $\text{CuIn}_{1-x}\text{Ga}_x\text{Se}_2$ par Spectroscopie Photoacoustique”, PhD , Dept electronic, Ferhat-Abbas University, Sétif, Algeria, 2007.
- [4]. I.Bouchama, “Contribution à l’amélioration des performances des cellules solaires $\text{CuIn}_{1-x}\text{Ga}_x\text{Se}_2$ ”, PhD , Dept electronic, Ferhat-Abbas University, Sétif, Algeria, 2012.
- [5]. A.Bouloufa, K. Djessas, and D. Todorovic, *Mat. Sci. Semicon. Proc.* 12, 2009.
- [6]. I. Bouchama, K. Djessas, F. Djahli and A. Bouloufa “Simulation approach for studying the performances of original superstrate CIGS thin films solar cells” *Thin Solid Films* vol 519 ,2011, pp.7280-7283.

Fabrication, sealing and hydrophilic modification of microchannels by hot embossing on PMMA substrate.

Alireza Shamsi, Saeed Delaram, Mehrnaz Esfandiari and Hasan Hajghassem

Abstract— In this paper, microchannel fabrication and sealing using a low cost hot embossing method with a simple technique to make them hydrophilic is presented. The proposed method uses low cost materials and procedure, with respect to previous methods and can be performed in a short time. The master is made from SU-8 on an inexpensive glass substrate which is patterned by standard lithography. Microchannels are replicated on a Polymethylmethacrylate (PMMA) stamp which is hydrophobic. A novel method is used to modify the surface of the Polymer to make it hydrophilic. The polymeric substrate is immersed in KI:I2 solution to be made hydrophilic. Effect of immersion time, which is a significant parameter, is discussed. Some sealing methods are compared and an optimum technique is used to seal microchannels. The microchannels are sealed by a PMMA sheet cap using thermal annealing bonding. Microchannels are imprinted by depth of 50 μ m and minimum width of 15 μ m.

Keywords— hydrophilicity, microchannel, sealing, microfluidics

I. INTRODUCTION

Microelectromechanical Systems (MEMS) have been used in numerous fields of science such as electronics, navigation, chemical industry and biology in recent years [1]-[2]. Although in most cases, silicon and glass-based processes are the first choice for MEMS device fabrication, they exhibit some limitations due to their complex procedures, geometrical design restrictions and cost involved [3]-[4]. On the other hand, because of low bio-compatibility, no transparency and low robustness of Silicon, it has limited applications in some technologies such as Optics and Bio-MEMS.

In contrast, due to the major advantages of polymer-based processes, such as simplicity, low cost, convenience to batch fabrication and less using of any harmful chemical etchants

[1]-[3], Polymer microfabrication has become a popular alternative to the established silicon and glass-based MEMS fabrication technologies [5]. Some significant features of polymers including biocompatibility, flexibility, transparency, low electrical conductance, high chemical stability and low cost of polymers are unrivaled and make them as a main material instead of silicon and glass for some MEMS devices, particularly, in microfluidics and lab-on-a-chip (LOC) applications [3],[6].

In recent years, polymer-based fabrication techniques, called soft lithography, have been developed and a wide range of soft lithography methods such as injection molding, casting, hot embossing and laser ablation are offered. These methods are advantageous in fabrication of Bio-MEMS devices, chemical sensors and disposable analytical components [7]. Among them, hot embossing has attracted much interest due to its efficiency, ease of processing, accuracy, moderate cost, and possibility of batch fabrication [3],[8], which can be chosen as an adequate replacement for silicon based process [2],[7].

Hot embossing is stamping of patterns into a polymer substrate by increasing the temperature above the polymer's glass transition point (T_g) [6]. In this process, complicated and expensive micromachining process would be necessary to produce one master only. When the master is fabricated, the flipped structure can be imprinted on thermoplastic stamp for several times using hot embossing process [9]. Thermoplastic polymers differ from elastomers and thermoset plastics in the sense that they are able to reshape upon heating and save their chemical and physical properties after cooling down [10]. Generally, hot embossing is carried out in three basic steps. Firstly, mold and polymeric stamp, heated above the glass transition temperature of stamp to make it deformable. Next, the mold is pressed to substrate by a certain pressure and pattern of the mold replicates on substrate. Finally, when the preset embossing time is spent, the system cooled down below the transition point of substrate. At this temperature, mold and substrate are separated [1].

A variety of methods are used to produce a master. A considerable amount of literature has been published on master fabrication and hot embossing process. Depending on the material used to fabricate masters, they may be divided into soft and hard masters. Hard masters are commonly made by Silicon and metals which needs expensive and time consuming procedures [9]. Soft masters made from polymeric materials can be used in hot embossing at temperatures below their T_g where T_g of the stamp should be lower than this temperature

Alireza Shamsi is with the Engineering Dept., Islamic Azad University, Roudehen branch, Roudehen, Tehran, Iran (corresponding author to provide email: alireza.shamsi@gmail.com).

Saeed Delaram was with the Department of Electronic, Electrical Engineering research center, Tehran, Iran (email: Saeed_delaram_mut@yahoo.com).

Mehrnaz Esfandiari is with the Engineering Dept., Islamic Azad University, Roudehen branch, Roudehen, Tehran, Iran (email: me_esfandiari2000@yahoo.com).

Hasan Hajghassem is with the Electrical Engineering Department, Khaje Nasir Odin Toosi University of Technology, Tehran, Iran

[1]. Fabrication of these masters is easier, faster and cheaper than the hard type [11]. One of the polymeric materials used for fabrication of MEMS is called SU-8, which is employed in this paper. Many previous works have been reported on hot embossing by several master types [3],[7],[9],[12],[13].

On the other hand, some surface characteristics of BioMEMS devices based on PMMA, such as hydrophilicity, surface topology or interactions between substrate and reagent can lead to undesired analyte adsorption on the microstructure walls causing to inaccurate reaction analysis and sample loss [14]. Various methods have been reported to modify the surface of polymers in order to make it hydrophilic. But, they needed some equipments such as laser ablation and plasma asher systems [15].

In this paper, microchannels are fabricated on a polymeric stamp by Hot Embossing process and made hydrophilic by a novel method and sealed by another polymeric cap using thermal bonding. A soft master is fabricated by SU-8 on a glass substrate, which has a lower cost rather than silicon in Metwally and Mathur works [12]-[13]. The stamp is a polymethylmetacrylate (PMMA) sheet with 1mm thickness.

Hydrophilicity of microchannel is important specification in a microfluidic device for Water-based solution applications, such as blood. The hydrophilicity of imprinted PMMA is enhanced by immersion in the KI:I₂ solution, which usually use to etch Au in MEMS fabrications. This solution increases the surface roughness of the polymer and makes it more hydrophilic. This method does not need any plasma ashing and laser equipments.

In a microfluidic device, we usually need bonding process to have enclosed microchannels [10]. In this paper, a PMMA sheet as a cap is bonded at the top of the channels and reservoirs. The cap is drilled as the fluid input and outputs. The most common methods to bond two sheets of polymer are thermal and adhesion bonding [7],[10]. Both of these techniques are examined in this paper and the thermal bonding is used as optimum one, because of its simplicity and lower microchannel damage.

Among the wide range of polymers which can be used in master fabrication, SU-8 is selected, because of its excellent coating, planarization and processing properties as well as its mechanical and chemical stability [16]. SU-8 is an epoxy-based chemically enhanced, negative tone photoresist (Microchem, USA) and has good properties such as high optical transparency and low surface tension. Significantly, it can be coated in several thicknesses by controlling the spinning speed (from 500nm to 200mm) [17]. It is also a convenient material to make soft masters in virtue of its high T_g which is more than 200°C [16]. The robustness of structure and adhesion of SU-8 to glass is increased in this essay by some techniques regarding the glass substrate pretreatment and SU-8 bake considerations. After fabrication of SU-8 mold on glass substrate, hot embossing process is carried out at optimum temperature and pressure so microchannels will replicate on polymeric substrate.

The method presented in this paper is inexpensive due to use of glass as master substrate instead of silicon wafer. It is also simple because of hydrophilic surface is reached just by a

liquid without using any complicated equipments such as plasma asher. Masters are fabricated without any metal deposition and etching process. They are reachable just by spin coat and UV exposure mask aligner systems. Since our lithography is one step, no precision alignment is necessary. On the other hand, because of higher strength of glass substrate than Silicon, we can increase embossing pressure to reach high aspect ratio. In our experiments, hot embossing is used to imprint microchannels on PMMA substrate and making hydrophilic and sealing is carried out in order to fabricate a microfluidic device which can be used for chemical, biological and medical applications such as Micro Total Analysis Systems (μTAS) [18]-[19].

Glass transmission temperature of PMMA as substrate is 105°C, that is much lower than T_g of SU-8 master (>200°C). Therefore, we can raise the embossing temperature to more upper than 105°C. In such temperature, PMMA will have more softness and flexibility and as a result, imprinting can perform at lower pressure. Hence, as an another benefit, the master sustain lower force and protected from damage and breakage

At the follows, details of master fabrication, hot embossing process and some images of replicated microchannels are presented. Hydrophilicity of PMMA and bonding of microchannels is also explained in that section. After that, important embossing factors are discussed and quality of imprinted structure is evaluated among the different values of impacting factors and optimum temperature and pressures are extracted.

II. FABRICATION PROCESS

A. Master fabrication

The master is composed of a SU-8 structure on a glass substrate with thickness of 1mm. The major source of uncertainty in this type of soft molds is adhesion between SU-8 and its glass substrate. The low adhesion of SU-8 to glass results in the low robustness, reliability of master and its lifetime. The stickiness depends on surface roughness, clearance and uncontamination and also material of substrate. In addition, SU-8 lithography processing including coating and soft bake treatments, UV exposure time and hard bake have important influence on uniformity of SU-8 structure and its adhesion to glass [20]-[21].

To clean the substrate, we use standard RCA-I cleaning process. According to this process, first, glass substrate is submerged in ammonium hydroxide and hydrogen peroxide solution for 5 minutes at 80-90°C. Once rinsed by de-ionized water, it is dried by gentle air stream. Then, it is rinsed by acetone prior to dehydration. On completion of cleaning, the substrate is subjected to heat at 180°C for 20 minutes to be dehydrated [17],[20]. Our experiences showed that dehydration has huge effect on SU-8 to glass adhesion and prevents to appear some bobbles during prebake. Since the depth of microchannels should be 50μm, a SU-8 structure with thickness of 50μm is needed. We coated SU-8 2025 at the spin speed of 1750 rpm. The coating recommended procedure is explained in the Catalog of polymer.

After spin coating, the soft bake is performed from environment temperature to 65 in order to ensure good adhesion of SU-8 to glass, and after 50 minutes, the temperature is raised to 95°C for 20 minutes on hotplate. More prebake leads to more adhesion of SU-8 to substrate. The structure is patterned on SU-8 by standard UV lithography (exposed for 60 seconds) and its crosslink completed by Post Exposure Bake (PEB) at 65°C for 30 minutes and 95°C for 15 minutes on hotplate [17]. All cool down steps are carried out slowly to avoid thermal residual stress and consequently, improve adhesion of SU-8 to glass [20]. After PEB, the master is developed by immersion in standard SU-8 developer for 7 minutes and dried by gentle stream of air. At the end, the mold structure hard baked in 180°C for 20 minutes (on hot plate) to increase the robustness of the mold and eliminate the cracks on its surface. A microscopic image of a master fabricated by this method is illustrated in figure 1..

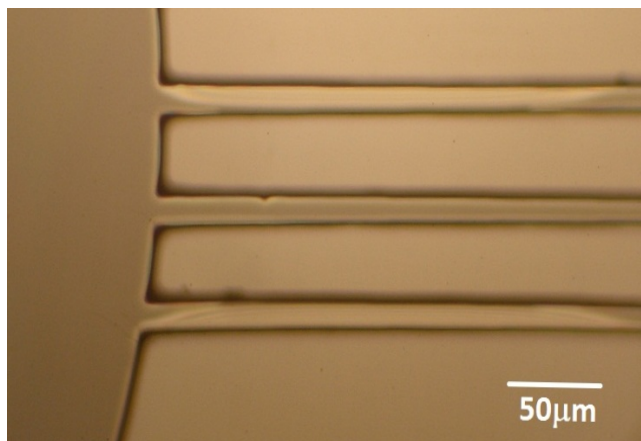


Fig. 1 Microscopic image of a master fabricated by SU-8 on glass

B. Hot Embossing process

In this study, the PMMA stamp is selected as Year Long's plexiglass sheet with 1mm thickness, which is sliced in 25×25mm pieces. It is clear that, the embossing temperature should be between the T_g of master and stamp. In such conditions, polymeric stamp is flexible but master structure is rigid without any deformation. T_g of PMMA and exposed SU-8 is 105°C and 240°C, respectively [6]-[7]. The embossing begins from environment temperature to optimum temperature which is 160°C and the pressure is applying up to 1.2MPa and is kept in that condition for 20 minutes. Then, the system is cooled down slowly to thwart the thermal residual stress. This stress causes some cracks on mold structure and adhesion between mold and stamp during de-embossing [9]. At 90°C, the pressure is removed to de-embossing the system.

Rising the temperature much higher than T_g of polymer substrate, makes it more formable. So that, we can apply lower pressure resulting in more master safety and life time, especially in soft molds. The residual stress at that temperature is low due to the small difference between the thermal expansion coefficient of master and stamp. The SEM image of

imprinted Microchannels and a reservoir is presented in Figure. 2.

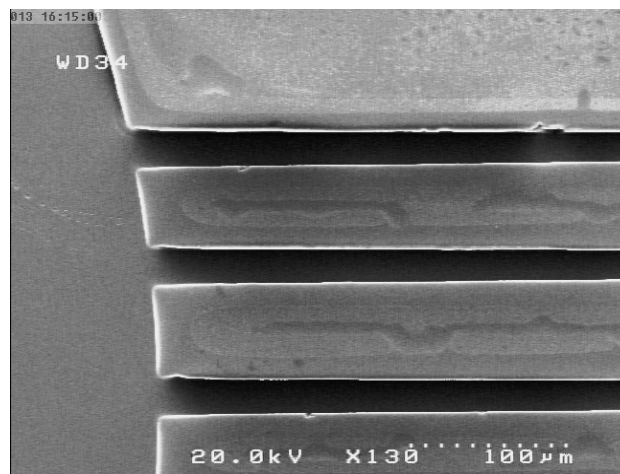


Fig 2 SEM image of imprinted microchannels

C. Hydrophilicity

Pristine PMMA sheets have not enough hydrophilicity and relatively are hydrophobic [15],[22]. PMMA microfluidic devices are commonly used for biological applications [5]. Surface characteristics of polymer-based Bio-MEMS devices and particularly the hydrophilicity have major impacts on the accuracy of the analysis of device [14]. For example, undesired absorption of proteins to surface of device is a significant problem and give the fact that hydrophobic surface absorbs intensely more proteins than hydrophilic surface [23]. Then, surface modification for PMMA is needed to have hydrophilic device surface.

Making polymers hydrophilic increases the adhesion strength and enhances their biocompatibility [24]. In addition, Surface roughness is a strong factor affecting on hydrophilicity of polymer materials and their contact angle values [15]. Many surface modification techniques are reported such as vacuum ultraviolet (VUV) irradiation with excimer lamp [25], UV/ozone graft polymerization [26], water-vapor plasma treatment [27], vapor-phase deposition of organic films [28], aminolysis [29] and surface-initiated atom transfer radical polymerization [14]. But, in this paper a novel method is used as immersing the structure in KI:I₂:DI water solution in 4:2:10 volume ratios, which is usually used for Au etching, for 10 minutes in ultrasonic and rinse by DI water. Our experience shows that the PMMA sheet had been become hydrophilic by this technique.

According to our observations, this solution will made the surface of the PMMA rough. An AFM image of surface topography of pristine and modified PMMA are shown in Figure 3. As can be seen from the Figure 3, the modified PMMA surface roughness is more than the pristine one. It can be simply seen the hydrophilicity of PMMA after immersion by applying a drop of water on its surface.

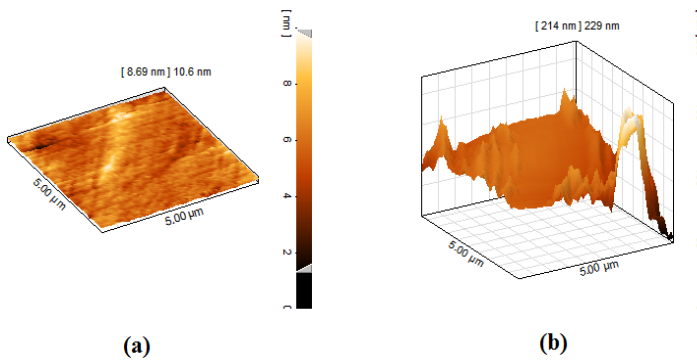


Fig. 3 AFM image of surface topography of PMMA substrates: (a) Pristine, (b) Modified PMMA

The contact angles of primitive and modified PMMA are illustrated in Figure 4.

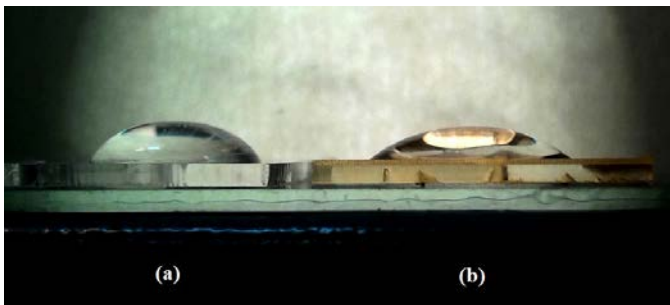


Fig. 4 Image of water-contact angles of the (a) pristine and (b) modified PMMA substrates.

We found that changing the immersion time has sensible impact on the contact angle. More immersion time causes more contact angle of water droplet. The immersion is carried out for some various times and the contact angle of water droplet is compared to each other. Figure 5 shows the measured contact angles for examined immersion times.

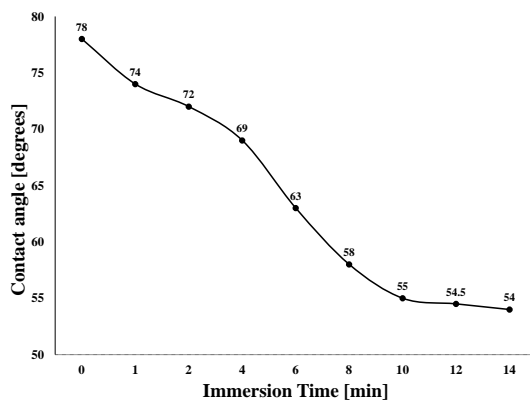


Fig. 5 Contact angle of modified PMMA Document Modification

D. Bonding

In a microfluidics, it is needed to seal the device to have enclosed structure. We used a PMMA sheet as a cap in order to seal the microchannels. There are different methods to bond two pieces of polymers which are generally classified into

direct and indirect bonding. The most common method used in microfluidic chip bonding is adhesion bonding [10] and Thermal fusion bonding which also known as Thermal annealing [7].

Both of these methods are carried out in this paper, we used SU-8 as an adhesive layer to bond the PMMA sheets. After coating SU-8 2002 on the cap, and a short prebake for 1 minute at 65°C, two parts are mated and exposure for 1 minute and post baked to complete polymerization of SU-8. This method has some defects such as leakage due to incomplete sealing and unclear microchannels. As shown in Figure 6, the adhesive SU-8 layer is entered to the channel and made it pinched.

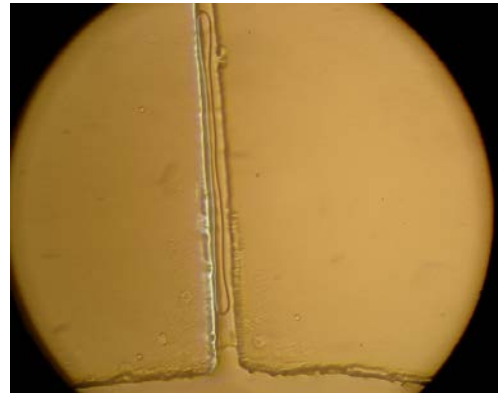


Fig. 6 The entered adhesive Su-8 layer to the channel

We used thermal bonding which is a kind of direct bonding as an alternative method which is simpler and does not need any adhesive material. In this technique, two polymer layers are heated to a temperature near the Tg of both then pressure is applied to increase mating contact force between the polymers [10]. Bonding temperature and pressure are impacting factors on adhesion of two layers. We evaluated some temperature and pressures. High temperature and pressure cause polymer to be more soft and flexible. This damages the channel walls and changes the shape of the structure which has been observed in channels with low depth. In contrast, by employing low temperature and pressure, the polymer sheets will not be adhesive enough and could be separated easily. The optimum temperature and pressure reached as 100°C and 0.2MPa. A microscopic image of bonded microchannels is shown in Figure 7(a). A dyed liquid is injected into microchannels to test their sealing as shown in Figure 7(b).

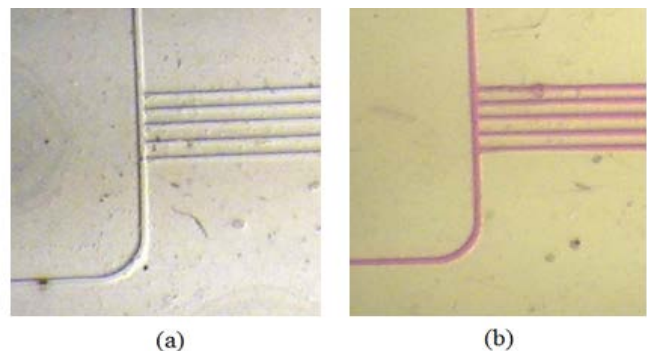


Fig. 7 (a)-bonded microchannels on PMMA. (b)-liquid injected

microchannels.

III. RESULTS AND DISCUSSION

In this section, we present the results of our experiments to optimize hot embossing process regarding to best quality, and repeatability. The quality of hot embossing process is conditioned by controlling contributory factors including temperature, pressure and the time of embossing [9]. We will investigate the effects of temperature and pressure on quality of embossing by applying different temperatures and pressures. The time of embossing should be big enough to let the flexible stamp flow in the free spaces of the master and take its shape. In this work, the best time of embossing is obtained as 20 minutes.

A. Effects of temperature and pressure

Here we analyze the effect of applied temperature and pressure on embossing quality by repeating the process for a wide range of temperatures and pressures. We observe that if the embossing temperature is low (around the T_g), the formability of polymer stamp would not be enough to take the shape of master correctly and sharp corners turn to curves. A top view of a microchannel with curved side walls is shown in Figure 8. On the other hand, aspect ratio of the structure will be low [9]. On the contrary, the soft master will be damaged in very high temperatures.

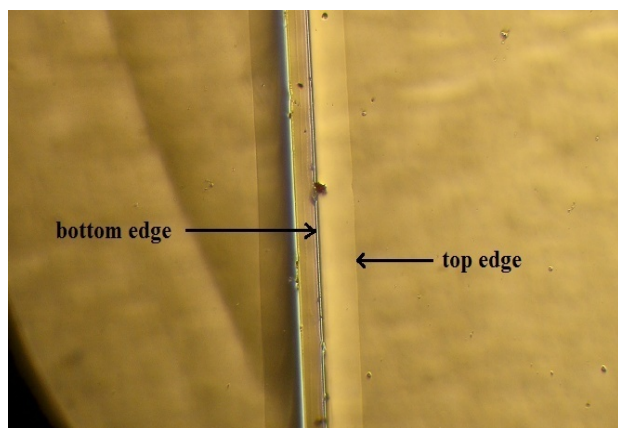


Fig. 8 Embossed structure at low temperature

Applied pressure is another important parameter in hot embossing. High pressure will make the master damaged and if the applied pressure is too low, the replication does not take place completely and deep patterns are not created correctly [9]. Our experienced showed that optimum embossing temperature and pressure are 160°C and 1.2Mpa , respectively.

IV. CONCLUSION

In this paper a low cost microchannels fabrication on a PMMA substrate and sealing of microchannels by thermal bonding is presented. Polymer surface is modified to be made hydrophilic by a novel simple method. The fabrication process described in this paper is focused on reducing complexity and

cost involved. Microchannels are imprinted using hot embossing method on a PMMA stamp and sealed by a drilled PMMA cap using thermal annealing bonding. The master is made from SU-8 on a glass substrate. In contrary to the Si-based processes, the presented method is a low cost and simple procedure and does not need any hazardous chemicals and complicated MEMS fabrication equipment. Embossing time, pressure and temperature are the main impacting parameters which have been optimized as 160°C and 1.2MPa . Thermal bonding performed at 100°C by the pressure of 0.2MPa . Conventional Au etchant, KI_2 solution is used to PMMA surface modification to make it hydrophilic. Minimum feature of $15\mu\text{m}$ and depth of $50\mu\text{m}$ with the aspect ratio of more than 3 are reached in this work and are adequate in comparison with the similar cases.

REFERENCES

- [1] Fan Yaxi, Tingjie Li, Woon-Ming Lau, and Jun Yang 2012 A Rapid Hot-Embossing Prototyping Approach Using SU-8 Molds Coated With Metal and Anti stick Coatings *J. Microelectromechanical systems*. **21**, pp.875-881
- [2] Wang W. and S. A. Soper 2007 Bio-MEMS Technologies and Applications (New York: CRC Press).
- [3] Chen S. C., M. C. Lin, R. D. Chien and W. L. Liaw 2005 Hot Embossing of Micro-Featured Devices Proc. Int. Conf. on Mechatronics, Taiwan.
- [4] Narasimhan J. and I. Papautsky (2004), Polymer embossing tools for rapid prototyping of plastic microfluidic devices, *J Micromech. Microeng.* 14:96-103, doi: 10.1088/0960
- [5] Becker H and Heim U (2000), Hot embossing as a method for the fabrication of polymer high aspect ratio structures, *J Sensors Actuators A*, 83:130-135.
- [6] Zhao Yongjun and Tianhong Cui (2003), Fabrication of high-aspect-ratio polymer-based electrostatic comb drives using the hot embossing technique, *J. Micromech. Microeng.* 13: 430-435
- [7] Koerner Terry, Laurie Brown, Ruixi Xie, Richard D. Oleschuk (2005), Epoxy resins as stamps for hot embossing of microstructures and microfluidic channels, sensors and actuators B, 107:632-639
- [8] Becker, H., Heim, U., and Rotting, O., The fabrication of polymer high aspect ratio structures with hot embossing for microfluidic applications, *Proc. SPIE (International Society for Optical Engineering)*, 3877, 74, 1999.
- [9] Mandy B. Esch, Sahil Kapur, Gizaida Irizarry, Vincent Genova (2003), Influence of master fabrication techniques on the characteristics of embossed microfluidic channels, *Lab Chip*, 3:121-127
- [10] Tsao Chia-Wen and Don L. DeVoe (2009), Bonding of thermoplastic polymer microfluidics, *J Microfluid Nanofluid*, 6:1-16, doi: 10.1007/s10404-008-0361
- [11] Harsono, H. J. Lu, Y. C. Liu, Y. C. Lam1 and X. C. Shan (2006), Experimental Studies on Polymer Deformation and Flow in Micro Hot Embossing, *Electronics Packaging Technology Conference, EPTC '06*, 8th, Singapore (This reference is not used in this paper)
- [12] Metwally Khaled, Laurent Robert, Roland Salut and Chantal Khan Malek (2012), SU-8-based rapid tooling for thermal roll embossing, *J Microsystem Technologies*, doi: 10.1007/s00542-012-1534-9
- [13] Mathur et al. 2011) Mathur A., S.S. Roy, M. Tweedie, S. Mukhopadhyay, S.K. Mitra (2009), J.A. McLaughlin, Characterization of PMMA microfluidic channels and devices fabricated by hot embossing and sealed by direct bonding, *J Current Applied Physics*, 9:1199-1202
- [14] Liu JK, Pan T, Woolley AT et al (2004) Surface-modified poly(methyl methacrylate) capillary electrophoresis microchips for protein and peptide analysis. *Anal Chem* 76:6948-6955.

- [15] Heng Qi, Tao Chen, Liying Yao and Tiechuan Zuo(2008), Hydrophilicity modification of poly(methyl methacrylate) by excimer laser ablation and irradiation, *J. Microfluid Nanofluid*, 5:139-143.
- [16] Campo A del, C. Greiner (2007), SU-8: a photoresist for high-aspect-ratio and 3D submicron lithography, *J. Micromech. Microeng.* 17: R81–R95.
- [17] www.micromech.com, Last modified :Jan. 2013.02.12
- [18] Lee G-B et al (2001), Microfabricated plastic chips by hot embossing methods and their applications for DNA separation and detection, *J Sensors Actuators B*, 75: 142–8.
- [19] Becker H., Dietz W. (1998), Microfluidic devices for μ -TAS applications fabricated by polymer hot embossing, *Proc. SPIE* 3515:177–82, doi: 10.1117/12.322081
- [20] Grist Samantha, Jasbir N. Patel, Moeed Haq, Bonnie L. Gray, Bozena Kaminska (2010), Effect of surface treatments/coatings and soft bake profile on surface uniformity and adhesion of SU-8 on a glass substrate, *J Microfluidics Biomems and Medical Microsystems VIII*, 7593:75930F-1-75930F-9.
- [21] Mao Xu, et al (2013), Two New Methode To Improve The Lithography Precision For SU-8 Photoresist On Glass Substrate, *J Microelectromechanical Systems* 22:124-130, doi: 10.1109/JMEMS.2012.2219295.
- [22] Ji-Yen Cheng, Cheng-Wey Wei, Kai-Hsiung Hsu, Tai-Horng Young (2004), Direct-write laser micromachining and universal surface modification of PMMA for device development, *J. Sensors and Actuators B*, 99:186-196.
- [23] Prime KL, Whitesides GM (1991) Self-assembled organic monolayers: model systems for studying adsorption of proteins at surfaces. *Science* 252:1164–1167.
- [24] P.K. Chua, J.Y. Chena, L.P. Wang, N. Huang, Plasma-surface modification of biomaterials, *Materials Science and Engineering*, 36 (2002) 143–206.
- [25] Hozumi A, Masuda T, Hayashi K et al (2002) Spatially defined surface modification of poly(methyl methacrylate) using 172 nm vacuum ultraviolet light. *Langmuir* Vol.18, pp. 9022–902.
- [26] Shah JJ, Geist J, Locascio LE et al (2006) Surface modification of poly (methyl methacrylate) for improved adsorption of wall coating polymers for microchip electrophoresis. *Electrophoresis* Vol.27, pp.3788–3796.
- [27] Long TM, Prakash S, Shannon MA et al (2006) Water-vapor plasmabased surface activation for trichlorosilane modification of PMMA. *Langmuir* Vol.22, pp. 4104–4109.
- [28] Hiratsuka A, Muguruma H, Lee KH et al (2004) Organic plasma process for simple and substrate-independent surface modification of polymeric BioMEMS devices. *Biosens Bioelectron* Vol.19, pp. 1667–1672.
- [29] Henry AC, Tutt TJ, Galloway M et al (2000) Surface modification of poly(methyl methacrylate) used in the fabrication of microanalytical devices. *Anal Chem* 72:5331–5337.

The arrangements of the locations of miR-619, miR-5095, miR-5096 and miR-5585 binding sites in the human mRNAs

Anatoly T. Ivashchenko, Olga A. Berillo, Anna Y. Pyrkova, Raigul Y. Niyazova, Shara A. Atambayeva

Abstract—The binding of 2,563 human miRNAs with the mRNAs of 12,175 human genes was studied. It was established that miR-619-5p, miR-5095, miR-5096 and miR-5585-3p bind with high affinity to the mRNAs of the 1215, 832, 725 and 655 genes, respectively. These unique miRNAs have binding sites in the 3'UTRs, CDSs and 5'UTRs. Groups of mRNAs in which the ordering of the miR-619-5p, miR-5095, miR-5096 and miR-5585-3p binding sites differed were established. The possible functional properties of these miRNAs are discussed.

Keywords—cancer, human, miRNA, mRNA.

I. INTRODUCTION

MiRNAs, as a part of the RNA-induced silencing complex, bind to mRNAs and interfere with translation or promote mRNA destruction [2]. The study of the properties of miRNAs and their influences on the expression of the genes that participate in all key processes of cells was established in the last 20 years. The actions of miRNAs on the cell cycle [3], apoptosis [4], differentiation [5], growth and development in animals [6] have been shown. Connections among miRNA expression and the development of various diseases have been established. miRNA concentrations change in cancer [7]. Metabolic disturbances necessarily change miRNA concentrations in cells [8]. It is possible to normalize some processes using miRNAs [9]. The aforementioned roles do not encompass the full list of the biological processes in which miRNAs participate, which proves the importance of their biological functions.

This study was supported by a grant obtained from the Ministry of Education and Science, Kazakhstan Republic.

A.T. Ivashchenko with the National Nanotechnology Laboratory, al-Farabi Kazakh National University, Almaty, Kazakhstan, 050038 (phone/ fax: +7 (727) 3773202; e-mail: a_ivashchenko@mail.ru).

O.A. Berillo with the National Nanotechnology Laboratory, al-Farabi Kazakh National University, Almaty, Kazakhstan, 050038 (e-mail: devolia18@mail.ru).

A.Y. Pyrkova with the National Nanotechnology Laboratory, al-Farabi Kazakh National University, Almaty, Kazakhstan, 050038 (e-mail: Anna.Pyrkova@kaznu.kz).

R.Y. Niyazova with the National Nanotechnology Laboratory, al-Farabi Kazakh National University, Almaty, Kazakhstan, 050038 (e-mail: raiguln@mail.ru).

S.A. Atambayeva with the National Nanotechnology Laboratory, al-Farabi Kazakh National University, Almaty, Kazakhstan, 050038 (e-mail: shara79@mail.ru).

Despite the appreciable successes in the study of miRNA properties, there are obstacles to establishing the target genes of miRNAs. There are miRNAs that bind to many mRNAs, and one mRNA can be the target of many miRNAs. These circumstances significantly complicate the study of the properties of miRNAs and their diagnostic and medical applications. There are more than 2,000 miRNAs in the human genome, and they are thought to act on 50% or more of genes. It will be difficult to draw unique conclusions about the participation of miRNAs in specific biological processes, and until those conclusions can be drawn, the connections between the majority of miRNAs and their target genes will remain unknown. Recently, we found a set of unique miRNAs that have hundreds of target genes and bind to mRNAs with high affinity. The binding sites unique to miRNAs are located in the 3'UTRs, CDSs and 5'UTRs of mRNAs. In present work, we studied some unique miRNAs that bind to the mRNAs of several hundred human genes.

II. MATERIAL AND METHODS

The human gene mRNAs were taken from GenBank (<http://www.ncbi.nlm.nih.gov>) using Lextractor002 script (<http://sites.google.com/site/malaheenee/software>). The nucleotide sequences of human miR-619-5p, miR-5095, miR-5096 and miR-5585-3p were taken from the miRBase site (<http://mirbase.org>).

The target genes for the tested miRNAs were revealed using the MirTarget program, which was developed in our laboratory. This program defines the following features of binding: a) the origin of the initiation of miRNA binding to mRNAs; b) the localization of miRNA binding sites in the 5'-untranslated regions (5'UTRs), the coding domain sequences (CDSs) and the 3'-untranslated regions (3'UTRs) of the mRNAs; c) the free energy of hybridization (ΔG , kJ/mole); and d) the schemes of nucleotide interactions between the miRNAs and the mRNAs. The ratio $\Delta G/\Delta G_m$ (%) was determined for each site (ΔG_m equals the free energy of an miRNA binding with its perfect complementary nucleotide sequence). The miRNA binding sites located on the mRNAs had $\Delta G/\Delta G_m$ ratios of 90% or more. We also noted the positions of the binding sites on the mRNA, beginning from the first nucleotide of the mRNA's 5'UTR. This program found hydrogen bonds between adenine (A) and uracil (U), guanine (G) and cytosine (C), G and U, and A and C. The distances between A and C were equal to those between G and C, A and U, and G and U. The numbers of hydrogen bonds in the G-C,

A-U, G-U and A-C interactions were found to be 3, 2, 1 and 1, respectively. The free binding energies of these nucleotide pairs were taken as the same values (i.e., 3, 2, 1, and 1, respectively).

III. RESULTS

A. Features of miR-619-5p, miR-5096, miR-5585-3p and miR-5095

The binding powers between the 2,563 tested hsa-miRNAs and the mRNAs of 12,175 human genes were calculated. Some of these miRNAs have greater numbers of target genes than others. For example, miR-619-5p, miR-5095, miR-5096 and miR-5585-3p are found to be capable of binding more 600 genes each. These miRNAs were termed unique miRNAs (umiRNAs). Additionally, the binding sites for these unique miRNAs are unusually located in the mRNAs. miR-619-5p, miR-5095, miR-5096 and miR-5585-3p have different miRNA binding site origins, lengths, quantities and miRNA binding site properties, among other features. Some characteristics of these unique miRNAs are outlined below.

With a length of 22 nt, miR-619-5p is coded in an intron of the slingshot protein phosphatase 1 gene (*SSH1*). We found that miR-619-5p has 1811 binding sites on 1215 target mRNAs. Of those, 1772 miR-619-5p binding sites are located in 3'UTRs, 26 sites are located in 5'UTRs and 13 sites are located in CDSs. The mRNAs of 197 genes have completely complementary binding sites for miR-619-5p. The mRNAs of 27 genes have four binding sites. Seven genes have five binding sites, and the mRNAs of the *CATADI*, *ICAIL*, *GK5*, *POLH*, and *PRR11* genes have six miR-619-5p binding sites. The mRNAs of the *OPA3* and *CYP20A1* genes have eight and ten binding sites, respectively. All of these sites are located in 3'UTRs.

With a length of 21 nt, miR-5096 is coded in an intron of the BMP2 inducible kinase gene (*BMP2K*). We found that miR-5096 has 997 binding sites on 832 target mRNAs. Of these, 984 miR-5096 binding sites are located in 3'UTRs, nine sites are located in 5'UTRs and four sites are located in CDSs. The mRNAs of 42 genes have completely complementary binding sites for miR-5096. The mRNAs of the *IP09* gene have four binding sites. The *PRR11* gene have five binding sites. The mRNAs of the *OPA3* and *CYP20A1* genes have six and 11 miR-5096 binding sites, respectively. All of these sites are located in 3'UTRs.

With a length of 22 nt, miR-5585-3p is coded in an intron of the transmembrane protein 39b gene (*TMEM39B*). We found that 725 target gene mRNAs have 844 binding sites for miR-5585-3p. Nine of these binding sites are located in 5'UTRs, two sites are located in CDSs and 833 sites are located in 3'UTRs. The mRNAs of the *CYP20A1* and *GPR155* genes each has four binding sites.

With a length of 21 nt, miR-5095 is coded in an intron of the sterol carrier protein 2 gene (*SCP2*). We found that 655 target gene mRNAs have 734 binding sites. 14 of these binding sites are located in 5'UTRs, eight sites are located in CDSs and 712 sites are located in 3'UTRs. The mRNAs of two genes have completely complementary binding sites for miR-5095. The

mRNAs of the *OPA3*, and *SPN* genes each has four binding sites.

B. miRNA binding sites in 5'UTRs, CDSs and 3'UTRs

The miR-619-5p, miR-5095, miR-5096 and miR-5585-3p binding sites in the 5'UTRs, CDSs and 3'UTRs of several genes were predicted using the MirTarget program. Multiple miRNA binding sites are revealed to be in the 5'UTRs of several genes. For example, miR-619-5p has two binding sites in each of the 5'UTRs of the *ANAPC16*, *CYB5D2* and *PRR5* mRNAs and three binding sites in the *DNASE1* mRNA.

The mRNAs of some genes have binding sites for miR-619-5p, miR-5095, miR-5096 and miR-5585-3p within their 5'UTRs and 3'UTRs or CDSs and 3'UTRs. For example, the 5'UTRs and 3'UTRs of the *ATAD3C* and *CYB5RL* genes have miR-619-5p binding sites. The CDSs and 3'UTRs of the *C8orf44*, *ISY1* and *ZNF714* genes have miR-619-5p binding sites.

The 5'UTR and 3'UTR of the *ANAPC16* gene have miR-5095 miR-5096 and miR-5585-3p binding sites. The 5'UTR and 3'UTR of the *ATAD3C* gene have miR-5095 and miR-619-5p binding sites. The 5'UTRs and 3'UTRs of the *C14orf182* and *CYB5RL* genes have miR-5096 and miR-619-5p binding sites, respectively.

miR-5095 and miR-619-5p binding sites were found in the CDS and 3'UTR of the *ISY1* gene. The CDS and 3'UTR of the *ZNF714* gene have binding sites for miR-5096 and miR-619-5p, and the *C8orf44* mRNA has only a miR-619-5p binding site.

C. The arrangements of the locations of umi-RNA binding sites

The mRNAs that are targeted by miR-619-5p, miR-5096, miR-5095 and miR-5585-3p were established. The 5'UTRs of three target genes contained these miRNA-binding sites (Fig. 1). The degree of homology of the nucleotide sequences in these genes is high not only in the binding sites of the studied miRNAs but also across all mRNA 178 nt sequences. The distance between the miR-5095 and miR-5096 binding sites is 57-59 nt and that between the miR-5096 and miR-5585-3p binding sites is 46-47 nt. The miR-5095 and miR-619-5p binding sites partially overlapped. The greatest numbers of miR-619-5p, miR-5096, miR-5095 and miR-5585-3p binding sites are located in the 3'UTRs, and it is therefore possible that many target genes have umiRNAs binding sites. The data about the locations of the miR-619-5p, miR-5096, miR-5095 and miR-5585-3p binding sites and the degrees of homology of the corresponding nucleotide sequences in the mRNAs of 21 genes are presented in Fig. 2. The distances between the miR-5095 and miR-5096 binding sites are all 57-60 nt. The distances between the miR-5095 and miR-5096 binding sites in the mRNAs of 78 genes averaged 58.6 ± 0.9 nt. Thus, the distances between miR-5095 and miR-5096 binding sites are highly conserved. The distances between the miR-5096 and miR-5585-3p binding sites are all 46-49 nt. The distances between the miR-5096 and miR-5585-3p binding sites in the mRNAs of 325 genes averaged 47.3 ± 1.1 .

The degree of homology of the nucleotide sequences containing the miR-619-5p, miR-5096, miR-5095 and miR-5585-3p binding sites is high. These areas contain binding sites for miRNAs other than the studied umiRNAs. Other miRNA binding sites are not present in all genes, and these binding sites have lower affinities (data not shown). It is possible that there are conserved domains in the nucleotide sequences of mRNAs.

D. Variability in the arrangement of umiRNA binding site locations

The miR-619-5p binding site is located at a distance of 6 nucleotides downstream of the miR-5095 site in the majority of genes containing arranged umiRNA sites. However, in another group of mRNAs, the beginnings of the miR-619-5p binding sites are located at distances of 7 nucleotides upstream of the miR-5585-3p binding sites Fig. 3. There is another group of genes in which the miR-619-5p binding sites are downstream of the miR-5095 sites and upstream of the miR-5585-3p sites. The distances between the positions of the two miR-619-5p binding sites in the mRNAs of these genes are constant at 112 nt. The nucleotide sequences of the mRNAs with miR-619-5p, miR-5095 and miR-5585-3p binding sites are highly homologous, which testifies to the strength of the selection pressure on these nucleotide sequences.

E. Connection of umiRNAs with mRNA of tumor suppressor genes

The miR-619-5p, miR-5095, miR-5096 and miR-5585-3p binding sites with mRNA of 455 tumor suppressor genes participating in breast cancer and lung cancer were predicted (Table 1). Free energy of the umiRNA:mRNA is equal to 95% - 100%. In this case, the umiRNAs have similar features as well as siRNAs, that is lead to mRNA degradation. Therefore, it is possible to assume that suppression of target gene expression via miR-619-5p, miR-5095, miR-5096 and miR-5585-3p can lead to tumorigenesis. For example, Reshmi et al. [21] established that in normal level of miR-5095 and miR-5096 concentration is much less, than in cancer cells.

IV. DISCUSSION

In this study, it was established that miR-619-5p, miR-5095, miR-5096 and miR-5585 can bind to the mRNAs of the 1215, 832, 725 and 655 genes, respectively. The nucleotide sequences of these miRNAs form hydrogen bonds with the mRNAs, and the free energy of these bonds is equal to or greater than 90% of the maximum possible free energy. The miR-619-5p, miR-5095, miR-5096 and miR-5585-3p binding sites are generally located in the 3'UTRs of target genes. Obviously, maintaining nucleotide sequences for the binding site of one umiRNA in the CDSs of such a high number of genes is complicated. Approximately 180 nucleotides of the mRNAs of many target genes containing binding sites for the miRNAs and the placement of these nucleotide sequences for the binding sites of two and more miRNA are highly conserved. The miRNA binding sites are located in the 5'UTRs of some genes; however, the number of such genes is small.

The mRNAs of some genes have multiple miR-619-5p, miR-5095, miR-5096 and miR-5585-3p binding sites. It is possible that the identification of large number miRNA binding sites in the mRNAs of some genes will be necessary for reliable control of gene expression.

Some groups of genes with different patterns of localization of miR-619-5p, miR-5095, miR-5096 and miR-5585-3p binding sites were established in this work. First, the strict order of the binding sites was established based on the origin of the general nucleotide sequences (these data are not described here). Secondly, it is necessary to control the expression of the corresponding gene complexes that are functionally associated with the miRNAs.

The detection of a large number miRNA binding sites in the mRNAs of the genes studied here presumably indicates to new functional opportunities. It is possible that these umiRNAs are coordinators of gene expression that participate in many major biological processes. The influences of miRNAs on the expression of genes that code for transcription factors [10, 11] and proteins that participate in the cell cycle [3, 12-14], apoptosis [4, 15-17], stress responses, etc. [18] have previously been shown. If these proteins define the limiting stages of multistage processes, these proteins will need to be controlled to manage multistage processes. Specifically, an appreciable portion of the targets of miR-5095 and miR-5096 are genes for transcription factors. One or several umiRNAs regulating the expression of several hundreds of genes will create a system of interconnected processes in cells and organisms. Such role for these miRNAs is quite possible because these miRNAs circulate in the blood and nearly all cells of an organism are available to them [19, 20]. The normal functioning of the system of the interconnected processes in which the umiRNAs participate is maintained because insignificant deviations in the expression of protein-coding genes or typical miRNAs cannot significantly alter the function of the system. On the other hand, the system is also vulnerable because it can be broken by changes in umiRNA expression. For example, it has been established that the basal expression of miR-5096 in normal cells is low [21], but, in tumor cells, the expression of miR-5096 repeatedly elevated. These elevations result in suppression of the expression of many target genes and unbalanced and uncontrollable cell functioning. Some interconnected umiRNAs have to function in the cell and the organism to minimize the consequences of such events. These interactions can be carried out via the general target genes of miRNAs. Thus, the loss or augmentation of the influence of one component (miRNA) in the regulatory system will have less influence on the functioning of the entire system.

The present results provide the basis to study the systemic roles of unique and typical miRNAs in the regulation of gene expression in human cells based on new ideas of miRNA properties.

ACKNOWLEDGMENT

We thank Moldagaliyeva A. and Sagaydak S. for their help in preparing the materials for analysis. We would also like to thank Dr. Khaylenko V. for writing the Lextractor002 script.

REFERENCES

- [1] Y. Zhang a, Z. Wang a, R. A. Gemeinhart, "Progress in microRNA delivery", *Journal of Controlled Release*, vol. 172, pp. 962–974, 2013.
- [2] G. Tang, "siRNA and miRNA: an insight into RISCs", *Trends Biochem Sci*, vol. 30, pp. 106-114, 2005.
- [3] Q. Luo, X. Li, J. Li, X. Kong, J. Zhang, L. Chen, Y. Huang, L. Fang, "MiR-15a is underexpressed and inhibits the cell cycle by targeting *CCNE1* in breast cancer", *Int J Oncol*, vol. 43, pp. 1212-1218, 2013.
- [4] F. Huang, C. Lin, Y. Shi, G. Kuerban, "MicroRNA-101 Inhibits Cell Proliferation, Invasion, and Promotes Apoptosis by Regulating Cyclooxygenase-2 in Hela Cervical Carcinoma Cells" *Asian Pac J Cancer Prev.*, vol. 14(10), pp. 5915-5920, 2013.
- [5] S. Monticelli, "MicroRNAs in T helper cell differentiation and plasticity", *Seminars in Immunology*, vol. 25, pp. 291–298, 2013.
- [6] M. Y. Barozai, "The novel 172 sheep (*Ovis aries*) microRNAs and their targets", *Mol Biol Rep.*, vol. 39(5), pp. 6259-6266, 2012.
- [7] Q. Cheng, B. Yi, A. Wang, X. Jiang, "Exploring and exploiting the fundamental role of microRNAs in tumor pathogenesis", *Oncotargets Ther.*, vol. 6, pp. 1675-1684, Nov. 2013.
- [8] S. Swaminathan, K. Suzuki, N. Seddiki, W. Kaplan, M. J. Cowley, C. L. Hood, et al, "Differential regulation of the Let-7 family of microRNAs in CD4+ T cells alters IL-10 expression", *J Immunol*, vol. 188, pp. 6238-6246, 2012.
- [9] K. U. Tüfekci, R. L. Meuwissen, S. Genç, "The Role of MicroRNAs in Biological Processes", *Methods Mol Biol*, vol. 1107, pp. 15-31, 2014.
- [10] J. E. Yeh, P. A. Toniolo, D. A. Frank, "Targeting transcription factors: promising new strategies for cancer therapy", *Curr Opin Oncol.*, vol. 25(6), pp. 652-658, Nov. 2013.
- [11] C. Peng, M. Wang, Y. Shen, H. Feng, A. Li, "Reconstruction and Analysis of Transcription Factor-miRNA Co-Regulatory Feed-Forward Loops in Human Cancers Using Filter-Wrapper Feature Selection", *PLoS One*, vol. 8(10), e78197, Oct. 2013.
- [12] P. Wang, F. Zou, X. Zhang, H. Li, A. Dulak, R. J. Tomko, J. S. Lazo, Z. Wang, L. Zhang, J. Yu, "microRNA-21 negatively regulates Cdc25A and cell cycle progression in colon cancer cells", *Cancer Res*, vol. 69, pp. 8157-8165, 2013.
- [13] E. Das, N.R. Jana, N. P. Bhattacharyya, "MicroRNA-124 targets *CCNA2* and regulates cell cycle in STHdh (Q111)/Hdh(Q111) cells", *Biochem Biophys Res Commun*, vol. 437(2), pp. 217-24, Jun 2013.
- [14] Y. Wang, X. Zheng, Z. Zhang, J. Zhou, G. Zhao, et al, "MicroRNA-149 inhibits proliferation and cell cycle progression through the targeting of *ZBTB2* in human gastric cancer", *PLoS One*, vol. 7, e41693, 2012.
- [15] T. Bertero, I. Bourget-Ponzio, A. Puissant, A. Loubat, B. Mari, G. Meneguzzi, P. Auberger, P. Barbry, G. Ponzio, R. Rezzonico, "Tumor suppressor function of miR-483-3p on squamous cell carcinomas due to its pro-apoptotic properties", *Cell Cycle*, vol. 12(14), pp. 2183-2193, Jul 2013.
- [16] C. Li, S. M. Hashimi, D. A. Good, S. Cao, W. Duan, P. N. Plummer, A. S. Mellick, M. Q. Wei, "Apoptosis and microRNA aberrations in cancer", *Clin Exp Pharmacol Physiol*, vol. 39, pp. 739-746, 2012.
- [17] R. T. Lima, S. Busacca, G. M. Almeida, G. Gaudino, D. A. Fennell, M. H. Vasconcelos, "MicroRNA regulation of core apoptosis pathways in cancer", *Eur J Cancer*, vol. 47, pp. 163-174, 2011.
- [18] K. Cawley, S. E. Logue, A. M. Gorman, Q. Zeng, J. Patterson, S. Gupta, A. Samali, "Disruption of microRNA biogenesis confers resistance to ER stress-induced cell death upstream of the mitochondrion", *PLoS One*, vol. 8, e73870, 2013.
- [19] S. Kumar, R. Keerthana, A. Pazhanimuthu, P. Perumal, "Overexpression of circulating miRNA-21 and miRNA-146a in plasma samples of breast cancer patients", *Indian J Biochem Biophys*, vol. 50, pp. 210-214, 2013.
- [20] T. Smith-Vikos, F. J. Slack, "MicroRNAs circulate around Alzheimer's disease", *Genome Biol*, vol. 14, pp. 125, 2013.
- [21] G. Reshmi, S. S. Chandra, V. J. Babu, P. S. Babu, W. S. Santhi, S. Ramachandran, S. Lakshmi, A. S. Nair, M. R. Pillai, "Identification and analysis of novel microRNAs from fragile sites of human cervical cancer: computational and experimental approach", *Genomics*, vol. 97, pp. 333-340, 2011.

Process Hazard Management System (PROHAMS) based on PSM

A. M. Shariff, H. A. Aziz and K. H. Yew

Process Safety Research Group, Department of Chemical Engineering
Universiti Teknologi PETRONAS, Bandar Seri Iskandar, 31750 Tronoh, Perak, Malaysia
azmish@petronas.com.my, Tel: 605-3687570, Fax: 605-3656176

Abstract— The key contributing factors that could prevent major accidents, injuries and fatalities in the process industries are by controlling the process hazards within the process plant. However, accidents can still happen if the process hazards are inadequately managed. One of the established standards to manage process hazards is Process Hazard Analysis (PHA) of Process Safety Management (PSM) 29 CFR 1910.119(e). This paper presents a PHA management and implementation technique that could fulfil the 29 CFR 1910.119(e) requirements. The technique provides organized strategies to manage and track information, documents, and resolution of recommendations related to the process hazards. Piping and Instrumentation Diagram (P&ID) is used as a foundation for the PHA data management. The data is efficiently managed using a computer database prototype known as Process Hazards Management System (PROHAMS). Implementation of this technique could help the employers to manage process hazards successfully and compliance with PSM regulation.

Keywords— Managing Hazards, Process Hazard, Process Hazard Analysis, PSM

I. INTRODUCTION

Numerous major accidents in process industries such as at Bhopal (1984), BP Texas Refinery Plant (2005) and BP Deepwater Horizon Mexico (2010) caused high fatalities and damages to properties and environment due to failure of managing process hazards properly. In order to prevent such accidents, rigorous hazard identification techniques and preventive safety procedures are implemented. Some of the well-known techniques are Hazard and Operability Studies (HAZOP), Fault Tree Analysis (FTA) and What-if analysis. Despite all the prevention efforts, accidents are still occurring worldwide. Investigations on these accidents have revealed that inadequate hazards review and improper hazards managements were the main factors that contribute to the accidents [1, 2].

To prevent major accidents from occurring, regulatory bodies worldwide posted certain industrial process safety standards that come in many forms, including mandatory standards, voluntary standards and consensus codes. One of the established mandatory standards that addressed the above issues is Occupational Safety and Health Administration

(OSHA) Process Safety Management (PSM) of Highly Hazardous Chemicals (HHC), 29 CFR 1910.119 [3]. The industries and regulatory bodies worldwide agreed that the implementation of PSM could prevent accidents if process plants follow the regulation as intended [4, 5].

Currently, the practical implementations of PSM are varied from plant to plant due to lacking of established technique for industries to comply with PSM requirements and maintaining the effective process safety programs [6, 7]. PSM auditing costs are high, and people are doubtful about its effectiveness [8]. PSM documentation is a very tedious process and requires strict management. Furthermore, good documentation is just a beginning and proper utilization is again difficult without a systematic filing system [9]. In general, the PSM implementation requires a lot of effort and time but pays off well if implemented fully [10].

The PSM standard contains 14 elements, including Process Hazard Analysis (PHA) 29 CFR 1910.119(e). The PHA is the heart of PSM standard that aims for systematically identifies, evaluates, and mitigates potential hazards in process plant [11]. This article proposes a structured technique using Piping and Instrumentation Diagram (P&ID) as a platform to manage PHA implementation that complies with OSHA PSM.

II. METHODOLOGY

A. Compliance with PHA of PSM Requirements

OSHA does not provide any specific methodology to be used for the implementation of PHA in order to comply with PSM regulation. However, there are numbers of general guidelines provided such as from CCPS [12-13]. Since particular methodology is not publicly available, therefore many companies developed the system based on their own interpretation and understanding from PSM guidelines. This paper introduces a technique to establish a PHA system that can comply with PSM regulation.

A framework in Fig. 1 summarizes vital information and strategy to manage and implement PHA as required by 29 CFR 1910.119(e). The detail explanation on the technique is given in the case study at section IV.

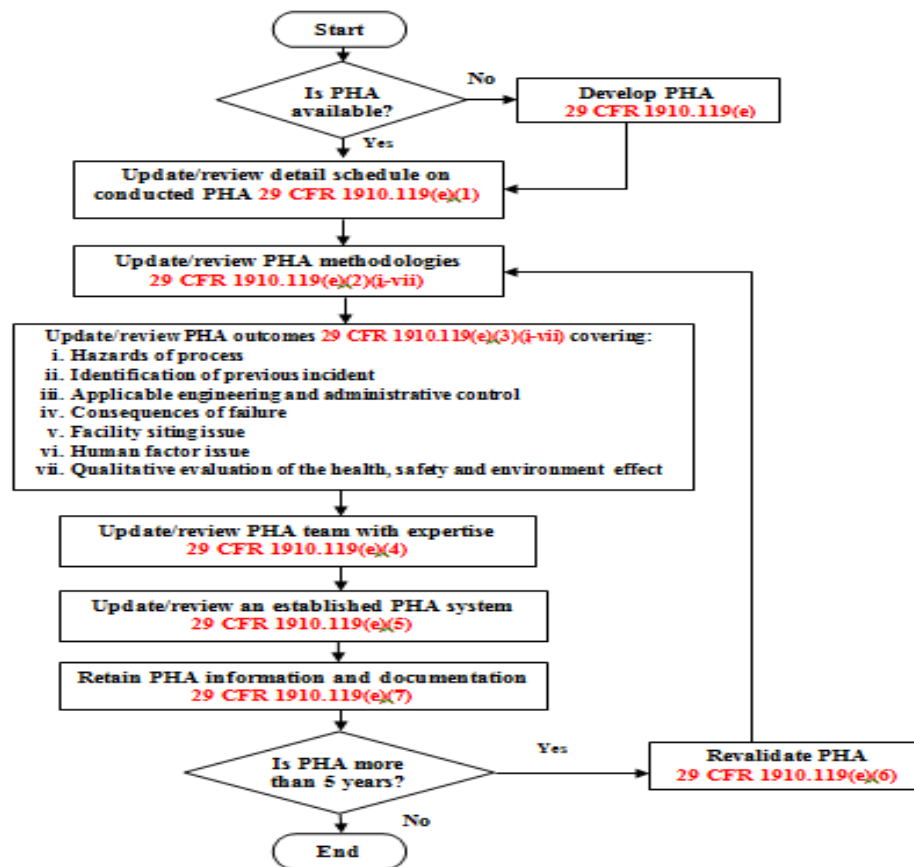


Fig. 1 Framework of PHA based on 29 CFR 1910.119(e)

B. Using P&ID as a Foundation for Data Management

A node system based on P&ID is used for managing and tracking written information of PHA. The P&ID is divided into several nodes. The number of nodes selected depends on the design intent and the number of equipment within the process plant which is considered manageable by the end users. The PHA implementation for each node is carried out according to 29 CFR 1910.119(e) standards as shown in Fig. 1. After all the information has been updated, the end users can select the next node to review or update the data. The updating information process will continue until all nodes in the P&ID are completed. For some cases, the node size may be quite large depending on the scope of the process. One P&ID may not capture the whole process well. Regardless of the numbers of P&IDs involved; similar steps should be adopted until the entire process plant is covered.

III. PROCESS HAZARD ANALYSIS MANAGEMENT SYSTEM (PROHAMS)

Even though the provision contained in OSHA PHA can be done manually, the best results can be obtained through a computer database system for efficient management of data and time. A prototype database management system known as PROHAMS was developed to demonstrate the concept using Microsoft Office Access 2010.

PROHAMS interfaces contain details of the mandatory requirements for employers to comply with PHA element of PSM. The information to be compiled may be found in

hardcopy and softcopy forms, such as log book, report and plant layout. The system allows for capturing information at any specific location. It also provides an effective communication process to all relevant personnel by allowing access to the information and acknowledged them for any process changes. Any database can be used to adopt the technique introduced to suit with the plant's requirements and size of the data to be managed.

IV. CASE STUDY

A case study was conducted using real data from LPG treating unit (LPGU) of typical oil and gas refinery in Malaysia using PROHAMS. The LPGU is used to remove hydrogen sulphide (H₂S) content in various LPG blend stock. The P&ID was divided into several nodes according to its design intention. Fig. 2 shows the selected node that consists of a phase separator (V-201) with inlet and outlet streams.

A. PHA Schedule 29 CFR 1910.119(e)(1)

Priority order for conducting initial PHA was based on the extent of process hazards, number of potentially affected employees, age of process and operating history [14]. Fig. 3 shows PROHAMS interface for PHA schedule. The system assists authorized personnel to plan, record, monitor, and update the information related to PHA development activities. In this case, the schedule for all the activities has been recorded and ready to be accessed by relevant personnel.

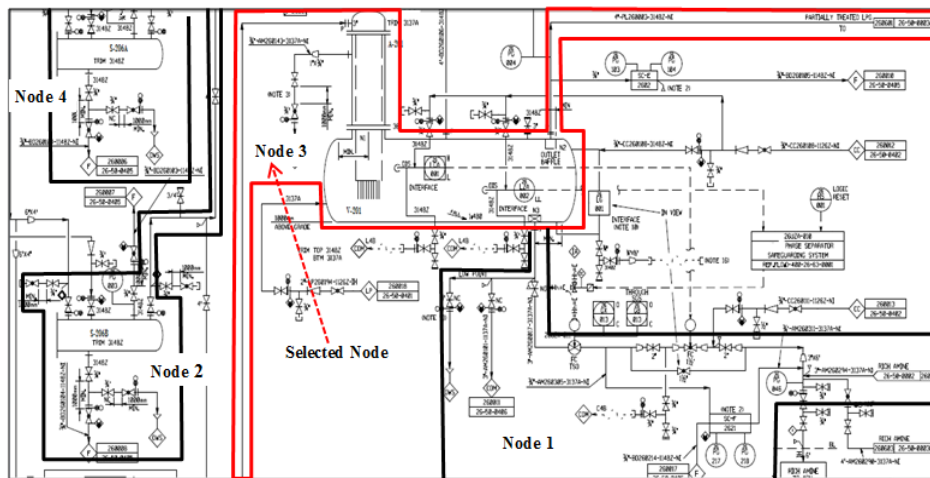


Fig. 2 Part of LPGU P&ID showing Phase Separator (V-201)

B. PHA Methodology 29 CFR 1910.119(e)(2)

Fig. 4 shows PROHAMS interface for PHA methodology. Any appropriate PHA methodology can be used to perform hazard identification and assessment, including HAZOP, FTA or any other established methodology. In this case, HAZOP was used to analyse process hazards on the selected node. PROHAMS captured the HAZOP report at C:\Amin_Treater-V-201\PHA\HAZOP_Report-2012.pdf. The document can be tracked by referring to the date of document as given in the 'Revision date' column.

C. PHA Outcomes 29 CFR 1910.119(e)(3)

PHA outcomes are important to ensure that employer and employees are alerted of process hazards so that the appropriate control measures can be implemented. Fig. 5 shows the interface for PHA outcomes. The interface prompts the authorized personnel to describe the availability of information as covered in the "Description" column. The evidence of the documented information can be referred to in the "Evidence location" column.

Once the information of the PHA outcomes completed, the authorized personnel can tick the "Complete" check box. The incomplete information can be tracked for the necessary actions. Any suitable personnel can be assigned by a superior in the "Action By" column with the due date at "Reply date" column. Therefore, the appropriate action can be taken, monitored and resolved effectively.

In this case, PROHAMS successfully captures information pertaining process hazards, previous accidents, engineering and administrative control of hazards, consequences due to the failure of control system, qualitative evaluation of safety and health effect of V-201. All the above information was recorded in HAZOP worksheet at C:\Amin_Treater-V-201\PHA\HAZOP_Worksheet-2012-013AI.pdf. Information of the previous accidents was recorded in the accident log book of LPGU and also at C:\Amin_Treater-V-201\PHA\Recent_Incident-2012-013AE.pdf. For incomplete information, "Norsyida" and "Ng Siew" have been assigned to compile and provide the information within the specified time frame.

D. PHA Team Members 29 CFR 1910.119(e)(4)

In this case, a PHA study for V-201 has been done by PHA team led by safety expert who is also knowledgeable of the HAZOP procedures. Other team members are involved directly with the identified unit operation within the node, hence capable to contribute in the PHA development.

E. PHA Recommendations and Required Actions 29 CFR 1910.119(e)(5)

PHA requires the measured excessive risk to be managed. Therefore, a tracking system is in place to ensure that necessary action will be taken timely based on the findings and recommendations by PHA team. PROHAMS can check the accessibility of the PHA information by the relevant personnel. The tracking was conducted by checking the last login date in PROHAMS. Hence, PHA outcomes, recommendations and required actions could be communicated effectively within the process plant. In this case, it was found that not all of them have completely accessed the PHA outcomes.

F. Validation of PHA Data 29 CFR 1910.119(e)(6)

PSM is primarily a performance-based regulation, thus an employer should determine appropriate frequency at least every five years for updating and revalidating PHA information. The 'Revalidate' column in PHA schedule of PROHAMS (Fig. 3) makes the planning process easier by providing the latest update of PHA information. The revalidation allows the employer to have an updated PHA, which is consistent with the current plant operation.

G. Retention Life of PHA Data 29 CFR 1910.119(e)(7)

Once PHA process is completed, the employer is required to retain all the PHA information. This includes the updated and revalidated data, as well as the records related to the resolution of recommendations as described in 29 CFR 1910.119(e)(5) for the life of the process plant. PROHAMS is designed to manage the above information in the database for easy retrieval. This system also assists the authorized personnel to assess the PHA data retention life based on the date of PHA process at 'Retention Date' column in the PHA schedule of Fig. 3.

Date	Description	Remarks	Revalidate (e)(6)	Retention time (e)(7)
4/19/2012	Pre Assessment of PHA	Overall LPGU	-	-
5/10/2012	Revalidation of Fire Safety Review	Overall LPGU	-	-
5/11/2012	Review of Recent Change	V-201	-	-
5/12/2012	Review of Recent Incident	V-201	5/12/2015	12 months
5/12/2012	Site Visit and Nodes revalidation	Overall LPGU	-	-
5/13/2012	Review HAZOP study	V-201	5/13/2015	12 months
5/16/2013	Revalidation of Risk Ranking	V-201	5/16/2015	12 months
5/16/2012	PHA Revalidation Recommendations	V-201	5/16/2015	12 months
6/6/2012	PSI errors for correction	Overall LPGU	-	-
8/15/2012	Address the PHA team's finding and recommendation actions	Overall LPGU	-	-

Fig. 3 PHA Schedule

PHA methodologies	Start date	End date	Evidence location	Revision date	Approved by
Hazard and Operability Study (HAZOP)	5/10/2012	5/16/2012	C:\Amine Treater-V-201\PHA\HAZOP Report -2012- Signed.pdf	7/17/2012	JJM

Fig. 4 PHA Methodology

Sub-standard	Requirement	Description	Evidence location	Complete	Incomplete	Remarks	Action by	Due date
1910.119(e)(3)(i)	Process hazard	Refer to possible cause column in HAZOP study	C:\Amine Treater-V-201\PHA\HAZOP Worksheet-2012-013A1.pdf	<input checked="" type="checkbox"/>	<input type="checkbox"/>			
1910.119(e)(3)(ii)	Previous accidents	Refer to review of recent incident	C:\Amine Treater-V-201\PHA\Recent Incident- 2012-013AE.pdf	<input checked="" type="checkbox"/>	<input type="checkbox"/>			
1910.119(e)(3)(iii)	Engineering and administrative controls	Refer to safeguards column in HAZOP study	C:\Amine Treater-V-201\PHA\HAZOP Worksheet-2012-013A1.pdf	<input checked="" type="checkbox"/>	<input type="checkbox"/>			
1910.119(e)(3)(iv)	Consequence due to failure of engineering and administrative controls	Refer to consequence column of HAZOP study	C:\Amine Treater-V-201\PHA\HAZOP Worksheet-2012-013A1.pdf	<input checked="" type="checkbox"/>	<input type="checkbox"/>			
1910.119(e)(2)(v)	Facility siting	Not available		<input type="checkbox"/>	<input checked="" type="checkbox"/>	On-going	Nbrasyids	6/28/2013
1910.119(e)(2)(vi)	Human factor	Not available		<input type="checkbox"/>	<input checked="" type="checkbox"/>	On-going	No Sign	7/31/2013
1910.119(e)(3)(vii)	Qualitative evaluation of safety and health effects	Refer to risk ranking column in HAZOP study	C:\Amine Treater-V-201\PHA\HAZOP Worksheet-2012-013A1.pdf	<input checked="" type="checkbox"/>	<input type="checkbox"/>			

Fig. 5 PHA Outcomes

V. CONCLUSION

A systematic technique towards PHA implementation in process plant based on PSM requirements is presented in this study. The technique for implementation and process data management is clearly tabulated through established PHA framework and P&ID study node Implementation of this technique could manage process hazards successfully that is in compliance with PSM regulation.

ACKNOWLEDGMENT

The researches would like to acknowledge University Teknologi PETRONAS for the support in terms of financial and research materials.

REFERENCES

- [1] P.P. Howell, "Plant Explosion Emphasizes Importance of Implementing PSM," *Process Saf. Prog.* vol. 29, no.2, pp. 144-149, 2010.
- [2] M. Kaszniak, "Oversights and Omissions in Process Hazard Analyses: Lessons Learned from CSB Investigations," *Process Saf. Prog.* Vol. 29, no. 3, pp. 264-269, 2010.
- [3] L.A. Long, "History of Process Safety at OSHA," *Process Saf. Prog.* vol. 28, no. 2, pp. 128-130, 2009.
- [4] J.F. Louvar, "Improving the Effectiveness of Process Safety Management in Small Companies," *Process Saf. Prog.* vol.27, no. 4, pp. 280-283, 2008.
- [5] H. A. Aziz, A. M. Shariff and R. Rusli, "Managing Process Safety Information Based on Process Safety Management Requirements," *Process Saf. Prog.* vol. 00, no. 00, pp. 1-8, 2013.
- [6] M. Kho, "Strengthening Process Safety Requirements in Hse Management System an Noc's Experience" AIChE PPSS Conference, Ernest N. Morial Convention Center, 2008.
- [7] W.F. Early, "Database Management Systems for Process Safety," *J. Hazard. Mater.* vol. 130, no. 1-2, pp. 53-57, 2006).
- [8] S. Arendt, "Continuously Improving Psm Effectiveness—a Practical Roadmap," *Process Saf. Prog.* vol. 25, no. 2, pp. 86-93, 2006.
- [9] P.R. Amyotte, A.U. Goraya, D.C. Hendershot, and F.I. Khan, "Incorporation of Inherent Safety Principles in Process Safety Management," *Process Saf. Prog.* vol. 26, no. 4, pp. 333-346, 2007.
- [10] M.I. Rashid, N. Ramzan, T. Iqbal, S. Yasin, and S. Yousaf, "Implementation Issues of Psm in a Fertilizer Plant: An Operations Engineer's Point of View," *Process Saf. Prog.* vol. 32, no. 1, pp. 59-65, 2013).
- [11] S.G. Kariuki and K. Löwe, "Integrating Human Factors into Process Hazard Analysis," *Reliab. Eng. Syst. Safe.* vol. 92, no. 12, pp. 1764-1773, 2007.
- [12] CCPS, "Guidelines for Implementing Process Safety Management Systems," American Institute of Chemical Engineers, New York, 1994.
- [13] CCPS, "Guidelines for Risk Based Process Safety," John Wiley & Sons, Inc. New Jersey, 2007.
- [14] D. Einolf and L. Menghini, "PSM/RMP Auditing Handbook: A Checklist Approach," Government Institutes, United States of America, 1999.

Prof. Dr. Azmi Mohd Shariff is a Professor in Chemical Engineering Department at Universiti Teknologi PETRONAS (UTP), Perak, Malaysia. He was conferred a PhD in Chemical Engineering from University of Leeds, United Kingdom (1996). He was with Universiti Kebangsaan Malaysia in 1989 as a tutor and was appointed as a lecturer in 1996 upon his return from University of Leeds. He joined Universiti Teknologi PETRONAS in 1997. He was appointed as the Head of Industrial Internship in 1998 and later he was appointed as Head of Chemical Engineering Department from 1999 until 2003.

His current research works are in the area of process safety and CO₂-NG separation. In the area of Process Safety, his research works are in the area of QRA, PSM, BBS and Inherent Safety. In the area of CO₂-NG separation, his research works are in the area of CO₂ Capture Technology, specifically on Absorption, Adsorption and Membrane. He can be reached at azmish@petronas.com.my.

Hanida Abdul Aziz is a PhD candidate in Process Safety at Universiti Teknologi PETRONAS, Malaysia. She received a MSc of Chemical Engineering from Universiti Sains Malaysia. Before joining UTP, She worked for Institut Teknologi PETRONAS as a lecturer. She is also has experienced as team member in conducting QRA for oil and gas related companies. She can be reached at hanidaaziz@gmail.com.

Kwang Hooi Yew is a lecturer in Computer and Information Sciences Department at Universiti Teknologi PETRONAS (UTP), Perak, Malaysia. Currently, he is doing PhD at Universiti Teknologi PETRONAS, Malaysia. He received a MSc of Engineering in Computer science, from Cornell University, New York, United States (2006). His current research works are in the area of Sentiment Analysis, Semantic Analysis, Natural Language Processing, Artificial Intelligence, Algorithm and data structure.

Predicted formation and deposition of slag from lignite combustion on pulverized coal boilers

Pakamon Pintana, and Nakorn Tippayawong

Abstract—Lignite is the main source of energy used to generate electricity in Thailand. Slag in pulverized coal boilers is normally the main problem associated with combustion of this solid fuel. In this work, numerical simulation was applied to Mae Moh coal fired power plant. Prediction of ash melting points was used to identify possibility of slag formation. CFD simulation of the boilers' wall temperatures and coal particle trajectories were used to predict and assess deposition potential of slag inside the boiler. It was found to have great potential to quantitatively and qualitatively predict and identify formation and deposition of slag in the boilers.

Keywords—slag, pulverized coal combustion, ash deposition, CFD simulation

I. INTRODUCTION

LIGNITE coal is a major source of energy in the North of Thailand. But, it is usually of poor quality, with high moisture, sulfur, and ash contents. Under management of Electricity Generating Authority of Thailand (EGAT), Mae Moh power plant is a steam power plant that utilizes this lignite as fuel. Its pulverized coal boilers are generating electricity with the total capacity of 2,400 MW, accounting for about 12% of the national electricity consumption. The fuel consumption is about 15-17 million tons per year, obtaining from the Mae Moh mine.

A major operation challenge faces by EGAT engineers is management of ash. For a pulverized coal boiler, there is always slag in the furnace. Soot blowers normally operate to remove the slag from the wall. However, if slag in the boiler becomes excessive, the soot blowers may not be able to handle it, and radiation heat transfer decreases, leading to lower overall boiler efficiency. Subsequent problems associated with slag such as loss of capacity, loss of heat, boiler equipment damage, loss of time and money in maintenance boiler will occur.

Slag consists of fused deposits or a re-solidified molten material that forms primarily on the walls of the furnace or on other surfaces predominately exposed to the radiant heat or excessively high gas temperatures [1]. Slag is caused by many

factors, such as the coal organic properties, coal mineral matter properties, mineral transformation and decomposition, temperature of the boiler furnace, the fluid dynamics, ash transport, vaporization and condensation of the ash species, deposit chemistry-specie migration and reaction etc. [2-3].

In this work, the slagging potential (combined effect of the slag liquid formation, ash flow distribution, and temperature profiles) in a pulverized coal fired boiler of EGAT Mae Moh power plant was investigated, using software programs.

II. METHODOLOGY

A. Lignite

The fuel properties of lignite coal were analyzed for proximate and ultimate composition, as well as its heating value. Additionally, its ash composition and ash fusibility temperatures were also analyzed [4-10]. Results are shown in Table 1.

B. Boiler Geometry

A furnace of 300 MWe Mae Moh tangentially fired boiler is shown in Fig. 1. The dimensions are 13.8 m in width and 15.3 m in breadth. The height from the lowest at hopper to the highest at the superheater and reheater is 54.3 m. On the walls, there are 4 windboxes for four corners to generate tangential fired balls. There are 4 secondary air panels, 5 panels for mixing of primary air and coal powder, an over fire air panel, a bottom air panel, and a warm up oil panel in 1 windbox.

C. FactSage Program

The FACTSAGE program has been developed as an efficient predictive tool for prediction of liquidus temperature, proportions of solids, mineral formation, and phase equilibria of ash samples [6-14]. FactSage is the fusion of two well-known software F*A*C*T/FACT-Win and ChemSage and it is the largest thermochemical package and database available for inorganic solid and slag in the field of computational thermochemistry. The package runs on a PC operating under Microsoft Windows [5].

The Equilib module (thermodynamic application calculations) and Phase Diagram module (phase diagram calculations) are used to incorporate the FactSage Gibbs energy minimizer [15]. It calculates the concentrations of chemical species when specific elements or compounds reacted or partially reacted, in order to reach a state of chemical equilibrium [16]. In this study, these modules were used to predict the ash behavior, the ash fusion temperature.

This work was supported by the Royal Golden Jubilee PhD program, Thailand Research Fund under grant no. PHD/0114/2552.

P. Pintana is with the Department of Mechanical Engineering, faculty of Engineering, Chiang Mai University, Chiang Mai 50200, Thailand (e-mail: p.pintana@gmail.com).

N. Tippayawong is with the Department of Mechanical Engineering, faculty of Engineering, Chiang Mai University, Chiang Mai 50200, Thailand (corresponding author: tel.: +66-5394-4146; fax: +66-5394-4146; e-mail: n.tippayawong@yahoo.com).

Table 1 Coal and ash properties

Proximate analysis (% w/w, as-received basis)	
Moisture content	35.07
Volatile matter	28.17
Fixed carbon	25.86
Ash	10.91
Ultimate analysis (% w/w, dry basis)	
Carbon (C)	58.54
Hydrogen (H)	3.00
Nitrogen (N)	1.89
Oxygen (O)	12.88
Sulfur (S)	5.49
Heating value (MJ/kg dry basis)	
HHV	22.80
LHV	22.15
Ash composition (% w/w)	
SiO ₂	21.28
Al ₂ O ₃	13.43
TiO ₂	0.24
CaO	11.08
Fe ₂ O ₃	28.03
Na ₂ O	1.87
MgO	4.02
K ₂ O	1.31
SO ₃	18.64
P ₂ O ₅	0.07
MnO ₂	0.04
Ash fusion temperature (°C)	
IT	1235
ST	1305
HT	1340
FT	1480

D. CFD Simulation

Computational fluid dynamics (CFD) has been used to simulate the firing of coal combustion under different operating conditions extensively [17-20]. In this work, a commercial CFD package, ANSYS Fluent, was used to predict gas flow, temperature distribution and particle trajectory that can adapt to predict slagging behavior [12, 21].

In generally, coal combustion in CFD models is used to solve for fluid flow, turbulence, particle trajectory, heat transfer, chemical reactions of the fuel, and the formation of pollutants [22]. In this study, FLUENT version 13.0 was used to predict the temperature and flow distribution inside a boiler. The wall heat flux was evaluated for comparison with real operating parameters. The information was combined with those from FactSage method to predict deposition of slag in the boiler furnace. All numerical simulation was performed at the University of Leeds.

A furnace was generated into 3-D geometry using ICEM CFD. The furnace geometry used approximately 470,000 computational grid cells with 4 blocks. The properties of coal particle was set at: as-received HHV = 14.82 MJ/kg, volatile molecular weight = 30 kg/kg mol, CO/CO₂ = 1 split in reaction products, high temperature volatile yield = 1.5, fraction of N in char = 0.7, and dry density = 800 kg/m³. The boundary conditions used for the CFD model were taken from the real operating condition in Mae Moh power plant.

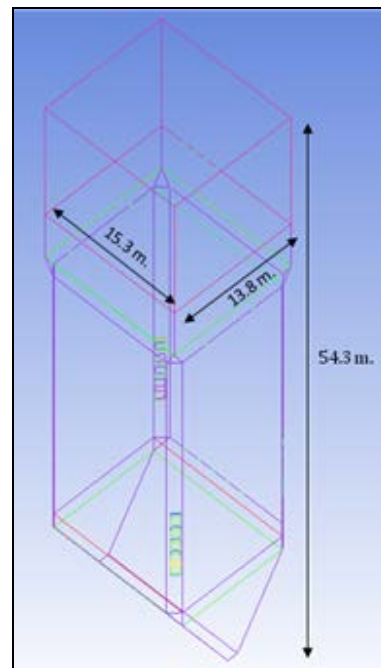


Fig. 1 The geometry of Mae Moh boiler

The inlet boundary condition was set to velocity inlet. The outlet boundary condition was set to outflow at the top of geometry. The wall boundary condition was divided into two parts; the bottom outlet was set to escape wall, all wall surface was set to no-slip condition, 4.572 mm thick with temperature = 673 K, internal emissivity = 0.8, and thermal conductivity of material = 1.5 W/m-K.

The RNG k- ϵ turbulence model was used. The Discrete Ordinate radiation model was commonly used in coal combustion. The combustion model used is the Eddy Dissipation with two step of chemical reaction.

III. RESULTS AND DISCUSSION

A. Slag Formation

Predicted mineral transformation and slag-liquid formation of the sample coal are shown in Table 2. It was found that as the temperature increases to 950°C, slag-liquid starts to form. The main solids at 800°C are hematite (Fe₂O₃), anhydrite (CaSO₄), and high-albite (NaAlSi₃O₈). They decreased at higher temperature. Unlike the main solid, the slag-liquid increased at higher temperature. Fig. 2 presents total slag formation. The equilib model can be used to predict quantity and identify the details of slag-liquid formed and composition at operating temperature, which can be applied to design temperature in the boiler furnace.

B. Ash Melting Temperature

The main compositions (SiO₂, Al₂O₃, CaO, and Fe₂O₃) in ash of blended coal were select to plot against with fusion temperature in ternary phase diagram. Fig. 3 presents the ash melting temperature predicted by phase diagram.

Table 2 The mineral matter output form Equilib model

Mineral composition (g/100g of lignite)	Temperature (°C)				
	800	1000	1200	1400	1600
Slag-liquid	0.0	0.7	8.7	14.2	14.3
Fe ₂ O ₃	5.1	5.1	4.5	0.0	0.0
CaSO ₄	4.9	2.5	0.0	0.0	0.0
NaAlSi ₃ O ₈	2.9	0.0	0.0	0.0	0.0
Mg ₂ Al ₄ Si ₅ O ₁₈	1.8	0.0	0.0	0.0	0.0
Mg ₄ Al ₁₀ Si ₂ O ₂₃	1.5	0.0	0.8	0.0	0.0
KAlSi ₂ O ₆	1.1	1.1	0.8	0.4	0.0
Mg ₂ SiO ₄	0.3	1.2	0.0	0.0	0.0
CaAl ₂ Si ₂ O ₈	0.0	4.4	0.0	0.0	0.0
NaAlSiO ₄	0.0	1.2	0.0	0.0	0.0
CaTiO ₃	0.0	0.1	0.0	0.0	0.0
Ca ₂ MgSi ₂ O ₇	0.0	0.0	0.0	0.0	0.0
CaMg ₂ Al ₁₆ O ₂₇	0.0	0.0	0.0	0.0	0.0

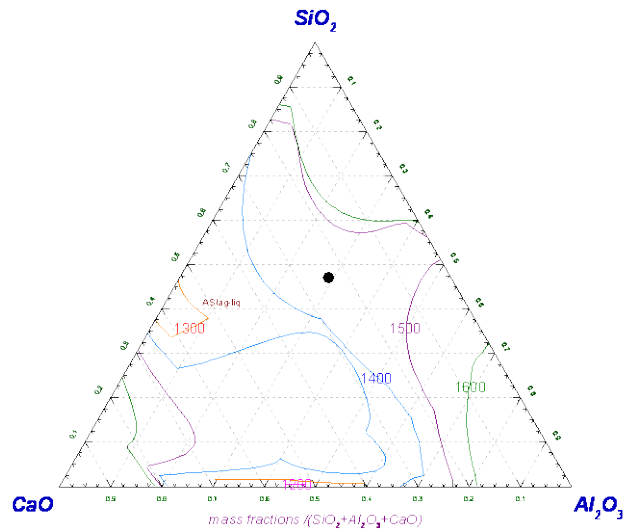


Fig. 3 Predicted ash melting point of SiO₂-Al₂O₃-CaO-Fe₂O₃ system

C. Potential of Slag Deposition

CFD simulation results are shown in Figs. 4-6. The wall temperature and the particle trajectory were applied with predicted deposition potential of slag inside the boiler furnace. The CFD simulation was conducted using the real operation information (coal properties and real operation) and it will be useful for comparison with the measured heat flux and flue gas outlet.

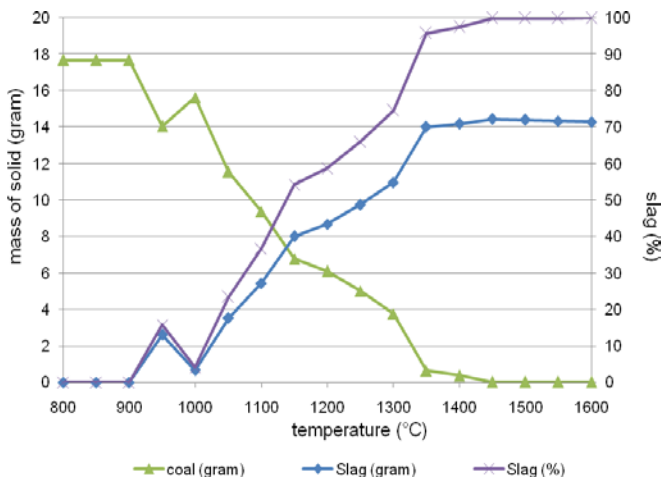


Fig. 2 Trend of slag formation

The superimpose function in FactSage was used in quaternary diagram. The possible reason for this behaviour is that the CaO, Fe₂O₃, SiO₂, and Al₂O₃ are significantly.

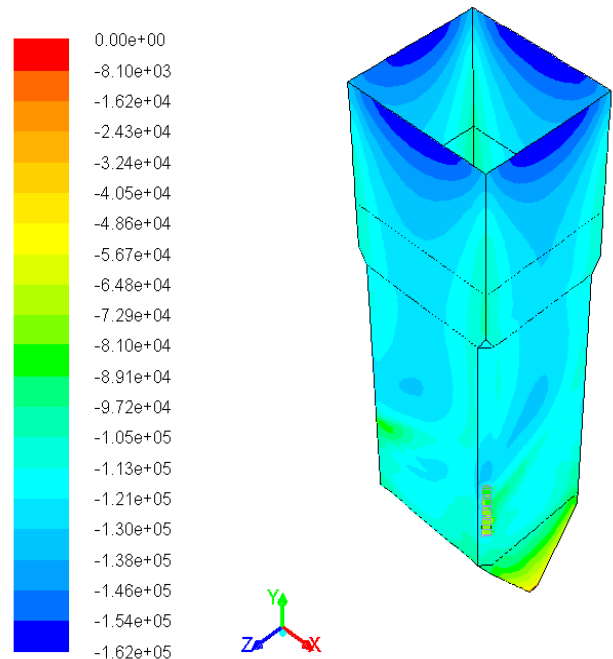


Fig. 4 Surface heat flux (W/m²)

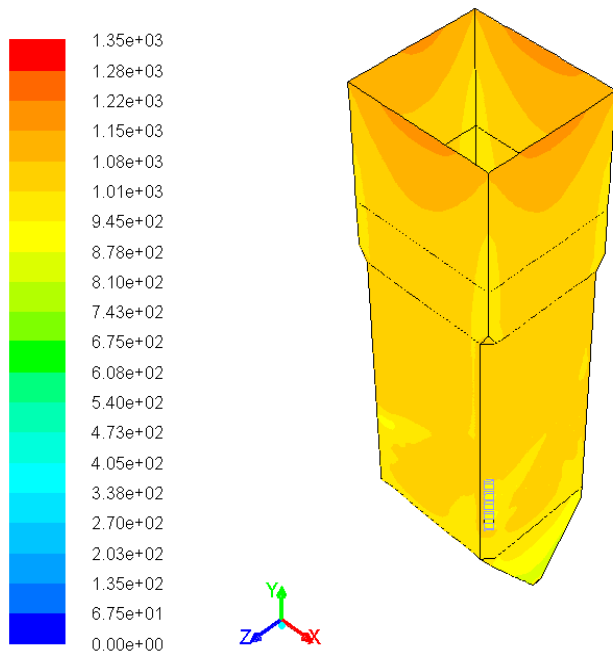


Fig. 5 Wall temperature inside boiler (K)

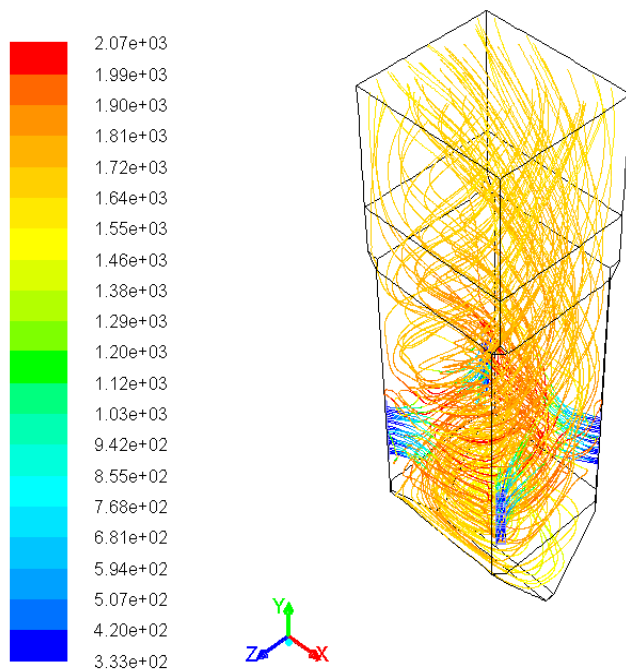


Fig. 6 Particle trajectory and temperature (K)

IV. CONCLUSION

The equilibrium and phase diagram models were found to be useful in identifying composition of slag and predicting ash fusion temperature. The CFD simulation results of gas temperature distribution, particle temperature and trajectory showed possibility of slagging deposition. The results of FactSage program may be used to compare with subsequent slag and ash fusion temperature experiments.

ACKNOWLEDGMENT

Technical assistance from the Energy Technology and Innovation Initiative, University of Leeds, is greatly appreciated, with special thanks to Profs. D. Ingham, M. Pourkashanian, A. Williams, J. Jones, and Dr L. Ma. We also wish to acknowledge support the EGAT Mae Moh power plant and its staff.

REFERENCES

- [1] J.G. Singer, "Combustion fossil power systems," INC., 1000 Prospect Hill Rd, Windsor, CT.
- [2] R.W. Borio, A.A. Levaseur, "Overview of coal ash deposition in boilers," 188th Meeting of the American Chemical Society, Philadelphia, USA, 1984, pp. 193-203.
- [3] K. Akiyama, H. Pak, Y. Takubo, T. Tada, Y. Ueki, R. Yoshiie, and I. Naruse, "Ash deposition behavior of upgraded brown coal in pulverized coal combustion boiler," *Fuel Processing Technology*, vol. 92, pp. 1355-1361, 2011.
- [4] S. Pipatmanomai, B. Fungtammanan, and S. Bhattacharya, "Characteristics and composition of Lignites and boilers ashes and their relation to slagging : The case of Mae Moh PCC boilers," *Fuel*, vol. 88, pp. 116-123, 2009.
- [5] J.C. van Dyk, "Understanding the influence of acidic components (Si, Al, and Ti) on ash flow temperature of South African coal sources," *Minerals Engineering*, vol. 19, pp. 280-286, 2006.
- [6] F.E. Huggins, D.A. Kosmack, and G.P. Huffman, "Correlation between ash-fusion temperatures and ternary equilibrium phase diagrams," *Fuel*, vol.60, pp. 557-584, 1981.
- [7] E. Jak, "Prediction of coal ash fusion temperatures with the F*A*C*T thermodynamic computer package," *Fuel*, vol. 81, pp. 1655-1668, 2002.
- [8] W. Song, L. Tang, X. Zhu, Y. Wu, Y. Rong, Z. Zhu, and S. Koyama, "Fusibility and flow properties of coal ash and slag," *Fuel*, vol. 88, pp. 297-304, 2009.
- [9] W.J. Song, L.H. Tang, X.D. Zhu, Y.Q. Wu, Z.B. Zhu, and S. Koyama, "Prediction of Chinese Coal Ash Fusion Temperatures in Ar and H₂ Atmospheres," *Energy&Fuel*, vol. 23, pp. 1990-1997, 2009.
- [10] L. Kong, J. Bai, Z. Bai, Z. Guo, and W. Li, "Effects of CaCO₃ on slag flow properties at high temperatures," *Fuel*, vol. 109, pp. 76-85, 2013.
- [11] J.C. van Dyk, F.B. Waanders, S.A. Benson, M.L. Laumb, and K. Hack, "Viscosity predictions of the slag composition of gasified coal, utilizing FactSage equilibrium modelling," *Fuel*, vol. 88, pp. 67-74, 2009.
- [12] L. Chen, S.Z. Yong, and A.F. Ghoniem, "Modeling the slag behavior in three dimension CFD simulation of a vertically-oriented oxy-coal combustor," *Fuel Processing Technology*, vol. 112, pp. 106-117, 2013.
- [13] W. Song, Y. Sun, Y. Wu, Z. Zhu, and S. Koyama, "Measurement and Simulation of Flow Properties of Coal Ash Slag in Coal Gasification," *AIChE Journal*, vol. 57, No. 3, pp. 801-818, 2011.
- [14] N. Wang, M. Chen, Z. Zou, Z. Zhang, Y. Xiao, and Y. Yang, "Liquidus and phase equilibria in CaO-Al₂O₃-FeOx-SiO₂ system under intermediate oxygen partial pressure," *Journal of Mining and Metallurgy, Section B: Metallurgy*, vol. 49, No. 2, pp. 139-144, 2013.
- [15] G. Eriksson, and E. Konigsberger, "FactSage and ChemApp :Two tools for the prediction of multiphase chemical equilibria in solutions," *Pure Appl. Chem.*, Vol. 80, No. 6, pp. 1293-1302, 2008.
- [16] R.H. Matjie, "Sintering and slagging of mineral matter in South African coals during the coal gasification process," Thesis of the degree Philosophiae Doctor in the Faculty of Engineering, Built Environment and Information Technology, University of Pretoria, 2008.
- [17] S. Black, J. Szuhanski, A. Pranzitelli, L. Ma, P.J. Stanger, D.B. Ingham, and M. Pourkashanian, "Effects of firing coal and biomass under oxy-fuel conditions in a power plant boiler using CFD modelling," *Fuel*, vol. 113, pp. 780-786, 2013.
- [18] A.H. Al-Abbas, J. Naser, and E.K. Hussein, "Numerical simulation of brown coal combustion in a 550 MW tangentially-fired furnace under different operating conditions," *Fuel*, vol. 107, pp. 688-698, 2013.
- [19] T. Asotoni, T. Yamashita, H. Tominaga, Y. Uesugi, Y. Itaya, and S. Mori, "Prediction of ignition behavior in a tangentially fired pulverized coal boiler using CFD," *Fuel*, vol. 87, pp. 482-490, 2008.

- [20] L. Ma, M. Gharebaghi, R. Porter, M. Pourkashanian, J.M. Jones, and A. Williams, "Modelling methods for co-fired pulverised fuel furnaces," *Fuel*, vol. 88, pp. 1448-1545, 2009.
- [21] C. Mueller, M. Selenius, M. Theis, B.J. Skrifvars, R. Backman, M. Hupa, and H. Tran, "Deposition behavior of molten alkali-rich fly ashes-development of a submodel for CFD applications," *Proceeding of the Combustion Institute*, vol. 30, pp. 2991-2998, 2005.
- [22] R.I. Backreedy, R. Habib, J.M. Jones, M. Pourkashanian, and A. Williams, "An extended coal combustion model," *Fuel*, vol. 78, pp. 1745-1754, 1999.

P. Pintana graduated with B.Eng. in agricultural engineering from Maejo University, Thailand and M.Eng. in energy engineering from Chiang Mai University, Thailand. She is currently pursuing her Ph.D. in mechanical engineering at Chiang Mai University. Her fields of specialization are Energy Engineering, CFD, and Ash Characterization.

N. Tippayawong graduated with B.Eng. in mechanical engineering and Ph.D. in IC engines from Imperial College London, UK. He is currently an associate professor at the Department of Mechanical Engineering, Chiang Mai University, Thailand. His fields of specialization are Energy Efficiency, Biomass Conversion, and Aerosol Technology.

Real Time IVUS Segmentation and plaque characterization by combining Morphological Snakes and Contourlet Transform

Mohamed Ali HAMDI , Karim Saheb Etabaa and Mohamed Lamine HARABI

Abstract – After the principal custom of the technics of intravascular ultrasound (IVUS) as an imaging technique for the coronary artery system 70th century until nowadays, the segmentation of the arterial wall boundaries and plaque characterization still an imperative problem. Much research has been done to give improved segmentation result for better diagnostics, therapy planning and evaluation. In this paper we present a new segmentation technics by combining Contourlet transform and Morphological Snakes which developed by Luis Alvarez used for IVUS segmentation followed by plaque characterization. The morphological snakes associate the morphological and differential operators used in the standard PDE based snake models. Results are presented and discussed in order to demonstrate the effectiveness of this approach in IVUS segmentation.

Keywords: Contourlet transform, IVUS Segmentation, Morphological Snakes, Plaque characterization

I. Introduction

From its improvement in the 1970s [1], Intra Vascular Ultra Sound (IVUS) has become a precious technique for diagnosis and the treatment of coronary artery diseases [3][5]. Intra Vascular Ultra Sound (IVUS) is a catheter-based system that give 2D cross sectional images of the coronary[14][16] arteries and offers information concerning the lumen and the vessel wall. In a typical IVUS image[4], we compare three regions: the lumen, the vessel wall, consisting of the adventitia and the intima layers and the media plus surroundings [3]. Characterization of the plaque composition remains difficult, Studies have exposed the advantage of IVUS in applications where precise quantification and visualization of atherosclerotic plaques[8] is required [6][7], such as assessing stent deployment or plaque progression – regression studies of lipid-lowering medical therapy

Despite the good susceptibility determination, IVUS has the difficulty that manual analysis of the huge amount of images is problematic, time-consuming, and subjective. Thus, there is a huge interest for the development of automatic segmentation technics for IVUS images. This present a challenge due to image quality and the noise.

Much of research [23][24][25] on this question has been done using different technics and algorithms like live wire, active contours, shape-driven. In this study, a new algorithm developed by combining Morphological snake, the so-called Morphological snake and the contourlet transform, this technic is employed to detect Lumen, Media /Adventitia [2]contours and plaque characterization. We used this new snake in a traditional segmentation pipeline: first, the preprocessing of the image, then, catheter circle detection and finally Snakes initialization.

II. Preprocessing

IVUS images are quite noisy, so to perform the segmentation [15] in an easier way, denoising it is a necessary step to apply filters. Many different types of filters were tested, wavelet transform, Curvelet transform and contourlet transform. Finally we have chosen the Contourlet transform which gave the best result.

Recently Do and Vetterli proposed an efficient directional multi resolution image representation called the contourlet transform. Contourlet transform has better performances in representing the image such as lines, edges, contours [18] and curves than wavelet and curvelet transform because of its directionality and anisotropy. The contourlet transform consists of two steps which is the sub band decomposition and the directional

transform. A Laplacian pyramid is first used to capture point discontinuities then followed by directional filter banks to link point discontinuity into lineal structure. The overall result is an image expansion using basic elements like contour segments thus the term Contourlet transform being coined [26].

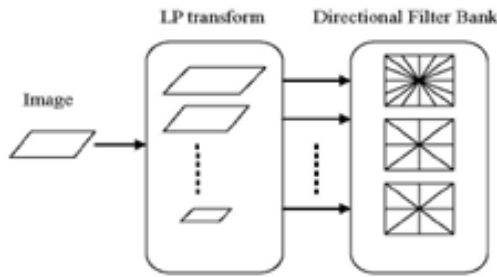


Fig. 1. The Contourlet transform framework

This Fig. shows a flow diagram of the Contourlet transform.

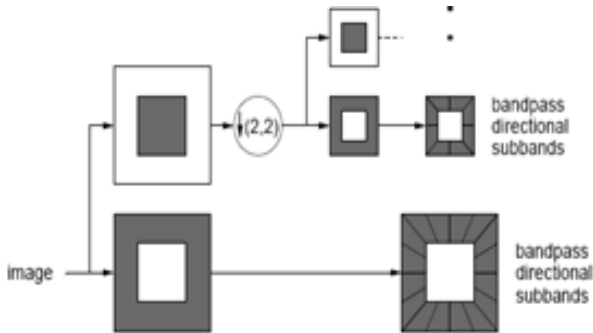


Fig. 2. The Contourlet filter bank [27]

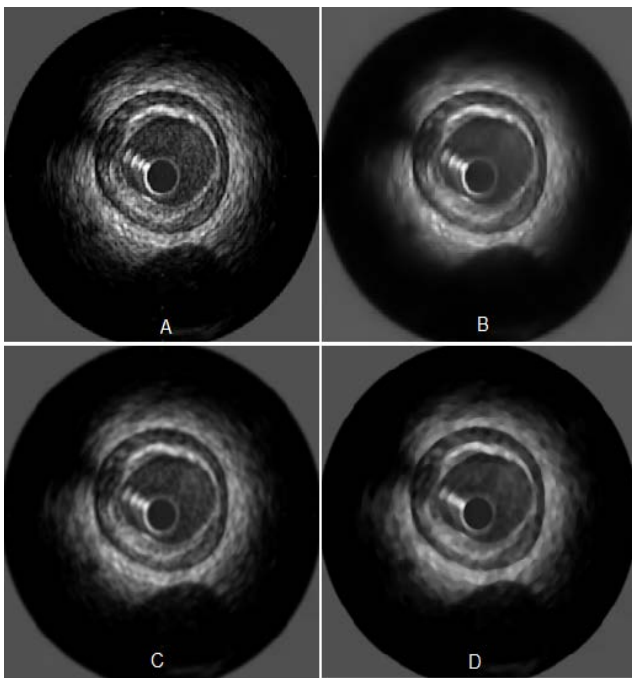


Fig. 3. An example of filtered image with three different low pass filters: (A) Original image. (B) Denoised image by using Contourlet transform. (C) Curvelet transform. (D) Wavelet transform

III. The Morphological Snake

Many technics were used like level set, active snakes, live wire [10-16] to detect the media-adventitia contour [2]. In our case we propose a solution based on morphological snake.

This algorithm developed by Alvarez [17] and his colleagues uses a morphological discretization of the Partial Differential Equations of curve evolution of the geodesic active contours in a level set framework. The main steps of this algorithm are:

- 1- The contour is represented in an implicit form included as the level set of an embedding function calculating the contour signed distance function [21] [22].
- 2- Solving the Partial Differential Equations in a contour narrow band . .
- 3- Keeping the stability of the algorithm by reinitializing of the distance function and the contour [17].

Let C a parameterized 2D curve ; $C : [0,1] \rightarrow \mathbb{R}^2$ and I an image $I : \mathbb{R}^2 \rightarrow \mathbb{R}$. Under the effect of the scalar field F the curve is deformed along its inwards normal vector, in other word $C_t = N \cdot F$.

In the geodesic active contours [18][21] : F is approached by:

$F = g(I)k + g(I)v - \nabla g(I) \cdot N$, with k is Euclidian curvature , v is a real parameter of the balloon force term [22] and $g(I)$ is a function low at the boundaries of image and selects the region which will attract the contour , In general $g(I)$ is defined by :

$$g(I) = \frac{1}{\sqrt{1 + \alpha |\nabla g \cdot \mathbf{n}|}} \quad (1)$$

At the boundaries of the image:

$$g(I) = |G_\sigma * I| \quad (2)$$

We define u as an implicit representation of C : $u : \mathbb{R}^2 \rightarrow \mathbb{R}$, $C(t) = \{(x, y); u(t, (x, y)) = 0\}$.

As illustrated previously, the curve evolution has the form $C_t = N \cdot F$ so we can see that the evolution of any function $u(x,y)$ embeds the curve such as one of its level set is :

$$\frac{\partial u}{\partial t} = F |\nabla u| \quad (3)$$

The curvature parameter K is calculated with the information on u : $k = \text{div}(\nabla u / |\nabla u|)$. Arranging all those equations , the geodesic active contours in a level set frame work became :

$$\frac{\partial u}{\partial t} = g(I) |\nabla u| (\text{div}(\nabla u / |\nabla u|) + v) + \nabla g(I) \cdot \nabla u \quad (4)$$

The solution of the previous equation can be spitted into in 3 terms : (1) the Balloon force term, (2) the smoothing term and (3) the attraction force term and we will explore those elements separately

III.1. The Balloon force term

The two known morphological operators erosion and dilatation defined respectively $(E_h u)(x) = \inf_{y \in B_h(x)} u(y)$ and $(D_h u)(x) = \sup_{y \in B_h(x)} u(y)$ with h is the operator radius, B_h is a disk with radius h . In terms of morphology continuous scale, the defined function $u_d(t, x) = D_t u_0(x)$ is the solution of the PDE :

$$\frac{\partial u_d}{\partial t} = |\nabla u_d| \quad (5)$$

With $u_d(0, x) = u_0(x)$, We can deduce that D_h is the infinitesimal generator of the partial differential equation proved by

$$\lim_{h \rightarrow 0^+} \frac{D_h u - u}{h} = |\nabla u| \quad (6)$$

The strength of each segment of the curve is controlled by $g(I)$ which acts as weight factor :when $g(I)$ increase, the corresponding segment moves away from target zone and the balloon force should be strong, otherwise, if $g(I)$ decrease, the corresponding segment approaches from its target and balloon force becomes neglected. In effect, according with the sign and value of v the remaining term $(v |\nabla u|)$ bring us to the dilatation and erosion PDEs [20] given above. At n iteration, the balloon force PDE applied over u^n may be using the morphologic approach [17]:

$$u^{n+1}(x_i) = \begin{cases} (D_d u^n)(x_i) & \text{if } g(I)(x_i) > \theta \text{ and } v > 0 \\ (E_d u^n)(x_i) & \text{if } g(I)(x_i) > \theta \text{ and } v < 0 \\ (u^n)(x_i) & \text{otherwise} \end{cases}$$

With E_d and D_d are the discrete forms of erosion and dilatation. The structure element is formed with eight neighbors of the pixel. E_d and D_d are executed by iterations of 8 or 5 neighborhood minima (or maxima) computation with homogeneous Neumann type borders condition. In our case we used the 5 neighbors version. Additional advantageous option to make evolves this Balloon force term is to use an image interval value: [17-20]

III.2. The smoothing term

Let B a set of all line segments with length of 2 centered at the origin of R^2 . We define the morphological line operators as:

$$(F_h u)(x) = \frac{(S_h u)(x) + (I_h u)(x)}{2} \quad (7)$$

The called Koepller -Catté-Dibos- scheme [19] [17] relates the operator F_t with the mean curvature motion in the following way:

$$(F_h u)(x) = u(x) + h^2 \frac{1}{4} |\nabla u| \operatorname{div} \left(\frac{\nabla u}{|\nabla u|} \right) (x) + O(h^3) \quad (8)$$

And $g(I)$ is a weight factor which controls the strength of the smoothing operation at each point. By discretizing it another time by means of a threshold t_2 the above PDE can be approached by using these line morphological operators in this numerical scheme (approximates mean curvature motion):

$$u^{n+1} = \begin{cases} (S_h \circ I_h u^n)(x) & \text{if } g(I) \geq t_2 \\ u^n(x) & \text{otherwise} \end{cases} \quad (9)$$

With S_h and I_h are discrete forms of the above morphological continuous line operators.

Both S_h and I_h have their specific form of the set B, P , which is a group of four discretized segments centered at the origin:

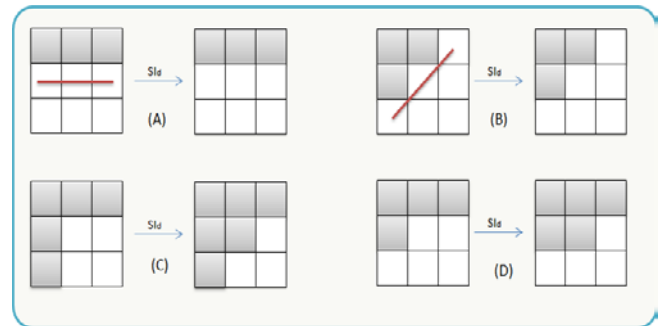


Fig. 4. Some illustrations of the effect of the SID. In those examples where a straight line is found (striking in red), the central pixel remains white ((a)and(b)). When the central pixel don't belong to a straight line of white pixels, it is made inactive ((c)and(d)).

IV. Implementation

As explained above, the active contour equation (4) is made up of three different components: a smoothing force, a balloon force and an attraction force. And these components may be solved with morphological operators, so the algorithm is very easy, in each iteration we will apply the morphological smoothing, the morphological balloon force and the discretized attraction over the embedded level-set function u .

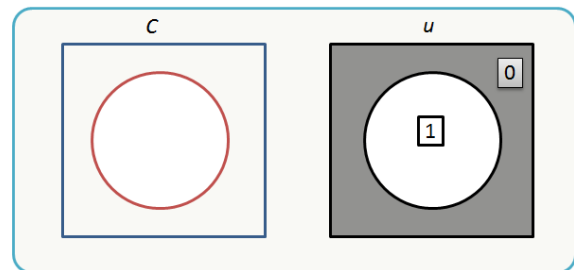


Fig. 5. The curve C and its embedded level-set binary function u .

At n iteration, let $u^n: R^2 \rightarrow \{0, 1\}$ and u^{n+1} from u^n using the following schemes:

$$u^{n+\frac{1}{3}}(x) = \begin{cases} (D_{\alpha} u^n)(x) & \text{if } |v|g(I)(x) > t_1 \text{ and } v > 0 \\ (E_{\alpha} u^n)(x) & \text{if } |v|g(I)(x) > t_1 \text{ and } v < 0 \\ (u^n)(x) & \text{otherwise} \end{cases}$$

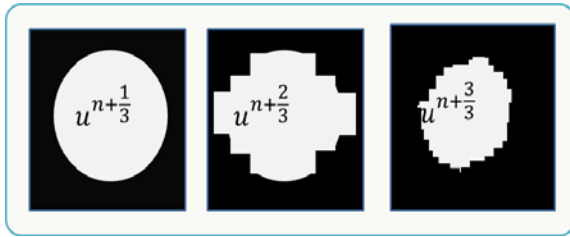


Fig. 6.The level set function u in different iteration

Which represent the morphological implementation of the PDE. Just a reminder , the input and the output level set is a binary image in other words, these 3 numerical systems are morphological that they don't make extra level set values, , [17-20]. The snake is initialized automatically by detecting the catheter circle which detected by using Hough transform .

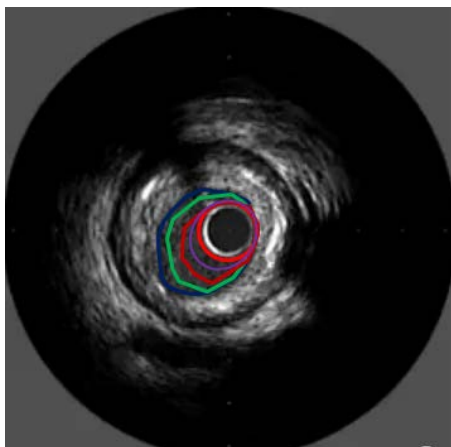
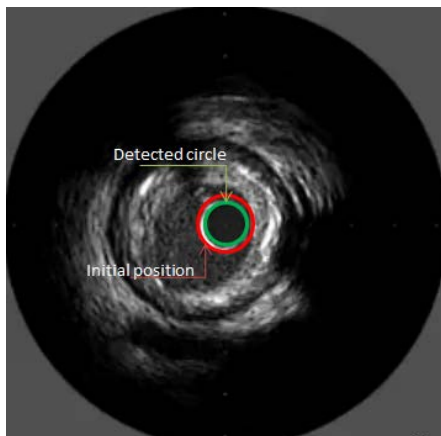


Fig. 7.Snakes initialization .(A) Detection of the catheter circle (green) and the initial position of the Lumen (red)contour snake .(B) Initial position of the Media/Adventitia contours(red)

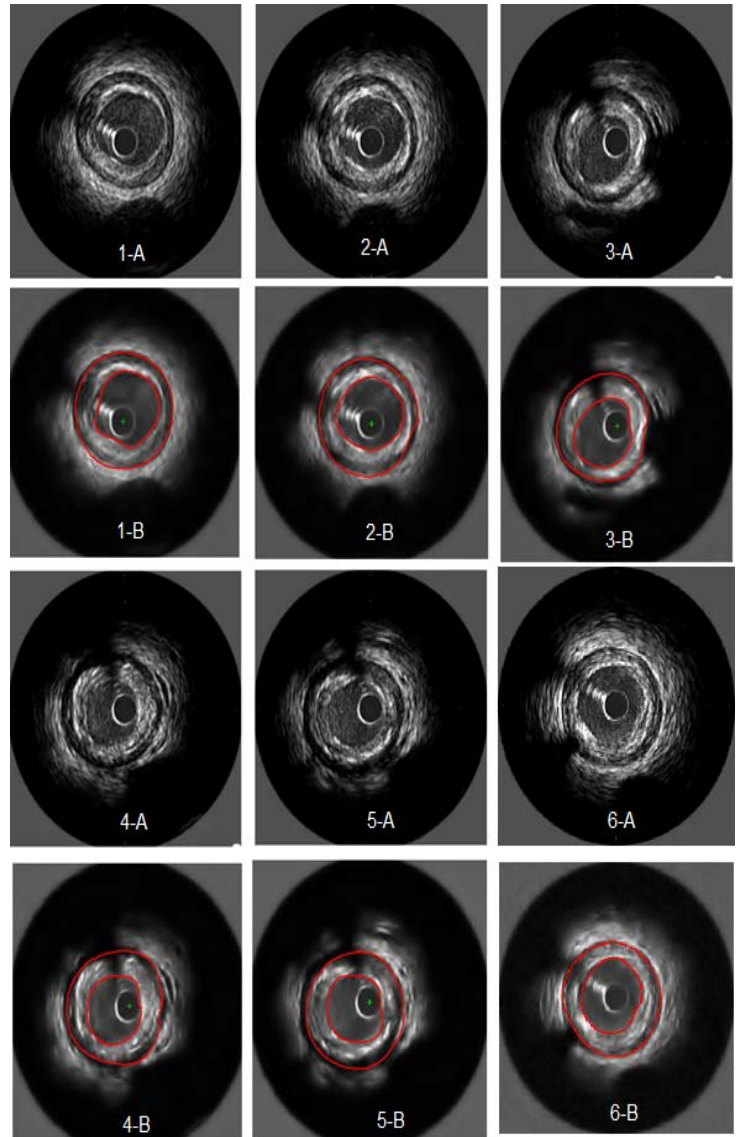


Fig.8.Six Samples from obtained results

The mentioned algorithm was tested by using LabVIEW with 50 IVUS images were acquired with a 20 MHz mechanical catheter using motorized pullback (1mm/s) .Image size was 356 X 356 , those images were analyzed by one experienced observer. The observer used a semi-automatic segmentation method to obtain lumen and vessel contours which were then manually corrected where necessary. No images were excluded and different configurations with calcified plaque, shadows, sidebranches, and drop-out regions were present. The pixel size is 27 x 27 μm^2

IV.1. Plaque characterization

In standard IVUS gray-scale images, calcified regions of plaque and dense fibrous components usually reflect ultrasound energy well and thus appear bright and

homogeneous on IVUS images. Conversely, regions of low echo reflectance in IVUS images are usually labeled "soft" or "mixed" plaque. However, this visual interpretation has been demonstrated to be very inconsistent in accurately determining plaque composition and does not allow real-time assessment of quantitative plaque constituents. Histogram analysis of the image permits detailed evaluation of plaque composition.

After segmentation, ROI is extracted for plaque classification based on gray level median of echogenicity. The following histogram show the distribution of gray scale intensities within the plaque

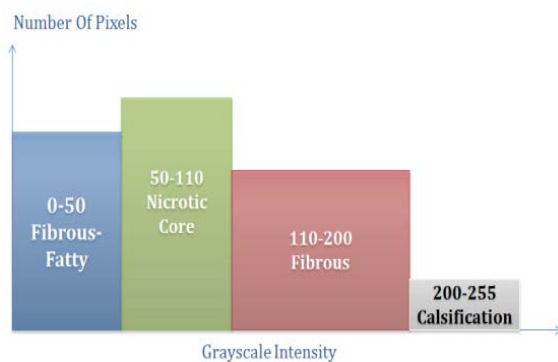


Fig. 9. Grayscale thresholds for plaque classification

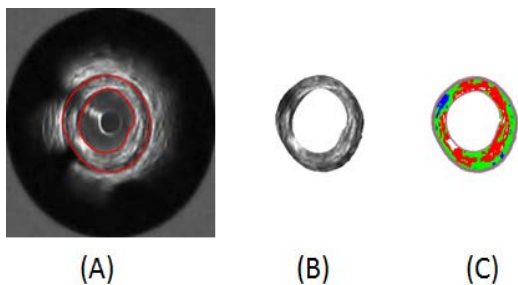


Fig. 10. (A) segmented IVUS images , (B) extraction of RIO and (C) plaque characterization

Calcified and fibrous plaques can be identified in most of the cases , Calcified zones are identified by their hyper echoic appearance and distal shadowing and might be related with acoustic reverberation. Fibrous lesions yield homogeneous echo reflections without distal shadowing. However, the structure of lipid-containing and mixed (fibrous, lipid-calcified) plaques remains unknown in most of the cases.[23, 24,25]

V. Result

For the 50 tested IVUS images, the paired difference between our method and observer, we found a mean difference of $-0,04 \pm 0,47 \text{ mm}^2$ for the vessel, and $0,06 \pm 0,26 \text{ mm}^2$ for the lumen cross-sectional areas

TABLE1. AREA DIFFERENCES BETWEEN THE AUTOMATIC SEGMENTATION AND THE MANUAL EXPERT SEGMENTATION FOR LUMEN AND MEDIA/ADVENTITIA CONTOURS .

	Area Difference (mm^2)
Lumen Contours	$0,06 \pm 0,26$
Media/Adventitia contours	$-0,04 \pm 0,47$

In addition, linear regression analysis revealed that the obtained result was strongly correlated with the reference manual, and yielded the following results for Lumen and Media / adventitia contours respectively : $y = 0.944x + .0278$, $r = 0.9$; $y = 0.616x + 2.564$, $r = 0.78$. As shown, the performance of the automated segmentation was remarkably high, even in poor quality IVUS images due to artifacts, calcifications, or speckles noise , additional supporting the detection efficiency of our segmentation approach . With respect to the manual segmentation method, the required analysis time for the dataset of 50 selected images reduced by 98% with our method (2 s per image for morphological snakes versus 105 s per image for manual segmentation), suggesting that apart from applicable and reliable, the method we propose is markedly rapid .

TABLES AND FIGURES

Please insert your figures with "inline wrapping" text style, as in this template (see Fig. 1).

Please do not use colors in the figures unless it is necessary for the proper interpretation of your figures. Place figure captions below the figures; place table titles above the tables. Tables and figures must be centered. Large figures and tables may span both columns. If your figure has two parts, include the labels "(a)" and "(b)". Letters in the figure should be large enough to be readily legible when the drawing is reduced. Do not forget to include the label, unit for each axis and the legend when they are required. Use the abbreviation "Fig." even at the beginning of a sentence. Do not abbreviate "Table." Tables are numbered with Roman numerals. Please do not include captions as part of the figures. Do not put captions in "text boxes" linked to the figures. Do not put borders around the outside of your figures. Do not use color for the proper interpretation of your figures. The title of the Table must be centered; it has to be 8 pt typed in capital letter. Leave one line space of 10 pt after the Table.

VI. Conclusion

In this paper we have presented a new approach for IVUS segmentation based on combining Contourlet transform and morphological snakes .The new approach has been applied to IVUS images which were segmented ; Lumen and Adventitia /Media contours were detected automatically and compared with expert-corrected contours. Results show good

correlation between agents and observer for the lumen areas with $r = 0.78$, and good correlation for the vessel areas with $r = 0.74$. In future, we plan to focus on detecting calcifications and branch openings. We will also take advantage of the continuity of images in the IVUS pullback sequences and enhance our algorithm by extending it to 3D.

References

- [1] Lee JT, White RA. Basics of intravascular ultrasound: an essential tool for the endovascular surgeon. *SemVascSurg* 2004;17(2):110–8.
- [2] Klingensmith JD, Shekhar R, Vince DG. Evaluation of three-dimensional segmentation algorithms for the identification of luminal and medial-adventitia borders in intravascular ultrasound images. *IEEE Trans Med Imaging* 2000;19(10).
- [3] Nissen SE, Yock P. Intravascular ultrasound: Novel pathophysiological insights and current clinical applications. *Circulation* 2001;103: 604–616
- [4] Mintz G, Nissen S, Anderson W, Bailey S, Erbel R, Fitzgerald P, Pinto F, Rosenfield K, Siegel R, Tuzcu E, Yock P. American College of Cardiology Clinical Expert Consensus Document on Standards for Acquisition, Measurement and Reporting of Intravascular Ultra-sound Studies (IVUS). A report of the American College of Cardiology Task Force on Clinical Expert Consensus Documents. *J Am Coll Cardiol* 2001;37:1478–1492.
- [5] Nissen SE. Shortcomings of coronary angiography and their implications in clinical practice. *Cleveland Clin J Med* 1999;66(8): 479–85
- [6] Mintz GS, Painter JA, Pichard AD, Kent KM, Satler LF, Popma JJ, Chuang YC, Bucher TA, Sokolowicz LE, Leon MB. Atherosclerosis in angiographically normal coronary artery reference segments: an intravascular ultrasound study with clinical correlations. *J Am Coll Cardiol* 1995;25(7):1479–85.
- [7] Tuzcu EM, Berkalp B, De Franco AC, Ellis SG, Goormastic M, Whitlow PL, Franco I, Raymond RE, Nissen SE. The dilemma of diagnosing coronary calcification: angiography versus intravascular ultrasound. *J Am Coll Cardiol* 1996;27(4):832–8.
- [8] Hausmann D, Johnson JA, Sudhir K, Mullen WL, Friedrich G, Fitzgerald PJ, Chou TM, Ports TA, Kane JP, Malloy MJ, Yock PG. Angiographically silent atherosclerosis detected by intravascular ultrasound in patients with familial hypercholesterolemia and familial combined hyperlipidemia: correlation with high density lipoproteins. *J Am Coll Cardiol* 1996;27(7):1562–70.
- [9] Hoffmann R, Mintz GS, Popma JJ, Satler LF, Kent KM, Pichard AD, Leon MB. Overestimation of acute lumen gain and late lumen loss by quantitative coronary angiography (compared with intravascular ultrasound) in stented lesions. *Am J Cardiol* 1997;80(10):1277–81.
- [10] Moraes, M.C An automatic media-adventitia border segmentation approach for IVUS images. *IEEE Computing in Cardiology*. 2010. p 389 - 392
- [11] Unal, G. Bucher, S.; Carlier, S.; Slabaugh, G.; Tong Fang; Tanaka, K. . Shape-Driven Segmentation of the Arterial Wall in *Intravascular Ultrasound Images*. *Information Technology in Biomedicine, IEEE Transactions on* .2008. p 335 – 347
- [12] Katouzian, A. Angelini, E.; Carlier, S.; Suri, J.; Navab, N.; Laine, A. A State of The Art Review on Segmentation Algorithms in Intravascular Ultrasound (IVUS) Images *Information Technology in Biomedicine, IEEE Transactions on* .2012 Feb .p1
- [13] Cardinal MHR, Meunier J, Soulez G, Maurice R, Therasse E, Cloutier G. "Intravascular Ultrasound Image Segmentation: A Three-Dimensional Fast-Marching Method Based on Gray Level Distributions" *IEEE Trans. Med. Imag.* 2006 May;vol.25(5):590–601.
- [14] Giannoglou GD, Chatzizisis YS, Koutkias V, Kompatsiaris I, Papadogiorgaki M, Mezaris V, Parissi E, Diamantopoulos P, Strintzis MG, Maglaveras N, Parcharidis GE, Louridas GE. "A novel active contour model for fully automated segmentation of intravascular ultrasound images: In vivo validation in human coronary arteries" *Computers Biol. Med.* 2007 Sep;37:1292–1302.
- [15] Brusseau E, de Korte C, Mastik F, Schaar J, van der Steen A. "Fully automatic luminal contour segmentation in intracoronary ultrasound imaging - A statistical approach" *IEEE Trans. Med. Imag.* 2004;vol.23:554–566.
- [16] Giannoglou GD, Chatzizisis YS, Sianos G, Tsikaderis D, Matakos A, Koutkias P, Diamantopoulos N, Maglaveras GE, Parcharidis GE, Louridas V. "In-vivo validation of spatially correct three-dimensional reconstruction of human coronary arteries by integrating intravascular ultrasound and biplane angiography" *Coron Artery Dis.* 2006;vol.17(6):533–43.
- [17] L. Alvarez, L. Baumela, P. Marquez-Neila and P. Henriquez. "Morphological Snakes", *CVPR 2010, San Francisco, U.S.A.* <http://www.sciweavers.org/publications/morphological-snakes>
- [18] V. Caselles, R. Kimmel, and G. Sapiro. "Geodesic active contours", *International Journal of Computer Vision*, 22(1):61–79, 1997.
- [19] F. Catté, F. Dibos, and G. Koepfler. "A morphological scheme for mean curvature motion and applications to anisotropic diffusion and motion of level sets", *SIAM Journal on Numerical Analysis*, 32(6):1895–1909, 1995.
- [20] F. Guichard, J. Morel, and R. Ryan. "Contrast invariant image analysis and PDE's". <http://mw.cmla.ens-cachan.fr/~morel/JMMBookOct04.pdf>.
- [21] M.A. Hamdi "A Comparative Study in Wavelets, Curvelets and Contourlets as Denoising Biomedical Images" *International Journal of Image, Graphics and Signal Processing* Year: 2012 Vol: 4 Issue: 1 Pages/record No.: 44-50
- [22] M.A. Hamdi "Combining an alternating sequential filter (ASF) and curvelet for denoising coronal MRI images " *Contemporary Engineering Sciences*, Vol. 5, 2012, no. 1-4, 85-90.
- [23] Potkin BN, Bartorelli AL, Gessert JM, et al. Coronary artery imaging with intravascular high-frequency ultrasound. *Circulation*. 1990;81:1575–1585.
- [24] Yock PG, Linker DT. Intravascular ultrasound: looking below the surface of vascular disease. *Circulation*. 1990;81:1715–1718.
- [25] Nissen SE, Ziada K, Tuzcu EM. Detection of atherosclerosis and identification of vulnerable plaque: potential role of intravascular ultrasound. In: Fuster V, ed. *The Vulnerable Atherosclerotic Plaque: Understanding, Identification and*

Modification. New York, NY: Futura Publishing Co Inc; 1999:87-109.

- [26] M.A. HAMDI and M.A. MRABTI "Combination of Morphological Snakes and Curvelet Transform for IVUS Contours Detection", *International Journal of Tomography and simulation*, 2012, volume 21, issue3, 48-57
- [27] M.A. HAMDI, "Combining Contourlet Transform and Watershed for Robust Multi-Scale Image Segmentation", *International Journal of Imaging and robotics*, Volume 8, Issue 2, 2012, 49-54.

Preliminary proteomic analysis and biological characterization of the crude venom of *Montivipera bornmuelleri*; a viper from Lebanon

Accary, C., Hraoui-Bloquet S., Hamze M., Sadek R., Hleihel W., Desfontis J.-C. and Fajloun Z.

Abstract— *Viperidae* snakes venoms represent a source of efficient bioactive components that have already led to the development of several new drugs. Here, we analyze the proteome of the *Montivipera bornmuelleri* venom using liquid chromatography coupled to electrospray ionisation mass spectrometry, sephadex G-75 gel filtration and sodium dodecyl sulfate-polyacrylamide gel electrophoresis. We have demonstrated the presence of proteins with molecular masses corresponding to metalloprotease III, serine-protease and phospholipase A2 in three fractions collected after gel filtration. In parallel, the crude venom was explored for its biological properties; it presents an antibiotic activity on different strains of bacteria revealing a potential effect against *Staphylococcus aureus* and *Morganella morganii* strains. In human plasma, it showed pro-coagulant and anti-coagulant activities at different concentrations. Indeed, for venom concentrations ranging from 0.1 to 3.125 µg/mL, the prothrombin time is way above the normal value indicating an anti-coagulant activity whereas for the activated partial thromboplastin time, the high concentration of the venom showed an anti-coagulant activity, but a pro-coagulant effect was occurred when the venom concentration decreases to 50 and 25 µg/mL. Also, the venom reveals an anti-platelet aggregation effect when the test is not interrupted by the formation of blood clots associated with the pro-coagulant propriety and finally, it shows an ability to induce an inflammatory response by acting on L- α -phosphatidylcholine used as substrate. Our data concerning the *Montivipera bornmuelleri* venom give evidence of a rich and complex content aiding the exploration of new bioactive molecules for biopharmaceuticals purposes.

Keywords— *Montivipera bornmuelleri*, proteome analysis, blood clotting, anti-platelet aggregation effect

I. INTRODUCTION

The evolution of the venomous function of snakes and the diversification of their bioactive proteins has been of tremendous research interest and considerable debate. Only about 20% of the advanced snakes (belonging to families *Atractaspididae*, *Elapidae* and *Viperidae*) have front-fanged delivery systems, and are typically regarded as of major medical interest (Fry et al, 2003).

The *Viperidae* snakes venoms are toxic secretions produced by a pair of specialized exocrine glands connected to the fangs by ducts (Mackessy and Baxter, 2006). *Viperidae* venoms may contain well over 100 protein components. This heterogeneous nature of venom composition was evidenced since the earliest analytical studies, and hence associated with the wide variety of bioactivities, both *in vitro* and *in vivo*, that were observed clinically or experimentally (Angulo and Lomonte, 2009). However, majority compounds of the *Viperidae* snakes venom can be grouped into a few major protein families, including enzymes (serine-proteinases, Zn²⁺-dependent metalloproteases, and group II phospholipase A2 isoenzymes) that interfere with the coagulation cascade, the normal homeostatic system and tissue repair, and proteins with no enzymatic activity such as C-type lectin-like proteins (Angulo and Lomonte, 2009; Juárez et al., 2004; Calvete et al., 2007). Human envenomations are often characterized by clotting disorders, hypofibrinogenemia, and local tissue necrosis (Ayvazyan and Ghazaryan, 2012).

Montivipera bornmuelleri is one of venomous viper species found in Lebanon and Syria mountains (Hraoui-Bloquet et al., 2002; Hraoui-Bloquet et al., 2012; McDiarmid et al., 1999; Mallow et al., 2003). It grows to a maximum length of about 75 cm, but usually much less. The original subtypes were collected in Lebanon from 1800 m in altitude by Werner, 1898. In 1967, Mertens raised the name *bornmuelleri* to valid rank for the Lebanese populations. This species is classified as Endangered according to the IUCN Red List of Threatened Species (IUCN Red List 2006) due to its limited and fragmented geographic distribution and because of continued decline in the area, extent and/or quality of its habitat.

This work was supported in part by the National Council for Scientific Research of Lebanon (CNRS-Lebanon) and Francophone University Agency (AUF).

Accary C. Hamze M and Fajloun, Z. are with Azm Center for Research in Biotechnology and its Applications, Doctoral School for Sciences and Technology, Lebanese University, El Mittein Street, Tripoli, Lebanon (corresponding author to provide phone: 961 6 213 383; fax: 961 6 213 383/Ext 103; e-mail: zfajloun@ul.edu.lb)

Hraoui-Bloquet S. is with Faculty of Sciences II (Fanar), Lebanese University, B.P. 90656 Jdeidet El Maten, Lebanon

Sadek R. is with American University, Department of Marine Sciences, Beirut, Lebanon

Hleihel W. is with Faculty of medical sciences, Holy Spirit university of Kaslik, Kaslik, Lebanon

Desfontis J.C. is with LUNAM, Oniris, Dermatology, Parasitology Mycology Unit, Nantes, France

Here we describe the proteomic analysis and some biological properties of the venom of *Montivipera bornmuelleri* vipers, collected from Lebanese mountains namely Sannine and Makmel Mountains (Fig.1). LC-ESI-MS, Sephadex G-75 gel filtration and SDS PAGE techniques were employed to analyze samples of the venom, with the specific aim to examine the diversity of protein molecules distributed. The antibacterial activities and the coagulation, anti-platelet aggregation, pro-inflammatory effects of the crude venom were also studied in this work.

II. MATERIALS AND METHODS

II. A. Materials

Venom was manually milked from *Montivipera bornmuelleri* vipers, freeze-dried into crystal shape, and stored at -20°C in a dry, cold and light-free place. Sephadex G-75, ammonium bicarbonate, formic acid (FA), SDS, Tris-glycine buffer, Coomassie Brilliant blue, ethanol, acetic acid, methanol, mercaptoethanol, glycerol, bromophenol blue, acetonitrile (ACN), L- α -phosphatidylcholine, Triton X-100, calcium chloride (CaCl), chloridric acid (HCl), sodium chloride (NaCl), phenol red, and sodium hydroxide (NaOH), trifluoroacetic acid (TFA) were from Sigma-Aldrich (USA). Muller Hinton broth, Muller Hinton agar, imipenem disc and cefoxitin disc were purchased from Bio-Rad. Bacterial strains were obtained from a bank strains at Azm center for the research in biotechnology and its applications. Pacific Hemostasis Thromboplastin-DS, Pacific Hemostasis aPTT XL, Pacific Hemostasis Calcium Chloride reagents were obtained from Fisher Diagnostics Company. The products: Collagen/EPI and Collagen ADP cartridges were purchased from Siemens Healthcare Diagnostics.

II. B. Methods

II. B.1. LC-ESI-MS analysis

On-line LC-ESI-MS analysis of lyophilized venom samples dissolved in 0.01% FA/H₂O to a concentration of 2mg/mL was performed on a Restek Ultra II C18 column. A 90 min linear gradient from 0 to 100% of buffer B [0.1% (v/v) FA/ACN] in buffer A [0.1% (v/v) FA/H₂O], at a flow rate of 1ml/min ($\lambda = 215$ nm) was applied to the column. Samples were injected manually into the LC-ESI-MS system and analyzed in positive ion mode. ESI spectra were acquired using an Esquire 3000 type from Bruker. Data processing was performed with the aid of the following Softwares: 44.0 Hystar Version 3.2, Hystar Post Processing, Esquire Control Version 1.3 and Data analysis compass.

II. B.2. Sephadex G-75 purification

The crude venom of *Montivipera bornmuelleri* was loaded on a Sephadex G-75 column (1 \times 40cm) previously equilibrated with 50mM ammonium acetate buffer, pH 7.45 and flowed with the same buffer. Fractionation was carried out at room temperature at a flow rate of 30ml/h and all fractions were lyophilized and subjected to a mass spectrometry analysis.

II.B.3. Sodium Dodecyl Sulphate Polyacrylamide Gel Electrophoresis (SDS-PAGE)

Freeze dried *Montivipera bornmuelleri* venom mixed with Tris-HCl 1.25M pH 6.8, SDS 10%, 2-Mercaptoethanol, Glycerol, Bromophenol Blue 0.1%, water was subjected to 10% SDS- PAGE according to a modified technique of Laemmli, 1970. Electrophoresis study was carried out using Tris-glycine (pH 8.3) with SDS (10%) buffer for 2 h at 60V at room temperature. The gel was stained with 0.1% Coomassie brilliant blue R-250 for detection of the protein bands and destained in water with 10% ethanol and 7.5% acetic acid.

II.B.4. Antibacterial activity

Inoculum preparation: from pure culture on a nutrient agar base (Bio-rad®, France), aged 18-24 hours, we prepared a bacterial suspension on Muller-Hilton (MHB; Bio-rad®, France) according to the turbidity of 0.5 McFarland approximately 10^8 CFU/mL.

Culturing: the bacterial suspension was diluted to 1/100 and inoculated on the surface of Muller-Hilton agar base (MHA; Bio-rad®, France).

Testing: A sterile disc filter, 7mm diameter, was placed on the cultured agar; then 30 μ l of the venom at 4mg/mL concentration were deposited on the filter. To control the sensitivity of strains, we used the imipenem disc (10 μ g; Bio-rad®, France) for *Pseudomonas aeruginosa*, *Morganella morganii*, *Salmonella Typhi* and *Escherichia coli*. The cefoxitin disc (30 μ g; Bio-rad®, France) was used for the *Staphylococcus aureus* strain. A blank with sterile saline solution instead of venom served as negative control. A disk loaded with ammonium acetate buffer was used also as negative control. The bacterial plates were incubated 18 hours at 37°C ; inhibition zone was measured in millimeter diameters. The antibacterial test was performed in duplicate.

II.B.5. Minimum inhibitory concentration (MIC) and Minimum bactericidal concentration (MBC)

The bacterial suspension for every strain was prepared from pure isolate on a nutrient agar for 18 hours, which was suspended in NaCl solution with turbidity of 0.5 McFarland. Then, the bacterial suspension was diluted to 1/100 in MHB medium (10^6 CFU/mL). The bacteria were counted in the decimal dilution method, according to Qaiyumi (2007). Therefore, the total number in 1mL was calculated (N/mL). For the determination of MIC and MBC, a series of dilutions of the venom were carried out in MHB through 1/2 dilution. 1mL from the inoculum was added for every tube (containing 1mL diluted venom), and a series of venom concentrations were obtained (100, 50, 25, 12.5, 6.25, 3.125, 1.56, 0.78, 0.39, 0.195, 0.097, 0.048 μ g/mL). A strong vortex was carried out on each tube, which was incubated at 37°C for 18 hours. To identify the bactericidal effect, the number of live colonies from each dilution in 1mL (Ni) was counted. Therefore, the percentage of killing effect was calculated as follows: $\text{Ni}/\text{N} \times 100 = \% \text{ survival}$.

II.B.6. Human plasma coagulation effect

PT and aPTT tests were performed in a certificated medical laboratory using Behring coagulation system according to the manufacturer's instructions. Freshly aspirated blood from healthy volunteer who had not taken any drugs for at least 2 weeks prior to sampling was collected in 3.2% sodium citrate

III. B. Sephadex G-75 purification

In the second step, 30mg of the *Montivipera bornmuelleri* venom proteins were separated by size-exclusion chromatography (SEC) on Sephadex G-75 and 30 fractions of 500 μ l volume each were manually collected in "Eppendorf" tubes. These fractions were subjected to a mass spectrometry analysis using off-line mode and for three fractions collected the results obtained are correlated with those of the whole crude venom where the same molecular weights were found and presented in bold in Table 1. Indeed, the ESI mass spectrum analysis of fraction 2 obtained by SEC reveals a protein with a molecular mass of 65361.8 Daltons (Fig.3A). This mass corresponds to the range of masses reported for the vast majority of snake venom metalloprotease III. The Fig. 3B shows the ESI mass spectrum of the unique compounds of fraction 3 that reveals a mass of 27328.3 Daltons which corresponds to serine-protease. The ESI mass spectrum of the only compounds of fractions 13 shows a mass of 13664.7 Daltons which corresponds to PLA2 represented in Fig. 3C. However, definitive assignment of a protein family detected in *Montivipera bornmuelleri* venom can only be done through demonstrated structural studies such as N-terminal sequencing. In parallel, the other fractions also analyzed by ESI-MS have showed heterogeneous content of proteins with similar molecular weights to those obtained during mass analysis of whole venom but none pure molecular mass corresponding to a prevalent protein was revealed. In further work, the combined strategy of purification and structural studies such as N-terminal sequencing will be used to identify and to assign definitively the different proteins detected in *Montivipera bornmuelleri* venom.

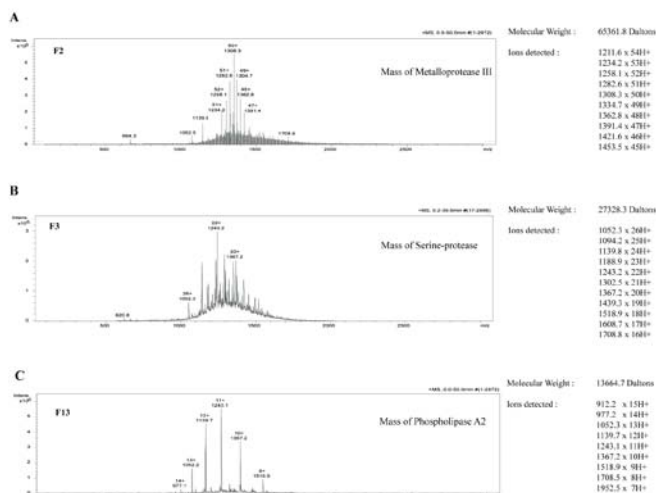


Fig. 3. (A) MS profile corresponding to mass of Metalloprotease III distributed across fraction 2; (B) MS profile corresponding to mass of Serine-protease identified in fraction 6 and (C) MS profile corresponding to mass of PLA2 identified in fraction 13. Molecular masses obtained and different ions detected for each MS analysis of the three fractions are represented. F2, F3 and F13 were obtained by SEC on Sephadex G-75.

III. C. Antibacterial activity

The crude venom of *Montivipera bornmuelleri* demonstrates a significant antibacterial activity against Gram+ and Gram- bacteria. It exhibits large inhibition zones by the disk diffusion method on both strains *Staphylococcus aureus*

and *Morganella morganii*. Indeed, diameters of the inhibition zones perimeters correspond to 21mm and 18mm respectively. For the other strains, *Escherichia coli*, *Salmonella Typhi* and *Pseudomonas aeruginosa*, diameters of the bacterial inhibition zones were respectively 12, 13 and 14 mm (Fig. 5). For *Staphylococcus aureus*, the diameter is closed to the sensible limit of the cefoxitin. For *Morganella morganii*, it is between the both limit. As for other stains the inhibition zone diameters are under the lower limit but still not far. According to the French Society of Microbiology (SMF) recommendations published in 2012 (SMF, 2012), a bacterial strain is sensitive to cefoxitin when the diameter of the inhibition zone is more than 22mm and resistant for a diameter less than 15mm. For imipenem, a bacterial strain is sensitive for an inhibition zone diameter more than 24mm and resistant when it is less than 17mm lower. Thus, on the basis of SMF recommendations and since we use a sample of crude venom corresponding to a heterogeneous mixture of proteins, the results could be regarded very promising and we will probably have in future studies excellent antibacterial activities by purification bioactive molecules in the venom.

Since the antibacterial activity of the crude venom was the most significant on *Staphylococcus aureus* and *Morganella morganii*, those two strains were selected for MIC and MBC determination. MIC is the lowest concentration of an antimicrobial to which there is no visible haze. The MBC is the lowest concentration of antimicrobial agent which gives at most 0.01% surviving bacteria of the initial inoculum. The MIC value tested on *Staphylococcus aureus* was 12.5 μ g/mL as for *Morganella morganii* is 25 μ g/mL. The MBC values tested for those two strains were also 12.5 μ g/ml for *Staphylococcus aureus* and 25 μ g/mL for *Morganella morganii*. As described in the literature (Vonk et al, 2011), the different substances including in the vipers venom like proteins and enzymes are responsible for its biological activities. Therefore, these compounds may interact with specific molecules of some bacteria while not affecting other strains. Vargas and collaborators have shown in 2012 that PLA2 can have antibacterial effects, and while *Montivipera bornmuelleri* venom has shown PLA2 in its protein components analyzed, this may be responsible for its antibacterial properties. Since the potential of *Montivipera bornmuelleri* crude venom for antimicrobial activity has been established and since the results obtained are very promising especially those concerning the activity against *Staphylococcus aureus* which presents a high resistance against ciprofloxacin, amoxicillin, and chloramphenicol, the further works will certainly aim to purify the active antimicrobial component from the viper venom and to screen equally a wider range of other bacterial strains in order to discover other antibacterial potential effects of *Montivipera bornmuelleri* venom.

III.D. Human plasma coagulation and anti-platelet aggregation effects

PT, aPTT and anti-platelet aggregation tests were performed to evaluate the effect of *Montivipera bornmuelleri* venom on the blood coagulation cascade. Results obtained for PT and aPTT tests shown in Table 3 are compared to the standard used for system calibration. For venom concentration ≥ 0.05 mg/mL, there was a total anti-coagulation activity in PT

test with time exceeding 200 seconds. This effect decreases with a lower concentration of the crude venom, even a concentration of 0.003125mg/mL still exhibit an anti-coagulant activity. In aPTT test, the venom has shown an anti-coagulant action with high concentration 0.1mg/mL but when concentration decreases to 0.05mg/mL and 0.025mg/mL, the clotting time went down the normal value pointing to a pro-coagulant activity of the crude venom of *Montivipera bornmuelleri*. Below these concentrations, the crude venom has no action on blood coagulation and aPTT value returns to normal. The crude venom of *Montivipera bornmuelleri* showed both pro-coagulant and anti-coagulant activities with different concentrations; PT and aPTT are both disrupted suggesting that the defect lies in multiple pathways or in the common pathway of the coagulation cascade.

The anti-platelet aggregation activity of *Montivipera bornmuelleri* venom was not successfully evaluated due to formation of blood clots within the samples after addition of the venom. A “flow obstruction” occurred in blood samples with venom during the test even after several steps of dilution. This issue was faced in previous work on the *Echis carinatus* venom (Kashani et al, 2012). We attempted to get one value for a venom concentration of 0.0625mg/mL tested with Collagen/Epinephrin, CT was higher than 300 seconds exceeding by far the normal value. Anti-platelet aggregation results obtained using DADE Platelet Function and Analyzer PFA-100 system are shown in Table 4.

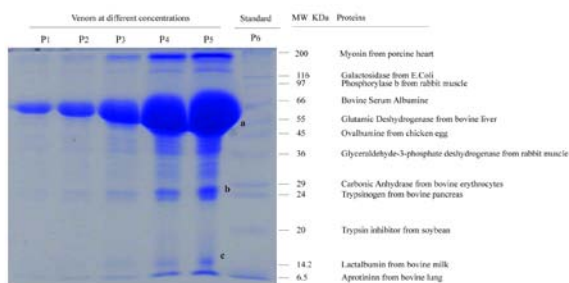


Fig. 4. SDS PAGE at 10% (w/v) gel for *Montivipera bornmuelleri* venom at different dilutions [P1 (more diluted) to P5 (less diluted)]. Marker or standard (P6): different proteins listed in the right of this figure. The gel was stained for 20 min with 0.2% (w/v) Coomassie Brilliant Blue G-250 and destained by 7% (v/v) acetic acid. The molecular weight standards are compared to these unknown proteins (a, b, c) within the venom in order to identify their sizes and possibly correspond to Metalloprotease III, Serine-protease and PLA2 respectively.

Viperidae venoms mainly cause hemorrhaging and coagulation disorders. Over the years, many toxins affecting blood circulation have been isolated and characterized from various snake venoms (Suntravat et al, 2010). Some affect platelet aggregation, whereas others affect blood coagulation cascade. Venom proteins that affect blood coagulation can be classified as pro-coagulant or anti-coagulant proteins based on their ability to shorten or prolong the blood-clotting process (Matsui et al, 2000; White, 2005). Pro-coagulant proteins are either serine-proteases or metalloproteases (Kini et al, 2002). These factors inhibit blood coagulation by different mechanisms. Some of these anti-coagulant proteins exhibit enzymatic activities, such as PLA2 and proteinase, whereas others do not exhibit any enzymatic activity (Meier, et al. 1991; Kornalik, 1991). In addition, several platelet aggregation inhibitors have been purified and characterized from various snake venoms. They include enzymes, such as

PLA2 enzymes, nucleotidases, and fibrinogenases, and nonenzymatic polypeptides, such as disintegrins and mambin. Moreover, Dambisya et al. (1994) discussed previously the presence of numerous molecules in the compound venomous of the *Viperidae* family that can possess both pro-coagulant and anti-coagulant properties. In fact, these authors reported that the different concentrations of *Calloselasma hodostoma* (Malayan pit viper) venom showed the dual effects (pro and anti-coagulant). These observations are relevant to our results obtained of the *Montivipera bornmuelleri* venom on the coagulation cascade. Furthermore, we can explain firstly, the appearance of “flow obstruction” due to the formation of blood clots associated with the pro-coagulant propriety of the viper venom and secondly, the high specific anti-platelet aggregation observed using venom at 0.0625mg/ml concentration associated to the anti-platelet or anti-coagulant properties. In future work, confirmation tests should be done for better analysis and in order to localize the action of the crude venom to certain activation step(s) in the cascade.

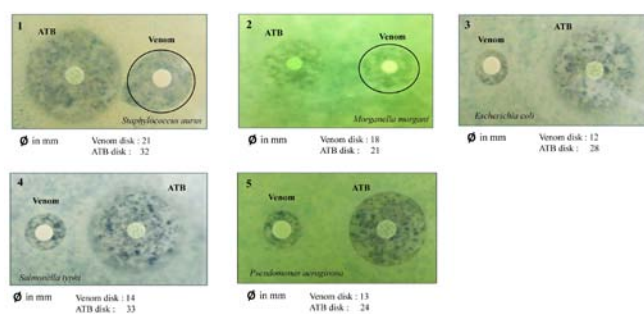


Fig. 5. The antibacterial activity of the crude venom of *Montivipera bornmuelleri* is measured using standard disk-diffusion susceptibility tests on Muller Hinton agar and performed on strains of (1) *Staphylococcus aureus*, (2) *Morganella morganii*, (3) *Escherichia coli*, (4) *Salmonella Typhi* and (5) *Pseudomonas aeruginosa*. On the first two strains, the venom incorporates the highest antibacterial activity; the perimeter of the zone of inhibition induced by the crude venom is indicated by black circle. On the other strains, the antibacterial activity of the venom persists and the perimeters of the zones of inhibition were evaluated considerably for a crude viper venom. For the five antibacterial tests performed, the diameters of the zones inhibitions corresponding to two effects: crude venom and antibiotics are indicated in mm.

III. E. Pro-inflammatory activity

Montivipera bornmuelleri crude venom has shown a pro-inflammatory activity expressed by a decrease in absorbance measured at 558nm when the different concentrations of the venom are added to the L- α -phosphatidylcholine substrate (see materials and methods). The reaction was triggered by the same absorbance at T_0 before the addition of the venom ($A_{558} = 0.575$). Fig. 6 shows the variation in absorbance at T_5 (after 5 minutes) according to *Montivipera bornmuelleri* crude venom concentration. Compared to the control at T_5 ($A_{558} = 0.544$), an important decrease in absorbance when the crude venom is added to the phosphatidylcholine solution can be observed indicating the presence of pro-inflammatory activity. The change in absorbance between t_0 and t_5 is caused by the acidification of the medium due to the liberation of fatty acids and proportional to the concentration of venom. According to the literature, the pro-inflammatory effect of snake crude venom is due to its toxins activity mainly phospholipases (Teixeira et al, 2003). We can therefore conclude that the venom of *Montivipera bornmuelleri* has a pro-inflammatory activity due possibly to the action of PLA2 since the specificity of the substrate.

Table 3

Crude venom concentrations mg/mL	PT in seconds	aPTT in seconds
Blank	13.1	36.7
Control +	12.2	33.4
Standard	13	25-40
0.4	>200	>150
0.2	>200	>150
0.1	>200	>150
0.05	>200	16.9
0.025	51.5	18.6
0.0125	31.3	22.6
0.00625	31.3	26.8
0.003125	26.5	34.2

Results of prothrombin time (PT) and activated partial thromboplastin time (aPTT) performed using Behring coagulation system.

Table 4

Samples	Mediators	CT in seconds
Standard	ADP	126
	Epinephrine	165
+Control	ADP	88
	Epinephrine	106
-Control	ADP	100
	Epinephrine	117
Venom 0.250 mg/mL	ADP	Flow obstruction
	Epinephrine	Flow obstruction
Venom 0.125mg/mL	ADP	Flow obstruction
	Epinephrine	Flow obstruction
Venom 0.0625mg/mL	ADP	Flow obstruction
	Epinephrine	>300

Anti-platelet aggregation results obtained using DADE Platelet Function Analyzer PFA-100 system.

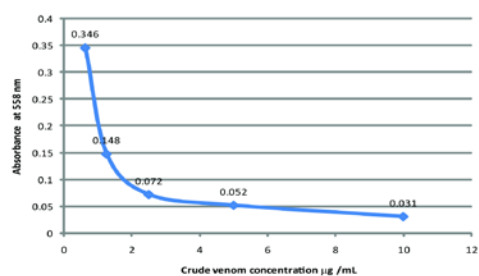


Fig. 6. Decrease in absorbance of phenol red of phosphatidylcholine solution after 5 minutes incubation with different concentrations of the crude venom of *Montivipera bornmuelleri*. Five concentrations 10µg/mL, 5µg/mL, 2.5µg/mL, 1.25µg/mL and 0.625µg/mL were tested to evaluate the pro-inflammatory effect of the venom.

IV. CONCLUSIONS

In conclusion, different components of the proteome of *Montivipera bornmuelleri* venom have been identified in our LC-ESI-MS results, even without definitive information such as N-terminal sequencing. The venom has been characterized for its biological properties. This crude venom exhibited antimicrobial activity against *Staphylococcus aureus*, and *Morganella morganii*, inhibitory effect on platelet aggregation, pro and anti-coagulant reactions and its ability to induce an inflammatory response. These biological effects came to support the results obtained in the proteomic analysis. We have demonstrated that PLA2 is present in the venom and could be able to induce an inflammatory response. Also, we have put in evidence the existence of metalloprotease III and serine-protease by analyses of the molecular masses of the corresponding compounds and the anti-coagulant activity performed on human plasma. We also supposed the presence of bradykinin-potentiating peptide, C-type lectin, sarafotoxin, acetylcholinesterase, prothrombin activator and L-amino oxidase proteins within the venom. Further studies will focus

on purification of PLA2 from this venom to determine its mechanisms of action and potential pharmacological applications. However, histopathology studies of the effect of the *Montivipera bornmuelleri* crude venom on mouse tissues are in progress.

ABBREVIATIONS

LC-ESI-MS: Liquid Chromatography coupled to Electrospray Ionisation Mass Spectrometry; RP-HPLC: Reverse Phase High Pressure Liquid Chromatography; SDS-PAGE: Sodium Dodecyl Sulphate Polyacrylamide Gel Electrophoresis; MHB: Muller Hinton Broth; MHA: Muller Hinton Agar; MIC: Minimal Inhibitory Concentration; MBC: Minimal Bactericidal Concentration; PT: Prothrombin Time; aPTT: activated Partial Thromboplastin Time; Collagene/EPI: Collagene/Epinephrine; Collagene/ADP: Collagene/Adenosine Diphosphate; IUCN: International Union for Conservation of Nature; CFU: Colony Forming Unit.

REFERENCES

- Angulo, Y., Lomonte B., 2009. Biochemistry and toxicology of toxins purified from the venom of the snake *Bothrops asper*. *Toxicon* 54, 949-957.
- Ayvazyan, N.M., Ghazaryan N.A., 2012. Lipid bilayer condition abnormalities following *Macrovipera lebetina obtusa* snake envenomation. *Toxicon* 15, 604-613.
- Bazaa, A., Marrakchi, N., El Ayeb, M., Sanz, L., Calvete, J.J., 2005. Snake venomomics: Comparative analysis of the venom proteomes of the Tunisian snakes *Cerastes cerastes*, *Cerastes vipera* and *Macrovipera lebetina*. *Proteomics* 5, 4223-4235.
- Calvete, J.J., Marcinkiewicz, C., Sanz, L., 2007. Snake Venomomics of *Bitis gabonica gabonica*. Protein family composition, subunit organization of venom toxins, and characterization of dimeric disintegrins bitisgabinin-1 and bitisgabinin-2. *Journal of Proteome Research* 6, 326-336.
- Cesar, J.M., De Miguel, D., GarcíaAvello, A., Burgaleta, C., 2005. Platelet Dysfunction in Primary Thrombocytopenia Using the Platelet Function Analyzer, PFA-100. *American Journal of Clinical Pathology* 123, 772-777.
- Dambisya, Y.M., Lee, T.L., Gopalakrishnakone, P., 1994. Action of *Calloselas marhodostoma* (Malayan pit viper) venom on human blood coagulation and fibrinolysis using computerized thromboelastography (CTEG). *Toxicon* 32, 1619-1626.
- De Oliveira, M., Palma, M.S., 1998. Polybitoxins: a group of phospholipases A2 from the venom of the neotropical social *Wasp Paulistinha*. *Toxicon* 36, 198-199.
- French Society of Microbiology (SFM), Antibioqram Committee, edition. January 2012. Fry BG,
- Wüster, W., Ramjan, S.F.R., Jackson, T., 2003. Analysis of *Colubroidea* snake venoms by liquid chromatography with mass spectrometry: evolutionary and toxicological implications. *Rapid Commun Mass Spectrom.* 17, 2047-2062.
- Hraoui-Bloquet, S., Sadek, R.A., Sindaco, R., Venchi, A., 2002. The herpetofauna of Lebanon: new data on distribution. *Zoology in the Middle East* 27, 35-46.
- Hraoui-Bloquet, S., Sadek, R., Accary, C., Hleihel, W., Fajloun, Z., 2012. An ecological study of the montane *Montivipera bornmuelleri* (Werner, 1898) viper including preliminary biochemical characterization of venom. *Lebanese Science Journal* 13, 89-101.
- IUCN 2006. The status and Distribution of Reptiles and Amphibians of the Mediterranean Basin. IUCN Red List of Threatened Species – Mediterranean Region Assessment
- Juárez, P., Sanz, L., Calvete, J.J., 2004. Snake venomomics: characterization of protein families in *Sistrurus barbouri* venom by cysteine mapping, N-terminal sequencing, and tandem mass spectrometry analysis. *Proteomics* 4, 327-338.
- Kashani, T.M., Vatanpour, H., Zolfagharian, H., Tehrani, H.H., Hossein Heydari, M.H., Kobarfard, F., 2012. Partial fractionation of venoms from two

- Iranian Vipers, *Echis carinatus* and *Cerastes persicus fieldiand* evaluation of their anti-platelet activity. Iranian Journal of Pharmaceutical Research, in press.
- Kammoun, M., Miladi, S., Ben Ali, Y., Damak, M., Gargouri, Y., Bezzine, S., 2011. In vitro study of the PLA2 inhibition and antioxidant activities of *Aloe vera* leaf skin extracts. *Lipids in Health and Disease* 10, 30-35.
- Kini, R.M., Rao, V.S., Joseph, J.S., 2002. Pro-coagulant proteins from snake venoms. *Haemostasi*, 31, 218-224.
- Kornalik F. 1991. The influence of snake venom proteins on blood coagulation. In: Harvey AL. (ed.) *Snake Toxins*. Pergamon Press, New York, pp 323-383.
- Laemmli, U.K., 1970. Cleavage of structural proteins during the assembly of the head of bacteriophage T4. *Nature* 227, 680-685.
- Mackessy, S.P., Baxter, L.M., 2006. Bioweapons synthesis and storage: the venom gland of front-fanged snakes. *Zoologischer Anzeiger* 25, 147-159.
- Mallow, D., Ludwig, D., Nilson, G., 2003. True vipers: natural history and toxinology of old world vipers. Krieger Publishing Company, Malabar, Florida, 359 pp.
- Matsui, T., Fujimura, Y., Titani, K., 2000. Snake venom proteases affecting hemostasis and thrombosis. *Biochim Biophys Acta*. 1477, 146-156.
- McDiarmid, R.W., Campbell, J.A., Touré, T., 1999. Snake species of the world: a taxonomic and geographic reference. The Herpetologists League, Washington 1, 511 pp.
- Meier, J., Stocker, K., 1991. Effects of snake venoms on hemostasis. *Crit. Rev. Toxicol.* 21, 171-182.
- Mertens, R., 1967. Über *Lachesislibanotica* und den Status von *Vipera bommuelleri*. *Senckenbergiana Biologica*, 48, 153-159.
- Qaiyumi, S., 2007. Macro- and Microdilution Methods of Antimicrobial Susceptibility Testing. In: R. Schwalbe, L. Steele-Moore and A. C. Goodwin, Eds., *Antimicrobial Susceptibility Testing Protocols*, CRC Press, Boca Raton, London, New York. pp 75-79.
- San, T.M., Vejayan, J., Shanmugan, K., Ibrahim, H., 2010. Screening antimicrobial activity of venoms from snakes commonly found in Malaysia. *Journal of Applied Sciences* 10, 2328-2332.
- Suntravat, M., Nuchprayoon, I., Pérez, J.C., 2010. Comparative study of anti-coagulant and pro-coagulant properties of 28 snake venoms from families *Elapidae*, *Viperidae*, and purified Russell's viper venom-factor X activator (RVV-X). *Toxicon* 56, 544-553.
- Teixeira, C.F., Landucci, E.C., Antunes, E., Chacur, M., Cury, Y., 2003. Inflammatory effects of snake venom myotoxic phospholipases A2, *Toxicon* 42, 947-962.
- Tsai, I.H., Wang, Y.M., Hseu, M.J., 2010. Mutagenesis analyses explore residues responsible for the neurotoxic and anti-coagulant activities of Trimucrotoxin, a pit-viper venom Asn(6)-phospholipase A(2). *Biochimie* 9, 277-85.
- Vargas, L.J., Londoño, M., Quintana, J.C., Rua, C., Segura, C., Lomonte, B., 2012. An acidic phospholipase A2 with antibacterial activity from *Porthidium nasutum* snake venom. *Comparative Biochemistry and Physiology*, 161, 341-347.
- Vonk, F.J., Jackson, K., Doley, R., Madaras, F., Mirtschin, P.J., Vidal, N., 2011. Snake venom: from fieldwork to the clinic. *Bio Essays* 33, 269-79.
- Werner F., 1898. Übereinigeneue Reptilien und einenneuen Froschausdemcilicischen Taurus. *Zoologischer Anzeiger* 2, 217-223.
- Werner F., 1922. Synopsis der Schlangenfamilien der Amblycephalidae und *Viperidae*. *Archivfür Naturgeschichte* 88A, 185-244.
- White J., 2005. Snake venoms and coagulopathy. *Toxicon* 45, 951-967.

A computational model of the modulation of basal ganglia function by dopamine receptors

Mohammad Reza Mohagheghi-Nejad, Fariba Bahrami, and Mahyar Janahmadi

Abstract— The basal ganglia (BG) play an important role in motor control and their malfunction is implicated in several disorders including Parkinson’s disease (PD), in which dopamine concentration in BG is greatly reduced. This is evidenced by increase in the firing rate of output nuclei of BG and synchronization between neurons of different micro-circuitry in basal ganglia. The most effective way to alleviate PD symptoms is to take Levodopa, which replenishes dopamine storage in the brain. However, long-term use of Levodopa results in motor fluctuations and dyskinesia. Here, we developed a computational model of BG that considers modulatory effects of dopamine on its target nucleus, that is on striatum. The present computational model can be used to investigate the effect of variations of the dopamine concentration in BG on motor fluctuations. Moreover, the effect of applying deep brain electrical stimulation on different nuclei of basal ganglia can be investigated through the proposed model.

Keywords— Basal ganglia, Conductance-based computational model, Motor fluctuations, Parkinson’s disease.

I. INTRODUCTION

Parkinson’s disease (PD) is the second most common age-related neurodegenerative disorder after Alzheimer disease. It is caused by dysfunction of basal ganglia (BG). In PD, dopaminergic neurons within BG are degenerated and the level of neurotransmitter dopamine (DA), decreases. Striatum (STR) is the main input site of the BG that receives stimulations from different areas in the cerebral cortex (CX). Its neuronal activity is modulated via DA. Degeneration of dopaminergic neurons in the final analysis will result in hyperactivation of the output nuclei of BG and this in turn leads to over-inhibition of the thalamus (TH) [1].

There are different mathematical models that describe the function of basal ganglia (BG) from different points of view. Terman and colleagues [2] developed a conductance-based computational model of subthalamopallidal circuit in the indirect pathway of the BG. Their model is capable of showing both correlated rhythmic activity and irregular autonomous

patterns of activity by varying striatal (STR) input and intrapallidal inhibition parameters. These two types of activity are in correspondence with parkinsonian and normal cases, respectively. Internal part of the globus pallidus (GPi) as the output nucleus of BG which provides inhibitory input to the thalamus was also considered in their model. In the proposed model, TH is a relay station whose task is to relay sensorimotor signals faithfully in normal condition. They used this model to investigate how high frequency stimulation of subthalamic nucleus (STN) alleviates PD symptoms [2]. Since in this model [2] the structure of STR and thereby, the functions of dopamine are not directly considered, motor fluctuation which is one of the side effects of Levodopa cannot be observed. Moreover, it should be noticed that deep brain stimulation is usually applied to the PD patients who are taking Levodopa.

In [3] and [4] another a mean-field model of basal ganglia-thalamocortical system (BGTCS) is introduced, in which comparatively a more detailed structure of BG is used to investigate the dynamics of the neuronal network of basal ganglia in both PD and normal conditions. However, mean-field modeling approach can be used properly when there is no temporal structure in the subpopulation [3]. Additionally, although it can be a good representation for firing rate as a macroscopic model, it can hardly represent different firing patterns of neurons.

Computational model of action selection is another model developed for the BG [6-7]. The purpose of developing this model was to investigate how action selection is performed in the BG. In addition, in this work, the authors explained quantitatively “how do different BG nuclei contribute to action selection?” and “what is the importance of DA in regulating BG function?” [4, 5]. However, this model cannot represent different behaviors within BG on the cellular level.

Therefore, the purpose of the present study is to develop a computational model of BG in order to further investigate the effect of changes in the dopamine content on motor fluctuations in PD as well as to assess the effects of other therapeutic methods including different types of deep brain electrical stimulations and different types of dopamine receptor agonists and antagonists as medication.

II. METHOD

Here, we developed a computational model of BG which is capable of showing DA effect (Fig 1.). The model consists of

M. R. Mohagheghi-Nejad is with the School of Electrical and Computer Engineering, College of Engineering, University of Tehran, Tehran, Iran. (e-mail: m.mohaghegh@ut.ac.ir).

F. Bahrami is with the Control and Intelligent Processing Center of Excellence, School of Electrical and Computer Engineering, College of Engineering, University of Tehran, Tehran, Iran (corresponding author, e-mail: fbahrami@ut.ac.ir).

M. Janahmadi is with the Neurophysiology Research Center and Department of Physiology, Medical School, Shahid Beheshti University of Medical Science, Tehran, Iran. (e-mail: janahmadi@sbmu.ut.ac.ir)

three parts. In the first part, the model developed by Rubin and Terman (RT model) [2] was implemented. In the second part, a biological realistic network of neurons in the STR was developed. Finally, an interface in BG to connect STR to the rest of the model was designed.

inhibitory impact on MSN population [7] (For further information about MSN and FSI equations and parameters, see [8] and [7], respectively).

There are two main types of MSN regarding the type of dopamine receptor, the first type is D1 MSN and the second one is D2 MSN in which DA has facilitatory and inhibitory

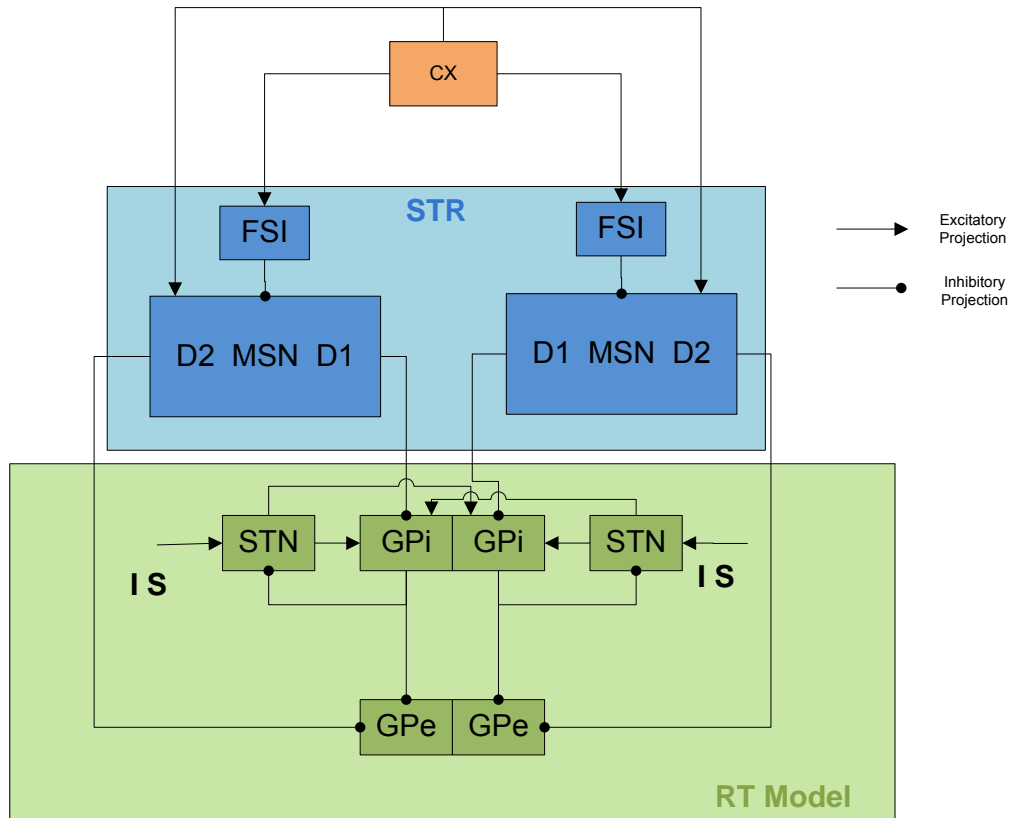


Fig. 1 Schematic structure of the model and their connection. Each nucleus has two clusters each is shown as a block. The blocks full name are as follow: CX: cerebral cortex, FSI: fast spiking interneuron, MSN: medium spiny neuron, STN: subthalamic nucleus, GPi: internal segment of globus pallidus, GPe: external segment of globus pallidus.

A. RT Model

Basal Ganglia (BG) consists of the following nuclei: striatum, globus pallidus which consists of external (GPe) and internal (GPi) segments, substantia nigra and subthalamic nucleus (STN). In the previous studies, conductance-based computational model of STN, GPe and GPi are developed [2, 6]. They consider 2 anatomically separated clusters each of which consists of 8 neurons. The way how each nucleus connected to each other is shown in Fig. 1.

B. Neural Network in the Striatum

The STR nucleus consists of three major types of neuron. Medium spiny projection neurons (MSNs) are the only output neurons of this nucleus which are 95% of the population of all neurons in the rat STR. The rest of the population consists of inhibitory fast spiking and cholinergic interneurons. In our modeling approach, we considered medium spiny projection type because of its dominant population and the fast spiking interneurons (FSIs) was also considered because of its strong

effects on them, respectively. We considered 2 clusters in the STR each of which has 35 MSNs of both types. Since there are recurrent connections in STR, we connected MSNs together with different ratio regarding different types. The ratio of their connections is given in Table. I [9]. The input to this network is provided by cerebral cortex which is generated using the algorithm developed in [8].

TABLE 1. PROPORTION OF RECURRENT CONNECTIONS IN STR

Presynaptic MSN type	Postsynaptic MSN type	Proportion
D1	D1	26%
D2	D2	36%
D2	D1	29%

C. Interface Connecting STR Network to the Rest of BG Nuclei

In RT model, the input to GPe, GPi and the recurrent connection in GPe is considered as the only parameters to distinguish between normal condition and PD. To connect our

developed STR network to the rest of BG model, we mapped the mean STR activity to the range mentioned in that model using an interface [10]. In addition, we considered that D1 dopamine receptors on MSNs in the STR network provide input to the GPi while D2 receptors provide input to GPe. While, we have 2 clusters in each nucleus, all of the connections among these nuclei are established in their corresponding clusters. The function we used for this purpose is a sigmoidal function of the general form of (1).

$$f(x) = A + \frac{B}{1 + \exp(-(v - v_{th})/\sigma_{th})} \quad (1)$$

TABLE 2. INTERFACE PARAMETERS

Modulatory Effect	A	B	v_{th}	σ_{th}
Indirect pathway	2.2	-4.2	0.05	2
Direct Pathway	1	2	0.05	2
GPe recurrent	0	0.3	0.05	-2

A, B, v_{th} and σ_{th} are the parameters of this interface and v is the postsynaptic potential induced by synaptic activity. We modeled the synaptic channel activity using the approach introduced in [11] which the related equations are mentioned in (2) and (3). The parameters of synaptic channel conductance are given in Table III.

$$[T](V_{pre}) = \frac{T_{max}}{1 + \exp(-(V_{pre} - V_T)/K_p)} \quad (2)$$

$$s' = \alpha[T](V - \theta)(1 - s) - \beta s \quad (3)$$

In (2), [T] is the concentration of neurotransmitter in synaptic cleft over time and V_{pre} is presynaptic membrane voltage. Substituting [T] in (3) yields synaptic channel activity which is used as the variable in (1).

TABLE 2. PARAMETERS OF THE CONDUCTANCE OF SYNAPTIC CHANNEL

T_{max}	V_T	K_p	α	β	θ
1	-57	2	0.01	0.01	20

III. MODEL VALIDATION

We validated our model by means of synchronization index and over-activation of GPi in PD.

A. Synchronization Index

According to some studies, clusters are anatomically

separated in both normal and PD conditions. In the normal case, neurons within each cluster are synchronized, but there is less synchronization between neurons of different clusters. However, in the case of PD clusters become more correlated and synchronized [12]. Here, we used the synchronization index introduced in [13]. Since we have 16 neurons in each nucleus, we took the average of synchronization index over time which is a number between 0 and 1 and use it as a synchronization measure [14]. Fig. 1 shows increased synchronization in GPi, GPe and STN.

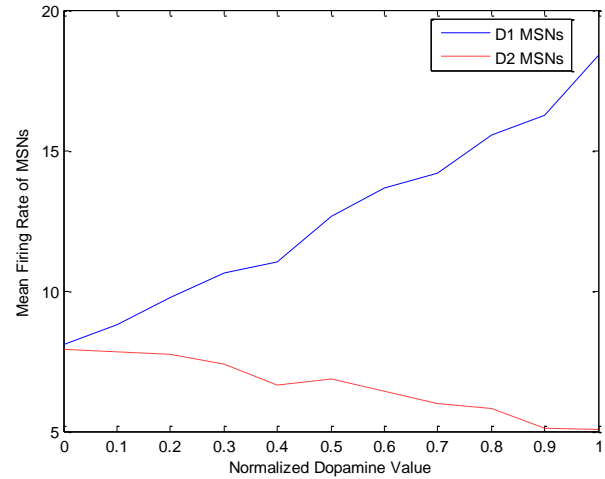


Fig. 2 The effect of variation of DA content on D1 and D2 MSNs in a recurrent network. As DA increases, mean firing rate of D1 MSNs increases while mean firing rate of D2 MSNs decreases.

B. Over-activation of GPi in PD

Although, we can validate our STR network in the similar way, there is also another fact to validate developed STR network. The activity of neurons in the direct and indirect pathways in the BG changes in transition from normal to PD. PD symptoms appear when more than 80% percent of dopaminergic neurons in the BG degenerate. In this condition the concentration of dopamine become much less than normal state. DA has facilitatory effect on D1 MSN therefore; the activity of this kind of neuron becomes less. Since D1 and D2 receptors have opposing effect, the activity of D2 MSN becomes more (Fig. 2). Then, less inhibition delivers to GPi via direct pathway and causes over-activation of GPi. In indirect pathway, there are two contributing effect which has the same overall effect. The first path is STR-GPe-GPi where over-inhibition caused by D2 MSNs leads to decrease GPe activity which provides less inhibition to GPi. Therefore GPi becomes more active. The second path is STR-GPe-STN-GPi where lower GPe activation causes STN become more active. While STN-GPi connection is excitatory, it leads to increase GPi activity. The net result is over-activation of GPi that provides over-inhibition to the TH [15].

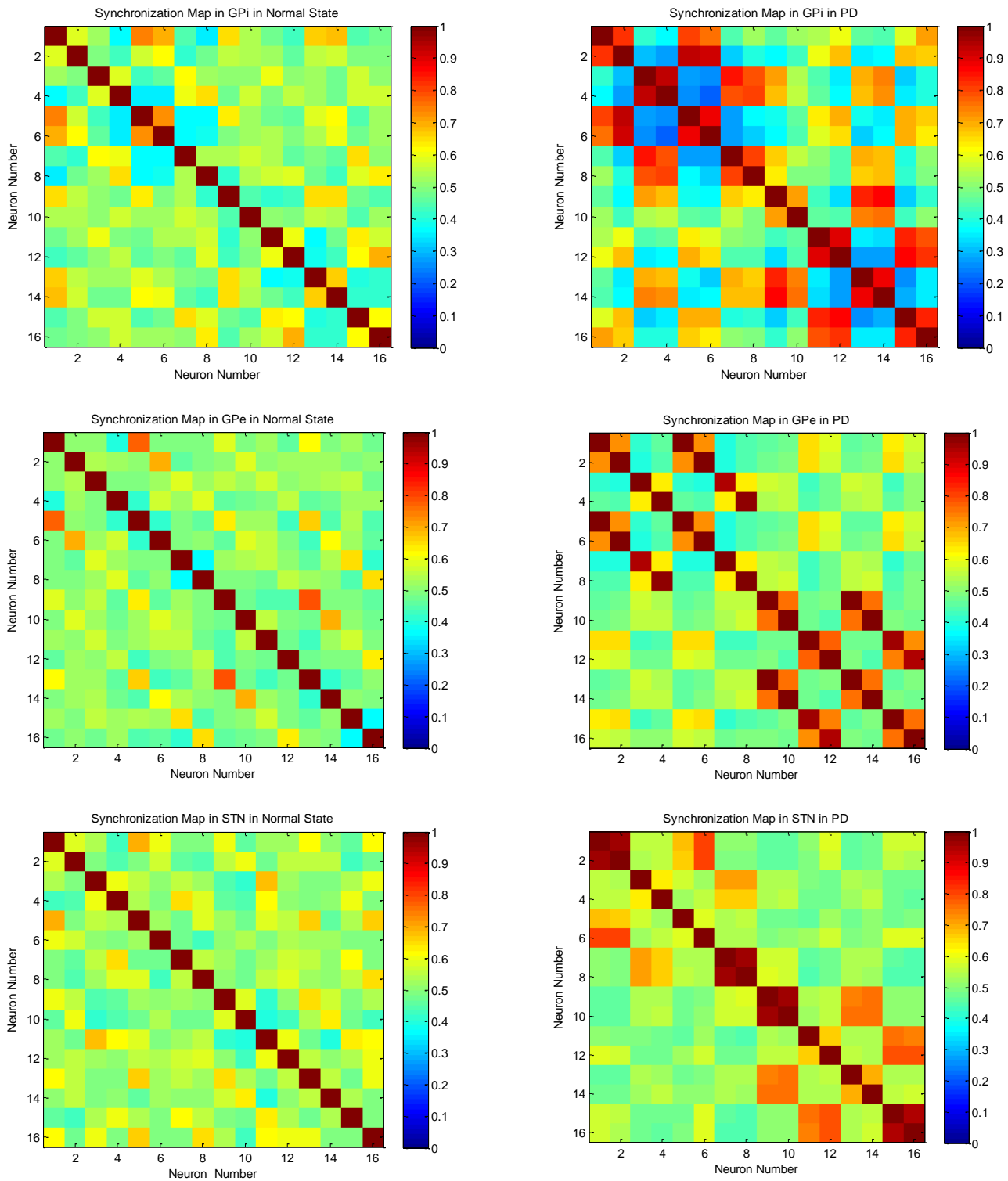


Fig.3 Synchronization map over GPI, GPe and STN in both normal state and PD. The leftmost maps are synchronization maps of the mentioned nuclei in normal state and the rightmost are in PD. As it is obvious, there is overall synchrony enhancement in PD. As stated previously, each nucleus contains 2 cluster each of which has 8 neurons. The first 8 neurons belong to the 1st cluster and the second 8 neurons belong to the 2nd cluster.

IV. CONCLUSION

We developed a computational model of BG which considers the modulatory effect of dopamine on STR activity. In our future studies, we will develop a conductance-based

computational model of BGTCS to investigate the effect of dopamine variation caused by levodopa uptake in motor fluctuation in PD. It will be also useful to analyze the effect of different types of deep brain electrical stimulation in PD symptoms alleviation.

REFERENCES

- [1] W. Dauer and S. Przedborski, "Parkinson's disease: mechanisms and models," *Neuron*, vol. 39, pp. 889-909, 2003.
- [2] J. E. Rubin and D. Terman, "High frequency stimulation of the subthalamic nucleus eliminates pathological thalamic rhythmicity in a computational model," *Journal of computational neuroscience*, vol. 16, pp. 211-235, 2004.
- [3] R. Bertram. (12/10/2013). *Single-Cell and Mean Field Neural Models*. Available: http://www.math.fsu.edu/~bertram/lectures/neural_models.pdf
- [4] K. Gurney, T. J. Prescott, and P. Redgrave, "A computational model of action selection in the basal ganglia. I. A new functional anatomy," *Biological cybernetics*, vol. 84, pp. 401-410, 2001.
- [5] K. Gurney, T. J. Prescott, and P. Redgrave, "A computational model of action selection in the basal ganglia. II. Analysis and simulation of behaviour," *Biological cybernetics*, vol. 84, pp. 411-423, 2001.
- [6] D. Terman, J. Rubin, A. Yew, and C. Wilson, "Activity patterns in a model for the subthalamopallidal network of the basal ganglia," *The Journal of neuroscience*, vol. 22, pp. 2963-2976, 2002.
- [7] M. D. Humphries, R. Wood, and K. Gurney, "Dopamine-modulated dynamic cell assemblies generated by the GABAergic striatal microcircuit," *Neural Networks*, vol. 22, pp. 1174-1188, 2009.
- [8] M. D. Humphries, N. Lepora, R. Wood, and K. Gurney, "Capturing dopaminergic modulation and bimodal membrane behaviour of striatal medium spiny neurons in accurate, reduced models," *Frontiers in computational neuroscience*, vol. 3, 2009.
- [9] S. Taverna, E. Ilijic, and D. J. Surmeier, "Recurrent collateral connections of striatal medium spiny neurons are disrupted in models of Parkinson's disease," *The Journal of Neuroscience*, vol. 28, pp. 5504-5512, 2008.
- [10] P. Suffczynski, S. Kalitzin, and F. Lopes Da Silva, "Dynamics of non-convulsive epileptic phenomena modeled by a bistable neuronal network," *Neuroscience*, vol. 126, pp. 467-484, 2004.
- [11] G. B. Ermentrout and D. H. Terman, *Mathematical foundations of neuroscience* vol. 64: Springer, 2010.
- [12] H. Bergman, A. Feingold, A. Nini, A. Raz, H. Slovlin, M. Abeles, *et al.*, "Physiological aspects of information processing in the basal ganglia of normal and parkinsonian primates," *Trends in neurosciences*, vol. 21, pp. 32-38, 1998.
- [13] M. Amiri, G. Montaseri, and F. Bahrami, "On the role of astrocytes in synchronization of two coupled neurons: a mathematical perspective," *Biological cybernetics*, vol. 105, pp. 153-166, 2011.
- [14] C. Hauptmann and P. A. Tass, "Restoration of segregated, physiological neuronal connectivity by desynchronizing stimulation," *Journal of neural engineering*, vol. 7, p. 056008, 2010.
- [15] A. Nambu, Y. Tachibana, K. Kaneda, H. Tokuno, and M. Takada, "Dynamic model of basal ganglia functions and Parkinson's disease," in *The Basal Ganglia VIII*, ed: Springer, 2005, pp. 307-312.

GSM Based Artificial Pacemaker Monitoring System

Santhosh Ganesh, Lavanya Jagannathan, Sasikala Thirugnanasambandam and Mahesh Veezhinathan

Abstract—The incidence of cardiac abnormalities has seen an unprecedented increase and the pacemaker has been instrumental in expanding the life span of patients. The internally implanted pacemakers are guaranteed 8-10 years of life but get dysfunctional within 4 years due to a variety of problems. The pacemakers which survive this encounter problems with the pace timing leading to a serious problem, pacemaker syndrome. A system to continuously monitor the parameters and battery levels is required. The existing technology uses short range telemetry and scanning transmission method. But these methods have a limited range. The integration of the monitoring system with a GSM communication module can be a feasible solution to this problem. A system has been developed with alarms for amplitude delivery, pacing rate and synchronization errors. Also, a battery level indicator with messages for every 10% discharge and an on-demand delivery of pacemaker parameters and pacing pulse is included. All these are communicated to the user and physician via GSM operated cell phones and uses LabVIEW platform for monitoring and programming.. This can be extended to programming the pacemaker and other medical devices as well.

Keywords— GSM, LabVIEW, Pacemaker alarm, Synchronous pacing.

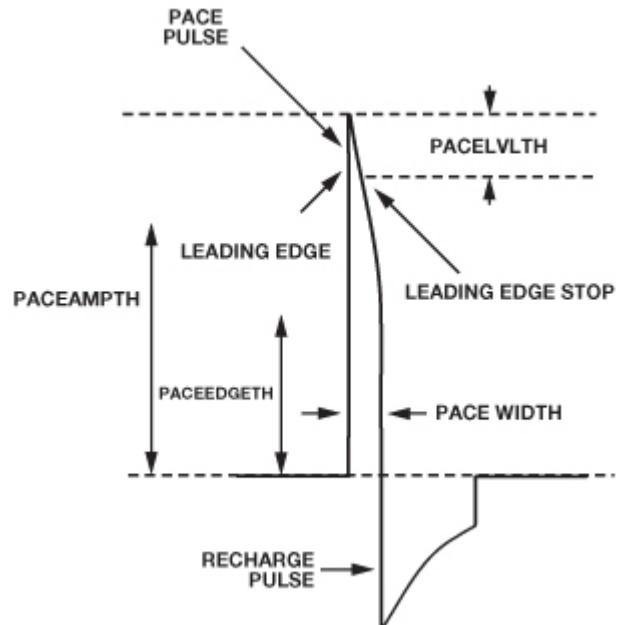
I. INTRODUCTION

Since the introduction of the modern artificial pacemakers in 1972 by Greatbatch [1], there has been more than 75% improvement in the life expectancy of patients with chronic cardiac abnormalities. There have been 2.9 million patients with permanent cardiac pacemaker implants in the USA between 1993 and 2009. The use of dual-chamber pacemakers alone has increased from 62% to 82% in 2009 while single chamber ventricular pacemaker fell to 14% [2]. This indicates the importance of dual chamber pacemakers in prolonging the life of cardiac patients. The internal pacemaker uses Li ion batteries which are expected to last 8-10 years depending on the physiological activity of the human cardiovascular system and its effects on the pacing system. The battery powers the sensing, pace timing and pulse production functions of the pacemakers. The discharge levels of the batteries adversely affect the functions of pacemaker and ultimately lead to its failure. The failure of pacemakers is a major problem and 26% of pacemakers fail well before the expected lifespan of the system [3].

Cardiac pacemakers can be of two types: synchronous and asynchronous. An asynchronous pacemaker

constantly produces pulses, even when the heart is functioning normally. A lot of power is wasted. Thus, the synchronous pacemaker was developed. In synchronous pacemakers, pulses are produced only when the system does not detect a QRS complex. The disadvantages of asynchronous pacemakers are partially overcome by the synchronous pacemakers.

An ideal pacing pulse (Figure 1) has a fast rising edge. Once the maximum amplitude is reached, a capacitive droop follows and then a trailing edge occurs. The polarity of the pulse is then changed for the recharge portion [4]. This is required so that the heart tissue is left with a net charge of



zero.

Fig 1: Ideal pace artifact

The pacemaker encounters various errors during its operation which can cause problems with the natural pacing causing disorders like pacemaker syndrome. Pacemaker syndrome consists of the cardiovascular signs and symptoms of heart failure and hypotension induced by right ventricular pacing. The reported incidence of pacemaker syndrome likely approaches 26% in rate modulated ventricular-based pacing. Over the last three decades the understanding of pacemaker syndrome has evolved [5]-[7].

This problem has to be addressed and is mainly caused due to the problems associated with the electronic malfunction of the pacemakers. This side of the pacemaker has been overlooked and has seeped as a major problem in the use of pacemakers. The problem can only be solved by building in a continuous monitoring of pacemaker functions

Mahesh Veezhinathan is with the department of Biomedical engineering at SSN College of Engineering, Kalavakkam, Chennai 603110, India. Phone: +91-44-27469700; fax: +91-44-27469772; E-mail: maheshv@ssn.edu.in. Santhosh Ganesh, Lavanya Jagannathan and Sasikala Thirugnanasambandam are with SSN College of Engineering, Kalavakkam, Chennai 603110, India.

and a communication protocol to alert the user and associated physician regarding the problem. Also, an on-demand communication of signals is necessary for the monitoring of the instrument.

Another important problem is the battery induced errors in the functioning of a pacemaker. This makes the monitoring of battery levels also a very integral part in the maintenance of the pacemaker's health. This necessitates a system to estimate power of the battery in a non-loading way and communicating the level at periodic signals. The monitoring protocol can bring about a change in the way people perceive the safety of pacemakers and their utility. GSM is a universal protocol of mobile communication and can be used to communicate the error messages and the waveform on demand.

The pacemaker, as a part of its function records the ECG for use in feedback purposes. This can be extracted and used to monitor the patient from time-to-time. This wave can indicate all data of the circulatory function such as the heart rate and the various pathological conditions associated with it. This can also be incorporated into a system where the waveforms are delivered via the GSM system whenever the physician requires monitoring the patient.

In this work, the use of LabVIEW platform to monitor the pacemaker properties and identify the errors has been proposed. The identified errors prompt the GSM server to send the messages and also the waveforms when user requests to send the data. The system is used to integrate the alarm software algorithm and the hardware including the pacemaker, battery circuit and the GSM modem.

II. SYSTEM REPRESENTATION

A. LabVIEW Block

Figure 2 illustrates the different parameters which are monitored in a pacemaker system and how the thresholds are set for the different values.

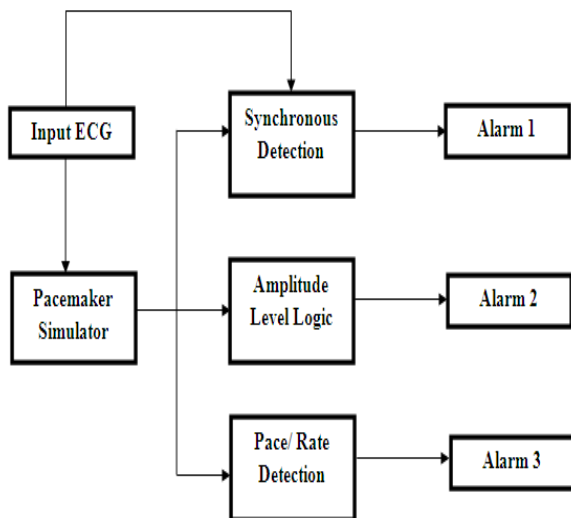


Fig 2: Pacemaker monitors using LabVIEW

The pacemaker simulator gets the input ECG which is processed and the output pulse is delivered if the pace is below the set threshold. The generated pacing pulse is usually a square pulse waveform with low duty cycle. The pulse usually encounters 3 types of errors [8]-[9]. The amplitude threshold and pace rate detector use simple comparator logic. The synchronous detector merges the input and output waveforms with time equalization and thus helps in eliminating the synchronous collision of the signals which may result in arrhythmic excitation and pacemaker syndrome.

B. LabVIEW Block

Figure 3 indicates the input and output of the GSM modem. The input is from the system which gives information on the detection of errors. This activates the modem to modulate and send the alarms to the destination.

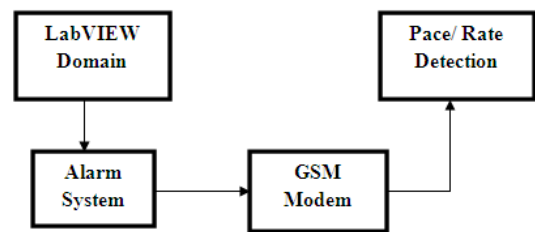


Fig 3: Alarm communication system

Figure 4 shows the double way on-demand data communication from one domain to another. The user can send the request to the GSM modem, which in turn acquires the data from the pacemaker and delivers it as a data file to the user.

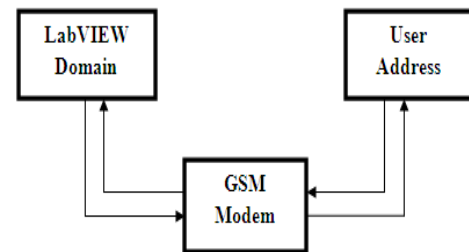


Fig 4: On-demand data communication

III. MATERIALS

This section describes the software and hardware resources used in the fault detection and notification systems.

A. NI LabVIEW

LabVIEW (Laboratory Virtual Instrument Engineering Work-bench) is a platform and development environment for a visual programming language. It can be used as a platform to integrate signal acquisition, processing and transmission of the

processed signal. It is a graphical programming environment. LabVIEW simplifies the most complex coding problems. The Software also includes a wide variety of blocks for mathematical functions, filters (IIR, FIR) and other blocks like SMTP which can be used to export data from LabVIEW. The software allows the user to create stand alone executables which can be distributed to a number of systems and be reused unlimitedly.

The GSM interface module available in the software has already been used in several medical telemetry applications [10].

B. GSM Modem

GSM (Global System for Mobile Communications) is a standard developed by the European Telecommunications Standard Institute. It was developed to describe a set of protocols for the second generation (2G) digital cellular networks. GSM Technology can be used to deliver data or signals from an instrument or device to the doctors. The device needs to be integrated with a SIM (Subscriber Identity Module) and is programmed with a telephone number. On trigger, the SIM establishes connection with the network and broadcasts the data to the destination as specified by the programmer. The dimension of a SIM card does not exceed 25mmX15mm.

GSM Modems are used to integrate the technology with LabVIEW. An example of a MODEM used is RTD GSM 35. It is a GSM/GPRS enabled Modem that is capable of sending and receiving data. It works on frequencies 900MHz and 1800MHz. It is compact in size [11].

IV. METHODS

This section describes the process, protocols and methodologies used in the fault detection and notification systems.

A. Pacemaker simulation

The initial requirement of a pacemaker was needed for the testing and evaluation of the system and algorithms. The use of a real pacemaker was replaced by a simulated one so as to increase the testing range of the algorithm. A simple algorithm was used to simulate the pacemaker and the input was given through the synthesized ECG. This code for ECG synthesis was retrieved from the AAMI database which is used as standard test for pacing devices. The pacemaker simulators amplitude and pace were controlled manually and there was a provision to introduce synchronizing error as well.

The battery level was also simulated using a DC power supply integrated into the device through a DAQ device.

B. Fault detection and monitoring

The monitoring system incorporates three parameters of the pacemaker

- Amplitude
- Pacing rate
- Pacing synchronisation.

Each of these parameters were extracted from the pacing pulse and compared with a threshold continuously. The comparator, in case of the first two and a synchronous detector for the third parameter were built in LabVIEW and tested using the built-in simulator.

A straightforward amplitude comparator was used for the amplitude monitoring while a timed counter was used for the pacing rate monitor. The LED alarms were used in the case of the simulation and a GSM prompt was given to the GSM modem interfaced with the device.

C. Battery level monitor

The battery monitor consisted of two parts – the hardware interface and the comparator. The battery is connected to a load circuit and then a DAQ to interface it with LabVIEW. This is then compared with a threshold and converted into a percentage. The battery monitor was set to generate messages at every 10% interval and was set to alarm at a discharge level of 25%, as it is the level at which most pacemakers fail [12].

The levels of indication, when executed through the circuit, were not very accurate and also resulted in the loading of the power source. Considering this, a simple algorithm was devised in the Arduino platform, to measure the battery level and provide indications for each 10% reduction in its power as well as an alarm when it goes below 25%.

D. Communication module

The communication protocol used is a GSM system to transmit alarm messages and signals on demand. The monitoring system is integrated with a GSM modulation tool which is prompted on the activation of any alarm. The GSM module communicates to the server, the string message generated. The string is then sent to the destination address. Systems to show error on disconnect or network non-availability problem is also built.

The second system involves an on-demand delivery of pacemaker parameters and pacing waveforms. This involves the user/physician dialing into the pacemaker by sending in a request to send the information. The GSM tool, on receiving the message connects with the pacemaker monitor and acquires the data from the system. The data is encoded as a MMS and sent to the destination address.

E. ECG storage

The ECG is continuously recorded as a part of the pacemaker system and an additional program of retrieving the recorded ECG from the pacemaker is done so as to deliver the patient ECG to the device whenever a request is made. This is done by the program which converts the ECG data into a 3-4KB data packet and then sends it to the encoder and GSM modem to be transmitted to the device.

V. RESULTS

The pacemaker monitoring system has been designed and tested using the synthesized ECG at different rates. The error tolerance rates for different pacing rates are given in Table 1

S.No	Pacing Rate	Tolerance (%)
1	5	0.13
2	10	0.15
3	20	0.26
4	25	0.22
5	30	0.4
6	40	0.46

Table 1: Pacing error tolerance rates

The pacing alarm tolerance exhibits a low value which states the efficiency of the system. This in addition with the average tolerance of the amplitude error, which was found to be 0.1% also, retains the performance of the system. The performance of the GSM system was also evaluated and a VI was developed for the simulation of the pacemaker and its monitor. The VI was used for transmitting the messages regarding the pacemaker parameters and warnings as well.

The communication module to supply parameters and waveform was also produced. The VI was generated for this communication also. The data was transmitted using the 900 and 1500 Hz modulation frequencies also. The network response errors were not received and the system worked perfectly well in distances over 35-40 kil tested.

long distances as it is a universal satellite controlled system. The interferences provided by the body also are very less for this system due to optimal frequencies used.

The method can also be developed for further changing pacing modes and giving further instructions which are currently done manually and by using the scanning transmission method.

VII. CONCLUSIONS

Failure of a Pacemaker can lead to serious complications. It is thus important to integrate alarm systems into the device which would notify the doctors in case of any fault with the device. Also, this system enables the patients to self evaluate the condition of the device [13].

The system designed using LabVIEW was tested for simulated error conditions i.e. Pacing, Synchronization and Amplitude errors. It proved to have high tolerance to errors and also has high efficiency. Further, plans to test the system with real time ECG signals and faulty temporary pacemakers and analyze the efficiency are considered.

To implement this system into a real time pacemaker, a hardware module needs to be developed. The hardware system will consist of a set of circuits designed to detect the pacing, amplitude and synchronization errors. A circuit to measure the battery level to monitor the rate of discharge of the battery should also be included. A PIC or an Arduino processor can be used to integrate the circuits with the GSM modem. The GSM Modem has to be programmed with a unique SIM card according to the requirements of the physician.

Fig 4: On-demand data communication



VI. DISCUSSIONS

The pacemaker alarm system using GSM (shown in Figure 4) is a very different one in comparison with existing technology such as the scanning memory transmission and other telemetry units used. The battery level indicating messages and the on-demand will improve the performance and the efficiency of the pacemaker by enabling continuous monitoring. The GSM also enables the communication over

REFERENCES

- [1] Max Schaldach, Seymour Furman M.D. "Engineering in Medicine" in *Advances in Pacemaker Technology*, 1st ed. vol. 1, Seymour Furman, Ed. New York: Springer, 1975.
- [2] "A review of JACC Journal Articles on the Topic of Interventional Cardiology: 2011-2012", vol. 62, 2013, Journal of the American College of Cardiology.

- [3] Greenspon AJ, Patel JD, et al, “Trends in permanent pacemaker implantation in the United States from 1993 to 2009: increasing complexity of patients and procedures”, 2010.
- [4] John Kruse and Catherine Redmond, “Detecting and Distinguishing Cardiac Pacing Artifacts”, vol. 46, November 2012, Analog Dialogue.
- [5] “Guidelines for cardiac pacing and cardiac resynchronization therapy: 2007-2008”, European Heart Journal.
- [6] D. Michael Farmer, N. A. Mark Estes, Mark S. Link, “New Concepts in Pacemaker Syndrome”, 2012, Indian pacing and electrophysiology journal.
- [7] William G. Stevenson and Paul D, et al, “ACCF/AHA/HRS Focused Update of the 2008 Guidelines for Device-Based Therapy of Cardiac Rhythm Abnormalities”, 2008.
- [8] A. Yilmaz, “Studies on cardiac pacing: emphasis on pacemaker sensor and resynchronization therapy”, 2005
- [9] Bruce Kleinman, MD; Margaret Baumann, MD; Charles Andrus, MD, “Faulty Design Resulting in Temporary Pacemaker Failure”, 2001.
- [10] Manita Rajput, Sadhana Pai, Umesh Mhapankar, “Wireless Transmission of Biomedical Parameters Using GSM Technology”, 2013.
- [11] Karima Djabella, Michel Sorine, “A differential model of controlled Cardiac pacemaker cell”, 2006.
- [12] Geoffrey Davies and Harold Siddons, “Prediction of battery depletion in implanted pacemakers.”, 1978.
- [13] Medtronic Electricals. “Manual for Adapta/Versa”, 2009.
- [14] John.G.Webster. “Medical Instrumentation: Analysis and Applications”, 2006.

Effect of genetic lines and season on body weights of chicks

Hani N. Hermiz¹, Kamarn A. Abas, Aram M. Ahmed, Tahir R. Al-Khatib, Shayma M. Amin, Dastan A. Hamad

Abstract— The experiment was conducted at Hawler Research Station. A total number of 442 chicks were hatched at three seasons namely spring, summer and autumn 2011 and belongs to five genetic lines (Line 1 = Black with Brown Neck, Line 2 = Isa Brown, Line 3 = White, Line 4 = Spotty, Line 5 = Pure Black). Chicken genotypes were kept in replicates and their average body weights were recorded at 1-day of their age and weekly till 5 weeks on a sensitive scale to the nearest 0.1 g, also their weekly body weight gains were calculated. The chicks were fed with a ration include in average 21.5 % CP and 2800 K.cal/kg, in addition to vitamins. In order to get natural resistance to disease, the chicks were vaccinated by Newcastle only. General linear model within SAS Programme was used to investigate the effect of genetic line and season on studied traits. Duncan Multiple Range Test was conducted to diagnosing the significant differences between the means of the levels of each factor.

The overall mean of chicks body weights at 1 day, 1, 2, 3, 4, and 5 weeks of age were 40.72, 82.90, 128.34, 191.28, 262.09 and 355.47 gm respectively. Genetic lines was found to have a significant effect on body weights of chicks at 1 day, 1, 2, 3, 4, and 5 weeks of age where the chicks of line 1 (Black with Brown Neck) exceed the others at all ages. The effect of season of hatching was found to be significant on body weights of chicks at 1, 2, 3, and 5 weeks of age, while the differences between the chicks hatched in different seasons were not significant in their body weights at 1 day and 4 weeks of age. Weekly body weight gains for all lines of chicks at the 1st, 2nd, 3rd, 4th, and 5th week of their age averaged 42.18, 45.44, 62.94, 70.82 and 93.38 gm respectively. The differences between genetic lines were significant on all of weekly body weight gains of chicks. The chicks of line 1 (Black with Brown Neck) exceed significantly the others at all ages except at the 4th week where the chicks of line 5 (Pure Black) gained significantly higher than the chicks of lines 2, 3 and 4. The season affect all weekly body weight gains of chicks belongs to all lines significantly, where the chicks hatched in Summer surpassed those hatched in Spring and Autumn in their weekly body weight gain at the 1st and 2nd week, while the chicks hatched in Autumn surpassed the others in their weekly body weight gain at the 4th and 5th week.

The conclusion: it was observed that chicks hatched from line 1 (Black with Brown Neck) exceed the others in their body weights and weekly gains at all ages, so the farmers could be advised to breed the male chicks of this line to get

high carcass weights beside egg production from females of the same line.

Keywords— Poultry Genetic Lines, Season, Chicks Body Weights.

I. INTRODUCTION

THE genetic improvement considered as one of the most important methods used to increase the productivity of poultry through selecting the best animals and improving their genetic merit. The industry of poultry is one of the pillars of the economies of many countries because of its benefit in fast capital turnover and to secure food sources of high nutritional value for humans including white meat and egg. This industry depends heavily on poultry, which shows a rapid and important improvement in various fields including the genetic and breeding improvement, so the researchers focus in their work on developing specialized and commercial strains of chickens by following new strategies [1]. These distinguished strains led to a lot of studies to have a knowledge about their requirements including feeding, breeding, management and mating system to express their genetic potential [2].

Similar to other economically important traits, most chicken growth and fitness traits are controlled by multiple genes [3]. Strain of chicken affects body weights and gains at different ages [4] and [5]. Understanding the genetic control of growth in chickens will provide an opportunity for genetic enhancement of production performance and physiology. Falconer [6] discussed the role of G × E interactions in animal breeding in considerable detail. Typical macro-environments are resulting from climatic differences such as those between seasons or regions [7] and [8]. This research aims to study and compare body weights of chicks of Isa Brown and four local genetic lines as well as the effect of different seasons on studied traits, in order to diagnosing which line is better to be used in relating with genetic programs to improve and bred for meat purposes.

II. MATERIALS AND METHODS

The present study was conducted at Hawler Research Station, Animal Production Department, Directorate of Agricultural Research–Erbil, Iraq. A total number of 442 chicks were hatched at three seasons namely spring, summer and autumn 2011 and belong to five strains (Line 1 = Black with Brown Neck, Line 2 = Isa Brown, Line 3 = White, Line 4 = Spotty, Line 5 = Pure Black) (Table 1). Chicken genotypes were kept in replicates and their average body weights were recorded at 1-day of their age and weekly till 5 weeks on a sensitive scale to the nearest 0.1 g, also their weekly body weight gains were calculated.

¹ Corresponding address Dr. Hani N. Hermiz (profdrhani59@gmail.com), College of Agriculture, University of Salahaddin, Erbil, Kurdistan Region, Iraq.

Chicks were bred in a clean well ventilated hall, previously fumigated with formalin and potassium permanganate with ratio (2:1). The hall was provided with heaters to adjust the environmental temperature. The chicks were fed with a ration include in average 21.5 % CP and 2800 K.cal/kg, in addition to vitamins. Water was available at all times. In order to get natural resistance to disease, the chicks were vaccinated by Newcastle only.

Table 1. Number of chicks according to their line and season of hatching:

Lines	season of hatching		
	Spring	Summer	Autumn
Line 1	22	18	19
Line 2	57	33	15
Line 3	19	31	28
Line 4	69	49	16
Line 5	25	30	11

Statistical Analysis: General linear model (GLM) within SAS Program [9] was used to investigate the effect of genetic line and season on studied traits. Duncan Multiple Range Test [10] was conducted to diagnosing the significant differences between the means of the levels of each factor.

III. Results and Discussion

The overall mean of chicks body weights at 1 day, 1, 2, 3, 4, and 5 weeks of age were 40.72, 82.90, 128.34, 191.28, 262.09 and 355.47 gm respectively (Table 2). Genetic lines was found to have a significant effect on body weights of chicks at 1 day, 1, 2, 3, 4, and 5 weeks of age where the chicks of line 1 (Black with Brown Neck) exceed the others at all ages (Table 2). Earlier investigators including Leeson et al. [4], Taha et al. [5], Farran et al. [11], Nadia et al. [12], Ajayi and Ejiofor [13], and Enaiat et al. [14] also obtained similar results using different strains and breeds. While in Iraq, Ali [15] revealed to a non significant differences between three broiler hybrids (Lohman, Ross and Hubbard) in their body weights at 1, 14, 28, 42, and 56 days of age. The effect of season of hatching was found to be significant on body weights of chicks at 1, 2, 3, and 5 weeks of age, while the differences between the chicks hatched in different seasons were not significant in their body weights at 1 day and 4 weeks of age (Table 2). Such effects could be attributing to climatic effects, heat stress, as well as, on the health and feed consumption of chicks. Several studies found that the heat-stress effect was more pronounced in fast-growing commercial broiler stocks than in non selected broiler lines [16] and [17] or broiler lines selected for traits other than growth rate [16], [18] and [19]. Natural heat stress also reduces growth rate. Settar et al. [20] in his work on commercial Arbor Acres broilers reared to sexual maturity and to produce two hatches, in spring and summer, revealed that body weight of chicks at 4 week of age was lower in summer than in spring by about 36%.

Weekly body weight gains for all lines of chicks at the 1st, 2nd, 3rd, 4th, and 5th week of their age averaged 42.18,

45.44, 62.94, 70.82 and 93.38 gm respectively (Table 3). The differences between genetic lines were significant on all of weekly body weight gains of chicks. The chicks of line 1 (Black with Brown Neck) exceed significantly the others at all ages except at the 4th week where the chicks of line 5 (Pure Black) gained significantly higher than the chicks of lines 2, 3 and 4 (Table 3). These results agreed with those obtained earlier by Deeb and Lamont [3], Leeson et al. [4], Taha et al. [5], Enaiat et al. [14], Rondelli et al. [21], and Zhao et al. [22]. They found significant genetic differences between different strains in growth rate and weight gain at different stages of life. On the other hand, Ali [15] stated that the differences between three broiler hybrids (Lohman, Ross and Hubbard) were not significant in their body weight gains from 15-28 and from 29-42 days of age. The season affect all weekly body weight gains of chicks belongs to all lines significantly, where the chicks hatched in Summer surpassed those hatched in Spring and Autumn in their weekly body weight gain at the 1st and 2nd week, while the chicks hatched in Autumn surpassed the others in their weekly body weight gain at the 4th and 5th week (Table 3). Growth rate of contemporary commercial broilers are significantly depressed by environmental stress caused by high ambient temperatures (AT) [8], [19] and [23]. Settar et al. [20] revealed that body weight gain of chicks at 0 to 4 weeks of age was lower in summer than in spring by about 38% in his work on commercial Arbor Acres broilers. Therefore, high AT has been a major factor hindering poultry meat production in hot climates, especially in developing countries where farmers cannot afford costly artificial control of AT in broiler houses.

IV. CONCLUSION

From the results of this study, it was observed that chicks hatched from line 1 (Black with Brown Neck) exceed the others in their body weights and weekly gains at all ages, so the farmers could be advised to breed the male chicks of this line to get high carcass weights beside egg production from females of the same line.

Acknowledgment

The authors thank and appreciate Mr. M.K. Ala-Adin and Mr. J.S. Toma (Directorate of Agricultural Research-Ministry of Agriculture-Erbil) for their assistance during the period of conducting the study.

Table 2. Means \pm S.E. for the factors affecting body weight of different lines of chicks:

Effects	Body Weights at different ages (g)					
	1 st Day	1 st Week	2 nd Week	3 rd Week	4 th Week	5 th Week
Overall mean	40.72 \pm 0.7	82.90 \pm 1.2	128.34 \pm 2.6	191.28 \pm 4.2	262.09 \pm 4.6	355.47 \pm 6.9
Genetic lines						
Line 1	43.81 \pm 2.3 a	88.56 \pm 3.4 a	138.99 \pm 7.2 a	208.25 \pm 13.1a	282.10 \pm 10.7a	399.83 \pm 14.6 a
Line 2	38.03 \pm 0.8 c	78.90 \pm 1.9 b	126.71 \pm 3.2ab	187.89 \pm 8.7 b	252.97 \pm 6.6bc	350.79 \pm 15.7 b
Line 3	39.27 \pm 0.6 bc	78.87 \pm 1.4 b	118.51 \pm 6.4 b	176.98 \pm 5.5 b	238.58 \pm 6.7c	336.56 \pm 18.8 b
Line 4	39.86 \pm 0.9abc	82.38 \pm 1.8 ab	127.98 \pm 5.6ab	191.15 \pm 9.9 b	260.80 \pm 4.8abc	348.61 \pm 8.3 b
Line 5	42.64 \pm 1.5 ab	85.80 \pm 1.8 a	129.52 \pm 4.0ab	192.12 \pm 6.0 b	276.03 \pm 12.3ab	341.58 \pm 12.3 b
Season of hatching						
Spring	42.40 \pm 1.5 a	84.33 \pm 2.2 a	125.04 \pm 5.5 b	198.82 \pm 6.7 a	251.93 \pm 9.2 a	348.22 \pm 9.8 b
Summer	40.16 \pm 0.6 a	84.66 \pm 1.9 a	140.26 \pm 2.4 a	206.79 \pm 5.3 a	268.18 \pm 6.6 a	329.57 \pm 8.2 c
Autumn	39.61 \pm 1.3 a	79.71 \pm 1.7 b	119.71 \pm 1.7 b	168.23 \pm 2.4 b	266.17 \pm 7.9 a	388.63 \pm 10.3 a

Means having different letters within each factor/column differ significantly ($P < 0.05$) according to Duncan (1955).

Table 3. Means \pm S.E. for the factors affecting body weight gain of different lines of chicks:

Effects	Body Weights Gain at Different Ages (g)				
	1 st Week	2 nd Week	3 rd Week	4 th Week	5 th Week
Overall mean	42.18 \pm 0.7	45.44 \pm 1.8	62.94 \pm 2.4	70.82 \pm 4.3	93.38 \pm 7.1
Genetic lines					
Line 1	44.76 \pm 2.4 a	50.42 \pm 3.9 a	69.26 \pm 6.3 a	73.86 \pm 5.1 ab	117.72 \pm 21.1 a
Line 2	40.87 \pm 1.3 ab	47.81 \pm 2.6 a	61.18 \pm 5.9 ab	65.08 \pm 9.8 b	97.82 \pm 14.2 ab
Line 3	39.59 \pm 1.0 b	39.64 \pm 5.4 b	58.47 \pm 4.8 b	61.60 \pm 7.9 b	97.98 \pm 16.8 ab
Line 4	42.51 \pm 0.9 ab	45.60 \pm 4.0 ab	63.18 \pm 6.7 ab	69.64 \pm 7.6 b	87.81 \pm 11.2 ab
Line 5	43.15 \pm 0.9 ab	43.72 \pm 3.5 ab	62.60 \pm 4.3 ab	83.91 \pm 15.3 a	65.55 \pm 10.9 b
Season of hatching					
Spring	41.93 \pm 1.0 ab	40.71 \pm 3.6 b	73.77 \pm 2.4 a	53.12 \pm 3.3 b	96.29 \pm 4.2 b
Summer	44.50 \pm 1.5 a	55.61 \pm 0.9 a	66.53 \pm 3.4 a	61.39 \pm 2.2 b	61.39 \pm 2.2 c
Autumn	40.10 \pm 0.5 b	40.00 \pm 0.1 b	48.51 \pm 1.8 b	97.94 \pm 6.1 a	122.46 \pm 16.1 a

Means having different letters within each factor/column differ significantly ($P < 0.05$) according to Duncan (1955).

REFERENCES

- [1] North, M.O. (1984). Commercial Chicken Production Manual. 3rd Edition. AVI. Publishing Company Inc. West Port. USA.
- [2] Havenstein, G.G., Ferket, P.R., Scheideler, S.E. and Larson, B.T. (1994). Growth, livability and feed conversion of 1957 vs 1991 broilers when fed "typical" 1957 and 1991 broiler diets. *Poultry Sci.*, 73:1795–1804.
- [3] Deeb, N. and Lamont, S.J. (2002). Genetic Architecture of growth and body composition in unique chicken population. *J. Heredity*. 93: 107-118.
- [4] Leeson, S., Caston, L. and Summers, J.D. (1997). Layer Performance of Four Strains of Leghorn Pullets Summers Subjected to Various Rearing Programs. *Poultry Sci.*, 76: 1–5.
- [5] Taha, A.E., Abd El-Ghany, F.A. and Sharaf, M.M. (2010). Strain and sex effects on productive and slaughter performance of developed local Egyptian and Canadian chicken strains. *Egypt. Poultry Sci.*, 30 (IV): 1059-1072.
- [6] Falconer, D.S. (1989). Introduction to Quantitative Genetics. Third edition, Longman House, London.
- [7] Mathur, P.K. and Horst, P. (1994). Genotype by environment interaction in laying hens based on relationship between breeding values of sires in temperate and tropical environments. *Poultry Sci.*, 73:1777–1784.
- [8] Yalcin, S., Settar, P., Ozkan, S. and Cahaner, A. (1997). Comparative evaluation of three commercial broiler stocks in hot versus temperate climates. *Poultry Sci.*, 76: 921–929.
- [9] SAS. (2005). SAS/STAT User's Guide for personal computers. Release, 8.2. SAS Institute, Inc., Cary , NC, USA.
- [10] Duncan, D.B. (1955). Multiple Range and Multiple Test. *Biometrics*. 11: 1-42.
- [11] Farran, M.T., Khalil, R.F., Uwayjan, M.G. and Ashkarian, V.M. (2000). Performance and carcass quality of commercial broiler strains. *J. App. Poultry Res.*, 9: 252-257.
- [12] Nadia; A.E., Rizk, R.E., Bahie El-Deen, M. and Shalan, H.M. (2001). Effect of strain and dietary regimen on the performance of local chickens. *Egypt Poultry Sci.* 21(IV): 1021- 1038.
- [13] Ajayi, F.O. and Ejiofor, O. (2009). Effects of genotype X sex interaction on growth and some development characteristics of Ross and Anak broiler strains in the high rainforest zone of Nigeria. *Asian J. Poultry Sci.* 3: 51-56.
- [14] Enaiat, M.M., Amina, A.S. and Eman, M.A. (2010). A comparative study of productive and physiological performance between two local strains of chicks. *Egypt Poultry Sci.* 30 (I): 297-316.
- [15] Ali, E.A. (2006). Effect of dietary supplementation with organic chromium on productive, physiological and immunological traits of three hybrids of Broiler chicken. M.Sc. Thesis, College of Agriculture, Baghdad University, Iraq. (In Arabic).
- [16] Washburn, K.W., El-Gendy, E. and Eberhart, D.E. (1992). Influence of body weight on response to a heat stress environment. Pages 53–56 in: Proceedings of 19th World's Poultry Congress, Vol. 2. Amsterdam, Netherlands.
- [17] Eberhart, D.E. and Washburn, K.W. (1993). Assessing the effects of the naked neck gene on chronic heat stress resistance in two genetic populations. *Poultry Sci.* 72:1391–1399.
- [18] Leenstra, F.R. and Cahaner, A. (1991). Genotype by environment interactions using fast-growing, lean or fat broiler chickens, originating from The Netherlands and Israel, raised at normal or low temperature. *Poultry Sci.* 70:2028–2039.
- [19] Cahaner, A. and Leenstra, F.R. (1992). Effects of high temperature on growth and efficiency of male and female broilers from lines selected for weight gain, favorable feed conversion, and high or low fat content. *Poultry Sci.* 71:1237–1250.
- [20] Settar, P., Yalcin, S., Turkmut, L., Ozkan, S. and Cahaner, A. (1999). Season by genotype interaction related to broiler growth rate and heat tolerance. *Poultry Sci.*, 78: 1353–1358.
- [21] Rondelli, S., Martinez, O. and Garcia, P.T. (2003). Sex effect on productive parameters, carcass and body fat composition of two commercial broilers lines. *Rev. Bras. Cienc. Avic.* 5, 3: 169 – 173
- [22] Zhao, J.P., Chen, J.L., Zhao, G.P., Zheng, M.Q., Jiang, R.R. and Wen, J. (2009). Live performance, carcass composition, and blood metabolite responses to dietary nutrient density in two distinct broiler breeds of male chickens. *Poult. Sci.* 88: 2575-2584.
- [23] Howlider, M.A.R. and Rose, S.P. (1989). Rearing temperature and the meat yield of broilers. *Br. Poultry Sci.* 30:61–67.

On the Optimization of non-Dense Metabolic Networks in non-Equilibrium State Utilizing 2D-Lattice Simulation

Erfan Khaji

Graduate Student, Applied Physics Department, University of Gothenburg, Gothenburg, Sweden.

Abstract

Modeling and optimization of metabolic networks has been one of the hottest topics in computational systems biology within recent years. However, the complexity and uncertainty of these networks in addition to the lack of necessary data has resulted in more efforts to design and usage of more capable models which fit to realistic conditions. In this paper, instead of optimizing networks in equilibrium condition, the optimization of dynamic networks in non-equilibrium states including low number of molecules has been studied using a 2-D lattice simulation. A prototyped network has been simulated with such approach, and has been optimized using Swarm Particle Algorithm the results of which are presented in addition to the relevant plots.

Introduction

The objective of Systems Biology is to study the complex biological processes as integrated systems of many interacting components [14]. Current metabolic engineering processes allow manipulating metabolic networks to improve the desired characteristics of biochemical systems [1]. While researches and investigations are still ongoing on the subject of metabolic networks and genome scale modeling, two crucial approaches are frequently utilized. The first approach is to consider all the reactions in our favorite pathway to be occurred with fixed rate which usually happens when the whole system is in steady state. Therefore, optimizing the yield of desired product is strait forward as the problem is a linear programming with linear cost function and constraints. The second approach is dynamical modeling which allows reactions to occur with any non-linear rate which is indicative of a system in

non-equilibrium system. Kinetic models describe the complete dynamics of the network, and have proven useful to implement optimization and control over the network, such as in [2]. The creation of reliable kinetic models involves the estimation of parameters, the complexity of this task increasing with the size of the network considered [1].

Optimizing a metabolic network is directly dependent on the network's model. Several strategies has been introduced in order to optimize the kinetics of networks some of which are [3] [4-12]. The majority of these approaches are based upon mixed-integer linear programming (MILP) that employ integer variables to capture the discrete nature of decision making required to analyze, curate and redesign metabolic networks. [13].

When optimizing a metabolic network for a given objective two different questions should be answered. The first is to find which branch or branches must be manipulated. The second is to determine what type of alterations must be done. Strategies such as OptKnock [8] and the work in [9] address the first problem. In this work a strategy for the second problem is described.

In this paper, we introduced 2-D lattice simulation for modeling dynamic and sparse metabolic

networks and optimized this model utilizing Particle Swarm Optimization. In the following sections, firstly, the preliminary assumptions of 2-D lattice simulation are presented. In section 2, a prototyped network is introduced which has been used in many scientific works on the same subject. In section 3, we present the result of the optimization, and discuss the results.

2-D Lattice Simulation

Consider a 2-D lattice where each cell can be referred to a molecule or a blank space. Should a molecule is larger than the rest particles in a pathway, allocating more than one cell to that molecule is achievable with ease. Moreover, consider a neighborhood area in which a molecule can react with the other particles. Regularly, a neighborhood of one cell from each side of a cell can be considered as the sensitive area. However, this point is also adaptable to the type of the molecule in hand similar to its size. If two types of molecules which can react with each other are

placed in their sensitive area in a 2-D lattice, then the reaction will take place in the way that those cells will convert to the products of the reaction they are involved. This process includes any kind of reactions such as those with enzymes or the reactions which have many substrates but much less products. Assuming that in each period of time just one reaction can take place, the algorithm of this simulation can be presented as follows:

- 1- Generate a 2-D lattice with the expected size.
- 2- Allocate each cell to a molecule or blank space according to the initial volume of each material.
- 3- Determine the total number of steps.
- 4- For each step pick a random cell from the lattice.
- 5- If a relevant molecule exists in the pre determined sensitive area of the chosen cell, substitute the cells with products with the probability of P .
- 6- Repeat steps 2-5.

Figure 1: samples of variant molecules in red and their sensitive area in blue in a 5*5 lattice.

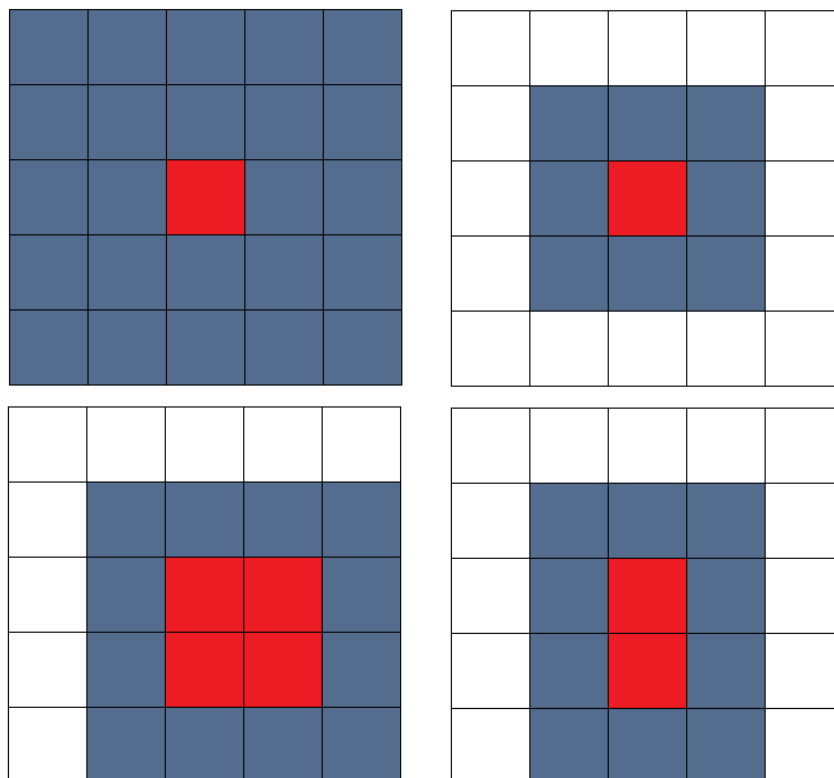


Figure 2: Result of 2-D lattice simulation of equation (1): Change in concentrations over time for enzyme E, substrate S, complex ES and product P in a (100*100) lattice with 0% neutralized molecules.

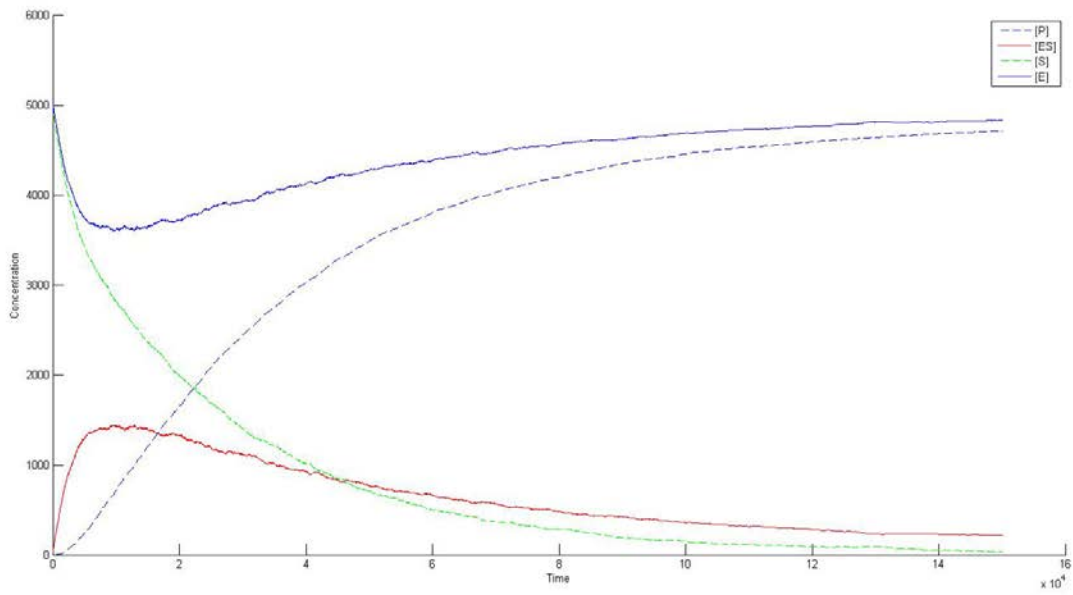


Figure 3: Result of 2-D lattice simulation of equation (1): Change in concentrations over time for enzyme E, substrate S, complex ES and product P in a (100*100) lattice with 50% neutralized molecules.

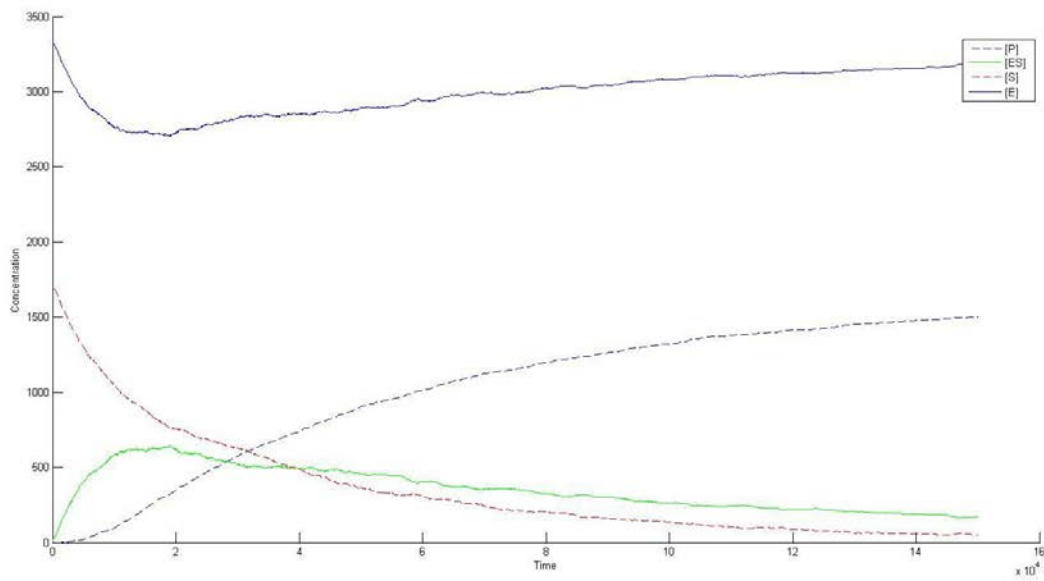


Figure 4: Result of 2-D lattice simulation of equation (1): Change in concentrations over time for enzyme E, substrate S, complex ES and product P in a (100*100) lattice with 75% neutralized molecules.

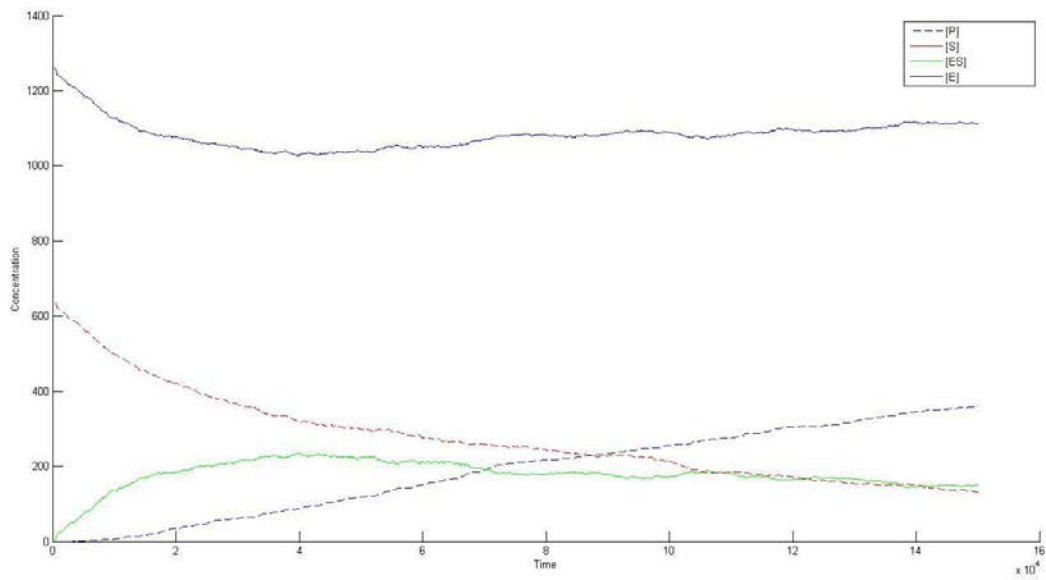
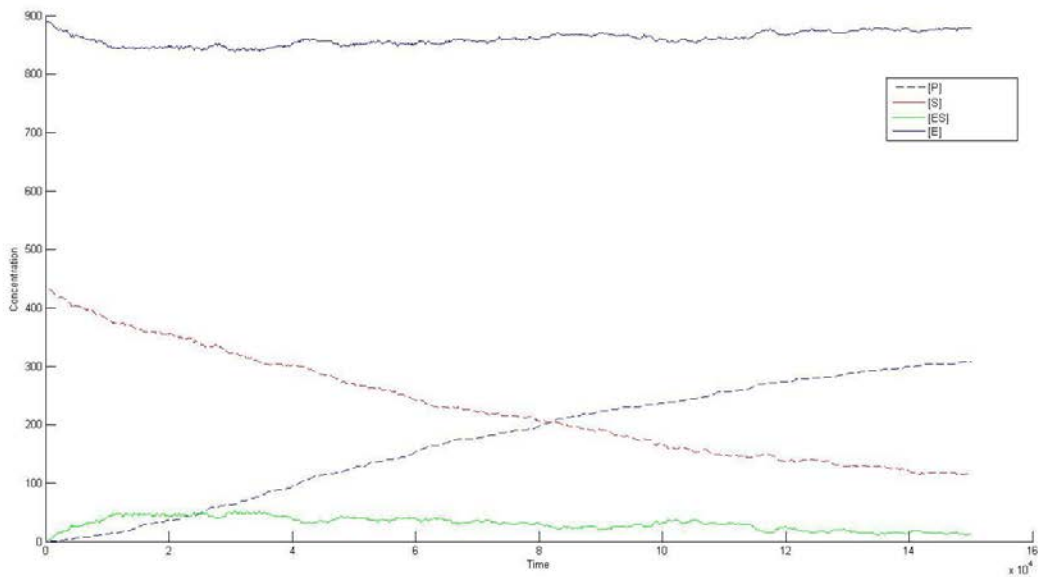
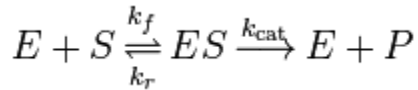


Figure 5: Result of 2-D lattice simulation of equation (1): Change in concentrations over time for enzyme E, substrate S, complex ES and product P in a (100*100) lattice with 81% neutralized molecules.



Before applying this method into a real life problem, we have examined with some simple, theoretical problems such as Michaelis-Menten equation. The results pretty match the solution of equation in the case of large number of molecules and in large scale 2-D lattice.



Time Scaling

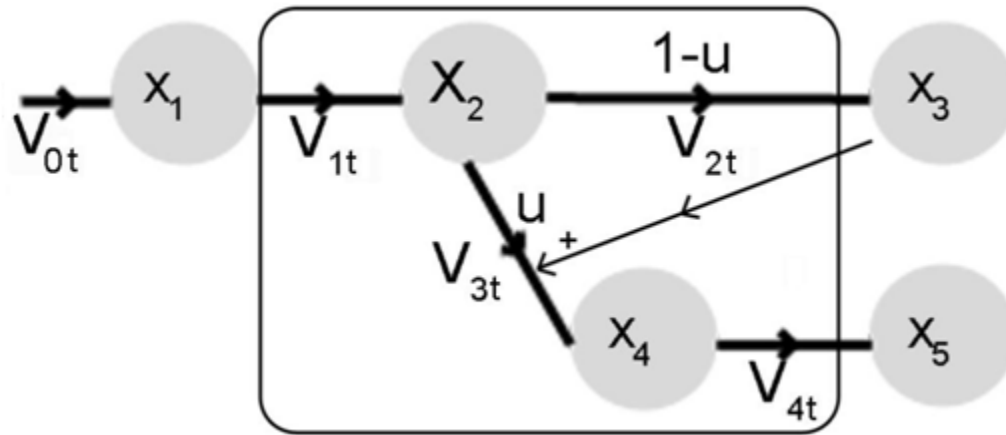
As one time step in simulation is a short period, and its length is not clear, one should illustrate

the length by realizing the duration of time that a pathway terminates in reality. For instance, should a pathway terminates after 30 seconds while its simulation after 12000 steps, it indicates that each time step has the length of $30/12000=0.0025$ s.

Prototype Network

The prototyped network is the one tested in [BMC] which is itself a modified version of [16]. There are however, some changes in the figure due to different considerations in this paper. A graphical representation of the network is shown in Figure 2:

Figure 6: Prototype network. The circles correspond to metabolites and the arrows to fluxes with the reaction rates indicated. The figure is a regulated version of the figure presented in [1].



Here the states $x_i, i = 1, \dots, 5$ are metabolite concentrations at the network nodes, $v_{it}, i = 1, \dots, 4$ are fluxes associated to the metabolic network branches in time t . In the figure, u represents a control function that allows redirecting the flux between the branches $x_2 \rightarrow x_3$ and $x_2 \rightarrow x_4$. Assuming that x_3 represents a precursor of the cellular objective (such as growth) and x_5 the desired product, if $u(t)$ is biased towards the branch of v_2 this yields the formation of x_3 but little or no production of x_5 . If $u(t)$ is biased towards the branch of v_3 the production of x_5 will be affected by the low concentration of x_3 (since there is a forward feedback). Thus, there is an optimal profile for $u(t)$ to maximize the concentration of x_5 at the final time t_{final} .

Optimization Problem

The optimization problem associated with prototyped network is finding the time in which the pathway should be switched from reaction (2) to (3) so that the yield of product (5) will be at its maximum. While in the literature time has been always considered as an integer value, here we assumed it as a contentious value. Moreover, there are other assumptions which were considered in this paper:

- 1- $V_{0t}=0$ for $t \in [0, t_{final}]$,
- 2- The probability for a molecule of each substrate to be placed in a cell of the lattice

after each time step is similar for all substrates.

- 3- Initial concentration of X_0 and the concentrations of all the enzymes related to each reaction are the same.
- 4- Each reaction needs just one enzyme.

Two different simulations were designed associated with the number of blank cells or neutralized molecules in the lattice, and each of them were run for 5 times. The lattice size was 100×100 for both simulations. The number of steps was supposed 100,000; however, this time should be regulated according to the problem in hand. The optimization algorithm

utilized in this paper was Particle Swarm Algorithm with 10 number of swarms and 10 number of generations. The fitness of the SPO algorithm was considered ($1/[X_5]$). Since the nature of the simulation is probabilistic, each simulation had to be run for five times.

The results are in agreement with the fact that the denser the biological systems, the less time we demand to achieve the maximum yield of desired product. The Switching times for the lattice where 50% and 20% of the molecules are neutralized are 3.1628×10^4 and 2.1088×10^4 respectively.

Figure 7: The result of optimization process on the 100×100 lattice model with 0% of neutralized molecule after 10 generations.

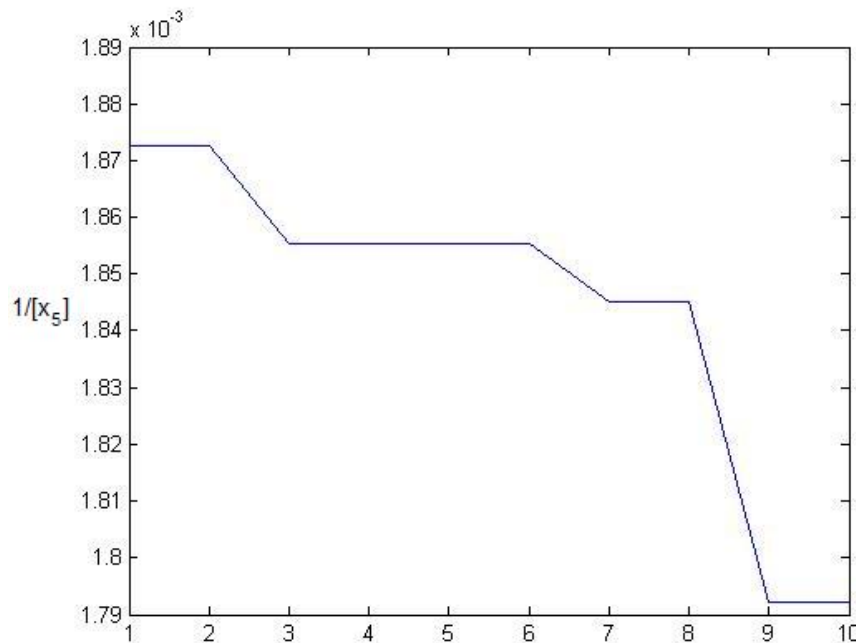


Figure 8: The result of optimization process on the 100*100 lattice model with 50% of neutralized molecules after 10 generation.

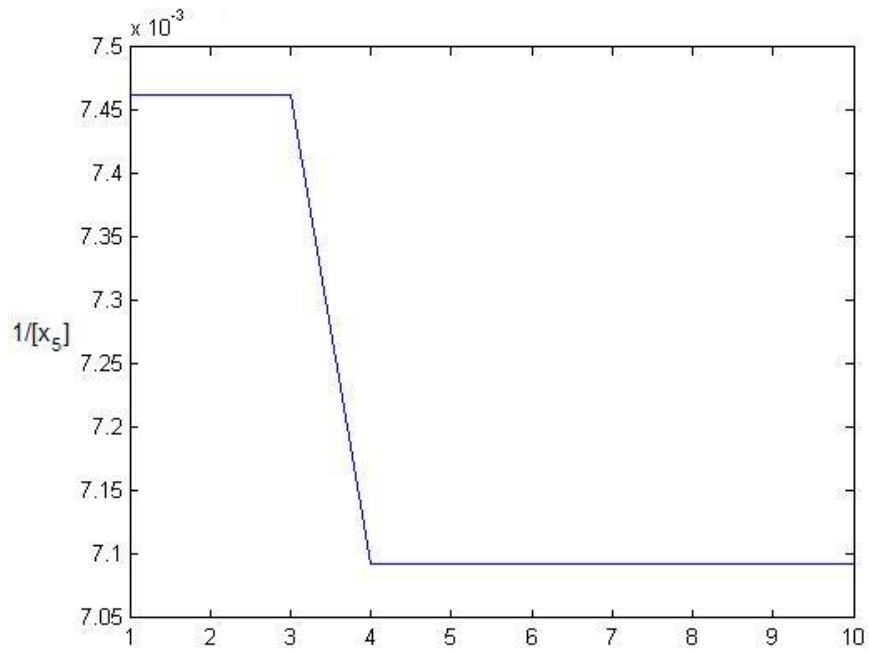


Figure 9: The Network dynamics where regulation time is equal to 2.1088e+004.

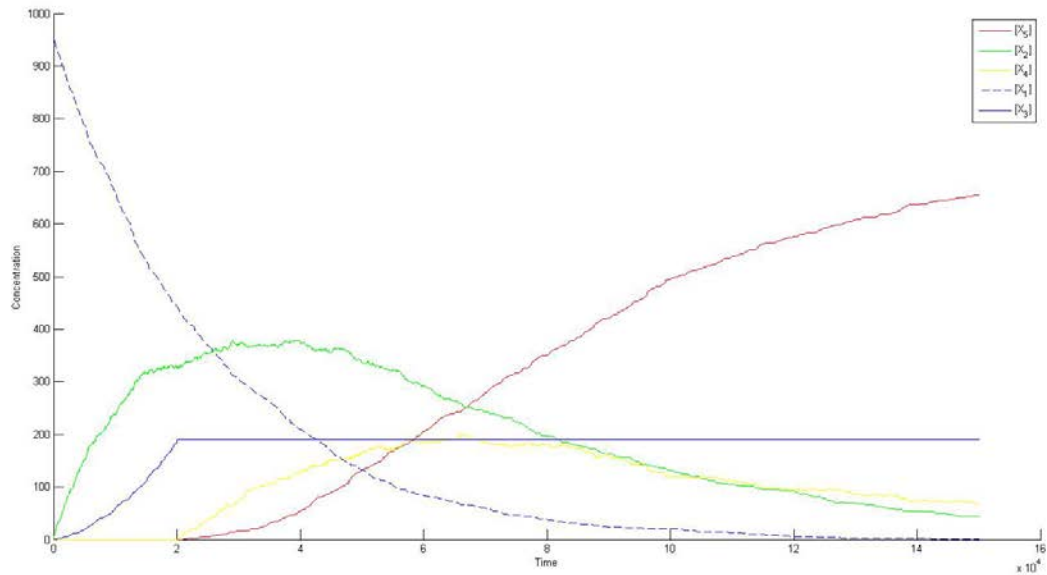
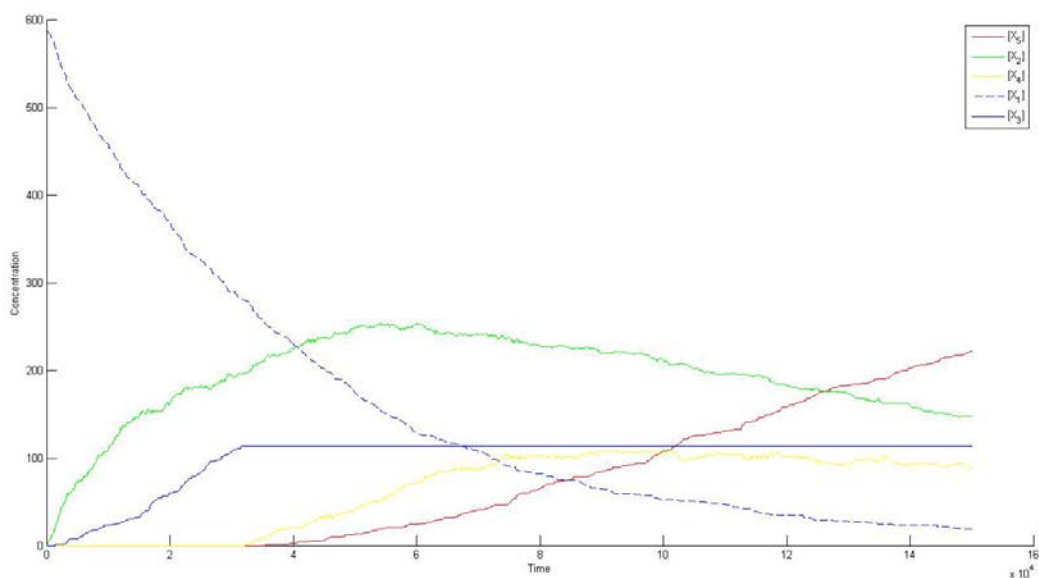


Figure 10: The Network dynamics where regulation time is equal to $3.1628e+004$.

Conclusion

2-D lattice simulation has been introduced as a tool to model the kinetics of metabolic networks in an efficient way. It has been shown that networks with low number of molecules can modeled, and optimized with heuristic algorithm (SPO).

It should be emphasized that the presented results are achieved based on the assumptions about the movement of molecules in each time step, the lattice size, and also the size of the molecules. In order to have more accurate achievements and better performance in special cases, those factors should be changed accordingly. These changes do not necessitate challenging efforts, and can be applied with ease.

The 2-D lattice simulation has also the capability of being modified according to more complex networks impacted by perturbations. Also, the equilibrium condition can also be simulated using this strategy all of which are to be presented in future works.

Reference

1. Nielsen J: **Metabolic engineering**. *Appl Microbiol Biotechnol* 2001, **55**(3):263-83.
2. Chu WB, Constantinides A: **Modeling, optimization, and computer control of the cephalosporin C fermentation process**. *Biotechnol Bioeng* 1988, **32**(3):277-88. [Chu, W B Constantinides, A United States Biotechnology and bioengineering *Biotechnol Bioeng*. 1988 Jul 20;32(3):277-88.]
3. Rocha I, Maia P, Evangelista P, Vilaca P, Soares S, Pinto JP, Nielsen J, Patil KR, Ferreira EC, Rocha M: **OptFlux: an open-source software platform for in silico metabolic engineering**. *BMC Syst Biol* **4**:45.
4. Edwards JS, Covert M, Palsson B: **Metabolic modelling of microbes: the flux-balance approach**. *Environ Microbiol* 2002, **4**(3):133-40.
5. Varma A, Palsson BO: **Stoichiometric flux balance models quantitatively predict growth and metabolic by-product secretion in wild-type Escherichia coli W3110**. *Appl Environ Microbiol* 1994, **60**(10):3724-31.
6. Schilling CH, Edwards JS, Letscher D, Palsson BO: **Combining pathway analysis with flux balance analysis for the comprehensive study of metabolic systems**. *Biotechnol Bioeng* 2000, **71**(4):286-306
7. Llaneras F, Pico J: **Stoichiometric modelling of cell metabolism**. *J Biosci Bioeng* 2008, **105**:1-11. [Llaneras, Francisco Pico, Jesus Research Support, NonU.S. Gov't Review Japan Journal of bioscience and bioengineering *J Biosci Bioeng*. 2008 Jan;105(1):1-11.]
8. Burgard AP, Pharkya P, Maranas CD: **Optknock: a bilevel programming framework for identifying gene knockout strategies for microbial strain optimization**. *Biotechnol Bioeng* 2003, **84**(6):647-57.
9. Rocha M, Maia P, Mendes R, Pinto JP, Ferreira EC, Nielsen J, Patil KR, Rocha I: **Natural computation meta-heuristics for**

- the in silico optimization of microbial strains.** *BMC Bioinformatics* 2008, **9**:499.
10. Koh K, Kim S, Mutapic A, Boyd S: **GGPLAB: A simple Matlab toolbox for Geometric Programming.** 2006.
 11. Boyd SP, Vandenberghe L: *Convex Optimization.* Cambridge University Press; 2004.
 12. Marin-Sanguino A, Voit EO, Gonzalez-Alcon C, Torres NV: **Optimization of biotechnological systems through geometric programming.** *Theor Biol Med Model* 2007, **4**:38.
 13. Zomorodi A. R, Suthers P.F, Ranganathanb S, Maranas. C D: **Mathematical optimization applications in metabolic networks,** *Metabolic Engineering* 14 (2012) 672–686
 14. Tomar N, Rajat K.De: **Comparing methods for metabolic network analysis and an application to metabolic engineering,** Volume 521, Issue 1, 25 May 2013, Pages 1–14
 15. Sorribas A, Hernandez-Bermejo B, Vilaprinyo E, Alves R: **Cooperativity and saturation in biochemical networks: a saturable formalism using Taylor series approximations.** *Biotechnol Bioeng* 2007, **97**(5):1259-77.

Antibacterial Study of Copper Oxide Nanoparticles synthesized by Microemulsion Technique

Harish Kumar*, Renu Rani

Department of Chemistry, Ch. Devi Lal University, Sirsa (Haryana) 125 055, India

* Corresponding Author: harimoudgil1@rediffmail.com

Abstract- Monoclinic CuO nanoparticles were synthesized by microemulsion technique. XRD, TEM and FT-IR techniques were used to characterize the nanoparticles. Antibacterial activity of CuO nanoparticles were tested against bacterial strains *S. epidermidis*, *S. aureus*, *E. faecalis*, and *M. luteus* using the agar diffusion method. Minimum Inhibitory Concentration (MIC) of these four bacterial strains *S. epidermidis*, *S. aureus*, *E. faecalis*, and *M. luteus* were found to be 0.1, 0.2, 0.6 and 0.8 µg/ml, respectively.

Keywords- Antibacterial activity, FTIR, TEM, Nanoparticles, XRD.

I. INTRODUCTION

With recent advances in nanotechnology, various types of metal and metal oxide nanoparticles with antimicrobial (microbiocidal or growth-inhibiting) activity have been synthesized [1-9]. Metal nanoparticles containing magnesium oxide [6], copper [7, 8], silver [1-5], iron [10], zinc oxide [11-13], and nickel oxide [14, 15] are exhibit antimicrobial properties.

The antimicrobial activity has been observed to vary as a function of surface area in contact with the microbe; therefore nanoparticles with large surface area ensure a broad range of reactions with the bacterial surface [16].

Compare to other methods, the reverse micelle method is one of the most promising wet chemistry synthesis approaches [17] of synthesis of metal nanoparticles. This method provides a favorable microenvironment for controlling the chemical reaction. As such the reaction rate can be easily controlled, and it is possible to obtain a narrow nanoparticle size distribution [18]. The size of the core of the reverse micelle can also be controlled by changing water to surfactant ratio [19]. Reverse micelle microemulsions are transparent, isotropic, and thermodynamically stable [20, 21].

In continuation of our earlier reported work on nickel, zinc, and silver nanoparticles [22-25], CuO nanoparticles were synthesized using microemulsion technique. Characterization of CuO nanoparticles were carried out using TEM, XRD, and

FTIR. Antibacterial activity of CuO nanoparticles were also investigated against four bacterial strains.

II. EXPERIMENTAL

A. Materials and method:

All chemicals used in experiment were of analytical grade. The stable reverse micelle microemulsion was prepared by mixing a non-ionic surfactant Triton X-100 [(C₁₄H₂₂O(C₂H₄O)_n] (Qualigen Chem. Pvt. Ltd.), Polyvinyl pyrrolidone (PVP) (K85-95) (Merk) and 1:9 ratio of cyclohexane (Qualigen Chem. Pvt. Ltd.) and triple distilled water (conductivity less than 1×10⁻⁶ S cm⁻¹) (W/S ratio 5). The microemulsion was mixed rapidly with continuous stirring for five minutes. CuSO₄.5H₂O (Qualigen Chem. Pvt. Ltd.) solution (0.5 M) was added drop by drop to microemulsion with continuous stirring. A sky blue colour mixture was obtained. PVP was used as a stabilizing agent. After half an hour of equilibration, 2.0 M hydrazine hydrate (Qualigen Chem. Pvt. Ltd.) solution was added drop by drop with continuous stirring at room temperature. The mixture gradually changed from sky blue to reddish brown without precipitation. The reverse micelles were broken by adding THF (Merk).

CuO nanoparticles were subsequently washed with ethanol and triple distilled water to remove residual PVP and surfactant molecules. After washing CuO nanoparticles were dried in oven at 100.0 °C for 48 hours.

B. Characterization techniques:

Structural and optical properties of the CuO nanoparticles were determined by using Transmission Electron Microscopy (TEM) (Hitachi: H-7500; Resolution: 2 Å), X-ray Diffraction (XRD) (Rikagu Mini-2 using CuKα1, λ = 0.15406 nm radiations), and Fourier Transform Infra- Red spectroscopy (FTIR) (Thermo-USA, FTIR-380) in the wavelength range of 400 - 4000 cm⁻¹.

C. Antibacterial Activity:

Bacterial strains were obtained from the Microbial Type Culture Collection (MTCC), Institute of Microbial Technology

(Chandigarh). The culture media; Beef extract and Agar-agar Type-1 (Hi-Media Pvt. Ltd., Bombay), and chemicals; Peptone, Sodium Chloride (Qualigen Chemicals Pvt. Ltd., Bombay) were used for the growth of bacteria.

D. Antibacterial Activity in Solid Method:

Antibacterial activity of CuO nanoparticles were tested against two gram negative bacterial strains of *Staphylococcus epidermidis* (MTCC 1809), *Staphylococcus aureus* (MTCC 3160), *Enterococcus faecalis* (MTCC 2729), and *Micrococcus luteus* (MTCC 1809) using the agar well diffusion assay method [26]. Approximately, 25.0 ml of molten and cooled nutrient agar media were poured in the sterilized petri dishes. The plates were left over night at room temperature to check for any contamination to appear. The bacterial test organism *S. epidermidis*, *S. aureus*, *E. faecalis*, and *M. luteus* were grown in nutrient broth for 24 hours at 37 °C. A 100 µl nutrient broth culture of each bacterial organism was used to prepare bacterial lawns. Agar wells were prepared with the help of a sterilized stainless steel cork borer. Agar wells were prepared with the help of a sterilized stainless steel cork borer. The wells in each plate were loaded with 100 µl of different concentrations i.e. 0.10, 0.20, 0.40, 0.60, 0.80, 1.0 and 1.2 µg/ml of copper oxide nanoparticles.

E. Antibacterial Activity in Liquid Method:

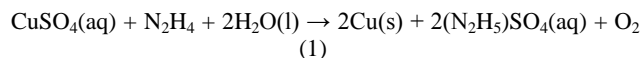
A 100 µl nutrient broth culture of each bacterial organism was added to 100 ml solution of different concentrations i.e. 0.10, 0.20, 0.40, 0.60, 0.80, 1.0 and 1.2 µg/ml of copper oxide nanoparticles and incubated at 37 °C for 24 hrs. To study the bacterial concentration, the optical density values were taken at 600 nm.

III. RESULTS AND DISCUSSION

A. Synthesis

Copper sulfate pentahydrate contains Cu (II) in a geometry best described as distorted octahedral. Here Cu (II) is bound to four water molecules in a square-planar geometry and two oxygen atoms of sulfate ions. Due to the solvating action, $\text{CuSO}_4 \cdot 5\text{H}_2\text{O}$ dissolves in water to produce the pale-blue colour $[\text{Cu}(\text{H}_2\text{O})_6]^{2+}$ ions, in which two of the water molecules are less tightly held than the others.

Addition of $\text{N}_2\text{H}_4 \cdot \text{H}_2\text{O}$ to the aqueous solutions of copper sulphate pentahydrate results to produce the reddish brown precipitates of Cu nanoparticles inside the reverse micelle core. PVP stabilize these Cu nanoparticles. The surfactant and PVP molecules adhere to the surface of nanoparticles which serve as a protective layer to prevent the further reaction. The Cu nanoparticles are oxidized into CuO nanoparticles in the presence of atmospheric O_2 gas at 100 °C. The reaction motile of formation CuO nanoparticles can be followed as:



There are two important factors that affect the exchange rate of reverse micelles in microemulsions; the dimer stability and the size of channels between the dimmers [27]. The dimer stability, which depends on the intermicellar attractive potential, determines the interdroplet transfer of reactants. On the other hand, the size of channels which depends on the rigidity of interfacial film in the microemulsion, determines the Ostwald ripening contribution [28].

B. Transmission Electron Microscopy and X-Ray Diffraction Analysis

Spherical shape of CuO nanoparticles were observed from TEM images (Figure 1a, and b). The average size of copper oxide nanoparticles was found to be 5.0 – 8.0 nm. It was indicate that surfactant molecules form a film over the surface of CuO nanoparticles which prevented the agglomeration of nanoparticles.

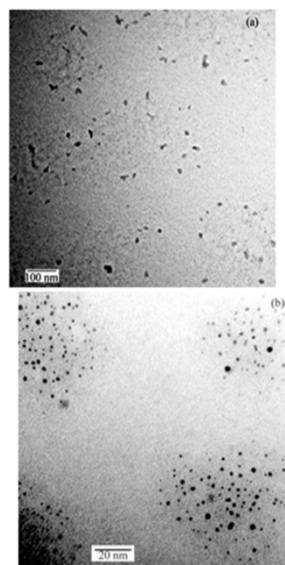


Fig. 1 (a, b) TEM images of CuO nanoparticles

XRD diffraction patterns of CuO nanoparticles are shown in Figure 2. The peaks are indexed as 33.72° (111), 35.86° (002), 39.46° (200), 46.68° (112), 49.06° (211), 53.85° (020), 58.92° (202), 62.06° (113), 66.72° (311), 67.98° (220) and 73.04° (311), respectively [29]. All diffraction peaks of sample correspond to the characteristic monoclinic structure of copper oxide with lattice constant of $a = 0.46837$ nm, $b = 0.34226$ nm and $c = 0.51288$ nm. Similar peaks of copper oxide nanoparticles were reported by A. K. Lagashetty and his coworkers [30] and Fei-Fei Cao et. al. [31]. Average particle size of copper oxide nanoparticles calculated using Scherrer equation [32] was 6.0 nm respectively.

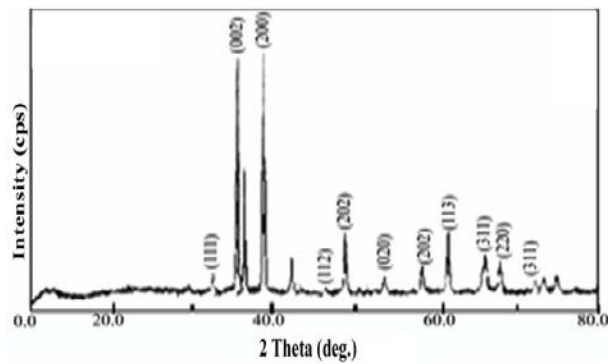


Fig. 2 X-ray diffraction patterns of CuO nanoparticles.

C. FTIR Spectroscopy

Figure 3 shows FTIR spectra of the nanoparticles. The peak at 3765.57 cm^{-1} may be due to O–H bond stretching assigned to H_2O present and at 1163.29 cm^{-1} may be due to O–H bond deformation assigned to the water adsorption. The peaks at 3266.33 and 3227.63 are attributed to the $\equiv\text{C-H}$ symmetrical and asymmetrical stretching modes, respectively. The peak at 2910.55 cm^{-1} due to $-\text{C-H}$ bond stretching assigned to alkyl group. The peak at 974.02 cm^{-1} is attributed due to C–H out of plane deformation and C–O stretching assigned due to the peaks at 1090.10 and 1051.35 cm^{-1} coordinate to the metal cations [33]. The peaks at 1599 and 1508.20 cm^{-1} are correspond to the Cu–O symmetrical and asymmetrical stretching and the peaks at 641.72 and 634.92 cm^{-1} are correspond to the Cu–O deformation vibration. The metal-oxygen frequencies observed for the respective metal oxides are in close agreement with literature values [34, 35].

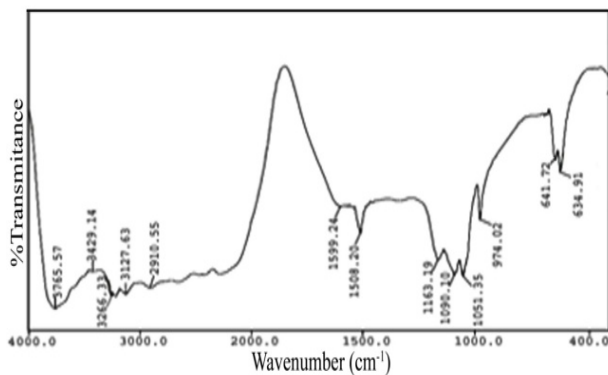


Fig. 3 FTIR spectra of CuO nanoparticles.

D. Antibacterial Activity

The effect of different concentration of CuO nanoparticles like B, C, D, E, F, G, and H as 0.1, 0.2, 0.4, 0.6, 0.8, 1.0, and 1.2 $\mu\text{g/ml}$, respectively shows in Figure 4 (a, b, c, and d).

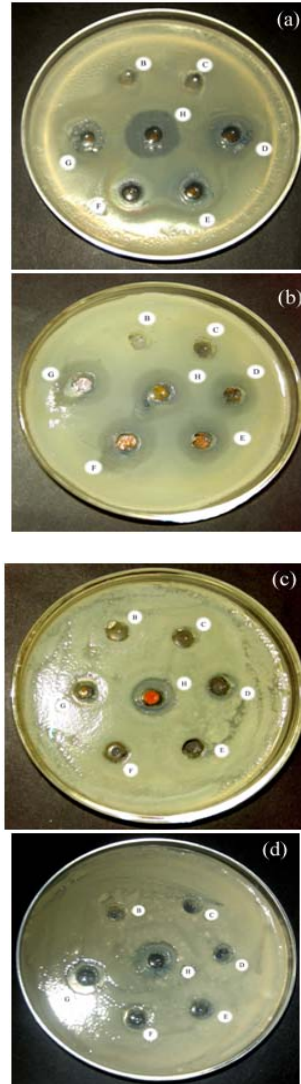


Fig. 4 Antibacterial activity of CuO nanoparticles at different concentrations against *S. epidermidis*, *S. aureus*, *E. faecalis*, and *M. luteus* as a, b, c, and d, respectively.

Figure 5 shows increase of the inhibition zone measurements with increase the concentration of CuO nanoparticles.

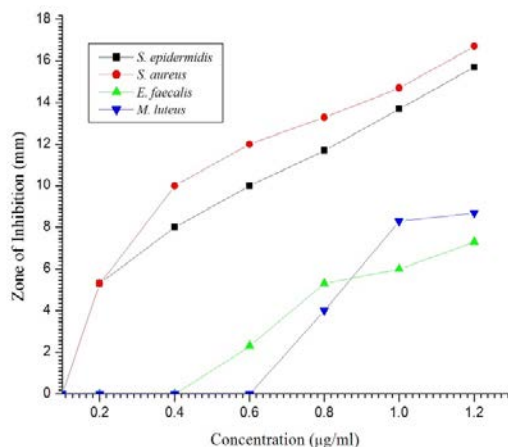


Fig. 5 Zone of inhibition (mm) shown by CuO nanoparticles at different concentration.

Minimum inhibition concentration (MIC) of copper oxide nanoparticles also determined on the basis of diameter of zone of inhibition as shown in Figure 6. Minimum inhibitory concentration of these four bacterial strains *S. epidermidis*, *S. aureus*, *E. faecalis*, and *M. luteus* were found to be 0.1, 0.2, 0.6 and 0.8 µg/ml, respectively.

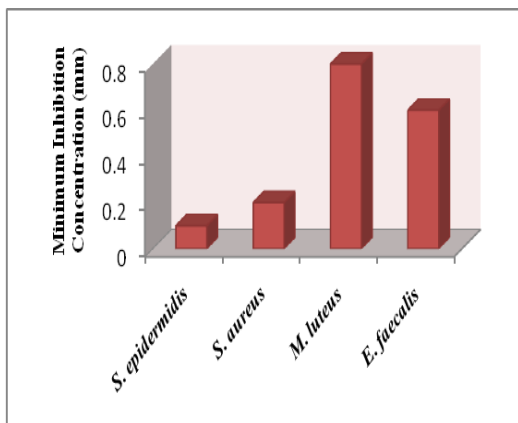


Fig. 6. Minimum Inhibitory Concentration (mm) of CuO nanoparticles against *S. epidermidis*, *S. aureus*, *E. faecalis*, and *M. luteus*.

IV. CONCLUSION

CuO nanoparticles were synthesized by microemulsion technique. TEM images indicate spherical shape of CuO nanoparticles of 5.0 – 8.0 nm in diameter. It is suggests that surfactant molecules form a film over the surface of CuO nanoparticles which prevented the agglomeration of nanoparticles. Monoclinic structure of CuO nanoparticles with average particles size of 6.0 nm in W/S ratio of 5.0 was observed

by XRD. FTIR spectra confirm the presence of metal oxygen bond. Antibacterial characterization has been demonstrated against four bacterial strains i.e. *S. epidermidis*, *S. aureus*, *E. faecalis*, and *M. luteus* using the agar well diffusion assay method. CuO nanoparticles adhered to the cell wall of bacteria and penetrated through the cell membrane. This resulted into inhibition of bacterial cell growth and multiplication, which finally leads to death of the cell.

REFERENCES

- [1] Alt V., Bechert T., Steinrcke P., Wagener M., Seidel P., Dingeldein E., Domann U., Schnettler R., 2004, *Biomater. Biomater.*, 25, pp. 4383-4389.
- [2] Furno F., Morley K. S., Wong B., Sharp B. L., Arnold P. L., Howdle S. M., Bayston R., Brown P. D., Winship P. D., H. Reid, 2004, *J. Antimicrob. Chem.*, 54, 1019.
- [3] Jeong S. H., Yeo S. Y., Yi S. C., 2005, *J. Mater. Sci.*, 40, 5407.
- [4] Chou W. L., Yu D. G., Yang M. C., 2005, *Poly. Adv. Technol.*, 16, 600.
- [5] Sambhy V., MacBride M. M., Peterson B. R. Sen, A., 2006, *J. Amer. Chem. Soc.*, 128, 9798.
- [6] Stoimenov P. K., Klinger R. L., Marchin G. L., Klabunde K., 2002, *Lang.*, 18, 6679.
- [7] Hsiao M. T., Chen S. F., Shieh D. B., Yeh C. S., 2006, *J. Phys. Chem. B*, 110, 205.
- [8] Theivasanthi T., Alagar M., 2011, *Ann. Bio. Res.*, 2, 368.
- [9] Morones J. R., Elechiguerra J. L., Camacho A., Holt K., Kouri J. B., Ramirez J. T., Yacaman M. J., 2006, *Nanotechnol.*, 16, 2346.
- [10] Lee C., Kim Y., Lee W. I., Nelson K. L., Yoon J., Sedlak D. L., 2008, *Environ. Sci. Technol.*, 42, 4927.
- [11] Zvekic D., Srdic V. V., Karaman M. A., Matavulj M. N., 2011, *Proc. App. Cer.*, 5, 41.
- [12] Rajendran R., BalaKumar C., Ahammed H. A. M., Jayakumar S., Vaideki K., Rajesh E. M., 2010, *Int. J. Engg. Sci. Technol.*, 2, 202.
- [13] Gondal M. A., Dastageer M. A., Khalil A., Hayat K., Yamani Z. H., 2011, *J. Nanopart. Res.*, 133, 423.
- [14] Wangsaprom K., Maensiri S., 2010, *Proceed in 3rd Int. Nanoelec. Conf.*, 1044.
- [15] Kavitha T., Yuvaraj H., 2011, *J. Mater. Chem.*, 21, 15686.
- [16] Holister P., Weener J. W., Vas C. R., Harper T., 2003, *Nanoparticles-Technology white papers 3*, Cientific Ltd., London.
- [17] Arriagada F. J., Osseo-Asare K., 1999, *J. Coll. Inter. Sci.*, 211, 210.
- [18] Bae D. S., Jungkim E., Bang J. H., Kim S.W., Han K. S., Kyulee J., Kim B. I., Adair J. H., 2005, *J. Met. Mater.-Int.*, 11, 291.
- [19] Ganguli A. K., Vaidya S., Ahmad T., 2008, *J. Bull. Mater. Sci.*, 3, 415.
- [20] Bae D. S., Park S. W., Han K. S., Adai J. H., 2001, *J. Met. Mater.-Int.*, 7, 399.
- [21] Pileni M. P., 1989, *Structure and reactivity in reverse micelles*, Elsevier, Amsterdam, New York.
- [22] Kumar H., Rani R., Salar R. K., 2010, *Proceed in Europ. Conf. Adv. Cont-Chem. Engg. Mech. Engg.* 88.

- [23] Kumar H., Rani R., Salar R. K., 2011, Res. J. Chem. Sci., 1, 1.
- [24] Kumar H., Rani R., 2013, Int. Let. Chem. Phys. Astro., 14, 26.
- [25] Kumar H., Rani R., 2013, Int. J. Engg. Inno. Technol., 3, 344.
- [26] Perez C, Paul M, Bazerque P., 1990, Act. Bio. Med. Exp., 15, 113.
- [27] Quintillán S., Tojo C., Blanco M. C., López-Quintela M. A., 2001, Lang., 17, 7251.
- [28] Dodoo-Arhin D., Leoni M., Scardi P., 2012, Mole. Crys. Liq. Crys., 555, 17.
- [29] Joint Committee on powder diffraction standards (2000) Diffraction data file, No. 05-0661.
- [30] Lagashetty A., Havanoor V., Basavaraja S., Balaji S. D., Venkatarman A., 2007, Sci. Tech. Adv. Mat., 8, 484.
- [31] Cao F.-F., Xin S., Guo Y. G., Wan L.-J., 2011, Phys. Chem. Chem. Phys., 13, 2014.
- [32] Cullity B. D., 1987, Elements of X-ray diffraction, second ed., Addison-Wesley, USA.
- [33] Bernson A., Lindgren J., Huang W., Frech R., 1995, Pol., 36, 4471.
- [34] Rao C. N. R., 1963, Chemical Applications of Infrared spectroscopy, Academic Press, New York and London.
- [35] Markova-Deneva I., 2010, J. Univ. Chem. Tech. Metal., 45, 351.

Dr Harish Kumar is Assistant Professor and Incharge, Department of Chemistry, Ch. Devi Lal University, Sirsa (Haryana) 125 055, India since 2004. Before that he lectured in Israna Engg. College, Panipat (Haryana). He has published more than 50 research papers and four books on Physical Chemistry. He is an editorial board member of various scientific journals. His main sphere of interest is in material science and electrochemistry. He may be contacted at harimoudgill@rediffmail.com

Renu Rani born in Meerut, India has received her M. Sc. Chemistry and Ph.D. degree from Ch. Devi Lal University, Sirsa in year 2008 and 2013, respectively. She is currently working as Research Associate in the area of 'Electrochemical Biosensor for the Detection of Biological Weapon' in Ch. Devi Lal University, Sirsa, India. She presented her research papers in ten International and National conferences. She has published seven papers in reputed international and national journals. Her current areas of interest are Biosensors, Nanoscience and nanotechnology and role of nanotechnology in combating cancer disease.

Authors Index

Abas, K. A.	184	Gaálová, J.	113	Mourão, A. P.	51
Abe, T.	55	Ganesh, S.	179	Naeem, M. A.	125
Accary, C.	167	Ganin, A. A.	40, 92	Nagahashi, H.	34, 55
Ahmed, Am. M.	82	Garcia, N. A.	47	Narkbuakaew, W.	34
Ahmed, Ar. M.	184	Gonçalves Jr., R. G.	51	Niyazova, R. Y.	102, 144
Al-Fariss, T. F.	125	Gonzalez, V.	47	Nowak, W.	67
Al-Khatib, T. R.	184	Hachol, A.	67	Ortuño, F.	61
Alonso, T. C.	51	Hajghassem, H.	138	Oudadesse, H.	130
Amin, S. M.	184	Hamad, D. A.	184	Ovseenko, L. V.	108
Aoki, K.	34	Hamdi, M. A.	160	Pallavicini, P.	71
Arafat, Y.	125	Hamze, M.	167	Paspalakis, E.	30
Atambayeva, S. A.	144	Harabi, M. L.	160	Pesavento, M.	71
Atupelage, C.	55	Hashiguchi, A.	55	Pintana, P.	155
Avilov, S. V.	79	Hermiz, H. N.	184	Ponomarev, A.	27
Aziz, H. A.	150	Hleihel, W.	167	Pyrkova, A. Y.	102, 144
Bahrami, F.	174	Hraoui-Bloquet, S.	167	Rani, R.	197
Barbier Jr., J.	113	Ivashchenko, A. T.	102, 144	Rebai, T.	130
Berillo, O. A.	102, 144	Jagannathan, L.	179	Rojas, I.	61
Bityutskaya, L. A.	40, 79, 92	Janahmadi, M.	174	Roujeinikova, A.	76
Bityutskaya, L. A.	121	Jebahi, S.	130	Ruiz-García, G.	61
Bobenko, N.	27	Jirátová, K.	113	Sadek, R.	167
Bormontov, E. N.	40, 79, 92	Keskes, H.	130	Sakamoto, M.	55
Bormontov, E. N.	121	Khaji, E.	188	Shamsi, A.	138
Bouloufa, A.	134	Khelif, M.	97	Shariff, A. M.	150
Boviatsis, J.	30	Kimura, F.	55	Shevchonok, A. A.	108
Bradai, C.	97	Klempa, J.	113	Šolcová, O.	113
Cennamo, N.	71	Kosionis, S. G.	30	Tassoult, H.	134
Chico, F.	47	Krutko, N. P.	108	Thirugnanasambandam, S.	179
D'Agostino, G.	71	Kubota, Y.	34	Tippayawong, N.	155
Delaram, S.	138	Kumar, H.	197	Titova, L. V.	108
Desfontis, J.-C.	167	Lorias, D.	47, 87	Tuchin, A. V.	40, 79, 121
Donà, A.	71	Luchenok, A. R.	108	Ulyanova, T. M.	108
Egorushkin, V.	27	Magnoux, P.	113	Valenzuela, O.	61
Eissa, H. M.	82	Masmoudi, N.	97	Veezhinathan, M.	179
El Feki, H.	130	Maupin, I.	113	Villalobos, J.	87
Elfeki, A.	130	Melnikova, N.	27	Vitiaz, P. A.	108
Ellouz, Z.	130	Mijoin, J.	113	Yamaguchi, M.	55
Elsehely, E. A.	82	Minor, A.	87	Yew, K. H.	150
Esfandiari, M.	138	Misiuk-Hojlo, M.	67	Zeni, L.	71
Estrella, F.	61	Mohagheghi-Nejad, M. R.	174	Zhukalin, D. A.	40, 79
Ettabaa, K. S.	160	Molski, M.	23		
Fajloun, Z.	167	Moncivalles, E.	87		